NBS SPECIAL PUBLICATION 716

U.S. DEPARTMENT OF COMMERCE / National Bureau of Standards

PROCEEDINGS OF THE SEVENTEENTH INTERNATIONAL SYMPOSIUM ON FREE RADICALS

Snow Mountain Ranch

Colorado, USA

August 18-23, 1985

The National Bureau of Standards[1] was established by an act of Congress on March 3, 1901. The Bureau's overall goal is to strengthen and advance the nation's science and technology and facilitate their effective application for public benefit. To this end, the Bureau conducts research and provides: (1) a basis for the nation's physical measurement system, (2) scientific and technological services for industry and government, (3) a technical basis for equity in trade, and (4) technical services to promote public safety. The Bureau's technical work is performed by the National Measurement Laboratory, the National Engineering Laboratory, the Institute for Computer Sciences and Technology, and the Institute for Materials Science and Engineering.

The National Measurement Laboratory

Provides the national system of physical and chemical measurement; coordinates the system with measurement systems of other nations and furnishes essential services leading to accurate and uniform physical and chemical measurement throughout the Nation's scientific community, industry, and commerce; provides advisory and research services to other Government agencies; conducts physical and chemical research; develops, produces, and distributes Standard Reference Materials; and provides calibration services. The Laboratory consists of the following centers:

- Basic Standards[2]
- Radiation Research
- Chemical Physics
- Analytical Chemistry

The National Engineering Laboratory

Provides technology and technical services to the public and private sectors to address national needs and to solve national problems; conducts research in engineering and applied science in support of these efforts; builds and maintains competence in the necessary disciplines required to carry out this research and technical service; develops engineering data and measurement capabilities; provides engineering measurement traceability services; develops test methods and proposes engineering standards and code changes; develops and proposes new engineering practices; and develops and improves mechanisms to transfer results of its research to the ultimate user. The Laboratory consists of the following centers:

- Applied Mathematics
- Electronics and Electrical Engineering[2]
- Manufacturing Engineering
- Building Technology
- Fire Research
- Chemical Engineering[2]

The Institute for Computer Sciences and Technology

Conducts research and provides scientific and technical services to aid Federal agencies in the selection, acquisition, application, and use of computer technology to improve effectiveness and economy in Government operations in accordance with Public Law 89-306 (40 U.S.C. 759), relevant Executive Orders, and other directives; carries out this mission by managing the Federal Information Processing Standards Program, developing Federal ADP standards guidelines, and managing Federal participation in ADP voluntary standardization activities; provides scientific and technological advisory services and assistance to Federal agencies; and provides the technical foundation for computer-related policies of the Federal Government. The Institute consists of the following centers:

- Programming Science and Technology
- Computer Systems Engineering

The Institute for Materials Science and Engineering

Conducts research and provides measurements, data, standards, reference materials, quantitative understanding and other technical information fundamental to the processing, structure, properties and performance of materials; addresses the scientific basis for new advanced materials technologies; plans research around cross-country scientific themes such as nondestructive evaluation and phase diagram development; oversees Bureau-wide technical programs in nuclear reactor radiation research and nondestructive evaluation; and broadly disseminates generic technical information resulting from its programs. The Institute consists of the following Divisions:

- Inorganic Materials
- Fracture and Deformation[3]
- Polymers
- Metallurgy
- Reactor Radiation

[1] Headquarters and Laboratories at Gaithersburg, MD, unless otherwise noted; mailing address Gaithersburg, MD 20899

[2] Some divisions within the center are located at Boulder, CO 80303.

[3] Located at Boulder, CO, with some elements at Gaithersburg, MD.

Proceedings of the Seventeenth International Symposium on FREE RADICALS

Snow Mountain Ranch
Granby, Colorado 80446 (U.S.A.)
August 18-23, 1985

Edited by

Kenneth M. Evenson
Time and Frequency Division
National Bureau of Standards
Boulder, Colorado 80303

Sponsored by

National Bureau of Standards
Laser Analytics Division of Spectra Physics, Inc.†
National Aeronautics and Space Administration
Smithsonian Astrophysical Observatory
Lambda Physik
Oriel Optics

†sponsorship included partial funding for the printing of this publication

U.S. DEPARTMENT OF COMMERCE, Malcolm Baldrige, Secretary

NATIONAL BUREAU OF STANDARDS, Ernest Ambler, Director

Issued April 1986

Library of Congress Catalog Card Number: 86-600529

National Bureau of Standards Special Publication 716
Natl. Bur. Stand. (U.S.), Spec. Publ. 716, 788 pages (Apr. 1986)
CODEN: XNBSAV

U.S. Government Printing Office
Washington: 1986

For sale by the Superintendent of Documents, U.S. Government Printing Office, Washington, DC 20402

DEDICATION

I would like to dedicate my efforts in arranging this 17th International Free Radicals Meeting to the memory of Dr. Herb Broida. Herb was one of the founding fathers of this meeting, head of the free radical program at NBS, and a continuing inspiration to his colleagues and students. He also was a Colorado native who climbed many of Colorado's highest peaks. Thus, it is especially appropriate to make this dedication at the first U. S. meeting since his death in 1978. I am especially indebted to Herb for encouraging me to come to the National Bureau of Standards in Boulder.

PREFACE

The 17th International Conference on Free Radicals has been an exciting conference for me personally, and I am most pleased to have been a co-chairman of this conference.

We strived to make this a "science first" conference by isolating ourselves at the Snow Mountain Ranch; I believe that we achieved this goal.

We also attempted to facilitate personal discussions by presenting most of the papers as posters with two-minute introductions; this seemed to be a very successful innovation. We had an excellent group of invited speakers who provided the core of the meeting. I would like to thank them personally.

Finally, I would like to acknowledge the financial help that we received from the National Atmospheric and Space Administration, the National Bureau of Standards, the Smithsonian Astrophysical Observatory, the Laser Analytics Division of Spectra Physics, Oriel Optics, and Lambda Physik.

I would like to acknowledge the local organizing committee: Dr. H. E. Radford and Dr. R. F. Curl, my co-chairmen; Yvonne Dunn, Conference Coordinator; and especially our wives, for the tremendous job they all performed in arranging the conference.

Finally, I especially acknowledge the outstanding performance of Patsy Tomingas of the Time and Frequency Division in gathering these papers and assembling them for this publication.

Ken Evenson

Ken Evenson

PROCEEDINGS OF THE

SEVENTEENTH INTERNATIONAL SYMPOSIUM ON FREE RADICALS

Granby, Colorado U. S. A.
August 18-23, 1985

ORGANIZING COMMITTEE

K.M. Evenson, National Bureau of Standards, Boulder, USA, Co-Chairman
H.E. Radford, Smithsonian Astrophysical Observatory, Cambridge, USA, Co-Chairman
R.F. Curl, Rice University, Houston, USA, Co-Chairman
A.M. Bass, National Bureau of Standards, Washington, USA
B.G. Ellison, University of Colorado, Boulder, USA
C.J. Howard, National Oceanic and Atmospheric Administration, Boulder, USA
D.A. Jennings, National Bureau of Standards, Boulder, USA
M. Mizushima, University of Colorado, Boulder, USA

INTERNATIONAL COMMITTEE

S. Leach, CNRS, Orsay, France (Chairman)
W.E. Jones, Dalhousie U., Halifax, Canada (Secretary)
A.M. Bass, NBS, Washington, USA
A. Carrington, Oxford U., Oxford, UK
S. Claesson, U. Uppsala, Sweden
R. Colin, Universite Libre de Bruxellex, Belgium
P.A. Giguere, U. Laval, Montreal, Canada
G. Herzberg, NRC, Ottawa, Canada
E.K.C. Lee, U. California, Irvine, USA
Y. Morino, Sogami Res. Cent., Kangawa, Japan
M. Peyron, Inst. Nat. Sc. Appl., Villeubanne, France
G. Porter, Roual Inst. London, UK
D.A. Ramsay, NRCC, Ottawa, Canada
F.S. Rowland, U. California, Irvine, USA
G. Semerano, U. Bologna, Italy
V.L. Talrose, Acad. Sciences, Moscow, USSR
I. Tanaka, Tokyo Inst. Tech., Tokyo, Japan
B.A. Thrush, U. Cambridge, UK

CONTENTS

Proceedings of the
Seventeenth International Symposium on Free Radicals

Kenneth M. Evenson, Editor

Time and Frequency Division
National Bureau of Standards
Boulder, Colorado 80303

This publication contains papers presented at the Seventeenth International Symposium on Free Radicals, held at Snow Mountain Ranch in Granby, Colorado, on August 18-23, 1985.

The Symposium was attended by 147 people, representing industry, government, and academia, from 18 countries. A total of 67 papers appear in written form in this document.

Key words: free radicals; 17th international symposium on free radicals

The Quenching of $PH(A^3\Pi_i)$ by H_2 and D_2

J. E. Allen, Jr. and R. J. Cody
Astrochemistry Branch, NASA/Goddard Space Flight Center, Greenbelt, MD, U.S.A.

The Jovian and Saturnian systems are examples of reducing planetary atmospheres in which the major constituent is molecular hydrogen. Phosphine (PH_3) has been identified as a minor but important constituent in these atmospheres. Since photolysis of PH_3 can lead to the production of the phosphinidene radical (PH), proper modeling of these systems requires that the reaction and quenching rates of PH, particularly with H_2, be known. Aside from their direct application to astrophysical and aeronomical problems, these rates contribute to a data base for the development of reaction and quenching rate theories which in turn are used to estimate experimentally undetermined rates. To provide such information, a study of the quenching of $PH(A^3\Pi_i)$ by H_2 and D_2 has been undertaken.

The experimental arrangement used for the present experiments is illustrated in Figure 1. Using a 3/8" diameter circular aperature, the central portion of the beam was selected from the output of an excimer laser operating on argon fluoride (λ = 193 nm, pulse energy = 200 mJ, pulse width = 10 ns). The unfocused beam was then directed through a brass photolysis cell. For some measurements metal screens were inserted in the beam path to vary the laser intensity, and the laser energy was monitored by a reflection from the front window of the cell. The resulting ($A^3\Pi_i \rightarrow X^3\Sigma^-$) fluorescence from the PH radical was viewed at right angles to the beam path either by a photomultiplier tube/interference filter arrangement or a 0.32 m monochromator. Two different methods were used to monitor the emission. In the first case the fluorescence was scanned by the monochromator with a resolution of 0.3 nm and

detected photoelectrically. The spectra were recorded either by a picoammeter/strip chart recorder combination or a signal processing system (PAR 4400). The 4400 system was operated in the static gate mode with a gate width of 700 ns and was triggered simultaneously with the excimer laser by a pulsed delay generator at a repetition rate of 40 Hz. In the second method the total fluorescence was monitored using the interference filter which has a peak transmission at 340 nm and a bandwidth of 12 nm. The signal was again processed with the 4400 system this time operating in scanning gate mode with a gate width of 5 ns. Fluorescent decays were measured from which lifetime information could be extracted by using the exponential fitting routine of the 4400. For quenching experiments pure PH_3 at a pressure of 3 mtorr or mixtures of 3 mtorr PH_3 in varying pressures of H_2 and D_2 - up to 1 torr - were flowed through the cell and fluorescent decays measured for various gas pressures.

The photolysis of ammonia, the analog of phosphine, at 193 nm has been the subject of numerous studies[2] and a reasonable understanding of this system is beginning to emerge. Less attention has been devoted to phosphine, although photolysis of PH_3 at 193 nm has previously been shown to produce PH_2 by a one-photon process and PH(A) by a two-photon process.[3] To verify the effect of laser intensity on PH(A) production, measurements were made of PH(A) fluorescence at varying laser powers for a PH_3 pressure of 3 mtorr and an initial laser power of ~15 MW/cm^2. A log-log plot of fluorescent intensity versus laser power appears as Figure 2. For relative laser powers less than 0.4 the graph is linear with a slope of 1.7 which is indicative of a two-photon process. A slope less than 2.0 and the deviation of the curve from linearity at higher laser powers suggest that saturation effects and/or competing processes may be important.

Like NH only the v=0 vibrational level of the $A^3\Pi_i$ state is substantially populated in PH; however, unlike NH the A state of PH is split into three spin-orbit subcomponents: $^3\Pi_0$, $^3\Pi_1$, and $^3\Pi_2$. Spectral scans showing the three components clearly resolved are illustrated in Figure 3 for 3 mtorr of PH_3 and mixtures of PH_3 with 600 mtorr of He, H_2 and D_2. Close examination of the spectra indicates effective rotational relaxation within the various components which is manifested as a broadening of the $^3\Pi_0$ component and the appearance of a shoulder on the long wavelength side of the $^3\Pi_2$ component. That rotational relaxation occurs is consistent with observations of a similar effect in NH.[2]

Fluorescent decays obtained with the filter represent a composite of the three subcomponents and exhibited nonexponential behavior which can be ascribed to variations in lifetimes of the radiating levels. At a PH_3 pressure of 3 mtorr the composite radiative lifetime of the PH(A) state was determined to be (320±50) ns which is in agreement with the earlier laser study[3] but slightly shorter than that measured by phase shift techniques.[4] Preliminary composite quenching rates for the PH(A) state were determined by plotting the reciprocal of the lifetime versus quencher pressure. Such a plot for quenching by the parent molecule is illustrated in Figure 4 and yields a rate of 4.2×10^{-10} cc/molec·s which is faster than the previously reported value.[3] Similar plots for quenching by H_2 and D_2 yielded rates of $\sim 2.2 \times 10^{-11}$ cc/molec·s and $\sim 8.2 \times 10^{-12}$ cc/molec·s for H_2 and D_2, respectively.

Very crude estimates of quenching efficiency for the various spin-orbit components were made by comparing peak heights and areas of the spectral scans at different quencher pressures. Even though only qualitative comparisons can be made, there appears to be slight variations which are summarized below.

H_2: $k_Q(\Pi_1) > k_Q(\Pi_0) > k_Q(\Pi_2)$

D_2: $k_Q(\Pi_1) \sim k_Q(\Pi_0) > k_Q(\Pi_2)$

An intercomparison of H_2 and D_2 quenching efficiencies for the same component indicates qualitatively that H_2 is a stronger quencher of the Π_2 components, while D_2 is more effective in quenching the Π_1 and Π_0 components.

References

(1) D. F. Strobel, Int. Rev. Phys. Chem. 3, 145 (1983).
(2) A. Hofzumahaus and F. Stuhl, J. Chem. Phys. 82, 3152 (1985) and references therein.
(3) C. L. Sam and J. T. Yardley, J. Chem. Phys. 69 (1978).
(4) E. Fink and K. H. Welge, Z. Naturforsch Teil A 19, 1193 (1964).

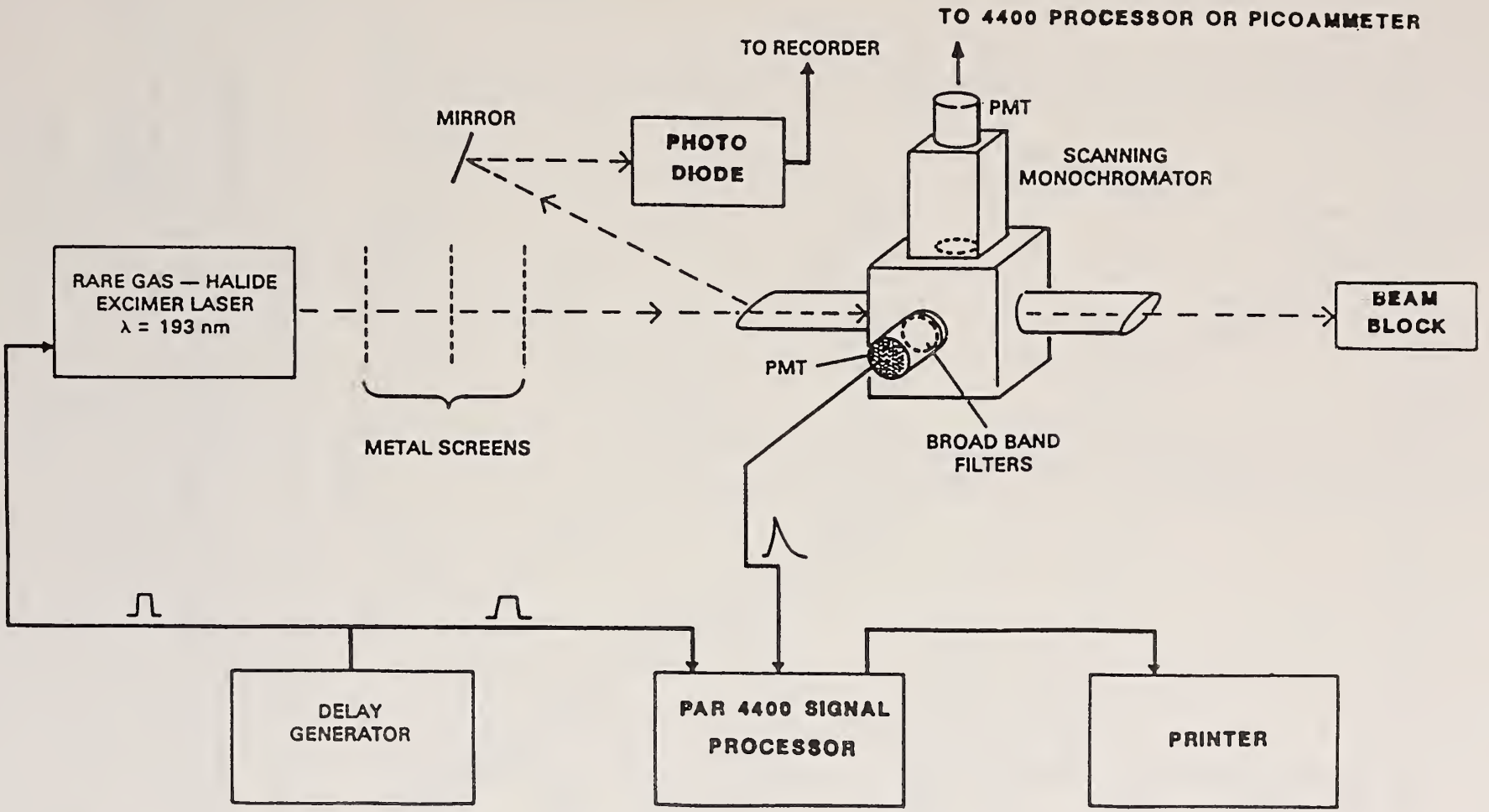

FIG. 1. EXPERIMENTAL APPARATUS

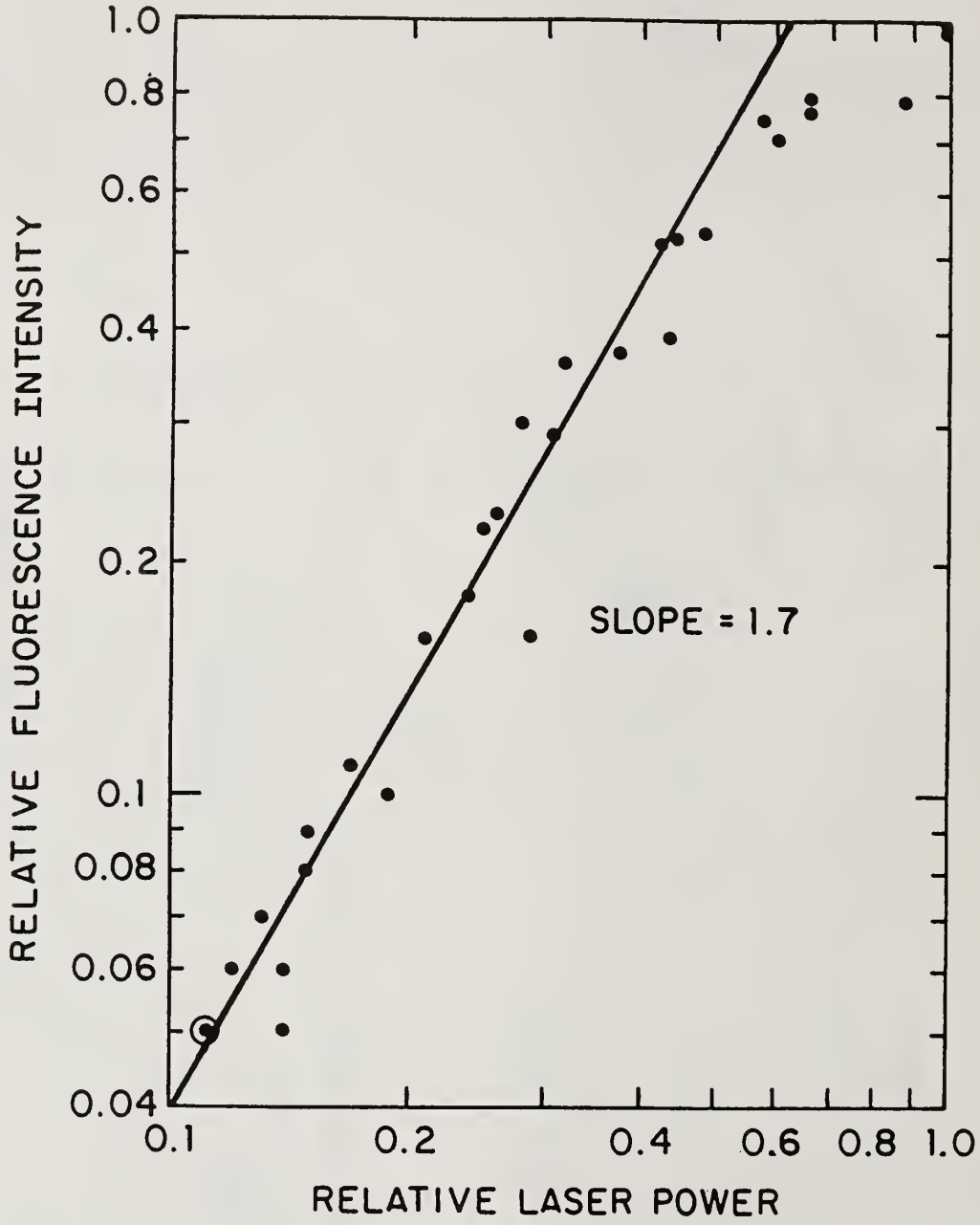

FIG. 2. POWER CURVE FOR THE PH (A→X) FLUORESCENCE.

THE LOGARITHM OF THE RELATIVE FLUORESCENT INTENSITY IS PLOTTED VERSUS THE LOGARITHM OF THE RELATIVE LASER POWER. THE GRAPH IS LINEAR FOR RELATIVE LASER POWER <0.4 AND YIELDS A SLOPE OF 1.7. AT HIGHER LASER POWERS SATURATION EFFECTS AND/OR COMPETING PROCESSES MANIFEST THEMSELVES AS A REDUCTION OF PH (A) FLUORESCENCE, WHICH RESULTS IN A DEVIATION OF THE CURVE FROM LINEARITY. METAL SCREENS WERE INSERTED IN THE PATH OF THE LASER BEAM TO VARY THE POWER.

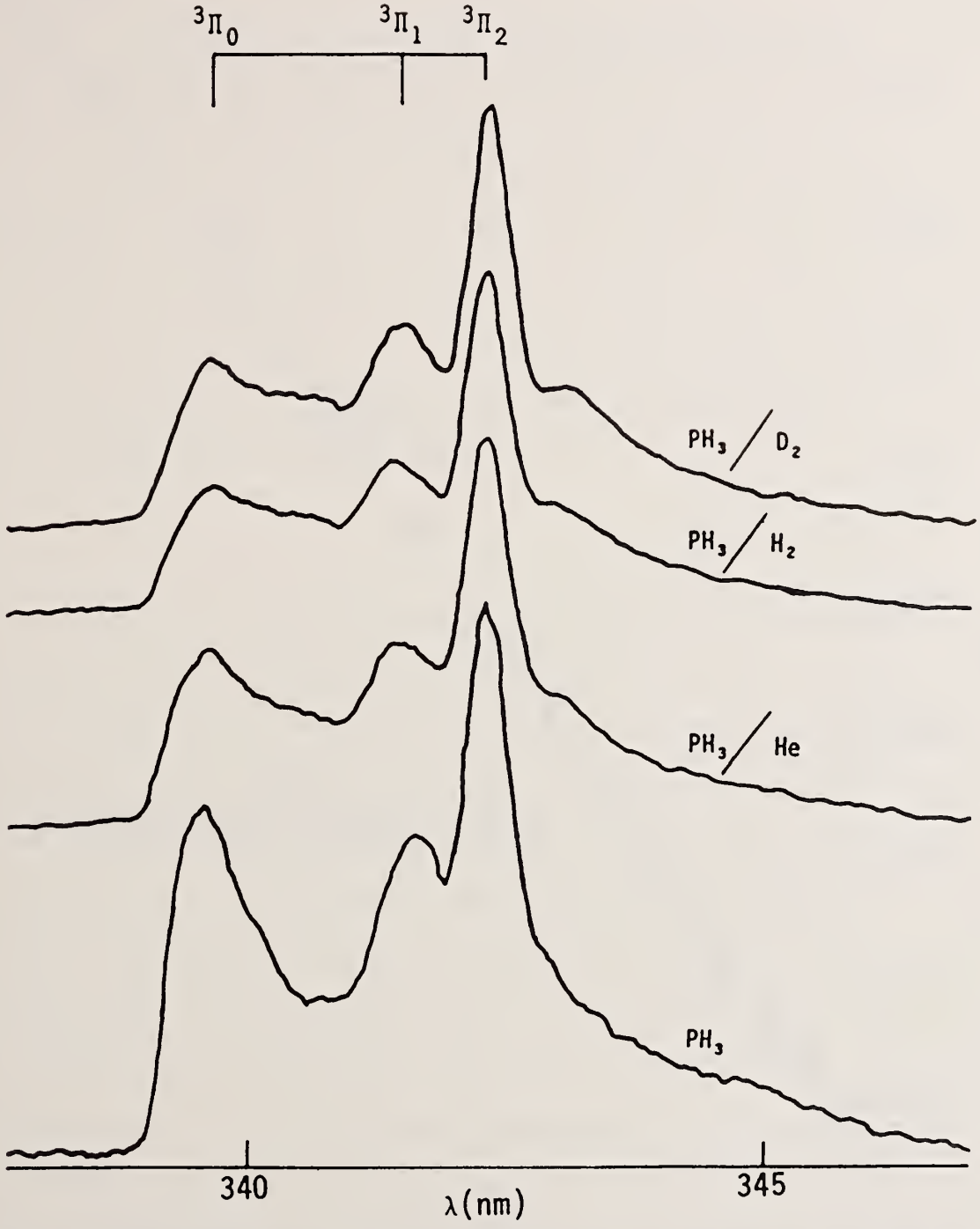

FIG. 3. SPECTRAL SCANS OF THE MULTIPLET STRUCTURE OF THE PH (A-X) FLUORESCENCE WITH DIFFERENT QUENCHING GASES. THE RESOLUTION OF THE MONOCHROMATOR WAS 0.3 NM. THE FLUORESCENT SIGNAL WAS MEASURED BY THE PICOAMMETER AND DISPLAYED ON A STRIP CHART RECORDER.

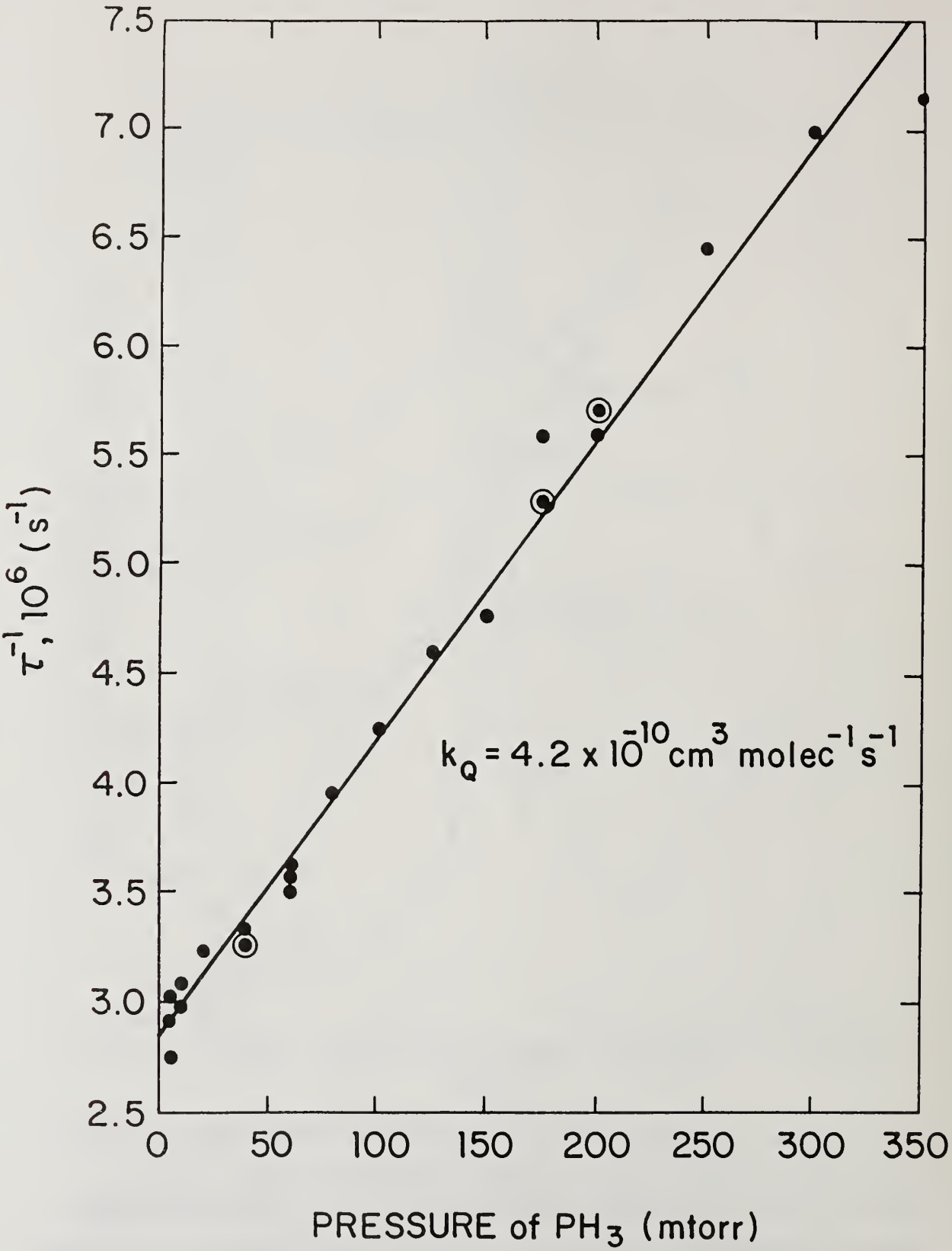

FIG. 4. QUENCHING PLOT OF THE INVERSE OF THE PH (A→X) FLUORESCENT LIFETIME, τ^{-1}, VERSUS PRESSURE OF PH_3. METAL SCREENS WERE INSERTED IN THE PATH OF THE ArF LASER BEAM TO MAINTAIN THE POWER IN THE LINEAR REGION OF THE POWER CURVE.

DIFFERENCE FREQUENCY LASER SPECTROSCOPY OF POLYATOMIC IONS

T. Amano

Herzberg Institute of Astrophysics, National Research Council,
Ottawa, Ontario, Canada K1A 0R6.

Since the first detection of the infrared spectrum of H_3^+ by Oka(**1**), the progress of the infrared spectroscopy of molecular ions has been truly remarkable. In 1983, a series of papers were published by Saykally's group at Berkley and Oka's group at Chicago on HCO^+(**2**), HN_2^+(**3**), H_3O^+(**4**), and NH_4^+(**5**,**6**). These ions were detected by using the Gudeman and Saykally's velocity modulation technique. The significance of this technique lies in two points. The first is that it can pick out the signals of ions from vast majority of much stronger neutral species. The second point is that it is much more sensitive method than the source frequency modulation method which was used in earlier experiments (**1**,**7**,**8**). On the other hand, we use a hollow cathode discharge cell in almost all recent experiments, and a great improvement of the sensitivity has been achieved by combining a multi-pass absorption cell(**9**). A hollow cathode cell cannot be used with the velocity modulation method. However, an examination of the magnetic field effect provides a useful tool to discriminate the lines due to ions from those of neutral species (**9**,**10**). The minimum absorption we can detect with our system is about 0.02 %. In this report, I will present the summaries of our recent results on $HCNH^+$, $HOCO^+$, and HON_2^+.

$HCNH^+$

$HCNH^+$ is one of the key ions of astrophysical importance, and the first spectroscopic detection of this ion was made by the Chicago group(**11**). They observed and analyzed the ν_1 and ν_2 bands. Later we detected the ν_1 band of $DCNH^+$(**12**). The further measurements of a few other iosotopic species, $HCND^+$ and $H^{13}CNH^+$, and the hot bands from the bending vibrational excited states, have been done since then. The measurements of the isotopic species enabled us to determine the substitution molecular structure of the ion. $HCNH^+$ was generated by a hollow cathode discharge through a gas mixture of HCN or DCN(about 20 mTorr) and H_2(about 300 mTorr). All the measurements were done with water cooled discharge. Figure 1 shows a section of the spectrum. The strong line at the middle is the $R(6)$ transition of the ν_1 fundamental band. There are two pairs of lines, and they are easily assigned as the hot band lines, since the splittings are clearly the ℓ-type doubling splittings. The figure also shows a weak feature which is the $R(8)$ line of the ^{13}C species in natural abundance. The assignment was confirmed by observing the lines with a 20 % enriched ^{13}C sample. The analyses are straightforward, and the finer details of the results will be found in our forthcoming paper(**13**).

$HOCO^+$

In 1981, Thaddeus, Guelin, and Linke suggested that the three consecutive millimeter-wave lines detected towards SgrB2 would likely be either due to $HOCO^+$ or HOCN(**14**). Several attempts were made in several microwave laboratories to observe the microwave or millimeter-wave lines of $HOCO^+$ or HOCN for conclusive confirmation of their tentative assignment. About a year ago, Bogey *et al* finally detected the submillimeter-wave transitions of $HOCO^+$ in the

laboratory(**15**) giving a definite conclusion that the astrophysical lines are really of $HOCO^+$. Our success in observing the ν_1 fundamental band of this ion was brought by the use of a hollow cathode discharge cell(**16**). It has been essential in the sense that we have not yet observed the spectra in the positive column of conventional glow discharges. The experimental details were described in our recent paper(**17**). Briefly, the spectra were observed with the discharge in a gas mixture of H_2 and CO_2 with the current of about 500 mA. The discharge was cooled by flowing cooled methanol through copper tubing which was directly soldered on the cathode. The details of the analysis were presented in our recent two papers (**16**,**17**). In Ref.(**17**), we gave predictions of the transition frequencies for the rotational lines in the ground state. Quite recently Destombes *et al* managed to observe more submillimeter-wave lines of K_a upto 5(**18**). The lines appeared within a few standard errors of our prediction. We have observed several other branches which are unassingned and presumably are the branches of $K_a \geq 4$. Now as the ground state rotational transitions for such higher K_a states are available, the assignment of our unassingned branches will be readily done in near future.

HON_2^+

We have subsequently detected the protonated N_2O in the 3 μm region. Although this ion has been well known by mass spectrosocpy, no high resolution spectroscopic identification has been made. Bohme, Mackay, and Schiff measured the proton affinity of N_2O, and their result shows that it is larger than that of CO_2(**19**). This work will provide the first spectroscopic detection of this ion. There arose two questions at the beginning of this work. 1)Which isomer is the more stable form? 2)What is the molecular structure? Our preliminary result indicates the species detected is a well-bent molecule like HN_3.

The experimental setup is similar to that used in our previous work (**9**). The protonated N_2O is detected in a hollow cathode discharge in a fast flowing gas mixture of N_2O(15 mTorr) and H_2(250 mTorr). At the initial stage of the search, many lines(many of them are diamagnetic neutral species) were observed. Examination of the behavior of these lines in the presence of an axial magnetic field applied to the hollow cathode discharge revealed a series of lines which showed characteristics of ion signals. It was found that the neutral lines could be suppressed greatly by using a fast pumping speed and a low N_2O pressure. We could easily identify the characteristic *b*-type *Q*-branch lines at about 3350 cm^{-1}(K_a=1← 0) and at about 3310 cm^{-1}(K_a=0← 1). This observation immediately led to a conclusion that the molecule we have detected here is a bent molecule that has an approximate *A* rotational constant of 20 cm^{-1}, which is similar to that of HN_3.

A preliminary least-squares fit with an effective Hamiltonian in the A-reduced representation revealed that the K_a=0, 1, and 2 lines could not be fit simultaneously. Also a plot of the *Q*-branch line frequencies in terms of $J(J+1)$ appeared abnormal for the K_a=1← 0 branch, while the K_a=0←1 branch appeared to be normal. We could assign the K_a=0 *a*-type *P*- and *R*-branch lines and the K_a=0← 1 *b*-type *Q*-branch lines unambiguously. By taking the combination differences, subsequently the K_a=1 *a*-type lines and the K_a=1← 0 *b*-type *Q*-branch lines were assigned. We found that the K_a=0 and 2 lines were fit reasonably well with the effective Hamiltonian. However, the lines which have the K_a=1 levels of the excited states as an upper state showed a systematic deviation. The deviation seems to be caused by either a Fermi interaction or an *a*-type Coriolis interacion. The least squares fit was done by two steps. The first step was the fit including the K_a=0 and 2 *a*-type lines and the K_a=0← 1 *Q*-branch lines. From the fit the spectro-

scopic constants listed in Table I were obtained. The second step was done with the K_a=1 a-type lines and the K_a=1← 0 Q-branch lines, with the ground state constants constrained to the values obtained from the first step. The A rotational constant in the excited state was also fixed to the number obtained from the first step. The sub-band origin of the K_a=1 a-type branch is about 0.5 cm^{-1} lower than the expected from the analysis of the K_a=0 and 2 branches. The B rotational constant in the excited state for the K_a=1 states is found to be about 28 MHz smaller. On the other hand, the C rotational constant for the K_a=1 state is almost the same. We are now extending our measurement to other branches such as the K_a=2← 1,and 1← 2 Q-branches and K_a=3, 4 a-type branches to elucidate a detail of the perturbation.

Figure 1. The R-branch lines around 3500 cm^{-1}.

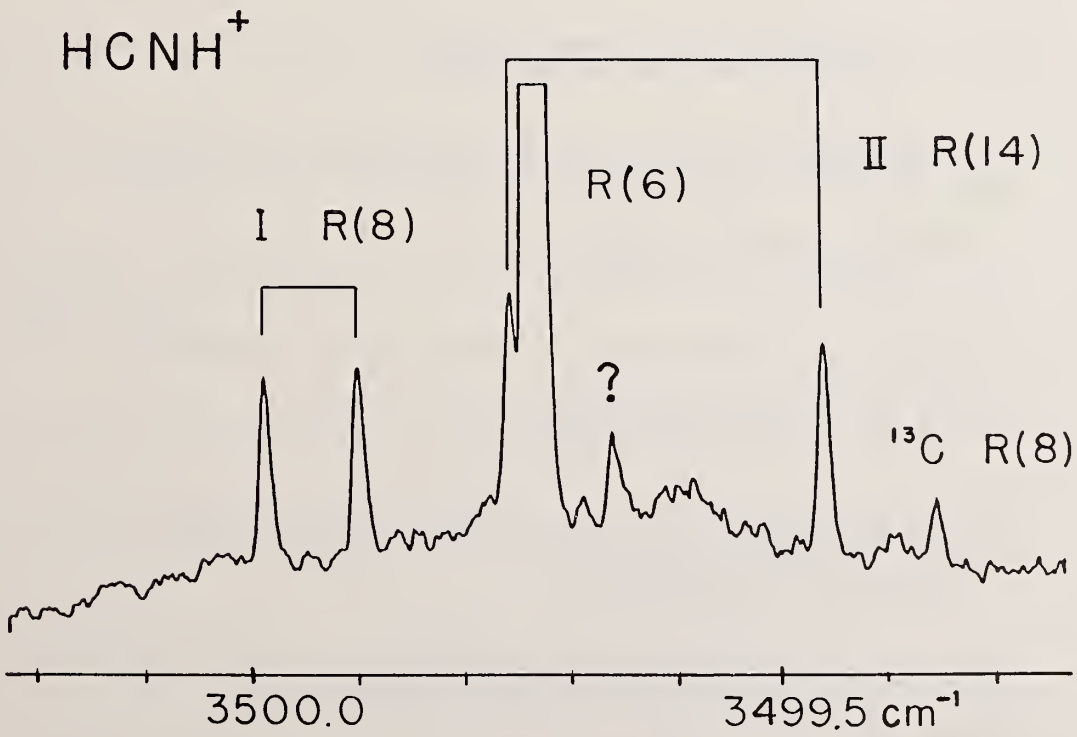

Table I. Molecular constants of $HONN^+$ (in MHz).

	$v_1 = 1$ state	ground state
A	603 899.5(90)	625 687.4(94)
B	11 272.2(46)	11 301.71(41)
C	11 044.5(21)	11 083.27(48)
Δ_J	0.023 96(85)	0.003 87(84)
Δ_{JK}	-3.208(53)	0.506(52)
Δ_K	[0]^a	[0]^a
δ_J		0.002 20(51)
ν_0	99 858 213.3(65)	

^{a} fixed.

REFERENCES

(1) T. Oka, Phys. Rev. Lett.**45**,531(1980).

(2) C. S. Gudeman,M.H.Begemann,J. Pfaff, and R. J. Saykally, Phys.Rev.Lett.**50**,727(1983).

(3) C.S.Gudeman,M.H.Begemann, J. Pfaff, and R. J. Saykally, J. Chem. Phys. **78**,5837(1983).

(4) M.H.Begemann, C.S.Gedeman, J.Pfaff, and R.J.Saykally, Phys.Rev.Lett.**51**,554(1983).

(5) M.Crofton and T.Oka,J.Chem.Phys.**79**, 3157(1983).

(6) E.S.Schafer, M.H.Begemann,C.S.Gedeman, and R. J. Saykally, J. Chem.

Phys.**79**,3159(1983).

(7) P. F. Bernath and T. Amano, Phys. Rev. Lett.**48**,20(1982).

(8) M. Wong, P. F. Bernath, and T. Amano, J. Chem. Phys. **77**,693(1982).

(9) T. Amano, J. Opt. Soc. Am. **B2**,790(1985).

(10) K. Kawaguchi, C. Yamada, S. Saito, and E. Hirota, J. Chem. Phys.**82**, 1750(1985).

(11) R. S. Altman, M. W. Crofton, and T. Oka, J. Chem. Phys. **80**,3911(1984). R. S. Altman, M. W. Crofton, and T. Oka, J. Chem. Phys. **81**,4255(1984).

(12) T. Amano, J. Chem. Phys.**81**,3350(1984).

(13) T. Amano and K. Tanaka, J. Mol. Spectrosc. to be published.

(14) P. Thaddeus, M. Guelin, and R. A. Linke, Astrophys. J. **246**,L41(1981).

(15) M. Bogey, C. Demuynck, and J. L. Destombes,Astron. Astrophys. **138**,L11(1984).

(16) T. Amano and K. Tanaka, J. Chem. Phys. **82**,1045(1985).

(17) T. Amano and K. Tanaka, J. Chem. Phys. **83**,3721(1985).

(18) J.L.Destombes and C.Demuynck,private communication.

(19) . K. Bohme, G. I. Mackay, and H. I. Schiff, J. Chem. Phys. **73**,4976(1980).

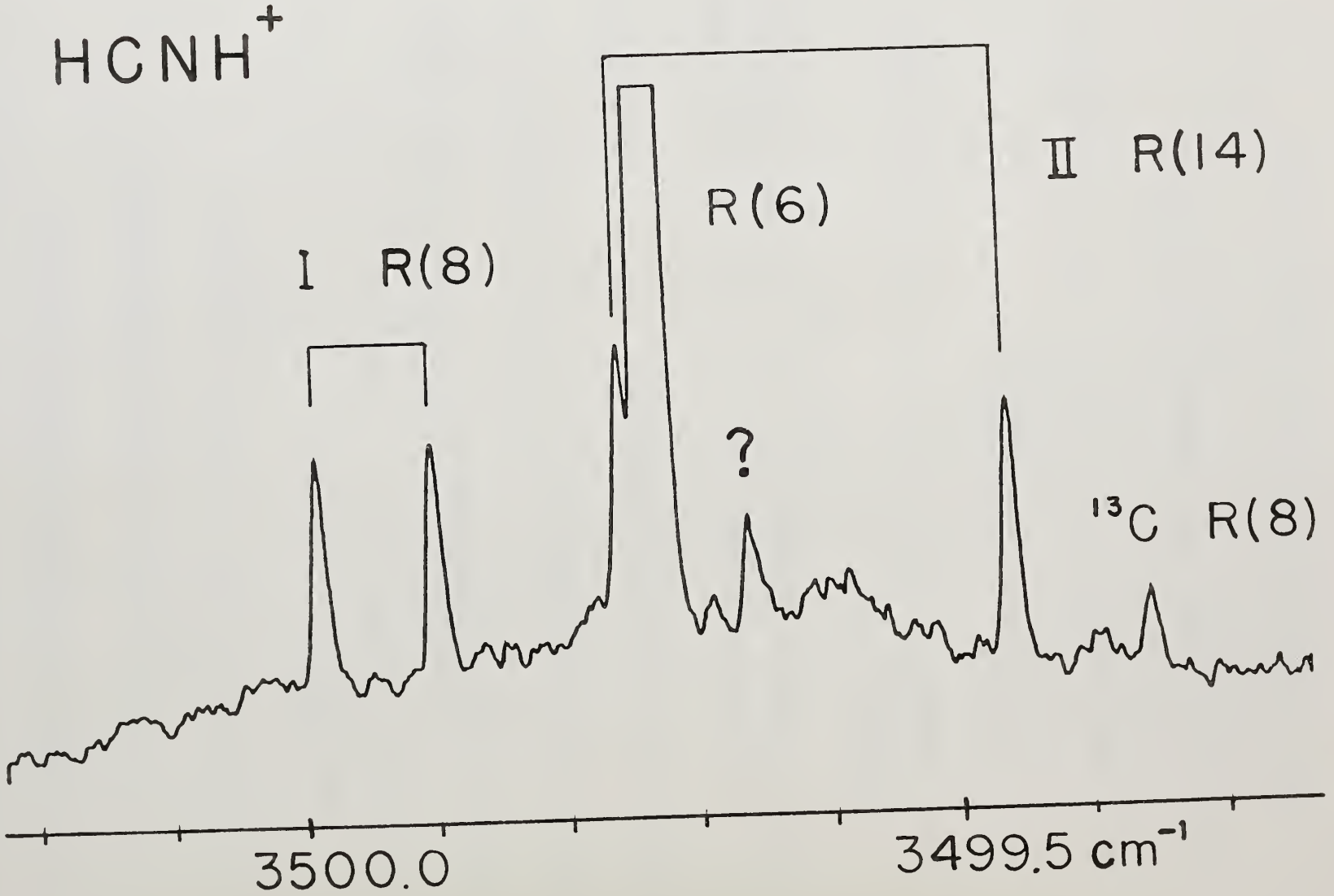
HCNH+
I R(8)
R(6)
II R(14)
?
13C R(8)
3500.0
3499.5 cm-1

KINETICS OF HYDROXYL RADICAL REACTIONS WITH ALKYL RADICALS

Larry G. Anderson and Juan L. Bonilla

Department of Chemistry

University of Colorado at Denver

Denver, Colorado 80202 U.S.A.

Proceedings of the Seventeenth International Symposium on Free Radicals

Snow Mountain Ranch, Colorado U.S.A.

August 18 - 23, 1985

KINETICS OF HYDROXYL RADICAL REACTIONS WITH ALKYL RADICALS

Larry G. Anderson and Juan L. Bonilla

Department of Chemistry, University of Colorado at Denver, Denver, Colorado 80202 U.S.A.

INTRODUCTION

Reactions of hydroxyl radicals with alkanes play an important role in both atmospheric chemistry and combustion chemistry. The homogeneous gas phase kinetics of the reactions of hydroxyl radicals with alkanes have been extensively reported. These reactions are believed to proceed by a hydrogen abstraction route:

$$HO + RH \text{ ---† } H_2O + R^{\cdot} \qquad (1)$$

producing water and an alkyl radical. In the study of HO - alkane reaction kinetics, secondary reactions may occur which complicate the interpretation of the primary kinetics results. The most important of these secondary reactions is the reaction of the HO radical with the product alkyl radical produced in reaction (1).

$$HO + R^{\cdot} \text{ ---† Products} \qquad (2)$$

It has been recognized for quite some time that the reaction of HO radicals with alkyl radicals can complicate the interpretation of HO - alkane kinetics results. Greiner[1] attempted to correct his data for this effect by assuming a rate constant of about 1.7×10^{-10} cm^3 $molecule^{-1}$ s^{-1} for the HO + alkyl radical reaction. In that work, relatively high initial HO concentrations were used, about 3×10^{13} radicals/cm^3. In some cases, the corrections to the rate constants for the HO + alkane reactions amounted to as much as 30%. Overend et al.[2] have evaluated the effects of secondary reactions, including the HO - alkyl reaction upon the observed kinetics for HO + alkane reactions. If one assumes a gas-kinetic collision rate for reaction (2), the

observed rate of HO radical decay can be as much as two times the actual rate due to reaction (1). These biggest discrepancies were found to occur at lower concentrations of alkanes and higher concentrations of HO radicals.

Perry et al.[3] tested for the influence of secondary reactions in their studies of HO + n-butane by doubling the flash energy used to produce the HO radicals, and observing no variation in the rate constant. Hence, they concluded that secondary reactions were negligible. Paraskevopoulos and Nip[4] found no significant effects of secondary reactions for test reactions which were a factor of three or more slower than the HO + n-butane reaction. They assumed that there would be no significant effect of secondary reactions on the HO + n-butane reaction, since they used HO radical concentrations a factor of 4 - 8 times lower than in their tests.

The purpose of this research is to investigate the possible importance of secondary reactions upon certain previous kinetic studies of HO radicals with n-butane. The second major goal of this work is to develop a technique for analyzing HO radical kinetic data to determine the rate of the HO radical reaction with alkyl radicals.

EXPERIMENTAL

The experimental data, which is analyzed in this work, was collected using a discharge flow-resonance fluorescence system[5]. Hydroxyl radicals were produced in the flow system by passing a dilute mixture of hydrogen in helium through a microwave discharge to form hydrogen atoms. The hydrogen atoms are allowed to react with an excess of NO_2 to form the HO radicals and NO. After sufficient time was allowed for the formation of HO radicals, the alkane reactants were added through eight fixed injection ports. Downstream of the reaction zone, the unreacted HO radicals were detected by resonance fluorescence. The signals were detected by a photomultiplier after the light had

passed through an interference filter. The experimental data to be discussed in this work was collected at 250 K and approximately 1 torr pressure.

RESULTS AND DISCUSSION

During the previous work,[5] some very preliminary data was collected which suggested that the observed kinetics were markedly different when studied at "high" hydroxyl radical concentrations versus the results at "low" hydroxyl radical concentrations. At "high" HO radical concentrations, two reactions are expected to contribute significantly to the loss of HO radicals from the system. These processes include the direct reaction of the HO radical with the n-butane, reaction (3), which is expected to be the only reaction of significance when the HO radicals are at "low" concentrations. In this reaction, the HO radical is expected to abstract a hydrogen atom from the n-butane, forming a butyl radical. At "high" HO radical concentrations, it is possible that sufficient product (butyl radical) is formed to allow the secondary reaction of hydroxyl radicals with the butyl radical, reaction (4), to contribute significantly to the decay of the hydroxyl radicals.

Figure 1 shows the results of a pair of nearly identical experiments performed in the study of the HO radical reaction with n-butane. The main difference in this pair of experiments was the initial HO radical concentration. The "high" HO radical concentration (lower data) was about 9×10^{11} radicals/cm^3, while the "low" HO radical concentration (upper data) was about 2×10^{11} radicals/cm^3. For the "low" hydroxyl radical case, a plot of the ln(HO fluorescence) versus time showed the normal linear plot, consistent with the pseudo-first-order decay of HO radicals in the presence of excess n-butane. For the "high" hydroxyl radical case, the ln plot showed considerable curvature. This curvature is presumably due to the occurrence of secondary reactions. The solid lines shown in this figure are the results of chemical

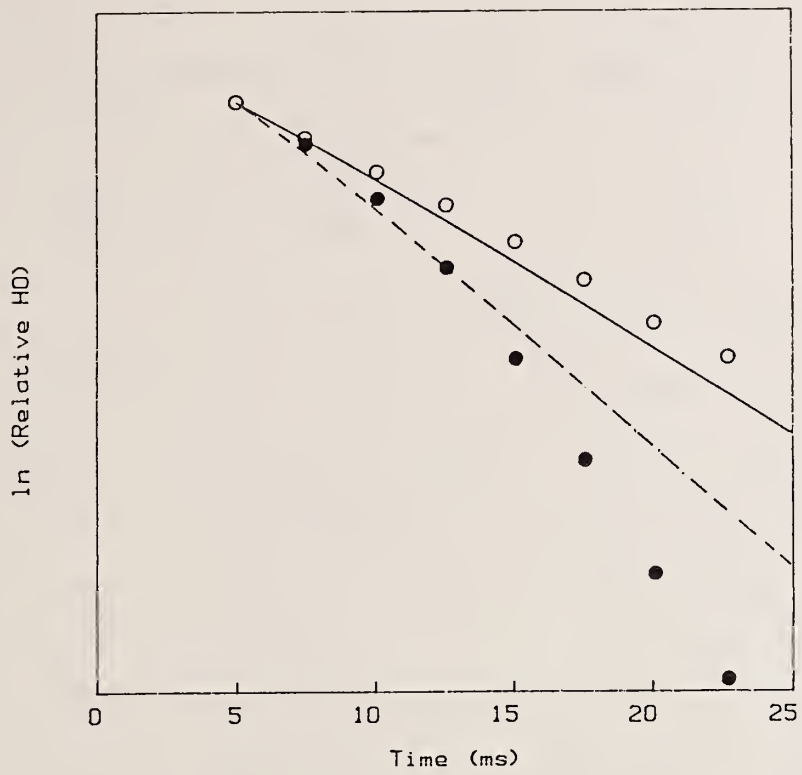

Figure 1. Plot of the ln of the relative HO fluorescence versus reaction time. In all of the figures, the open set of data points corresponds to "low" initial HO radical concentrations (about 2 x 10^{11} radicals/cm^3) and the closed set of data points corresponds to "high" initial HO radical concentrations (about 9 x 10^{11} radicals/cm^3). The solid line is the result of model calculations for the "low" HO case and the dashed line is for the "high" HO case. The model calculations were performed using the chemical mechanism and rate constants listed in table 1.

model calculations, which were performed using the reaction mechanism and rate constants listed in table 1. The model calculations show a faster decay for "low" HO radical concentrations than does the experimental data. This is because the rate constant used for reaction (3) was determined in the previous work[5] by assuming that secondary reactions are insignificant. The comparison between the model calculations and the data suggest that secondary reactions have a significant effect on the kinetics, even at "low" HO concentrations. The major effect of the secondary reactions is due to reaction (4), which has been assumed to occur at nearly a gas-kinetic rate. In addition, there is a small effect on the kinetics due to the reaction of HO with butene, reaction (10). Butene was assumed to be the product of the HO + butyl radical reaction.

Table 1. Reaction Mechanism used in Simulations of HO - n-Butane Reactions

Reaction	Rate Constant (cm^3 $molecule^{-1}$ s^{-1})	Reference
3) HO + n-butane ---† H_2O + butyl	1.46×10^{-12}	5
4) HO + butyl ---† butene (??)	2.0×10^{-10}	est.
5) HO + HO (+ M) ---† H_2O_2	2.2×10^{-14}	6
6) HO + H_2O_2 ---† H_2O + HO_2	1.7×10^{-12}	6
7) HO + NO_2 (+ M) ---† $HONO_2$	8.3×10^{-14}	6
8) HO + NO (+ M) ---† HONO	2.2×10^{-14}	6
9) HO + $HONO_2$ ---† H_2O + NO_3	1.3×10^{-13}	6
10) HO + butene ---† products	3.0×10^{-11}	ave.
11) HO + HO ---† H_2O + O	1.9×10^{-12}	6
12) HO ---† Wall	2 (s^{-1})	5

If the rate constant for reaction (4) were reduced, one would find better agreement between the "low" HO data and simulations. However, if we look at the "high" HO data and the associated simulation, one finds that the simulation tends to underpredict the decay rate for HO radicals. This suggests that the rate constant for the HO + butyl radical reaction, (4), has been underestimated. Due to the preliminary nature of the current data, no attempt has been made to force the fits to the data any further.

Figure 2 shows a plot of some additional preliminary data on the n-butane concentration dependence of the observed pseudo-first-order rate constant, measured for "low" HO concentration (lower data) and "high" HO concentration (upper data). Clearly, there is a significant difference in these two sets of data. The solid curves that are shown are the results of model simulations,

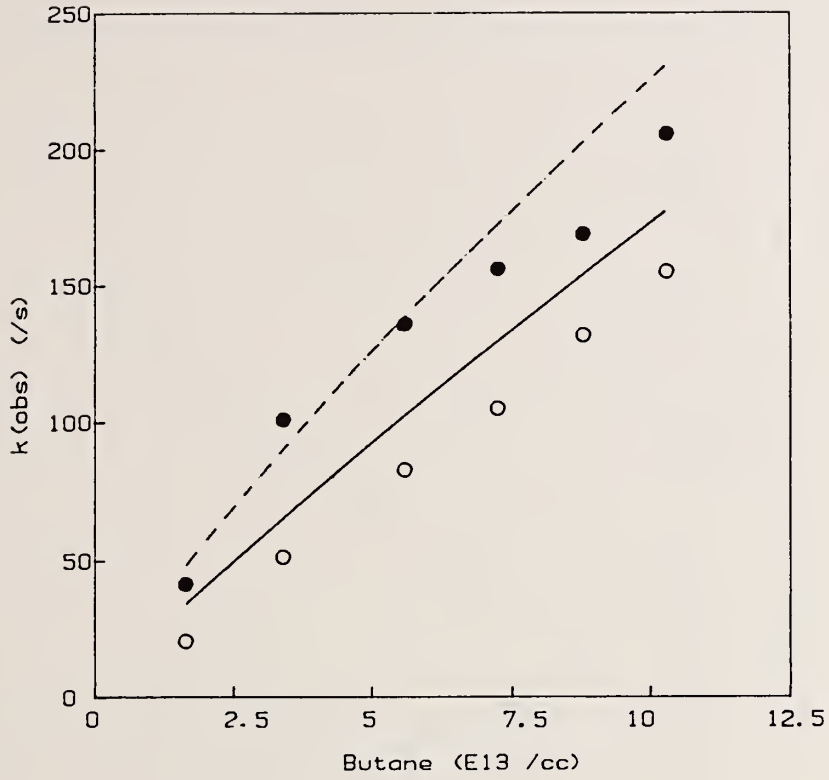

Figure 2. Plot of the pseudo-first-order rate constant for HO decay as a function of the butane concentration. The symbols are described in the caption for figure 1. The model calculations were performed using the chemical mechanism and rate constants listed in table 1.

using the mechanism listed in table 1. There is an obvious overprediction of k_{obs} for the "low" HO radical concentrations. This overprediction is due to the consideration of the effects of secondary reactions. Figure 3 shows the comparison between the "low" HO radical concentration data and the computed results, when one ignores secondary reactions and only reaction (3) is considered.

The data presented above suggests that the "low" HO concentration data is affected significantly by secondary reactions. Hence, the rate constant used for reaction (3), which was determined by ignoring such secondary reactions, must be too large. Figure 4 shows a plot of the same data on the n-butane

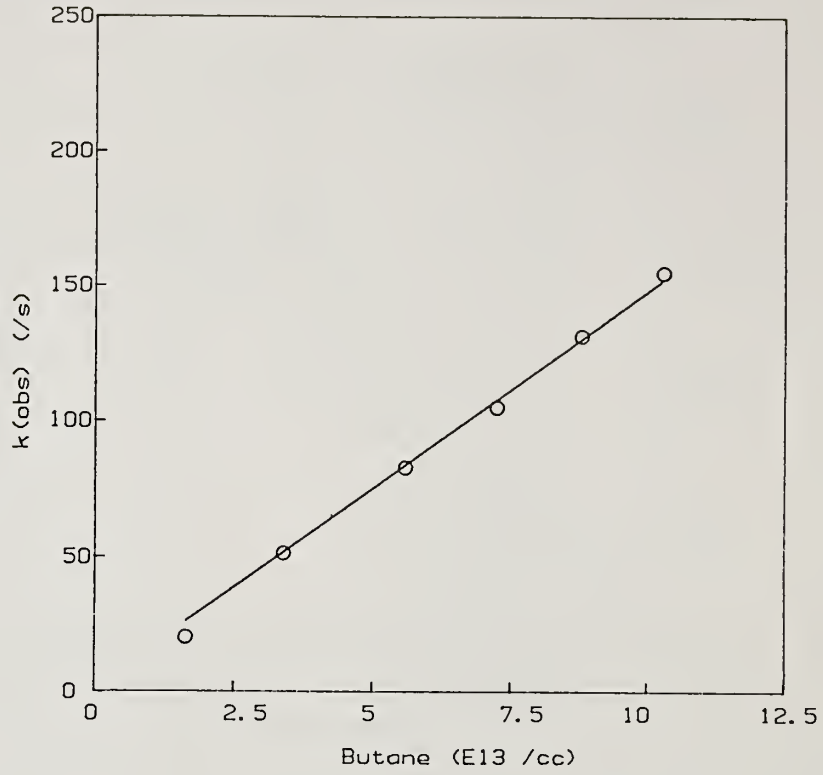

Figure 3. Plot of the pseudo-first-order rate constant for HO decay as a function of the butane concentration for "low" initial HO radical concentrations. The calculated curve ignores the influence of secondary on the HO radical concentration, considering only reaction (3).

concentration dependence of k_{obs} compared to the model simulations, in which a smaller rate constant of 1.2×10^{-12} cm^3 $molecule^{-1}$ s^{-1} is used for reaction (3). This reduction in the rate constant for reaction (3) clearly provides a much better fit to the "low" HO concentration data. There is still reasonable agreement between the calculated and experimental results for "high" HO concentrations.

These model results suggest that the rate constant for the HO + n-butane reaction is less than the 1.46×10^{-12} cm^3 $molecule^{-1}$ s^{-1} reported at 250 K[5]. This is in spite of the fact that the rate constants reported by Anderson and Stephens[5] at room temperature are smaller than all of the values reported

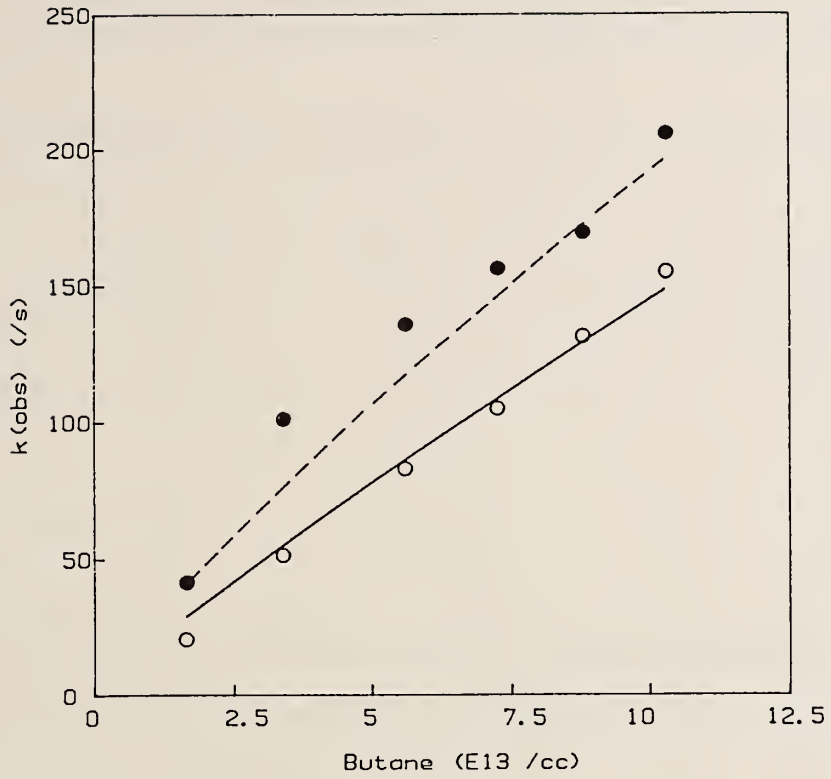

Figure 4. Plot of the pseudo-first-order rate constant for HO decay as a function of the butane concentration. The symbols are described in the caption for figure 1. The model calculations were performed using the chemical mechanism and rate constants listed in table 1, except the rate constant for reaction (3) was reduced to 1.2×10^{-12} cm^3 $molecule^{-1}$ s^{-1}.

previously (Table 2). These model results also suggest that the principle secondary reaction, that of the HO radical with the butyl radical, occurs with nearly a gas kinetic rate.

Some preliminary work has been done to try to evaluate the importance of the secondary reactions on the results of the other previously reported experiments. It is clear that there is a significant contribution in the experiments of Greiner[1], Morris and Niki[7], and Paraskevopolous and Nip[4]. It is also clear that the specific experimental conditions of concentrations and time scale must be modeled, in order to properly assess the role of the possible secondary reactions. In addition, it was found that there is often insuffi-

Table 2. Previous Direct Studies of the HO + n-Butane Reaction

k_{298} (cm^3 $molecule^{-1}$ s^{-1})	Method	Reference
2.57×10^{-12}	FP-KS	1
4.1×10^{-12}	DF-MS	7
2.35×10^{-12}	FP-RF	8
2.72×10^{-12}	FP-RF	4
2.67×10^{-12}	FP-RA	3
1.68×10^{-12}	DF-RF	5

FP - flash photolysis; DF - discharge flow; KS - kinetic spectroscopy; MS - mass spectroscopy; RF - resonance fluorescence; RA - resonance absorption

cient data presented to allow one to adequately evaluate the potential influence of secondary reactions. For example, Perry et al.[3] do not present any quantitative or even semi-quantitative information about the HO concentration used in their system. Typically, flash photolysis- resonance fluorescence studies of HO reactions are performed at low HO concentrations, hence secondary reactions are not likely to adequately explain the differences between the work of Anderson and Stephens[5] and that of Perry et al.[3] and Stuhl[8].

Experiments in which the radical concentration is doubled or the flash energy is doubled are frequently reported as resulting in no "significant" variation in the rate constant for the reaction. These experiments do not really provide an adequate test of the importance of secondary reactions. In order to be able to rule out the effects of secondary reactions on kinetics studies, it is suggested that some experiments be performed under conditions where there are obvious effects of these processes. These experiments will

provide a basis for more accurately assessing the influence of such secondary reactions.

In this work, a technique has been used to evaluate the rate constant for HO + alkyl radical reactions. By collecting more data over a broader range of initial HO radical concentrations and using detailed chemical modeling of the processes involved, one should be able to make reliable estimates of the rate constants for HO radical reactions with alkyl radicals.

REFERENCES

1. N. R. Greiner, J. Chem. Phys., 53, 1070-1076 (1970).

2. R. P. Overend, G. Paraskevopoulos and R. J. Cvetanovic, Can. J. Chem., 53, 3374-3382 (1975).

3. R. A. Perry, R. Atkinson and J. N. Pitts, Jr., J. Chem. Phys., 64, 5314-5316 (1976).

4. G. Paraskevopoulos and W. S. Nip, Can. J. Chem., 58, 2146-2149 (1980).

5. L. G. Anderson and R. D. Stephens, "Absolute rate constants for the reactions of OH radicals with alkanes", General Motors Research Publication GMR-4087, General Motors Research Laboratories, Warren, MI, 1982.

6. W. B. DeMore, M. J. Molina, R. T. Watson, D. M. Golden, R. F. Hampson, M. J. Kurylo, C. J. Howard and A. R. Ravishankara, "Chemical kinetic and photochemical data for use in stratospheric modeling. Evaluation number 6". JPL Report 83-62, Jet Propulsion Laboratory, Pasadena, CA, 1983.

7. E. D. Morris and H. Niki, J. Phys. Chem., 75, 3640 (1971).

8. F. Stuhl, Z. Naturforsch., 28A, 1383 (1973).

PRODUCTION AND REACTIONS OF THE ISOPROPOXY RADICAL

R. Jeffrey Balla*, H.H. Nelson, and J.R. McDonald
Chemistry Division, Naval Research Laboratory,
Washington, D.C. 20375-5000

We report the first laser-induced fluorescence (LIF) and direct chemical kinetics measurements on the isopropoxy radical (i-PrO). Arrhenius parameters for its reaction with O_2, NO, and NO_2 are measured over the temperature range of 22 to 105°C. We have performed the first direct measurements of the unimolecular decomposition as a function of temperature and pressure. Finally, the fluorescence excitation spectrum is measured over a 40 nm range (330-370 nm).

The i-PrO radical is prepared by 355 nm photolysis of isopropyl nitrite and probed by LIF via the A-X transition around 340 nm. The reaction of i-PrO with O_2 produced the following Arrhenius expression.

$(1.51 \pm 0.70) \times 10^{-14} \exp(-390 \pm 280/RT)$ cm^3/sec

The temperature dependence of this system will be compared with those of other alkoxy reactions.

With both NO and NO_2, i-PrO reacts via two channels: a bimolecular hydrogen abstraction and a termolecular combination reaction. In both cases, the latter reaction predominates. The following Arrhenius expressions result for NO and NO_2 respectively.

$(1.22 \pm 0.28) \times 10^{-11} \exp(+620 \pm 140/RT)$ cm^3/sec

$(1.48 \pm 0.76) \times 10^{-11} \exp(+520 \pm 320/RT)$ cm^3/sec

All uncertainties represent 2 . Data taken during the i-PrO + NO_2 reaction lead us to propose that $O(^3P)$ reacts with i-PrO with a nearly gas kinetic rate constant.

Alkoxy radicals are known to undergo thermal decomposition. Few experimental measurements of this reaction have been made and none are by direct methods. Our data indicates that this reaction is in the fall-off region at both 105 and 133°C using between 1 and 300 Torr N_2 as a buffer gas.

*NRC/NRL Postdoctoral Research Associate

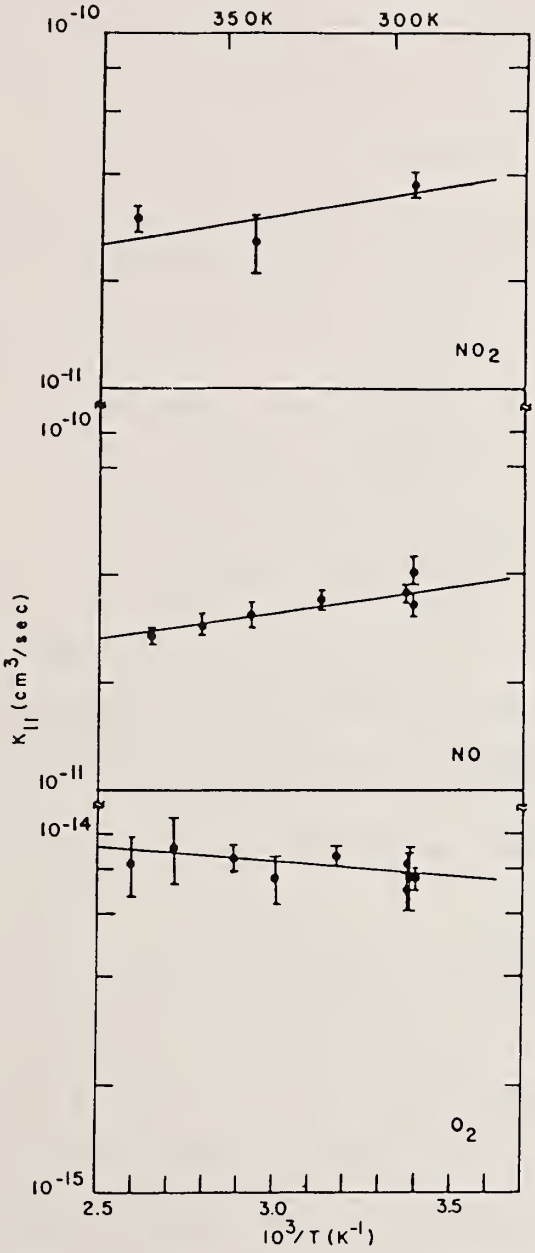

Arrhenius plots for the reaction of i-PrO with O_2, NO, and NO_2

THE FAR-INFRARED ROTATIONAL SPECTRUM OF $X^2\Pi$ OH

Geoffrey A. Blake[1],

Jam Farhoomand[2],

and Herbert M. Pickett[2]

[1]Department of Chemistry, California Institute of Technology.

[2]Jet Propulsion Laboratory, California Institute of Technology.

THE FAR-INFRARED ROTATIONAL SPECTRUM OF $X^2\Pi OH$

We have previously reported the direct (zero-field) measurement of the fundamental rotational transitions of the hydroxyl radical using a recently developed far-infrared (FIR) laser sideband spectrometer (1). This note presents a more extensive set of measurements of the pure rotational spectrum of OH, which we combine with existing microwave, infrared, and optical data to produce an optimized set of molecular constants.

Hydroxyl radicals were created in a 1 m DC glow discharge cell containing approximately 100 μm of water vapor, through which currents of 50 - 100 mA were passed. The FIR laser sideband spectrometer has previously been described in detail (1,2), and was used for all of the measurements described here. Lasing transitions of CH_2F_2 at 1891.3 and 2448.0 GHz, and of CH_3OH at 2522.8 and 3195.2 GHz, have been mixed with radiation from klystrons in the 50 - 90 GHz range to produce the tunable FIR source utilized in these experiments. Lines of CO and HDO were used as reference gases to calibrate our measured laser frequencies(1). The CO frequencies were obtained from K. M. Evenson and the HDO frequencies from J. W. C. Johns.

In addition to the fundamental rotational transitions at 1835 and 2510 GHz reported previously, we have also measured the $\Omega + 1/2$, $J = 3/2 \rightarrow 5/2$ lines at 3036 GHz and the cross-ladder ($\Delta\Omega = 1$) $J = 7/2 \rightarrow 5/2$ transitions at 2603 GHz. Table 1 presents our measured frequenices along with the predictions of Brown et al.(3), deduced from an extensive FIR laser magnetic resonance study of OH, which are listed in Table II. The term values of Coxon(4), which we have used for states with $J + 1/2 = 21$ and $J + 1/2 = 31$, have been assigned an uncertainty of 0.020 cm^{-1}, while the sixteen infrared combination differences obtained from the difference frequency laser work of Amano(5) have an estimated accuracy of 0.001 cm^{-1}. Frequencies for the Λ-doubling lines have been taken from Beaudet and Poynter(6), who analyzed the rotational spectrum of OH with a three-state Hamiltonian first described by Dousmanis, Sanders, and Townes(7).

We have chosen, however, to analyze the combined data set using an effective two-state Hamiltonian as applied by Coxon(4), whose constants are also listed in Table II. Within the larger pure rotational structure, the hyperfine interactions have been modeled by the $^2\Pi$ Hamiltonian of Meerts and Dymanus(8). As one can see, the constants listed in Table 2 are, in general, quite similar though a number of them disagree at the 1σ level. The present constants are considerably more precise, however, and have allowed the pure rotational spectrum of the OH radical to be predicted to better than 10 MHz throughout the FIR and mid-IR spectral regions. All transitoins below a J of 7/2 have estimated uncertainties of less than 1 MHz. The observed - calculated rms error for the microwave and far-infrared lines is only 0.062 MHz, while that for the infrared combination differences is less than 0.0036 cm^{-1}. The overall rms error is approximately 0.97 MHz. The brief nature of this note is such that a presentation of our predictions is inappropriate. A complete listing of the predicted transitions frequencies is available upon request from the authors or the editor.

ACKNOWLEDGEMENT

We would like to thank E. A. Cohen for his help and useful discussions during the course of these experiments. We would also like to thank K. M. Evenson and J. W. C. Johns for providing the calibration frequencies prior to publication. The research described in this paper was performed by the Jet Propulsion Laboratory, California Institute of Technology, under contract with the National Aeronautics and Space Administration.

REFERENCES

1. J. Farhoomand, G. A. Blake, and H. M. Pickett, Ap. J. (Letters) 291, L19-22 (1985).

2. J. Farhoomand, G. A. Blake, M. A. frerking, and H. M. Pickett, J. Appl. Phys. 57, 1763-1766 (1985).

3. T. M. Brown, J. E. Schubert, K. M. Evenson, and H. E. Radford, Ap. J. (Letters) 258, 899-903 (1982).

4. J. A. Coxon, Can. J. Phys. 58, 933-949 (1980).

5. T. Amano, J. Mol. Spec. 103, 436-454 (1984).

6. R. A. Beaudet and R. L. Poynter, J. Phys. Chem. Ref. Data 7, 311-362 (1978).

7. G. C. Dousmanis, T. M. Sanders, and C. H. Townes, Phys. Rev. 100, 1735-1754 (1955).

8. W. L. Meerts and A. Dymanus, Can. J. Phys. 53, 2123-2141 (1975).

Table 1: Observed Spin-Rotation Transition Frequencies of $^2\Pi_{1/2}$ and $^2\Pi_{3/2}$ OH

Ω	Transitions[1] $JP' \rightarrow JP''$	$F' \rightarrow F''$	Observed Frequency(σ) (MHz)	Observed - Calculated (MHz)	LMR Predictions[2](σ) (MHz)	Calibration Frequency	Calibration Species
1/2	$3/2^- \rightarrow 1/2^+$	1 → 1	1834735.51(0.5)	0.22	1834734.7(3.0)	1956018.066	CO
		2 → 1	1834737.35(0.5)	0.22	1834746.6(3.0)		
		1 → 0	1834750.42(0.5)	0.22	1834749.6(3.0)		
3/2	$5/2^+ \rightarrow 3/2^-$	2 → 2	2509935.44(0.5)	-0.02	2509933.7(3.0)	2528172.080	CO
		3 → 2	2509949.43(0.5)	-0.02	2509947.7(3.0)		
		2 → 1	2509988.61(0.5)	-0.02	2609986.9(3.0)		
3/2	$5/2^- \rightarrow 3/2^+$	2 → 2	2514298.83(0.6)	-0.02	2514297.1(3.0)		
		3 → 2	2514317.17(0.5)	-0.01	2514315.5(3.0)		
		2 → 1	2514353.96(0.5)	-0.01	2514352.3(3.0)		
3/2 → 1/2	$5/2^+ \rightarrow 7/2^-$	2 → 3	2603399.52(0.5)	-0.06	2603402.(>3.0)	2592522.734	HDO
		3 → 4	2603424.86(0.5)	-0.01	2603428.(>3.0)		
1/2	$3/2^- \rightarrow 5/2^+$	2 → 2	3036257.77(0.5)	-0.07	3036260.(>3.0)	3037103.857	HDO
		1 → 2	3036269.61(0.5)	-0.07	3036272.(>3.0)		
		2 → 3	3036275.58(0.5)	-0.07	3036278.(>3.0)		
1/2	$3/2^+ \rightarrow 5/2^-$	2 → 2	3036573.51(0.5)	-0.08	3036576.(>3.0)		
		1 → 2	3036643.73(0.5)	-0.07	3036646.(>3.0)		
		2 → 3	3036645.05(0.5)	-0.06	3036647.(>3.0)		

[1] Quantum numbers for the upper state are denoted by primes and those for the lower state by double primes. Superscripts on the J quantum numbers indicate the parity of the states according to Brown et al.(3).

[2] Taken from Brown et al.(3) σ in MHz.

Table II: Optimized constants for the $X^2\Pi$ state of OH

Constant	Present (σ) (MHz)	Coxon[1] (σ) (MHz)
A	-4168684.47(93)	-4168731.7(348)
A_D	11.634(84)	-
B	555547.329	555546.63(102)
D	57.2349	57.2085(71)
H	$4.319(26) \times 10^{-3}$	$4.23607(145) \times 10^{-3}$
L	$-4.42(19) \times 10^{-7}$	$-3.83734(908) \times 10^{-7}$
γ	-3517.000000[2]	-3594.097(5519)
γ_D	0.679(29)	0.7396(240)
p	7053.2686(13)	7051.56099(354)
p_D	-1.55047(14)	-1.55075(43)
p_H	$1.546(37) \times 10^{-4}$	$1.670(005) \times 10^{-4}$
p_L	$3.7(34) \times 10^{-8}$	$2.0(33) \times 10^{-8}$
q	-1160.07750(41)	-1159.55593(151)
q_D	0.441971(23)	0.4418957(875)
q_H	$-8.238(29) \times 10^{-5}$	$-8.3507(402) \times 10^{-5}$
q_L	$1.348(85) \times 10^{-8}$	$1.46(10) \times 10^{-8}$
a	86.1119(25)	86.1109(37)
b_F	-73.2593(52)	-73.1524(63)
c	130.652(11)	130.6390(152)
d	56.6845(39)	56.658
d_D	-0.02279(18)	-0.02285(14)
C_1	-0.09978(61)	-0.10016(85)
C_1	0.00671(18)	0.00649(11)

[1]Taken from ref. (4), σ in MHz.
[2]Fixed to value in ref. (5).

Kinetics of Reactions between CH_2-Radicals and Hydrocarbons in the Temperature Range 296 K $\leq$ T $\leq$ 728 K

T. Böhland, S. Dóbé, F.Temps, and H.Gg. Wagner
Max-Planck-Institut für Strömungsforschung, Bunsenstr. 10,
3400 Göttingen, W.-Germany

1. Introduction

Reactions of methylene radicals (CH_2) play a central role in many fields in chemistry such as organic synthesis, theoretical chemistry, combustion processes, or chemical activation studies of unimolecular reactions (see e.g. [1-3]). CH_2-radicals have a triplet electronic ground state $\tilde{X}\ ^3B_1$ (hereafter referred to as $^3CH_2$). Besides, there exists a low-lying singlet first excited state $\tilde{a}\ ^1A_1$ (hereafter $^1CH_2$). The chemical properties of both spin states are completely. The basic mechanism for reactions of CH_2 and hydrocarbons have been qualitatively inferred from the observed end products [2,3]. $^1CH_2$-radicals insert into C-H bonds and add stereospecifically to double bonds. On the contrary, $^3CH_2$-radicals react with saturated hydrocarbons via abstraction of an H-atom and add nonstereospecifically to double bonds. The reaction systems are further complicated by an efficient collision induced intersystem crossing between both spin states.

Despite their importance, very little is known experimentally about the kinetics of the elementary reactions between CH_2 and organic reactants. For reaction of $^3CH_2$ with hydrocarbons no direct kinetic studies had previously been published. In the case of $^1CH_2$, rate constants had been measured for the overall removal by various reactants [4,5]. However, an experimental separation between removal via intersystem crossing or reactive channels had not been possible. The present paper is concerned with a series of direct investigations of reactions of CH_2 in both spin states with saturated as well as unsaturated organic molecules.

Firstly, the branching ratios were measured for the deactivation channels (D) in the removal of $^1CH_2$ by selected hydrocarbons HR

$$^1CH_2 + HR \longrightarrow {}^3CH_2 + HR \qquad (1D)-(8D)$$
$$\longrightarrow \text{other products} \qquad (1S)-(8S)$$

for HR = CH_4 (1), C_2H_6 (2), C_3H_8 (3), i-C_4H_{10} (5), C_2H_4 (7).

Secondly, the rate constants were determined for direct H-atom abstraction by $^3CH_2$ from selected molecules HR

$$^3CH_2 + HR \longrightarrow CH_3 + R \qquad (1T)-(6T)$$

for HR = CH_4 (1), C_2H_6 (2), C_3H_6 (3), n-C_6H_{14} (4), i-C_4H_{10} (5), CH_3CHO (6).

Thirdly, the rate constants were measured for addition of $^3CH_2$ to C_2H_4 and C_2H_2

$$^3CH_2 + C_2H_4 \longrightarrow \text{products} \qquad (7T)$$
$$^3CH_2 + C_2H_2 \longrightarrow \text{products} \qquad (8T)$$

The reactions were investigated in the temperature regime 296 K $\leq$ T $\leq$ 728 K in isothermal flow reactors using the method of Laser Magnetic Resonance (LMR) as a direct monitor for $^3CH_2$. The results summarized here have been described in more detail in a series of recent papers [6].

2. Experimental

The experimental set-up is shown in Figure 1. The reactions were investigated in thermostated pyrex flow systems equipped with a movable probe. $^3CH_2$-radicals were detected with a far infrared LMR spectrometer which operates in the wavelength regime 40 μm $\leq \lambda \leq$

1250 μm. The spectrometer can also be used for direct time-resolved LMR studies although this has not yet been applied to CH_2. A full description of the spectrometer can be found elsewhere [7]. For all $^3CH_2$ concentration measurements the transition at λ = 159 μm, B_0 = 0.323 Tesla in π-polarization [8] was used. Vacuum UV resonance absorption allowed the simultaneous detection of atomic species.

CH_2-radicals were generated in two different sources. The first method was the reaction

$$O + CH_2CO \quad ---> \quad CH_2 + CO_2 \qquad (9)$$

which produces $^3CH_2$ as main products [9] and also allows the determination of absolute CH_2 concentrations. O-atoms generated in a microwave discharge of O_2 diluted in He were admixed to a large excess of CH_2CO within the moveable probe.

The second source was the photodissociation of CH_2CO with an exciplex laser at λ = 308nm or 193 nm

$$CH_2CO + h\nu \quad ---> \quad CH_2 + CO \qquad (10)$$

Photolysis of CH_2CO at λ = 308 nm yields practically exclusively $^1CH_2$-radicals [10,11]. Photodissociation at λ = 193 nm has a two orders of magnitude larger cross section and can also populate the $\tilde{b}\ ^1B_1$ state. In the presence of a large excess of inert gases excited CH_2-radicals are rapidly deactivated to the ground state [4,5]. The CH_2CO was photolysed in a cell attached sidewards to the main flow tube under conditions such that the residence time of the gas within the cell was short compared to the time between two laser shots. Hence, the gas flow carried a pulse of radicals through the reactor and the LMR sample region. The radical pulse was detected with the LMR using low time constants of 3 - 10 ms and accumulated in a signal averager. Further details have been reported in [6b].

3. Deactivation of $^1CH_2$ by Hydrocarbons

3.1 Results

The branching between intersystem crossing (deactivation,D) and reaction (S) in the removal of $^1CH_2$ by HR

$$^1CH_2 + HR \longrightarrow {}^3CH_2 + HR \qquad (1D)\text{-}(8D)$$
$$\longrightarrow \text{other products} \qquad (1S)\text{-}(8S)$$

was studied at room temperature relative to $^1CH_2$ quenching by He and, to a minor extent, CH_2CO

$$^1CH_2 + He \longrightarrow {}^3CH_2 + He \qquad (11)$$
$$^1CH_2 + CH_2CO \longrightarrow {}^3CH_2 + CH_2CO \qquad (12D)$$
$$\longrightarrow C_2H_4 + CO \qquad (12S)$$

by monitoring the yields of $^3CH_2$ from photodissociation of CH_2CO at λ = 308 nm in the absence and the presence of varying concentrations of HR. Assuming the quantum yield for $^1CH_2$ formations at λ = 308 nm to be Φ_1 = 1 [10,11] the ratio of the $^3CH_2$ concentrations with and without HR is given by

$$\gamma = \frac{[^3CH_2]_{+HR}}{[^3CH_2]_{-HR}} \cdot \frac{k'_{Q+HR}}{k'_{Q-HR}} = 1 + \frac{k_{iD}\,[HR]_i}{k_{11}\,[He]}$$

with i=1-8, $k_{iQ} = k_{iD} + k_{iS}$, $k'_{Q-HR} = k_{11}[He] + k_{12Q}\,[CH_2CO]$, and $k'_{Q+HR} = k_{11}[He] + k_{12Q}[CH_2CO] + k_i^Q[HR]_i$. More details of the analysis can be found in [6b]. The results are given in Table 1 and Figure 2. At room temperature the branching ratios k_{iD}/k_{iQ} were found to be for

CH_4	$k_{1D}/k_{1Q} = 0.17 \pm 0.05$
C_2H_6	$k_{2D}/k_{2Q} = 0.19 \pm 0.05$
C_3H_8	$k_{3D}/k_{3Q} = 0.24 \pm 0.07$
$i\text{-}C_4H_{10}$	$k_{5D}/k_{5Q} = 0.28 \pm 0.08$
C_2H_4	$k_{7D}/k_{7Q} = 0.12 \pm 0.06$

3.2 Discussion

The experimental data proove that intersystem crossing is only a minor channel in the removal of $^1CH_2$ by hydrocarbons, as has been suggested earlier [4,5]. The exact results depend somewhat on the quantum yield ϕ_3 for direct formation of $^3CH_2$ at λ = 308 nm. The data for C_2H_4 set an upper limit of $\phi_3 < 0.12$. In case that $0 < \phi_3 < 0.12$ the present branching ratios would have to be considered as upper limits.

Figure 3 shows a semilogarithmic plot of the cross sections for collision induced intersystem crossing as a function of the reduced Lennard-Jones energy well depths for a variety of collision partners. Within experimental error the present data fit well into the correlation.

4. Reactions of $^3CH_2$ with Saturated Molecules

4.1 Results

The rate constants for reactions of $^3CH_2$ with saturated hydrocarbons HR

$$^3CH_2 + HP \longrightarrow CH_3 + R \qquad (1T)-(6T)$$

were measured between 296 K $\leq$ T $\leq$ 705 K by monitoring the decay of $^3CH_2$ with the LMR under pseudo first order conditions with HR present in large excess. The experimental data have been given in [6a,6c] and are summarized in Tables 2-7. In Figure 4 the measured rate constants are plotted in Arrhenius form. The data are decribed by the following experimental rate expressions

CH_4	$k_{exp} = 10^{(13.1 \pm 0.7)}$	$\exp(-4800\pm1000\ K/T)\ cm^3/mol\ s$
C_2H_6	$k_{exp} = 10^{(13.34\pm0.37)}$	$\exp(-4360\pm 500\ K/T)\ cm^3/mol\ s$
C_3H_8	$k_{exp} = 10^{(13.11\pm0.31)}$	$\exp(-3650\pm 380\ K/T)\ cm^3/mol\ s$
$n\text{-}C_6H_{14}$	$k_{exp} = 10^{(13.22\pm0.20)}$	$\exp(-3380\pm 240\ K/T)\ cm^3/mol\ s$

$i\text{-}C_4H_{10}$ $k_{exp} = 10^{(12.84\pm0.18)} \exp(-3090\pm 210\ K/T)\ cm^3/mol\ s$
CH_3CHO $k_{exp} = 10^{(12.40\pm0.18)} \exp(-1910\pm 180)K/T)\ cm^3/mol\ s$

4.2 Discussion

The reactions of $^3CH_2$ with HR may proceed via two different pathways. The direct reaction of $^3CH_2$ with HR is generally accepted to proceed via abstraction of an H-atom. A second pathway is opened by thermal excitation of $^3CH_2$ to $^1CH_2$ in collisions with He, CH_2CO, or HR followed by rapid consecutive reactions of $^1CH_2$

$$^3CH_2 + HR \longrightarrow CH_3 + R \qquad (T)$$
$$^3CH_2 + M \longrightarrow {}^1CH_2 + M \qquad (E)$$
$$^1CH_2 + M \longrightarrow {}^3CH_2 + M \qquad (D)$$
$$^1CH_2 + HR \longrightarrow \text{products} \qquad (S)$$

With the rate constants for intersystem crossing of $^1CH_2$ obtained in section 3 and [4,5] and the thermodynamic equilibrium constant K_{ST} for $^3CH_2 \rightleftharpoons {}^1CH_2$ the rate constants for consumption of $^3CH_2$ via the $^1CH_2$ pathway (E, D, S) are calculated to be

$$k_{iSeff} = K_{ST}\ k_{iS}/(1+k_{1S}[HR]/k'_D) \qquad (II)$$

with i=1-6, $k'_D = k_{iD}[HR]_i + k_{11}[He] + k_{12D}[CH_2CO]$. The experimentally measured rate constants are given by the sums

$$k_{iTexp} = k_{iT} + k_{iSeff} \qquad (III)$$

Correcting all data points for reactions (2T)-(6T) the Arrhenius parameters for direct H-abstraction by $^3CH_2$ were obtained to be

C_2H_6 $k_{2T} = 10^{(12.81\pm0.61)} \exp(-3980\pm 840\ K/T)\ cm^3/mol\ s$
C_3H_8 $k_{3T} = 10^{(12.69\pm0.38)} \exp(-3330\pm 460\ K/T)\ cm^3/mol\ s$
$n\text{-}C_6H_{14}$ $k_{4T} = 10^{(12.89\pm0.24)} \exp(-3080\pm 280\ K/T)\ cm^3/mol\ s$
$i\text{-}C_4H_{10}$ $k_{5T} = 10^{(12.40\pm0.14)} \exp(-2710\pm 150\ K/T)\ cm^3/mol\ s$
CH_3CHO $k_{6T} = 10^{(12.22\pm0.16)} \exp(-1760\pm 160\ K/T)\ cm^3/mol\ s$

In the hydrocarbons studied, H-abstraction is possible from a C-H bond in methane as well as from primary, secondary, tertiary, or aldehydic sites. The data given above can be used to obtain Arrhenius parameters per C-H bond (in units of cm^3/mol s):

$k_M = 1.1\ 10^{12} \exp(-42\ \text{kJ mol}^{-1}/RT)$ $\Delta H_{R_0}^0{}_{298} = -\ 21$ kJ/mol
$k_P = 1.08\ 10^{12} \exp(-33\ \text{kJ mol}^{-1}/RT)$ $\Delta H_{R_0}^0{}_{298} = -\ 49$ kJ/mol
$k_S = 1.03\ 10^{12} \exp(-26\ \text{kJ mol}^{-1}/RT)$ $\Delta H_{R_0}^0{}_{298} = -\ 62$ kJ/mol
$k_T = 1.09\ 10^{12} \exp(-20.5\ \text{kJ mol}^{-1}/RT)$ $\Delta H_{R_0}^0{}_{298} = -\ 71$ kJ/mol
$k_A = 1.08\ 10^{12} \exp(-13.2\ \text{kJ mol}^{-1}/RT)$ $\Delta H_{R}^0{}_{298} = -\ 100$ kJ/mol

The C-H bond strength in the reactants studied varies over a wide range. In Figure 5 the activation energies are plotted as a function of the C-H bond dissociation energies. The data points are described by a linear Evans-Polanyi relation $E_A = 0.406\ (D_{C-H} - 336$ kJ/mol). The correlation and the per bond Arrhenius expressions will enable the estimation of rate parameters for H-abstraction from other reactants, e.g. H_2, C_2H_4, C_2H_2, or other unsaturated hydrocarbons.

The measured activation energy for reaction (1) is much lower than the value expected from the Evans-Polanyi plot. For CH_4 the $^3CH_2$ consumption pathway via thermal excitation to $^1CH_2$ always dominates the reaction system. Hence, the measured activation energy $E_A(1) = 40$ kJ/mol is equal to the singlet triplet splitting in CH_2. The value is in good agreement with the more precise spectroscopic results [12].

Kinetic measurements for H-abstraction reactions by $^3CH_2$ have not been reported before. However, the rate parameters obtained here can be compared to those of the isoelectronic reactions of $O(^3P)$ [13]. On the average, the activation energies for $^3CH_2$ are about 7 kJ/mol higher than for O. This contrasts with the much higher bond energies in CH_3 than in OH. The preexponential factors for $^3CH_2$ are lower by a factor of 5 - 15 reflecting the higher steric requirements. Earlier BEBO estimates for activation energies of

$^3CH_2$ reactions [14] are in marked disagreement with the experimental data largely because of the set of BEBO parameters used. Partly in order to throw some light on the discrepancies, partly in an attempt to obtain more insight into the trends observed and the analogies between $^3CH_2$ and O, the Arrhenius parameters for H-abstraction were evaluated using semi-empirical transition state theory as described in [15-17]. The results have been given in [6d] and are summarized in Tables 8-9. The calculations are in general agreement with the experimental data and the various trends observed are well represented by the modells. However, the calculated absolute values should be treated with caution because of the numerous approximations involved.

5. Reactions of $^3CH_2$ with C_2H_4 and C_2H_2

5.1 Results

The rate constants for reactions of $^3CH_2$ with C_2H_4 and C_2H_2

$$^3CH_2 + C_2H_4 \quad ---> \quad \text{products} \qquad (7T)$$
$$^3CH_2 + C_2H_2 \quad ---> \quad \text{products} \qquad (8T)$$

were measured under pseudo first order conditions between 296 K $\leq$ T $\leq$ 728 K using both reactions (9) and (10) as CH_2 sources. The experimental results are compiled in Tables (10)-(11) and are illustrated in Figure 6. The points are described by the experimental Arrhenius expressions

$$C_2H_4 \quad k_{exp} = 10^{(12.69\pm0.12)} \exp(-2810\pm140 \text{ K/T}) \text{ cm}^3/\text{mol s}$$
$$C_2H_2 \quad k_{exp} = 10^{(13.42\pm0.13)} \exp(-3620\pm140 \text{ K/T}) \text{ cm}^3/\text{mol s}$$

5.2 Discussion

The rate expression for the direct reaction of $^3CH_2$ with C_2H_4 (7T) excluding the pathway via thermal excitation to $^1CH_2$ was evaluated to be

C_2H_4 $k_{7T} = 10^{(12.50\pm0.10)} \exp(-2660\pm110\ K/T)\ cm^3/mol\ s.$

The direct reaction of $^3CH_2$ with C_2H_4 proceeds via addition yielding a highly energized triplet trimethylene intermediate which may either be collisionally stabilized to cyclopropene, isomerize to propylene or, at the low pressures used here, dissociate to fragments H + allyl [18-20]. Redissociation of the excited trimethylene addition complex to reactants is concluded to be negligible, since the rate constants were found to be pressure independent and no CH_2-radicals could be detected as products of the reaction $^3CD_2 + C_2H_4 \rightarrow {}^3CH_2 + CH_2CD_2$ ($\Delta H_R{}^0{}_{298} = -4$ kJ/mol). A further investigation of the mechanism and products of reaction (1T) using unimolecular rate theory is underway [6e].

An evaluation of the rate constant for the direct reaction of $^3CH_2$ with C_2H_2 from the experimental data has to await future studies of the deactivation of $^1CH_2$ by C_2H_2 [6e]. The reaction proceeds via an addition complex yielding propyne and allene as stabilized products or, at low pressures, H + C_3H_3.

References

[1] M. Jones and R.A. Moss, Carbenes, Vol. 1-2, New York, 1975.
[2] P.P. Gaspar and G.S. Hammond, in Ref [1], pp 207.
[3] A.H. Lauffer, Rev. Chem. Intermediates 4, 225 (1981).
[4] M.N.R. Ashfold, M.A. Fullstone, G. Hancock, and G.W. Ketley, Chem. Phys. 55, 245 (1981)
[5] A.O. Langford, H. Petek, and C.B Moore, J. Chem. Phys. 78, 6650 (1983).
[6] S. Dobe, T. Bohland, F. Temps, and H.Gg. Wagner, Ber. Bunsenges. Phys. Chem. 89, 432 (1985);
--, --, 89, 000 (~ 9/1985);
--, --, 89, 000 (~ 11/1985);
--, Max-Planck-Institut fur Stromungsforschung, Report 11/1985;
--, to be published.
[7] T. Bohland, F. Temps, and H. Gg. Wagner, Zeitschr. Physik. Chemie, in press.
[8] T. Sears, P.R. Bunker, A.R.W. McKellar, K.M. Evenson, D.A. Jennings, and J.M. Brown, J. Chem. Phys. 77, 5348 (1982).
[9] N. Washida, S. Hatakeyama, H. Takagi, K. Kyogoku, and S. Sato, J. Chem. Phys. 78, 453 (1983).
[10] P.M. Kelley and W.L. Hase, Chem. Phys. Lett. 38, 171 (1976).
[11] C.C. Hayden, D.M. Neumark, K. Shobutake, R.K. Sparks, and Y.T. Lee, J. Chem. Phys. 76, 3607 (1982).
[12] A.R.W. McKellar, P.R. Bunker, T.J Sears, K.M. Evenson, R.J. Saykally, and S.R. Langhoff, J. Chem. Phys. 79, 5251 (1983); D.G. Leopold, K.K. Murray, and W.C. Lineberger, J. Chem. Phys. 81, 1048 (1984).
[13] R.E. Herron and J.T. Huie, Progr. React. Kinet. 8, 1 (1975).
[14] R.W. Carr, J. Phys. Chem. 76,1581 (1972).
[15] S.W. Benson, Thermochemical Kinetics, New York, 1976.
[16] H.S. Johnston, Gas Phase Reaction Rate Theory, New York, 1966. .
[17] M.S. Zahniser, B.M Berquist, and F. Kaufman, Int. J. Chem. Kin. 10, 15 (1978).
[18] S. Krzyzanowski and R.J. Cvetanovic, Can. J. Chem. 45, 665 (1967).
[19] F.S. Rowland, C. McKnight, and E.K.C. Lee, Ber. Bunsenges. Phys. Chem. 72, 236 (1968).
[20] R.J. Cvetanovic, H.E. Avery, and R.S. Irwin, J. Chem. Phys. 46, 1993 (1967).

Table 1: Experimental results for deactivation of $^1CH_2$ by hydrocarbons

a) form [4,5]

HR	$\bar{v}$ [m/s]	[He] [mol/cm^3]	[CH_2CO] [mol/cm^3]	$[CH_2]_o$ [mol/cm^3]	k_{iQ} a) [cm^3/mols]	k_{iD} [cm^3/mols]
CH_4	11.7	$7.0 \cdot 10^{-8}$	$6.1 \cdot 10^{-10}$	$1.9 \cdot 10^{-13}$	$4.3 \cdot 10^{13}$	$0.75 \cdot 10^{13}$
C_2H_6	14.9	$5.5 \cdot 10^{-8}$	$3.0 \cdot 10^{-10}$	$0.5 \cdot 10^{-13}$	$1.1 \cdot 10^{14}$	$2.2 \cdot 10^{13}$
	25.9	$11.0 \cdot 10^{-8}$	$1.8 \cdot 10^{-10}$	$0.9 \cdot 10^{-13}$		$2.3 \cdot 10^{13}$
	11.7	$6.8 \cdot 10^{-8}$	$6.7 \cdot 10^{-10}$	$2.6 \cdot 10^{-13}$		$2.0 \cdot 10^{13}$
C_3H_8	16.1	$7.1 \cdot 10^{-8}$	$4.4 \cdot 10^{-10}$	$1.2 \cdot 10^{-13}$	$1.4 \cdot 10^{14}$	$3.3 \cdot 10^{13}$
i-C_4H_{10}	13.6	$5.6 \cdot 10^{-8}$	$4.9 \cdot 10^{-10}$	$1.6 \cdot 10^{-13}$	$1.6 \cdot 10^{14}$	$4.5 \cdot 10^{13}$
C_2H_4	13.6	$6.3 \cdot 10^{-8}$	$5.5 \cdot 10^{-10}$	$1.6 \cdot 10^{-13}$	$9.0 \cdot 10^{13}$	$1.1 \cdot 10^{13}$

Table 2: Experimental results for reaction (1T)

T [K]	p [mbar]	$\bar{v}$ [m s^{-1}]	[CH_2CO] [10^{-9} mol cm^{-3}]	$[O_2]_o$ [10^{-13} mol cm^{-3}]	[CH_4] [10^{-9} mol cm^{-3}]	$k_{2T}^{exp}[CH_4]$ [s^{-1}]	k_{2T}^{exp} [cm^3 mol^{-1} s^{-1}]
545	3.36	19.6	0.89	5.1	29.9	50	$1.7 \cdot 10^9$
625	2.00	21.4	0.63	11.5	11.3	76	$6.7 \cdot 10^9$
	2.15	22.6	0.59	11.0	16.0	107	$6.7 \cdot 10^9$
705	1.65	23.1	0.65	10.6	3.19	47	$1.5 \cdot 10^{10}$
	1.69	24.3	0.62	10.0	5.15	67	$1.3 \cdot 10^{10}$
	1.76	25.6	0.61	9.5	7.23	89	$1.2 \cdot 10^{10}$

Table 3: Experimental results for reaction (2T)

T [K]	p [mbar]	$\bar{v}$ [ms^{-1}]	$[CH_2CO]$ [10^{-9} mol cm^{-3}]	$[O_2]_o$ [10^{-13} mol cm^{-3}]	$[C_2H_6]$ [10^{-9} mol cm^{-3}]	$k_{2T}^{exp}[C_2H_6]$ [s^{-1}]	k_{2T}^{exp} [$cm^3 mol^{-1} s^{-1}$]
502	3.23	13.9	0.79	7.2	15.3	75	$4.9 \cdot 10^9$
545	2.44	14.3	0.94	3.3	6.35	45	$7.1 \cdot 10^9$
	2.51	20.6	0.60	4.8	13.3	88	$6.6 \cdot 10^9$
	2.48	23.8	0.66	4.2	18.4	110	$6.0 \cdot 10^9$
	3.52	20.4	0.69	2.3	21.5	160	$7.4 \cdot 10^9$
633	1.65	21.0	0.74	9.3	2.16	52	$2.4 \cdot 10^{10}$
	1.65	23.7	0.59	4.6	5.68	126	$2.2 \cdot 10^{10}$
	1.65	23.7	0.59	8.3	5.69	121	$2.1 \cdot 10^{10}$
	1.67	32.0	0.44	6.4	7.09	172	$2.4 \cdot 10^{10}$
	1.71	42.1	0.28	4.9	7.52	148	$2.0 \cdot 10^{10}$
693	1.40	24.0	0.48	9.4	2.09	113	$5.4 \cdot 10^{10}$
	1.56	22.8	0.55	9.9	3.67	124	$3.4 \cdot 10^{10}$
	1.52	24.9	0.45	9.0	5.04	217	$4.3 \cdot 10^{10}$

Table 4: Experimental results for reaction (3T)

T [K]	p [mbar]	$\bar{v}$ [ms^{-1}]	$[CH_2CO]$ [10^{-9} mol cm^{-3}]	$[O_2]_o$ [10^{-13} mol cm^{-3}]	$[C_3H_8]$ [10^{-9} mol cm^{-3}]	$k_{3T}^{exp}[C_3H_8]$ [s^{-1}]	k_{3T}^{exp} [$cm^3 mol^{-1} s^{-1}$]
393	3.89	8.54	1.3	12.0	17.9	35	$2.0 \cdot 10^9$
432	2.31	15.8	0.82	6.3	9.57	24	$2.5 \cdot 10^9$
	2.44	15.0	0.87	6.7	10.1	20	$2.0 \cdot 10^9$
477	2.45	16.4	0.86	6.2	9.21	60	$6.5 \cdot 10^9$
504	2.32	18.3	0.82	5.5	8.23	70	$8.5 \cdot 10^9$
	3.25	16.9	0.65	5.9	9.00	79	$8.8 \cdot 10^9$
544	2.45	13.5	1.1	7.5	2.63	38	$1.4 \cdot 10^{10}$
	2.45	14.1	1.9	8.0	4.34	74	$1.7 \cdot 10^{10}$
	2.45	17.5	0.70	5.7	7.91	129	$1.6 \cdot 10^{10}$
	3.81	23.5	0.54	4.3	12.5	183	$1.5 \cdot 10^{10}$
	2.51	23.0	0.54	4.4	15.4	173	$1.1 \cdot 10^{10}$
625	1.69	19.5	0.57	9.5	1.55	66	$4.3 \cdot 10^{10}$
635	1.73	20.1	0.55	9.3	2.71	109	$4.0 \cdot 10^{10}$
	1.71	29.2	0.41	3.3	3.11	137	$4.4 \cdot 10^{10}$
	1.71	22.8	0.49	8.1	6.65	243	$3.7 \cdot 10^{10}$
695	1.57	23.4	0.50	5.2	2.59	254	$9.8 \cdot 10^{10}$

Table 5: Experimental results for reaction (4T)

T [K]	p [mbar]	$\bar{v}$ [ms^{-1}]	$[CH_2CO]$ [10^{-9} mol cm^{-3}]	$[O_2]_o$ [10^{-13} mol cm^{-3}]	$[n\text{-}C_6H_{14}]$ [10^{-9} mol cm^{-3}]	$k_{4T}^{exp}[nC_6H_{14}]$ [s^{-1}]	k_{4T}^{exp} [$cm^3 mol^{-1} s^{-1}$]
413	2.51	18.2	0.63	6.3	8.89	45	$5.1 \cdot 10^9$
413	2.16	16.2	0.90	7.5	14.5	59	$4.1 \cdot 10^9$
413	1.67	27.8	0.51	4.4	21.4	105	$4.9 \cdot 10^9$
520	2.24	41.1	0.35	2.4	1.85	46	$2.5 \cdot 10^{10}$
527	2.63	17.9	0.53	6.8	3.46	96	$2.8 \cdot 10^{10}$
527	3.05	19.9	0.48	6.1	5.26	153	$2.9 \cdot 10^{10}$
527	2.35	44.1	0.21	2.8	6.59	161	$2.4 \cdot 10^{10}$
535	2.59	17.9	0.53	6.8	2.15	83	$3.9 \cdot 10^{10}$
633	2.51	15.0	0.71	18.0	2.30	144	$6.3 \cdot 10^{10}$
633	1.93	22.0	0.47	12.2	2.89	211	$7.3 \cdot 10^{10}$
707	2.09	25.0	0.62	11.0	0.94	145	$1.5 \cdot 10^{11}$
707	2.11	23.7	0.66	11.9	1.30	205	$1.6 \cdot 10^{11}$

Table 7: Experimental results for reaction (6T)

T [K]	p [mbar]	$\bar{v}$ [ms^{-1}]	$[CH_2CO]$ [10^{-9} mol cm^{-3}]	$[O_2]_o$ [10^{-13} mol cm^{-3}]	$[CH_3CHO]$ [10^{-9} mol cm^{-3}]	$k_{6T}^{exp}[CH_3CHO]$ [s^{-1}]	k_{6T}^{exp} [$cm^3 mol^{-1} s^{-1}$]
296	2.41	9.37	1.7	11.0	4.3	24	$5.6 \cdot 10^9$
335	2.41	10.6	1.2	9.6	4.5	48	$1.1 \cdot 10^{10}$
373	2.44	17.2	0.72	5.8	1.1	19	$1.7 \cdot 10^{10}$
	2.45	17.3	0.71	5.7	2.4	35	$1.5 \cdot 10^{10}$
	3.87	11.0	1.1	9.0	2.5	33	$1.3 \cdot 10^{10}$
	2.49	13.0	8.9	7.6	3.0	42	$1.4 \cdot 10^{10}$
	3.93	13.0	0.95	7.6	4.4	62	$1.4 \cdot 10^{10}$
431	2.45	15.3	0.76	6.5	2.4	60	$2.5 \cdot 10^{10}$
471	4.15	8.20	1.4	12.0	0.65	23	$3.5 \cdot 10^{10}$
	2.49	25.7	0.52	3.9	1.1	36	$3.3 \cdot 10^{10}$
	4.17	12.7	0.97	7.8	1.1	47	$4.3 \cdot 10^{10}$
	3.59	14.8	0.83	6.7	1.7	65	$3.8 \cdot 10^{10}$
	2.48	16.5	0.74	6.0	2.3	80	$3.5 \cdot 10^{10}$
	2.91	18.5	0.67	5.4	2.7	105	$3.9 \cdot 10^{10}$
	2.89	18.6	0.67	5.4	3.3	127	$3.8 \cdot 10^{10}$
632	1.80	25.4	0.52	9.5	0.27	49	$1.8 \cdot 10^{11}$
	1.68	19.7	0.74	12.0	0.35	52	$1.5 \cdot 10^{11}$
	1.68	29.0	0.54	8.4	0.61	79	$1.3 \cdot 10^{11}$
	2.19	22.0	0.66	11.0	0.74	99	$1.3 \cdot 10^{11}$
	1.80	26.4	0.50	9.2	1.6	253	$1.6 \cdot 10^{11}$

Table 6: Experimental results for reaction (5T)

T [K]	p [mbar]	$\bar{v}$ [$m\,s^{-1}$]	$[CH_2CO]$ [10^{-9} mol cm^{-3}]	$[O_2]_o$ [10^{-13} mol cm^{-3}]	$[i\text{-}C_4H_{10}]$ [10^{-9} mol cm^{-3}]	$k_{5T}^{exp}[i\text{-}C_4H_{10}]$ [s^{-1}]	k_{5T} [$cm^3\,mol^{-1}\,s^{-1}$]
296	2.78	11.1	1.3	12.0	13.1	3	$2.3 \cdot 10^8$
	2.78	11.1	1.3	12.0	21.3	7	$3.3 \cdot 10^8$
375	2.39	12.6	1.2	8.3	8.69	21	$2.4 \cdot 10^9$
	2.39	14.2	1.0	7.1	16.4	33	$2.0 \cdot 10^9$
394	2.44	14.7	1.1	6.8	15.9	45	$2.8 \cdot 10^9$
429	2.36	14.7	1.3	6.2	7.47	37	$5.0 \cdot 10^9$
472	2.39	15.5	1.2	6.4	5.47	56	$1.0 \cdot 10^{10}$
	2.37	15.9	0.80	5.5	6.85	64	$0.93 \cdot 10^{10}$
	2.43	15.6	1.2	6.4	7.00	79	$1.1 \cdot 10^{10}$
	2.57	15.2	0.93	6.5	9.48	69	$0.73 \cdot 10^{10}$
	2.31	17.7	0.80	5.5	10.6	114	$1.1 \cdot 10^{10}$
	2.44	16.6	0.86	6.0	10.8	106	$0.98 \cdot 10^{10}$
	2.71	15.8	0.89	6.3	15.1	120	$0.79 \cdot 10^{10}$
503	2.50	16.3	0.89	6.1	6.70	75	$1.1 \cdot 10^{10}$
544	2.44	13.2	1.0	7.5	2.73	67	$2.5 \cdot 10^{10}$
	2.49	20.2	0.60	6.9	5.96	129	$2.2 \cdot 10^{10}$
	2.48	22.9	0.58	4.3	7.38	119	$1.6 \cdot 10^{10}$
	2.73	24.9	0.55	4.0	9.36	186	$2.0 \cdot 10^{10}$
556	2.39	13.7	1.0	7.4	1.94	57	$2.9 \cdot 10^{10}$
	2.43	17.9	0.72	5.6	2.86	84	$2.9 \cdot 10^{10}$
	2.36	19.4	0.54	5.2	5.52	158	$2.9 \cdot 10^{10}$
634	1.65	28.3	0.38	3.6	1.28	79	$6.2 \cdot 10^{10}$
	1.60	30.5	0.35	3.3	2.37	141	$5.9 \cdot 10^{10}$
	1.67	40.7	0.46	2.5	2.94	151	$5.1 \cdot 10^{10}$
	1.69	42.9	0.34	2.4	5.03	219	$4.4 \cdot 10^{10}$
	2.08	42.0	0.30	2.4	5.15	336	$6.5 \cdot 10^{10}$
698	1.52	24.1	0.67	10.0	2.00	210	$1.0 \cdot 10^{11}$

Table 8: Comparison of calculated and experimental preexponential factors

R-H	$\Delta S^{\neq}_{300}$ [J/mol K]	$\langle C_p^{\neq} \rangle$ [J/mol K]	A_{calc}(500 K) [cm^3/mol s]	A_{exp} [cm^3/mol s]
CH_3-H	- 113	3.3	$4.9\ 10^{12}$	$4.4\ 10^{12}$
C_2H_5-H	- 114	6.4	$5.5\ 10^{12}$	$6.5\ 10^{12}$
$(CH_3)_2CH$-H	- 124	8.8	$2.1\ 10^{12}$	$2.1\ 10^{12}$
$(CH_3)_3C$-H	- 132	12	$0.9\ 10^{12}$	$1.1\ 10^{12}$

Table 9: Results of BEBO calculations

a) values in parentheses are for $O(^3P)$

R-H	$n^{\neq}_{C-H}$	$\Delta E_0^{0\neq}$(calc) a) [kJ/mol]	E_A(exp) a) [kJ/mol]
CH_3-H	0.57 (0.45)	44 (40)	42 (38)
C_2H_5-H	0.66 (0.58)	30 (24)	33 (24)
$(CH_3)_2CH$-H	0.69 (0.64)	26 (18)	26 (19)
$(CH_3)_3C$-H	0.72 (0.67)	19 (14)	21 (140

Table 10: Experimental results for reaction (7T)

T [K]	p [mbar]	$\bar{v}$ [ms^{-1}]	$[CH_2CO]$ [10^{-10} $molcm^{-3}$]	$[O_2]_o$ a) [10^{-12} $molcm^{-3}$]	$[C_2H_4]$ [10^{-9} $molcm^{-3}$]	$k_{7T}^{exp} \cdot [C_2H_4]$ b) [s^{-1}]	k_{7T}^{exp} c) [$cm^3 mol^{-1} s^{-1}$]
296	2.31	5.5	20.9	2.3	23.2	8	$3.5 \cdot 10^8$
	2.32	10.8	14.3	1.7	23.5	10	$4.3 \cdot 10^8$
385	2.39	13.6	8.5	2.2	9.39	34	$3.6 \cdot 10^9$
	2.33	14.6	9.7	2.0	12.3	43	$3.5 \cdot 10^9$
	2.48	15.3	9.3	2.0	21.1	75	$3.6 \cdot 10^9$
397	1.93	35.9	1.4	-	15.0	62	$4.1 \cdot 10^9$
	3.35	18.0	2.8	-	27.0	112	$4.1 \cdot 10^9$
434	3.01	26.7	2.3	-	20.3	148	$7.3 \cdot 10^9$
511	1.67	41.1	1.3	-	8.34	118	$1.4 \cdot 10^{10}$
535	1.97	47.0	3.5	0.60	3.74	95	$2.5 \cdot 10^{10}$
	7.52	15.2	7.6	2.0	4.63	142	$3.1 \cdot 10^{10}$
	0.48	14.2	9.8	2.1	4.68	109	$2.3 \cdot 10^{10}$
	3.52	15.2	8.3	1.9	5.27	152	$2.9 \cdot 10^{10}$
	0.92	16.5	11.6	2.0	5.46	107	$2.0 \cdot 10^{10}$
	1.79	14.9	10.9	1.9	5.47	140	$2.6 \cdot 10^{10}$
	1.81	22.2	7.3	1.3	5.73	167	$2.9 \cdot 10^{10}$
	0.48	16.1	8.6	1.9	6.05	138	$2.3 \cdot 10^{10}$
	0.92	14.9	11.1	2.0	7.10	145	$2.0 \cdot 10^{10}$
	0.92	15.9	9.9	1.9	8.17	161	$2.0 \cdot 10^{10}$
	3.52	15.4	7.3	1.8	10.4	243	$2.3 \cdot 10^{10}$
601	2.24	52.5	1.5	-	4.86	173	$3.6 \cdot 10^{10}$
618	2.60	46.0	1.7	-	6.74	298	$4.4 \cdot 10^{10}$
660	2.19	22.5	6.3	1.3	2.03	174	$8.6 \cdot 10^{10}$
689	3.11	21.9	7.7	1.4	1.18	150	$1.3 \cdot 10^{11}$
	3.12	22.0	7.7	1.4	1.73	186	$1.1 \cdot 10^{11}$
728	2.21	59.3	1.3	-	1.82	194	$1.1 \cdot 10^{11}$
	1.93	54.4	1.4	-	3.36	338	$1.0 \cdot 10^{11}$

a) For data points with $[O_2]_o = 0$ $^3CH_2$ was generated by photolysis of CH_2CO;

Table 11: Experimental results for reaction (8T)

T [K]	p [mbar]	$\bar{v}$ [ms^{-1}]	$[CH_2CO]$ [10^{-10} mol cm^{-3}]	$[O_2]_o$ [a)] [10^{-12} mol cm^{-3}]	$[C_2H_2]$ [10^{-9} mol cm^{-3}]	$k_{8T}^{exp} \cdot [C_2H_2]$ [s^{-1}]	k_{8T}^{exp} [$cm^3 mol^{-1} s^{-1}$]
347	2.35	24.1	5.5	2.4	22.4	11	$9.8 \cdot 10^8$
397	2.07	18.9	9.5	3.2	11.2	38	$3.4 \cdot 10^9$
	3.15	14.8	11.0	4.2	22.2	63	$2.8 \cdot 10^9$
	3.05	18.0	2.4	-	24.2	60	$2.5 \cdot 10^9$
	3.48	16.9	2.6	-	31.2	88	$2.8 \cdot 10^9$
	2.92	14.3	11.1	4.3	37.1	101	$2.7 \cdot 10^9$
456	2.52	34.1	0.5	-	12.5	101	$8.1 \cdot 10^9$
465	2.71	19.8	2.2	-	1.37	13	$0.95 \cdot 10^{10}$
	2.91	21.9	2.0	-	2.49	28	$1.1 \cdot 10^{10}$
	2.89	22.8	3.4	-	3.91	45	$1.2 \cdot 10^{10}$
	3.28	21.7	3.6	-	13.6	126	$0.93 \cdot 10^{10}$
	3.20	23.8	1.9	-	20.4	198	$0.97 \cdot 10^{10}$
542	2.48	21.0	1.9	-	2.26	79	$3.5 \cdot 10^{10}$
	2.37	23.0	7.4	2.6	2.67	94	$3.5 \cdot 10^{10}$
	2.07	24.2	7.0	2.5	4.71	165	$3.5 \cdot 10^{10}$
	2.11	24.4	6.9	2.5	6.83	233	$3.4 \cdot 10^{10}$
	3.41	31.2	1.3	-	10.8	362	$3.4 \cdot 10^{10}$
699	1.83	32.0	5.4	1.8	1.08	173	$1.6 \cdot 10^{11}$
	1.89	33.2	7.2	1.7	1.98	291	$1.5 \cdot 10^{11}$

a) For data points with $[O_2]_o = 0$ $^3CH_2$ was generated by photolysis of CH_2CO

FIGURE 1 : EXPERIMENTAL SET-UP

AL: ALUMINIUM RODS; CO_2: CO_2 LASER PUMP BEAM; CT: GOLD COATED COPPER TUBE; DI: DISCHARGE; DP: DIAPHRAGM; EL: EXCIPLEX LASER BEAM; FIR: FIR OUTPUT BEAM; FR: FLOW REACTOR; H_0: DIRECTION OF MAGNETIC FIELD; IS: IRIS; LMR: LMR ABSORPTION VOLUME; M1: FIR LASER MIRROR; M2: FIR LASER MIRROR; MC: MODULATION COIL; MP: MOVEABLE PROBE; OC: OUTPUT COUPLER; PC: PHOTOLYSIS CELL; QT: QUARTZ TUBE; RA: RESONANCE ABSORPTION CELL; VUV: VUV RADIATION TO MONOCHROMATOR.

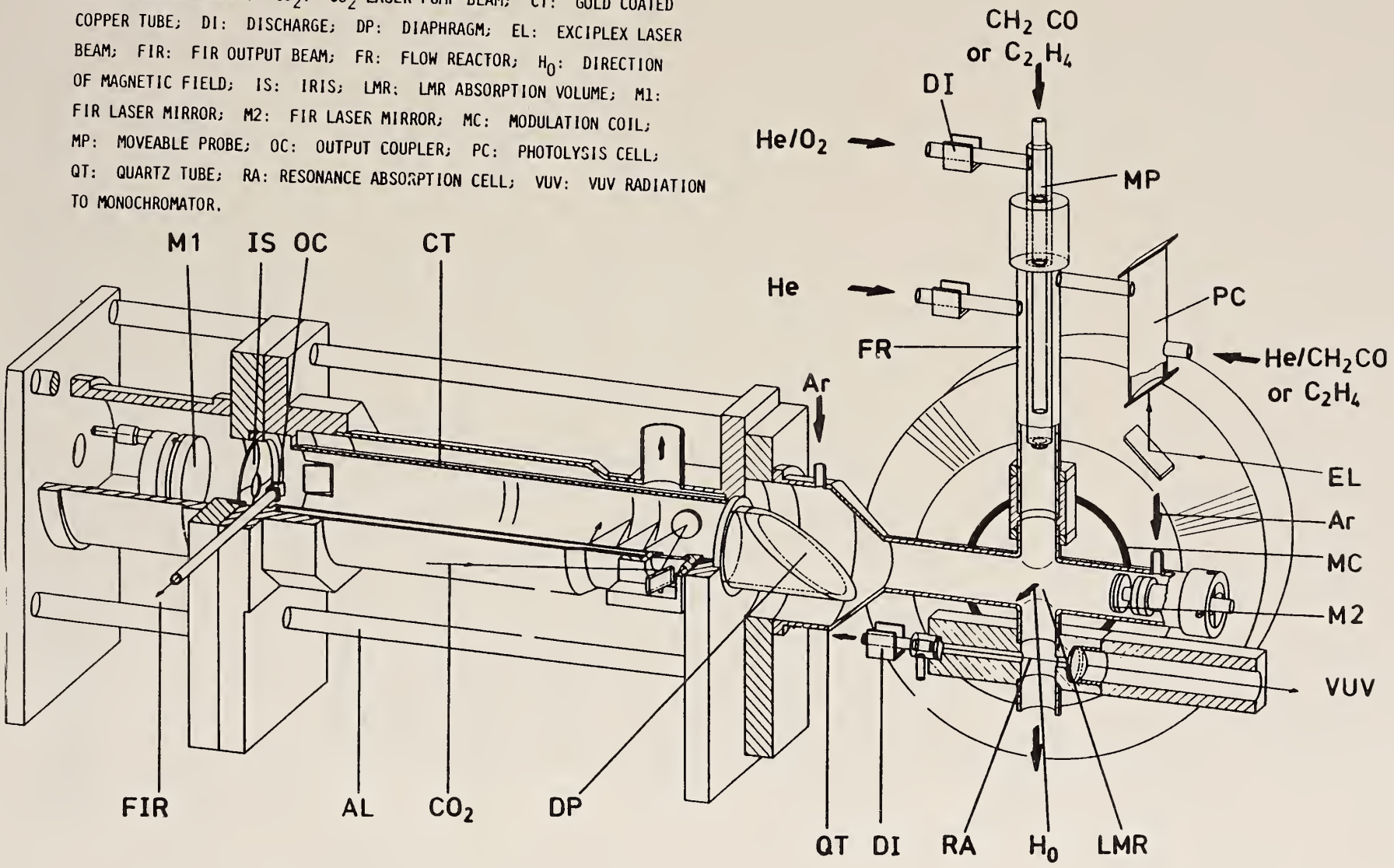

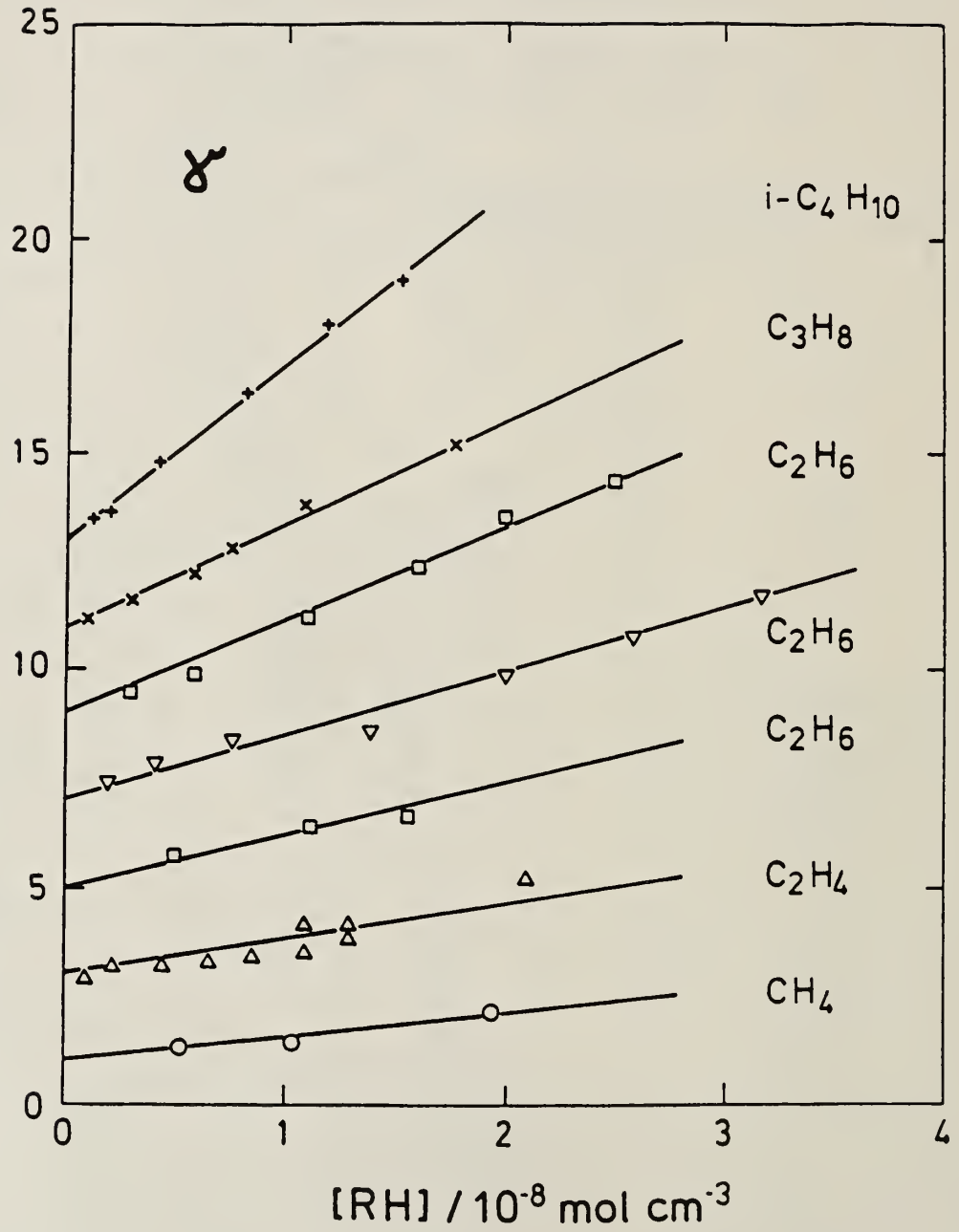

Figure 2: Plot of the ratio γ as function of [HR]

For clarity, tha data corresponding to different runs have been displaced by 0, 2, 4, ...

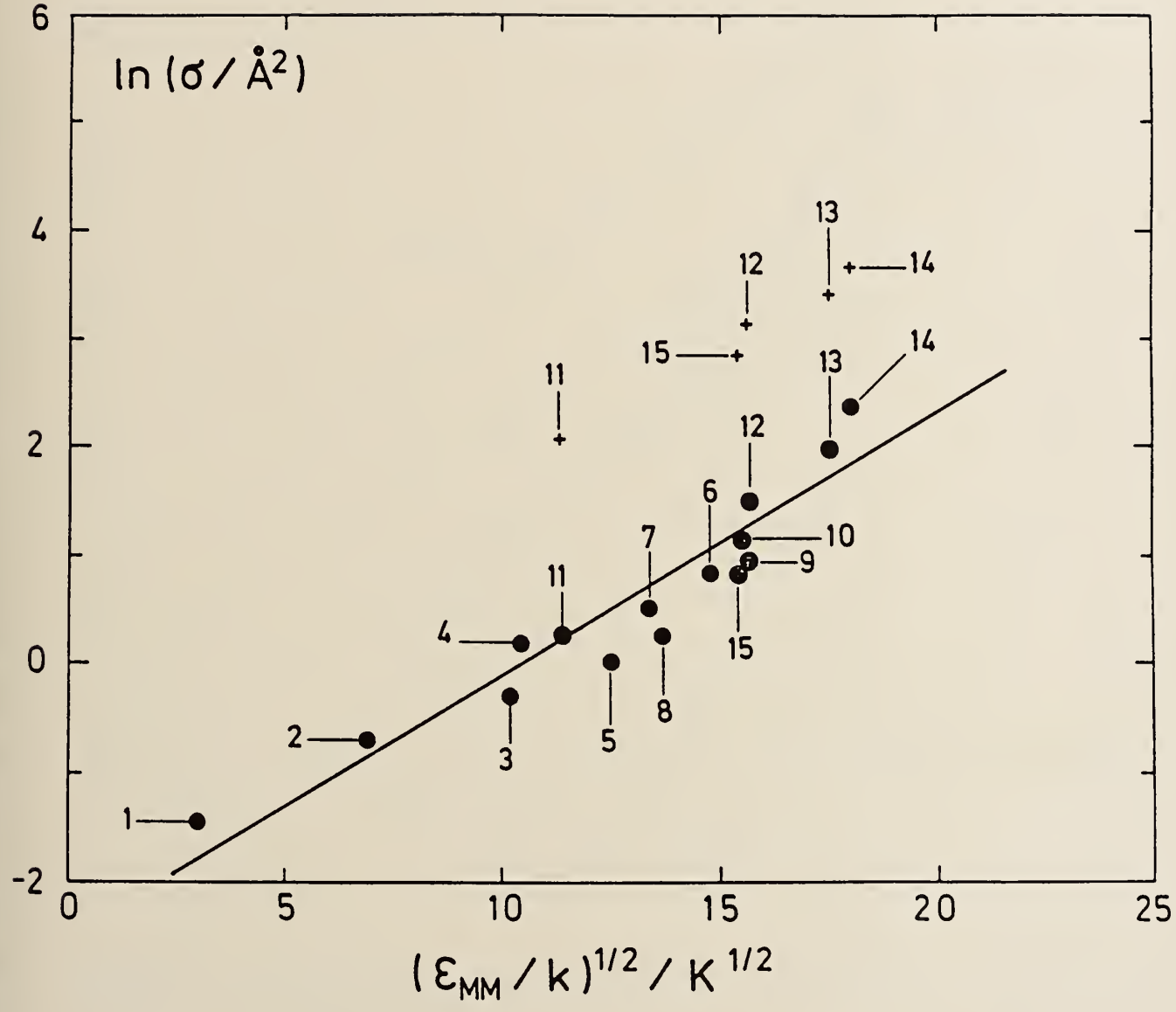

Figure 3: Parmenter-Seaver correlation for deactivation of $^1CH_2$

+ overall removal of $^1CH_2$ by HR
● intersystem crossing channels only
1: He, 2: Ne, 3: Ar, 4: N_2, 5: Kr, 6: Xe, 7: CF_4, 8: SF_6, 9: N_2O, 10: C_2F_6, 11:CH_4, 12: C_2H_6, 13: $^2C_3H_8$, 14: $i\text{-}C_4H_{10}$, 15: C_2H_4
for references see [4,5] and [6b]

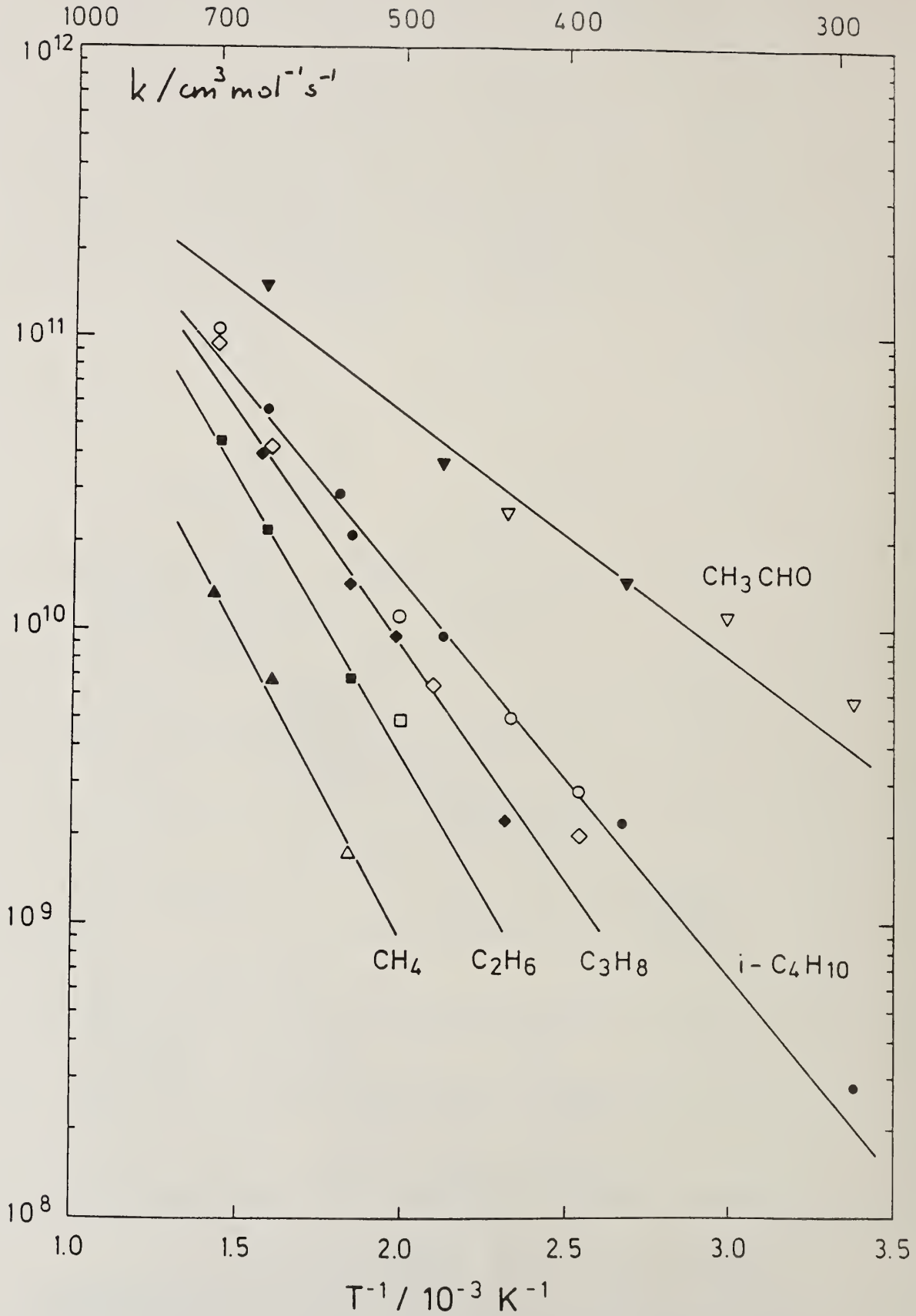

Figure 4: Experimental Arrhenius plots for reactions (1T)-(6T) For clarity, the points for reaction (4T) are omitted.

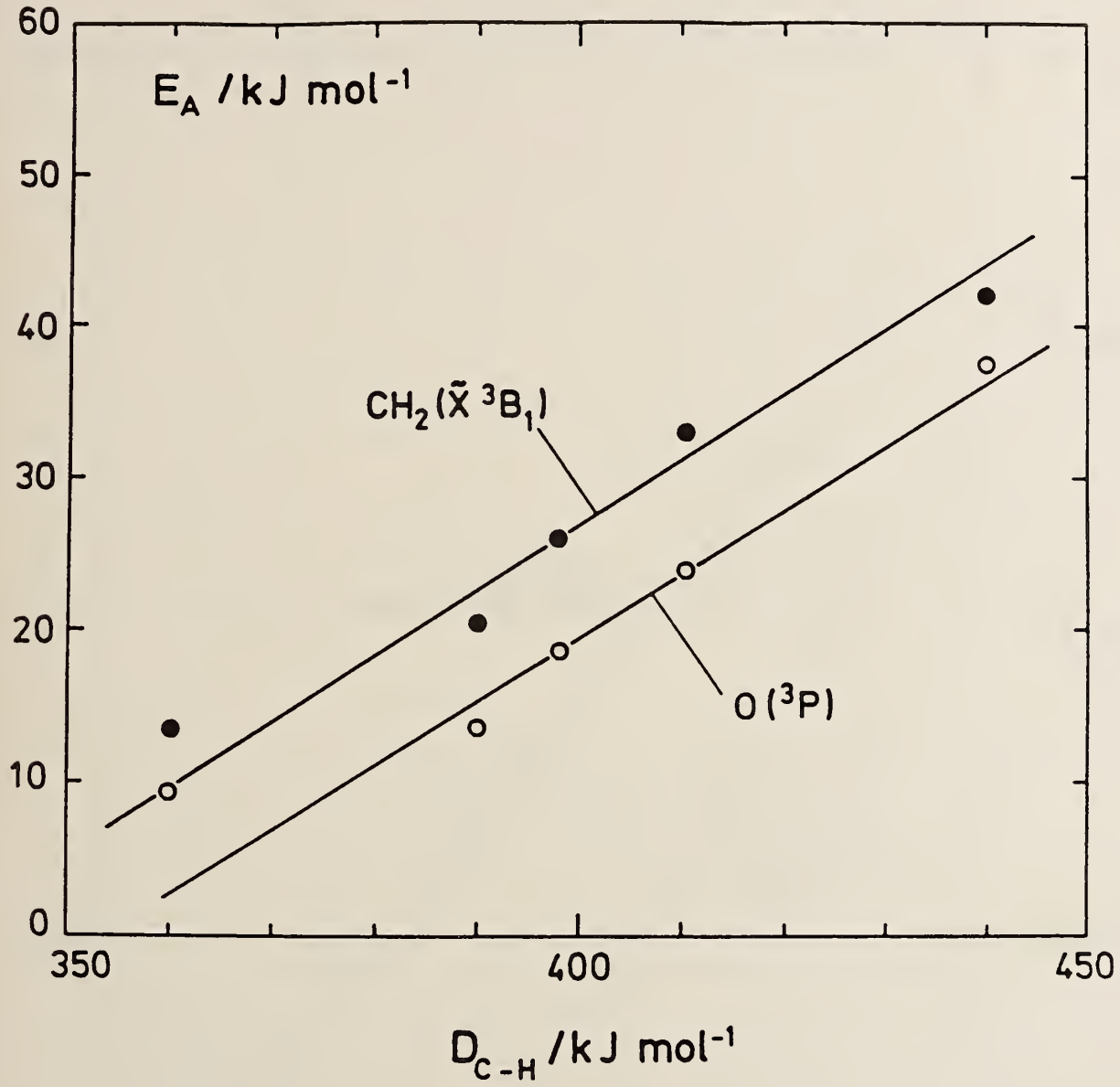

Figure 5: Evans-Polanyi correlation for H-abstraction by $^3CH_2$ and O(^{3}P)

Data for O from [13]

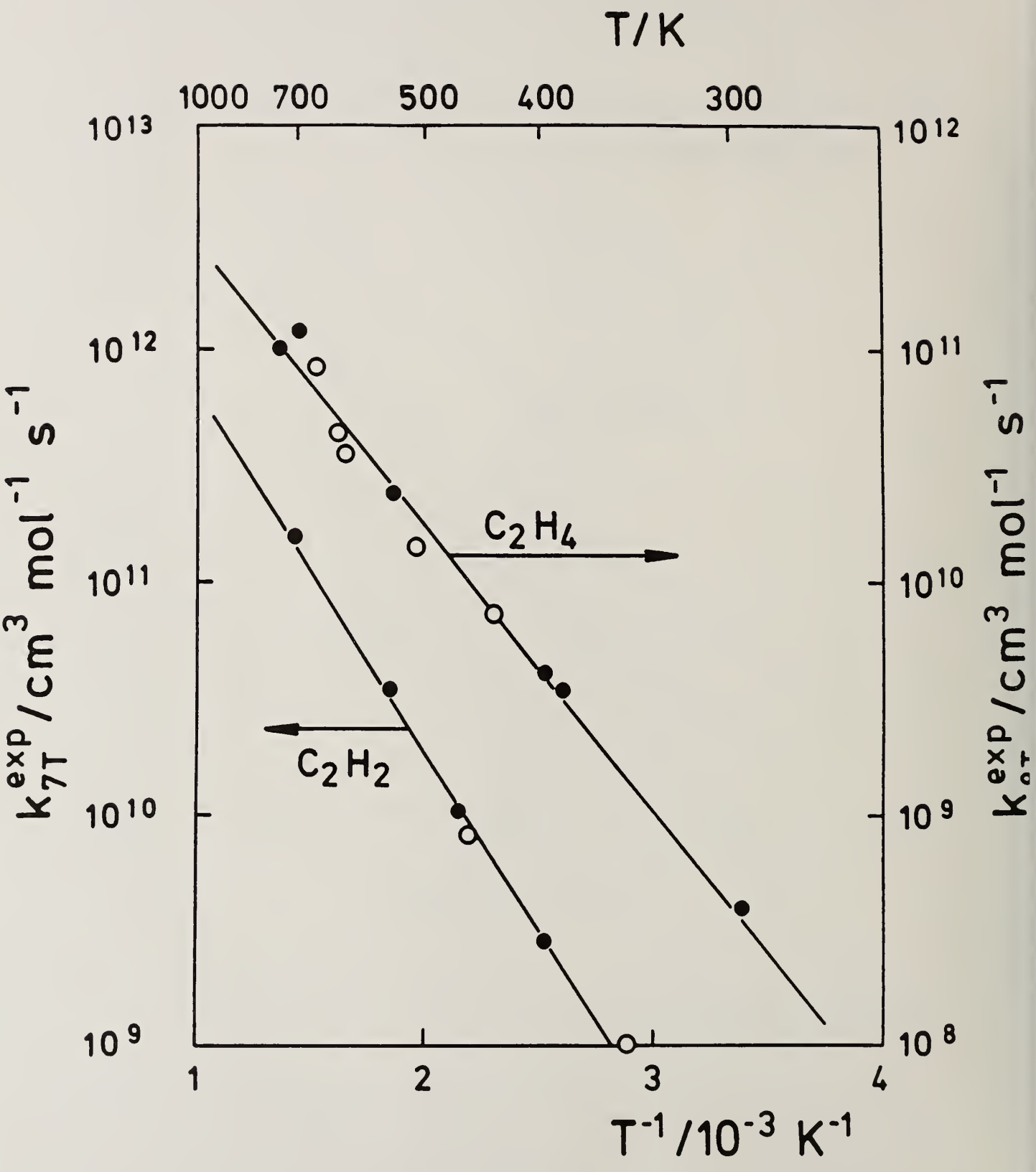

Figure 6: Experimental Arrhenius plots for reactions (7T) and (8T)

Vibration Rotation Spectroscopy of Open-Shell Molecular Ions. Faraday-LMR of DCl^+ in a DC-Discharge

W.Bohle, J.Werner, D.Zeitz, A.Hinz, W.Urban
Institut für Angewandte Physik, Universität Bonn
Wegelerstr. 8, D-5300 Bonn 1

Abstract

We report rotationally resolved vibrational spectra of the DCl^+ molecular ion for v=1 - 0 to v=6 - 5 with a Faraday LMR spectrometer. The ions were generated in a DC-excited discharge of the anomalous type. A small probe modulation coil allowsd spatial resolution of the concentration profile along the discharge. Comparisons of such profiles between anomalous and normal discharge conditions are presented. Spectroscopic constants for DCl^+ up to v=6 are reported. We also suggest a model for the strongly nonthermal distribution of vibrational excitation.

Introduction

In recent years vibration rotation spectra of numerous closed shell molecular ions have been observed particualarly by velocity modulation techniques /1/. Normally LMR spectroscopy provides the sensitivity for open shell species, but no positive results have been obtained in the mid infrared with the commonly employed intracivitiy LMR technique. This may be due to the fact that this technique has poor sensitivity for detecting species inside an electric discharge. This seems to be confirmed by the relatively poor signal to noise ratio obtained for pure rotational spectra of HBr^+ and HCl^+ and most recently HF^+ using the intrinsically more sensitive FIR-LMR intracavity spectroscopy /2,3,4/. A variation of the LMR-technique has been developed in our group /5/, that does not suffer to the same extend from modulation pickup via the discharge plasma as the intracavity arrangement /6/. This extracavity Faraday-LMR provides the means for detection of open

shell molecular ions in the medium IR with fairly good signal to noise ratio /7,8/ and produced the only positive results in the mid infrared for open shell mulecular ions, until recently the vibrational spectrum of CO_2^+ was obtained by diode laser spectroscopy using concentration modulation /9/.

Our preliminary results were reported in /8/. We have improved the ion generation and are able now to detect quite an unexpected variety of hot band transitions.

Experimental arrangement

The experiments have been performed with an extracavity Faraday-LMR system (Fig.1). The details of the experimental setup based on a superconductive solenoid with a maximum field of 3.1 Tesla, have been described elsewhere /7/ and will not be repeated here.

In the experiments previously reported /7,8/, the electrodes for the longitudinal discharge were outside the solenoid and thus only part of the positive column extended into the modulation coil defining the active region.

In the present experiments, the electrodes were extended into the central region of the solenoid so that the discharge is just in the homogeneous part of the magnetic field. A total length of 30 cm is modulated. Our present experiments use single pass arrangement (Fig.1), permitting direct measurement of the Doppler shift produced by ion drift in the DC-discharge.

If we use a very short modulation coil, the signal will be proportional to the concentration of the paramagnetic species in the modulated volume, thus providing a method of monitorung the concentration profile along the discharge axis, by slipping the short coil stepwise along this axis. This technique enables us to monitor directly the spatial concentration distribution of DCl^+ under various discharge conditions. We find considerable difference between the so called anomalous discharge and the normal discharge. The HCl^+ concentration in the anomalous discharge is higher by more than one order of magnitude with

the maximum concentration occuring in the region of negative glow, which is much more extended in the anomalous discharge. Fig.2 shows the intensity distributions for three different discharge conditions. These direct observations are in perfect agreement with the indirectly deduced results of De Lucia et al. /10/ for positive ions.

There is one further observation that seems worthwhile reporting. Since we used single pass arragement, reversal of the discharge polarity should give a shift of the line positions. Our experiments show that in spite of the much better signal to noise ratio no shift was detectable in the anomalous discharge. Fig. 3a and 3b give examples for both cases, using an unshifted line of an uncharged species for reference.

The same behaviour was observed by C.Woods /11/ who noticed even a slight drift of the ions in the opposite direction which he attributed to fast electrons present in the region of the negative glow. In our experiments we did not observe this effect perhaps as a result of higher total gas pressures.

These observations give some evidence that velocity modulation is ineffective under anomalous discharge conditions. On the other hand, switching from normal to anomalous condition will result in an effective concentration modulation. This happens obviously in the case reported by Kawaguchi et al. /9/, where magnetic field modulation was used at zero external field in connection with a continuously tunable IR-laser.

This investigation of the concentration distribution in the production of open shell molecular ions has resulted in the improvement of the signal by almost two orders of magnitude compared to the results reported in the previous publication /8/.

The spectra are also somewhat sensitive to the temperature. Cooling of the discharge down to 150 K allowed a better resolution of the hyperfine splitting and gives a signal increase of

a factor of 5 compared to room temperature (Fig.4). This can be explained by the increased rotational population and narrowed line width.

Using the improved production method, we are able not only to get more precise line positions and more lines of the DCl^+ fundamental band but also to observe hot bands up to v=6-5 in the He, DCl-discharge (Fig.5a-d). Spectroscopic constants for the species $D^{35}Cl^+$ and $D^{37}Cl^+$ up to vibrational levels of v=6 could be derived and are presented in Table I.

Discussion

The non-thermal vibrational excitation raises the question of the production mechanism of DCl^+ in this system. Various experimental facts lead to the conclusion that the vibrational excitation takes place in the DCl neutral and is then transferred into to ionized state by Penning ionization. Ab-inition calculations by Bettendorf et al./12/ show a crossing between the ground state of HCl and HCl^- that could explain the population of DCl up to v=5. A strong enhancement of vibrationally excited HCl in the HCl-discharge has accidentally been observed by Davies et al /13/ in their diode laser spectra of HCl^+. A more detailed analysis of the processes involved in the dynamics generating DCl^+ is underway.

Acknowledgements

We appreciate valuable and critical comments particularly by R.F.Curl and E.E.Ferguson. The ab initio calculations have been brought to our attention by S.D.Peyerimhoff. The results on HCl^+ have been made available by P.D.Davies prior to publication. This work has been supported by the Deutsche Forschungsgemeinschaft through "Sonderforschungsbereich 42".

References

/1/ C.S.Gudemann, R.J.Saykally
Am.Rev.Phys.Chem. 35, 387-418 (1984)

/2/ R.J.Saycally, K.M.Evenson
Phys.Rev.Letters 43, 515-518 (1979)

/3/ D.Ray, K.G.Lubic, R.J.Saykally
Molec.Phys. 6, 217-212 (1982)

/4/ D.C.Hoode, E.Schäfer, S.E.Straham, C.A.Ferrari, D.Ray,
K.G.Lubic, R.J.Saykally
Molec.Phys. 52, 245-249 (1984)

/5/ A.Hinz, J.Pfeiffer W.Bohle, W.Urban
Molec.Phys. 45, 1131-1139 (1982)

/6/ W.Urban, A.Hinz, W.Bohle, D.Zeitz
Proceedings of the 7th International Congress "Laser `85"
W.Waidlelich (Edit.) Optoelectronics in Engeneering
Springer Verlag (1985)

/7/ A.Hinz, D.Zeitz, W.Bohle, W.Urban
Apll.Phys. B 36, 1-4 (1985)

/8/ A.Hinz, W.Bohle, D.Zeitz, J.Wernr, W.Seebass, W.Urban
Molec.Phys. 53, 1017-1021 (1984)

/9/ W.Kawaguchi, C.Yamada, E.Hirota
J.Chem.Phys. 82, 1174-117 (1985)

/10/ F.C.De Lucia, B.Herbst, G.M.Plummer, G.A.Blake
J.Chem.Phys. 78, 2312-2316 (1983)

/11/ R.C.Woods, H.E.Warner, W.T.Conner
J.Chem.Phys. 81, 5413-5416 (1984)

/12/ M.Bettendorf, R.J.Buenker, S.D.Peyerimhoff
Molec.Phys.50, 1363-1380 (1983)

/13/ P.B.Davies, P.A.Hamilton, S.A.Johnson
J.Chem.Phys. (in print)

Figure Captions

Fig. 1
Experimental setup of the Faraday-LMR. The modulated region extends to 30cm, the homogeneous part of the superconductive solenoid. For the experiments described in Fig.2 a very short modulation coil was used, that could be slipped along the discharge glasstube. The anomalous discharge could only be sustained with specially shaped electrodes.

Fig. 2
Intensity distribution of DCl^+ along the discharge axis for various discharge conditions, monitored by a short modulation coil. With increasing voltage the negative glow extends more an more into the center region of the magnetic field (anomalous dicharge conditions).

Fig. 3
Line shift with polarity change of DC-discharge.
a) normal discharge conditions, the signals are due to DCl^+ concentration in the positive column. A Doppler-shift is observed for ionic species as compared to lines from uncharged radicals.
b) anomalous discharge conditions, no Doppler-shift resolved. The DCl^+ detected in the negative glow, eteding into the modulated region of the discharge.

Fig. 4
Both linewidth and intensity change accordig to the temperature of the discharge, indicating translational and rotational thermal equilibrium.

Fig. 5
Faraday-LMR spectra of DCl^+ in anomalous discharge for the vibrational fundamental and various hot-bands.

Fig.5a: DCl^+ v=1-0

Fig.5b: DCl^+ v=2-1

Fig.5c: DCl^+ v=5-4

Fig.5d: DCl^+ v=6-5

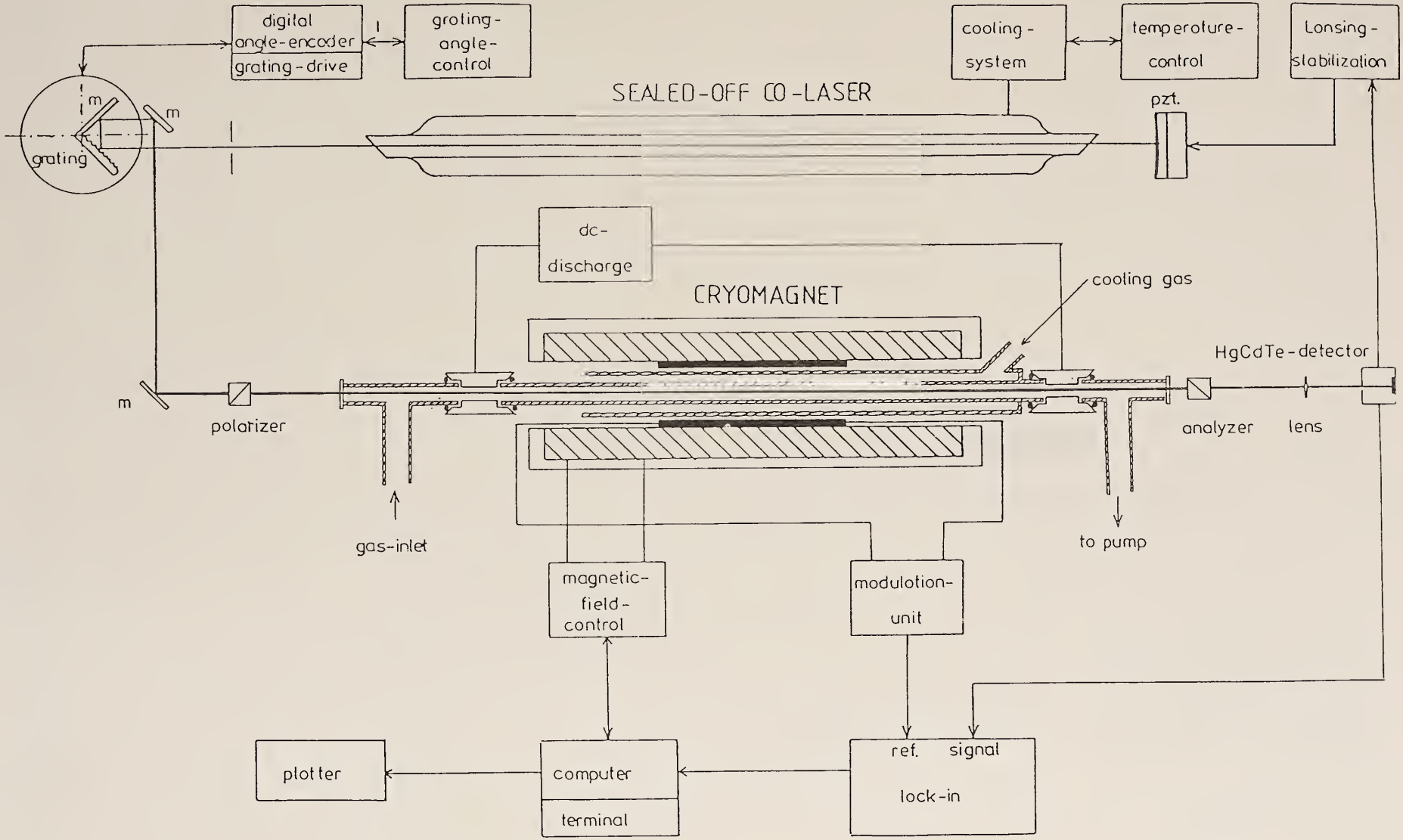
digital angle-encoder
grating-drive
grating-angle-control
cooling-system
temperature-control
Lonsing-stabilization
SEALED-OFF CO-LASER
pzt.
m
m
grating
dc-discharge
CRYOMAGNET
cooling gas
HgCdTe-detector
m
polarizer
analyzer
lens
gas-inlet
to pump
magnetic-field-control
modulation-unit
plotter
computer
terminal
ref.
signal
lock-in

Fig. 1

DCL^+-DISTRIBUTION IN ANOMALOUS DC-DISCHARGE

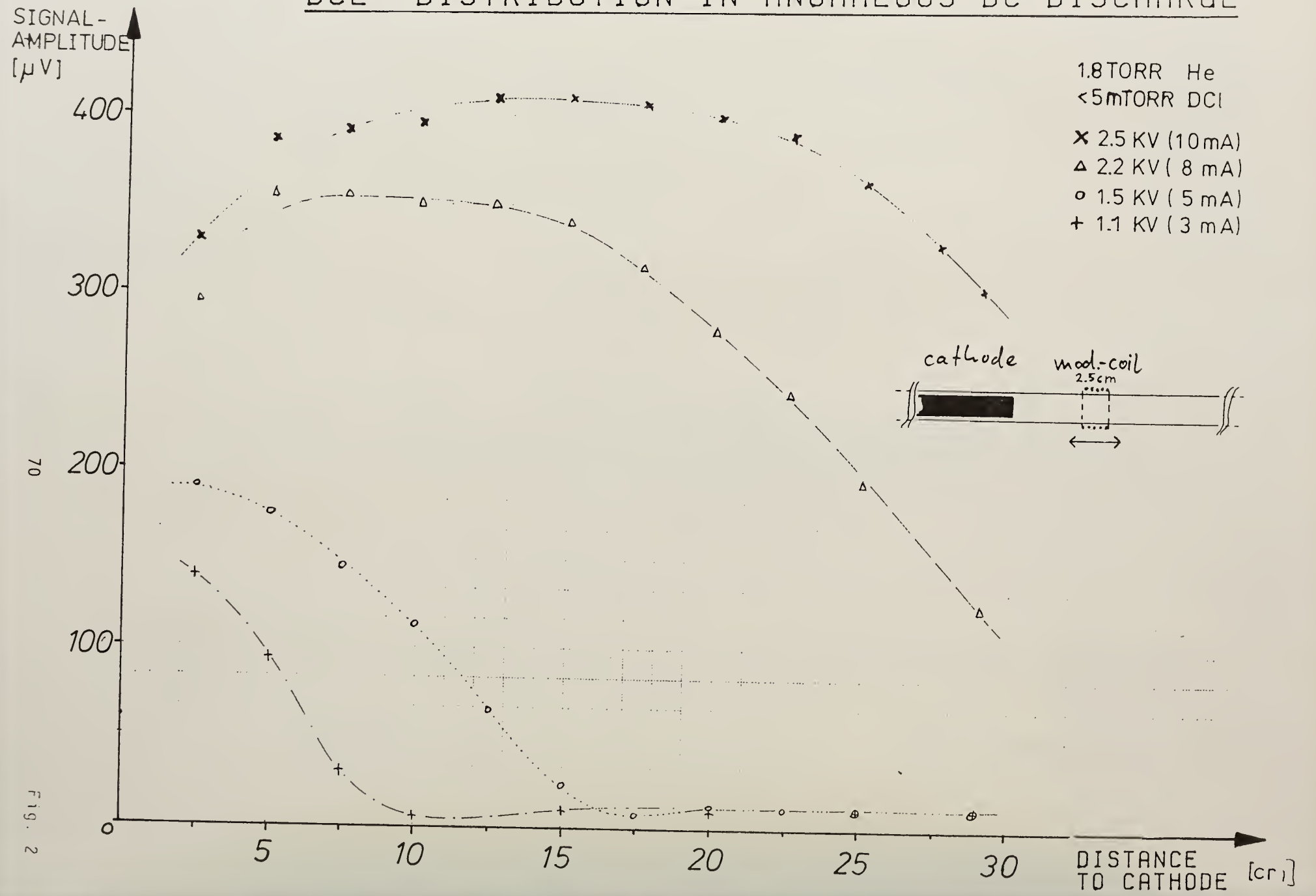

Fig. 2

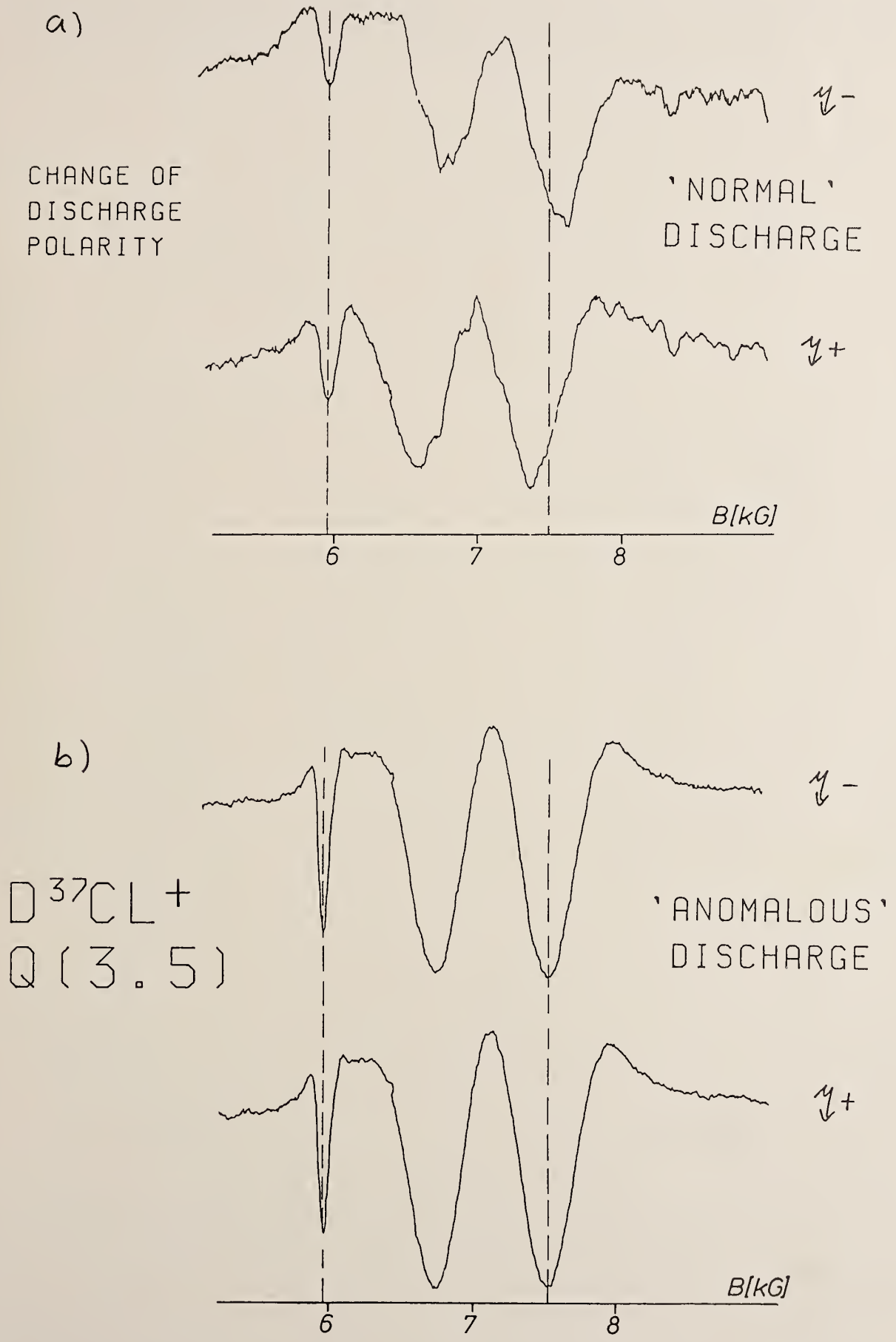
a)
CHANGE OF
DISCHARGE
POLARITY
'NORMAL'
DISCHARGE
y-
y+
B[kG]
6
7
8
b)
D37CL+
Q(3.5)
'ANOMALOUS'
DISCHARGE
y-
y+
B[kG]
6
7
8

Fig. 3

DCL^+, Q(1.5) in cooled anomalous discharge

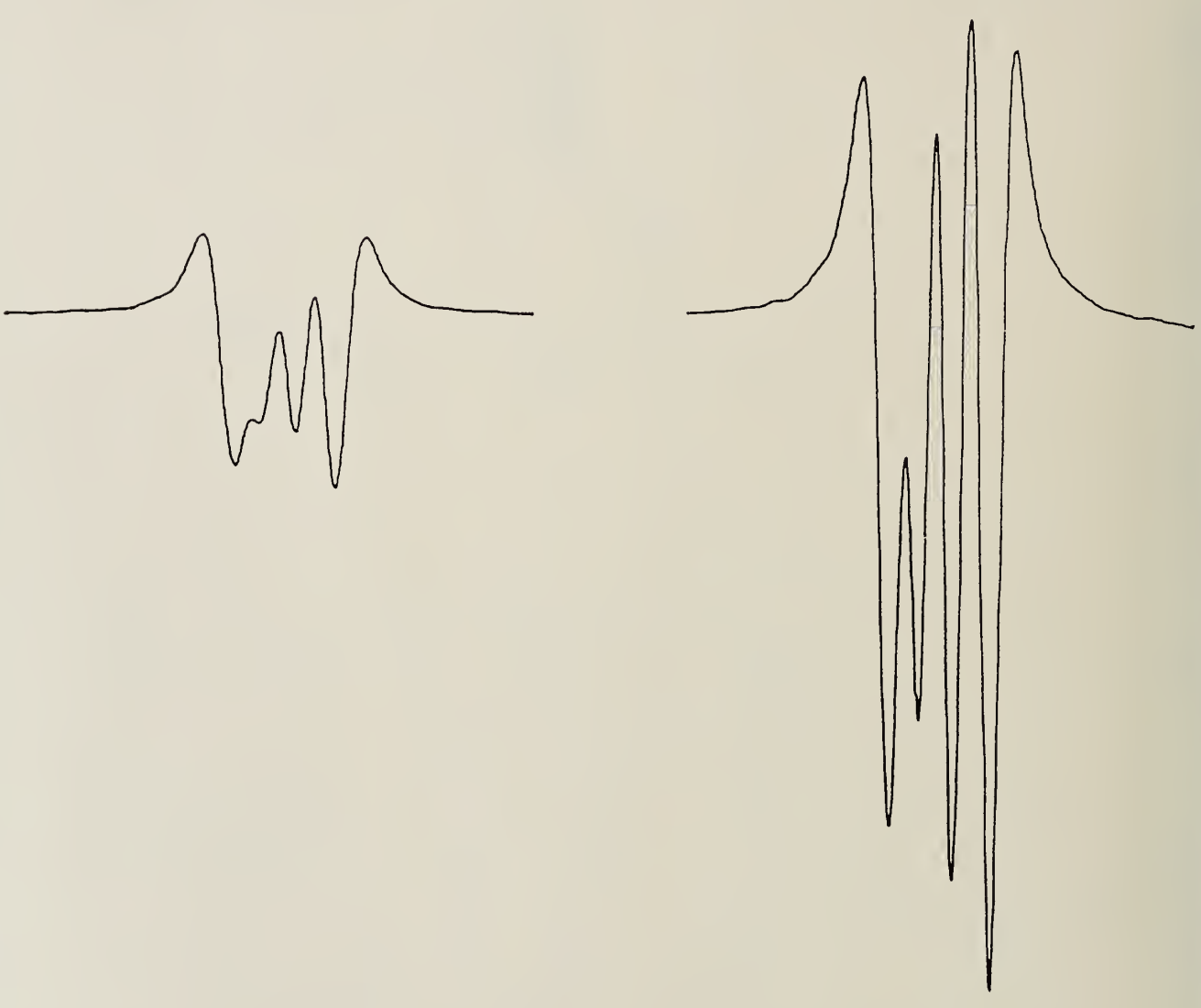

280 K

150 K

Fig. 4

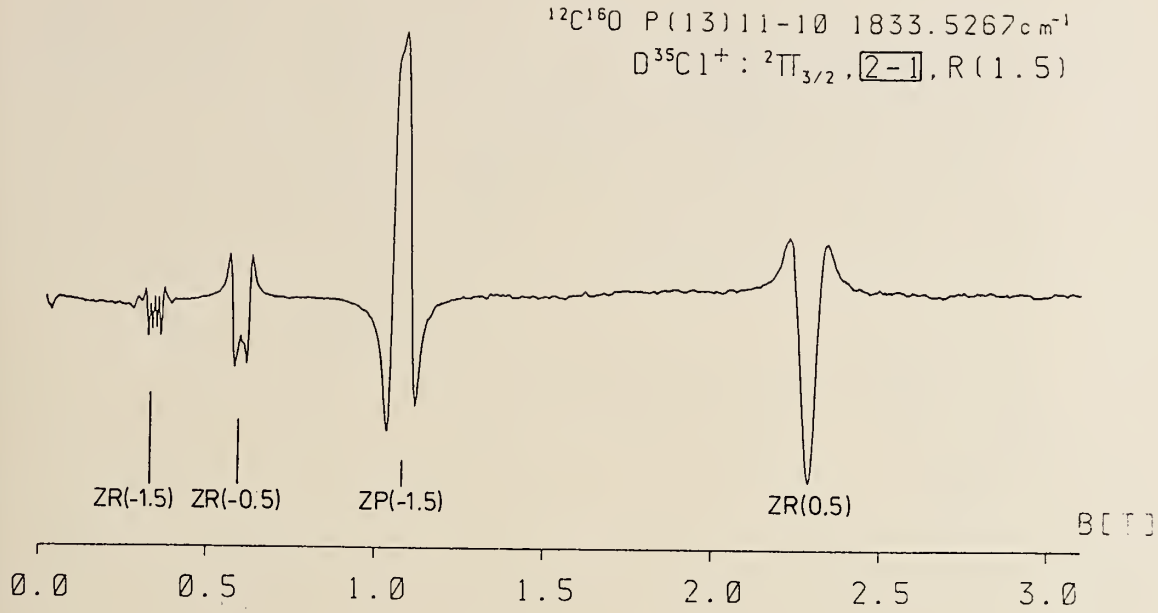
$^{12}C^{16}O$ P(13) 1-10 1833.5267cm^{-1}
$D^{35}Cl^+$: $^2\Pi_{3/2}$, 2-1, R(1.5)
ZR(-1.5)
ZR(-0.5)
ZP(-1.5)
ZR(0.5)
B[T]
0.0
0.5
1.0
1.5
2.0
2.5
3.0

Fig. 5b

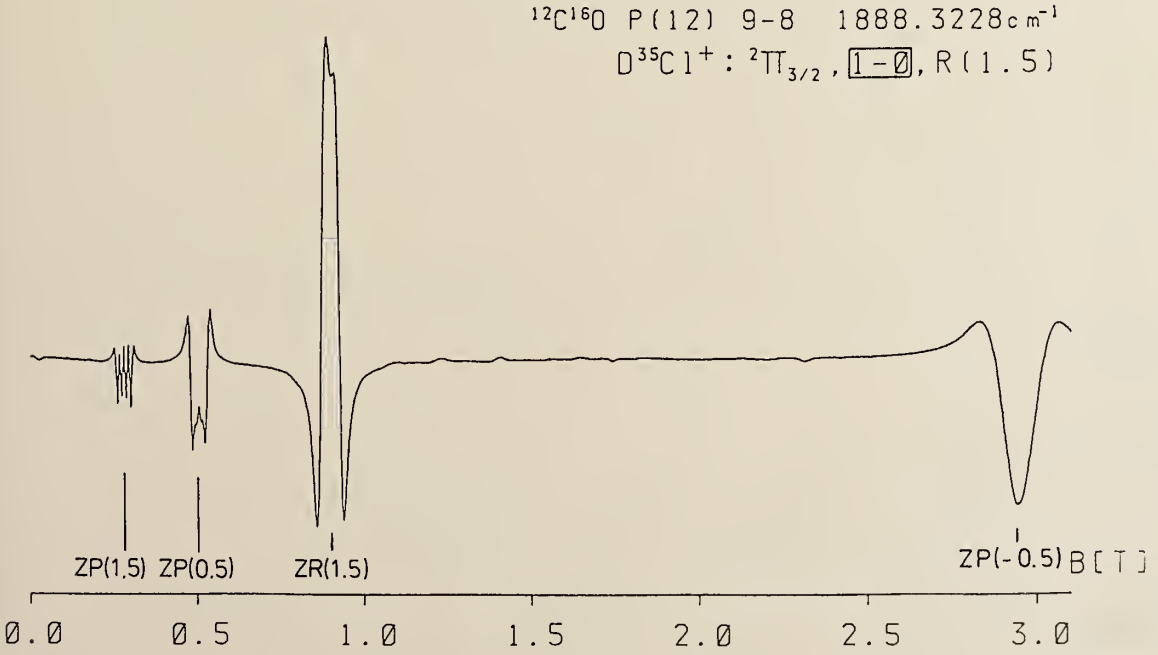
$^{12}C^{16}O$ P(12) 9-8 1888.3228cm^{-1}
$D^{35}Cl^+$: $^2\Pi_{3/2}$, 1-0, R(1.5)
ZP(1.5)
ZP(0.5)
ZR(1.5)
ZP(-0.5)
B[T]
0.0
0.5
1.0
1.5
2.0
2.5
3.0

Fig. 5a

$^{12}C^{16}O$ P(16)20-19 1597.93596cm^{-1}
$D^{37}CL^{+}$: $^{2}\Pi_{3/2}$, 6-5, Q(1.5)

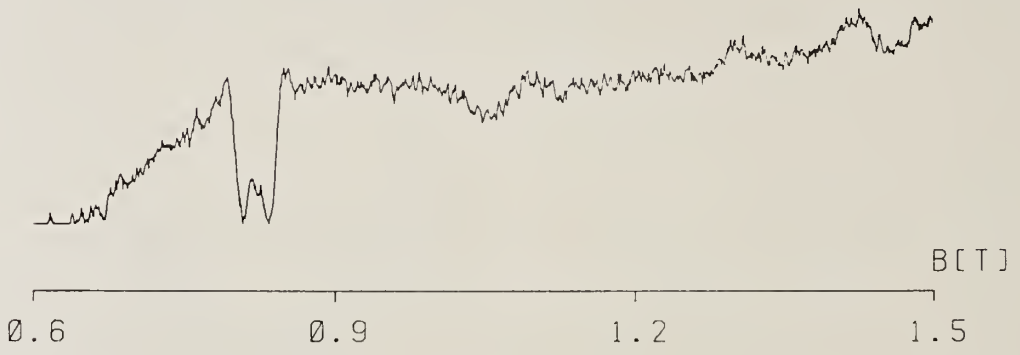

Fig. 5d

$^{12}C^{16}O$ P(15)18-17 1650.8108cm^{-1}
$D^{35}Cl^{+}$: $^{2}\Pi_{3/2}$, 5-4, Q(1.5)+Q(2.5)

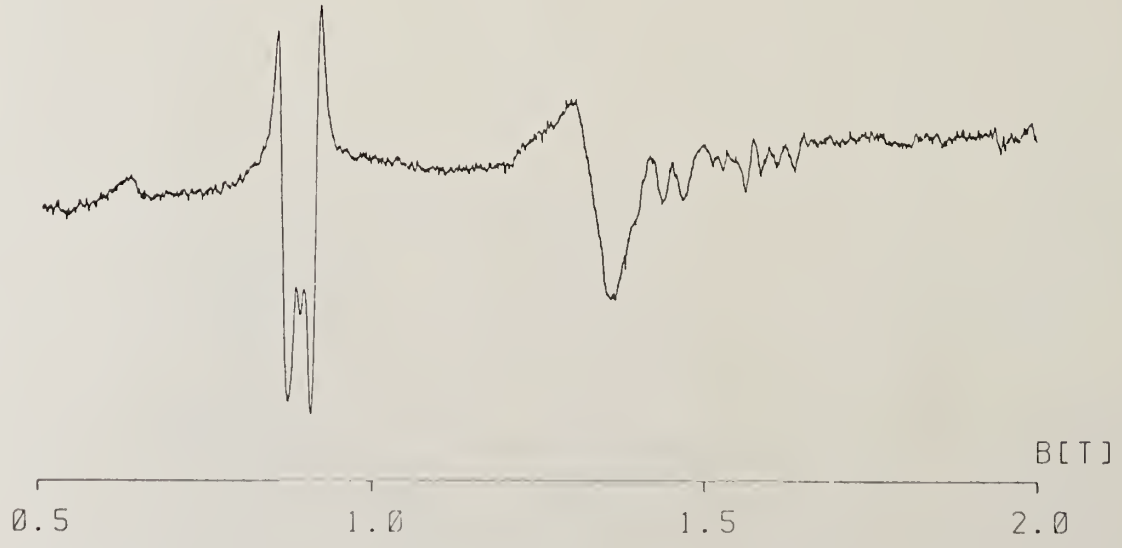

Fig. 5c

Table Caption

Table I
Spectroscopic constants for both isotopic species with ^{35}Cl and ^{37}Cl, derived from 80 Zeeman-components in 18 vib-rot-transition of the fundamental band and 80 Zeeman-components in 33 hot band transitions.

CALCULATED MOLECULAR CONSTANTS OF $DCL^+, X\,^2\Pi_{3/2}$

(ALL VALUES IN CM^{-1})

	$D^{35}CL^+$	$D^{37}CL^+$
ω_e	1919.47702(67)	1916.6443(19)
$\omega_e x_e$	27.91068(43)	27.8274(15)
$\omega_e y_e$	.14384(10)	.14284(46)
$\omega_e z_e$ 10^3	.2187(78)	.260(46)
B_e	5.120338(27)	5.105178(34)
α_e	.120446(20)	.119756(45)
γ_e 10^3	.6491(36)	.612(11)

(uncertainty in brackets $\hat{=}$ 1σ)

THE LOW-TEMPERATURE MEASUREMENTS OF THE "DIMOL" EMISSION FROM SINGLET MOLECULAR OXYGEN

Andrew P. Billington and Peter Borrell
Keele University, Staffordshire, England.
Nathan H. Rich
Memorial University, Newfoundland, Canada.

Abstract.

Preliminary Results are reported on the emissivity of the cooperative dimol transition of $O_2(a^1\Delta_g)$ between 100 and 323 K. Below 200 K, it was found that the emissivity is enhanced and that the temperature dependence compares well with that predicted from the previously determined absorption spectrum.

Introduction.

The unusual bimolecular emission from singlet molecular oxygen,

$$O_2(a^1\Delta_g) + O_2(a^1\Delta_g) = O_2(X^3\Sigma_g^-) + O_2(X^3\Sigma_g^-) + h\nu \qquad (1)$$

discovered by Ogryzlo and his co-workers[1,2], continues to fascinate because the nature of the transition and the emitting species is still not fully understood. Above room temperature the emission increases approximately with $\sqrt{T}$, as expected from simple collision theory, and above ~900 K it is further enhanced by contributions from hot vibrational bands[3,4]. A clue to the possible behaviour at low temperatures is provided by the work of McKellar, Rich and Welsh[5] who studied the absorption of gaseous oxygen at high pressures, and found an enhancement at low temperatures. It seemed worthwhile therefore to look for the corresponding effect in emission.

Experimental.

The emission was observed at one point in a cooled flow tube and relative measurements made of the emission at a given temperature to that at room temperature.

Our apparatus for low temperature work has recently been described in some detail(6). $O_2(a^1\Delta_g)$ is generated by passing O_2 at ~6 torr pressure

through a 2450 MHz microwave discharge. Mercury vapour is also passed through the discharge to remove oxygen atoms. The flow, typically at 1.06 mmol s^{-1} (linear flow rate 0.90 m s^{-1}) is then passed through the central 32 mm diameter tube of a triple-walled, double-jacketed, flow tube (length 0.4 m). The outer jacket is evacuated and the cooling is achieved by passing chilled gaseous nitrogen through the inner jacket. The lowest temperatures are obtained by cooling the N_2 with liquid nitrogen and the temperature is controlled to ±2 K by regulating the flow rate. The outside of the vessel is blown with hot air to prevent condensation.

Temperatures above ambient were obtained by circulating heated oil through the inner jacket of a similar vessel.

The observations were made between 0.1 and 0.35 m downstream of the the constricted inlet to the flowtube[6] with a photomultiplier (EMI 9658B) and an interference filter (Balzer) with a half-height bandwidth of 10 nm. The output was registered with a digital voltmeter.

Results.

As $O_2(a^1\Delta_g)$ passes along the flow tube it is deactivated collisionally and at the wall:

$$O_2(a^1\Delta_g) + O_2 = 2O_2 \qquad (2)$$

$$O_2(a^1\Delta_g) + \text{wall} = O_2 \qquad (3)$$

The decay in concentration follows a first-order rate law[6] but the rate constants, k_2 and k_3, both change with temperature. Furthermore, at the constant pressure used in the experiment, the density of the the gas changes with T^{-1} so that the emission ratio, (I'/I") for two temperatures T' and T" is given by:

$$\frac{I'}{I''} = \frac{k'}{k''}\left(\frac{T''}{T'}\right)^2 \frac{\exp(-2\{k_2'[O_2] + k_3'\}\ell/V')}{\exp(-2\{k_2''[O_2] + k_3''\}\ell/V'')} \qquad (4)$$

The squared term and factor 2 arise from the bimolecular nature of the emission, V' is the linear flow velocity at temperature T', and (k'/k") is the emissivity ratio, the value of which is sought.

The rate constants, k_2 and k_3, have been determined previously[6] between 100 and 350 K by measuring the fall in concentration along the tube so that all the terms in equation (4) are known except the emissivity ratio. To see the form of equation (4), the ratio can be set to one and in this way the full lines in figure 1 were plotted for two sets of flow

conditions; they show the way in which the relative emission should vary with temperature if the emissivity is independent of temperature. The behaviour is complicated because of the differing dependencies on T of the density and k_2, which increase, and k_3, which decreases, with temperature.

The runs were made by setting the photomultiplier at a fixed position, establishing the required flow rate and pressure at room temperature, and then recording the intensity. Then the temperature was reduced and a series of readings taken to cover the range of temperatures shown in figure 1. Further readings were taken as the apparatus was allowed to warm up and the room-temperature value checked at the end of the run.

The experimental values for I(T)/I(292 K) under two typical flow conditions are shown as points on the diagram. It can be seen that at the lower temperatures the emission ratio is greater than that of the line, for which the ratio is one. The relative emissivity is determined from the ratio of the experimental to the theoretical values.

Some 20 determinations were made under varying conditions of flow rate, pressure and observation point in the tube. The values of the emissivity ratio at each temperature were averaged; at 100 K, for example, the value was found to be 1.32 ± 0.03. From the averages, the values of $k_1(T)$ were determined using the value for k_1(295 K) recommended by Borrell and Rich[7]. While the results at the lowest temperatures have the greatest uncertainties, the enhancement of the emission is clearly seen.

Discussion.

The only other low temperature measurement is that of Arnold, Browne, and Ogryzlo[2] whose single value at 208 K falls below ours. It is however possible to compare the results with absorption measurements using the Einstein equation[7] to convert absorptivity to the bimolecular rate constant. The results of McKellar, Rich and Welsh[5] are plotted in figure 2. Considering the totally different experimental techniques and conditions, the agreement is good.

The temperature dependence of the absorption was interpreted[7] in terms of the theory, developed by Van Kranendonk[8], for pressure-induced transitions. The full line on figure 2 is derived from the theory and fitted to the results; the form is well reproduced between 100 and 300 K. The theory treats the transition in terms of a collision-induced dipole moment, and the agreement therefore suggests that the origin of the emission in this temperature range is wholly to be found in collisional processes with no participation from bound dimers.

While the agreement between theory and experiment is good, a problem

remains in reconciling the theory with the emissivities observed at high temperatures[2,3,4] where a dependence of the emission on $\sqrt{T}$ is found.

Acknowledgements.

We wish to thank the S.E.R.C and the USAF (Grant AFOSR-84-0035) for supporting this work. A.P.B thanks the University of Keele for the award of a studentship and N.H.R. thanks the Nuffield Foundation for a travel grant.

References.

1. S.J.Arnold, E.A.Ogryzlo and H.Witzke, J.Chem.Phys., 1964, **40**, 1769
2. S.J.Arnold, R.J.Browne and E.A.Ogryzlo, Photochem. and Photobiol., 1965, 4, 963
3. P.Borrell, P.M.Borrell and K.R.Grant, J.Chem.Soc.,Faraday Trans.2, 1980, **76**, 1442
4. R.Boodaghians, P.M.Borrell, P.Borrell and K.R.Grant, J.Chem.Soc., Faraday Trans.2, 1982, **78**, 1195
5. A.R.W.McKellar, N.H.Rich and H.L.Welsh, Canad.J.Phys., 1972, **50**, 1
6. A.P.Billington and P.Borrell, J.Chem.Soc.,Faraday Trans.2, to be published.
7. P.Borrell and N.H.Rich, Chem. Phys. Letters, 1983, **99**, 144
8. J.Van Kranendonk, Physica, 1958, **24**, 347

-oOo-

Captions for Figures.

Figure 1. Variation of the relative emission with temperature. The conditions for the top curve were: presure, 7 torr; linear flow rate, 54 cm s^{-1}; observation point, 54 cm along the tube; the conditions for the bottom were 5.2 torr, 43 cm s^{-1}, and 33 cm. The full lines are predicted from equation (4) assuming the emissivity to be constant with temperature; the points are experimental.

Figure 2. The rate constant for the dimol emission at low temperatures. ○ : this work(emission); △ and ◇ : reference 5(absorption). The full line is fitted with the theoretical equation from reference 5.

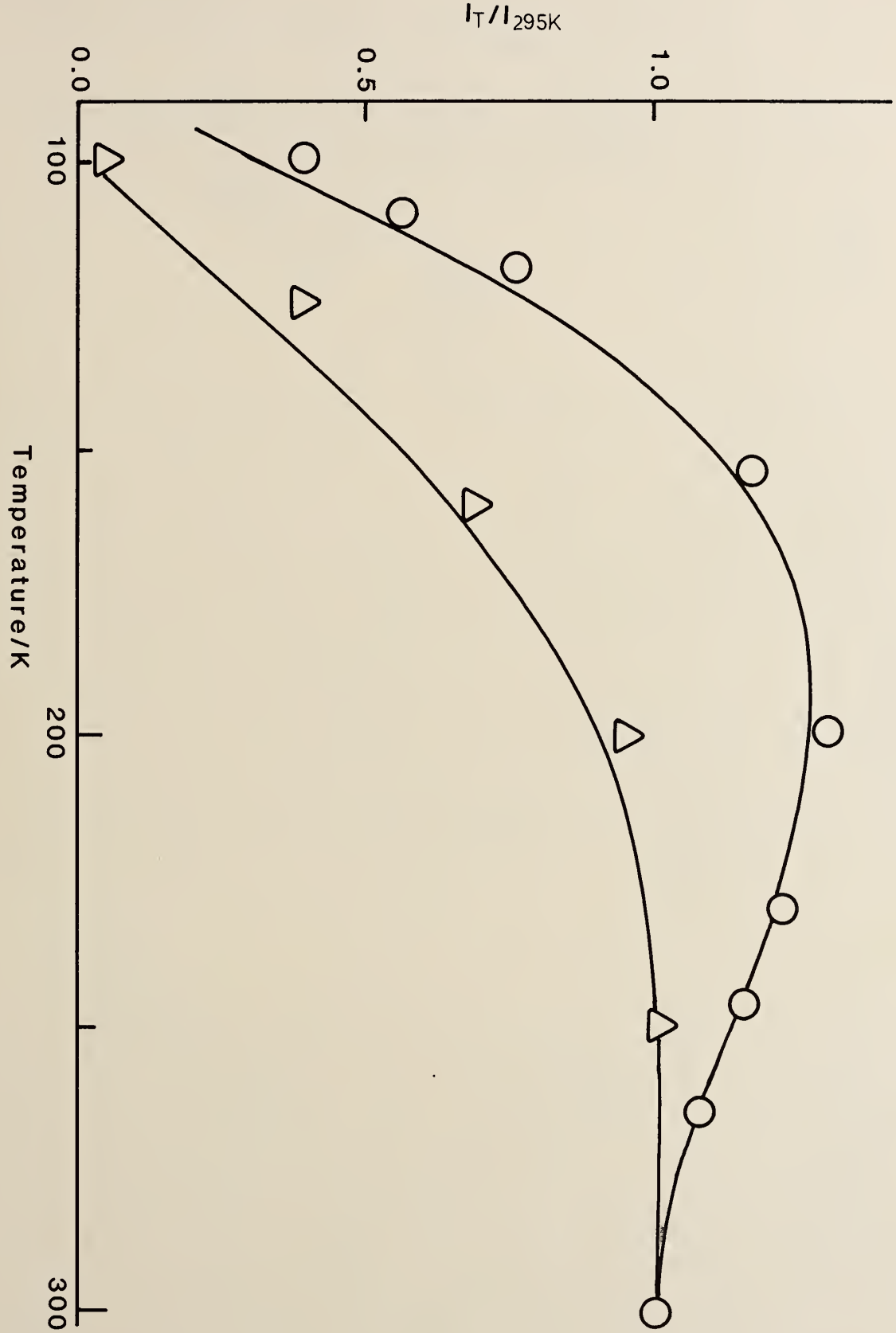

Fig. 1

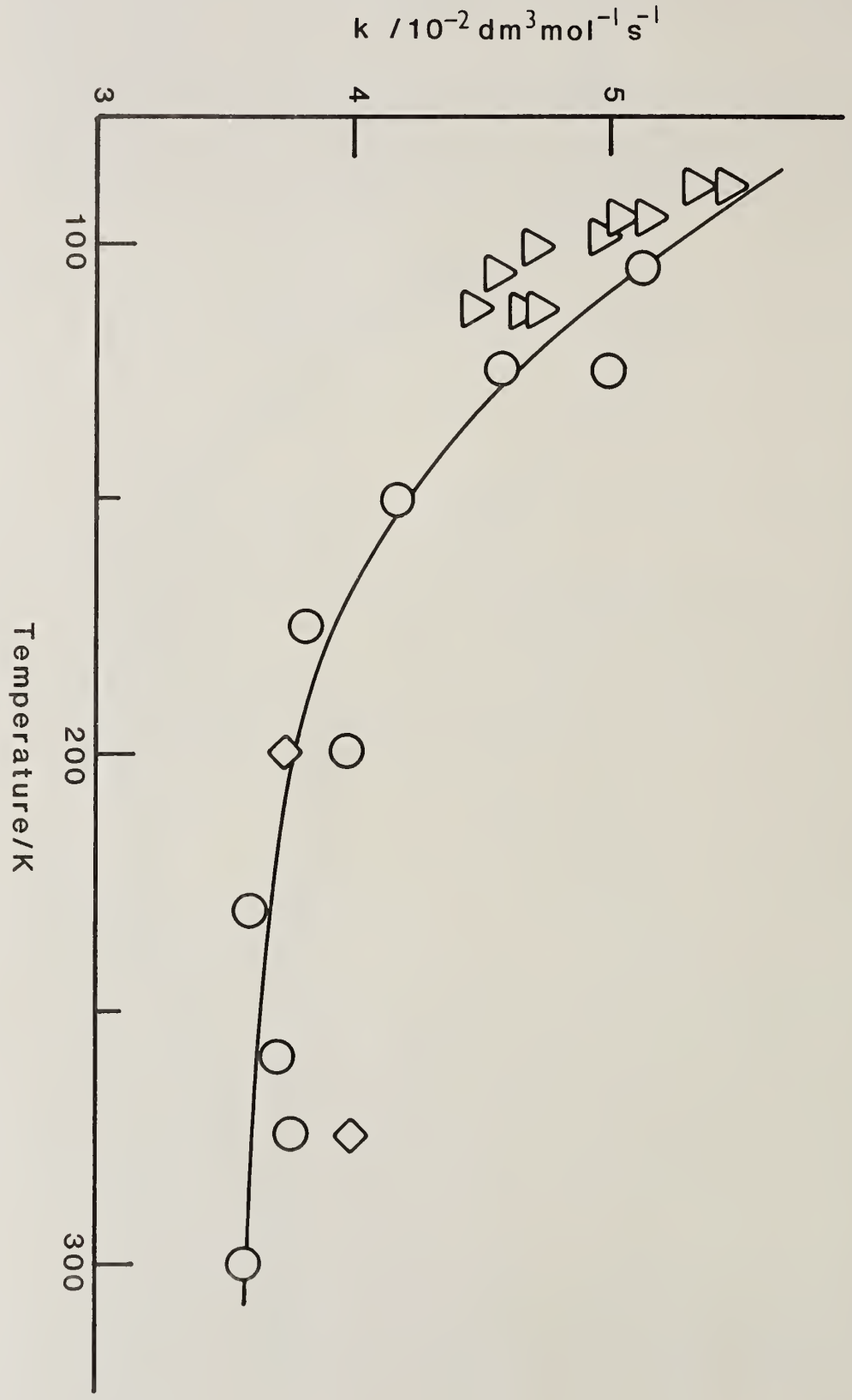

Fig. 2

LASER SPECTROSCOPY OF MgO : THE $d^3\Delta$ AND $c^3\Sigma^+$ STATES. APPLICATION TO THE $Mg(^3P,^1P) + N_2O$ REACTION KINETICS.

Bernard BOURGUIGNON and Joëlle ROSTAS

Laboratoire de Photophysique Moléculaire du CNRS*
Bâtiment 213 - Université de Paris-Sud

91405 - ORSAY Cédex France.

We report the analysis of the 363-365 nm laser induced fluorescence and excitation spectra of MgO produced by the reaction between $Mg(^1P, ^3P)$ and N_2O in a Broida oven. Features at 363.39, 363.80, 363.82 and 363.87 nm have been shown to be respectively the Q_1, Q_2, Q_{3f} and Q_{3e} heads of the $d^3\Delta$-$a^3\Pi$(1-0) band. Partial analysis of the (0-0) and (1-0) bands of this transition has provided improved molecular parameters for the $d^3\Delta$ state. In addition, a band around 364.0 nm has been assigned to the forbidden $c^3\Sigma^+$-$A^1\Pi$ (3-0) band. This assignment is substantiated by partial rotational analysis, ab initio calculations and earlier spectroscopic work. The $c^3\Sigma^+$ state arising from the same configuration ...$\pi^3\pi$, as the $d^3\Delta$, $D^1\Delta$, $C^1\Sigma^-$ and $E^1\Sigma^+$ states, has been characterized for the first time. This new spectroscopic data on MgO provides a tool to understand the $Mg(^3P, ^1P) + N_2O$ + He kinetics at room temperature. The $Mg(^3P) + N_2O$ reaction produces directly both the $A^1\Pi$ and $a^3\Pi$ states. The $A^1\Pi$ is efficiently depleted by reaction with $Mg(^1P)$ producing chemiluminescent MgO states. In contrast, there is no efficient secondary reaction involving the $a^3\Pi$ state.

I. Introduction

The dynamics of the reactions of excited $Mg(^3P)$ and (^1P) atoms with oxydants (O_2, N_2O ...) under bulk [1-4] and single collision [5-8] conditions has been extensively investigated. Most of the experimental data concerning dynamical properties such as branching ratios, rovibronic population distributions and reaction cross sections relie on the analysis of chemiluminescent spectra for the radiative states and laser excitation spectra for the dark states of the MgO product. In addition to the $X^1\Sigma^+$ ground state, MgO presents two low lying states, $a^3\Pi$ and $A^1\Pi$, at 2550 and 3500 cm^{-1} respectively, and a $(b)^3\Sigma^+$ state calculated to lie around 8000 cm^{-1} above the ground state [9]. According to correlation rules or energetic considerations, all these states may be formed in the $Mg(^3P) + N_2O / O_2$ reactions. However until recently the lack of spectroscopic data on the triplet manifold precluded reliable probing of the low lying triplet states rovibronic populations.

The emission and laser excitation UV spectra of MgO consists of numerous bands in the 359-400 nm region ([10-19]). Among them, only some $\Delta v = 0, -1$ sequence bands of the $C^1\Sigma^-$, $D^1\Delta$-$A^1\Pi$ transitions have been rotationally and vibrationally analyzed ([13-14]). In addition, the most intense system around 372 nm had been assigned to the $d^3\Delta$-$a^3\Pi$ (0-0) system ([15,17]) and bands at 386 nm had been tentatively assigned to the $\Delta v = 0$ sequence of the $c^3\Sigma^+$-$a^3\Pi$ transition ([16]). No rovibronic population analysis can be made from such crude spectroscopic data.

There has been recently several laser spectroscopic studies involving the MgO triplet states. The $a^3\Pi$ state, which was first located by perturbation in the $X^1\Sigma^+$ state ([18]), has been observed directly through the intermultiplet B-a ([20]) and D-a systems ([21]) observed respectively at 573.0 and 367.2 nm. We have used the $a^3\Pi$ $v = 0$ and $v = 1$ parameters derived from rotational analysis of some of these bands to reassign the main features of the 372 nm band to the $d^3\Delta$-$a^3\Pi$ $\Delta v = 0$ sequence ([19]). In addition, preliminary values for the $d^3\Delta$, $v = 0$ and 1 molecular parameters were obtained. In a previous study ([3,22]) of the reaction of Mg + N_2O, we had investigated the MgO fluorescence spectrum induced by excitation with the 363.8 nm Ar^+ laser line. Unexpectedly, the low resolution spectrum showed many bands, most of which could not be assigned because of the lack of reliable spectral data in the relevant region. Therefore, we undertook a detailed investigation of the MgO laser excitation spectrum in the UV region. In this paper, we present the analysis of the 363-365 nm region, showing that at least four different electronic transitions of MgO are observed in this region, namely **i)** the d-a $\Delta v = +1$ sequence **ii)** the D-A (2-0) band **iii)** the C-a $\Delta v = 0$ sequence, **iv)** a band involving a new electronic state which could be identified as the $c^3\Sigma^+$ state arising from the same configuration as the $d^3\Delta$ state. In addition, several bands could not be assigned. From this analysis, immediatly follows assignment of most of the bands observed in the Ar^+ LIF spectrum and further understanding of the kinetics of the Mg (^3P, ^1P) + N_2O reaction. In particular, it is shown that the MgO ($A^1\Pi$) + Mg (^1P) → MgO ($d^3\Delta$, $D^1\Delta$, $C^1\Sigma^-$) + Mg (^1S) occurs. In contrast, the corresponding reaction of MgO ($a^3\Pi$) is not observed.

II. EXPERIMENTAL

The experimental arrangement has been described previously ([3-18]). Magnesium vapor is produced in a Broida oven and excited through a dc discharge. The vapor is carried by Helium gas along to the reaction zone where excited (^3P and ^1P) Magnesium atoms are mixed with N_2O producing MgO in several electronic states. Product MgO is detected in the reaction zone by exciting fluorescence with a tunable, excimer pumped dye laser. The laser band width is 0.2 cm^{-1}. Fluorescence is detected with an EMI 9558 BQ photomultiplier after passing either through a broad band interference filter (350-390 nm) or through a 50 cm focal length monochromator. In several cases the monochromator was used as a optical band pass filter

(FWHM $\sim$ 4 nm) to discriminate between different molecular transitions. This arrangement provided a drastic improvement of the signal to noise ratio by eliminating laser scattered light and allowing an increase of two orders of magnitude of the amplification of the detection. In some cases, the monochromator was used to record low resolution ($\sim$ 3 Å) laser induced fluorescence spectra.

Absolute wavelength calibration is made to an accuracy of 0.3 cm^{-1} using available data on known electronic transitions of MgO and Mg. Interpolation between reference wavelengths is made using a 0.85 cm^{-1} FSR Fabry-Perrot. The relative positions of unblended lines is determined to better than 0.1 cm^{-1}.

Rotational and vibrational temperatures of the $a^3\Pi$ and $A^1\Pi$ states produced in our experimental conditions have been estimated in a previous study ([19]) by comparaison of simulated and observed laser excitation spectra of $C^1\Sigma^-$, $D^1\Delta$ - $A^1\Pi$ and $D^1\Delta$ - $a^3\Pi_1$ $\Delta v = 0$ transitions. A rotational temperature of $T_R \sim 300$ K has been found for both states. The vibrational population distribution which is not well represented by a Boltzmann distribution, is markedly different in the two states, corresponding crudely to vibrational temperatures of 800 and 1200 K respectively for the $a^3\Pi$ and $A^1\Pi$ state.

III. DESCRIPTION OF THE SPECTRUM

The MgO 363 - 365 nm laser excitation spectrum is shown in Fig. 1b. It consists of several different systems the overlap of which results in the observed complex structure. Wavelength of the main features are listed in Table 1. Up to now, four systems could be identified :

-1- The peak at 363.48 nm is exactly at the calculated position for the Q head (27504.0 cm^{-1}) of the $D^1\Delta$ - $A^1\Pi$ (2-0). The simulated spectrum for T_{rot} = 300 K exhibits a prominent narrow Q head explaining that it can be seen despite the small Franck-Condon factor (0.4×10^{-5}) calculated for this band.

-2- The $C^1\Sigma^-$ - $a^3\Pi$ (0,0), (1,1), (2,2) Q heads expected at 364.15, 364.41 and 364.69 respectively contribute to the complex structure observed on the red handside of the 364 nm peak.

-3- Assignment of the 363.39, 363.80, 363.82 and 363.87 nm peaks to the Q heads of the d-a (1-0) band will be discussed in the next section.

-4- It will be shown in section V that the narrow peak at 364.0 involves a new electronic state of MgO.

Few strong peaks have not yet been assigned (Table 1).

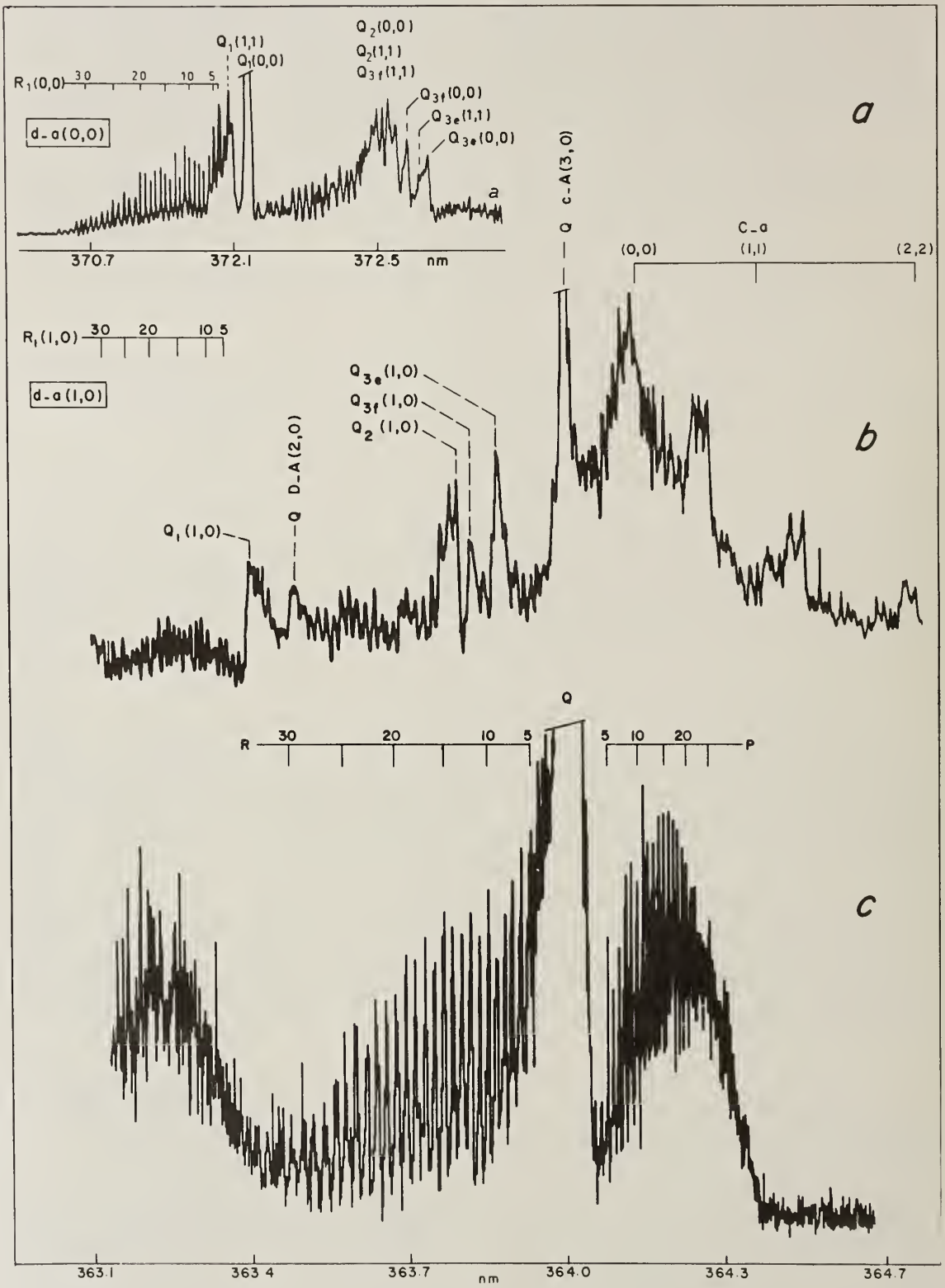

Fig. 1. Laser excitation spectra of MgO

a) In the 372 nm region
b) c) In the 364 nm region
Fluorescence between 350 and 390 nm was collected in a) and b), and between 384 and 388 nm in c).

TABLE 1 - Main band heads in the MgO 363-365 nm laser excitation spectrum.

λ (nm)	ν (cm^{-1})	I [a]	Direction of degradation	Assignment
363.391	27510.7	14	R	Q_1 d-a(1-0)
363.480	504.0	8	R	Q D-A(2-0)
363.797	480.0	23	V	Q_2 d-a(1-0)
363.824	478.0	16	R	Q_{3f} d-a(1-0)
363.872	474.4	23	M	Q_{3e} d-a(1-0)
364.010	463.9	100	R	Q c-A(3-0)
364.115	456.0	19	M	Q C-a(0-0)
364.137	454.4	19	M	-
364.271	444.3	14	M	-
364.450	430.8	11	M	Q C-a(1-1)
364.472	429.1	11	V	-
364.666	414.5	6	M	Q C-a(2-2)

a *estimated relative intensity.*

IV. THE $d^3\Delta$ STATE

The $d^3\Delta$ state was first identified by Schamps and Gandara ([15],[17]) who tentatively assigned four intense peaks near 372 nm to the Q branch heads of the d-a (0-0) band. The $d^3\Delta$ - $a^3\Pi$ system of MgO exhibits a very congested structure, not only because of the 54 rotational branches expected for a $^3\Delta$ - $^3\Pi$ transition but also because of heavy overlap of sequence bands due to the similarity of the MgO $a^3\Pi$ and $d^3\Delta$ states. This congested structure precluding a detailed rotational analysis, Schamps and Gandara based their assignment on ab initio calculation predictions. Recently, investigation of the 372 nm laser excitation spectrum of MgO produced at room temperature in a Broida oven enabled us ([19]) to reassign unambiguously the main peaks to Q heads of the $\Delta v = 0$ ($v = 0$, 1 and 2) sequence of the $d^3\Delta_3$ - $a^3\Pi_2$ subband (Q_1 heads). Comparison of observed and simulated spectra not only gave conclusive argument for the assignment, but also provided preliminary constants for the $d^3\Delta$ $v = 0$ and $v = 1$ levels, since the $a^3\Pi$ $v = 0$ and $v = 1$ constants were known from an independent work ([20]). In the present work, Q band heads of the d-a (1-0) band were easily assigned (Table 1 and Fig. 1b) by comparison of the observed spectrum with a simulated one, calculated using the relevant molecular constants. The shape of the individual Q heads, which are governed by the $\Delta B = B^{eff}_{\Delta} - B^{eff}_{\Pi}$ values varies notably from the $\Delta v = 0$ to the $\Delta v = +1$ bands (Fig. 1a and 1b) : in the

$\Delta v = 0$ sequence, the Q_1 branches are narrow and undegraded while Q_2 and Q_3 are broader and violet degraded ; in the (1-0) band, the Q_1 head is broad and red degraded and the Q_3 are sharp and prominent. In both the (0-0) and (1-0) bands, the R_{11} branches are almost free from overlap (Fig. 1a and 1b) and easily numbered in J (Table 2). This partial rotational analysis yielded approximate values $B_0 = 0.5048$ and $B_1 = 0.4994$ cm^{-1} and consequently $B_e = 0.5102$ cm^{-1} and $\alpha = 0.0054$ cm^{-1} and an accurate value $\Delta G\ 1/2 = 646.4$ cm^{-1} for the $d^3\Delta$ state. The observation of the (1-0) band and the partial rotational analysis of the (1-0) and (0-0) bands further confirm our assignments for the 372 nm peaks. The $d^3\Delta$ rotational and spin-orbit fine structure will be discussed in detail elsewhere ([23]).

TABLE 2 - Wavenumbers in (cm^{-1}) of the rotational lines and Q heads assigned in the $d^3\Delta - a^3\Pi$ bands of MgO.

	1 - 0					0 - 0				
J	R_{11}	Q_{11}	Q_{22}	Q_{3f}	Q_{3e}	R_{11}	Q_{11}	Q_{22}	Q_{3f}	Q_{3e}
0										
1										
2	27514.13									
3	514.97									
4	515.80					26869.81				
5	516.86					870.61				
6	517.69					871.55		26834.20 H		
7	513.53					872.41				
8	519.36					873.43				
9	520.19					874.36			26831.88 H	
10	521.18					875.38				
11	522.01					876.17				
12	522.69					877.18				26828.14 H
13	523.60					877.98				
14	524.21		27480.02 H			878.99				
15	525.04	27510.73 H		27477.99 H		879.93				
16	525.72				27474.36 H	880.80	26864.04 H			
17	526.56					881.74				
18	527.39					882.75				
19	527.85					883.54				
20	528.68					884.84				
21	529.36					885.78				
22	530.04					887.01				
23	530.88					887.80				
24	531.71					888.82				
25	532.39					889.76				
26	-					890.70				
27	534.06					891.79				
28	-					892.73				
29	-					893.74				

H Q heads, the J numbering is approximate.

V. IDENTIFICATION OF THE $c^3\Sigma^+$ STATE

The most prominent feature of the 363 - 365 nm laser excitation spectrum shown in Fig. 1b is a very narrow and intense peak at 364.0 nm, which can not be assigned to any hitherto identified system of MgO. In order to obtain some information about the lower state of this transition, the fluorescence spectrum induced by laser excitation at 364.0 nm was dispersed at low resolution. Six main peaks were observed (Fig. 2). Their wavelengths and relative intensities are listed in Table 3. The peaks at 372.6 nm and

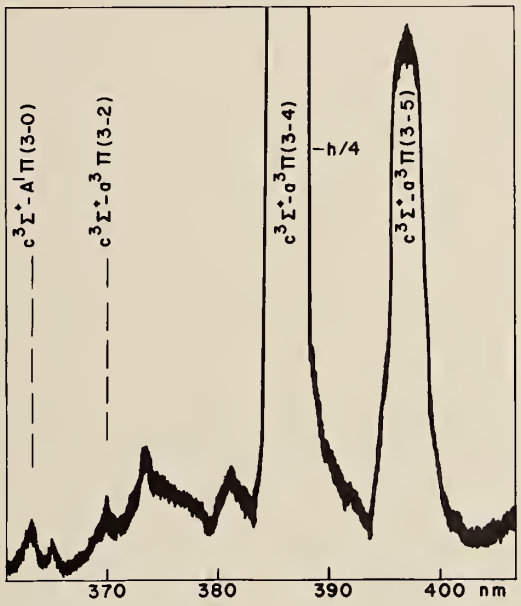

Fig. 2. MgO Laser Induced Fluorescence Spectrum. The pulsed dye laser wavelength is 364.01 nm.

TABLE 3 - Low resolution laser induced fluorescence bands observed by excitation at 364.0 nm.

λ (nm)	I_{MgO} [a]	MgO transition	
		Fluorescence	Excitation
364.0	1	c-A (3-0)	c-A (3-0)
369.5	1	c-a (3-2)	c-A (3-0)
372.6	7	d-a (1-1)	d-a (1-0)
380.9	5	D-A (2-2)	D-A (2-0)
386.0	100	c-a (3-4)	c-A (3-0)
396.6	32	c-a (3-5)	c-A (3-0)

[a] *Observed relative intensities.*

380.9 nm are readily assigned to the d-a (1-1) and D-A (2-2) bands which originate respectively from the d, v = 1 and D, v = 2 levels. However, the most intense peaks at 386.0 nm and 396.6 nm can not be related to any known system. Since the main fluorescence occurs around 386 nm, an excitation spectrum was recorded by selectively collecting the 384 - 388 nm fluorescence. The result is spectacular as shown in Fig. 1 where the two excitation spectra are compared (Fig. 1b and 1c). The complex structure described previously is absent and instead a regular RQP branch structure is observed. Upon detailed

TABLE 4 - Wavenumbers and second-combination differences (in cm^{-1}) of the lines assigned in the 364.0 nm band [a].

J	R	P	Δ_2F''	Δ_2F'' ($A^1\Pi$) [b]
0				
1				
2				5.03
3				7.05
4	27469.36	27459.99		9.06
5	470.55	459.15	11.02	11.07
6	471.69	458.34	13.15	13.08
7	472.82	457.40	15.14	15.09
8	473.92	456.55	17.04	17.10
9	475.18	455.78	19.02	19.11
10	476.45	454.90	21.08	21.12
11	477.77	454.10	23.16	23.13
12	479.07	453.29	25.20	25.14
13	480.33	452.57	27.21	27.15
14	481.60	451.86	29.18	29.16
15	482.86	451.15	31.16	31.16
16	484.26	450.44	33.07	33.17
17	485.59	449.79	35.12	35.17
18	487.02	449.14	37.10	37.18
19	488.38	448.49	39.17	39.18
20	489.79	447.85	41.17	41.18
21	491.12	447.21	43.14	43.18
22	492.67	446.65	45.08	45.18
23	494.03	446.04	-	47.18
24	495.67	-	-	49.18
25	497.37	-	51.03	51.17
26	498.63	444.64	53.14	53.17
27	500.29	444.25	55.21	55.16
28	501.95	443.42	-	57.15
29	503.58	-	59.12	59.14
30	504.97	442.83	61.17	61.13
31	506.82	442.41	62.98	63.11
32	508.45	441.99	-	-

[a] *Q head at 27462.8 cm^{-1}*

[b] *From ref. 20.*

inspection, it appears that most of the lines are not single. The R and P lines were easily numbered (Table 4), and appropriate combination differences R(J-1) - P(J+1) provides $\Delta_2F''(J)$ which identify unambiguously the $A^1\Pi$ v = 0 level as the lower level of the 364.0 nm band. A value of B = 0.5124 cm^{-1} is obtained for the upper state from Δ_2F'. Since the $A^1\Pi$, v = 0 level lies at 3503 cm^{-1} above the $X^1\Sigma^+$ v = 0 level (which will be taken as origin throughout), the upper state is located at 30966 cm^{-1}. The nearest singlet levels are the $C^1\Sigma^-$ v = 1 and $D^1\Delta$ v = 2 levels lying respectively at 30626 and 31010 cm^{-1}. No other singlet level is expected in this region. The new level lies between the v = 2 ($\sim$30660 cm^{-1}) and v = 3 ($\sim$31290 cm^{-1}) levels of the $d^3\Delta$ state. In addition to the $d^3\Delta$ state, two triplet states arising from the same $...2\pi^3\ 6\sigma^2\ 3\pi$ configuration are predicted to occur in this region. They are **i)** a $^3\Sigma^-$ state which, in first approximation, is degenerated with the $C^1\Sigma^-$ state (30000 cm^{-1}) and is expected to be either repulsive or weakly bound, and **ii)** a $^3\Sigma^+$ state which is the lowest state arising from this configuration and which has been calculated at $\sim$ 27650 cm^{-1} ([9]). Therefore, according to ab initio predictions, possible assignments for the 364.0 nm band upper level is either the $(e)^3\Sigma^-$ v = 0 (or v = 1) or $c^3\Sigma^+$ v = 3 (or v = 4) level. Previous conventional spectroscopic studies can help to choose between these possibilities. The most useful data concerning the MgO triplet states are those reported in 1954 by Brewer and Porter ([10]) and more recently by Schamps ([15]). Brewer and Porter observed the MgO UV bands in emission and absorption at medium resolution (0.67 Å/mm) from a King type furnace (T $\sim$2550 K). They tentatively classified about 30 band heads. Later ([13],[14]), vibrational and rotational analysis of high resolution spectra has shown that some of the bands belong to the singlet C-A and D-A transitions, but many bands had not yet been identified. Among them, there are two series (at 370 and 380 nm) of three violet degraded heads separated by $\sim$700 cm^{-1} . The spacing of $\sim$60 cm^{-1} between two adjacent heads of each group is characteristic of the $a^3\Pi$ spin-orbit splitting. The triple head structure strongly suggests that these bands arise from a $^3\Sigma$ - $^3\Pi$ transition. The 380 nm heads have been observed both in emission and absorption, while the 370 nm bands have been seen only in absorption. It seems therefore reasonnable to assign the 380 nm and 370 nm band heads respectively to the (0-0) and (1-0) bands of a $^3\Sigma$ - $a^3\Pi$ transition. If this is correct the $^3\Sigma$ v = 0 and v = 1 levels would lie respectively at 28910 and 29610 cm^{-1} above the $X^1\Sigma^+$ v = 0 level, and the upper state of the laser excitation spectrum 364 nm band would, indeed, be the v = 3 level of this electronic state. The parity of the observed $^3\Sigma$ state will remain ambiguous, since it lies between the calculated positions (27650 and 30100 cm^{-1} for the $^3\Sigma^+$ and $^3\Sigma^-$ states respectively), until a detailed rotational analysis establishes the $^3\Sigma$ state fine structure. Appropriate high resolution spectra of this band are presently being recorded. There are however several arguments suggesting that the observed state is the $c^3\Sigma^+$. The rota-

tional constant $B_e \simeq 0.5360\ cm^{-1}$ (obtained from extrapolation of $B_{v=3} = 0.5124\ cm^{-1}$ assuming $\alpha = 0.0050\ cm^{-1}$) and vibrational frequency ($\sim 705\ cm^{-1}$) are notably larger than those for the states arising from the same configuration (Table 8), as observed for the corresponding states of CO. The empirical relationship ([24]) ω_e/B_e^2 holds fairly well for the observed electronic states of MgO. In addition, this assignment places the $c^3\Sigma^+$ below the $d^3\Delta$ state as expected from ab initio calculations.

The identification of the $c^3\Sigma^+$ state proposed here, disagrees with its position given in the literature ([16]), which is based on a tentative assignment by Evans and Mackie ([16]) of a band around 386.0 nm to the c-a $\Delta v = 0$ sequence bands. This assignment which is reported as uncertain by Huber and Herzberg ([25]) relies on the observation of a very broad band in the very low resolution absorption spectrum of shock heated $Ar/O_2/MgO$ vapor ; according to Evans and Mackie, this band is unsuitable for quantitative spectroscopic study because of the presence of overlapping Mg lines between 383 - 384 nm. This assignment which is not supported by any spectroscopic argument can be ruled out. The present assignment is, indeed, further confirmed by observation of most of the c-a (1-0) and (0-0) band heads both in Schamps' hollow cathode spectrum and laser excitation spectra that we recorded. In these spectra, however, the triplet structure is hidden because many other bands interperse with them explaining why they had not yet been identified.

The wavenumbers of the band heads assigned to the $c^3\Sigma^+ - a^3\Pi$ transition, observed in the present work and/or in earlier studies, are collected in Table 5. The proposed assignment are further supported by the analysis of the Ar^+ LiF spectrum as discussed below.

TABLE 5 - Wavenumbers (in cm^{-1}) of the band heads assigned to the $c^3\Sigma^+ - a^3\Pi$ transition.

$a^3\Pi$ \ $c^3\Sigma^+$	0	1	2
	26418.0 [a,b,c]	27118.1 [a,b]	-
0	26358.6 [a,b]	27055.0 [a,b,c]	-
	26291 [b]	26988.9 [a,b]	-
	25770 [c]	-	27161.4 [c]
1	25717.5 [c]	26418.0 [c]	27105.4 [c]
	25663.4 [c]	-	27040.2 [c]

[a] *This work*

[b] *Ref. 10*

[c] *Ref. 15*

VI. ANALYSIS OF THE Ar^+ 363.8 nm LASER INDUCED FLUORESCENCE SPECTRUM

The main purpose for investigating the 363 - 365 nm region of the MgO spectrum was originally to assign the low resolution fluorescence spectrum observed in a previous work ([3],[22]) by excitation of MgO with the 363.8 nm Ar^+ laser line. Fig. 3 shows the spectra obtained at low resolution ($\sim$1000) at low (3a) and high (3b) concentration of the metastable $Mg(^3P)$ state. The spectrum consists of 12 bands which are listed in Table 6. These bands can be classified into two sets according to their intensity dependence upon the $Mg(^3P)$ concentration ; **i)** the 372 nm and 383.5 nm bands whose intensity increases linearly with $Mg(^3P)$ concentration, and **ii)** the ten remaining bands showing first a linear increase of the intensity which goes through a maximum and fades out rapidly at high $Mg(^3P)$ concentration (Fig. 4). The 372 nm peak is assigned to $d^3\Delta_2$ - $a^3\Pi_1$ (1-1) lines excited by (1-0) $Q_2(15)$ lines. According to the rotational assignments of the c-A (3-0) band given in Table 4, the Ar^+ 363.86 nm (27480.9 $\pm$ 3 cm^{-1}) excites the R(13) c-A line and the fluorescence peaks observed at 369.4, 377.4, 386.0 and 395.1 nm can be readily assigned to lines originating from the $c^3\Sigma^+$ v = 3, J = 14 level and involving respectively the v = 2, 3, 4 and 5 levels of the $a^3\Pi$ state. The relative intensity of these bands are in agreement with the calculated Franck-Condon factors (Table 6). The positions and relative intensities of the LiF spectrum bands are,indeed,further evidence of the validity of our assignment of the 364 nm feature to the $c^3\Sigma^+$ - $A^1\Pi$ (3-0) band. There are still some unassigned bands in the photoluminescence spectra excited by the 364.0 and 363.8 nm lines suggesting that one (or more) molecular transitions lie in the 363 - 365 nm region. These transitions which are obviously associated with the still unassigned peaks in the laser excitation spectrum may involve either the $(b)^3\Sigma^+$ state of MgO or a more complex molecule as MgO_2 or MgOH since no more transition involving the X, a and A states of MgO are expected in this region.

VII. KINETICS OF THE Mg + N_2O REACTION

The above assignments for the Ar^+ 363.8 nm LiF spectrum bands demonstrate that both the $a^3\Pi$ and $A^1\Pi$ states of MgO are produced in reactions occurring at room temperature and under flow conditions in the $Mg(^3P)/N_2O$ mixture. This allows further interpretation of the data obtained in our previous kinetic study of this system ([3],[22]). In addition, investigation of the $Mg(^3P)$ + $N_2O(O_2)$ reaction under single collision conditions by Dagdigian et al ([5],[6]) provided dynamical data, in particular the relative rates of formation for the $X^1\Sigma^+$, $a^3\Pi$ and $A^1\Pi$ states. On the other hand, the interpretation of the reaction dynamics is greatly facilitated by ab initio calculation of selected points on the lowest $^1A'$ and $^3A'$ potential energy surfaces carried out

TABLE 6 - Low resolution laser induced fluorescence bands observed by excitation with the 363.8 nm Ar^+ laser line.

λ (nm)	I_{MgO} [a]	$f(I_{Mg})$ [b]	MgO Transition	
			Fluorescence	Excitation [d]
360.0	2	β	c-a (3-1) 0.089 [c]	c-A (3-0)
360.5	3		-	-
369.4	100	β	c-a (3-2) 0.394 [c]	c-A (3-0)
372.0	8	α	d-a (1-1)	d-a (1-0)
373.5	8		-	-
377.4	7	β	c-a (3-3) 0.010 [c]	c-A (3-0)
379.5	4		D-A (2-2)	D-A (2-0)
386.0	95	β	c-a (3-4) 0.208 [c]	c-A (3-0)
388.0	5		-	-
391.0	< 1		-	-
395.3	10	β	c-a (3-5) 0.180 [c]	c-A (3-0)
397.0	< 1			

[a] *Approximate relative intensities*

[b] *Dependence of* I_{MgO} *on* $I_{Mg} = I\,[Mg(^3P-^1S)]$: α = linear dependence, $\beta \propto \frac{I_{Mg}}{K'+K''\,I_{Mg}^2}$

[c] *Franck-Condon factors calculated from the molecular constants given in Table 8.*

[d] *According to Table 4, the 363.8 nm* Ar^+ *laser line coincides with* $R_2(13) + {}^RQ_{32}(13)$ *of* $c^3\Sigma^+ - A^1\Pi$ *(3-0).*

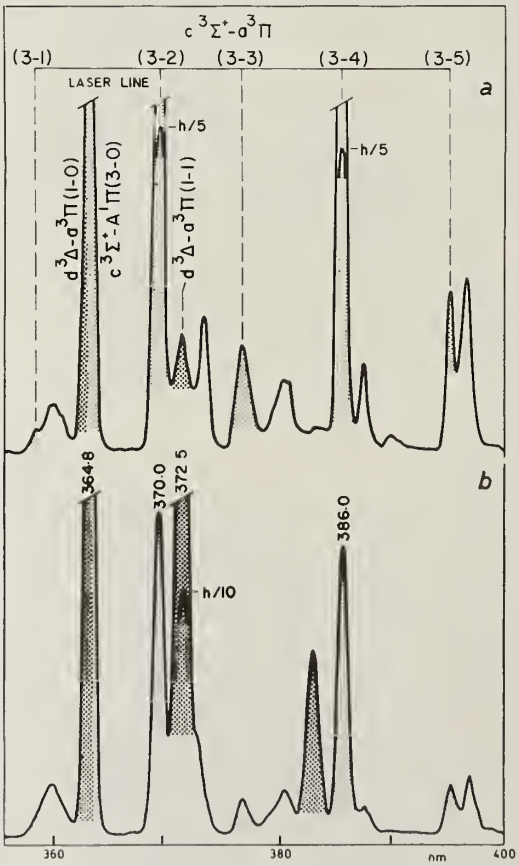

Fig. 3. MgO Laser Induced Fluorescence Spectrum excited by the Ar^+ laser 363.8 nm line.
a) low $Mg(^3P)$ concentration
b) high $Mg(^3P)$ concentration.

recently by Yarkony ([26]).

The reaction scheme given in Table 7 takes into account all the presently available information on the Mg + N_2O reaction kinetics and dynamics and on MgO spectroscopy.

TABLE 7 - Reaction scheme for the $Mg(^3P, ^1P) + N_2O$ + He system.

(1)	$Mg(^3P) + Mg(^3P) \rightarrow Mg(^1P) + N_2O$		
(2)	$Mg(^3P) + N_2O \rightarrow MgO(a^3\Pi) + N_2$	(0.43)	2a
	$\rightarrow MgO(X^1\Sigma^+) + N_2$	(0.33)	2b
	$\rightarrow MgO(A^1\Pi) + N_2$	(> 0.04)	2c
	$\rightarrow MgO(b)^3\Sigma^+ + N_2$	*	2d
(3)	$Mg(^1P) + N_2O \rightarrow MgO(B^1\Sigma^+) + N_2$		3a
	$\rightarrow MgO(A^1\Pi, X^1\Sigma^+) + N_2$		3b
(4)	$MgO(A^1\Pi) + Mg(^1P) \rightarrow MgO(d^3\Delta, D^1\Delta, C^1\Sigma^-) + Mg(^1S)$	**	

* *The $MgO(b)^3\Sigma^+$ state is not known.*

** *The occurrence of this reaction is inferred from kinetic arguments but there is no direct experimental evidence that the observed $d^3\Delta$, $D^1\Delta$ and $C^1\Sigma^-$ chemiluminescent states are formed through it (see text).*

In contrast, the analogous reaction $MgO(a^3\Pi) + Mg(^1P) \rightarrow MgO(d^3\Delta, c^3\Sigma^+) + Mg(^1S)$ does not seem to proceed.

It consists of four types of reactions :

(1) Energy pooling reaction populating very efficiently the $Mg(^1P)$ state. Up to now, there has been no evidence that $Mg(^1P)$ is a direct product. An alternate mechanism is the direct formation of $Mg(4^1S)$ in a resonant step, then cascade to $Mg(^1P)$, although attempts to observe $Mg(3\ P) \leftrightarrow Mg(4^1S)$ emission have failed ([27]).

(2) Primary reactions involving $Mg(^3P)$. They have been extensively studied by Dagdigian ([5],[6]) who measured the branching ratios given in brackets. Using the assignement that we established for the 372 nm system, we have been able to derive a consistent vibrational distribution for the $a^3\Pi$ state formed under single-collision conditions. The $a^3\Pi$ state exhibits a population inversion in favor of the v = 2 level. This analysis and the dynamical implications are discussed in detail elsewhere ([29]). There is no experimental evidence that the reaction 2d occurs, since the MgO $(b)^3\Sigma^+$ state has not yet been observed. According to Yarkony's theoretical work, it should not be significantly populated.

(3) Primary reactions involving $Mg(^1P)$. The reaction 3a produces the radiative $B^1\Sigma^+$ state which is detected through chemiluminescence. This reaction was invoked in our previous study ([3]) to explain the kinetic observations. This reaction is possible because the $Mg(^1P)$ effective lifetime is significantly lenghtened by radiation trapping and therefore the collision probability of $Mg(^1P)$ with N_2O is increased. Formation of the B state by reaction of $Mg(^1P)$ with N_2O was proved unambiguously by Breckenridge ([8]) who observed the (B-X) chemiluminescence in absence of $Mg(^3P)$ by direct laser excitation of $Mg(^1P)$. There is still no evidence that other MgO states are formed by this reaction since Breckenridge probed only the B state, and kinetic measurements are not conclusive because of the simultaneous occurrence of the $Mg(^3P) + N_2O$ reaction.

(4) Electronic energy transfer. Chemiluminescence from $d^3\Delta$, $D^1\Delta$, and $C^1\Sigma^-$ MgO states is observed under our experimental conditions. From kinetic arguments we concluded that these states were not populated directly by $Mg(^3P,^1P) + N_2O$. This was later confirmed by Dagdigian ([5]) and Breckenridge et al ([8]) experimental observations. These states must therefore be populated by electronic energy transfer. In our experimental conditions, $Mg(^3P)$ and $Mg(^1P)$ are the only energy reservoirs;since the reaction $Mg(^3P) + MgO(X^1\Sigma^+, a^3\Pi, A^1\Pi) \rightarrow MgO(d^3\Delta, D^1\Delta, C^1\Sigma^-) + Mg$ is highly endothermic, electronic energy can only be transferred from $Mg(^1P)$. This is in agreement with the observed dependence of $MgO(A^1\Pi)$ population with the $Mg(^3P)$ concentration as shown in Fig. 4, and consistent with the occurrence of reactions 2c and 4a. The low intensity of the $C^1\Sigma^-$, $D^1\Delta \rightarrow A^1\Pi$ chemiluminescence precludes measurement of the $C^1\Sigma^-$ and $D^1\Delta$ formation rate dependence upon $Mg(^3P)$ concentration. For the more intense $d^3\Delta - a^3\Pi$ chemiluminescence, the intensity dependence is found to be consistent with the reaction scheme of Table 7 only at relatively low $Mg(^3P)$ concentration (Fig. 5). In conclusion, we think that the occurrence of reaction 4a is demonstrated. Formation of the $MgO(d^3\Delta)$ through this spin-forbidden mechanism is still questionable. In any case, the $d^3\Delta$ state is also populated by another reaction which could not be identified. The analogous reaction involving $Mg(^3P)$ is not observed, giving evidence for a strong spin selectivity.

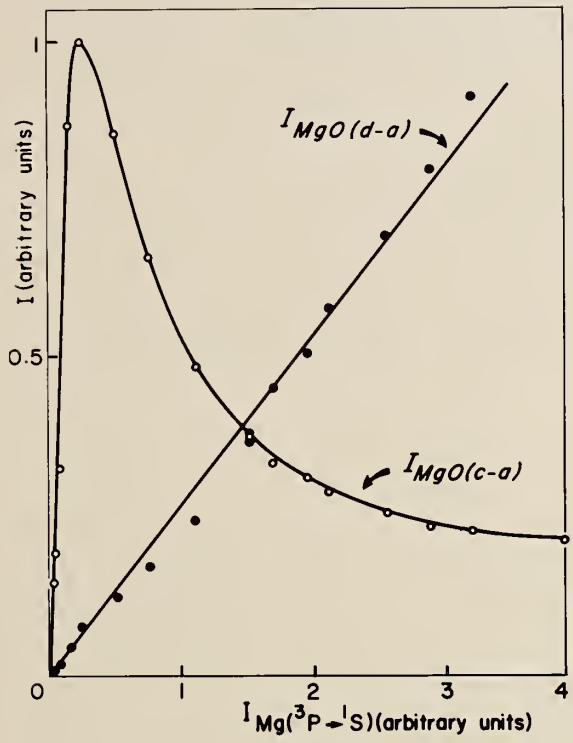

Fig. 4.

Dependence of the $c^3\Sigma^+ - a^3\Pi$ (3-2) and $d^3\Delta - a^3\Pi$ (1-1) LiF intensities as a function of the $Mg(^3P - ^1S)$ emission intensity. The c-a (3-v) fluorescence resulting from the c-A(3-0) transition pumping, monitors the $A^1\Pi$ population. The d-a(1-1) resulting from the d-a(1-0) pumping, monitors the $a^3\Pi$ population. (see section 6 and table 6).

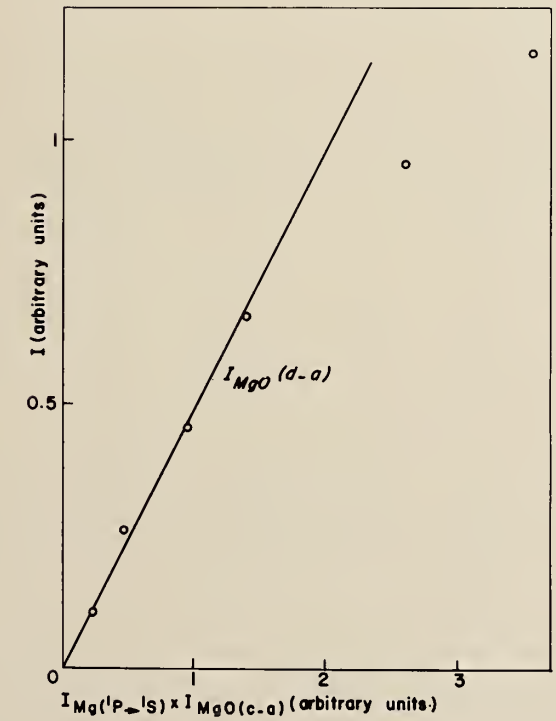

Fig. 5.

Dependence of the $MgO(d^3\Delta - a^3\Pi)$ chemiluminescence intensity as a function of the product of the $Mg(^1P - ^1S)$ emission intensity times the $MgO(c^3\Sigma^+ - a^3\Pi)$ (3-2) LiF intensity. The $MgO(d^3\Delta - a^3\Pi)$ chemiluminescence monitors $MgO(d^3\Delta)$ population, the $MgO(c^3\Sigma^+ - a^3\Pi)$ LiF monitors the $MgO(A^1\Pi)$ population. A linear dependence of $[MgO(d^3\Delta)]$ on $[MgO(A^1\Pi)] \times [Mg(^1P)]$ would be in agreement with the formation of $MgO(d^3\Delta)$ by reaction 4 of Table 7.

VIII. SUMMARY AND CONCLUSION

Detailed investigation of laser induced fluorescence and laser excitation spectra of MgO produced at room temperature from the Mg(^{3}P, ^{1}P) + N_2O reaction in a Broida oven has provided new spectroscopic data on the ...$\pi^3\pi$ triplet states of MgO. The assignments for the $d^3\Delta$ - $a^3\Pi$ Δv = 0 band heads that we proposed previously have been confirmed by the observation of the (1-0) band and rotational analysis of the R_1(0-0) and R_1(1-0) branches. The $c^3\Sigma^+$ state has been characterized for the first time from the assignment of a band at 364.0 nm to the forbidden $c^3\Sigma^+$ - $A^1\Pi$ (3-0) band. This assignment is substantiated by partial rotational analysis and earlier spectroscopic work.

Preliminary values for the equilibrium molecular constants (T_e, ω_e, B_e) of the $c^3\Sigma^+$ and $d^3\Delta$ states have been obtained. They are compared with the ab initio values ([9]) in Table 8, where are given the relevant values for the MgO electronic states arising from the three lowest configurations. The excellent agreement between observed and calculated ω_e values for the $d^3\Delta$ is fortuitous since the calculated ω_e values are about 10 % too small for the other states of the same configuration. The calculated values for B_e are also consistently too small ($\sim$3 %). The calculated position (T_e) for the C, D, d and c states is higher than observed. The difference, of 400 - 700 cm^{-1} for

TABLE 8 - Observed and calculated molecular constants for MgO (cm^{-1}) [a].

	T_e			ω_e		B_e	
	obs.	calc. [d]	obs.-calc.	obs.	calc. [d]	obs.	calc. [d]
$E^1\Sigma^+$	37722			705		0.5249	
$C^1\Sigma^-$	30030.6	29634	447	632.4	566.8	0.5008	0.4849
$e^3\Sigma^-$		-					
$D^1\Delta$	29851.6	29339	513	632.5	573.2	0.5014	0.4866
$d^3\Delta$ [b]	29452	28731	721	652.4	649.3	0.5102	0.4976
$c^3\Sigma^+$ [b]	28950	27654	1296	706	666.8	0.5360	0.5037
$8^1\Sigma^+$	19984.0	20804	- 820	824.1	853.7	0.5822	0.5841
$(b)^3\Sigma^+$	-	8272		-	715.7	-	0.5473
$A^1\Pi$	3563.3	3487	76	664.4	733.8	0.5056	0.5097
$a^3\Pi$ [c]	2620.0	2402	218	648.3	715.5	0.5028	0.5090
$X^1\Sigma^+$	0.0	0	-	785.1	875.9	0.5743	0.5671

[a] *All observed parameters are taken from ref. 25 except otherwise stated.*

[b] *Observed values from this work.*

[c] *Observed values from ref. 19 and 20.*

[d] *Calculated values from ref. 9.*

the C, D and d states, is about 1300 cm^{-1} for the c state. This questionned our assignment of the $c^3\Sigma^+$ vibronic levels, which should be confirmed further by more experimental data. We plan to carry out further investigation in particular to study the other MgO isotopic species.

The present spectroscopic analysis giving evidence that both the $a^3\Pi$ and $A^1\Pi$ states are pumped by the 363.8 nm Ar^+ laser line was a key for the detailed understanding of the $Mg(^3P, ^1P) + N_2O + He$ kinetics. The $Mg(^3P) + N_2O$ reaction produces directly both the $A^1\Pi$ and $a^3\Pi$ states. The $A^1\Pi$ is efficiently depleted by reaction with $Mg(^1P)$ producing chemiluminescent MgO states. In contrast, there is no efficient secondary reaction involving the $a^3\Pi$ state.

The above results have to be considered in the general framework of collision-induced electronic transfer as well as chemical reactivity. Because of the difficulty to isolate a particular chemical or physical process in a bulk experiment, still in question are the detailed mechanisms responsible for several important experimental observations for example : **i)** the anomalous $a^3\Pi$ Λ-doublet population distribution ([20]) in $Mg(^1S)/N_2O/Ar$ flames ; **ii)** the occurrence of reaction such as $MgO(a^3\Pi) + CO \rightarrow Mg(^3P) + CO_2$ ([4]) which, suggested long ago, was recently demonstrated in a Mg beam experiment ([30]) ; **iii)** the possibility of chemical pumping of Mg ground state atoms into $Mg(^3P)$ by reacting $Mg(^1S)$ atoms with N_2O/CO/mixture ([31]).

Acknowledgments

We thank Guy Taïeb for stimulating discussions. We also thank Jacques Lefevre for his help with the figures, and Odile Dubost for skillfull and patient typing of the manuscript.

---

* *Laboratoire associé à l'Université de Paris-Sud.*

References

1 - G. Taïeb and H.P. Broida, J. Chem. Phys. 65 (1976) 2914.

2 - G. Taïeb, J. Phys. (Paris) 42 (1981) 537.

3 - B. Bourguignon, J. Rostas and G. Taïeb, J. Chem. Phys. 77 (1982) 2979.

4 - D.J. Benard and W.D. Slafer, J. Chem. Phys. 66 (1977) 1017.

5 - P.J. Dagdigian, J. Chem. Phys. 76 (1982) 5375.

6 - J.W. Cox and P.J. Dagdigian, J. Phys. Chem. 86 (1982) 3738.

7 - J.W. Cox and P.J. Dagdigian, J. Phys. Chem. 88 (1984) 2455.

8 - W.H. Breckenridge and H. Umemoto, J. Phys. Chem. 87 (1983) 1804.

9 - C.W. Bauschlicher Jr., B.H. Lengsfiled III, D.M. Silver and D.R. Yarkony, J. Chem. Phys. 74 (1981) 2379.

10- L. Brewer and R.F. Porter, J. Chem. Phys. 22 (1954) 1867.

11- D. Pesic and A.G. Gaydon, Proc. Phys. Soc. 73 (1959) 244.

12- D. Pesic, Proc. Phys. Soc. London A, 76 (1960) 844.

13- L. Brewer, S. Trajmar and R.A. Berg, Astrophys. J. 135 (1962) 955.

14- S. Trajmar and G.E. Ewing, Astrophys. J. 142 (1965) 77.

15- J. Schamps, Thèse d'Etat, Université de Lille (1973).

16- P.J. Evans and J.C. Mackie, Chem. Phys. 5 (1974) 277 ; J. Molec. Spectrosc. 65 (1977) 169.

17- J. Schamps and G. Gandara, J. Molec. Spectrosc. 62 (1976) 80.

18- T. Ikeda, N.B. Wong, D.O. Harris, and R.W. Field, J. Molec. Spectrosc. 68 (1977) 452.

19- B. Bourguignon, J. McCombie and J. Rostas, Chem. Phys. Lett. 113 (1985) 323.

20- P.C.F. Ip. PhD Thesis, Massachussetts Institute of Technology (1983).

21- P.C.F. Ip., K.J. Cross, R.W. Field, J. Rostas, B. Bourguignon and J. McCombie, to be published.

22- B. Bourguignon, Thèse de 3ème cycle, Université de Paris-Sud, Orsay (1982).

23 - B. Bourguignon and J. Rostas, to be published.

24 - G. Herzberg, Electronic spectra of diatomic molecules, (Van Nostrand, 1950).

25 - D.L. Albritton, A.L. Schmeltekopf and R.N. Zare, (private communication).

26 - D.R. Yarkony, J. Chem. Phys. 78 (1983) 6763.

27 - W.H. Breckenridge, W.L. Nikolai and J. Stewart, J. Chem. Phys. 74 (1981) 2073.

28 - A.T. Pritt Jr., D. Patel and D.J. Benard, Chem. Phys. Lett. 105 (1984) 667.

29 - B. Bourguignon, J. Rostas, G. Taïeb, J. McCombie, and M. Gargoura, Laser Chemistry (1985).

30 - H.H. Michels and R.A. Meinzer, Chem. Phys. Lett. 98 (1983) 6.

31 - R.A. Meinzer, H.H. Michels and R. Tripodi, V Gas Combustion Conference, Oxford 1984.

LASER SPECTROSCOPY OF ORGANOMETALLIC FREE RADICALS

C.R. Brazier, P.F. Bernath, S. Kinsey-Nielsen,
L.C. Ellingboe and A.M.R.P. Bopegedera
Department of Chemistry, University of Arizona, Tucson, AZ 85721

Abstract

Recently we observed a large number of new organometallic free radicals (1). Calcium, strontium and barium have been found to react in the gas phase with a wide variety of organic molecules including aldehydes, ketones, alcohols, carboxylic acids and hydrogen isocyanate. The reaction products are free radical metal salts with electronic states that are closely related to the alkaline earth monohalides.

The alcohols, ketones, aldehydes and hydrogen isocyanate react to produce metal free radicals of the form:

$M^+—O^=—R$ M = Ca, Sr, Ba

R = CH_3, C_2H_5, C_3H_7, C_4H_9, CN

The bonding in these molecules is largely ionic and the observed electronic transitions occur between M^+ centered atomic-like orbitals perturbed by an ^-O-R ligand.

Acetic and formic acids react with Ca, Sr and Ba to produce metal monoacetates and monoformates of the form:

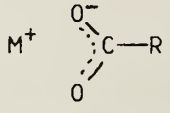

R = H, CH_3

M = Ca, Sr and Ba

The observed electronic spectra differ from the alkoxides because the local symmetry is C_{2v} rather than linear.

The molecules are all produced in a flowing metal plus organic oxidant reactor (Broida oven) and detected via laser induced fluorescence. We are presenting data on the electronic structure and vibrational frequencies of these novel species.

Introduction

The interaction of metals with organic molecules is one of the principal themes of modern chemistry. Recently, we have discovered a large number of new gas phase organometallic free radicals produced by the reaction of Ca, Sr and Ba with aldehydes, ketones, alcohols, carboxylic acids and hydrogen isocyanate. In this paper we report on the alkaline earth monoalkoxide, monocarboxylate and monocyanate radicals.

The smallest members of the alkaline earth alkoxide (M-O-R; M = Mg, Ca, Sr, and Ba) series are the triatomic monohydroxides (R = H). The alkaline earth monohydroxide radicals commonly occur in flames containing traces of alkaline earth salts (2). The flame observations date back to the work of Herschel (3) in 1823, although it was not until 1955 that James and Sugden (4) correctly assigned the carrier of the emission to the alkaline earth monohydroxides. ESR spectra of matrix-isolated BeOH (5) and MgOH (6) suggested that, like the alkali hydroxides, the alkaline earth hydroxides are linear. More recently infrared spectra of matrix isolated SrOH and BaOH were observed by Kauffman, Hauge and Margrave (7).

The key discovery in the alkaline earth alkoxide work was that substantial quantities of cool (500 K) MOH could be produced in a Broida oven (8) by the reaction of alkaline earth metal vapors with H_2O (9,10). Rotational analyses of the $\tilde{A}^2\Pi$-$\tilde{X}^2\Sigma^+$ and $\tilde{B}^2\Sigma^+$-$\tilde{X}^2\Sigma^+$ electronic transitions by laser techniques provided bond lengths and vibrational frequencies (11-16). Wormsbecher and Suenram (17) prepared the next member of the alkoxide series in a Broida oven by the reaction of Ca and Sr metal vapors with CH_3ONO.

During an unsuccessful attempt to make alkaline earth acetylides in a Broida oven, we discovered that acetone reacted with Sr vapor to produce two new free radicals (1). Further experiments proved that the major product was strontium isopropoxide, $SrOCH(CH_3)_2$. The initial strontium isopropoxide observations encouraged us to explore the gas phase chemical reactions of alkaline earth metals with alcohols.

Inspired by these results with alcohol oxidants, we extended our investigation by including the reactions of calcium and strontium with formic and acetic acid. The spectra are interpreted as arising from the bidentate

organometallic molecule, $M^+ \overset{O^-}{O}CH\text{-}R$.

Most recently, our work has included hydrogen isocyanate as the oxidant (18). The spectra are interpreted as arising from the linear ionic $M^+\text{-}^-OCN$ molecule. The spectra presented here are the first to be assigned to metal-monocyanate complexes, i.e. M-O-C≡N.

Experimental Methods

The alkaline earth monoalkoxides, monocarboxylates and monocyanates were made in a Broida-type oven (8) by the reaction of a metal vapor (Ca, Sr, or Ba) with a suitable oxidant. The metal was evaporated from a resistively heated alumina crucible and entrained in a flow of argon carrier gas. The total pressure was adjusted to about 8 torr by varying the pumping speed and argon flow rate in order to optimize the laser induced emission signal. For our initial strontium plus acetone experiments, it was found that the Sr $^3P_1\text{-}^1S_0$ atomic line overlapped the molecular transition (cf. Figure 1) and that excitation of the atomic line increased the signal by three orders of magnitude. Although the ground state atoms react at pressures of 8-10 torr, the $^3P_1$ excited atoms produce more product molecules. Thus for most of the experiments two cw dye lasers were used: a single-mode (1 MHz) Coherent 699-29 excited the $^3P_1\text{-}^1S_0$ atomic transition and a broadband (1 cm^{-1}) Coherent 599-01 excited the molecular transition. The dye lasers were operated with DCM or Pyridine 2 dyes and were pumped by Coherent Innova 20 and/or Coherent Innova 90 argon ion lasers. The dye laser output beams (200-1000 mW) were spatially overlapped and focused into the weakly chemiluminescent metal flames.

Laser excitation spectra were recorded by scanning the broadband dye laser and recording the total fluorescence with a photomultiplier-filter combination. Chopping the laser resonant with the atomic line provided product molecule concentration modulation and allowed lock-in detection.

Resolved fluorescence detection was accomplished by imaging the laser-induced fluorescence onto the slits of a 0.64 m monochromator equipped with an RCA C31034 photomultiplier and photon counting detection electronics. The monochromator (not the laser) was scanned to provide a dispersed fluorescence signal.

Results

The alkaline earth alkoxide and cyanate spectra all resemble the linear MOH spectra (which, in turn, resemble the MF diatomic spectra) so the observed electronic states will be named by analogy. Since the symmetry of the alkaline earth alkoxides is lower than linear this is not strictly correct. However, the M-O bond is very ionic so the electronic transitions involve non-bonding M^+ orbitals perturbed by an RO^- ligand. The M-O-C bond angle is 180°. Hence the local symmetry near the metal is linear, so for instance, there is always a "spin-orbit" splitting of ~65 cm^{-1} for the A state of the calcium containing species. The orbitals on the metal are only slightly affected by the nature of R on the ligand, so it is useful to utilize the effective linear symmetry in labelling the electronic states.

The observed band origins for calcium and strontium alkoxides and cyanate are reported in Table I and II. These data were recorded by monochromator scans of the laser-induced fluorescence (Figures 2 and 3 are typical examples). The hydroxides and methoxides produced resonance fluorescence while emission from the larger molecules was relaxed. The emission from the cyanates was partly relaxed and partly resonant (Figure 4). Vibrational relaxation, relaxation between $\tilde{A}_1$ and $\tilde{A}_2$ spin-components and relaxaion between $\tilde{B}$ and $\tilde{A}$ states were all prominent (but not complete) in the spectra. The two strong, broad features of Figures 1-4 are the $\tilde{A}_1{}^2\Pi_{1/2}$-$\tilde{X}^2\Sigma^+$ and $\tilde{A}_2{}^2\Pi_{3/2}$-$\tilde{X}^2\Sigma^+$ transitions. The peak positions were determined to an estimated accuracy of ±2-5 cm^{-1}.

The $\tilde{A}$-$\tilde{X}$ emission spectra (Figs. 2-4) show evidence of weak vibrational structure. Since the electronic transition involves a metal-centered, non-bonding electron the Franck-Condon factors for $\Delta v \neq 0$ transitions are expected to be small. Furthermore, any observed vibrational activity will be associated with the metal center.

The laser-induced fluorescence spectra (eg. Figs. 2-4) were all recorded by scanning the monochromator. In some spectra the detector amplifier gain was such that the strong features were off scale but the vibrational structure was clearer (eg. Figs. 5 and 6). The observed transitions could be assigned to activity in four normal modes: ν_B, the M-O-R bend; ν_S, the M-O stretch; ν_σ, the O-C stretch; and ν_β, the O-C-C bend.

The reaction of Sr with acetone (and acetaldehyde) produced two products. For instance (Fig. 6) when a large (several hundred millitorr) amount of acetone was present, the main product was $Sr-O-CH(CH_3)_2$. At lower acetone concentrations an additional molecule, tentatively assigned to $Sr-O-C(CH_3)=CH_2$, was observed. The strontium isopropoxide assignment is secure since a comparison spectrum (obtained from Sr plus isopropanol) is available. The reaction of Ca with acetone (or acetaldehyde) produced almost entirely the isopropoxide (ethoxide) while the corresponding Ba reactions have not been explored yet.

Figure 7 is a laser excitation spectrum of the Sr plus formic acid reaction. The reaction produced SrH and SrOH as well as a new molecule with peaks at 6785 and 6710 Å. We assign the carrier of this spectrum to the strontium monoformate radical with C_{2v} symmetry. The two main peaks are the $^2B_1$ and $^2B_2$ electronic states that correlate with the A $^2\Pi$ state of SrF. A new electronic transition was also found 1000 cm^{-1} below the 6785 Å peak. This new electronic state probably has $^2A_1$ symmetry and correlates with one component of the expected $^2\Delta$ states of strontium monohalides. The $^2\Delta$-$^2\Sigma$ transition has become allowed in a C_{2v} molecule.

Discussion

A. Vibrational Structure

The metal-centered character of the $\tilde{A}$-$\tilde{X}$ electronic transition both helps and hinders the vibrational analysis. Franck-Condon selection of only a few modes associated with the metal center makes the vibrational assignments relatively easy. However, almost all direct information about the nature of the alkyl group is suppressed.

As well as diagonal bands, emission was observed to excited vibrational levels of the ground state and from excited vibrational levels of the $\tilde{A}$ state. The metal-oxygen stretching frequency (ν_s) is usually the strongest mode (Fig. 4) and was easily assigned. The ground state ν_s frequencies are collected in Table III for comparison purposes. The values range from 606 cm^{-1} for CaOH to 247 cm^{-1} for $SrOC(CH_3)_3$, largely because of changes in the effective reduced mass. The M^+-O^- ionic bonding results in a similar M-O force constant for all

the observed molecules. By treating the OR unit as a single mass a diatomic-like "reduced mass" (μ) can be calculated. A plot of the stretching frequency versus $\mu^{-1/2}$ produces an approximately linear correlation with Ca-OR and Sr-OR (Ba has only three points) each producing a slightly different line (Figure 8). These empirical correlations are consistent with a locally linear model for these compounds, M-O-R, where the R group has essentially no effect on the metal oxygen bond.

The M-O-R bending mode (ν_B) is usually as prominent as the M-O stretching mode. In fact for Sr alkoxides with symmetry lower than $C_{\infty v}$ or C_{3v} ν_B is the strongest mode, occurring in the 65-90 cm^{-1} region except for MOH and $MOCH_3$. This is a remarkably low frequency even for a bending mode but the ionic M^+-O^- bond will produce a very flat bending potential. The low frequency is also consistent with the general trend in bending frequencies for CaOH (339 cm^{-1}) and $CaOCH_3$ (142 cm^{-1}).

B. Electronic Structure

The alkaline earth monoalkoxide and cyanate electronic spectra resemble those of the corresponding monohalides. The similarities are particularly strong for the isoelectronic MOH as OH^- is a pseudohalide. Since replacing H by R in MOH is not expected to change the basic character of the electronic states, our discussion of MOR electronic states is carried over from the corresponding MF states (19-21).

The ground $\tilde{X}^2\Sigma^+$ state of MOR arises almost entirely from the valence nsσ orbital of M^+ with a small admixture of npσ character. The first excited states (22) for Ca^+, Sr^+, and Ba^+ are the (n-1)d states with np states 10,000 to 15,000 cm^{-1} higher (n= 4, 5 and 6 for Ca, Sr and Ba, respectively). The O^--R ligand has effective linear symmetry and produces three molecular orbitals (n-1)dσ, (n-1)dπ and (n-1)dδ from the (n-1)d orbital and two molecular orbitals npσ, npπ from the np state. The npσ and (n-1)dσ mix to produce the $\tilde{B}^2\Sigma^+$ state while the npπ and (n-1)dπ result in the $\tilde{A}^2\Pi$ state (as well as higher lying $^2\Sigma^+$ and $^2\Pi$ states). The $\tilde{B}^2\Sigma^+$ and $\tilde{A}^2\Pi$ states form a unique perturber pair (23) connected by spin-orbit, rotation-electronic and vibronic interactions. The (n-1)dδ orbitals produce a $^2\Delta$ state which for BaCl (24) has been found to lie lower in energy than the $\tilde{A}^2\Pi$ state. The $^2\Delta$ states are difficult to locate because $^2\Delta$-$^2\Sigma$

transitions are forbidden even for pseudodiatomics like MOR. For the calcium and strontium monoformates where the local symmetry is C_{2v} rather than $C_{\infty v}$, the $^2\Delta$ state (or more accurately a $^2A_1$ state correlating with a $^2\Delta$ parent state) has been found about 1000 cm^{-1} below the $\tilde{A}$ state (25).

In both the Ca and Sr cyanate spectra the $\tilde{A}\leftarrow\tilde{X}$ transition consists of two components split by 72 and 291 cm^{-1}, respectively. This is similar to the spin-orbit splitting in Ca and Sr monohydroxide (73, 281 cm^{-1}) (11,15) and monoalkoxides (26). This is characteristic of locally linear bonding in the ionic molecule $M^+-{}^-OX$ (X= H, R, CN).

The splitting between the $\tilde{A}$ and $\tilde{B}$ states is a ligand field separaton between $d\sigma$ ($p\sigma$) and $d\pi$ ($p\pi$) orbitals. The various ligands can be arranged in a spectrochemical series (27) $F^- > OH^- > NH_2^- > O^-R > NCO^- > Cl^- > Br^- > I^-$ for the alkaline earths. The order is determined by the $\tilde{B}$-$\tilde{A}$ energy separation and reflects the strength of the ligand field interaction. The location of NH_2^- is from the work of Wormsbecher et al. (10).

Conclusion

A large number of new Ca, Sr and Ba containing free radicals have been discovered and characterized by laser spectroscopy. The alkaline earth organometallics were produced in the gas phase by the reaction of the metal vapor with the appropriate oxidant. The vibrational and electronic structure of the alkaline earth monoalkoxides has been explained in terms of an M^+ ion perturbed by an ionic ligand.

Acknowledgements

This research was supported by the National Science Foundation (NSF-8306504) and the Research Corporation. Acknowledgement is made to the donors of the Petroleum Research Fund, administered by the ACS, for partial support of this work. Partial support was also provided by the Office of Naval Research (ONR N 00014-84-K-0122).

References

(1) Brazier, C.R.; Bernath, P.F.; Kinsey-Nielsen, S; Ellingboe, L.C. J. Chem. Phys. 1985, **82**, 1043-1045.

(2) Alkemade, C.Th.J.; Hollander, Tj.; Snelleman, W.; Zeegers, P.J.Th. "Metal Vapours in Flames"; Pergamon Press: Oxford, 1982.

(3) Herschel, J.F.W. Trans. Roy. Soc. (Edinburgh) 1823, **9**, 445-460.

(4) James, C.G.; Sugden, T.M. Nature 1955, **175**, 333-334.

(5) Brom, J.M. Jr.; Weltner, W. Jr. J. Chem. Phys. 1976, **64**, 3894-3895.

(6) Brom, J.M. Jr.; Weltner, W. Jr. J. Chem. Phys. 1973, **58**, 5322-5330.

(7) Kauffman, J.M.; Hauge, R.H.; Margrave, J.L. High Temp. Sci. 1984, **18**, 97-118.

(8) West, J.B.; Bradford, R.S.; Eversole, J.D.; Jones, C.R. Rev. Sci. Instrum. 1975, **46**, 164-168.

(9) Benard, D.J.; Slafer, W.D.; Hecht, J. J. Chem. Phys. 1977, **66**, 1012-1016.

(10) Wormsbecher, R.F.; Trkula, M.; Martner, C.; Penn, R.E.; Harris, D.O. J. Mol. Spectrosc. 1983, **97**, 29-36.

(11) Hilborn, R.C.; Zhu Qingshi; Harris, D.O. J. Mol. Spectrosc. 1983, **97**, 73-91.

(12) Nakagawa, J.; Wormsbecher, R.F.; Harris, D.O. J. Mol. Spectrosc. 1983, **97**, 37-64.

(13) Bernath, P.F.; Kinsey-Nielsen, S.M. Chem. Phys. Lett. 1984, **105**, 663-666.

(14) Bernath, P.F.; Brazier, C.R. Astrophys. J. 1985, **288**, 373-376.

(15) Brazier, C.R.; Bernath, P.F. "Laser and Fourier Transform Spectroscopy of the $\tilde{A}^2\Pi - \tilde{X}^2\Sigma^+$ Transition of SrOH" J. Mol. Spectrosc. (in press).

(16) Kinsey-Nielsen, S.M.; Brazier, C.R.; Bernath, P.F. "Rotational Analysis of the $\tilde{B}^2\Sigma^+ - \tilde{X}^2\Sigma^+$ Transition of BaOH and BaOD" submitted to J. Chem. Phys.

(17) Wormsbecher, R.F.; Suenram, R.D. J. Mol. Spectrosc. 1982, **95**, 391-404.

(18) Ellingboe, L.C.; Bopegedera, A.M.R.P.; Brazier, C.R.; Bernath, P.F. "Laser Spectroscopy of Ca and Sr Cyanate" in prep.

(19) Dagdigian, P.J.; Cruse, H.W.; Zare, R.N. J. Chem. Phys. 1974, **60**, 2330-2339.

(20) Bernath, P.F.; Pinchemel, B.; Field, R.W. J. Chem. Phys. 1981, **74**, 5508-5515.

(21) Rice, S.F.; Martin, H.; Field, R.W. J. Chem. Phys. 1985, **74**, 5023-5034.

(22) Moore, C.E. "Atomic Energy Levels"; vol. I-III NSRDS-NBS 35, National Bureau of Standards: Washington, 1971.

(23) Zare, R.N.; Schmeltekopf, A.L.; Harrop, W.J.; Albritton, D.L. J. Mol. Spectrosc. 1973, **46**, 37-66.

(24) Martin, H.; Royen, P. Chem. Phys. Lett. 1983, **97**, 127-129.

(25) Brazier, C.R.; Ellingboe, L.C.; Kinsey-Nielsen, S.M.; Bernath, P.F. "Laser Spectroscopy of Alkaline Earth Monocarboxylates" in preparation.

(26) Brazier, C.R.; Ellingboe, L.C.; Kinsey-Nielsen, S.; Bernath, P.F. "Laser Spectroscopy of Alkaline Earth Monoalkoxide Free Radicals" submitted to J. Amer. Chem. Soc.

(27) Cotton, F.A.; Wilkinson, G. "Advanced Inorganic Chemistry" 4th ed.; Wiley: New York 1980; p. 663.

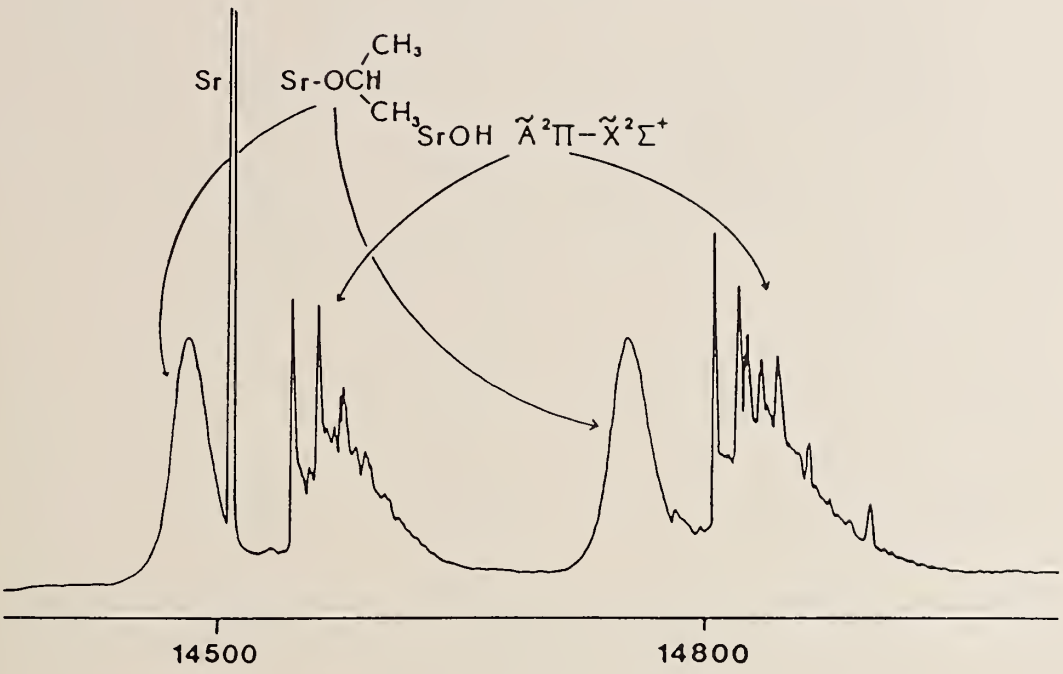

Figure 1. Laser excitation spectrum of the Sr plus acetone reaction products. The two broad peaks are due primarily to the strontium isopropoxide radical.

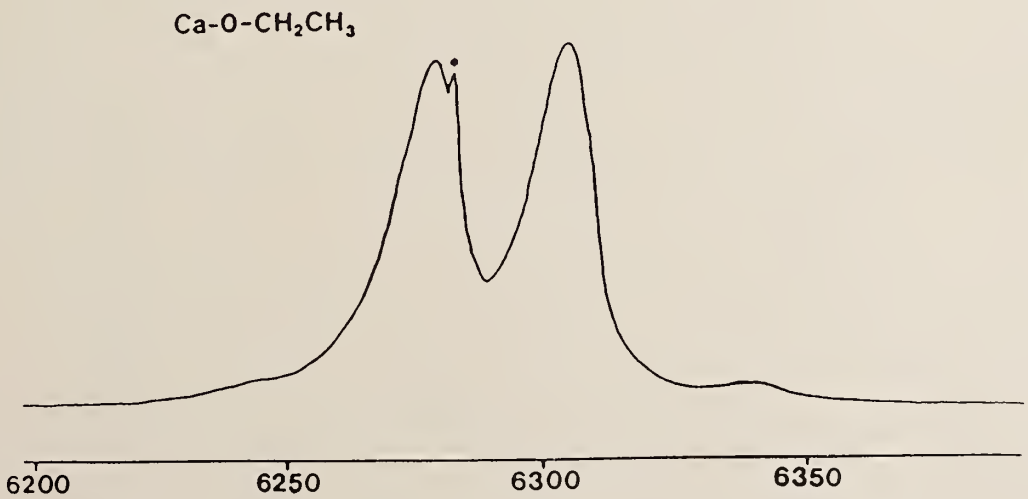

Figure 2. Laser-induced fluorescence from the $\tilde{A}-\tilde{X}$ transition of $CaOCH_2CH_3$. The asterisk marks scattered light from the dye laser exciting the $\tilde{A}_2{}^2\Pi_{3/2}-\tilde{X}^2\Sigma^+$ molecular transition. An additional laser excites the Ca $^3P_1-{}^1S_0$ transition at 6572 Å. The horizontal scale is in Å.

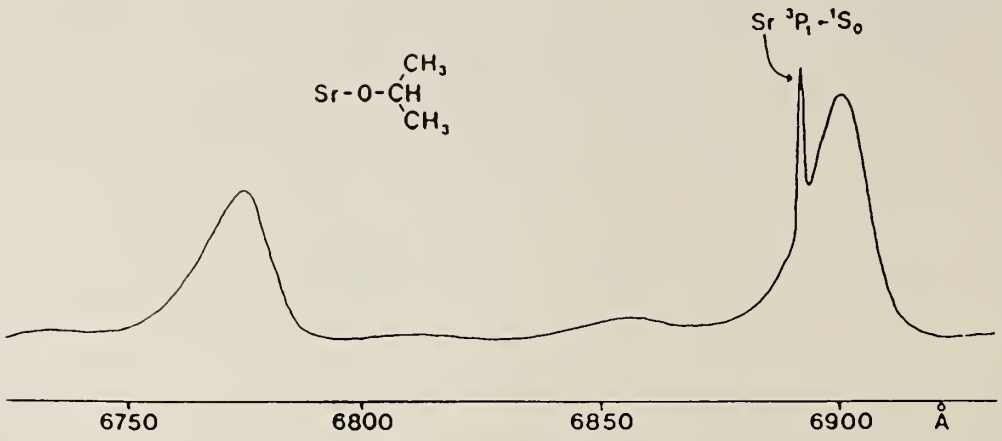

Figure 3. Laser-induced fluorescence from the $\tilde{A}$-$\tilde{X}$ transition of $SrOCH(CH_3)_2$. The laser is simultaneously exciting the atomic line at 6892 Å and the $\tilde{A}_1{}^2\pi_{1/2}$-$\tilde{X}^2\Sigma^+$ molecular transition.

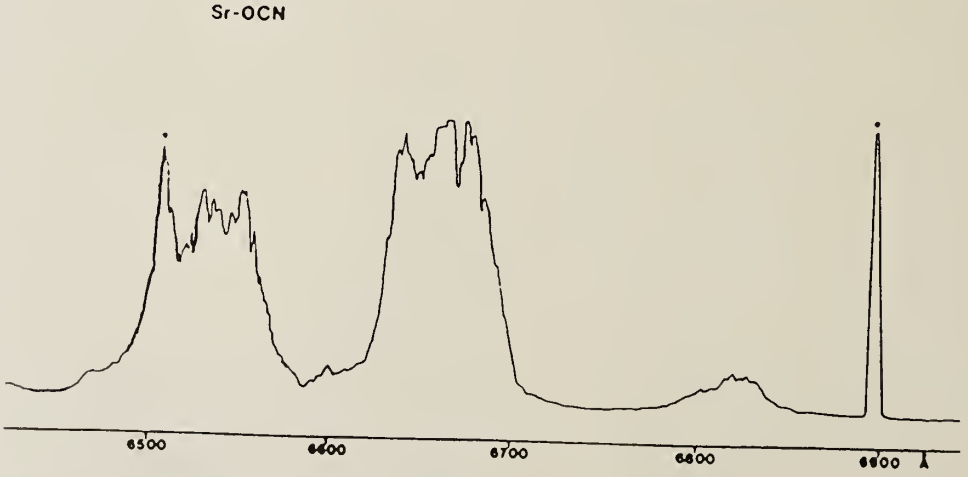

Figure 4. Laser-induced fluorescence from the $\tilde{A}\leftarrow\tilde{X}$ transition of SrOCN. The splitting between the two strong features is due to the spin-orbit splitting in the $\tilde{A}^2\Pi$ state. The asterisks mark the scattered light from the two exciting dye lasers on the atomic $^3P_1\leftarrow{}^1S_0$ transition and the $\tilde{A}_2{}^2\pi_{3/2}\leftarrow\tilde{X}^2\Sigma^+$ transition.

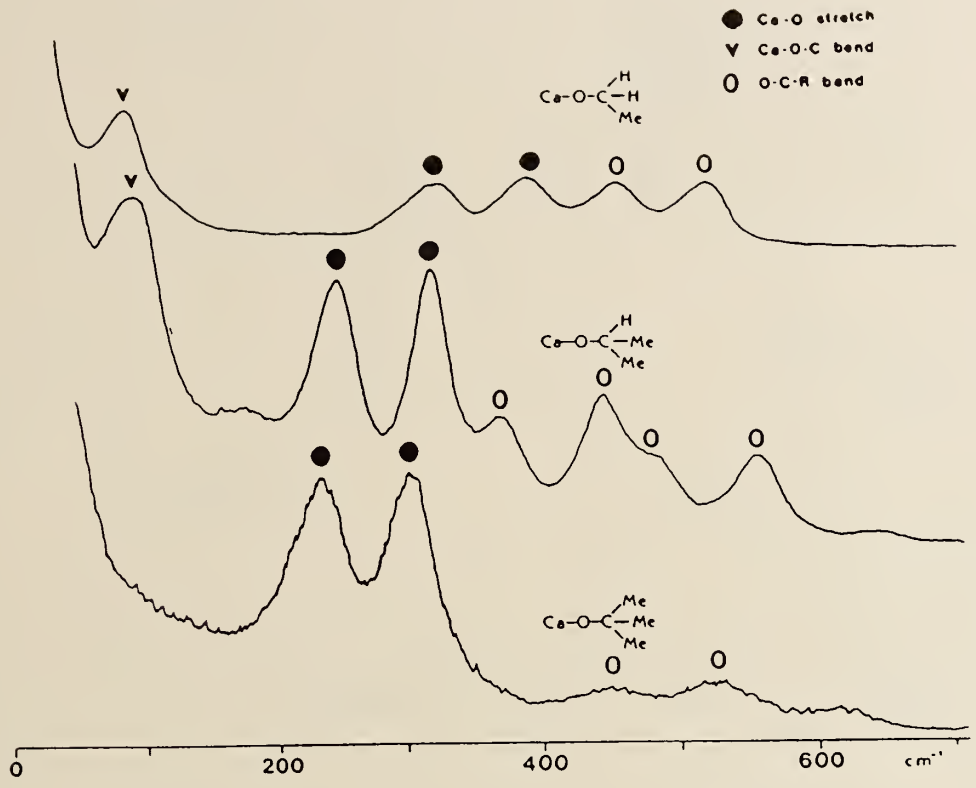

Figure 5. Laser-induced fluorescence spectra of the $CaOCH_2CH_3$, $CaOCH(CH_3)_2$, and $CaOC(CH_3)_3$ molecules (the 0-0 $\tilde{A}$-$\tilde{X}$ band emission is off scale). Each vibrational feature is doubled by the spin-orbit splitting (~65 cm^{-1}) of the $\tilde{A}$ state. The x-axis scale is set to zero for the $\tilde{A}_1{}^2\pi_{1/2} \leftarrow \tilde{X}^2\Sigma^+$ 0-0 band so the scale refers to the higher frequency component of any doublet. Each pair of lines corresponds to emission from the $\tilde{A}$ state into the vibrationally excited $\tilde{X}^2\Sigma^+$ state.

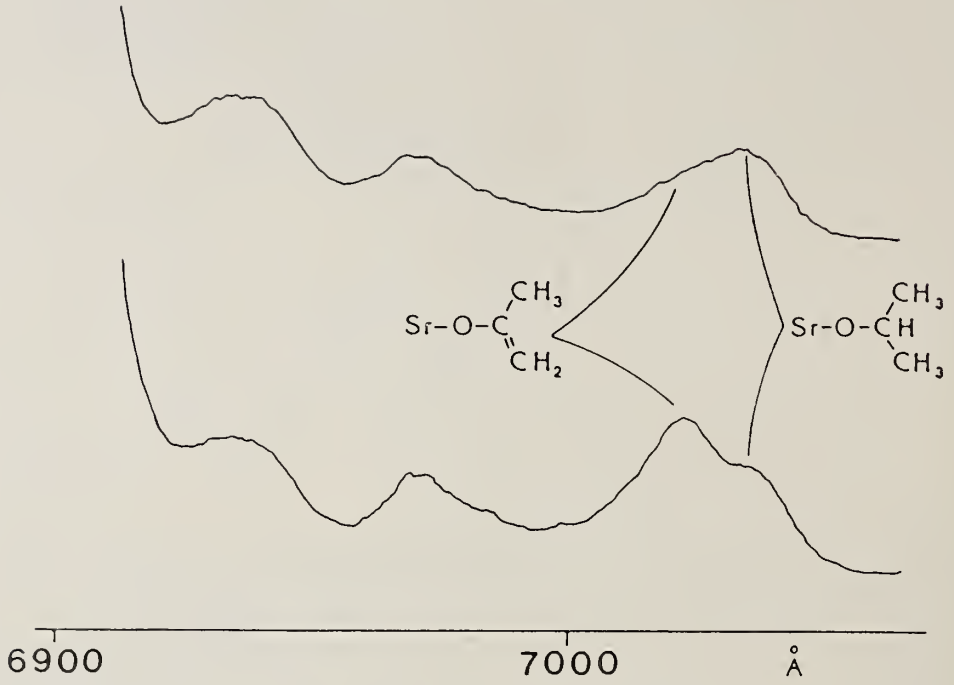

Figure 6. Laser-induced fluorescence spectra of the products of the Sr vapor plus acetone reaction. The $\tilde{A}_1{}^2\pi_{1/2}$-$\tilde{X}^2\Sigma^+$ transition is off scale near 6903 Å. The upper trace corresponds to a large amount (several hundred millitorr) of acetone oxidant while the bottom trace was recorded from a flame with less than 100 millitorr of acetone. The vibrational features arise from emission from v=0 of the $\tilde{A}_1{}^2\pi_{1/2}$ state into vibrationally excited levels of the ground $\tilde{X}^2\Sigma^+$ state.

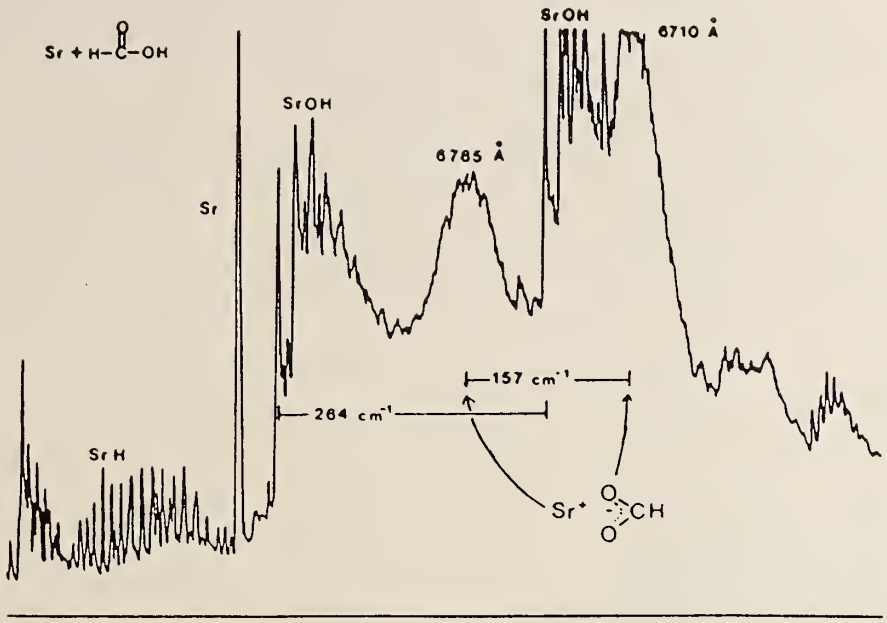

Figure 7. Laser excitation spectrum of the Sr plus formic acid reaction products. The strontium monoformate radical is responsible for the 6785 and 6710 Å peaks.

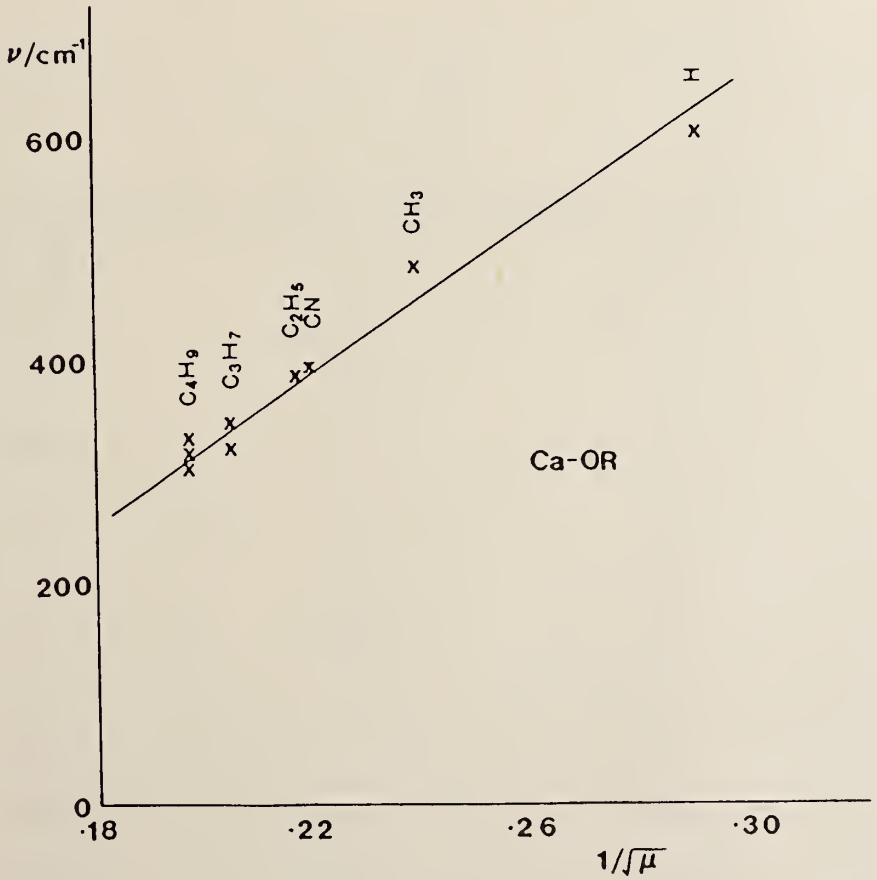

Figure 8. The variation of the Ca-O stretching frequency for the series Ca-OR (R= H, CH_3, C_2H_5, C_3H_7, C_4H_9, CN).

Table I. Band Origins of Calcium Monoalkoxides and Monocyanate (in cm^{-1}).

Molecule	$\tilde{A}_1{}^2\Pi_{1/2}$	$\tilde{A}_2{}^2\Pi_{3/2}$	$\tilde{B}^2\Sigma^+$
CaOH[a]	15965	16032	18022
$CaOCH_3$	15917	15982	17676
$CaOCH_2CH_3$	15850	15913	-
$CaOCH_2CH_2CH_3$	15860	15934	-
$CaOCH(CH_3)_2$	15823	15896	-
$CaO(CH_2)_3CH_3$	15853	15931	-
$CaOCH(CH_3)CH_2CH_3$	15813	15896	-
$CaOC(CH_3)_3$	15818	15886	-
CaOCN	16230	16303	17150

[a]Reference 14.

Table II. Band Origins of Strontium Monoalkoxides and Monocyanate (in cm^{-1})

Molecule	$\tilde{A}_1{}^2\Pi_{1/2}$	$\tilde{A}_2{}^2\Pi_{3/2}$	$\tilde{B}^2\Sigma^+$
SrOH[a]	14543	14806	16377
$SrOCH_3$	14520	14804	16098
$SrOCH_2CH_3$	14507	14767	16090
$SrOCH_2CH_2CH_3$	14512	14784	16176
$SrOCH(CH_3)_2$	14485	14756	16100
$SrO(CH_2)_3CH_3$	14508	14778	16173
$SrOCH(CH_3)CH_2CH_3$	14472	14745	16098
$SrOC(CH_3)_3$	14480	14749	16041
SrOCN	14972	15263	15970

[a]References 12 and 15.

Table III. Metal-Oxygen Stretching Frequencies (ν_s) for Alkaline Earth Monoalkoxides and Monocyanate (in cm^{-1})

Molecules	M = Ca	Sr	Ba
MOH	606[a]	528[b]	492[c]
$MOCH_3$	486	408	375
$MOCH_2CH_3$	385	345	-
$MOCH_2CH_2CH_3$	~349	279	-
$MOCH(CH_3)_2$	319	274	249
$MO(CH_2)_3CH_3$	-	~265	-
$MOCH(CH_3)CH_2CH_3$	330	-	-
$MOC(CH_3)_3$	302	247	-
$MOCH=CH_2$	-	306	-
$MOC(CH_3)=CH_2$	-	253	-
MOCN	395	332	-

[a]Reference 11.
[b]Reference 15.
[c]Reference 16.

Fourier transform detection of laser induced fluorescence from CCN and SrOH

C. R. Brazier, L. C. Ellingboe and P. F. Bernath

Department of Chemistry, University of Arizona, Tucson, AZ 85721

Abstract

We have observed laser induced fluorescence from gas phase free radicals using Fourier transform detection. The observations were made in the visible wavelength region using the Fourier transform spectrometer associated with the McMath solar telescope at Kitt Peak National Observatory. The combination of these two techniques provides the laser advantage of selective excitation of a small number of levels with the FT advantage of simultaneous detection of many transitions at high resolution.

Introduction

Previous studies of laser induced fluorescence (LIF), using Fourier transform (FT) detection, have involved species such as I_2 (1) and Te_2 (2) which can be made in relatively high concentration in a cell or heat pipe oven. The equivalent experiment for a free radical, such as SrOH or CCN, is more difficult, due to the problem of maintaining a sufficiently high concentration of the molecule in the region of interaction with the laser beam. The molecular concentration in an I_2 cell at room temperature is about 10^{16} molecules/cm^3. For free radicals concentrations 3 to 6 orders of magnitude less than this are typical.

The CCN molecule was first observed in absorption by Merer and Travis (3). Two studies of the $\tilde{A}^2\Delta - \tilde{X}^2\Pi$ transition using LIF by Kakimoto and Kasuya (4) and Kawaguchi et al (5), have provided accurate constants for the ground vibrational and excited bending levels respectively. Our work extends that of Hakuta and Uehara (6) who found that the 4658 Å line of an argon ion laser coincides with two rotational lines in the $\tilde{A}^2\Delta$ (010)Φ - $\tilde{X}^2\Pi$ (010)Δ vibronic

transition. They resolved the fluorescence through a small monochromator and were able to obtain the frequencies of the two stretching vibrations. Hakuta and Uehara could only obtain a resolution of about 3 cm^{-1} and hence could not resolve the rotational structure except for the resonantly excited lines. By repeating the experiment but with FT detection we obtained near Doppler-limited resolution and were able to perform a full rotational analysis for five ground state vibronic levels.

The visible bands of SrOH have been known for a very long time, the first observations being made by Herschel in 1823 (7). The carrier was not identified as SrOH until 1955 when James and Sugden (8) recognized the similarity with the bands of the isoeletronic strontium fluoride molecule. The bands of SrOH, like all the alkaline earth monohydoxides are so badly overlapped that rotational analysis was not possible before the development of the tunable dye laser. The first analysis of SrOH was carried out by Nakagawa, Wormsbecher and Harris (9) who studied the $\tilde{B}^2\Sigma^+ - \tilde{X}^2\Sigma^+$ system. The FT experiment described here represents part of a study of the $\tilde{A}^2\Pi - \tilde{X}^2\Sigma^+$ transition full details of which will be published elsewhere (10).

Experimental

Two Doppler-limited Fourier transform spectra of SrOH, produced in a Broida oven by the reaction of Sr vapor and water, were recorded. About 1 Watt of radiation from a Coherent 599-01 broadband dye laser (1 cm^{-1} bandwidth) was passed horizontally through the oven and the resultant fluorescence imaged onto the entrance aperture of the FT spectrometer. For one spectrum the laser was tuned to the $P_1 + Q_{12}$ band head and 13 scans were co-added in 1 1/2 hours. For the other the $^3P_1 - {}^1S$ Sr atomic line, which lies very near to the P_{12} branch band head (see Figure 3), was excited. In this case 14 scans were co-added in 1 hour of observation. The resolution of the Fourier transform spectrometer was 0.020 cm^{-1}.

The spectrum of CCN, produced by the reaction of acetonitrile and fluorine atoms, was recorded using on axis laser excitation. A small pick-off mirror was used to guide the laser beam into the reaction cell, with a

collimating lens placed behind it to focus the laser induced fluorescence onto the input aperture of the FTS. This arrangement results in more efficient collection of the fluorescence but a filter must be used to block the scattered laser light. As a result only transitions to excited vibrational levels of the ground state can be observed. A total of 42 scans were co-added in 2 1/2 hours of recording with a resolution of 0.05 cm^{-1}.

Results and Discussion

A low resolution spectrum of the CCN emission is shown in figure 2. Of the bands marked, all except the $(010)\Pi - (011)\Sigma^-$ transition have been analysed. The strongest band is the $(010)\Phi - (011)\Delta$ transition, a section of which is shown in figure 2. The argon ion laser populates two rotational levels in $(010)\Phi$, J=24.5 in the F_1 component and J=13.5 of F_2. A total of 12 resonant lines are observed back to the ground state, for example $Q_2(13.5)$ in figure 3. In addition rotational relaxation also occurs, leading to the weaker lines, which exhibit a Boltzmann distribution of population. The two bands originating from $(010)\Pi$ in the excited state are populated only by relaxation and hence are much weaker.

The $\tilde{A}^2\Delta$ $(010)\Phi$ state has been analysed by Kawaguchi et al (5), providing us with rotational constants. The analysis of Hakuta and Uehara (6) was used to make initial assignments of the resonant lines. The others were assigned by counting from the resonant transitions. The transitions to $(011)\Delta$ and $(012)\Delta$ both contained lines with good signal-to-noise and could be fitted fairly easily. The other strong transition terminating in $(110)\Delta$ is perturbed at J=9.5 in F_2 and J=20.5 in F_1. The F_1 perturbation is local, but none of the levels below J=9.5 in F_2 could be fitted with the rest of the band. Only a small number of lines were seen in the $(010)\Phi - (031)\Delta$ band, but these were sufficient to determine most of the rotational constants.

The $(010)\Pi - (011)\Sigma^+$ transition was very weak, and only Q branch lines could be picked out clearly. Several assignments were tried to reproduce these lines and the only one that did this, and also gave the positions of the P branch band heads correctly, resulted in a negative value for the

centrifugal distortion constant. While the Renner-Teller interaction makes this possible, the term which can make D negative (5) should be much smaller than the normal positive contribution. The constants for the 5 ground state vibronic levels analysed are given in table 1.

The first FT spectrum of SrOH was recorded with excitation at the P_1, Q_{12} bandhead. The corresponding R_1 branch shows strong resonant lines between J of 10.5 and 32.5. The intensities of the P_{12}, Q_1 and R_{12} branches which originate from the other lambda doubling component (f) show a Boltzmann distribution (T ~ 500 K) of population in the excited state f levels. There is no evidence of resonant ($\Delta J = 0$) transfer of population between e and f levels. However, the presence of a sustantial Boltzmann population in the f component does suggest that the e and f levels communicate with each other.

The second FT spectrum was recorded with excitation of the $^3P_1 - {}^1S$ Sr line at 6892 Å. There is no overlap of this line with the spectrum of SrOH. However, the P_{12} bandhead is only 0.4 cm^{-1} away so that it was excited by the 1 cm^{-1} bandwidth dye laser. The lines with J' = 83.5 to 96.5 which could have been directly excited are not the strongest lines however, instead the maximum occurs at J' = 71.5, as can be seen in figure 3. The most reasonable explanation of this is that a partial relaxation of the population has occurred. In the limit of an infinite number of collisions, a Boltzmann distribution of population will occur. We appear to be looking at a situation part way between the fully relaxed and the initial laser-excited distributions.

There is clear evidence in this spectrum of transfer to the e levels in the $^2\Pi$ state. In this case there is no strong Boltzmann background and the populations can be estimated fairly accurately, giving a value of 5:1 for the f:e ratio. The chance of a single collision causing a change of parity must be much less than this however, as each molecule must have undergone several collisions, at our pressure of 10 torr, before emitting.

It is also possible to make a comparison of the resonantly excited P_{12}, Q_1 and R_{12} branches. For a pure case a $^2\Pi - {}^2\Sigma^+$ transition these should have a 1:2:1 intensity ratio. If spin uncoupling is included in the intensity calculations (11), then the ratio becomes 1:2.6:1. The measured ratio is

1:2.6:1.6, the difference is thought to arise from a parallel contribution to the formally perpendicular transition dipole moment. Expressions for the relative intensities of $\Omega = 1/2$ states including this effect have been derived by Kopp and Hougen (12). Their expressions do not include spin uncoupling, but as the ratio of P/R branch intensity does not change due to uncoupling, an estimate of $\mu_{\parallel}$ may be made from the relative intensities of these two branches. The calculation gives

$$\mu_{\perp}/\mu_{\parallel} = 9.3$$

This contribution arises from contamination of the $^2\Pi_{1/2}$ state by spin-orbit mixing $[A(L_-S_+ + L_+S_-)]$ with the $\tilde{B}^2\Sigma^+$ state. The wavefunction for the $\tilde{A}$ state acquires a proportion of $^2\Sigma$ character and $\mu_{\parallel}$ can then make a contribution to the overall transition dipole moment.

The rotational constants for the $\tilde{A}^2\Pi$ - $\tilde{X}^2\Sigma^+$ transition, which were determined partly from the FT data, are given in table II.

Acknowledgements

This research was supported by the National Science Foundation (NSF-8306504) and the Research Corporation. Acknowledgement is made to the donors of the Petroleum Research Fund, administered by the ACS, for partial support of this work. Partial support was also provided by the Office of Naval Research (ONR N 00014-84-K-0122).

References

1. R. Bacis, S. Churassy, R. W. Field, J. B. Koffend and J. Verges, J. Chem. Phys. **72**, 34 (1980).
2. J. Verges, J. d'Incan, C. Effantin, D. J. Greenwood and R. F. Barrow, J. Phys. B **12**, L301 (1979).
3. A. J. Merer and D. N. Travis, Can. J. Phys. **43**, 1795 (1965).
4. M. Kakimoto and T. Kasuya, J. Mol. Spectrosc. **94**, 380 (1982).

5. K. Kawaguchi, T. Suzuki, S. Saito, E. Hirota and T. Kasuya, J. Mol. Spectrosc. **106**, 320 (1984).
6. K. Hakuta and H. Uehara, J. Chem. Phys. **78**, 6484 (1983).
7. J. F. W. Herschel, Trans. Roy. Soc. (Edinburgh) **9**, 445 (1823).
8. C. G. James and T. M. Sugden, Nature **175**, 333 (1955).
9. J. Nakagawa, R. F. Wormsbecher and D. O. Harris, J. Mol. Spectrosc. **97**, 37 (1983).
10. C. R. Brazier and P. F. Bernath J. Mol. Spectrosc. (in press).
11. L. T. Earls, Phys. Rev. **48**, 423 (1935).
12. I. Kopp and J. T. Hougen, Can. J. Phys. **45**, 2581 (1967).

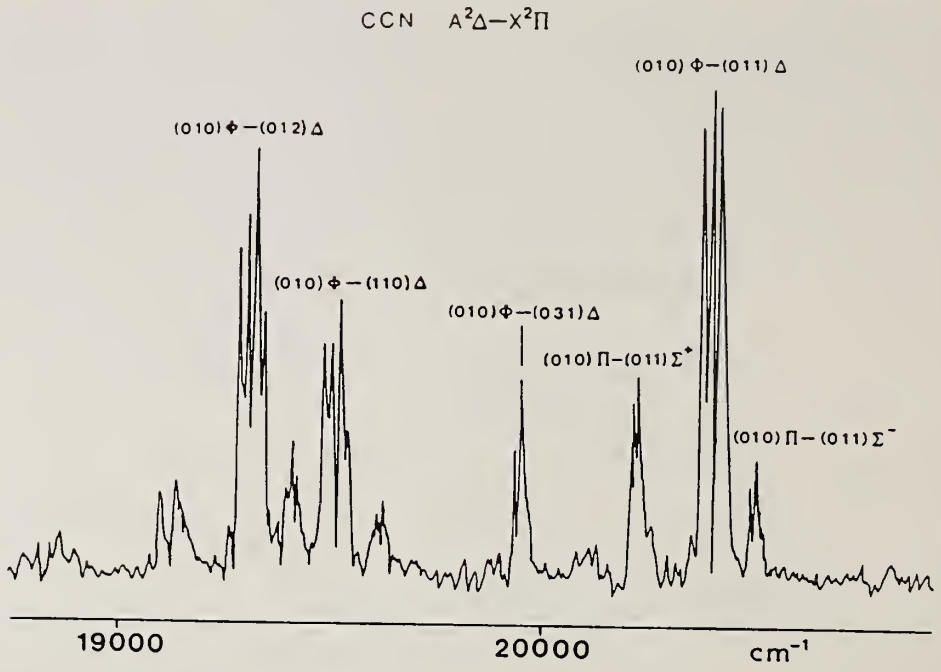

Figure 1. Low resolution spectrum of CCN showing all the observed vibronic bands.

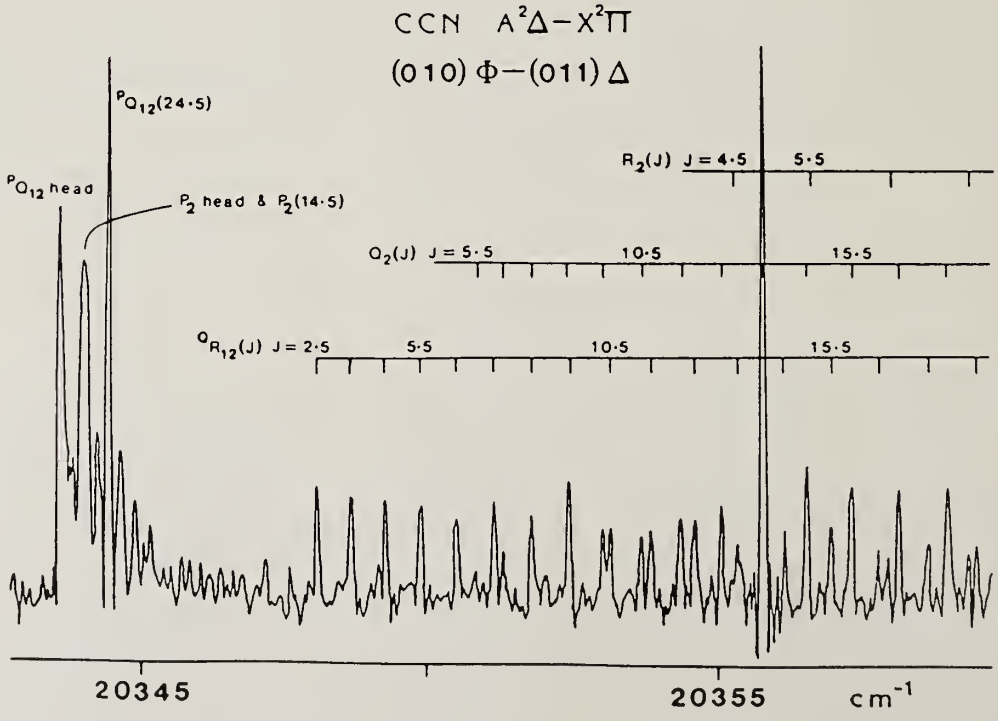

Figure 2. Part of the (010)Φ - (011)Δ vibronic band with both resonant and relaxed rotational lines.

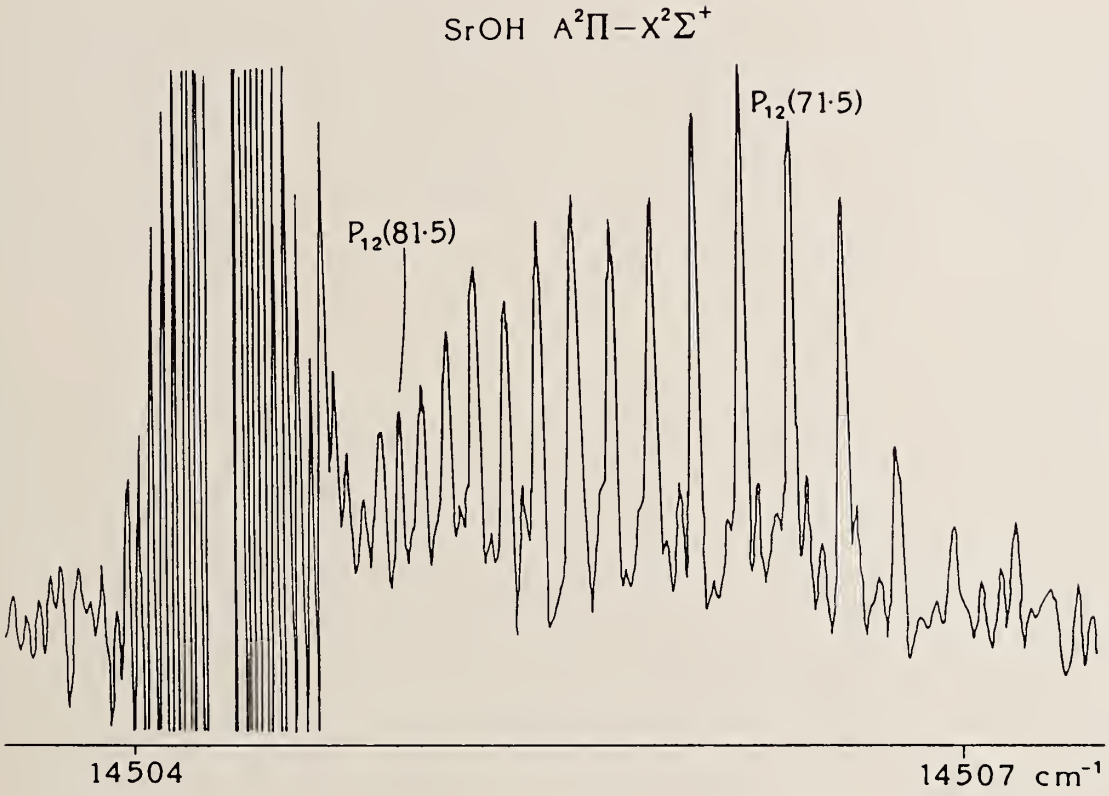

Figure 3.. Fourier transform detected emission from SrOH. The laser is exciting the $^3P_1$ - ^1S Sr atomic line which is about 3 orders of magnitude off scale, the structure near this line is an instrumental artifact.

Table I

Molecular constants for the $X^2\Pi$ state of CCN (cm^{-1})

	(011) $^2\Delta$	(011) $^2\Sigma^+$	(012) $^2\Delta$	(110) $^2\Delta$	(031) $^2\Delta$
A	36.0177(14)[a]		35.8067(26)	36.2047(50)	9.817(3
B	0.398572(27)	0.396112(35)	0.396060(30)	0.398313(46)	0.40447
$D \times 10^7$	2.99(25)	-8.76(50)	2.64(29)	0.79(53)	3.0[b]
γ	-0.00703(15)	0.00952(15)	-0.00417(27)	0.00057(63)	0.00401
ε[b]	1060.789(1)		2113.360(3)	1915.776(6)	1491.627(1

[a] The numbers in parentheses represent one standard deviation error estimates in the last quoted fi

[b] Constrained to this value.

[c] Energy relative to $(010)^2\Delta$.

Table II . Molecular constants for 000-000 band of the $\tilde{A}^2\Pi - \tilde{X}^2\Sigma^+$ transition of SrOH (in cm^{-1}, one standard deviation in parentheses).

Constant	$\tilde{X}^2\Sigma^+$ 000	$\tilde{A}^2\Pi$ 000
T_0	0.0	14 674.332(2)
B_0	0.2492032(27)	0.2538873(27)
$D_0 \times 10^7$	2.1801(30)	2.1735(30)
$\gamma_0 \times 10^3$	2.4273(53)	-
p_0	-	-0.1432006(86)
$q_0 \times 10^4$	-	-2.0000(133)
A_0	-	263.51741(34)
$A_J \times 10^5$	-	7.0046(68)

Atmospheric Free Radicals: Detection, Calibration, and Field Measurement

Martin Buhr and Donald H. Stedman, University of Denver, Denver, Colorado.

ABSTRACT

Presented herein are data pertaining to the calibration and field measurements of peroxy and oxy radicals in air using a modulated chemical amplification technique. Based on the chain reaction in which these molecules participate to oxidize NO and CO to NO_2 and CO_2, chainlengths on the order of 500 are documented. Field measurement of these radicals in clean air at a site near Bennett, Colo. yielded ambient concentrations on the order of 10^8 molecules cm^{-3}.

INTRODUCTION

The hydroxyl and hydroperoxy radicals are of paramount importance in any discussion or investigation involving atmospheric chemistry. They are involved in virtually every reaction pertaining to the oxidation of reduced atmospheric species. Consequently a great deal of effort has been expended developing measurement techniques. Laser induced fluorescence (LIF) has been used aboard aircraft (Davis, et al., 1976) and at ground level (Wang, et al., 1975), however there have been problems with this technique and the results are subject to considerable uncertainty (Selzer and Wang, 1979; Ortgies, et al., 1980; Davis, et al., 1981a, b; Wang, et al., 1981). Recently, Hard and Obrien (1984) have had success using LIF in conjunction with gas expansion at a few torr. Perner, et al. (1976) and Hubler, et al. (1982) have used UV absorption of HO$\cdot$ over long paths (several kilometers), and resonance fluorescence has been used in the stratosphere to measure HO$\cdot$ (Anderson, 1976) and $HO_2\cdot$ (Anderson, et al., 1981). Campbell, et al. (1979) have used the oxidation of ^{14}CO by atmospheric HO$\cdot$ to determine ambient HO$\cdot$ concentrations. The application of spin traps to atmospheric HO$\cdot$ measurements has been reported by Watanabe, et al. (1982), followed by EPR detection of the HO$\cdot$ complex. (We have recently experimented with the spin trapping of $HO_2\cdot$ in our laboratory and have found the data to be subject to artifacts and the spin traps very suceptible to non-radical induced complex formation.) Finally, atmospheric $HO_2\cdot$ detection has been reported using matrix isolation followed by EPR (Mihelcic, et al., 1978; Mihelcic, et al., 1982).

Our technique of measuring peroxy radicals by chemical amplification, (Cantrell, et al., 1984; Cantrell and Stedman, 1982; Stedman and Cantrell, 1982), uses the oxidizing chain reaction in which HO$\cdot$ and $HO_2\cdot$ participate

directly. Some $RO_2\cdot$ become $HO_2\cdot$ after a few reaction steps. The yield of NO oxidized to NO_2 by ambient radicals is measured, and an ambient total peroxy radical concentration (which in clean air is expected to be mostly $HO_2\cdot$) is inferred. Presented here are the results of laboratory calibrations of the detector and some ambient measurements.

EXPERIMENTAL

Apparatus. The chemical amplifier instrumentation is composed of three parts, which provide for (1) addition of reagent gases (CO or N_2 and dilute NO in N_2), (2) NO_2 prodution from the chain reaction and other sources, and (3) NO_2 detection. (Cantrell, et al., 1984)

The flow rate of reagent gases is controlled through flow restrictors (Mott Metallurgical) and delivered through 0.25 in. o.d. Teflon tubing to two three-way solenoid valves (General Valve). The valves control which reagent will be delivered to the reactor and which gas will be released to the atmosphere. The gas selected is mixed with the dilute NO and is delivered to a plenum on the interior of the stainless steel reactor (figure 1). The incoming air passes through a 1 cm diameter hole which is surrounded by 16 radial grooves leading from the plenum to which the reagents are delivered. The reactor has a total volume of 200 cm^3, which results in a reaction time of 4 seconds at a total flow rate of 3 L min^{-1}. The resultant mixture is drawn into the NO_2 detector which is based on the chemiluminescent reaction between NO_2 and 3-aminophthalhydrazide (luminol) described by Wendel, et al. (1983). Photons from the chemiluminescent reaction are detected by a blue sensitive photomultiplier tube (RCA) operated at a voltage of -1400 V (Venus Scientific, Inc.). The photocurrent generated is amplified by an electrometer (Analog Devices 310J) and is read on a chart recorder (Heath Schlumberger SR-204), through a variable gain select and passive RC low pass filter with a fixed 1 sec. time constant. Electrometer output is also collected by a IBM personal computer with a Labmaster interface (Tecmar, Inc.). The solenoid valve timing sequence is controlled by a Chrontrol CT-4 table top timer, or through opto-isolater relays if the data is computer aquired.

Reagents. The reagent gases used in the detection system are carbon monoxide, CP grade (Air Products), nitrogen, (AP), and nitric oxide in nitrogen (250 ppmv made in aluminum cylinders from high purity nitric oxide and oxygen-free nitrogen). The carbon monoxide is passed through a filter containing I_2/ Activated charcoal to remove carbonyls formed in the cylinder and the NO is filtered with $FeSO_4$ to remove NO_2 formed in the cylinder. The reagents used in the NO_2 detector solution are sodium sulfite (Baker analyzed reagent grade), sodium hydroxide, and luminol (3-

aminophthalhydrazide, 97%, Aldrich Chemical Co.,Inc.) used without further purification. Solutions are made with deionized water.

Procedure. The basis of the chemical amplifier technique has been described by Cantrell and Stedman, (1982). Briefly, air containing oxy ($HO\cdot$) or peroxy ($RO_2\cdot$ and $HO_2\cdot$) radicals is drawn into the stainless steel reactor to which is added the appropriate reagent gases. A partial mechanism for the reactions of the radicals and reagent gases is:

$$HO_2\cdot + NO \rightarrow NO_2 + HO\cdot \qquad (1)$$

$$HO\cdot + CO \rightarrow CO_2 + H\cdot \qquad (2)$$

$$H\cdot + O_2 + M \rightarrow HO_2\cdot + M \qquad (3)$$

Proper choice of [NO], [CO] and reaction time can produce several NO_2 molecules for each radical entering the system. Typical conditions are [NO] = 3 ppmv, [CO] = 10 %, and t_{rxn} = 4 sec. The amount of NO_2 produced from these reactions is limited by reactions which terminate the chain reaction. The most important radical sinks for reagent concentrations and reaction times in the range described above are:

$$HO\cdot + NO + M \rightarrow HONO + M \qquad (4)$$

$$HO_2\cdot + HO_2\cdot \rightarrow H_2O_2 + O_2 \qquad (5)$$

However under normal atmospheric $HO_2\cdot$ concentrations (<200pptv), reaction 5 is very slow and not very important in this system. Chemical kinetic modelling of reactions 1-5 using up to date rate constants (Demore, et al., 1983) leads to a predicted increase in nitrogen dioxide concentration approximately 3 orders of magnitude larger than the incoming radical concentration.

Since there are other sources of NO_2 in the atmosphere and in this system including ambient NO_2 and NO_2 produced from ambient ozone

$$NO + O_3 \rightarrow NO_2 + O_2 \qquad (6)$$

a modulated technique is used. Nitrogen is substituted for carbon monoxide one half of the time. The radical signal is then determined from the difference in NO_2 signal with and without CO present.

RESULTS AND DISCUSSION

Calibration. Determination of the chain length for a given set of instrumental conditions results in a calibration factor that makes the radical signal quantitative. There is however, the analytical problem of producing a known amount

of radicals. We circumvent this problem and achieve calibration by producing a high concentration (approximately 150 pptrv) steady state of hydroperoxyl radicals in a 1000 L Teflon gas bag and measuring the second order homogeneous decay of the $HO_2^{\cdot}$ radical forming H_2O_2 and O_2 (reaction 5). The radicals are produced using near UV fluorescent lights for photolysis by the following mechanism:

$$Cl_2 + h\nu \rightarrow 2\ Cl^{\cdot} \qquad (7)$$

$$Cl^{\cdot} + H_2 \rightarrow HCl + H^{\cdot} \qquad (8)$$

$$H^{\cdot} + O_2 + M \rightarrow HO_2^{\cdot} + M \qquad (9)$$

The radicals decay in the dark at a known rate and the following relationship results

$$\text{Chain length} = 2k_{recombination} / \text{slope}$$

where $k_{recombination}$ is given as $(1.6 + 1.2P) * 10^{-12}$ and the slope is that measured after plotting the inverse NO_2 mixing ratio versus time.A second order plot produced using our field instrument is shown in figure 2. Figure 3 is the actual chart tracing of an achieved steady state followed by dark decay starting at the star. Using this method of calibration we have measured chainlengths from 400 to 600, lower than predicted values but reproducible. Possible reasons for the chain lengths are unoptimized reagent gas flows or unaccounted for loss factors such as surface removal of radicals on the untreated stainless steel.

Field Measurements. Clean air ambient radical concentrations were measured in a collabrative effort with the National Center for Atmospheric Research at a field site 12 miles northeast of Bennett, CO. Data was aquired for selected days in the months of June and July, 1985. The radical reactor was positioned 2.5 meters off of the ground on the roof of a trailer parked in a wheat field. The NO_2 detector was mounted inside the trailer 1.5 meters below the reactor. Cylinders of reagent gases were positioned outside the trailer below the reactor. The site was chosen because of the availability of ancillary data being aquired by our collaborators.

Calculations of radical concentrations were made using a chainlength 350, resulting from calibrations made for the instrumental conditions maintained. Data for selected days in the month of June are shown in figure 4, along with corresponding $j(O_3)$ values and background measurements given as ppbv of NO_2. It is thought that the background may be attributed mainly to ozone because of the consistently low (< 1 ppbv) mixing ratios measured for NO_2. This assumption was carried through and the calculated values were used to

check instrumental NO_2 response and subsequently in the radical signal quantitation.

CONCLUSIONS

Using our technique of chemical amplification for the measurement of atmospheric free radicals we have built a field instrument, calibrated it in the laboratory, and carried out field measurements. Values of $[HO_2\cdot]$ in clean air reached a high value of $5 * 10^8$ molecules cm^{-3}, with consistent noon-peaking values of approximately $3 * 10^8$ molecules cm^{-3}. As data from our collaborators become available steady state calculations will be made and the relative accuracy of our numbers determined.

ACKNOWLEGEMENTS

We would like to thank Tony Delaney of NCAR for his help, facilities, and cooperation in our field efforts, and the National Science Foundation for their support of our research.

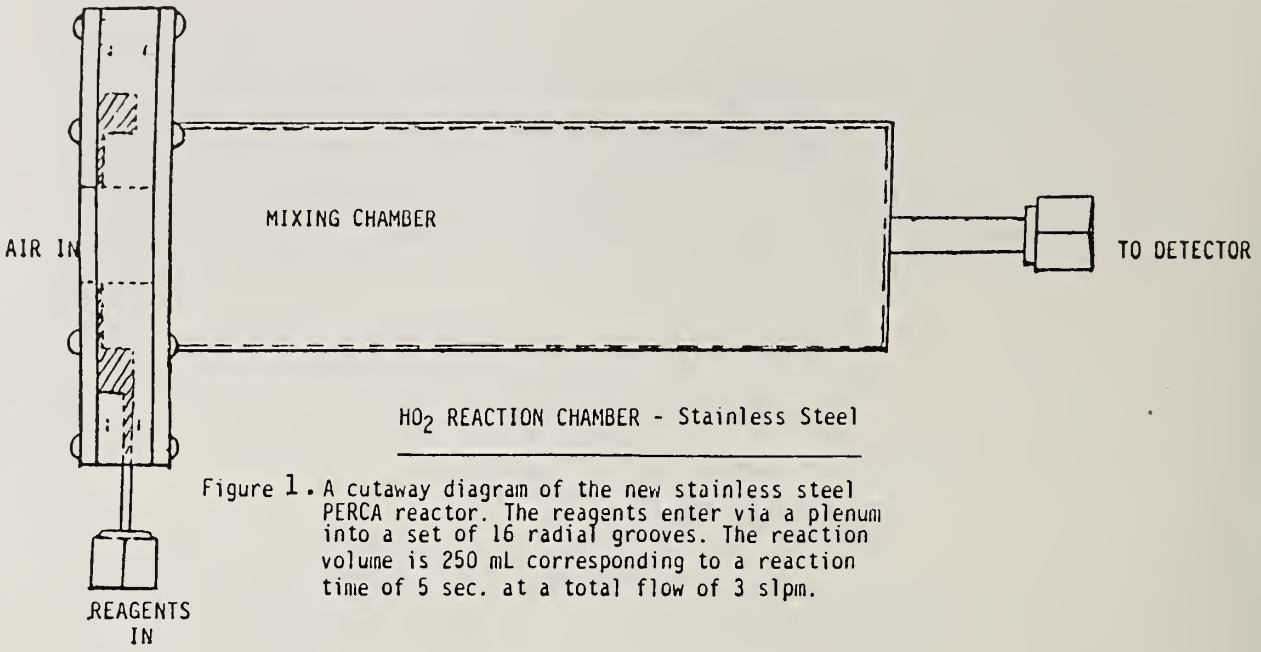

Figure 1. A cutaway diagram of the new stainless steel PERCA reactor. The reagents enter via a plenum into a set of 16 radial grooves. The reaction volume is 250 mL corresponding to a reaction time of 5 sec. at a total flow of 3 slpm.

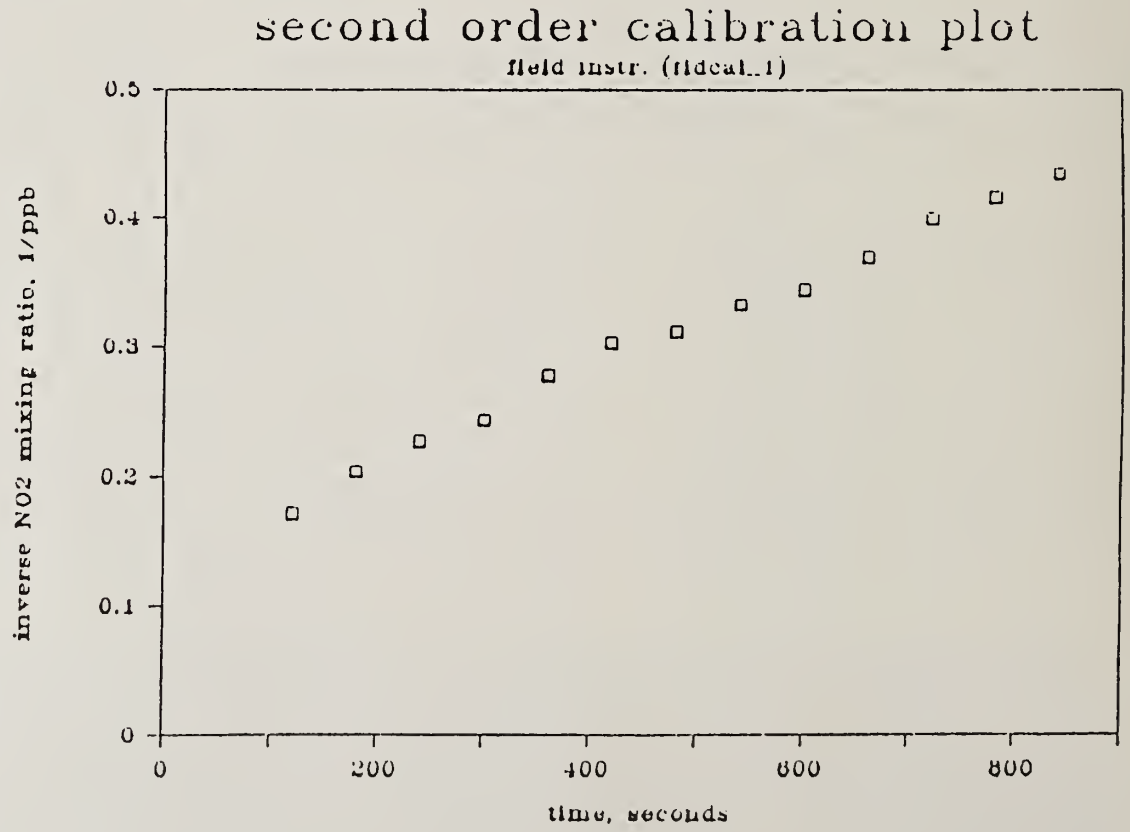

Figure 2. Plot obtained from gas bag decay. Chain length is calculated to be 350.

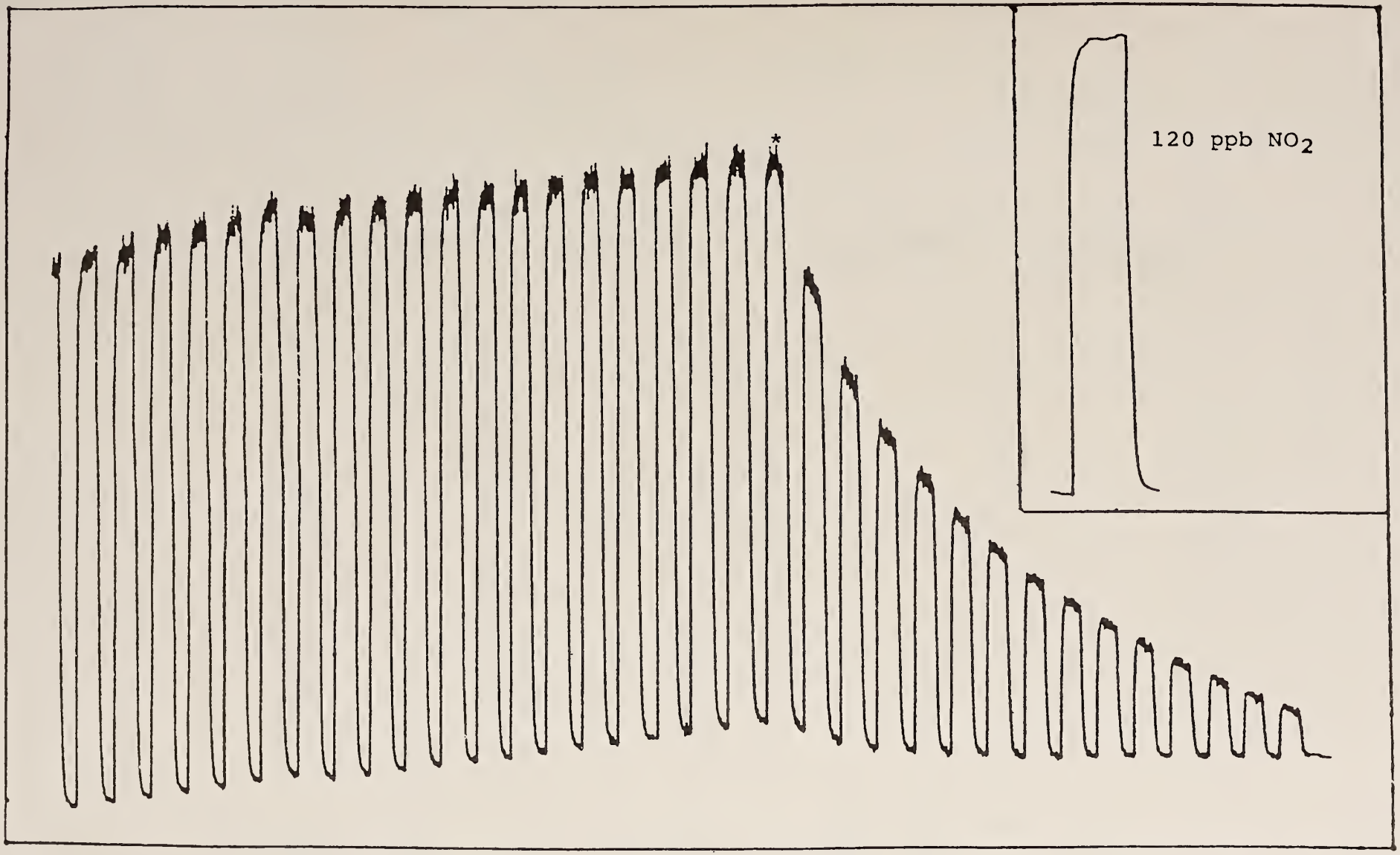

Figure 3. Actual chart tracing of a steady state radical signal and subsequent dark decay (*). Radicals were generated with a Cl_2/H_2/Air mixture in a Teflon gas bag.

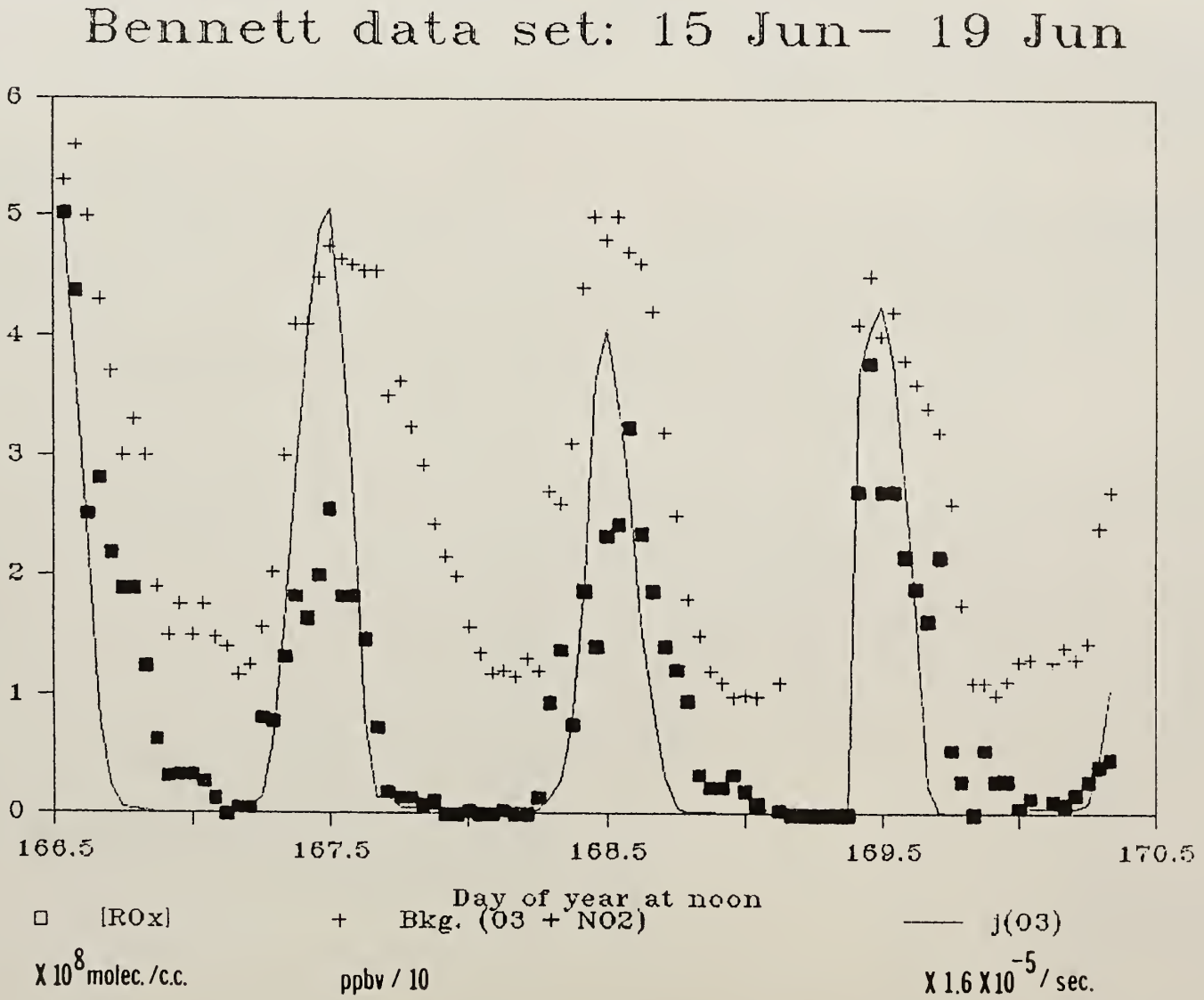

Figure 4. Selected ambient data from Bennett, CO. field site.

REFERENCES

Anderson, J.G.; Geophys. Res. Lett., 1976, 3, 165-168

Anderson.J.G.; Grassl, H.J.; Shetter, R.E.; Margitan, J.J.; Geophys. Res. Lett., 1981, 8, 289-292

Campbell, M.J.; Sheppard, J.C.; Au, B.F.; Geophys. Res. Lett.,1979, 3, 175.

Cantrell, C.A.; Stedman, D.H.; Geophys. Res. Lett., 1982, 9, 846-849.

Cantrell, C.A.; Stedman D.H.; Wendel, G.J.; Anal. Chem., 1984, 54, 1496-1502.

Davis, D.D.; Heaps, W.S.; Philen, D.; McGee, T.; Atmos. Environment, 1979, 13, 1197-1203

Davis, D.D; Rodgers, M.O.; Fischer, S.D.; Asai, K.; Geophys. Res. Lett., 1981a, 8, 73-76.

Davis, D.D.; Rodgers, M.O.; Fischer, S.D.; Heaps, W.S.; Geophys. Res. Lett., 1981b, 8, 73-76.

Demore, W.B.; Watson, R.T.; Golden, D.M.; Hampson, R.F.; Kurylo, M.; Howard, C.J.; Molina, J.J.; Ravishankara, A.R., JPL Publ., 1982, 24-33,88-89.

Hard, T.M.; O'Brien, R.J.; Chan, C.Y.; Mehrabzadeh, A.A.; Environmental Sci. and Tech., 1984, 18, 768-777.

Hubler, G.; Perner D.; Platt, U.; Toennissen, A.; Ehhalt, D.H.;Second Symposium on the Composition of the Nonurban Troposphere, 1982, 315-318.

Mihelcic, D.; Ehhalt, D.H.; Kulessa, G.F.; Klomfass, J.; Trainer, M.; Schmidt, A.; Rohrs, H.; Pure and Applied Geophysics, 1978. 116, 530.

Mihelcic, D.; Helten, M.; Fark, H.; Musgen, P.; Patz, H.W.; Trainer, M.; Kempa, D.; Ehhalt, D.H.; 2nd AMS Symp. on The Composition of the Nonurban Troposphere, 1982, 327-329.

Ortgies, G.; Gericke, K.H.; Comes, F.J.; Geophys. Res. Lett., 1980, 7, 905-908.

Perner, D.; Ehhalt, D.H.; Patz, H.W.; Platt, U.; Roth, E.P.; Volz, A.; Geophys. Res. Lett., 1976, 3, 466-468.

Selzer, P.M.; Wang, C.C.; J. Chem. Phys., 1979, 71, 3786-3791

Stedman, D.H.; Cantrell C.A.; Second Symposium on the Composition of the Nonurban Troposphere, 1982

Wang, C.C.; Davis, L.; Wu, C.H.; Japar, S.; Niki, H.; Weinstock, B.; Science, 1975, 189, 797-800.

Wang, C.C; Davis, L.; Selzer, P.M.; Munoz, R.; J. Geophys. Res., 1981, 86, 1181-1186.

Watanabe, T.; Yoshida, M.; Fujiwara, S.; Abe, K.; Onoc, A.; Hirota, M.; Igaraski, S.; Anal. Chem., 1982, 54, 2470-2474.

Wendel, G.J.; Stedman, D.H.; Cantrell, C.A.; Damrauer, L.D.; Anal. Chem., 1983, 55, 937-940.

Some studies of the atmospheric reactions of NO_3 and an FTIR matrix isolation spectrum of NO_3.

J.P.Burrows, G.S.Tyndall, W.Schneider, H.Bingemer, G.K.Moortgat and D.W.T. Griffith.

Max Planck Institut für Chemie, Mainz F.R.G.

Abstract.

Some recent investigations of the reaction rate coefficients for reaction of NO_3 with NO_2, CH_3SCH_3, SO_2, CS_2, CO, CH_4 and H_2O_2 are reported. The products of the reaction of NO_3 with CH_3SCH_3 have been studied and surprisingly the most exothermic channel, generating NO_2 and CH_3SOCH_3, appears to be of negligible importance. A matrix isolation FTIR study of NO_3 is also described and a spectrum tentatively assigned to NO_3.

Introduction.

The realisation of the important role played by the oxides of nitrogen (NO_x) in atmospheric chemistry[1,2] requires a detailed understanding of the elementary reactions involving NO_x. The detection of NO_3 at night in both the troposphere[3,4] and stratosphere[5] has focussed attention on the chemistry and atmospheric fate of this species.

NO_3 builds up in the atmosphere at night, being formed by the reaction of NO_2 with O_3:

$$NO_2 + O_3 \longrightarrow NO_3 + O_2 \qquad (1)$$

Since it strongly absorbs visible radiation and is photolysed, its daytime concentration is very low.

The relative concentrations of NO_2, NO_3 and N_2O_5 should be determined in the atmosphere at night by the equilibrium

$$N_2O_5 \rightleftharpoons NO_2 + NO_3 \qquad (2)$$

The establishment of this equilibrium does not lead to an overall loss of NO_x. However it has been pointed out that reactions of NO_3 with other atmospheric constituents might provide an atmospheric sink for NO_x.[6] Recent measurements of NO_3 at night in the troposphere support the view that NO_3 may be scavenged even in relatively unpolluted air.[7] Studies by Niki and coworkers[8] and Atkinson and coworkers[9] have shown that NO_3 reacts rapidly with unsaturated hydrocarbons and a wide range of naturally emitted hydrocarbon compounds, particularly monoterpenes.

Here results are presented from some recent kinetic investigations of the reactions of NO_3 with a variety of atmospheric constituents. We also present a FTIR matrix isolation study of NO_3 with a spectrum tentatively assigned to NO_3.

Experimental.

The apparatus used to study the chemistry of NO_3 is shown schematically in figure 1 and described in detail elsewhere.[10,11] The reaction vessel is a 145 cm-long quartz tube, which is surrounded by up to six fluorescent photolysis lamps. In this work both Philips TL08 black lamps (310-400 nm) and TUV lamps (254nm) were used. The gases enter the vessel through four inlets simultaneously and are pumped out of the vessel via three outlets. This ensures optimal mixing of reactant gases in the vessel, which approximates to a stirred flow reactor.

The photolysis lamps were powered by a 20kHz signal of up to 1kV amplitude and the lamps could be switched at photolysis frequencies between 2.5 kHz and 0.02 Hz. Also, the ratio of on-time to off-time could be varied between 0.1 and 9.

In most of the experiments described here reactants and products were monitored by UV and visible absorption spectroscopy. Two light sources were used for optical measurements, a D_2 lamp for UV work and a tungsten halogen lamp for the visible. The collimated beam of light passed once through the cell, and, after dispersion by a 0.3-m monochromator, was detected by a photomultiplier. The output from the monochromator was converted to a voltage and subtracted from a reference voltage before entering a signal averager, which was triggered by a signal from a photodiode positioned next to the photolysis lamps. The output from the signal averager and the reference voltage were sent at the end of a photolysis experiment to a microcomputer for mathematical manipulation. Relatively small absorptions could be measured in this manner, a noise level corresponding to an optical density of 5×10^{-6} being achieved in about 20 minutes.

In one set of experiments on the $NO_3 + CH_3SCH_3$ reaction part of the exit gases was by-passed through a teflon loop immersed in liquid N_2 in order to trap out condensible reaction products. The loop was then warmed rapidly to 298 K and the products analysed by gas chromatography. The gas chromatograph had a flame photometric detector for specific monitoring of sulphur species.

The reaction vessel may be connected to a microsampling cryostat, suitable for matrix isolation studies. Matrices were grown by repetitively opening and closing a solenoid valve, specially designed to deposit gas directly on the cold finger. Matrices of a few reaction mixtures containing NO_3

were deposited on a gold mirror surfaced copper cold finger cooled by an Air Products Helitran flow cryostat. The N_2 in the reaction mixture served as the matrix material. FTIR spectra of the matrices were recorded using a Bomem DA03.01 spectrometer with a globar source, Ge/KBr beam splitter, and liquid helium cooled Ge:Cu detector.

N_2O_5 was prepared by passing NO and ozonised oxygen repetitively between two traps held at 195 K. $ClONO_2$ was made by mixing freshly prepared Cl_2O and N_2O_5 at 195 K and allowing the mixture to warm slowly to 273 K. The resulting mixture was purified by several three trap distillations. ClNO was prepared by mixing an excess of NO with Cl_2 and then trapping the product at 195 K and pumping away the excess NO. The other chemicals used in these studies were purchased commercially.

Results.

In all experiments, the NO_3 concentration was determined by optical density measurements at 623 nm. The absorption spectrum determined in this laboratory for NO_3 at 298K is shown in figure 2 along with other published spectra.[11]

a) The N_2O_5 equilibrium.

The equilibrium constant, $K_{2,C}$, for the reaction:

$$N_2O_5 \rightleftharpoons NO_2 + NO_3 \qquad (2)$$

was measured as a function of temperature between 275 and 315 K, where

$$K_{2,C} = [NO_2] \times [NO_3] / [N_2O_5]$$

Flows of N_2O_5 in N_2 were passed through the cell and the concentrations of N_2O_5, NO_3 and NO_2 were determined by absorption measurements at 220 or 250 nm, 623 nm, and 370 or 400 nm respectively.

A plot of $\ln K_{2,C}$ against 1/T is shown in figure 3. Our values are compared with other recent measurements.

By combining the experimental data with a calculated value for $\Delta S_2^o{}_{298}$ we obtain the following expression for $K_{2,P}$:

$$-\ln K_{2,P} = -(18.2 \pm 1.5) + (11425 \pm 300)/T$$

From this expression the heat of formation of NO_3 may be calculated :

$$\Delta H_f^o{}_{298}(NO_3) = 73.1 \pm 4.2 \text{ kJ mole}^{-1}$$

These results are discussed and compared with other measurements in a recent publication[12].

b) Reactions of NO_3.

In order to measure rate coefficients for the reactions of NO_3 the NO_3 was produced by modulated photolysis in the presence of excess reactant, and monitored at 623 nm. In these studies NO_3 was generated in one of three ways: by the photolysis of mixtures of Cl_2-$ClONO_2$-N_2, F_2-HNO_3-N_2 or HNO_3-N_2.

$$Cl_2 + h\nu(310\text{-}400nm) \longrightarrow Cl + Cl \quad (3)$$

$$Cl + ClONO_2 \longrightarrow NO_3 + Cl_2 \quad (4)$$

$$F_2 + h\nu(310\text{-}400nm) \longrightarrow F + F \quad (5)$$

$$F + HNO_3 \longrightarrow NO_3 + HF \quad (6)$$

$$HNO_3 + h\nu(254nm) \longrightarrow OH + NO_2 \quad (7)$$

$$OH + HNO_3 \longrightarrow NO_3 + H_2O \quad (8)$$

The photolysis rates of Cl_2 and F_2 were measured in the static photolysis of mixtures of Cl_2-H_2-O_2 and F_2-H_2-O_2.[11] The decays of Cl_2 and F_2 were monitored at 310 nm and 330 nm respectively. k_3 was determined to be $(1.35\pm0.2)\times10^{-3}$ s^{-1} per lamp and k_5 to be $(7.4\pm1.3)\times10^{-5}$ s^{-1} per lamp at 298 K.

The photolysis rate of HNO_3 by 254 nm radiation, k_7, was estimated from a knowledge of the photolysis rate of ClNO by 254nm radiation and the absorption cross sections of HNO_3 and ClNO at 254nm, to be 6×10^{-5} s^{-1} per lamp.

The addition of an excess of reactant, A, which reacts with NO_3, to the flowing photolysis mixture reduces the NO_3 stationary state concentration and increases the rates of rise to, and decay from, stationary state. To a first approximation, the rate of change of NO_3 concentration, with the photolysis lights on, is given by :

$$d[NO_3]/dt = B - k[A][NO_3]$$

and for lights off :

$$d[NO_3]/dt = -k[A][NO_3]$$

where B represents the photolysis production rate of NO_3 and k the rate coefficient for the reaction between NO_3 and A. Consequently k may be determined from an analysis of the growth and decay of NO_3 concentration. An example is shown in figure 4 of the photolysis of a HNO_3-CH_3SCH_3-N_2 mixture.

In this manner, the reactions of NO_3 with NO_2, CH_3SCH_3, SO_2, CS_2, CO, CH_4 and H_2O_2 have been studied. NO_3 reacts rapidly with NO_2 and CH_3SCH_3 but only upper limits could be determined for the other reactions.

$$NO_3 + NO_2 + M \longrightarrow N_2O_5 + M \qquad \Delta H_2 = -94.9 \text{ kJ mole}^{-1}$$

$$NO_3 + CH_3SCH_3 \longrightarrow CH_3SOCH_3 + NO_2 \quad \Delta H_{9a} = -179.3 \text{ kJ mole}^{-1}$$

$$\longrightarrow CH_2SCH_3 + HNO_3 \quad \Delta H_{9b} = -48.3 \text{ kJ mole}^{-1}$$

$$\longrightarrow \text{products} \qquad (9c)$$

$$NO_3 + SO_2 \longrightarrow SO_3 + NO_2 \qquad \Delta H_{10} = -137 \text{ kJ mole}^{-1}$$

$$NO_3 + CO \longrightarrow CO_2 + NO_2 \qquad \Delta H_{11} = -321 \text{ kJ mole}^{-1}$$

$$NO_3 + CH_4 \longrightarrow CH_3 + HNO_3 \qquad \Delta H_{12} = 14 \text{ kJ mole}^{-1}$$

$$NO_3 + H_2O_2 \longrightarrow HO_2 + HNO_3 \qquad \Delta H_{13} = -58 \text{ kJ mole}^{-1}$$

$$NO_3 + CS_2 \longrightarrow \text{products} \qquad (14)$$

The results obtained are listed in Table 1.

In a separate study of the modulated photolysis of Cl_2-$ClONO_2$ mixtures, it was realised that Cl reacts rapidly with NO_3 and that this reaction competes with reaction (4) for the removal of Cl atoms:

$$NO_3 + Cl \longrightarrow ClO + NO_2 \qquad \Delta H_{15} = -57 \text{ kJ mole}^{-1}$$

From measurements of the stationary state concentration of NO_3 as a function of the concentrations of Cl_2 and $ClONO_2$, the ratio of rate coefficients k_{15}/k_4 was determined to be (2.4 ± 0.75). Using the literature value for k_4 of $(1.12 \pm 0.2) \times 10^{-11}$ cm^3 molecule^{-1} s^{-1} at 298 K, this expression yields a value for k_{15} of $(2.7 \pm 1.0) \times 10^{-11}$ cm^3 molecule^{-1} s^{-1} at 298 K.

The values obtained for the rate coefficients of reaction of NO_3 with Cl, NO_2, SO_2, CS_2, CO, CH_4 and H_2O_2 are discussed and compared with other determinations in a recent publication.[11] The determination of the rate coefficient for reaction of NO_3 with CH_3SCH_3 between 278 and 318 K is the first direct determination of this rate coeffient and is approximately a factor of 2 faster than the recent measurement by Atkinson et al.[13]

c) Product analysis in the reaction of NO_3 with CH_3SCH_3.

Two approaches were used to investigate the products of the reaction of NO_3 with CH_3SCH_3. The first method was to monitor optically the concentrations of N_2O_5, NO_3 and NO_2 and simultaneously to cryo-trap the contents of flowing mixtures

of N_2O_5-CH_3SCH_3-N_2 immediately after passage through the cell. These samples were then analysed by gas chromatography. The total pressure of N_2 was 20 torr and the residence time in the cell was 3 s.

N_2O_5 is in equilibrium with NO_3 and NO_2 and, if the NO_3 reacts with CH_3SCH_3 to produce NO_2, then the NO_3 concentration is depressed and NO_2 is increased. Optical measurements were made to determine NO_2, NO_3 and N_2O_5 concentrations, both prior to and after the addition of CH_3SCH_3. NO_2 was observed to increase and NO_3 was no longer observable on the addition of CH_3SCH_3 to the flowing mixture. However more NO_2 was observed than anticipated from the rate of thermal decay of N_2O_5.

Analysis of the GC samples also proved puzzling. The CH_3SCH_3 signals were observed to diminish on the addition of N_2O_5 but the only product observed with the column at 313 K was SO_2. When the temperature of chromatographic column was increased as a function of the time following sample injection, amounts of CH_3SOCH_3 in addition to the SO_2 were observed, as the column reached its maximum temperature 443 K.

The best explanation of these results is that CH_3SCH_3 reacts with N_2O_5 in the reaction vessel. This reaction is probably heterogeneous.

$$N_2O_5 + CH_3SCH_3 \longrightarrow \text{products} \qquad (16)$$

$$\longrightarrow \text{wall} \qquad (17)$$

However an estimate of an upper limit for any gas phase reaction between N_2O_5 and CH_3SCH_3 can be made from an analysis of the changes in NO_2 and CH_3SCH_3 concentration. This leads to an upper limit for $k_{16} < 1\times10^{-14}$ in 20 torr of N_2 at 298K.

The second attempt to determine the product of the reaction of NO_3 with CH_3SCH_3 was undertaken in the modulated photolysis of flowing mixtures of HNO_3-CH_3SCH_3-N_2.

NO_2 is generated in the primary photolysis step, reaction (7), and potentially by reaction (9a) between NO_3 and CH_3SCH_3. NO_3 absorption at 623 nm and NO_2 absorption at 350 nm were monitored in the absence and in the presence of CH_3SCH_3. No increase in the rate of production of NO_2 was observed on the addition of CH_3SCH_3 indicating that pathway (9a) is insignificant in 20 torr of N_2 at 298K. This indicates that the exothermic channel (9b) is likely to be the dominant pathway for reaction between NO_3 and CH_3SCH_3.

d) Matrix isolation FTIR spectrum of NO_3.

For the purpose of investigating its matrix isolation infrared spectrum, NO_3 was generated by continuously photolysing Cl_2-$ClONO_2$-N_2 and F_2-HNO_3-N_2 mixtures. The N_2 flow contained 6.4 ppm of N_2O for calibration of the matrix thickness.

A set of matrices were grown from a mixture containing Cl_2, 3.3×10^{16} molecule cm^{-3}, and $ClONO_2$, 2.7×10^{15} molecule

cm^{-3}, in 20.5 torr of N_2. The residence time in the cell was 20 s and the mixture was photolysed by one blacklamp. The NO_3 concentration was determined to be 2.6×10^{13} molecule cm^{-3} in the gas phase.

NO_3 is generated and removed from the cell by the following reactions :

$$Cl_2 + h\nu(310\text{-}400nm) \longrightarrow Cl + Cl \qquad (3)$$

$$Cl + ClONO_2 \longrightarrow Cl_2 + NO_3 \qquad (4)$$

$$Cl + NO_3 \longrightarrow ClO + NO_2 \qquad (15)$$

$$N_2O_5 \rightleftharpoons NO_2 + NO_3 \qquad (2)$$

$$ClO + NO_3 \longrightarrow OClO + NO_2 \qquad (17a)$$

$$\longrightarrow ClOO + NO_2 \qquad (17b)$$

Consequently an increase in the concentrations of NO_3 and N_2O_5 are expected on photolysis. Two parts of the FTIR matrix isolation spectrum of photolysed and unphotolysed Cl_2-$ClONO_2$ are shown in figure 5.

In photolysed mixtures of F_2-HNO_3-N_2, NO_3 is generated and removed from the system via the reactions :

$$F_2 + h\nu(310\text{-}400nm) \longrightarrow F + F \qquad (5)$$

$$F + HNO_3 \longrightarrow HF + NO_3 \qquad (6)$$

$$F + NO_3 \longrightarrow FO + NO_2 \qquad (18)$$

$$FO + NO_3 \longrightarrow FO_2 + NO_2 \qquad (19)$$

$$FO + NO_2 + M \longrightarrow FNO_3 + M \qquad (20)$$

In a set of experiments with a mixture containing F_2, 1.6×10^{16} molecule cm^{-3}, HNO_3, 6.8×10^{15} molecule cm^{-3}, in 55 torr of N_2, the NO_3 concentration was measured to be 1.0×10^{13} molecule cm^{-3}. The FTIR matrix isolation spectrum of the photolysed and unphotolysed mixtures is shown in figure 6.

In both the Cl_2-$ClONO_2$ and F_2-HNO_3 chemical systems, two weak absorption features appear around 1500 cm^{-1} and 761 cm^{-1}, which may be assigned to NO_3. The feature absorbing between 1495 and 1505 cm^{-1} in the Cl_2-$ClONO_2$ system and between 1492 and 1500 cm^{-1} in the F_2-HNO_3 system is assigned to the ν_3, e', vibration of NO_3, in agreement with a recent diode laser study in the gas phase.[14] The broadness of this feature in the matrix may be due to the degenerate nature of this vibration, whereas the slight shift in absorption regions between the two matrices may be due to the presence of Cl_2 in the Cl_2-$ClONO_2$ matrix. The other feature attributed to NO_3 occurs at 761cm^{-1} in both systems. This is assigned to the ν_2, a_2'', vibration of NO_3.

By assuming that the relative concentrations of N_2O and NO_3 are the same in the deposited N_2 matrix as in the gas phase and that the Beer-Lambert law is valid for matrix absorptions, then the ratio of band strengths $S_{NO3(v)}/S_{N2O(v3)}$ can be calculated for a vibration v of NO_3 from the integrated absorptions and gas phase concentrations. These values are listed in table 2.

Acknowledgement.

This work was supported by supported by the Deutsche Forschungsgemeinschaft under the Middle Atmosphere Program and by the Max Planck Gesellschaft.

References.

1) Crutzen, P.J.; Quart. J. Roy. Met. Soc. 96 (1970) 320.
2) Johnston, H.S. ; Science 173 (1971) 517.
3) Platt, U. ; Perner, D.; Winer, A.M.; Harris, G.W. ; Pitts, J.N.; Geophys. Res. Lett. 7 (1980) 89.
4) Noxon, J.F. ; Norton, R.B. ; Marovich, E. ; Geophys. Res. Lett. 7 (1980) 125.
5) Rigaud, P. ; Naudet, J.P. ; Huguenin, D. ; J. Geophys. Res. 88 (1983) 1463.
6) Winer, A.M. ; Atkinson, R. ; Pitts, J.N. ; Science 224 (1984) 156.
7) Noxon, J.F. ; J. Geophys. Res. 88 (1983) 11017.
8) Morris, E.D. ; Niki, H. ; J. Phys. Chem. 78 (1974) 1337. Japar, S.M. ; Niki, H ; J. Phys. Chem. 79 (1975) 1629.
9) Atkinson, R. ; Plum, C.N.; Carter, W.P.L. ; Winer A.M. ; Pitts, J.N.; J. Phys. Chem. 88 (1984) 1210. Atkinson, R. ; Aschmann, S. ; Winer, A.M.; Pitts, J.N. ; Environ. Sci. Technol. 18 (1984) 370.
10) Burrows, J.P. ; Griffith D.W.T. ; Moortgat G.K. ; Tyndall, G.S. ; J. Phys. Chem. 89 (1985) 266.
11) Burrows, J.P. ; Tyndall G.S. ; Moortgat, G.K. ; J. Phys. Chem. in press (1985).
12) Burrows, J.P. ; Tyndall G.S. ; Moortgat, G.K. ; Chem. Phys. Lett, 119, (1985) 193.
13) Atkinson R. ; Pitts J.N. ; Aschmann S.M. ; J. Phys. Chem. 88 (1984) 1584.
14) Ishiwata T. ; Tanaka I. ; Kawaguchi K. ; Hirota E. ; J. Chem. Phys. 82 (1985) 2196.
15) Graham R.A. ; Johnston H.S. ; J. Phys. Chem. 82 (1978) 254.
16) Platt U. ; Perner D. ; Schröder J. ; Kessler C. ; Toennissen A. ; J. Geophys. Res. 86 (1981) 11965.
17) Malko M.W. ; Troe J. ; Int. J. Chem. Kinet. 14 (1982) 399.
18) Tuazon E.C. ; Sanhueza E. ; Atkinson R. ; Carter W.P.L. ; Winer A.M. ; Pitts J.N. ; J. Phys. Chem. 88 (1984) 3095.
19) Perner D. ; Schmeltekopf A. ; Winkler R.H. ; Johnston H.S. ; Calvert J.G. ; Cantrell C.A. ; Stockwell W.R. ; J. Geophys. Res. 90 (1985) 3807.
20) Kircher C.C. ; Margitan J.J. ; Sander S.P. ; J. Phys. Chem. 88 (1984) 4370.

Table 1. Reaction rate coefficients of NO_3, studied in the modulated photolysis apparatus.

Reaction	N_2 torr	Temperature K	Rate Coefficient cm^3 molecule^{-1} s^{-1}
NO_3+NO_2	24	298	$(4.8\pm0.3)\times10^{-13}$
	40	298	$(5.8\pm0.8)\times10^{-13}$
$NO_3+CH_3SCH_3$	21	298	$(9.0\pm4)\times10^{-13}$
	21	318	$(1.0\pm0.4)\times10^{-12}$
	21	278	$(1.2\pm0.4)\times10^{-12}$
NO_3+Cl	20	298	$(2.7\pm1.0)\times10^{-11}$
NO_3+SO_2	20	298	$\lesssim 4\times10^{-16}$
NO_3+CS_2	20	298	$\lesssim 4\times10^{-16}$
NO_3+CO	20	298	$\lesssim 4\times10^{-16}$
NO_3+CH_4	20	298	$\lesssim 4\times10^{-16}$
$NO_3+H_2O_2$	20	298	$\lesssim 2\times10^{-15}$

Table 2. Band strengths for NO_3 vibrations relative to the v_3 vibration of N_2O.

chemical system	absorption cm^{-1}	assignt	$S_{NO3(v)}/S_{N2O(v_3)}$
$Cl_2+ClONO_2+hv$	1495-1505	v_3	0.2
	761	v_2	8.6×10^{-2}
F_2+HNO_3+hv	1492-1500	v_3	0.2
	761	v_2	7.7×10^{-2}

Figure captions.

Figure 1. Schematic diagram of the apparatus.

Figure 2. Visible absorption spectrum of NO_3 .

Figure 3. Plot of ln $K_{2,C}$ against 1/T.
⟷ Graham and Johnston[15]
△ Platt et al[16]
—·— Malko and Troe[17]
✳ Tuazon et al[18]
● Perner et al[19]
□ Kircher et al[20]
○ this work

Figure 4. NO_3 concentration variation in the modulated photolysis of a HNO_3-CH_3SCH_3-N_2 mixture.

Figure 5. FTIR matrix isolation spectra of unphotolysed (a) and photolysed (b) Cl_2-$ClONO_2$ mixtures.
(i) 600-900 cm^{-1}.
(ii) 1400-1700 cm^{-1}.

Figure 6. FTIR matrix isolation spectra of unphotolysed (a) and photolysed (b) F_2-HNO_3 mixtures.
(i) 600-900 cm^{-1}.
(ii) 1400-1700 cm^{-1}.

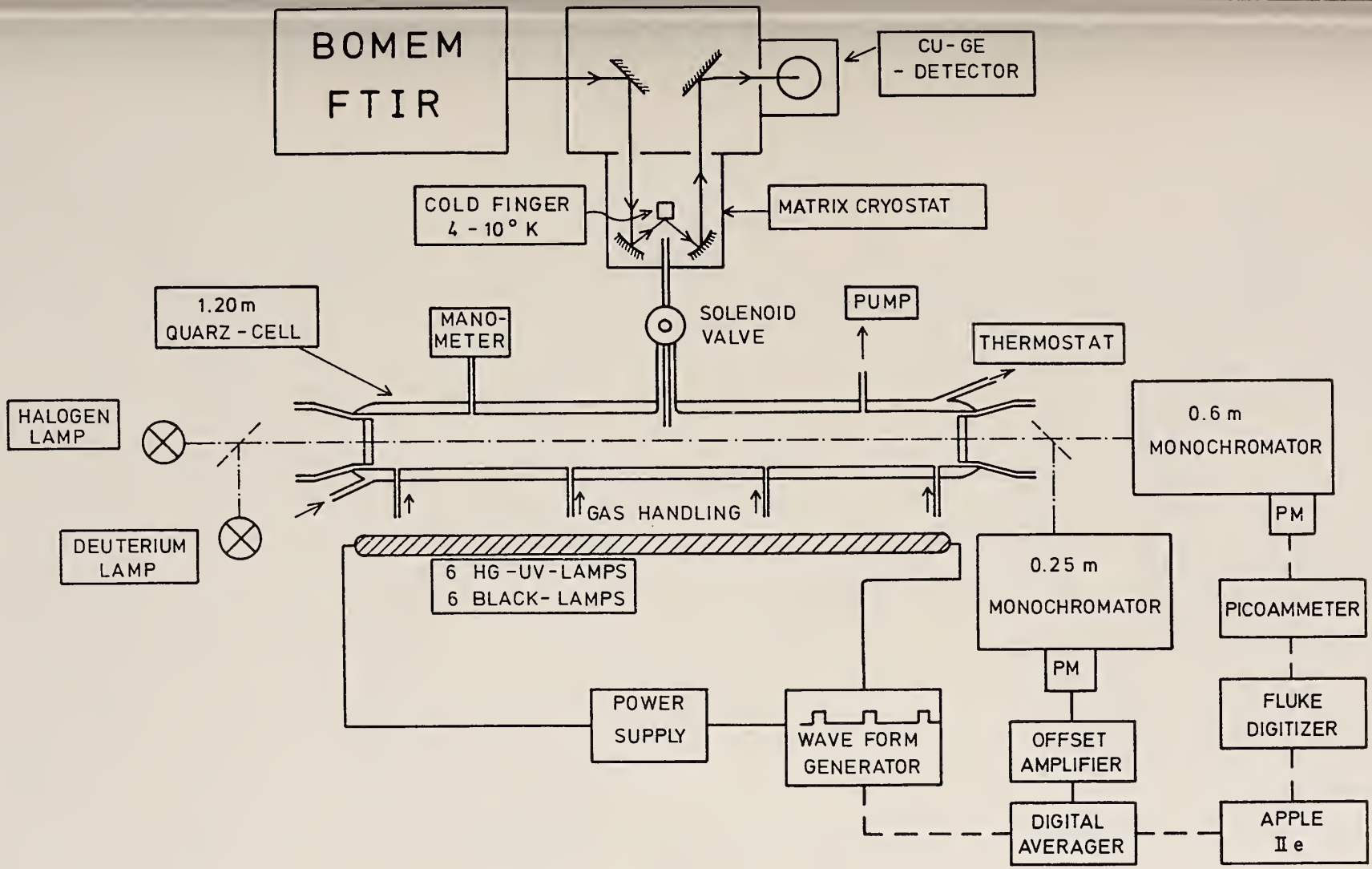

MATRIX ISOLATION FTIR, U.V.-VIS. ABSORPTION and MODULATED PHOTOLYSIS APPARATUS

Fig. 1

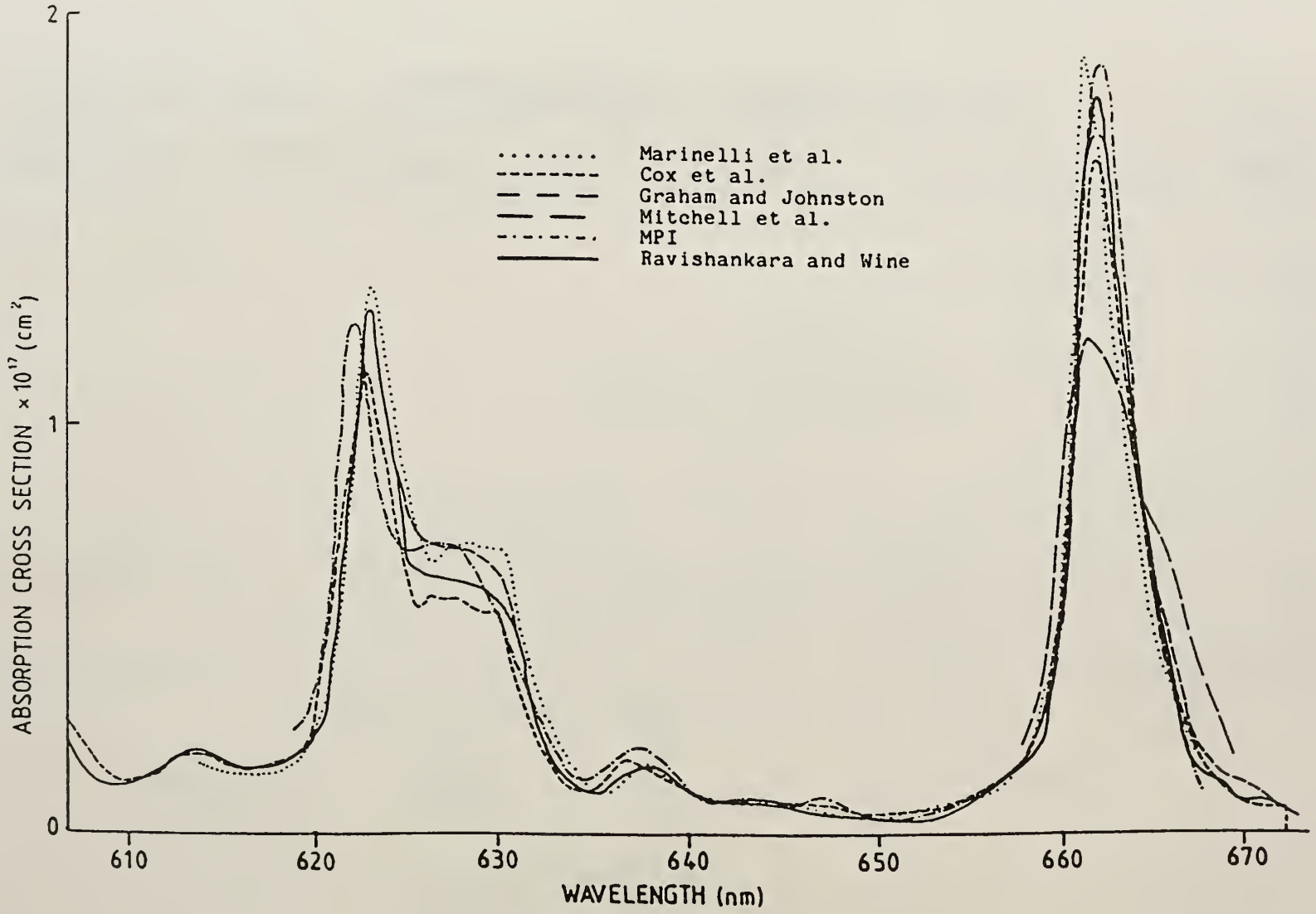
Marinelli et al.
Cox et al.
Graham and Johnston
Mitchell et al.
MPI
Ravishankara and Wine
ABSORPTION CROSS SECTION × 10^17 (cm^2)
WAVELENGTH (nm)
0
1
2
610
620
630
640
650
660
670

Fig. 2

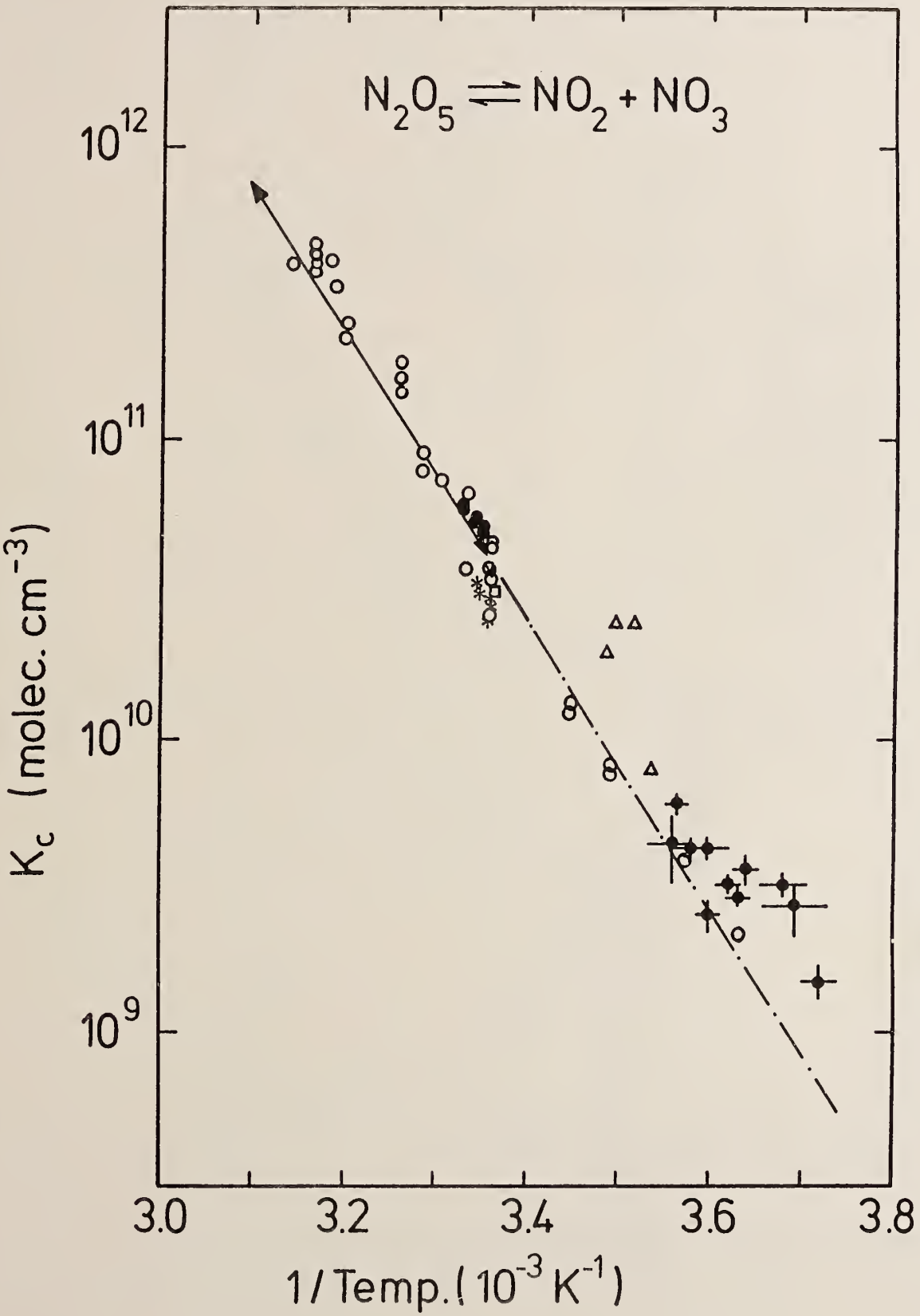
$N_2O_5 \rightleftharpoons NO_2 + NO_3$
10^{12}
10^{11}
10^{10}
10^{9}
K_c (molec. cm^{-3})
3.0
3.2
3.4
3.6
3.8
1/Temp.(10^{-3} K^{-1})

Fig. 3

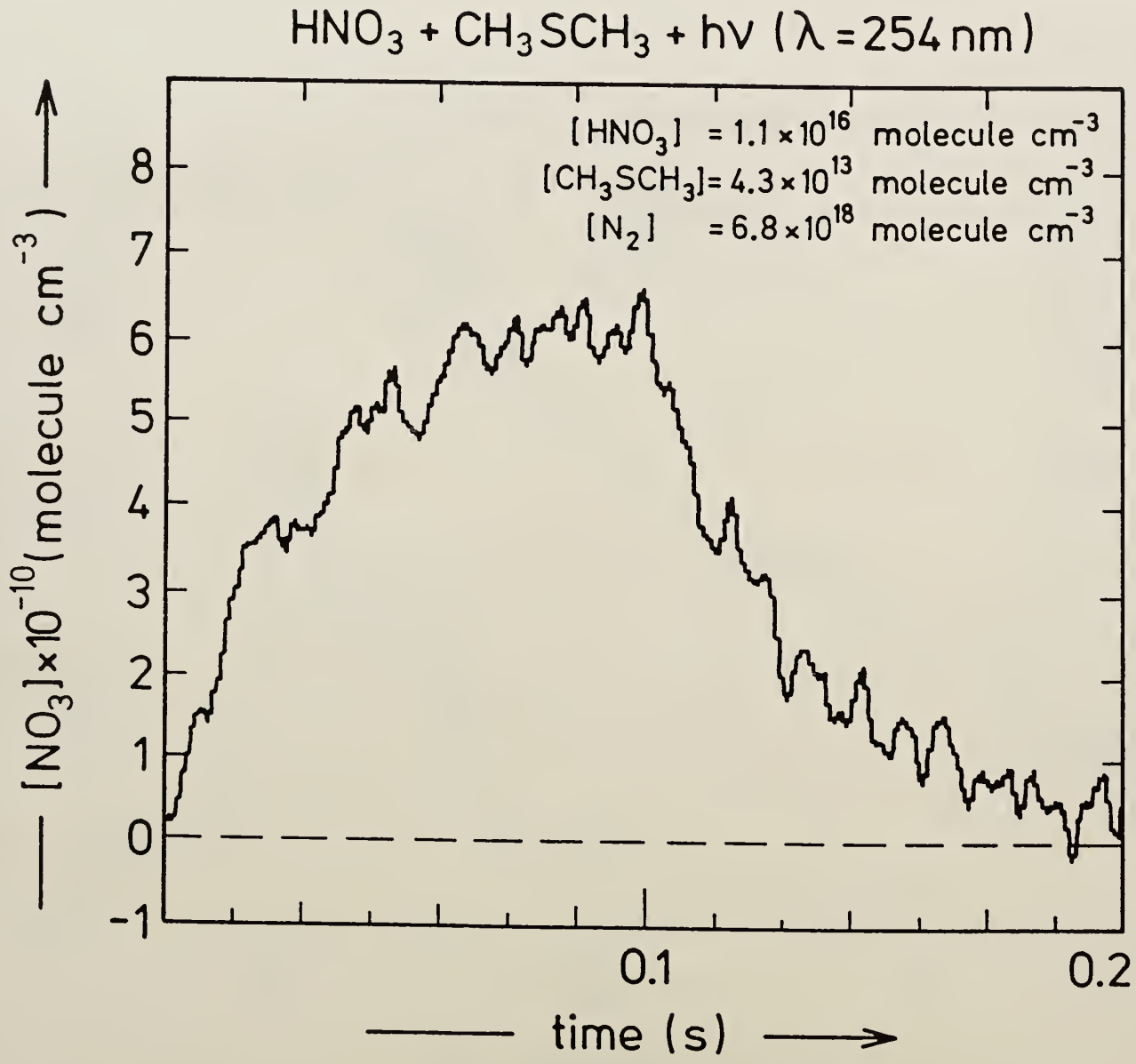
$HNO_3 + CH_3SCH_3 + h\nu$ ($\lambda = 254$ nm)
$[HNO_3] = 1.1 \times 10^{16}$ molecule cm^{-3}
$[CH_3SCH_3] = 4.3 \times 10^{13}$ molecule cm^{-3}
$[N_2] = 6.8 \times 10^{18}$ molecule cm^{-3}
$[NO_3] \times 10^{-10}$ (molecule cm^{-3})
8
7
6
5
4
3
2
1
0
-1
0.1
0.2
time (s)

Fig. 4

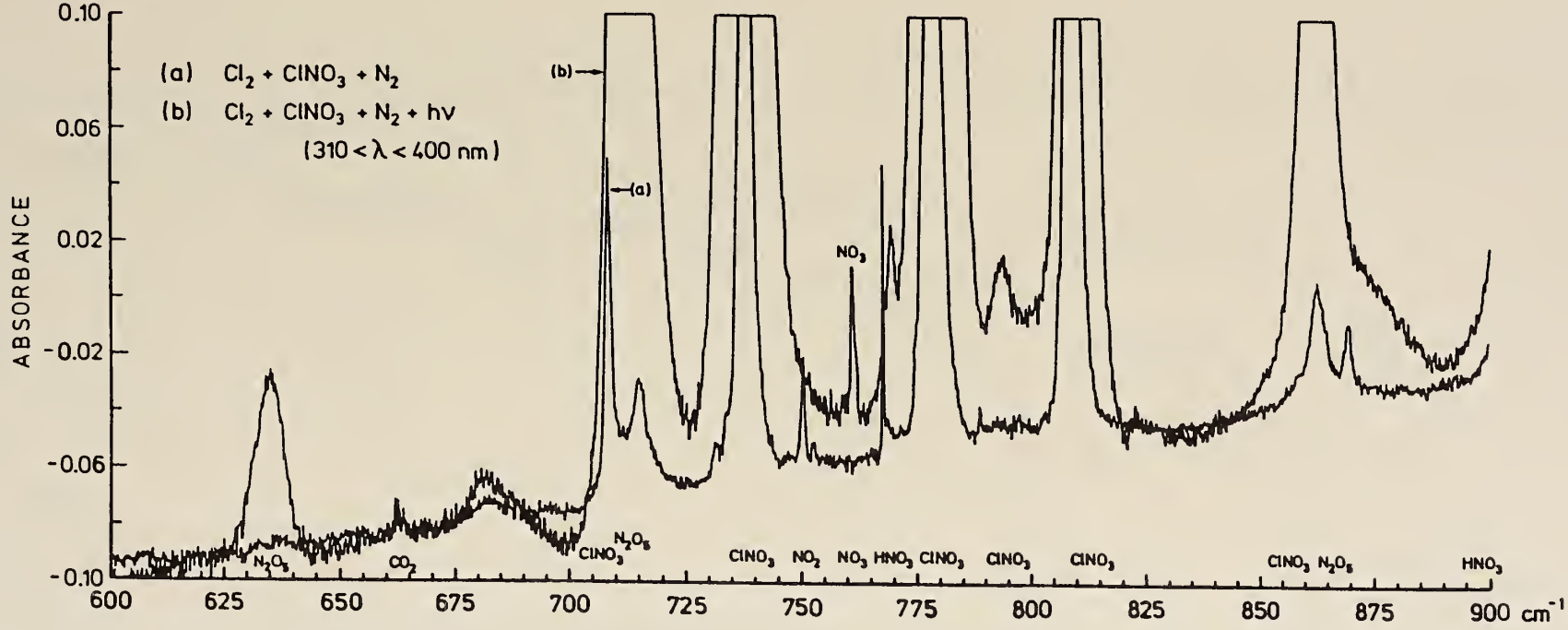
(a) $Cl_2 + ClNO_3 + N_2$
(b) $Cl_2 + ClNO_3 + N_2 + h\nu$
$(310 < \lambda < 400\ nm)$
ABSORBANCE
0.10
0.06
0.02
-0.02
-0.06
-0.10
(b)
(a)
NO_3
N_2O_5
CO_2
$ClNO_3$
N_2O_5
$ClNO_3$ NO_2 NO_3 HNO_3 $ClNO_3$ $ClNO_3$ $ClNO_3$
$ClNO_3$ N_2O_5
HNO_3
600 625 650 675 700 725 750 775 800 825 850 875 900 cm^{-1}

Fig. 5

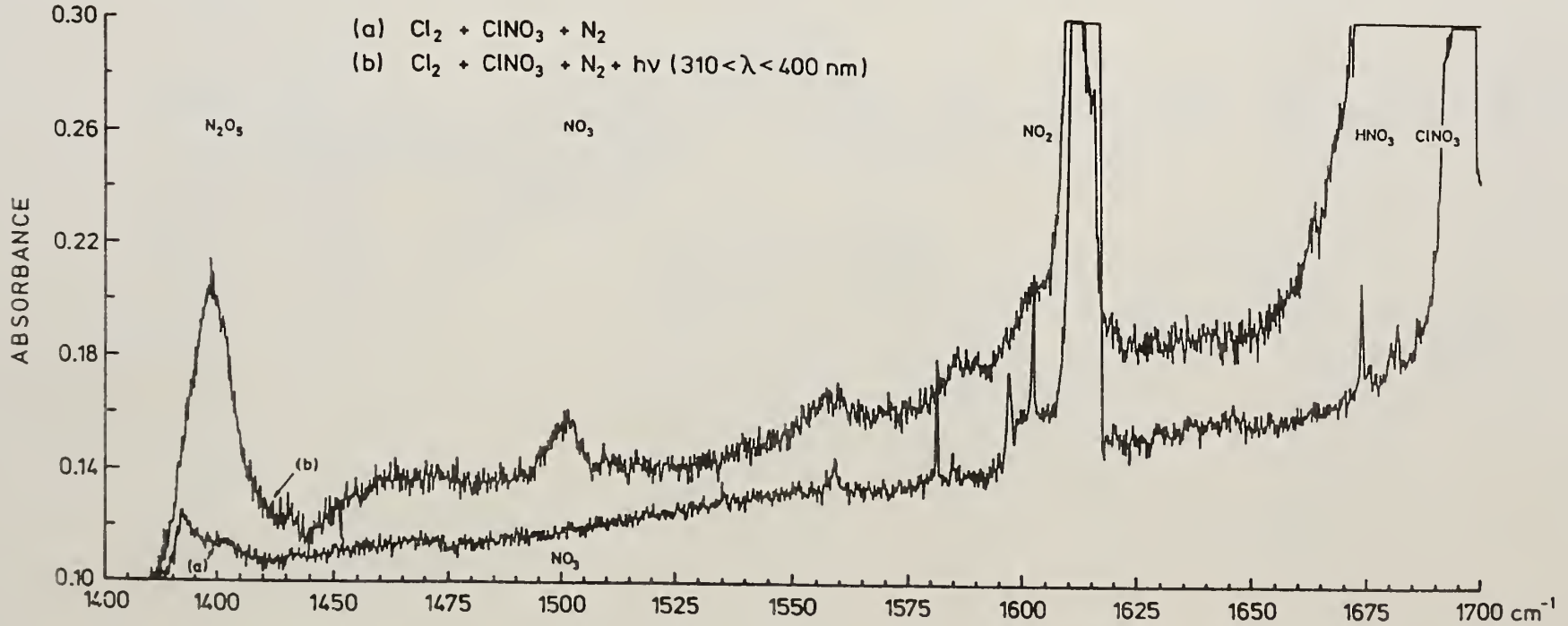
(a) Cl_2 + $ClNO_3$ + N_2
(b) Cl_2 + $ClNO_3$ + N_2 + hν (310<λ<400 nm)
N_2O_5
NO_3
NO_2
HNO_3
$ClNO_3$
(b)
(a)
NO_3
ABSORBANCE
0.30
0.26
0.22
0.18
0.14
0.10
1400
1400
1450
1475
1500
1525
1550
1575
1600
1625
1650
1675
1700 cm^{-1}

Fig. 6

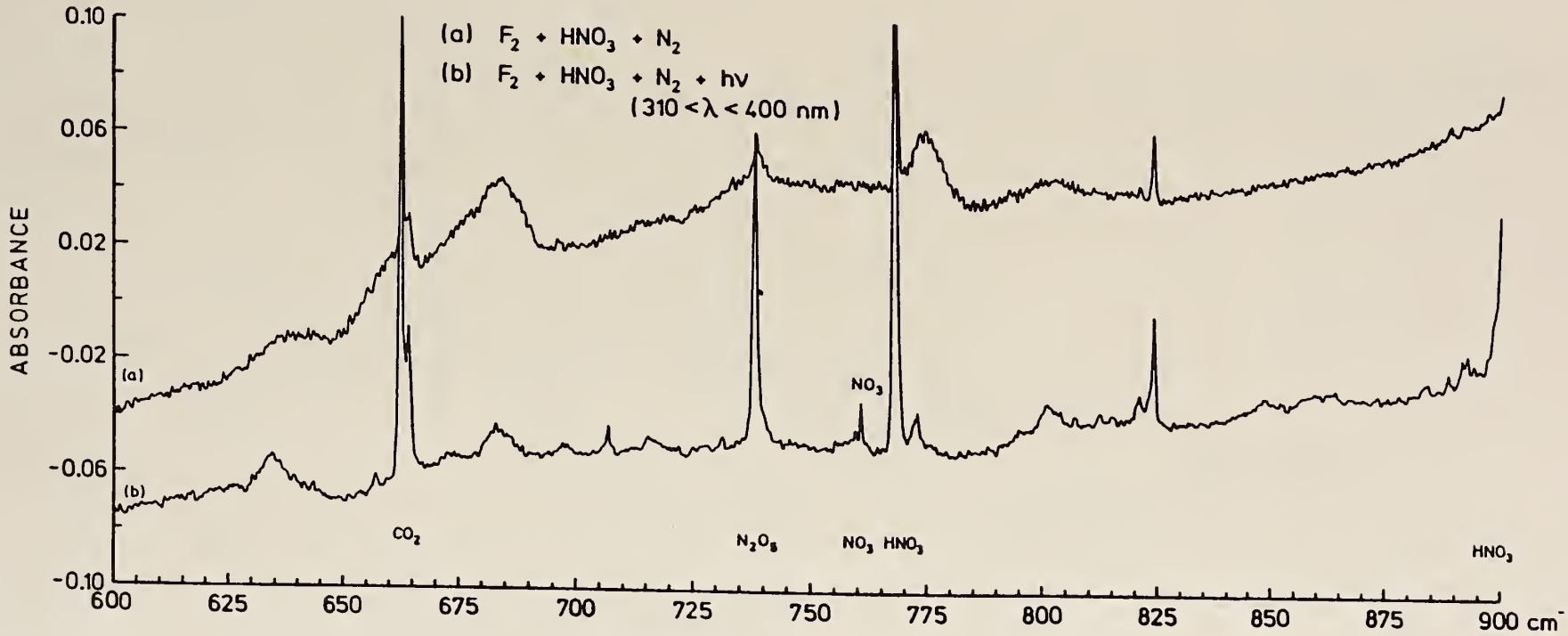
(a) F_2 + HNO_3 + N_2
(b) F_2 + HNO_3 + N_2 + hν
(310 < λ < 400 nm)
ABSORBANCE
0.10
0.06
0.02
-0.02
-0.06
-0.10
(a)
(b)
CO_2
N_2O_5
NO_3
NO_3 HNO_3
HNO_3
600
625
650
675
700
725
750
775
800
825
850
875
900 cm⁻¹

Fig. 7

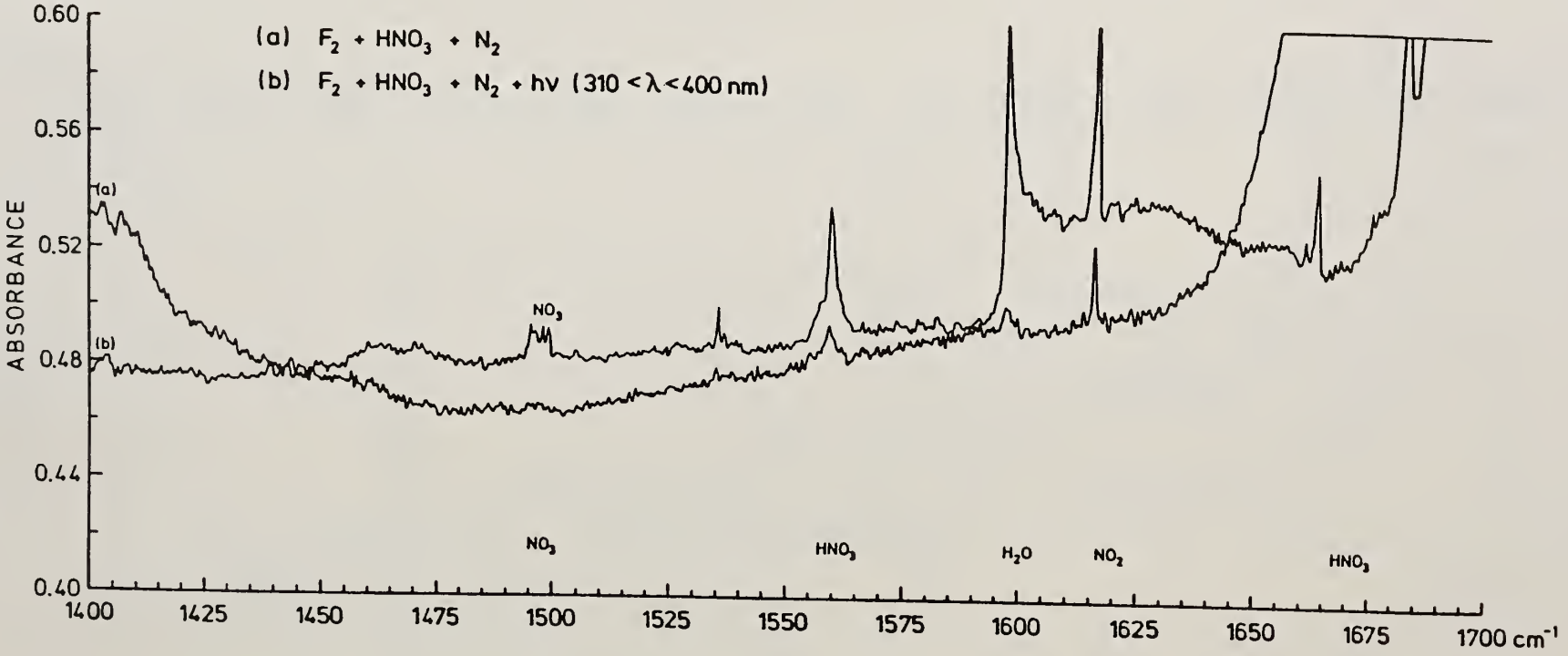
(a) $F_2 + HNO_3 + N_2$
(b) $F_2 + HNO_3 + N_2 + h\nu$ (310 < λ < 400 nm)
ABSORBANCE
0.60
0.56
0.52
0.48
0.44
0.40
(a)
(b)
NO_3
NO_3
HNO_3
H_2O
NO_2
HNO_3
1400
1425
1450
1475
1500
1525
1550
1575
1600
1625
1650
1675
1700 cm^{-1}

Fig. 8

THE FAR-INFRARED LMR SPECTRUM OF THE CN RADICAL

J.M. Brown
Physical Chemistry Laboratory, Oxford University, England.

K.M. Evenson
National Bureau of Standards, Boulder, CO, U.S.A.

Radicals in $^2\Sigma$ states have proved notoriously difficult to study by magnetic resonance techniques. The reason for this is that the electron spin is easily uncoupled from the molecular framework, even by modest magnetic fields. In consequence, those transitions with electric dipole intensity lose their tunability while magnetically tunable transitions lose their electric dipole intensity[1]. The only reported observation of such a free radical by LMR is that of C_2H [2] where a rotational transition was tuned into coincidence with the laser frequency at very low flux densities ($\sim$ 100 G) before the electron spin could be fully decoupled.

We have recently observed several rotational transitions of CN in its $X^2\Sigma^+$ state by far-infrared LMR spectroscopy. These data supplement the measurements of Dixon and Woods[3] and of Skatrud et al.[4] on the zero-field millimeter wave spectrum. The free radical was detected with good signal-to-noise in a variety of chemical reactions. It was possible to produce the molecule in sufficient concentration that its magnetic resonance transitions could be studied in the spin-decoupled region. The transitions studied were of the highly tunable type with very low, but not completely negligible, electric dipole intensity. Under these conditions, the Zeeman patterns are very different from the familiar ones for molecules in $^2\Pi$, $^3\Sigma$, etc. states. For example, there are about twice as many different M components for a given rotational transition. In addition, the relative intensities for perpendicular polarisation ($\Delta M_J = \pm 1$) look like those for a parallel spectrum and vice versa.

References

(1) J. Boland, J.M. Brown, A. Carrington and A.C. Nelson, Proc. Roy. Soc. London A360, 507 (1978).
(2) R.J. Saykally, L. Veseth and K.M. Evenson, J. Chem. Phys. 80, 2247 (1984).

(3) T.A. Dixon and R.C. Woods, J. Chem. Phys. 67, 4956 (1977).
(4) D.D. Skatrud, F.C. De Lucia, G.A. Blake and K.V.L.N. Sastry, J. Mol. Spectrosc. 99, 35 (1983).

INNER AND OUTER NITROGEN HYPERFINE STRUCTURE IN THE HN_2^+ MOLECULAR ION.

G.CAZZOLI, G.CORBELLI, C.DEGLI ESPOSTI and P.G.FAVERO.

Centro di Studio di Spettroscopia a Microonde.
Universita' di Bologna. Via Selmi 2, 40126 Bologna (Italia)

and

Istituto di Spettroscopia Molecolare del C.N.R.
Via de' Castagnoli 1, 40126 Bologna (Italia)

-INTRODUCTION.-

The pure rotational spectrum of HN_2^+ has been first observed in the interstellar medium by Thaddeus and Turner (1), and then at higher resolution by Snyder et al. (2). The first laboratory spectroscopic detection has been performed by Woods and co-workers (3) who confirmed the radioastronomical assignements.

In 1983 F.de Lucia and co-workers (4) discovered a powerful technique that enhances the concentration of molecular ions in the negative glow region of a discharge by two orders of magnitude.

We then decided to apply this technique in order to observe in laboratory the nitrogen hyperfine structure of the J=1-0 rotational transition of HN that has so far been only detected by radioastronomical observation.

-EXPERIMENTAL.-

HN_2^+ was produced in a glow discharge inside a pyres cell 3 m in length and 9 cm in diameter, cooled by liquid nitrogen. Around the cell is wound a solenoid which provides a magnetic field up to 200 G . A 1:1 mixture of H_2 and N_2 with an excess of argon was pumped through the cell, and the discharge current was regulated at 10 mA. The total pressure on the pump end of the cell was below 1 mTorr.

This apparatus is very similar to that used in ref.(4) except that the working pressure is lower and the pyrex tube has a larger section.

The best signal to noise ratio is obtained at a field of about 100 G.

The microwave radiation is produced by a crystal harmonic generator driven by a source modulated 30V12 OKI klystron phase-locked to a computer-controled synthesizer. The computer also performs the averaging and smoothing of the digitized spectrum. The radiation was detected using a home made photodetector which operates at 1.6 K.

Fig. 1 shows the low-dispersion spectrum of the J=1-0 transition of HN_2^+ while fig. 2 and 3 show the hyperfine structure

of the $\Delta F_1=1$ and $\Delta F_1=0$ transition due to the inner nitrogen nucleus.

The measured transition frequencies are listed in table I.

-ANALYSIS AND DISCUSSION.-

The expression of the hfs Hamiltonian used to fit the central line frequency, the two electric quadrupole coupling constants and the two N spin rotation coupling constants to the seven experimental line frequencies is:

$$H(hfs) = H(Q) + H(SR)$$

where

$$H(Q) = \sum_{i=1}^{2} \frac{(eQq_z)_i}{4I_i(2I_i-1)} (3\bar{I}_{zi}^2 - \bar{I}_i^2)$$

and

$$H(SR) = \sum_{i=1}^{2} C_i (\bar{J}.\bar{J}_i - \bar{J}_z \bar{I}_{zi})$$

The matrix elements of this Hamiltonian in the $|JIF\rangle$ representation (where $I=I_1+I_2$) are calculated using the expression given by Mizushima (5). In spite of this choice the energy levels are labeled with the quantum numbers J, F_1, F since this convention was followed in previous papers on HN_2^+. The results of the fit are collected in table II together with those from ref. (1).

No significant frequency shift, due to the motion of the ions in the electric field, was observed.

The central line frequency and the hyperfine structure constants are in good agreement with those reported in ref. (1).

In conclusion the results of this investigation show that the resolution obtained with our spectrometer compares quite well with that obtained by the best radioasronomical observation of this molecular ion (2).

-REFERENCES.-

1)P.Thaddeus and B.E.Turner,Astrophys.J. 201(1975)L25.
2)L.E.Snyder,J.M.Hollis,d.Buhl and W.D.Watson,Astrophys.J. 218(1977)L61.
3)R.J.Saykally,T.A.Dixon,T.G.Anderson,P.G.Szanto and R.C.Woods,Astrophys.J. 205(1976)L101.

4)F.C.de Lucia,E.Herbst,G.M.Plummer and G.A.Blake,J.Chem.Phys.
76(1983)2312.
5)M.Mizushima,"The theory of rotating diatomic molecules."(Wiley
,N.Y. 1975).

TABLE I
Observed transition frequencies of HN_2^+ (MHz)

J'F'F' - J F F	Obs.	Obs.-calc.(a)
110 011	93171.619	-0.006
112 012	93171.947	0.005
111 010	93172.078	0.000
122 011	93173.505	0.006
123 012	93173.809	-0.006
121 011	93174.016	0.000
101 012	93176.310	0.000

a)Calculated frequencies were obtained from the molecular parameters of table 2.

Table II
Spectral constants of HN_2^+ (MHz).

	This work	Ref. (1)
ν_0	93173.435(3)	93173.392(31)
$(eQq)_1$	-5.71(3)	-5.67(1)
$(eQq)_2$	-1.44(4)	-1.43(2)
C_1	0.012(4)	0.015(2)
C_2	0.011(4)	-
St.Dev.	0.0085	-

Captions for the figures 1,2,3.

Fig.1.The J=1-0 transition of HN_2^+.Scan from 93171 to 93177 MHz,marker every 0.25 MHz,time constant 0.3 s.The spectrum is the accumulation of two scans,followed by digital smoothing.

Fig.2.The J=0-1 ,F_1 = 2-1 transition of HN_2^+.Scan from 93173 to 93174.5 MHz,marker every 0.10 MHz,time constant 0.3 s.The spectrum is the accumulation of 15 scans,followed by digital smoothing.

Fig.3.The J=1-0,F =1-1 transition of HN_2^+.Scan from 93171.4 to 93172.5 MHz,marker every 0.10 MHz,time constants 0.3 s.The spectrum is the accumulation of 9 scans,followed by digital smoothing.

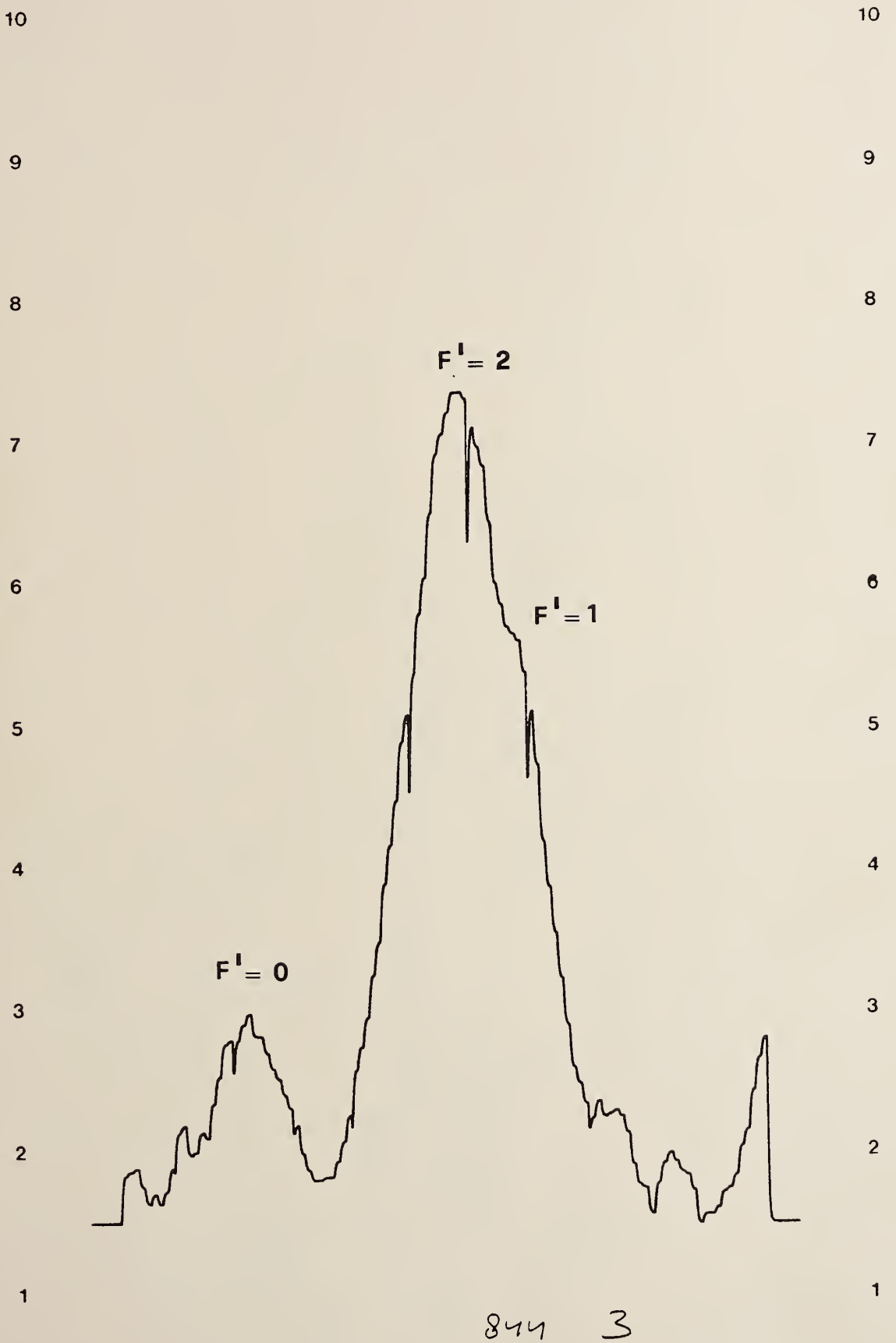

844 3

Fig. 1

42

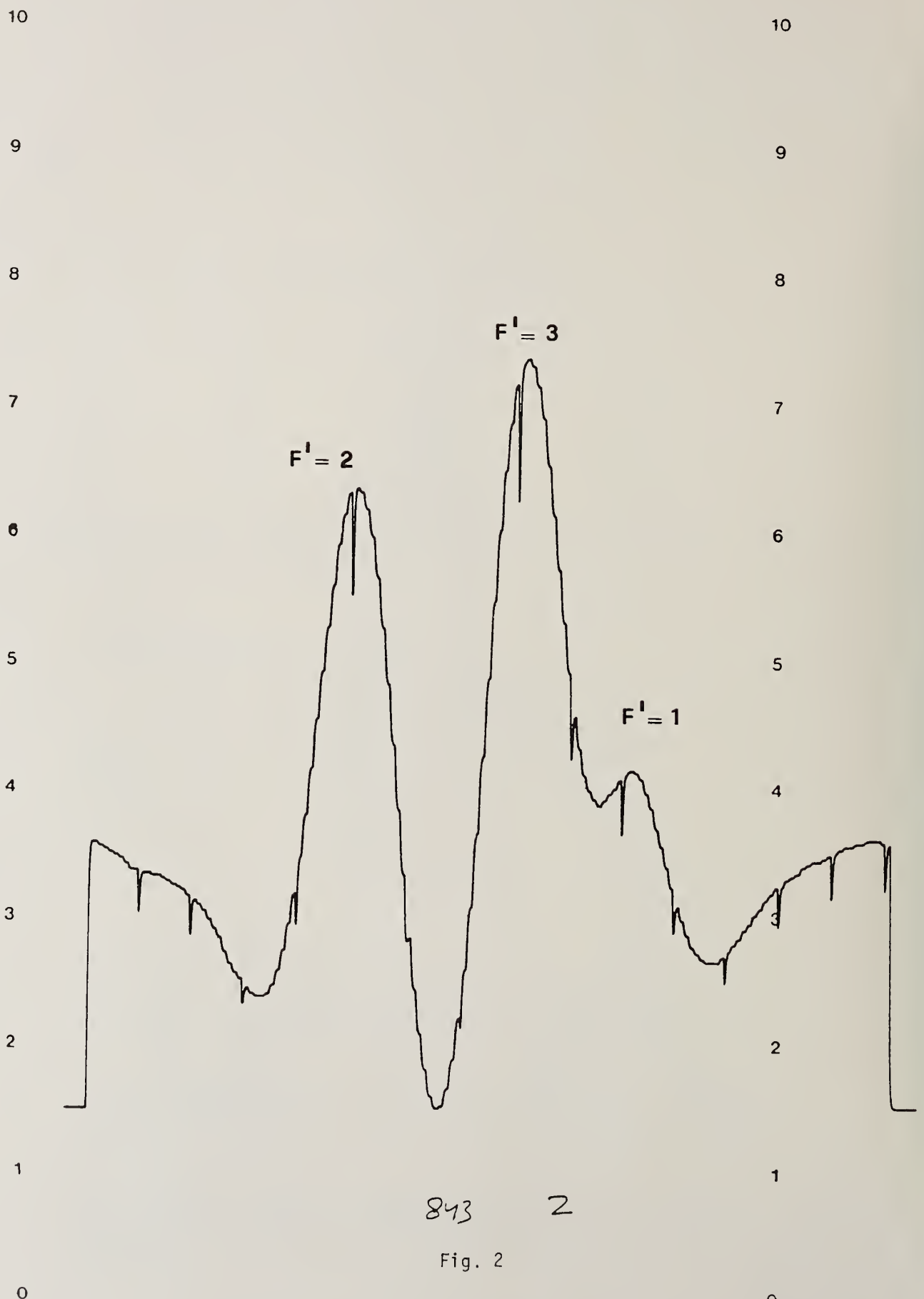

843 2

Fig. 2

421

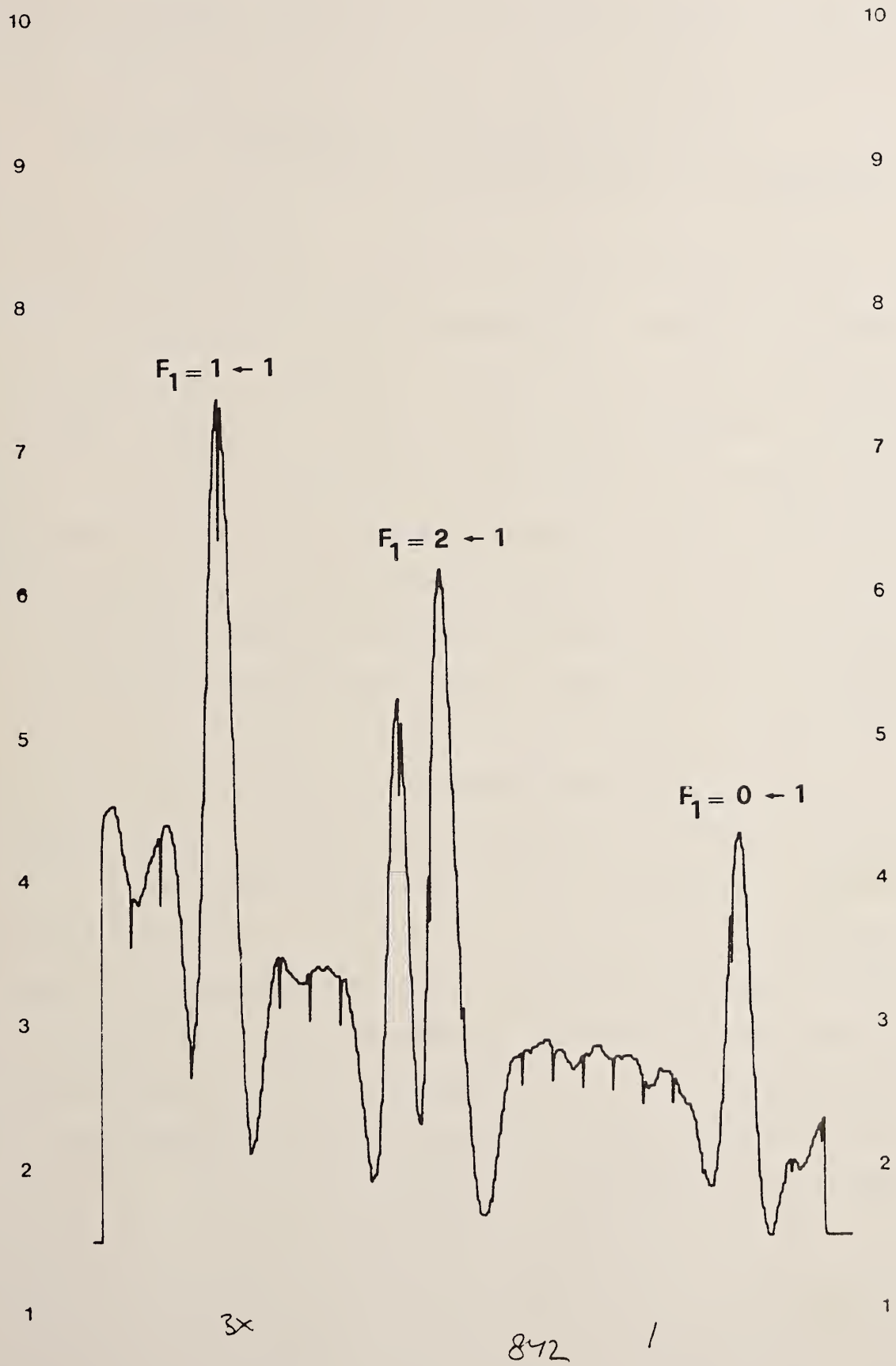

3x

842 1

Fig. 3

42 8

FAR-INFRARED MEASUREMENTS OF STRATOSPHERIC TRACE GASES

K.V. Chance, F.J. Lin and W.A. Traub
Harvard-Smithsonian Center for Astrophysics, Cambridge, MA, U.S.A.

The far-infrared/submillimeter region of the spectrum has become increasingly important for measuring trace species involved in stratospheric photochemistry. Among the reasons for this importance are: (1) the recent improvement of detectors and spectrometer design; (2) the ability of far-infrared instruments to make emission measurements of the stratosphere, allowing measurements in any direction and at any time of day or night; (3) the fact that a great number of the more important and interesting stratospheric molecules have strong spectral lines in this region, chiefly from molecular rotational transitions.

We present here a summary of measurements obtained with a balloon-borne Fourier transform spectrometer during two balloon flights in 1983. The spectrometer is a double-beam instrument having a resolution of 0.032 cm^{-1} (unapodized), which is sensitive from 80 to 220 cm^{-1}. It observes the atmosphere through a telescope with a 0.3^{o} field of view, stabilized to $\pm\ 0.02^{o}$ in absolute elevation. The species observed during these flights include OH, H_2O_2, H_2O, O_3, O_2, $O(^3P)$, HCl and HF. Most of the data have now been reduced to obtain altitude profiles of these species in the atmosphere.

MULTIPHOTON IONIZATION STUDIES OF UV-MULTIPHOTON FRAGMENTATION PROCESSES

Peter Chen, Joan B. Pallix, William A. Chupka, and Steven D. Colson

Sterling Chemistry Laboratory

Yale University, New Haven CT 06511

We report the copious production of neutral carbon atoms from ketene within the 5 ps pulsewidth of the dissociation laser. Since the observation[1] that the resonant multiphoton ionization of benzene with a strongly focussed laser yielded predominantly C^+ ions, experimental[2] and theoretical[3] studies of high-power laser photodissociation and photoionization have appeared widely, nearly always discounting the importance of neutral pathways. Dissociation is assumed to occur predominantly through the ionic manifold[4]. In a few instances[5], however, production of small neutral fragments by near-UV multiphoton dissociation has been reported, carbon atoms being produced abundantly from simple aromatic hydrocarbons in one case[5a]. Nevertheless, two fundamental mechanistic questions remain unaddressed experimentally:

1) In what manner is sufficient energy deposited in an isolated, neutral, polyatomic molecular system to cause production of atoms in much greater abundance than ions?

2) Through what intermediates, if any, is the neutral fragmentation occurring?

We would like to propose some answers to these questions based upon preliminary observations of extensive production of neutral fragments from ketene and a number of other organic precursors with time resolution.

Experiments were performed in a time-of-flight mass spectrometer. Dissociation was done under collision-free conditions in a pulsed free jet of roughly 4% of an organic precursor seeded in 2 atm. argon. Neutral fragments were detected by the wavelength dependence of the MPI signal produced by the dissociating laser pulse; only fragments produced within the laser pulsewidth

were detected. Nanosecond experiments were performed with the doubled output of a YAG-pumped dye laser. Typically used were 1.0 mJ pulses of 8 ns duration with 1 cm^{-1} bandwidth. Picosecond pulses from a mode-locked Ar^+-pumped dye laser were pulse-amplified and doubled to give, typically, 40 μJ, 5 ps UV pulses with 5 cm^{-1} bandwidth. The laser was focussed with a 15 cm lens for the nanosecond results, and a 6 cm lens for the picosecond work. Thus, typically, the fluence (photons cm^{-2}) in the picosecond case was about 15 times less than in the nanosecond case, but the flux (photons cm^{-2} sec^{-1}) about 100 times greater. Acetone, acetonitrile, and tetramethylsilane were of spectroscopic grade and used as received. Ketene was synthesized by the flash vacuum pyrolysis of acetic anhydride, and purified by multiple trap-to-trap distillations; purity was checked by mass spectroscopy. t-Butylnitrite was prepared by the action of acidic $NaNO_2$ on t-butanol and purified by distillation under reduced pressure; purity was checked by gas chromatography.

Using mass-selected wavelength scans with nanosecond pulses, we have detected atomic carbon, CH, CH_2, and CH_3 (where possible) by resonant multiphoton ionization. Results are summarized in Table 1. That the resonant signal is due to ionization of neutral fragments is unambiguous from the wavelength dependence. A representative spectrum for m/e=12 is shown in Fig. 1, and can be assigned to known atomic carbon transitions[6]. Band assignments for CH and CH_2 were confirmed by rotational analysis and comparison with known lower state combination differences. These spectra will be the subject of separate publications[7]. Observation of the $3p\ ^2A_2'' \leftarrow X\ ^2A_2''$ Rydberg transition of CH_3 reported by Hudgens[8] et. al. confirmed the presence of that radical in significant abundance. For ketene, t-BuONO, and acetone, absorption[9] of one photon (two at the one photon energy for TMS and acetonitrile) appears continuous, due either to line broadening or spectral congestion, in the spectral regions covered. At the laser powers used, there

Table 1

fragment precursor	$C(^3P_J)$	$C(^1D_2)$	$C(^1S_0)$	$CH(X^2\Pi_i)$	$CH_2(a^1A_1)$	$CH_3(X^2A_2'')$
ketene	yes	yes	no	yes	yes	---
t-BuONO	---	yes	no	yes	yes	yes
acetone	---	yes	---	yes	yes	yes
TMS	---	yes	yes	yes	---	yes
MeCN	---	yes	---	yes	---	yes

2+1 MPI SPECTRUM OF ATOMIC CARBON

from ketene

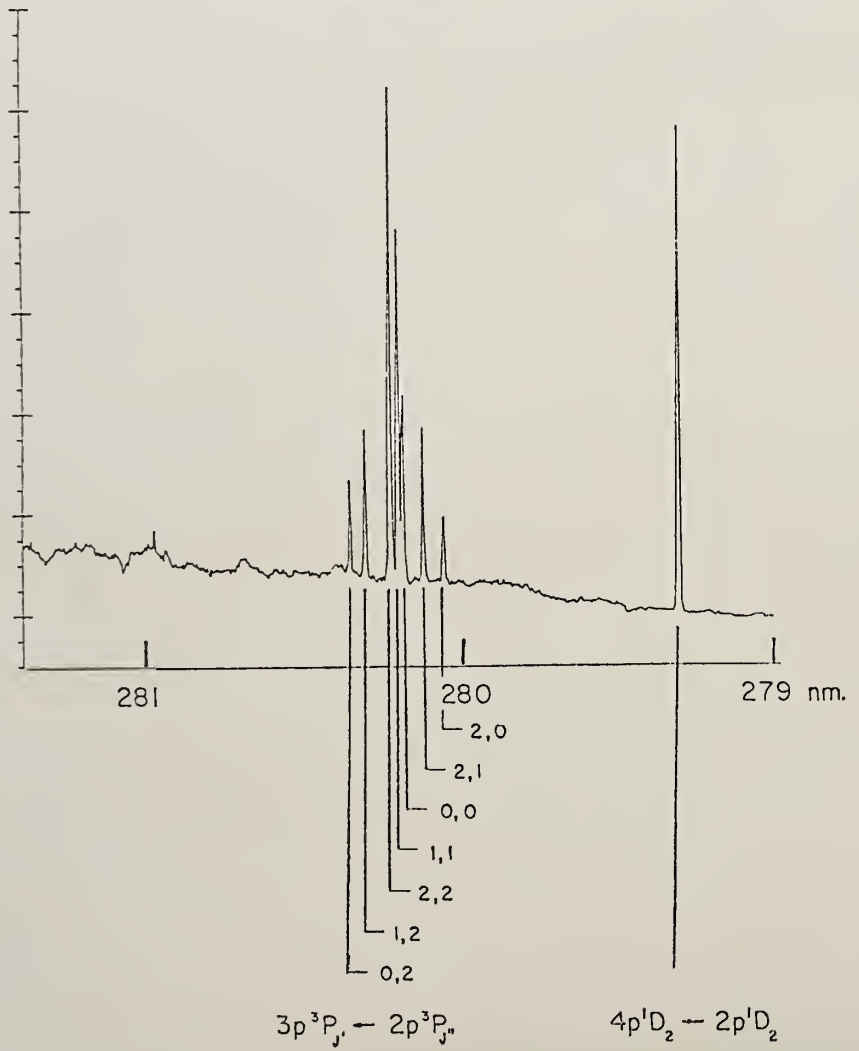

Figure 1.

WAVELENGTH DEPENDENCE IN THE MPI MASS SPECTRUM OF KETENE NEAR THE ATOMIC CARBON $3p\,^1S_0 \leftarrow 2p\,^1D_2$ LINE

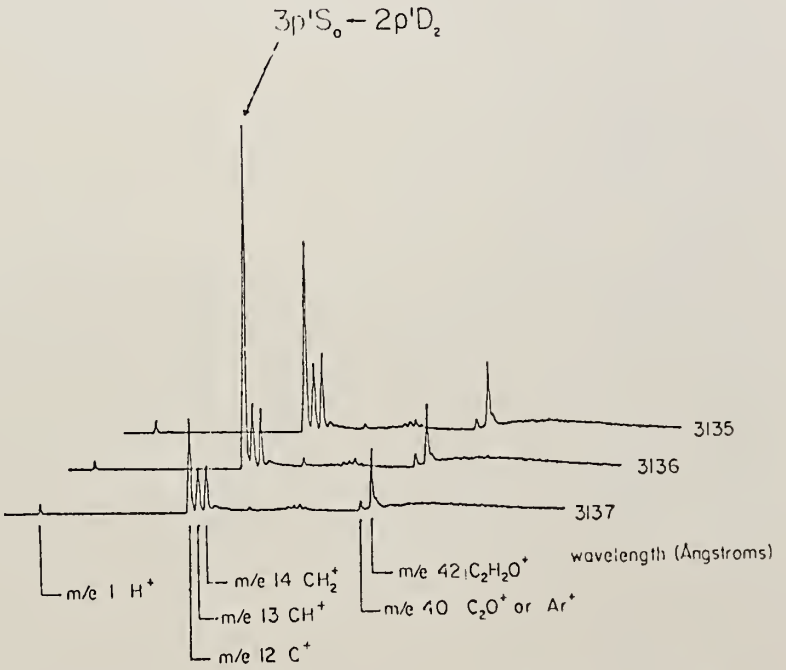

Figure 2. Pulsewidth: 25 ps; bandwidth: 0.1 nm; energy; 40 μJ per pulse.

is no strong wavelength dependence to fragment formation. By comparing the intensities of fragment resonant signals to that due to ionization of the parent molecule, we conclude that production of neutral carbon atoms, plus other neutral fragments, exceeds ionization of the parent molecule by at least two orders of magnitude.

Picosecond experiments searched for the $3p\ ^1S_0 \leftarrow 2p\ ^1D_2$ carbon resonance[6] because that peak was one of the most prominent in the nanosecond results. From ketene, neutral carbon atoms were found to appear within the 5 ps pulse duration. Picosecond mass spectra as the wavelength was scanned over the resonance line are shown in Fig. 2. In contrast, no enhancement of the m/e=12 peak at the carbon resonance was observed for acetone or t-butylnitrite under similar conditions. When the pulsewidth was stretched from 5 to 25 to 50 ps, the relative intensity of m/e=12 to m/e=42, the ketene parent mass, grew dramatically (see Figure 3), with the energy per pulse was held constant. Thus the relative increase in the extent of fragmentation occurred despite decreasing peak power. For comparison, the same carbon peak in the nanosecond mass spectrum is the only peak visible, the other masses being lost in the baseline. (The extent of fragmentation relative to ionization was found to be relatively insensitive to peak power for fixed pulsewidths. The ratio was invariant when power was halved; for much larger decreases the C^+ intensity dropped faster than the parent peak). These results imply that carbon atom formation from ketene occurs on a timescale such that the shortest pulses probe only its rising edge, and that some kinetic factor strongly favors the rapid appearance of carbon atoms from ketene as compared with the other compounds. We repeated the experiment using two 5 ps pulses separated in time by 330 ps. The results shown in Figure 4 indicate that a dark process increased the C^+ yield, as expected from the pulse stretching results. Similar fragmentation processes have been observed[10] in the UV excitation of SO_2.

PRODUCTION OF $^1D_2$ ATOMIC CARBON AT 3136 Å FROM KETENE BY PICOSECOND LASER EXCITATION

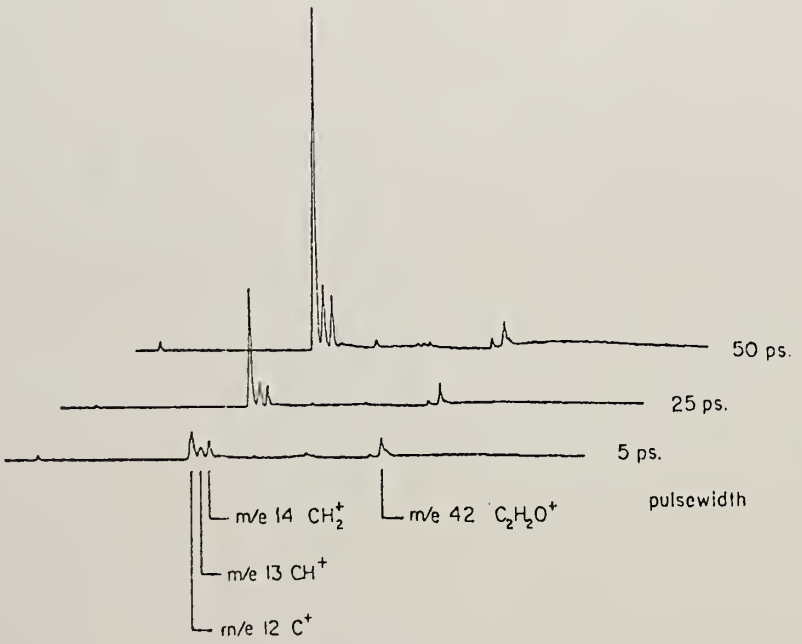

Figure 3. Bandwidth of both 5 and 50 ps laser pulses was measured to be about 0.1 nm.

PICOSECOND PUMP-PROBE DETECTION OF $^1D_2$ CARBON FROM KETENE

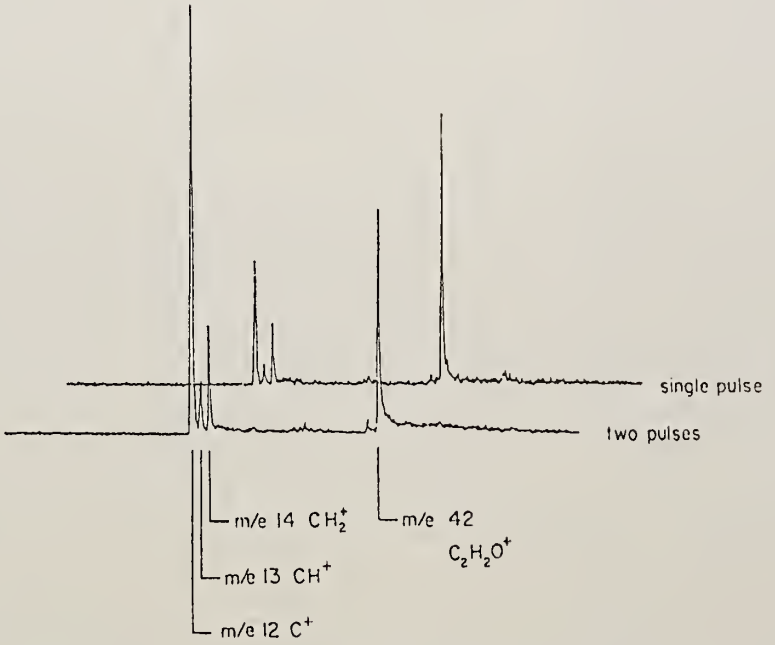

Figure 4. Each pulse had a width of 5 ps and an energy of 6 μJ. The second pulse is delayed by 330 ps. The laser wavelength is 313.6 nm.

To produce $^1D_2$ carbon, one can calculate from heats of formation[11] that a minimum of three photons is necessary. In addition, the exceedingly rapid appearance of the smallest possible fragments makes the thermodynamic threshold only a lower limit. Furthermore, while the energy of three photons ($\approx$96,000 cm^{-1}) far exceeds ketene's ionization potential ($\approx$77,000 cm^{-1})[12], the total ion yield was very small compared to the total yield of neutrals. To account for these observations, we propose a mechanism involving rapid, non-ionizing radiationless transitions which intervene to prevent the electronic energy of any abundant species from exceeding its I.P., although its total internal energy may do so. The radiationless transitions may include internal conversion (IC), intersystem crossing (ISC), and dissociation, and can be expected to occur, interspersed with additional photon absorption, in various combinations and sequences depending on the molecule, wavelength, and laser pulse characteristics. While the obvious mechanism of sequential photodissociations undoubtedly occurs when optical and kinetic factors are favorable, we point out a variant of the general mechanism which can be expected to enter especially for larger molecules where dissociation rates become smaller and IC or ISC rates can be very large. This is a cyclical or vibronic pumping mechanism first discussed by Woodward[13] et. al. for the photofragmentation of butadiene radical cation, whereby photon absorption by the molecule (or a fragment) is followed by a very rapid IC (or ISC), the sequence, or a similar one, repeating until termination by dissociation. If, in this sequence of excitations, the electronic energy remains far below the I.P. (even though the total internal energy exceeds it), predissociation will dominate vibrational autoionization, and extensive fragmentation can occur.

There are two plausible explanations for the absence of detectable carbon atoms in the picosecond mass spectra for t-butylnitrite and acetone. To the extent that RRKM theory is a valid model, the species with the fewest degrees

of freedom, i.e. ketene, will have the fastest dissociation rate. Alternatively, slower internal conversion in t-butylnitrite and acetone may retard cyclical pumping sufficiently to prevent deposition of enough energy in 5 ps to produce atomic fragments.

We have reported production of small neutral fragments from the UV multiphoton dissociation of ketene and other organic species on both nanosecond and picosecond timescales. These results are rationalized by a mechanism involving very rapid radiationless transitions, including cyclical pumping, which has no analog in conventional low-power photochemistry.

We would like to acknowledge funding from the Army Research Office, International Business Machine Corporation, and the Exxon Educational Foundation. One of us (P.C.) would like to thank the National Science Foundation Graduate Fellowship Program and Pfizer Inc. for financial support.

1. L. Zandee, R.B. Bernstein, J. Chem. Phys., 71, 1359, (1979).

2. T.E. Carney, T. Baer, J. Chem. Phys., 76, 5968, (1982). and references therein.

3. a) J. Silberstein, R.D. Levine, Chem. Phys. Lett., 74, 6, (1980).

   b) T. Baer, A.E. DePristo, J.J. Hermans, J. Chem. Phys., 76, 5917, (1982).

4. F. Rebentrost, A. Ben-Shaul, J. Chem. Phys., 74, 3255, (1981).

5. a) R.L. Whetten, K.J. Fu, R.S. Tapper, E.R. Grant, J. Phys. Chem., 87, 1484, (1983).

   b) D.L. Monts, T.G, Dietz, M.A. Duncan, R.E. Smalley, Chem. Phys., 45, 133, (1980).

6. C.E. Moore, "Atomic Energy Levels," vol. 1, NBS Cir. 467, (1949).

7. The CH band analysis has been submitted to Chem. Phys. Lett. for publication. CH_2 analysis is still underway.

8. J.W. Hudgens, T.G. DiGiuseppe, M.C. Lin, J. Chem. Phys., 79, 571, (1983).

9. a) W.C. Price, J.P. Teegan, A.D. Walsh, J. Chem. Soc., 920, (1951).

   b) P. Tarte, J. Chem. Phys., 20, 1570, (1952).

   c) O. Anner, H. Zuckermann, Y. Haas, J. Phys. Chem., 89, 1336, (1985).

10. D.T. Biernacki, S.D. Colson, unpublished results.

11. For the reaction, $CH_2CO^* \rightarrow C(^1D_2) + H_2 + CO$, $\Delta H^\circ = 186$ kcal/mol. While the energy of two photons approaches this value, the jet-cooled ketene nevertheless cannot supply the balance from internal energy. In addition, atomic carbon lines farther to the red were observed, where, clearly, three photons are needed to surmount the thermodynamic barrier.

12. C. Baker, D.W. Turner, Chem. Comm., 480, (1969).

13. A.M. Woodward, W.A. Chupka, S.D. Colson, J. Phys. Chem., 88, 4567, (1984).

QUENCHING OF NH ($A^3\Pi_i$) RADICALS BY H_2 AND D_2

R. J. Cody and J. E. Allen, Jr.
Astrochemistry Branch, NASA/Goddard Space Flight Center, Greenbelt, MD, U.S.A.

Although NH_3 is a minor component in the atmosphere of Jupiter, ammonia and its products play an important role in the atmospheric chemistry of this planet. Heretofore attention has been focused primarily on electronic ground state species, even though excited species could be formed either by chemical reactions or absorption of radiation and these could then contribute to the atmospheric chemistry. One possible candidate is the NH radical in its resonantly excited $A^3\Pi_i$ state. This paper reports the electronic quenching of this state by D_2 and H_2, the major component of the Jovian atmosphere.

Photodissociation of NH_3 by an ArF excimer laser (λ=193 nm) produces both ground and excited state NH_2 ($\tilde{X}^2B_1$, $\tilde{A}^2A_1$) radicals in single photon processes and excited state NH ($A^3\Pi_i$, $b^1\Sigma^+$) radicals by two-photon events.[1] The NH(A) radicals are formed predominately in the v'=0 vibrational level with a hot rotational distribution.[1,2] About 5% of the radicals are in the v'=1 level.[2] The decay of the NH(A) radicals is monitored by detection of the NH($A^3\Pi \rightarrow X^3\Sigma^-$) fluorescence at 336 nm.

A diagram of the experimental apparatus is Fig. 1. A pulsed delay generator, which has a repetition rate of 40 Hz, triggers simultaneously the ArF laser and the EG&G PAR Model 4400 Signal Processing System. The laser beam passes through three fine mesh metal screens which reduce the intensity below the saturation region and into the linear range of the power curve. The transmittance of each screen is 0.33. An 0.6x0.9 cm region is selected by a circular aperture from the center of the beam and passes through the photolysis cell. The relative laser power is measured

before the photolysis cell by using the reflection from the front cell window. The NH(A-X) fluorescence is viewed perpendicular to the direction of the laser beam. It is filtered by a broad band 0.2 meter monochromator (FWHM ~25 nm) centered at 336 nm and is detected by a photomultiplier. The signal is integrated by the PAR 4400 boxcar averager and stored on diskette. The boxcar averager scans in time over the NH(A) fluorescent decay curve with a gate width of 5 ns. Later, the decay curves are fitted by the single exponential curve program of the 4400 Signal Processor to yield the inverse of the fluorescent lifetime, τ^{-1}. A sample decay curve with its exponential fit is shown in Fig. 2.

Gas mixtures of NH_3 and H_2 or D_2 are made in storage bulbs and allowed to equilibrate for at least 1 1/2 hours before use. Both NH_3 and H_2 are purified before use, but the D_2 (research grade) is used directly from the cylinder. The gas mixture is slowly flowed through the photolysis cell. The NH(A) fluorescent lifetime is first measured in NH_3 alone at a pressure of 20 mTorr, and then, with added quenching gas at various pressures.

The inverse of the fluorescent lifetime, τ^{-1}, is plotted versus the pressure of H_2 or D_2, and the slope is the electronic quenching rate constant (k_Q). These plots for H_2 and D_2 are shown in Fig. 3. Table I contains the rate constants measured in this work and previous work. The cross sections, σ_Q, are calculated from

$$\sigma_Q = k_Q \left(\frac{\pi\mu}{8kT}\right)^{1/2} \qquad \text{where } T = 300 \text{ K}$$

TABLE I. Quenching Rate Constants for NH(A) Radical

Quenching Gas	k_Q (10^{-11} cm^3 molecule^{-1} s^{-1})	σ_Q (10^{-16} cm^2)
H_2	5.5 ± 0.5[a]	2.9
	5.5 ± 0.5[b]	2.9
	2.4[c]	1.3
D_2	3.4 ± 0.4[a]	2.4

(a) This work.
(b) Ref. 2.
(c) Ref. 3.

The quenching rate constant with H_2 measured here is in very good agreement with that measured by Hofzumahaus and Stuhl[2] for a hot rotational distribution in the v'=0 level of NH(A). It is a factor of ~2 higher than the value we reported earlier,[3] and the difference could be due to gas mixing problems in the earlier work. The rate constant for quenching by D_2 is ~40% smaller than that by H_2. Due to the velocity difference, the quenching cross section of D_2 is only ~20% smaller than the cross section for H_2. Both of these rate constants are fast. Since the radiative lifetime of NH(A) is 465 ns,[2] then for collisional quenching to compete on an equal basis with radiation in a planetary atmosphere, the pressure of H_2 or D_2 has to be ~1 Torr.

References

(1) V. M. Donnelly, A. P. Baronavski, and J. R. McDonald, Chem. Phys. 43, 271 (1979).
(2) A. Hofzumahaus and F. Stuhl, J. Chem. Phys. 82, 3152 (1985).
(3) R. J. Cody and J. E. Allen, Jr., 16th Int. Symp. on Free Radicals (1983), Lauzelle-Ottignies, Belgium.

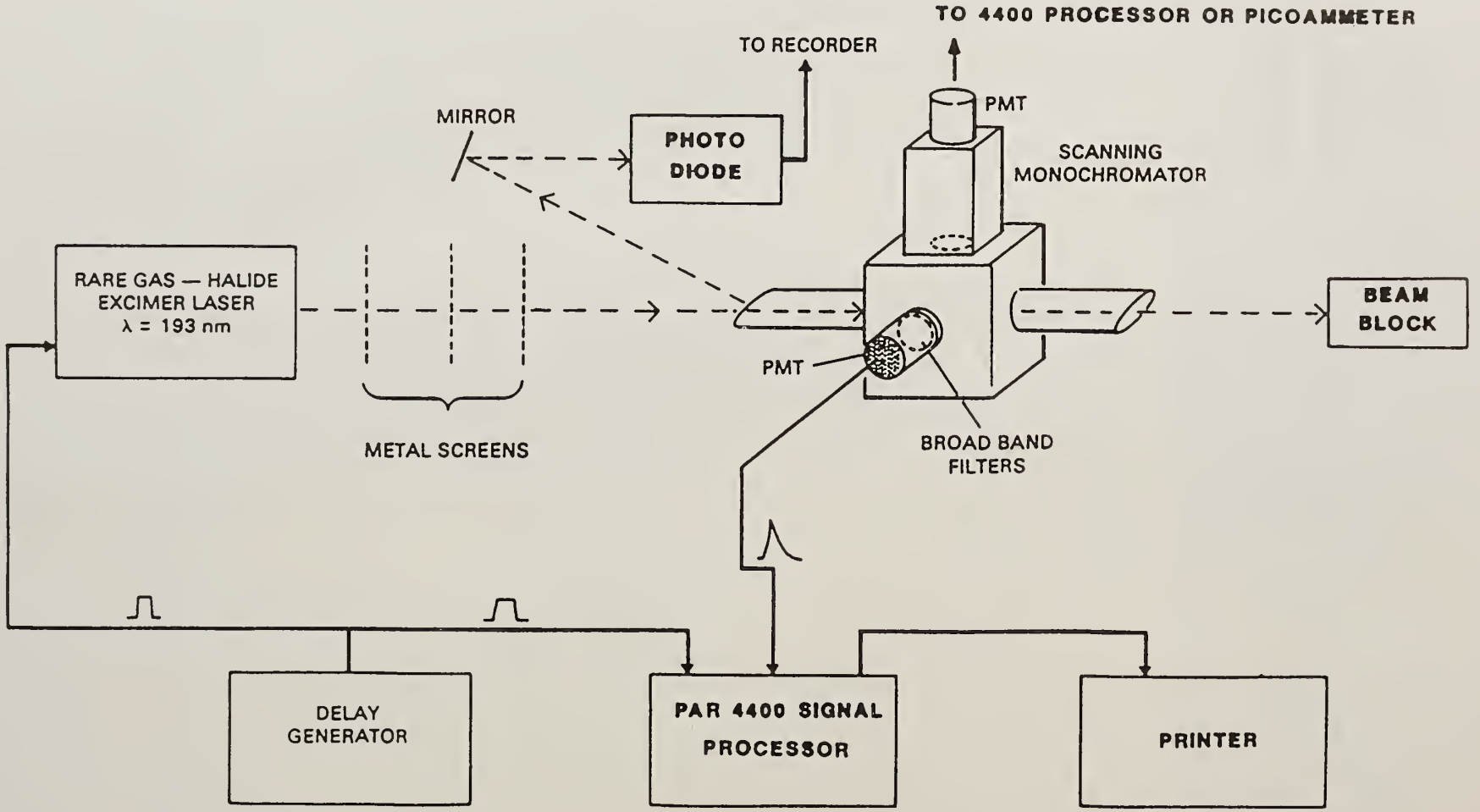

Fig. 1. Diagram of Experimental Apparatus

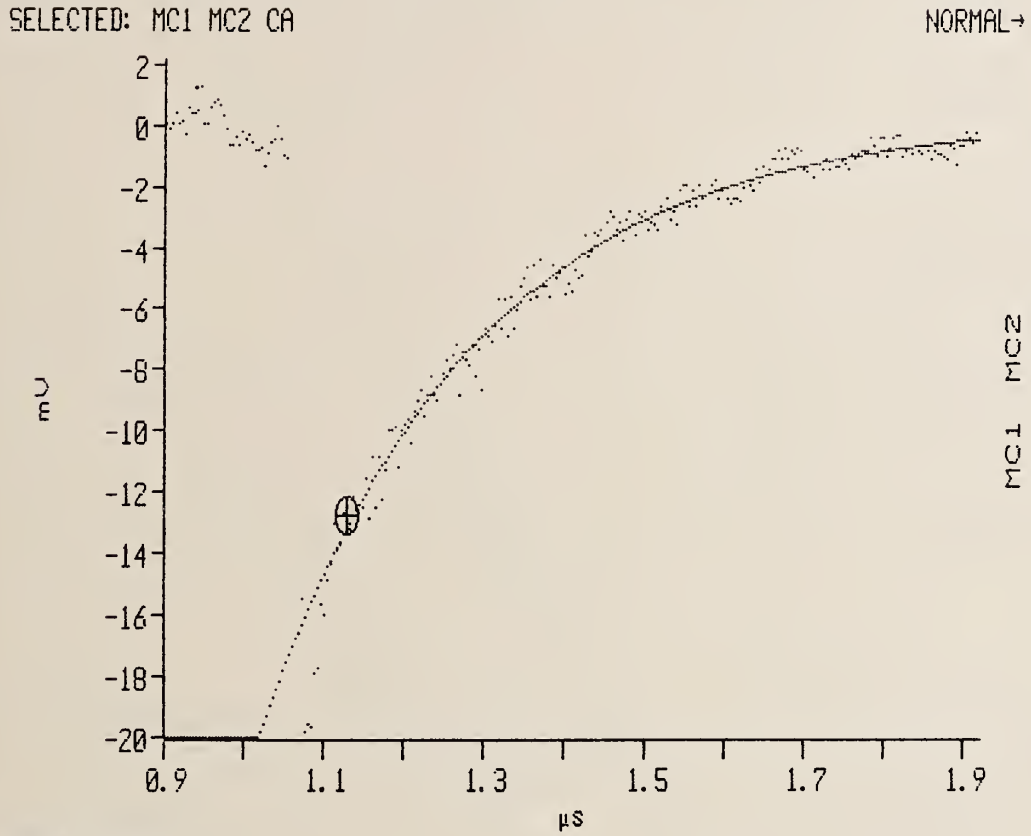

Fig. 2. Experimental NH(A-X) fluorescent decay curve with the exponential curve fit.

$R_1 = \tau^{-1}$ in μs.

$R_3 = \tau$ in ns.

P_{Total} = 800 mTorr of 2.5% NH_3/H_2 gas mixture.

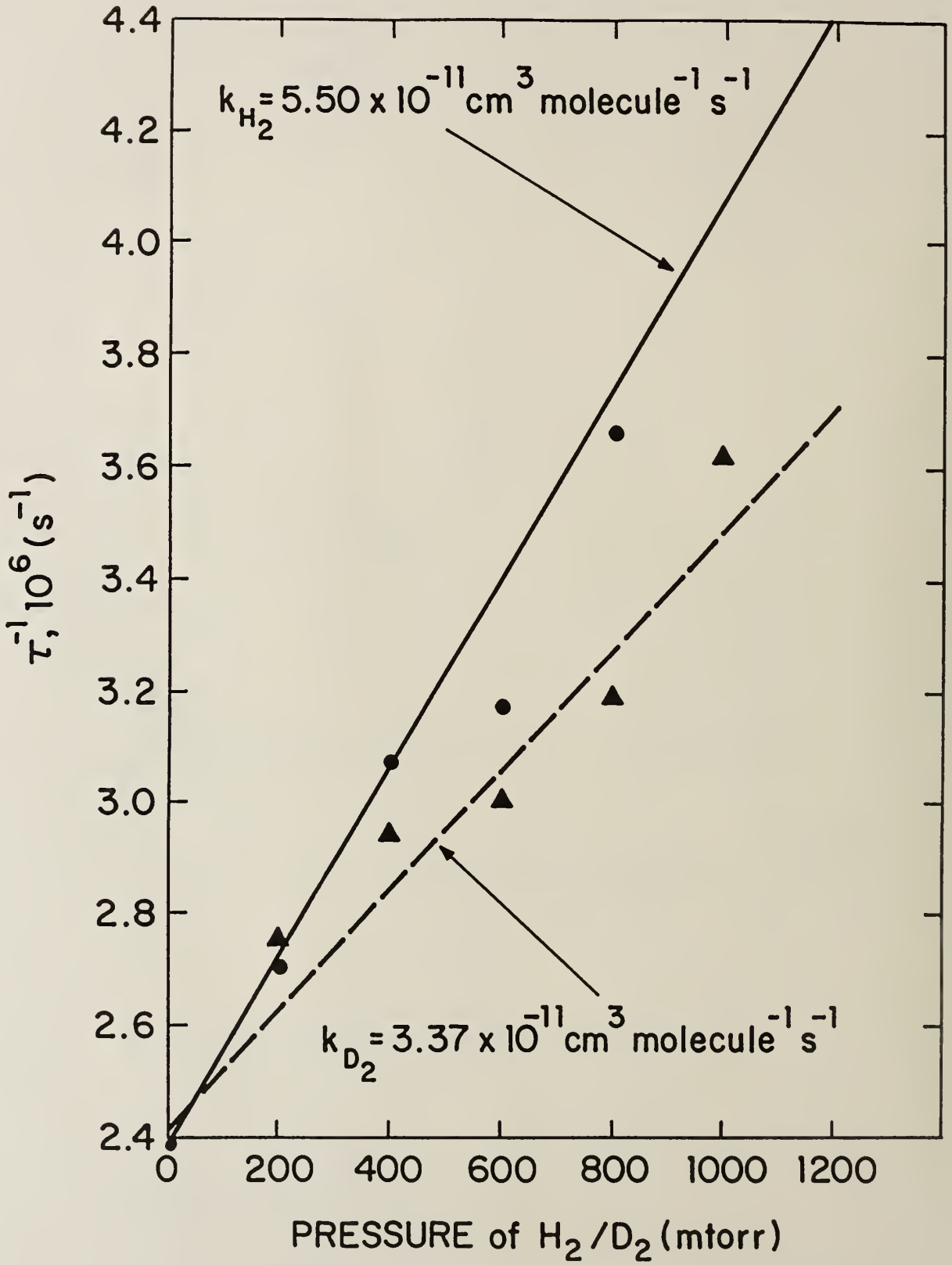

Fig. 3. Quenching plot of the inverse of the fluorescent lifetime, τ^{-1}, versus pressure of H_2 or D_2. ● —— H_2; ▲ ---- D_2.

ROTATIONAL CONTOUR ANALYSIS OF SELECTED VIBRONIC BANDS IN THE VISIBLE ABSORPTION SPECTRUM OF THE BENZYL RADICAL

C. Cossart-Magos[a] and W. Goetz[b]

[a] Laboratoire de Photophysique Moléculaire du C.N.R.S.
Bâtiment 213, Université Paris-Sud - 91405 Orsay Cédex, France

[b] Herzberg Institute of Astrophysics, N.R.C., Ottawa, Ontario K1A 0R6

Abstract

The three most intense vibronic bands in the visible absorption spectrum of benzyl are analyzed by the technique of rotational contour simulation. A', B' and C' values for the rotational constants of each of the three upper levels are obtained and discussed in the light of a previous vibronic analysis. Application of the present determination of rotation constants to the study of rotational contours recently observed in the laser induced fluorescence spectrum of supercooled benzyl is also considered.

Introduction

The visible absorption spectrum of benzyl was recorded for the first time in the gas phase in 1964[(1)]. Some years ago, Cossart-Magos and Leach[(2)] showed that its anomalous structure was due to vibronic interaction between the two first quasi-degenerate excited states assigned[(3)] as 1^2A_2 and 2^2B_2[(4)], in order of increasing energy.

The three bands considered in the present paper are, according to the notation of Ref. 2, A^1, A^2 and $6a_0^1$. They have as common lower level the zero-vibration level of the 1^2B_2 ground state. A^1 and A^2 are type A bands. Their upper levels, of B_2 symmetry, are vibronic mixed levels (mixing of the 2^2B_2 state with b_1 vibration levels of 1^2A_2). $6a_0^1$ is a type B band. Its upper level is an essentially unperturbed level of A_2 symmetry (mode 6a (a_1) is excited with v' = 1 in the 1^2A_2 state). We will show that the different ΔA, ΔB and ΔC values of the rotational constant variations obtained by rotational contour fitting can be related to the different vibronic composition of the upper levels of the three bands.

Experimental

The gas phase absorption spectrum of $C_6H_5CH_2$ was obtained by flash-photolysis of toluene, some years ago, at Ottawa (N.R.C.). The experimental conditions are given elsewhere[5]. The spectrum was photographed on a Eastman-Kodak I-O plate, in the 13th order of a 7.3 m focal length Ebert mount spectrograph at an inverse dispersion of 0.17 Å/mm. Reference spectra were provided by an iron hollow cathode lamp. Recording of band contours was done at Orsay with a double beam microdensitometer.

Band contour simulation results

The essential features of the rotational contours of the three bands presented above, $6a_0^1$, A^2 and A^1, can be observed in the microdensitometer trace given in Fig. 1.

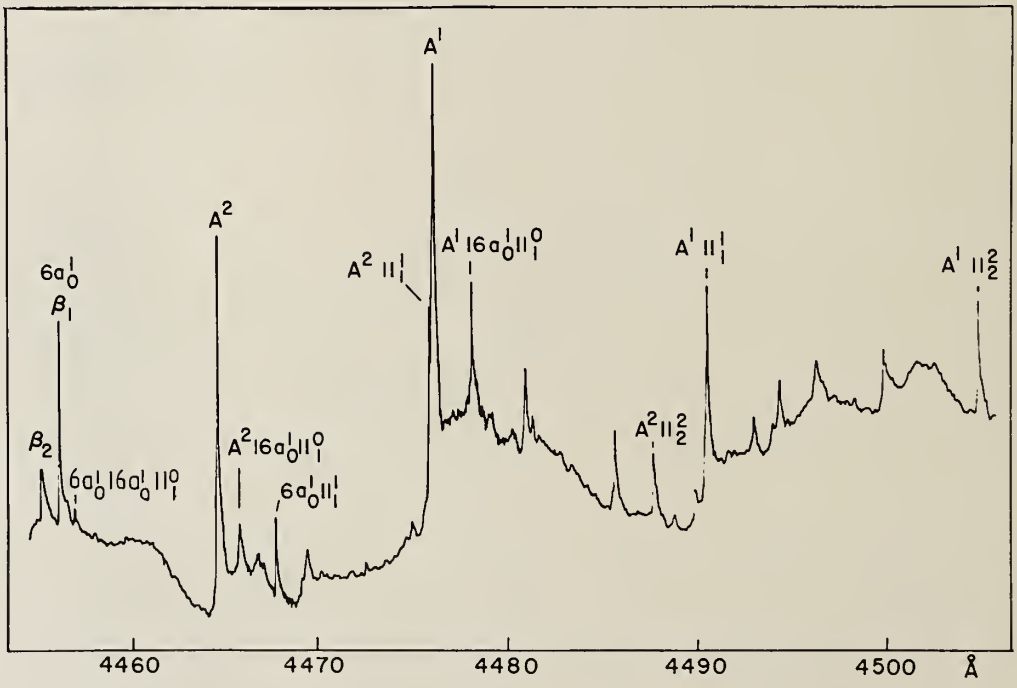

Fig. 1 - Microdensitometer trace of the gas phase absorption spectrum of benzyl between 4450 and 4510 Å.

In the figure are also given some hot band assignments involving two out-of-plane modes 16a (a_2) and 11b (b_2)[6].

It can be seen, in Fig. 1, that the type B, $6a_0^1$ band has a contour with two principal peaks (β_1, β_2) whereas the type A, A^1 and A^2 bands have contours with only one principal peak. The same characteristics were found for other benzyl bands of the same band-types studied at lower resolution in emission[3]. The present absorption spectrum resolution is high enough to allow observation of contour fine structure. As an example, Fig. 2 shows the microdensitometer trace of band A^2 in greater detail and compares it to the final calculated contour obtained with the asymmetric rotor program written by Birss [7].

For a rotational temperature equal to the room temperature 293 K, contours were calculated with $J_{max} = 100$ and $K_{max} = 60$. A triangle line profile with f.w.h.m. = 0.05 cm^{-1} was considered. It corresponds to the slit width used. The Doppler width is smaller, 0.03 cm^{-1}.

Nuclear spin statistical weights 9/7 for K_a even/K_a odd levels were included taking into account the B_2 vibronic symmetry of the initial state.

The rotational constants used for the ground state, given in Table 1, correspond to a particular geometric model defined in Ref. 3 with bond lengths estimated from calculated bond orders.

A"	B"	C"
0.18225	0.09033	0.06040

Table 1 : Benzyl radical ground state constants[3], in cm^{-1}.

Rotational band contours are more critically dependent on the values of the rotational constant variations ΔA, ΔB and ΔC accompanying the vibronic transition. The values corresponding to the best fit of the contour of each band $6a_0^1$, A^2 and A^1 are given in Table 2.

As an application of the present contour analysis results, contours at low temperature can be calculated for the same rotational parameter values and compared to those recently recorded for the laser induced fluorescence of benzyl in a supersonic free jet expansion[8]. As an example, Fig. 3 shows the contours obtained for

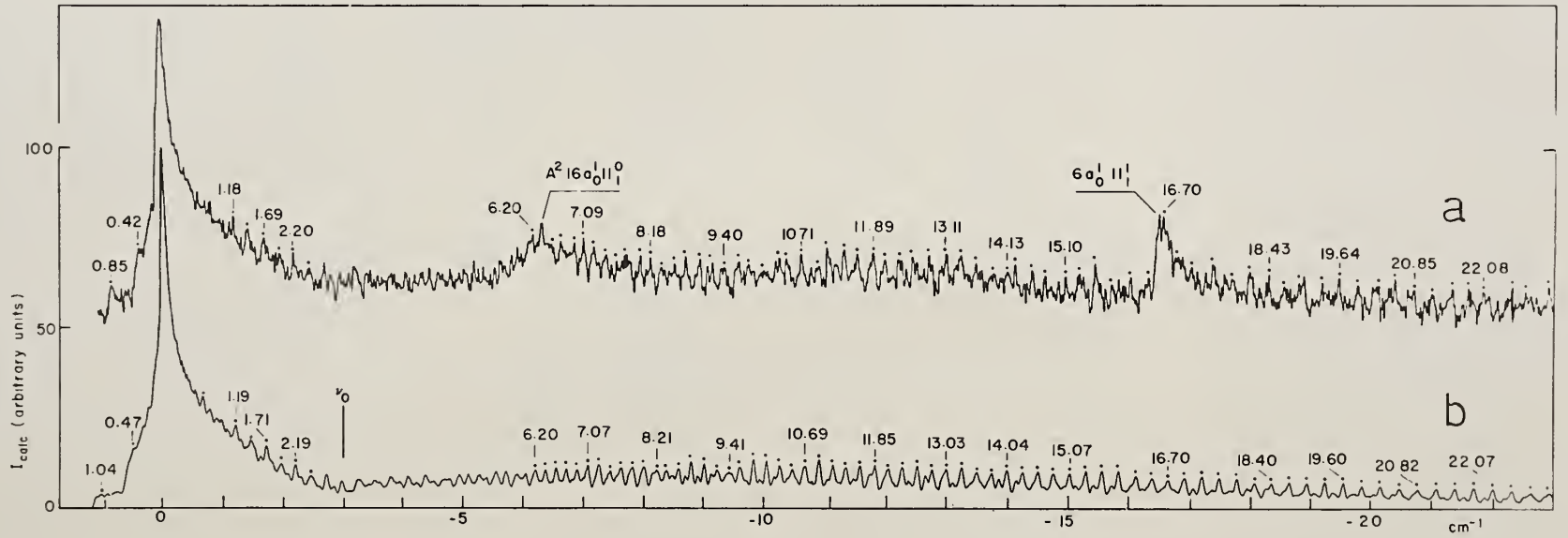

Fig. 2 - Benzyl absorption band A^2 : a) observed and b) calculated contour. Some peak frequencies are given relative to the principal peak observed at 22389.88 cm^{-1} (the complete list is published elsewhere[5]); ν_0 is the calculated vibronic origin at - 3.10 cm^{-1}. Frequencies were not measured in the low intensity region adjacent to the origin.

Table 2 : Benzyl radical rotational constant differences (10^{-4} cm^{-1}) for three bands of the visible absorption spectrum. Uncertainty is on ΔA and ΔB, < 1.0 x 10^{-4} cm^{-1}, on ΔC, < 0.5 x 10^{-4} cm^{-1}.

Band[a]	ΔA	ΔB	ΔC
$6a_0^1$	- 39.3	- 16.5	- 11.5
A^2	- 48.7	- 15.0	- 11.5
A^1	- 49.5	- 15.0	- 12.6

a) Notation of Ref. 2

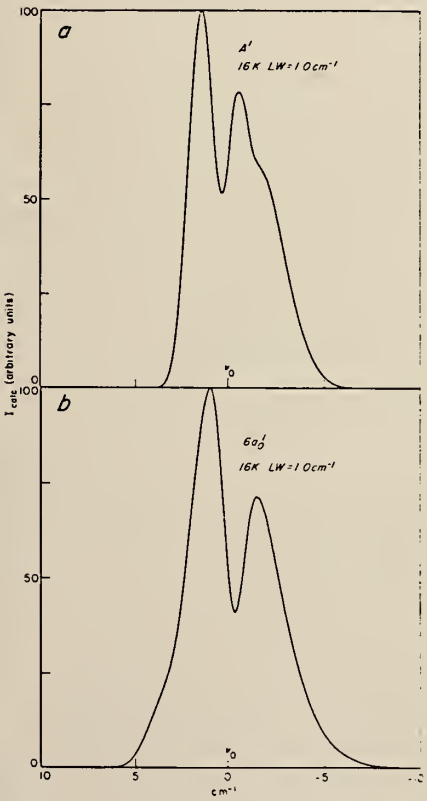

Fig. 3 - Low temperature rotational band contours of benzyl : rotational constants of Tables 1 and 2 for a) the type A band A^1 and b) the type B band $6a_0^1$; LW = 1.0 cm^{-1} and T_R = 16 K.

A^1 and $6a_0^1$ bands with a line width equal to 1.0 cm^{-1} and a rotational temperature of 16 K. These calculated contours approach well the observed doublet contours of the particular bands in the jet cooled benzyl laser induced fluorescence spectrum recently published[8].

Discussion

The question we wish to answer here is the following : do the rotational constants of the different vibronic levels considered reflect the different degree of 1^2A_2 and 2^2B_2 state mixing assigned to them according to the analysis of Ref. 2 ? The answer is positive for constant A, less clearly so for B and C.

In fact, one sees in Table 2, that the A^1 and A^2 upper levels (where there is mixing of 1^2A_2 and 2^2B_2 states[2]) have rotational constants A and B closer to each other than to the $6a^1$ level (which is an essentially unperturbed level of 1^2A_2[2]). No distinction among the levels can be made on the basis of ΔC values. It is also to be noted that the ΔA and ΔB values for the $6a_0^1$ band are closer to the values of these parameters obtained[3] at lower resolution for the emission bands 0_0^0, $6a_1^0$ and $6b_1^0$: -44_0, $-17_5 \times 10^{-4}$ cm^{-1} respectively. Again $\Delta C = -12_7 \times 10^{-4}$ cm^{-1} does not follow the same trend as the other two constants.

In order to confirm that ΔA and ΔB values for A^1 and A^2 levels indeed reflect mixing of the second excited state, 2^2B_2, into the first, 1^2A_2, (as compared to the upper levels of $6a_0^1$ or the emission bands, where there is no such mixing), one can compare our experimental values of ΔA and ΔB (and ΔC) with those calculated for pure 1^2A_2 and 2^2B_2 states, assuming reasonable geometrical models. The values given in Table 3 correspond to models in which the bond

Electronic Transition	ΔA	ΔB	ΔC
$1^2A_2 - 1^2B_2$	- 36	- 10	- 9
$2^2B_2 - 1^2B_2$	- 76	- 7	- 12

Table 3 : Benzyl radical rotational constant differences (10^{-4} cm^{-1}) corresponding to the calculated bond orders[3] of the electronic states of the two transitions in the visible.

lengths were obtained from a bond length-bond order relation and the bond angles those defined in model I, I' of Fig. 6 in Ref. 3.

One sees that the experimental ΔA value increases from $6a_0^1$ to A^1 and A^2 (cf. Table 2) in the same direction as the calculated ΔA value in going from the pure $1^2A_2 - 1^2B_2$ to the pure $2^2B_2 - 1^2B_2$ transitions, cf. Table 3. Similar sign agreement pertains for ΔB ; for ΔC, the expected behaviour is clearly found only for $6a_0^1 \rightarrow A^1$. It should be noted that to the rotational constants obtained for A^2 corresponds a slightly too great negative inertial defect $\Delta' = -0.3$ u.m.a. $\mathring{A}^2$ ($\Delta' = -0.2$ (A^1) : -0.1 ($6a_0^1$)[5]) which may reflect the existence of interactions, such as 2nd order Coriolis, neglected in the present analysis.

Conclusion

Three particular bands of the benzyl absorption spectrum were studied by the rotational contour simulation technique.

The rotational constants obtained are shown to be compatible with the results of a previous vibronic analysis of the same spectral region[2].

The three bands considered are those of highest intensity in the room temperature absorption spectrum and are the only bands observed in the jet cooled laser induced fluorescence recently recorded[8]. Transfer of the values of the rotational constants determined at high temperatures to the study of the low temperature observed contours, enables one to investigate the other parameters on which the latter depend, in particular, the rotational temperature of the jet.

References

1) G. Porter and R. Ward, J. Chim. Phys. 61, 1517 (1964).

2) C. Cossart-Magos and S. Leach, J. Chem. Phys. 64, 4006 (1976).

3) C. Cossart-Magos and S. Leach, J. Chem. Phys. 56, 1534 (1972).

4) x, y and z axes are chosen as in most previous work on benzyl, with the x axis in the molecular plane ; if x and y axes are interchanged, in accordance with Mulliken's recommendations (J. Chem. Phys. 23, 1997 (1955)), the B_1 and B_2 representations are interchanged.

5) C. Cossart-Magos and W. Goetz, to be published.

6) C. Cossart-Magos, Thèse d'Etat, Université Paris-Sud (1973).

7) F.W. Birss, J.M. Brown, A.R.H. Cole, A. Lofthus, S.L.N.G. Krishnamachari, G.A. Osborne, J. Paldus, D.A. Ramsay and L. Watmann, Can. J. Phys. 48, 1230 (1970).

8) M. Heaven, L. DiMauro and T.A. Miller, Chem. Phys. Lett. 95, 347 (1983).

IMPLANTED MUON STUDIES OF ORGANIC FREE RADICALS AND MOLECULAR RADICAL MODELS FOR THE MUONIUM CENTRES IN SEMICONDUCTORS

S F J Cox

Rutherford Appleton Laboratory, Oxfordshire OX11 0QX, UK

Abstract

Thermalised or near-thermalised positive muons will stick to lone pairs of electrons, reduce multiple bonds to form carbocations, or act as electron acceptors. The resultant cationic or atomic states can be the precursors to free radical products in which muonium, the light isotope of hydrogen, is incorporated in the molecule. The spectroscopic technique known as μSR, used to study these species is described, and its use in structural and dynamical studies of organic radicals is illustrated by examples from the μSR literature.

The reported spectroscopic studies of muonium-related paramagnetic centres in silicon, germanium and diamond are summarised. No microscopic model for the nature of these centres, ie their chemical and electronic states, has yet been substantiated. New molecular radical models are presented which appear to accommodate the experimental findings satisfactorily.

1. IMPLANTED MUON SPECTROSCOPY

Positive muons are short-lived elementary particles which, when implanted in gases, liquids or solids, play the role of lightweight protons. They have the same charge and spin as protons but only about one-tenth the mass. Like protons, muons are too reactive to remain as "bare" particles when thermalised in a medium but react rapidly at a diffusion limited rate. They will add to molecules of even weak basicity, "sticking" to lone pairs of electrons on polar molecules, for example. They will also accept and bind single excess electrons to form hydrogen-like atoms known as muonium, $Mu^{\bullet} = \mu^{+}e^{-}$, which is stable in sufficiently inert media. Atomic muonium has essentially the same Bohr radius and ionisation potential - the same size and binding energy - as atomic hydrogen. Chemically it is a genuine light isotope of hydrogen. So it is fascinating to explore the physical and chemical consequences of replacing hydrogen by muonium in molecules. Both the muonic cations and atomic muonium, whichever is formed initially, may subsequently react with solvent or solute to form a variety of species. I like to call these muonated (as opposed to deuterated or tritiated) molecules. The unprecedented mass ratio, Mu:H $\simeq$ 1:10, makes muonation a far more sensitive probe of molecular structure and dynamics than the more

common isotopic substitutions, with the lighter particle facilitating observation of specifically quantum dynamical effects.

Muonium is also a radioactive isotope of hydrogen. The muon decays with a lifetime of ca $2\mu s$, which is to be contrasted with the very much longer lifetime of tritium, and which defines the timescale of the dynamical and chemical processes which may be probed by muonation. It is the nature of this radioactive decay which enables the labelled molecules to be studied. This allows the evolution of the muon spin polarisation to be monitored,[1] rather as in magnetic resonance methods. The experimental technique is known as muon spin rotation, or μSR, and is illustrated in Figure 1.

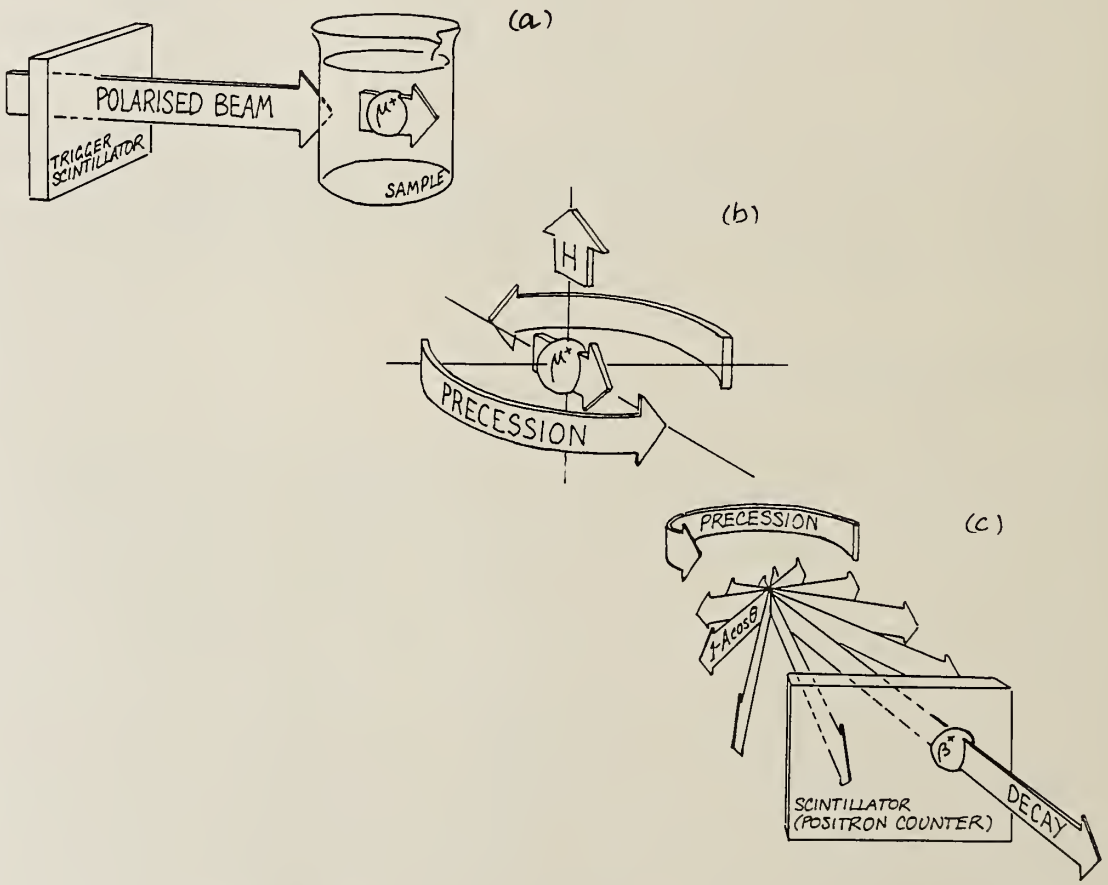

Figure 1. The μSR method. Implantation (a), Larmor precession (b) and radioactive decay (with detection of the emitted positron) (c) of spin-polarised muons. The polar diagram for the probability of positron emission rotates with the muon polarisation (just as that for γ-ray emission does in Perturbed Angular Correlation experiments).

In (a) the implantation of muons with a defined initial polarisation is depicted in a (liquid) sample. Polarised muon beams suitable for this

purpose are available at certain accelerator laboratories, notably at the so-called meson factories. In (b) the muon spins are shown precessing at their Larmor frequency in any transverse field they experience, be it applied externally or generated internally in the sample. The magnetic moment of the muon is about three times that of the proton, so that μSR frequencies are higher than the corresponding proton NMR frequencies by the same factor. In (c) the muon is shown indicating the orientation of its spin at the instant of its decay, by emitting the decay positron preferentially in that direction. This is a very fortunate consequence of parity violation in the radioactive decay process: it allows the muon precession to be displayed.[2] For a bunch of muons implanted at time zero, one can almost imagine a somewhat diffuse light-house beam of positrons shining out of the sample, sweeping around and periodically illuminating the detector.

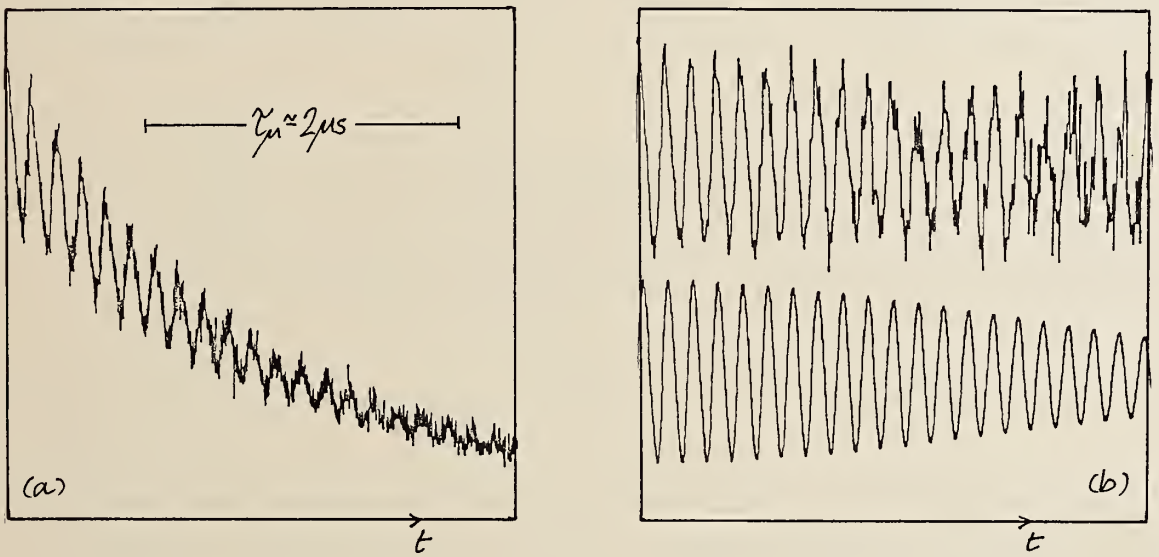

Figure 2. Positron countrate, ie number of counts as a function of muon lifetime inside the sample (a), and the extracted precession signal (b) (upper trace). The lower trace in (b) is an online computer fit, yielding precession frequency (here 6.5 MHz, appropriate to an applied field of 500 Gauss) and relaxation function. Notice the resemblance to Free Induction Decay signals obtained in NMR experiments following a 90^{o} pulse.

The positron countrate therefore shows this precession signal, but attenuated by the muon radioactive decay curve, as in the raw data of Figure 2(a). Compensation for the muon lifetime reveals the signal of interest (Figure 2b), which is exactly analogous to a Free Induction Decay obtained by pulsed NMR. Except that in μSR no rf fields are involved: the muons are implanted in a non-stationary state and the detection of their

precession benefits hugely in sensitivity from the "nuclear techniques" of single particle counting. This is "radioactively detected" magnetic resonance. This example emphasizes the analogy with proton NMR and is appropriate to muons in a diamagnetic environment. Such an environment may be a molecular cation or a neutral molecule, as is illustrated in the probable reaction sequence for muons implanted in water (1,2).[3]

$$\mu^+ + H_2O \rightarrow H_2OMu^+ \quad (1)$$

$$H_2OMu^+ + H_2O \rightleftharpoons H_3O^+ + MuOH \quad (2)$$

(I like to call this last species "light water"!).

Atomic muonium, Mu•, is also observed in the μSR spectrum of water, as in many inert solvents and insulating solids. (It is stable on the microsecond timescale which is characteristic of μSR, though in the presence of reactive solute a damping of the signal can indicate chemical reaction). The notation used here is as follows: Mu denotes muonium which is covalently bonded in a molecule. A dot emphasises the presence of an unpaired electron spin, as here in atomic muonium Mu•, and below in the molecular radicals, $\dot{Mu}S$. The symbol μ^+ is reserved for the incoming bare particle (possibly with some residual kinetic energy) and is to be distinguished from Mu^+ which, like H^+, denotes some cationic association of the thermalised particle.

In the paramagnetic species, the muon-electron hyperfine coupling generates other components in the μSR precession signal (typically at much higher frequencies than the single-component precession of Figure 2), so these are easily recognised. Figure 3 shows a frequency-domain spectrum which is typical of a radical, here the muonated phenyl ethyl radical, $Ph\dot{C}H.CH_2Mu$ observed in μSR studies of styrene.[4] The two characteristic lines correspond esssentially to flips of the muon spin alone (Figure 3b), the applied field here being high enough to decouple electronic and nuclear spins. The analogy is now with an ENDOR spectrum.[5] This spectrum was recorded in a liquid sample, so that the muon-electron hyperfine coupling is effectively isotropic, of the form $A\underline{I}.\underline{S}$. The hyperfine field at the muon reinforces or opposes the applied field according as the muon spin $\underline{I}$ and electron spin $\underline{S}$ are parallel or antiparallel, so that the coupling constant A may be measured directly and accurately from the two μSR frequencies.

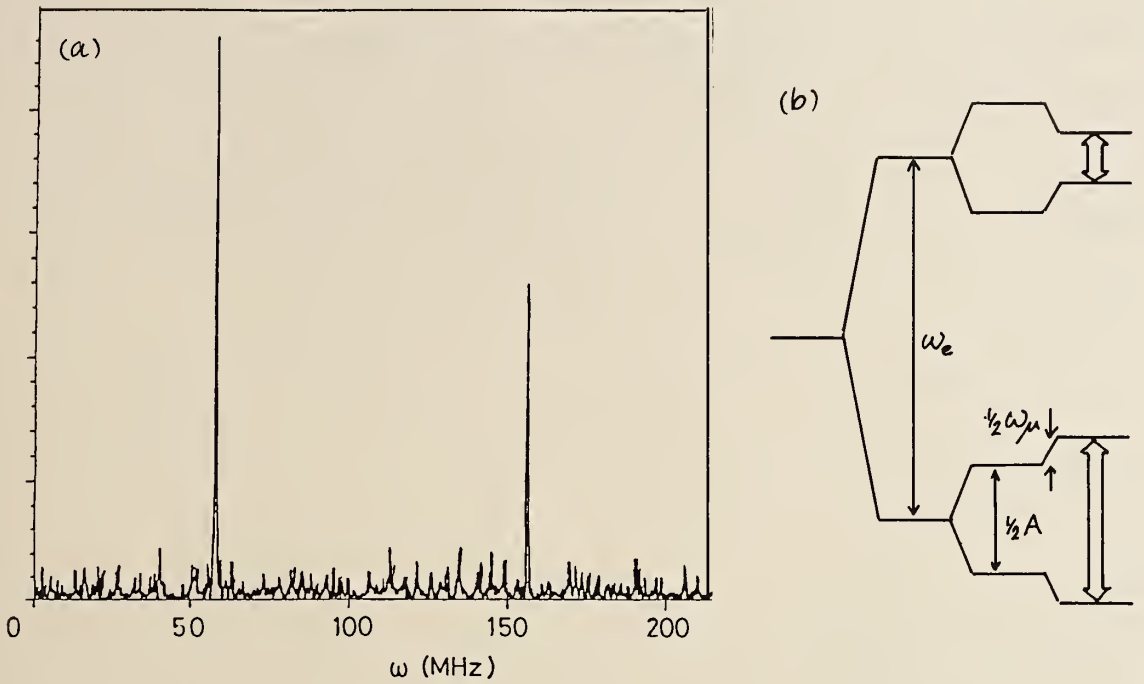

Figure 3. A typical 2-line μSR spectrum of a muonated radical (a) and its interpretation (b), illustrating the analogy with ENDOR spectra. A is the muon-electron hyperfine coupling constant. This spectrum is of the radical $\dot{C}HPh.CH_2Mu$ generated by muon implantation in styrene, (recorded at room temperature in 3kG).

2. DYNAMICAL STUDIES OF ORGANIC RADICALS

This measured coupling is a very sensitive source of information on the structure and dynamics of the radicals. Figure 4 illustrates this for the phenyl ethyl radical. Here the methyl group is shown muonated. The coupling represents hyperconjugation between the C-Mu σ-bond and the singly occupied orbital on the β-carbon atom, which has dominant p_z character. The coupling is maximum when the methyl group is oriented so that the muon eclipses this orbital ($\theta = 90^\circ$, Figure 4b). It is close to zero in the perpendicular configuration ($\theta = 0$) with the muon lying in the plane of the $-\dot{C}HPh$ moiety, ie the nodal plane of the p_z orbital. An angular dependence (3) is expected:

$$A(\theta) = A_o + B\cos^2\theta \qquad (3)$$

An unsubstituted methyl group $-CH_3$ is free to rotate in such a molecule, yielding an angular average for the methyl proton coupling given by equation (4).

$$A_H = A_o + B\langle\cos^2\theta\rangle = A_o + \tfrac{1}{2}B \qquad (4)$$

Substitution of a methyl proton destroys the symmetry of the rotor, however, and the methyl muon in $-CH_2Mu$ adopts a preferred orientation, executing small torsional oscillations only about $\theta = 90^o$. Its angular average, given by equation (5), is therefore somewhat greater, $A_{Mu} > A_H$ (by about 20% at room temperature). That is, there is a dynamic isotope effect in the hyperfine coupling.[6]

$$A_{Mu} = A_o + B\langle\cos^2\theta\rangle_{Mu} \qquad (5)$$

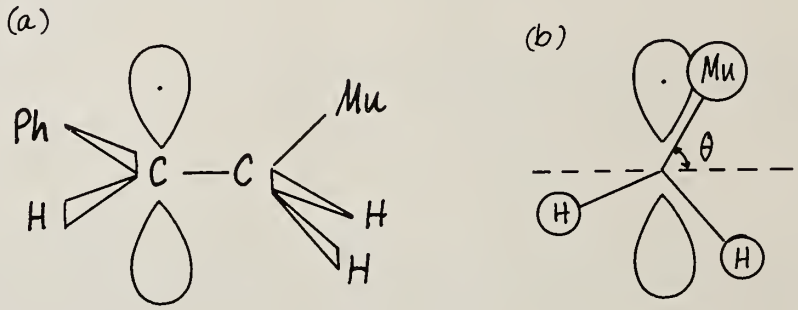

Figure 4. Structure of the phenyl-ethyl radical (a) indicating the singly occupied p_z orbital, perpendicular to the plane of the PhHC moiety. The (muonated) methyl group has some rotational freedom about the C-C bond (viewed along this bond in (b)) but adopts a preferred orientation, $\theta = 90^o$.

The preferred orientation of isotopically substituted methyl groups is of especial interest. Since the substituted group is no longer a symmetric rotor (ie it wobbles as it rotates - the inertial axis is no longer the geometrical axis), the effect must be at least partially dynamic in origin. Thus in diamagnetic molecules of similar structure, studied by Raman spectroscopy, a similar effect has been adequately interpreted in terms of a coupling between the rotational mode and the stretching modes of the methyl C-H bonds.[7] In the present case a coupling to the inversion (or "flapping" mode) of the planar moiety CHPh may also be significant.

It is often possible to simulate such dynamical couplings in terms of a static barrier to rotation, or equivalently, in terms of pairwise interactions between the methyl protons, deuterons or muons and the other atoms of the molecule. In this vein, the perpendicular orientation adopted by the muon has been ascribed to steric hindrance, the muon effectively occupying more volume in space, ie being "bulkier" than the proton, by

virtue of its greater zero point motion.[6] Predictions based solely on this interpretation fail in certain instances, however. Symons argues strongly that control of the orientation via σ-π hyperconjugation, ie via electron release from the methyl σ-bonds into, in this case, the singly occupied p_z orbital on the remote carbon atom, is particularly important in the paramagnetic species.[8] Electron release from the C-Mu bond will be more facile than from the C-H bonds, the C-Mu σ-bond being slightly longer and weaker. This is the more important consequence of the muons' greater zero point energy (and the anharmonicity of the electronic potential); it enhances the bonding character of the singly occupied molecular orbital. This stabilises the perpendicular configuration and, by the same token, increases spin-density on the muon. A distinct contribution of this sort to the isotope effect has not yet been generally acknowledged, however.

3. RADICAL REACTIONS

If the muonated radicals react chemically on a microsecond timescale, this will constitute a lifetime broadening of their spectral lines. There are other possible sources of line broadening but the dominant mechanism can often be identified systematically.[4] Thus from the temperature dependence of the linewidth in figure 3, which shows an unmistakable Arrhenius variation, it was possible to determine the rate constant for reaction (6). This is the encounter of radical with monomer to form dimer: in this example muon "labelling" allows a particularly direct measurement of the initial rate of polymerisation, en route to polystyrene.

$$Ph.HC{=}CH_2 + Ph.HC{-}CH_2Mu \rightarrow Ph.H\dot{C}{-}CH_2{-}CHPh{-}CH_2Mu \qquad (6)$$

In studies of this sort the product is not itself visible in the μSR spectrum, phase coherence being lost with respect to the incoming muon. Neither is the radical precursor directly visible, though its nature may sometimes be deduced from the initial phase of the observed precession signal. This is exploited in the following section.

4. RADICAL FORMATION MECHANISM

The muonated phenyl ethyl radical, depicted in Figures 3 and 4, is derived from the host molecules of styrene following implantation of positive muons (7):

$$Ph.HC{=}CH_2 \rightarrow Ph.HC{-}CH_2Mu \qquad (7)$$

Indeed, all the muonated organic radicals which have been identified to date are similarly formed by the reduction of multiple bonds in unsaturated materials. There is now an extensive world catalogue of such radicals.[9,10,12] Other archetypal examples are given below (8-1) (here the carbon atom which becomes saturated in the process is designated *):

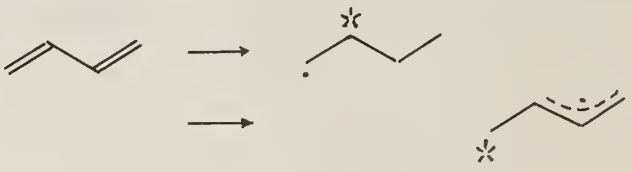

(8a)[12]

(8b)[12]

(9)[4,10,13,14]

(10)[15]

The singly occupied molecular orbital is increasingly delocalised by conjugation in examples 8b-10. (Note that in trans-polyacetylene it is also mobile, the bond-alternation defect or "soliton" being free to migrate along the chain).[15] Reduction of a carbon-carbon triple bond has also been demonstrated in one particular substance, phenyl acetylene (11).[16]

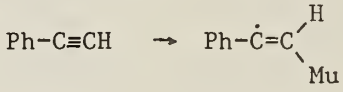

(11)

(12)

Likewise addition to the carbonyl bond (12) is known, forming the radical $(CH_3)_2\dot{C}$-OMu from acetone, for example.[10,13,17] In this case π-conjugation between carbon and oxygen gives substantial spin density which is α to the muon, and a corresponding negative contribution to the hyperfine coupling. Marked sensitivity to temperature and solvent effects result.[17] Very recent preliminary results indicate the formation of new muonated radicals from molecules of the formate, acetate, and formamide families.[18]

In every case, one muon and one electron have been added to the host molecule. Formally, therefore, the radicals are muonium adducts. It was originally thought that muonium formation, followed by an addition reaction, was the only route to radical production (13), indeed that muonium was the sole and unique precursor to all muonated species.[19] (This raises the question of how muonium itself is formed following the

implantation of energetic muons in a material, which is a matter of some controversy in the μSR literature.[20] Alternative routes to radical production (14-17) are depicted in Figure 5. These, (together with the muonium formation question) are considered in detail elsewhere[21] but may be summarised as follows:

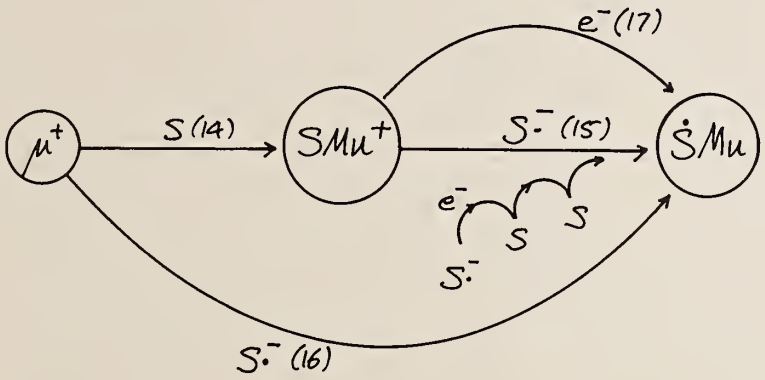

Figure 5. Ionic mechanisms of radical production (illustrating reactions 14 - 17).

$$S + Mu^{\bullet} \rightarrow \dot{S}Mu \quad (13)$$

$$S + \mu^{+} \rightarrow SMu^{+} \quad (14)$$

$$SMu^{+} + S^{\bullet -} \rightarrow \dot{S}Mu + S \quad (15)$$

$$\mu^{+} + S^{\bullet -} \rightarrow \dot{S}Mu \quad (16)$$

$$SMu^{+} + e^{-} \rightarrow \dot{S}Mu \quad (17)$$

Here S denotes a solvent or reactive solute molecule, and the scheme assumes the radiolytic production of excess electrons by the initially energetic muon (and also by secondary electron ejection). The majority of these electrons will return to their twin radical cations $S^{\bullet +}$, but some will solvate, or be trapped by individual solvent molecules as radical anions. Both species are denoted $S^{\bullet -}$. Figure 5 gives central importance to direct fixation (14) of the thermalised or near-thermalised muons, forming SMu^{+} carbocations, or similar species, in unsaturated material.[4,21,22] This is expected to be the radical precursor stage in basic hosts S (even if they are only weakly basic, in view of the high reactivity of the bare μ^{+} ion). Subsequent neutralisation by encounter with a radical anion, $S^{\bullet -}$, then yields the radical $\dot{S}Mu$ *via* reaction (15). Competitive parallel channels (16,17) may be favoured depending on the relative affinities of the host for electrons and protons (muons). A hopping transfer of the electron (or even of the muon) will in some circumstances enhance the effective mobilities of the ionic species and so facilitate their combination.

Such an ionic mechanism has been identified in styrene,[4] and found to contribute to radical production in acetone.[17,23] In solutions of benzene and of dimethyl butadiene, on the other hand, muonium addition is favoured.[23,24] The different behaviours of these materials can be reconciled with chemical expectations in terms of a more general scheme.[21] The exploitation of the angular phase of the μSR precession signal to distinguish diamagnetic and paramagnetic precursors[4] seems likely to become a standard diagnostic test. Likewise the use of additives to remove excess electrons by dissociative capture, or even to trap muonium atoms, is an invaluable diagnostic method.[23-26]

It is noteworthy that no muonated inorganic radicals have been reported to date in liquid hosts or in molecular materials. Direct muonium addition to P,Si or S, for instance, might be expected, yielding radicals in which the muon is α to the magnetic atom[8] (the additional valence of these atoms, in a higher row of the Periodic Table than carbon, should accommodate the extra electron). But in a radical search in phosphites, for example, only short-lived muonium was seen, indicating that the addition reaction is probably too slow for μSR detection of the product.[18]

The paramagnetic centres observed in certain crystalline solids, notably the elemental semiconductors, have all the character of molecular radicals, however, some of them with α-muon character. These centres are the subject of the final section.

5. MUONIUM-CENTRES IN THE DIAMOND-TYPE LATTICE

It is safe to conclude that for muonated organic radicals, the site of the muon within the molecule can be identified with certainty, the conformation and dynamics of the molecule may often be elucidated by μSR studies, and the electronic structure, the nature of the singly occupied molecular orbital and the origin of the muon-electron hyperfine coupling, are all reasonably well understood.

The same can hardly be said of the paramagnetic centres discovered by μSR in silicon, germanium and in diamond. No hydrogen centres are known to ESR studies in these materials, so the observation of muonium-related centres is especially interesting, and a real scoop for μSR spectroscopy. Yet these centres have also provided the subject with its most long-standing puzzle. The muon site or sites within the diamond-type lattice, the local

electronic structure, and the energy of these states (with respect to the valence and conduction bands - presumably they are somewhere in the gap), all remain unknown to date. Or at least unconfirmed. Even the models proposed below are conjectural, but they appear to be the first which satisfactorily accommodate the experimental findings. These findings are reviewed by Patterson,[27] for instance, and may be summarised as follows:-

Similar observations are made in Si, Ge and diamond. Two distinct paramagnetic centres are observed in each material, denoted Mu and Mu*. The muon-electron hyperfine coupling is isotropic for Mu, which appears to be mobile down to very low temperatures. This coupling is only ca 50% of the free muonium, or vacuum-state value, in Si and Ge however, and only 85% in diamond. For Mu*, the coupling is smaller again and highly anisotropic, with axial symmetry along the <111> directions. These are the X-X bond directions (X = C,Si or Ge). Spectra appropriate to Mu* from the three orthogonal <111> directions are observed, so Mu* is localised and immobile in the lattice. Mu and Mu* are observed simultaneously in μSR spectra, ie both are formed promptly on implantation of the muons, but some thermally activated conversion of Mu to Mu* can also be demonstrated. Mu* is therefore the more stable state.

Mu* is known as "anomalous muonium" and Mu, by default, as "normal muonium". But hyperfine couplings as low as 50% of the vacuum-state value are anything but normal, and indicate a substantial delocalisation of spin density. For comparison, normal muonium in quartz (a particularly inert medium with large interstitial cavities) has a coupling closely equal to the vacuum-state value, and when atomic hydrogen is trapped in a tight lattice, its hyperfine constant tends to be increased rather than decreased. Accordingly, couplings greater than 100% are found for H and Mu in the alkali fluorides.[28] The characteristics of Mu*, especially, may be taken as indicative of a molecular radical. And even Mu cannot retain hydrogenic character with so low a coupling, despite its apparently spherical symmetry. Perhaps this centre should be given a new name, such as Mu', to distinguish it from the free atom.[29]

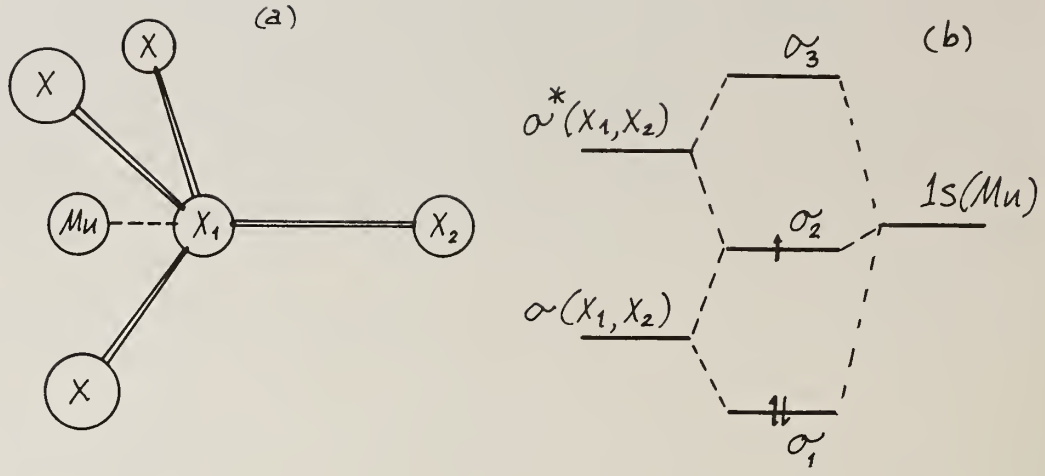

Figure 6. Structure A for the Mu' centre (a), and a qualitative level diagram (b) indicating the interaction of the σ and σ^* orbitals for the stretched bond X_1-X_2 with muonium. The singly occupied molecular orbital retains some hydrogenic character.

Figure 6 depicts a new model for Mu' [29] in which the muon and electron are localised by association with a particular X-X bond (X=C,Si or Ge). This entity (Structure A) is to be seen as intermediate between the limiting valence bond structures Mu̇...X-X and Mu-X...Ẋ, ie the product of a chemical reaction (18).

$$\text{Mu}\cdot + \text{X-X} \longrightarrow \text{Mu'...X...X} \qquad (18)$$

Evidence for such a tendency is given by reaction (19) which is known to occur in silicon chemistry.[30]

$$\text{H}\cdot + (\text{CH}_3)_3\text{Si-Si}(\text{CH}_3)_3 \longrightarrow (\text{CH}_3)_3\text{SiH} + \dot{\text{S}}\text{i}(\text{CH}_3)_3 \qquad (19)$$

Whereas (19) can proceed to completion, however, (18) is limited to structure A by coordination with the surrounding lattice. This constraint is most severe in diamond, and reaction (18) stops with only ca 15% transfer of spin density; ca 50% transfer is achieved in the softer semiconductors.

To account for the observed isotropy of the hyperfine coupling in Mu', a sufficiently rapid tunnelling between equivalent sites may be invoked. Local tunnelling between the crystallographically equivalent sites surrounding the centre of the "tetragonal interstice" is one possibility

(ie within a particular "cage" of host atoms). In a preliminary experiment,[18] no evidence of coupling to the naturally abundant ^{29}Si nuclei could be detected in the low-field spectrum of Mu', however. This negative result indicates that the ^{29}Si hyperfine coupling is motionally averaged to a low value and may be taken as confirming the long-range mobility of Mu'.

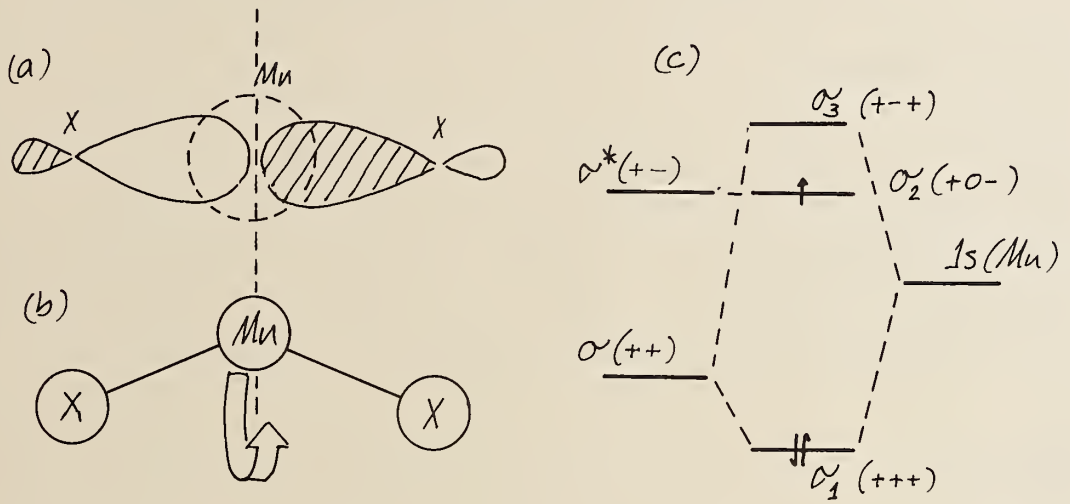

Figure 7. Structure B for Mu*, with the muon inserted at the centre of anelongated X-X bond (a), or off-axis (b), in both cases at the nodal plane of the σ^* orbital. In (b) rotation or rotational tunnelling maintains axial magnetic symmetry. The qualitative level diagram (c) indicates the interaction of the stretched X-X bond with muonium. In this geometry the singly occupied molecular orbital is non-bonding (contrast Figure 6).

Figure 7 depicts a model for Mu* due to Symons,[8] in which the muon is inserted at a bond centre, ie in the nodal plane of the σ^* orbital (Structure B). This is substantiated by a semiquantitative analysis of the coupling constants,[29] which reveals a negative isotropic component and an anisotropic component with point dipole character. Spin density on the muon is therefore zero, and the isotropic coupling originates in spin-polarisation of the bonding electrons. (For C, it happens to be exactly equal to the α proton coupling in the methyl radical). The effective muon-electron separation estimated from the dipolar coupling is unprecedentedly small, however. The structure B of Figure 7 is perhaps the only geometry which can satisfy such stringent requirements.

For muonium initially localised in structure A a certain activation energy will be required to reach the more stable structure B. This explains how

Mu' may be thermally converted to Mu* at sufficiently high temperatures. It remains to account for the simultaneous observation of Mu and Mu* in the μSR spectra, ie for the prompt formation of Mu*. Presumably the activation energy may also be provided by the residual kinetic energy of the muon itself. This would be the first clear indication of muonic radical formation by any such epithermal reaction.

ACKNOWLEDGEMENTS

I wish to acknowledge my collaboration with Martyn C R Symons, Emil Roduner, Christopher A Scott, David A Geeson, Alyson Hill and Roberto De Renzi for the organic radical studies, also discussions with Bruce F Patterson and Tom L Estle of their spectroscopic studies of Mu' and Mu*, and discussions with Paul W Percival of radiolysis aspects.

REFERENCES

1 J H Brewer, K M Crowe, F N Gygax and A Schenck in Muon Physics III, eds V W Hughes and C S Wu, Academic Press (1975) p3.

2 R L Garwin, L M Lederman and W Weinrich. Phys Rev 105 (1957) 1415.

3 P W Percival, E Roduner and H Fischer. Chemical Physics 32 (1978) 353-67.

4 S F J Cox, A Hill and R De Renzi. J Chem Soc. Faraday Trans 1, 78 (1982) 2975.

5 E Roduner and H Fischer. Chem Phys 54 (1981) 261.

6 M J Ramos, D McKenna, B C Webster and E Roduner. J Chem Soc, Faraday Trans 1, 80, (1984), 255 and 267.

7 D Cavagnat and J Lascombe. J Molecular Spectroscopy 92 (1982) 141-157.

8 M C R Symons. Hyperfine Int. 17-19 (1984) 771.

9 E Roduner, W Strub, P Burkhard, J Hochmann, P W Percival, H Fischer, M Ramos and B C Webster. Chem Phys 67 (1982) 275.

10 A Hill, G Allen, G Stirling and M C R Symons. J Chem Soc, Faraday Trans 1, 78 (1982) 2959.

11 D C Walker. Muon and Muonium Chemistry, Cambridge UP (1983).

12 E Roduner and B C Webster.
J Chem Soc, Faraday Trans 1, 79 (1983) 1939.

13 E Roduner in Exotic Atoms '79
eds K Crowe, J Duclos, G Fiorientini and G Torelli.
Plenum Press, NY, (1980) 379.

14 E Roduner, G A Brinkmann and P W F Louwrier.
Chem Phys 73 (1982) 117.

15 K Nagamine, K Ishida, T Matsuzaki, K Nishiyama, Y Kuno, T Yamazaki and H Shirikawa. Phys Rev Letters 53 (1984) 1763.

16 D A Geeson, M C R Symons, E Roduner, H Fischer and S F J Cox.
Chem Phys Letters 116 (1985) 186.

17 A Hill, M C R Symons, S F J Cox, R De Renzi, C A Scott, C Bucci and A Vecli. J Chem Soc, Faraday Trans 1, 81 (1985) 433.

18 D Geeson, M C R Symons, E Roduner, H Fischer, S F J Cox and C A Scott. (Unpublished).

19 G G Myasischeva, Yu V Obukhov, U S Roganov and V G Firsov.
High Energy Chem. 4 (1970) 398 and 463.

20 P W Percival, Radiochemica Acta 26 (1979) 1.

21 S F J Cox and M C R Symons. (To be published).

22 P W Percival and J Hochmann. Hyp Int 6 (1979) 421.

23 E Roduner. Chem Soc Faraday Discussion No. 78 (198 , in press;
also to be published elsewhere in full).

24 E Roduner. Hyperfine Int 17-19 (1984) 785.

25 Y C Jean, B W Ng, J H Brewer, D G Fleming and D C Walker.
J Phys Chem 85 (1981) 451.

26 P W Percival, J-C Brodovitch and K E Newman.
Faraday Discuss. Chem Soc 78 (1984).

27 B D Patterson in Muons and Pions in Materials Research.
Eds J Chappert and R I Grynszpan (North Holland, 1984) ch 10.

28 H P Baumeler, K W Blazey, W J Choyke, T L Estle, H Keller,
R F Kiefl, W Kundig, P F Meier, W Odermatt, B D Patterson,
S L Rudaz, J W Schneider and C Schwab. (To be published).

29 S F J Cox and M C R Symons. (Unpublished).

30 R Ellul, P Potzinger and B Reimann. J Phys Chem 88 (1984) 2793.

HIGH RESOLUTION LASER SPECTROSCOPY OF C_2

M.C.Curtis and P.J. Sarre
Department of Chemistry, University of Nottingham,
University Park, Nottingham, U.K. NG7 2RD

INTRODUCTION

We have recorded Doppler-limited and sub-Doppler electronic spectra of the Swan system ($d^3\Pi_g - a^3\Pi_u$) of C_2 produced by the reaction of sodium vapour with organic halides. Transitions with $\Delta\Omega = \pm 1$ are observed for the first time leading to improved molecular parameters, and sub-Doppler spectra of the $^{13}C_2$ molecule allow the determination of nuclear hyperfine parameters.

EXPERIMENTAL

The experimental details are described fully in a forthcoming paper[1] and are given here only in outline. Formation of C_2 radicals is achieved by the reaction of an organic halide, for example CCl_4 or C_2Cl_4 in a vapour of an alkali metal, usually sodium. A six-way stainless steel cross is used to contain the reaction and allows easy attachment of windows, baffle arms and the sodium reservoir. The entire cross is heated to ca. 500 K, and the organic halide is introduced through a nozzle at the bottom of the reservoir. A buffer gas is employed to keep the observation window clean, and the total pressure in the cell is 4 torr. A weak blue chemiluminescence is observed. The transitions are detected by laser-induced fluorescence of the $\Delta v = -1$ sequence with $v' = 0,1,2,3$ and 4. This indicates that the C_2 molecule has considerable vibrational excitation in addition to a high translational temperature of 3000 K. It is possible to generate C_2 radicals in many other, perhaps simpler, ways. We have developed this apparatus primarily with the aim of observing new radicals.

A Coherent CR-699-29 ring dye laser was employed in this work. It provides automatic wavelength calibration by reference to the well-known spectrum of I_2. For the sub-Doppler measurements the linearity of the scan of the tilting Brewster plate was checked against a 75 MHz FSR etalon.

DOPPLER-LIMITED SPECTRA

A detailed study of the 0-1 band of the Swan system was undertaken. In addition to the well-known P and R branches of the $\Delta\Omega = 0$ transitions between the three Ω components of the two $^3\Pi$ states, members of the Q branches were detected for the first time. Weak transitions obeying $\Delta\Omega = \pm 1$ were also observed. Taken together, these lines allow determination of an extensive set of molecular parameters for both $^3\Pi$ states. In the least squares fitting, we employed the $^3\Pi$ hamiltonian of Brown and Merer[2], and have obtained the molecular parameters given in table 1.

TABLE 1 Molecular Parameters for C_2

	$d^3\Pi_g(v'=0)$	$a^3\Pi_u(v''=1)$
T_{01}	17 760.441(1)	
A	-14.0022(30)[a]	-15.2522(28)
B	1.745573(45)	1.607434(43)
$10^6 D$	6.824(48)	6.447(43)
λ	0.0334(26)	-0.1544(24)
$10^4 \gamma_D$	-0.44(25)	-0.35(24)
$10^4 A_D$	5.07(48)[b]	2.27(41)[b]
o	0.6387(30)	0.6796(28)
p	-0.0252(23)	-0.0086(22)
$10^4 q$	-8.16(19)	-6.17(19)

a 3σ

b γ was set to zero as it is fully correlated with A_D

SUB-DOPPLER SPECTRA

The principal aim of this work on C_2 was to study the electronic structure of the molecule by resolution of nuclear hyperfine structure in spectra of $^{13}C_2$. Sub-Doppler spectra of $^{12}C_2$ were initially recorded

using two different saturation techniques. Intermodulated fluorescence spectra were readily obtained, but it was found that laser induced fluorescence probing of saturation produced better signal-to-noise. In this approach the laser beam (600 mW) was split into two counter-propagating beams of equal intensity. One beam was continuous and the other beam was mechanically chopped at 3kHz. The LIF signal due to interaction of the chopped beam with the sample produced dips in $^{12}C_2$ of almost 50% with a linewidth of 80 MHz.

Enriched $^{13}CCl_4$ was employed as the reactant gas to generate $^{13}C_2$ and good signal-to-noise spectra were obtained as shown in figure 1.

FIGURE 1 Sub-Doppler Spectrum of the $P_1(21)$ Line of the 0-1 Band of the Swan System of $^{13}C_2$

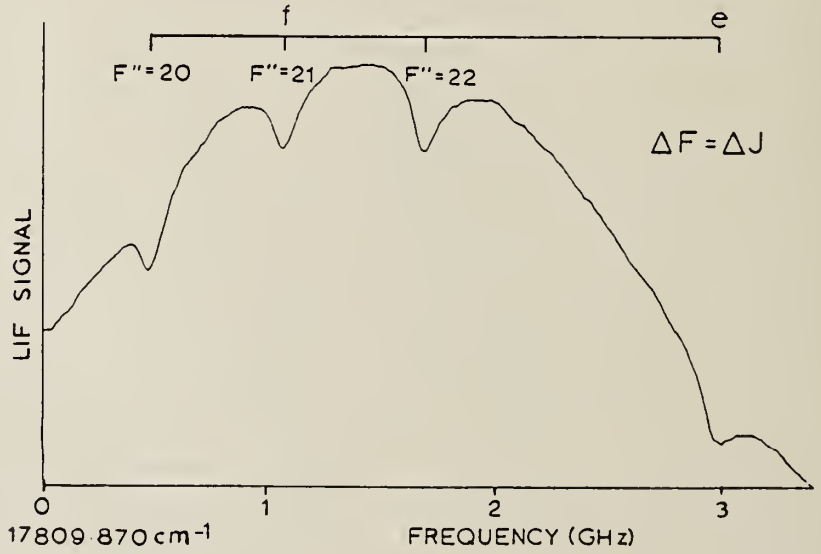

The hyperfine measurements were fitted using a published hamiltonian[3] and the hyperfine parameters obtained are given in table II. The parameters a, b_F, c and d have their usual meaning and are defined in reference (3).

TABLE II Hyperfine Parameters for $^{13}C_2$ in MHz

	$d^3\Pi_g(v=0)$	$a^3\Pi_u(v=1)$
a	159(15)†	170(20)
b_F	638(9)	27(11)
c	-62(21)	-47(25)
d	35(9)	41(9)

†3σ quoted

DISCUSSION

The $a^3\Pi_u$ and $d^3\Pi_g$ states arise from the configurations $2\sigma_u^2 1\pi_u^3 3\sigma_g^1$ and $2\sigma_u^1 1\pi_u^3 3\sigma_g^2$ respectively. The orbital hyperfine parameter a and the hyperfine doubling parameter d have contributions from the unpaired π electron only and should therefore assume the same value in both electronic states. We find that this is indeed the case. The spin-spin dipolar parameter c depends on both of the unpaired electrons and a simple interpretation of its magnitude and sign is not readily made. The most interesting result is the very substantial difference in the Fermi contact parameters for the two electronic states. To a first approximation there will be no contribution to the spin density at the nuclei from the unpaired π electron, and its influence is neglected in the following discussion. In the simplest LCAO approximation the $3\sigma_g$ wavefunction may be written as a linear combination of 2p atomic orbitals on the two centres. Using Slater-type 2p orbitals, we calculate a contact interaction of only 2 MHz. This is very much less than our experimental value of 27 MHz and indicates that some 2s character must be included in the wavefunction as expected. The contact interaction in the $d^3\Pi_g$ state is very much larger with a value of +638 MHz. In the simplest approximation, the wavefunction may be written as a linear combination of 2s atomic orbitals. Using Slater-type 2s orbitals, an overlap integral between the 2s orbitals of 0.43, and noting that an electron in a 2s orbital on a ^{13}C atom gives rise to a

contact interaction of 3777 MHz, we obtain an estimated value of 620 MHz. The very close agreement between experiment and this crude calculation is not meaningful given the approximations introduced, and without doubt some 2p character should be included in the LCAO basis. Nevertheless, this calculation gives a semiquantitative interpretation of the observed values without recourse to a full ab-initio calculation. It will be of interest to compare these experimental results with the results of a calculation of spin-densities in which a larger basis set and spin-polarisation effects are included.

REFERENCES

1. M.C.Curtis and P.J.Sarre, J.Mol.Spectrosc.(in press)
2. J.M.Brown and A.J.Merer, J.Mol.Spectrosc. 74, 488 (1979)
3. J.M.Brown, I.Kopp, C.Malmberg and B.Rydh, Phys. Scripta 17, 55 (1978)

ACKNOWLEDGEMENTS

We thank the SERC for a grant for the purchase of apparatus and for a studentship to MCC, and Coherent (UK) Ltd. for support under the CASE scheme.

Mid Infrared Diode Laser Spectroscopy of Transient Species

P.B. Davies
Department of Physical Chemistry, University of Cambridge, Lensfield Road, Cambridge CB2 1EP, U.K.

Introduction

Over the past decade a wealth of new information on free radicals, ions and other transient species has been derived from high resolution spectroscopy particularly with laser techniques.[1] In several cases the existence of new gas phase species, hitherto a matter of theoretical or mechanistic speculation, has been confirmed. The essential characteristics of the new techniques required for such studies are: sensitivity, specificity and high resolution. Many early successes were due to Laser Magnetic Resonance (LMR) with CO and CO_2 lasers.[2] At first mid infrared LMR was restricted to regions around 5 and 10μm but recent development of CO lasers has closed the gap between these regions.[3]

The complementary tunable laser techniques used for most spectroscopic applications are: the F-centre laser, difference frequency laser, and diode laser. Ternary lead salt alloy lasers cover the region from about 330 to 3700 cm^{-1}. However, the results described below concentrate on the mid infrared region of the spectrum. Finally it is important to remember the potential of the latest generation of FTIR spectrometers, especially for emission studies.[5] These instruments provide a complementary approach for Doppler limited spectroscopy which will become increasingly important.

Experimental Techniques

The sensitivity of diode laser absorption spectroscopy has been enhanced in several ways to facilitate the detection of free radicals, which almost always exist only in low concentrations. The modulation techniques employed include

a) Zeeman modulation (of paramagnetic species),

b) frequency modulation of the laser,

c) concentration modulation of transients produced in discharges.

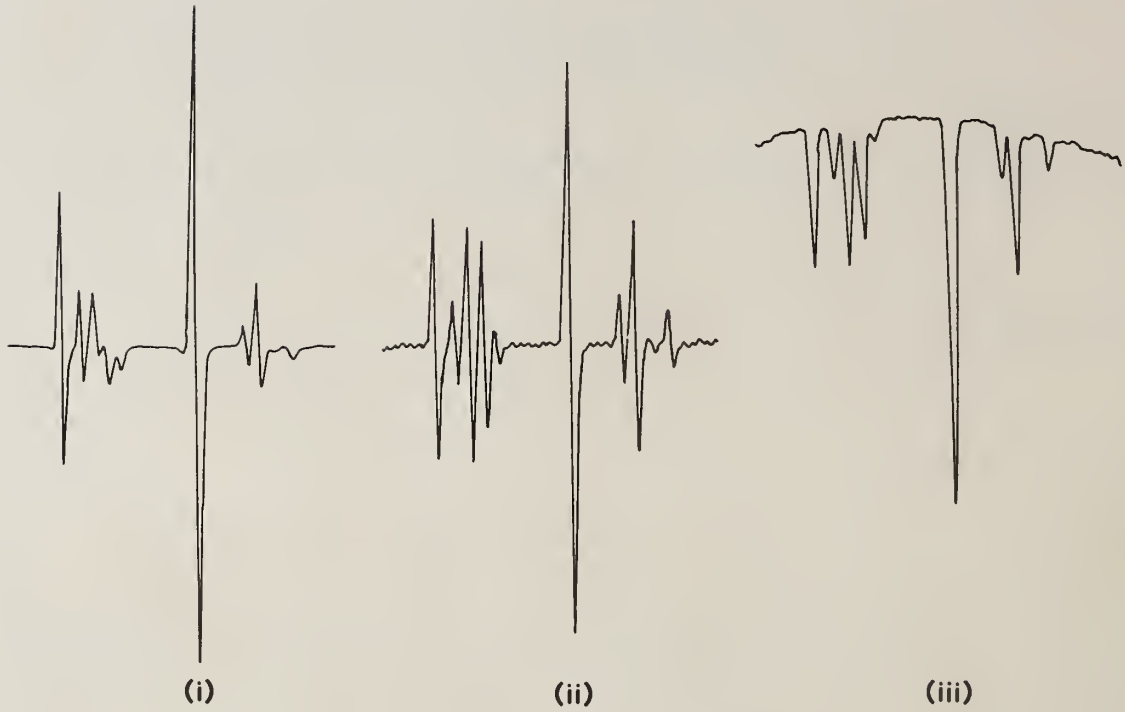

1. Diode laser absorption spectrum of the chlorine atom recorded with (i) Zeeman modulation (ii) source modulation and (iii) modulation of the laser beam with a mechanical chopper.

Another method used to improve signal to noise ratios is rapid scan spectroscopy for accumulating signal under computer control.[6] Figure 1 shows the results of using three different modulation techniques to detect the fine structure transition[7] in the Cl atom ($3p^5$, $^2P_{\frac{1}{2}} \leftarrow {}^2P_{3/2}$). The same concentration was used in each case and the atoms were generated in the side arm of a large multiple-pass 1 m long cell. Multiple-pass cells are in widespread use for increasing the absorption of both neutral and charged species. In many examples the radical, ion or transient is produced within the cell by electric discharge with the laser beam making one or more passes through the discharge medium.

Although the modulation methods outlined above have boosted sensitivity to $10^8/cm^3$ or better they tend to be non specific in

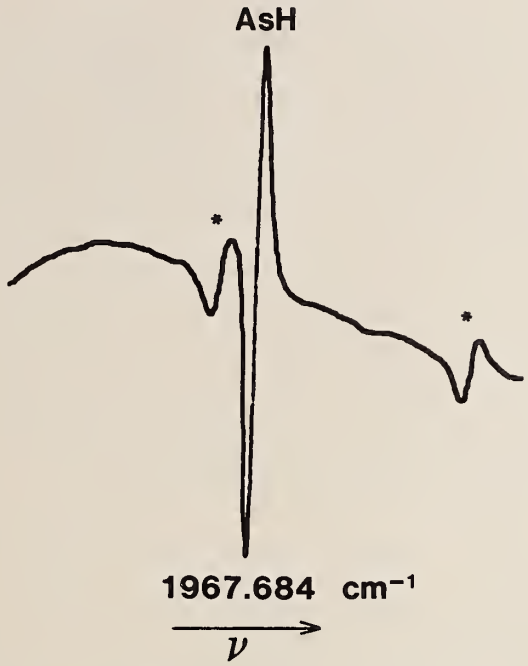

2. The P-branch transition N,J : 6,6 ← 7,7 of the ground $^3\Sigma$ state of AsH. The starred lines ar N_2O calibration peaks.

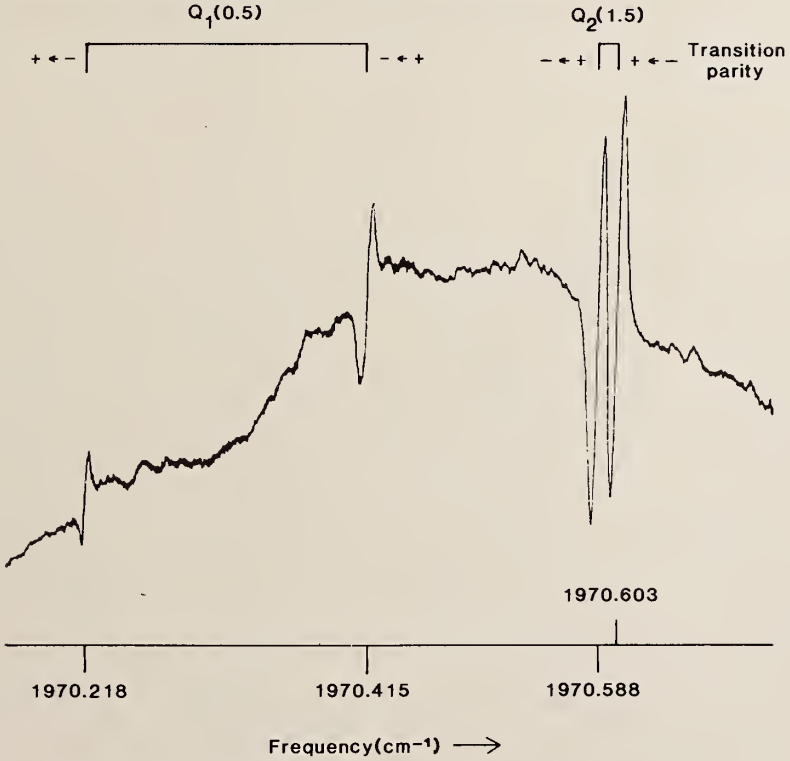

3. Lowest J Q-branch lines of the fundamental band of SiH showing resolved Λ doubling. The spectrum was recorded in 3 minutes using a 1 second time constant from a 2.5 kV, 60 mA discharge of 10% SiH_4 in H_2 at a pressure of 3 Torr.

selecting between ions and neutrals. One particularly effective method of preferential detection of charged species is velocity modulation[8] in which the ion is generated in an a.c. discharge. The ion absorption frequency is then significantly Doppler shifted at the discharge frequency and can be detected in the usual way by phase sensitive detection. A fuller account of the Cambridge velocity modulation experiments as applied to HCO^+ and HCS^+ cations is given elsewhere in these proceedings by W.J. Rothwell. Another useful method for identifying ion spectra has been to magnetically confine the discharge and employ amplitude modulation.[9]

When sensitivity and specificity have been optimised it remains to calibrate the spectra. In diode laser spectroscopy calibration against standard gases such as OCS, NH_3, CO_2 and N_2O is the most widely accepted method. Many of the calibration lines have been measured with heterodyne precision, usually well beyond the measurement accuracy of the diode laser experiment itself. In other regions where calibration data are sparse the FTIR results are extremely important for calibration standards.

Spectroscopic Results

1) AsH

Spectra of this radical have been detected in a d.c. discharge of hydrogen over arsenic.[10] The discharge tube was 1.5 m long and the laser made up to eight passes through the discharging gas. In appearance the spectra of AsH make an interesting contrast with those of PH. Both molecules have $^3\Sigma$ ground states and assuming the selection rule $\Delta N = \Delta J = \pm 1$ each rotational component of the fundamental band should be a triplet (in this approximation there is no Q-branch). In AsH, however, the 'spin-spin' parameter which determines the magnitude of the triplet splitting is very large, 58.8 cm^{-1} compared with 2.2 cm^{-1} in PH. Thus while the PH triplet splitting is almost ideally matched to the mode size of diode lasers[11] in AsH only single lines are usually observed for each mode (figure 2). Nevertheless twenty three transitions have been measured in $AsH(X^3\Sigma^-)$ and, combined with ground state data, yield the following equilibrium parameters:

α_e 0.2117(10) cm^{-1}

B_e 7.3067(5) cm^{-1}

γ_e 0.152315(5) nm

β_e 3(8) x 10^{-6} cm^{-1}

D_e 3.30(7) x 10^{-4} cm^{-1}

ω_e 2175 cm^{-1} $\omega_e x_e$ 49 cm^{-1}

Actually the ground state of AsH is much closer to Hund's case (c) than (b), unlike PH, and the above selection rules are incomplete. Many more transitions should be accessible if case (c) rules apply and these will be searched for when new diodes become available.

2) SiH

Much concern is currently being given to understanding silane decomposition reactions in electric discharges, and thermally and photochemically. Of particular interest is the role of gas phase Si species in thin film formation processes. In thermal and photochemical decompositions SiH_2 is believed to be very important while in electric discharges SiH_3 is abundant, at least near surfaces. Thus there are several transient or radical species of interest including : Si, SiH, SiH_2 and SiH_3, and at least one ion, SiH^+. The latter is also of possible importance in extra terrestrial chemistry. As part of a programme investigating the photochemical decomposition of SiH_4 with infrared lasers we have used a diode laser to monitor reaction products. This has revealed the infrared spectra of one or more transient species. In order to elucidate the chemistry of the various silane decomposition systems we have studied the species present in a discharge in SiH_4 and recorded several new lines in SiH[12], both in the fundamental and hot bands (2-1). The main objective of the work has been to observe and measure low J Q-branch lines of the fundamental, extending the data already available from FTIR and LMR.

Although SiH is a light radical and therefore might be thought to have a well dispersed spectrum, in its $^2\pi_{\frac{1}{2}}$ ground state it has a Q-branch as well as R and P branches. In addition, both $^2\pi_{\frac{1}{2}}$ and $^2\pi_{3/2}$ manifolds lie close to each other. Figure 3 shows the most distinctive feature of the spectrum, well resolved Λ doublets from the

lowest Q-branch components of both $^2\Pi_{\frac{1}{2}}$ and $^2\Pi_{3/2}$ SiH. A fuller account of this work will appear shortly.[12].

3) CO^+

This free radical cation is a species of fundamental interest both in laboratory spectroscopy and in astrophysics. Many impressive spectroscopic experiments involving CO^+ have been reported including the discovery of its microwave spectrum by Dixon and Woods.[13] We have used a similar experimental arrangement to Dixon and Woods, namely a liquid nitrogen cooled discharge in CO and helium, to detect the fundamental band of CO^+ near 2180 cm^{-1}. The spectra were recorded using velocity modulation at 50 kHz.

The $^2\Sigma^+$ ground state of this ion conforms to Hund's case (b) for which the selection rules exclude a Q-branch. However, each P- and R-branch component is split by the spin-rotation interaction and although it is not always completely resolved it is a useful guide to assignment. For the higher P and R components each transition consists

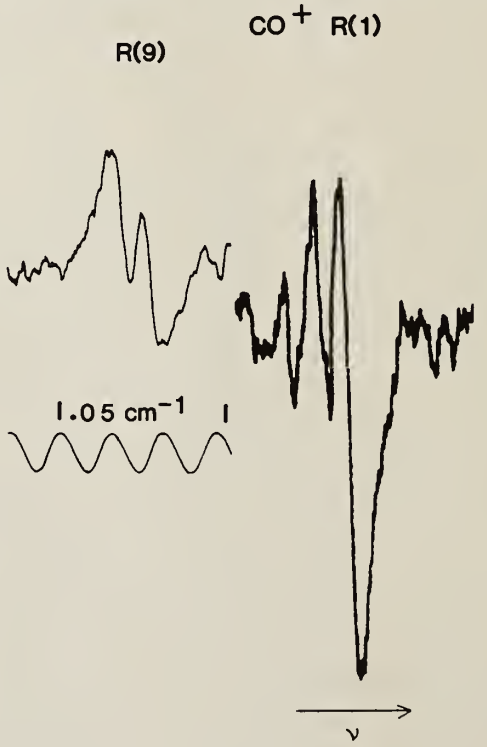

4. The R(9) and R(1) components of the fundamental band of CO^+. (The etalon fringe spacing applies to the R(9) transitions).

of a doublet given by the selection rule $\Delta N = \Delta J$ ($=\pm 1$) and provided N is not too large this splitting is given by the mean value of the spin-rotation parameter, $\gamma \sim 0.01$ cm^{-1}. Figure 4 shows such a relatively strong doublet R(9). A third component is also weakly allowed ($\Delta J = 0$) but at high N its intensity is very low and it is well displaced from its associated doublet. However, moving towards the band centre this third component increases in intensity and is located much closer to its associated $\Delta N = \Delta J$ pair so that, for example, at R(1) it forms part of a triplet, figure 4.

In a final fit to eighteen lines (with positions given elsewhere[14]) v=0 and 1 values of B, D and γ were set to their microwave values.[15] The fitted value of the band centre was ν_0 = 2183.9193(10) cm^{-1} which is in good agreement with a prediction from much earlier spectroscopy of Rao,[16] 2183.89 cm^{-1}. These CO^+ spectra are in many ways similar to those of isoelectronic CN. However, in CN spin-rotation splitting was only resolved in R(0) and P(1) probably due to the smaller value of $\bar{\gamma}$(.007 cm^{-1}). The above value of ν_0 combined with microwave rotational and fine structure parameters enables the positions of other transitions in CO^+ to be calculated with an accuracy of 10^{-3} cm^{-1} up to N=10.

4) HCl^+

This cation has been studied previously both by its electronic spectrum[17] ($A^2\Sigma \rightarrow X^2\Pi$ system) and more recently in the far infrared by LMR.[18] There has also been a preliminary account[19] of the fundamental band of DCl^+ detected by mid infrared LMR. Vibration-rotation transitions in HCl^+ were first detected[6] in 1983 with a diode laser and a d.c. discharge in weak mixtures of HCl in helium. This assignment was tentative as no specific method of identifying ion transitions was available. Nevertheless the Λ doubling of the observed lines corresponded well with that calculated from Sheasley and Mathews'[17] optical data. We have now confirmed the detection of HCl^+ using velocity modulation detection and extended it to many more transitions, limited at the

moment only by the diode lasers available.

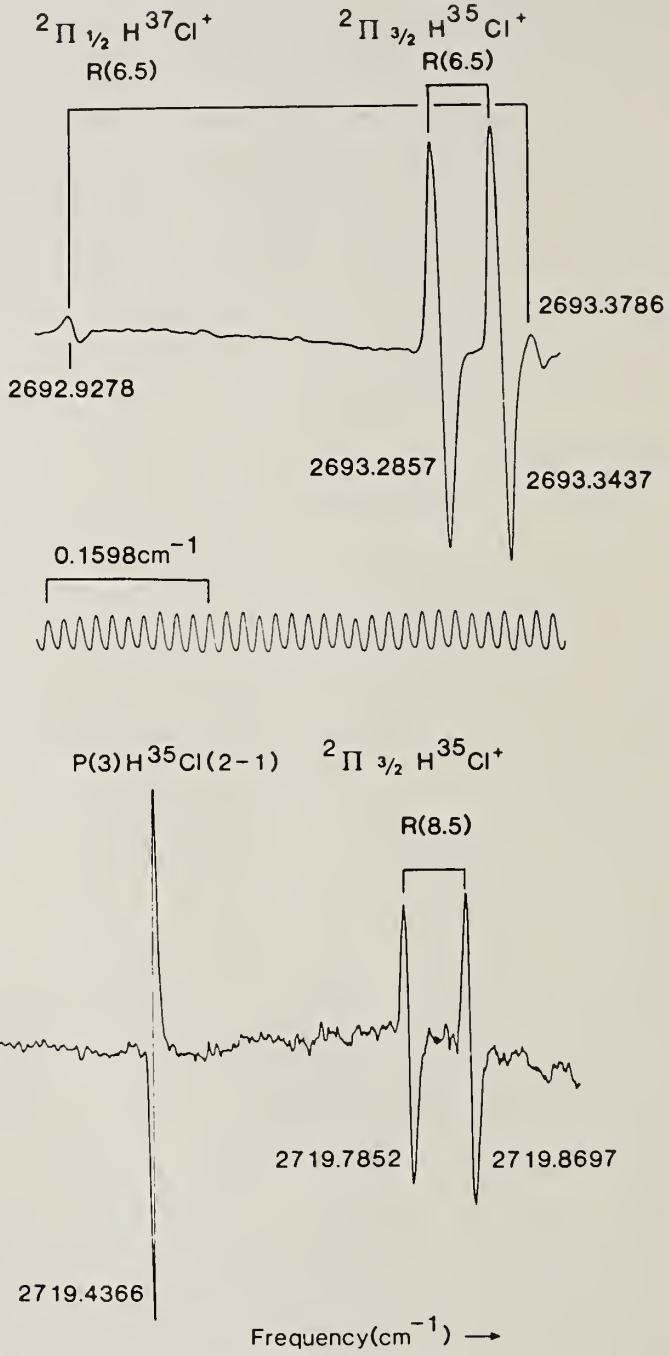

5. Velocity modulation spectra of the fundamental band of HCl^+ recorded with a 1 second time constant. The ion was generated by a 50 kHz discharge in a 1 m Torr HCl, 700 m Torr He mixture. The germanium etalon fringe pattern in the middle of the diagram refers to the upper spectrum.

In summary Q-and R-branch transitions in both $^2\pi_{\frac{1}{2}}$ and $^2\pi_{3/2}$ states of $H^{35}Cl^+$ and $H^{37}Cl^+$ have been measured in the fundamental band and, tentatively, a few hot band transitions have also been recorded. The optical data has turned out to be satisfactorily accurate in predicting both absolute line positions and Λ doublet splittings. Figure 5 shows typical spectra with lines from $^2\pi_{\frac{1}{2}}$ and $^2\pi_{3/2}$ HCl^+. Also observed was an intense line from HeH^+ which appeared when the HCl content of the discharge was reduced.

Seventeen transitions have been measured so far[20] and in later work will be used to obtain more accurate data for this ion to probe harmonic and anharmonic features of the rotational and fine structure parameters. It is also worth noting that there is extensive data on isoelectronic SH with which HCl^+ can be compared. Finally, with such good sensitivity (S/N ratios $\geq$ 200:1 on the strongest lines) it is worth speculating on the detection of other HCl^+ i.r. spectra. These include weaker "cross-stack" transitions between $^2\pi_{\frac{1}{2}}$ and $^2\pi_{3/2}$ states, with and without changes in the vibrational quantum number, and pure rotational transitions in the far infrared at 400 cm^{-1}.

5) $\underline{H_3O^+}$

This cation has been one of the most widely studied by infrared laser spectroscopy. Of particular relevance to mid infrared spectroscopy is the ν_2 'umbrella' mode of H_3O^+ (D_3O^+) which has now been studied in several laboratories using diode lasers over the past two years. Complementing the experiments have been several ab initio investigations aimed at predicting both vibrational frequencies and rotational constants. As the experimentally determined parameters became available the calculations have been refined and extended up the potential. Figure 6 shows the various components of the ν_2 mode in H_3O^+ and D_3O^+ measured by diode laser spectroscopy. In each case precise band centres and rotational constants were determined (see for example data in refs 21 and 22).

Liu and Oka[22] have used the results of diode laser spectroscopy in the $1^- \leftarrow 0^+$, $1^+ \leftarrow 0^-$ and $1^- \leftarrow 1^+$ components of ν_2 to

predict the $0^- \leftrightarrow 0_+$ 'pure inversion' spectrum which lies in the far infrared outside the range of diode lasers and is of direct astrophysical importance. One of these transitions has now been detected in the laboratory[23] within 25 MHz of its predicted position. In another development in collaboration with T.J. Sears, P.R. Bunker and V. Spiro[24] the accumulated infrared laser spectra of H_3O^+ and D_3O^+ have been fitted to the non rigid invertor hamiltonian to determine structural parameters for H_3O^+. This yielded : r_e = 0.9758A, $\alpha_e(\angle HOH)$ = 111.3^0 and a barrier height of 672 cm^{-1}. Lastly, although the far infrared transitions of H_3O^+ are outside diode laser range it is nevertheless possible to provide accurate wavenumbers of mid infrared transitions for astronomical searches. The latter usually employ heterodyne detection methods using N_2O and CO_2 laser local oscillators. We have recently measured[25] several H_3O^+ transitions likely to occur at low temperatures and which are close to suitable heterodyne standards.

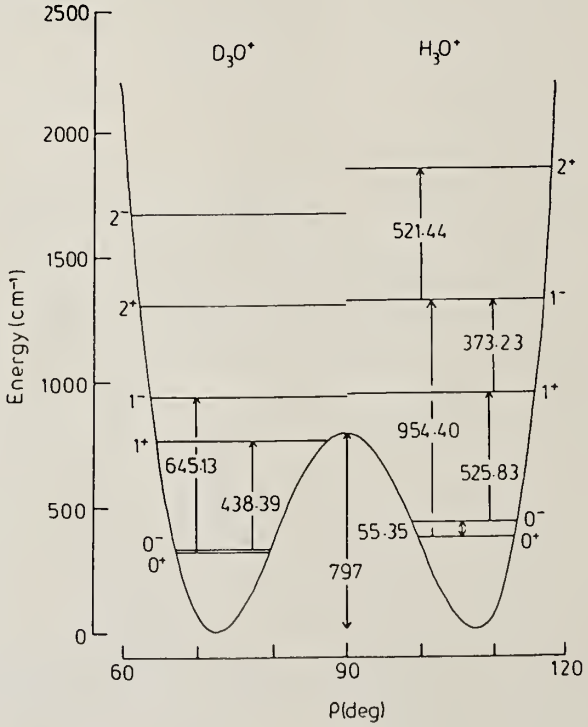

6. The inversion potential of H_3O^+ (D_3O^+) showing the lowest vibrational levels and the transitions so far detected by diode laser spectroscopy.

The vibrational term values of the ν_2 mode of H_3O^+ are markedly different from those of NH_3 by virtue of the much lower inversion barrier. One experimental consequence of this is an accidental bunching of three allowed transitions in the 500-600 cm^{-1} region (figure 6), leading to a dense pattern of lines. Unfortunately both diode and detector performance is poorer here than at higher frequencies. Thus to satisfactorily cover just 20 cm^{-1} band ($\nu_0 \sim 525$ cm^{-1}) required about five lasers. Nevertheless, the accumulated results on H_3O^+ derived from diode laser spectroscopy is formidable and shows the strength of the technique for studying ions, particularly when allied to velocity modulation detection.

Conclusions

The future of tunable infrared laser spectroscopy looks extremely promising. As sensitivity improves the detection of many more free radicals and ions can be expected including multiply charged cations as well as anions. So far the bulk of results have come from experiments over restricted pressure ranges e.g. 0.1 - 1 Torr in discharges. Two novel alternative methods of generating these species seem worth investigating: (a) Corona discharges in supersonic nozzle expansions[26] which could be important for simplifying the spectra of larger species and (b) infrared and ultraviolet laser photolysis which has already been used to produce transients in SiH_4[27] and HN_3[28] decomposition.

Acknowledgement

The results reported here on AsH, SiH, CO^+, HCl^+ and H_3O^+ were obtained in collaboration with colleagues in Cambridge and elsewhere whose names are cited in the references. I express my gratitude to them for participating in these projects and for many stimulating discussions on diode laser spectroscopy.

References

(1) E.Hirota, J.Phys. Chem. 87, 3375 (1983).
(2) A.R.W.McKellar, Far. Disc. Chem. Soc. 71, 63 (1981).
(3) T.X.Lin, W.Rohrbeck and W.Urban, Appl. Phys. B26, 73 (1981).

(4) A.S.Pine, Phil. Trans. R. Soc. Lond. A 307, 481 (1982).
(5) J.W.C.Johns, J. Mol. Spec. 106, 124 (1984).
(6) P.B.Davies, P.A.Hamilton, W.Lewis-Bevan and M.Okumura J. Phys. E : Sci. Instrum. 16, 289 (1983).
(7) P.B.Davies and D.K.Russell, Chem. Phys. Lett. 67, 440 (1979).
(8) C.S.Gudeman, M.H.Begemann, J.Pfaff and R.J.Saykally, Phys. Rev. Lett. 50, 727 (1983).
(9) B.Lemoine and J.L.Destombes, Chem. Phys. Lett. 111, 284 (1984).
(10) J.R.Anacona, P.B.Davies and S.A.Johnson, Mol. Phys. in press.
(11) J.R.Anacona, P.B.Davies and P.A.Hamilton, Chem. Phys. Lett. 104, 269 (1984).
(12) P.B.Davies, N.A.Isaacs, S.A.Johnson and D.K.Russell, J. Chem. Phys. in press.
(13) T.A.Dixon and R.C.Woods, Phys. Rev. Lett. 34, 61 (1975).
(14) P.B.Davies and W.J.Rothwell, J. Chem. Phys. in press.
(15) M.Bogey, C.Demuynck and J.L.Destombes, J. Chem. Phys. 79, 4704 (1983).
(16) K.N.Rao, Astrophys. J. 111, 50 (1950).
(17) W.D.Sheasley and C.W.Mathews, J. Molec. Spect. 47, 420 (1973).
(18) D.Ray, K.G.Lubic and R.J.Saykally, Mol. Phys. 46, 217 (1982).
(19) A.Hinz, W.Bohle, D.Seitz, J.Werner, W.Seebass and W.Urban, Mol. Phys. 53 1017 (1984).
(20) P.B.Davies, P.A.Hamilton and S.A.Johnson, J. Chem. Phys, in press.
(21) P.B.Davies, P.A.Hamilton and S.A.Johnson, J. Opt. Soc. Amer. B 2, 794 (1985).
(22) D.-J.Liu and T.Oka, Phys. Rev. Lett. 54, 1787 (1985).
(23) a) G.M.Plummer, E.Herbst and F.C.De Lucia, J. Chem. Phys. 83, 1428 (1985); b) M.Bogey, C.Demuynck, M.Denis and J.L.Destombes, Ast. and Astrophys. 148, July (II) 1985.
(24) T.J.Sears, P.R.Bunker, V.Spirko, P.B.Davies and S.A.Johnson, J.Chem. Phys. in press.
(25) P.B.Davies, P.A.Hamilton and S.A.Johnson, Ast. and Astrophys. 141, 19 (1984).
(26) A.T.Droege and P.C.Engelking, Chem. Phys. Lett. 96, 316 (1983).
(27) N.A.Isaacs, D.K.Russell, S.A.Johnson unpublished work.
(28) J.L.Hall, H.Adams, J.V.V.Kasper, R.F.Curl and F.K.Tittel, J. Opt. Soc. Amer. B 2, 781 (1985).

Molecular Photodissociation Dynamics in H_2O, D_2O and H_2O_2

M.P. Docker, A. Hodgson and J.P. Simons
Chemistry Department, The University, Nottingham NG7 2RD, England.

Summary Experimental studies of molecular photodissociation from both structured and continuum electronically excited states are reviewed, with particular reference to current investigations of H_2O, D_2O and H_2O_2. The studies of H_2O, D_2O include fully quantum state selected measurements of predissociation from the rotationally structured $\tilde{C}^1B_1$ state, the discovery of a weak bound-free fluorescence emission from $\tilde{C}^1B_1 \rightarrow \tilde{A}^1B_1$, the dynamics of molecular photodissociation in the $\tilde{B}^1A_1$ continuum and, in particular, the influence of molecular rotation on the dissociation dynamics and product branching ratios. A correlation of 'direct' trajectories on the $\tilde{B}^1A_1$ potential with high photofragment rotation and 'indirect' bending trajectories with low rotation, suggested by earlier scattering calculations is experimentally confirmed. The rotational alignment of OH/OD(A) fragments generated by direct excitation into the $\tilde{B}^1A_1 \leftarrow \tilde{X}^1A_1$ continuum decreases with the rotational quantum number N'. Photodissociation of H_2O_2 in the continuum near 248 nm generates OH(X) fragments exclusively in the ground vibrational level, predominantly in low rotational levels and with near equal populations of the two spin-orbit states. However, analysis of the Doppler profiles of the OH(X) l.i.f. spectra reveals a smooth progression from highly aligned translational motion of the photofragments with low rotation to near isotropic scattering into high rotational levels. Possible interpretations of this behaviour are discussed.

1. Introduction

In the study of elementary reaction dynamics the experimentalist tries to define, as closely as possible, the quantum states of the reagents and characterise as far as possible those of the products. The ideal is full quantum state selection in both the entry and exit channels - the 'before' and the 'after'. Of course, the real question

is what goes on in between - what are the dynamics of individual molecular collisions? They are usually inferred from state-to-state experiments, but pinning down the dynamics of individual collisions is clouded by the inevitable spread of impact parameters that must obtain in any bimolecular collision process. There is no doubt that the most penetrating experimental approach to these questions is through the spectroscopic study of photodissociation systems, either chemically bonded single molecules or van der Waals bonded molecular complexes. Absorption of tunable, monochromatic and polarised light can allow full definition of the initial quantum states when resolved rotational structure is retained on excitation; the spread of initial impact parameters in the half-collision dissociation process may also be closely restricted. Simultaneous spectroscopic analysis of the dissociation fragments via spontaneous, or laser induced fluorescence spectroscopy can lead to full quantum state selection - achieved for the first time in studies of H_2O and D_2O[1,2]. The time dependence of the dissociation dynamics can be inferred from measurements of the half-collisional anisotropies[3] and from the quantum-state dependence of the branching into alternative channels. This allows direct measurements of radiationless processes in small polyatomic molecules. A complementary approach to photodissociation dynamics, developed by Heller and Kinsey[4], focuses attention on the emission spectroscopy of the dissociating molecules themselves, excited into a short lived (unstructured) upper state. By tuning an intense laser source close to the peak of the dissociation continuum, it is possible to record long vibrational progressions in resonance Raman spectra of photo-dissociating molecules. Their temporal evolution can be displayed directly via an inversion of the spectrum from the frequency domain to the time domain[4]. When the photoexcited molecule has a lifetime long enough to support, at least partially, resolved vibrational and rotational structure, further information may be obtained on quantum state dependencies from the excitation spectrum of its weak fluorescence emission [5,6,7].

2. The photodissociation of H_2O and D_2O

The molecules of choice for full quantum state selection in a photodissociating system, are generally polyatomic hydrides (where

rotational congestion is minimised) excited into quasi-bound Rydberg levels (where the lifetimes are long enough to restrict the degree of line-broadening) predissociating into fluorescent hydride fragments (whose spectra are easily resolved and well understood). Such systems are likely to show many interesting rotational and vibrational state dependencies, since the predissociation pathways often involve the traversal of a number of surface intersections as the geometrical configuration changes. Current studies of the quantum state selected photodissociation of H_2O and D_2O provide a textbook example of the spectroscopic approach to molecular reaction dynamics. Coherent two photon absorption of frequency narrowed, tunable, krypton fluoride laser radiation at 248nm into the origin band of the rotationally structured $\tilde{C}^1B_1 \leftarrow \tilde{X}^1A_1$ Rydberg transition at 124nm allows population of individually selected rovibronic levels in a quasi-bound predissociating state. If the laser is tuned to (two photon) frequencies which lie between the resolved rotational features, the underlying absorption continuum - due predominantly (if not entirely) to the $\tilde{B}^1A_1 \leftarrow \tilde{X}^1A_1$ transition - may be accessed. Alternatively, the continuum may be accessed through radiationless transfer from the $\tilde{C}$ state, promoted by rotational coupling. Once in the $\tilde{B}$ state continuum, the HOH bond angle opens since the potential is dominated by the conical intersection with the ground state, $\tilde{X}^1A_1$, causing a deep well in the exit channel for linear geometries. The torque exerted by the bending motion on the $\tilde{B}$ state potential induces strong rotational excitation in the scattered photofragments $OH/OD(A^2\Sigma^+)$[8]. Simultaneous monitoring of (i) the energy resolved OH/OD(A→X) photofragment fluorescence and its polarisation (ii) the rotationally resolved predissociation spectrum of $H_2O/D_2O(\tilde{C}^1B_1)$ - monitored via the photofragment fluorescence and the (very weak) parent molecular fluorescence continuum $H_2O/D_2O(\tilde{C} \rightarrow \tilde{A})$, and (iii) the underlying $\tilde{B}^1A_1 \leftarrow \tilde{X}^1A_1$ photodissociation continuum has established the following principal results:-

The fluorescent fragments $OH/OD(A^2\Sigma^+)$ are produced via the $\tilde{B}^1A_1$ state continuum only. If the absorbed photons initially populate the structured Rydberg state, $\tilde{C}^1B_1$, then access to the continuum is gained through Coriolis coupling. The coupling is induced by out of plane

rotational motion about an axis perpendicular to the two-fold symmetry axis, i.e. the a-inertial axis, since this has the required symmetry (B_1). If the expectation value $\langle J_a^2 \rangle$ for the rotational angular momentum about this axis is zero, photofragment fluorescence is not observed.

An alternative dissociation path which involves <u>direct</u> coupling of the $\tilde{C}^1B_1$ Rydberg state into the lower-lying $\tilde{A}^1B_1$ continuum also contributes - but this leads to 'dark' products, i.e. electronically unexcited fragments H/D + OH/OD($X^2\Pi$). Of course, for levels with $\langle J_a^2 \rangle = 0$, this is the sole dissociation path. Thus rotational coupling in the dissociating molecule controls <u>electronic</u> branching into alternative products. The parent molecular fluorescence H_2O/D_2O ($\tilde{C} \rightarrow \tilde{A}$) is observed most strongly when $\langle J_a^2 \rangle = 0$ but falls monotonically as the heterogeneous predissociation rate increases[6].

Absolute values of the homogenous and rotationally dependent heterogeneous predissociation rates may be obtained from the experimental linewidths and relative intensities of the rotationally resolved fluorescence excitation (or REMPI) spectra using the calculated two-photon linestrengths for the $\tilde{C}^1B_1 \leftarrow \tilde{X}^1A_1$ absorption[9]. Modelling of the experimental spectrum leads to the following predissociation rates

	Homogeneous	Heterogeneous
H_2O	4×10^{11} s^{-1} (2.5ps)	$4 \times 10^{11}[\exp(0.2\langle Ja^2 \rangle - 1]$ s^{-1}
D_2O	1.7×10^{11} s^{-1} (6.0ps)	$1.7 \times 10^{11}[\exp(0.2\langle Ja^2 \rangle - 1]$ s^{-1}

Comparison of the relative intensity of the molecular and OH/OD(A→X) photofragment fluorescence intensities, coupled with the data above and a knowledge of the OH/OD(A) quantum yield averaged over all populated rovibronic levels, allows an estimate of the $\tilde{C}^1B_1 \rightarrow \tilde{A}^1B_1$ radiative lifetime. For D_2O, this takes the value $\tau_r \simeq 8$ns, as expected for a transition which correlates with Ne(3p→3s) in the united atom.

Once the $\tilde{B}^1A_1$ continuum is accessed and the molecule approaches linearity the energy separation between the $\tilde{B}^1A_1$ and the lower

lying $\tilde{A}^1B_1$ states tends to zero; they are Renner-Teller components of the degenerate $^1\Pi_u$ state of the linear H_2O/D_2O molecule. Following passage through this configuration the molecule may transfer into the lower component, which correlates with the non-fluorescent products H/D + OH/OD($X^2\Pi$). Like the $\tilde{C}\rightarrow\tilde{B}$ transfer, $\tilde{B}\rightarrow\tilde{A}$ transfer also involves Coriolis coupling which increases with $\langle J_a^2\rangle$[2]. As a result, the yield of fluorescent products OH/OD($A^2\Sigma^+$) passes through a maximum as $\langle J_a^2\rangle$ increases. It does not fall to zero, however, when a significant fraction of the dissociation trajectories can pass outside the region of degeneracy, at O-H/D bond distances (>1.6Å) beyond the conical intersection between the $\tilde{B}^1A_1$ and $\tilde{X}^1A_1$ potential surfaces.

Three dimensional quantum scattering calculations for the fragmentation on the $\tilde{B}^1A_1$ potential surface suggest that the dynamics may be enriched by scattering resonances associated with motion along the bending coordinate; Segev and Shapiro correlated the longer-lived trajectories/resonances with the population of rotationally unexcited fragments[10]. Resolved photofragment fluorescence excitation spectra for selected rotational levels N', in OD($A^2\Sigma^+$)v' = 0 show a correlation between high N' and high $\langle J_a'^2\rangle$, and hence the $\tilde{B}\rightarrow\tilde{A}$ crossing probabilities; the population of the fluorescent fragments in low rotational levels is sparse. This can be understood since the (potentially) long-lived trajectories are those most susceptible to 'leakage' via $\tilde{B}\rightarrow\tilde{A}$ transfer near linearity. Under these conditions OH/OD(A) will be generated predominantly via direct trajectories.

3. The photodissociation of H_2O_2 at 248 nm

The near u.-v absorption of H_2O_2 is entirely continuous though the number, identity and relative intensities of the contributing transitions remains obscure. Photodissociation at 248 nm is known to generate OH(X) fragments exclusively in the lowest vibrational level and with relatively low rotational excitation (maximum population at N" = 5), thereby providing an excellent, near monoenergetic, translationally excited OH radical source[11,12]. The energy disposal has been interpreted in terms of a quasi-diatomic model, with strong repulsion along the O-O axis[11]. Some anisotropy in the Doppler profiles of the OH(X) laser induced fluorescence was also indicated in earlier experiments and new measurements have now been made under

improved resolution in an effort to clarify further the spectroscopy and dissociation dynamics. (They also test the feasibility of detecting the ground state OH fragments produced via the predissociation of $H_2O(\tilde{C}^1B_1)$ - so far OH(X) has not been detected, presumably because of its high rotational excitation). The new results were interesting and unexpected.

Production of OH(X) fragments was monitored using counter-propagating photolysis (KrF, ~100mJ) and probe (frequency doubled dye, $\Delta\nu \sim 0.04$ cm^{-1}) laser beams, with a probe delay of 35 ns. The pressure of H_2O_2 was maintained at ~20 mtorr. In the lowest rotational levels, N"~2, the Doppler profiles display strong forward-backward symmetry, indicating recoil of the two OH(X) fragments perpendicular to the ε-vector of the photolysis beam and hence a transition moment in the parent molecule directed perpendicular to the O-O internuclear axis. Analysis of the Doppler profile gives an anisotropy parameter $\beta \simeq -1$. As the rotational quantum N" increases, however, the minimum in the Doppler profile fills in, disappearing at N" ~ 7 and assuming a near isotropic contour for levels with N" > 12. Rotational alignment of the fragments is absent at all N" and the two spin-orbit components $^2\Pi_{3/2}$ and $^2\Pi_{\frac{1}{2}}$ are near equally populated.

If the absorption continuum were 'fluorine-like' the principal contributing transition would be the analogue of the $^1\Pi_{1u} \leftarrow {}^1\Sigma_{o^+g}$ transition populating a steeply repulsive molecular potential. The 'perpendicular' orientation of the transition moment indicated by the Doppler profiles at low N" is consistent with this assignment, but the near equal population of the $\Omega = \frac{1}{2}$ and 3/2 spin-orbit states implies strong mixing of the potentials at large O-O distances[11,13]. The progression towards an isotropic product angular distribution might be associated with an overlapping transition having a 'parallel' transition moment orientation, but other explanations seem more probable, particularly in view of the monotonic rotational surprisals[11]. Rotation of the parent molecule during the dissociation period could account for the observed behaviour, either through a transfer of rotational angular momentum to the fragments or by an increase in the duration of the dissociative trajectories leading to the rotationally excited fragments. The loss of alignment would

reflect the magnitude of the average product $\langle\omega\tau\rangle$, where ω is the parent rotational frequency and τ the dissociation period. Experiments in progress using a jet-cooled source of H_2O_2 should help resolve the alternatives since rotational cooling would reduce ω but leave τ unchanged.

The authors are most grateful to Professor R N Dixon and Dr M N R Ashfold for their help in the 'water work', and to SERC for their support.

References

(1) A. Hodgson, J.P. Simons, M.N.R. Ashfold, J.M. Bayley and R.N. Dixon, Chem.Phys.Letters, 107, 1, (1984); Mol. Phys., 54, 351 (1985)
(2) R.N. Dixon, Mol. Phys. 54, 333, (1985)
(3) J.P. Simons and A.J. Smith, Chem.Phys.Letters, 97, 1, (1983) J.P. Simons, A.J. Smith and R.N. Dixon, J.Chem.Soc. Faraday II 80, 1489, (1984)
(4) D. Imre, J.L. Kinsey, A. Sinha and J. Krenos, J.Phys.Chem. 88, 3956 (1984)
(5) Y.-C. Hsu, M.A. Smith and S.C. Wallace, Chem.Phys.Letters 111, 219 (1984)
(6) M.P. Docker, A. Hodgson and J.P. Simons, Mol.Phys., in press.
(7) R.N. Dixon, Chem.Phys. 93, 293 (1985)
(8) T. Carrington, J.Chem. Phys., 41, 2012 (1964)
(9) M.N.R. Ashfold, J.M. Bayley and R.N. Dixon, Chem.Phys. 84, 35 (1984)
(10) E. Segev and M. Shapiro, J.Chem. Phys., 77, 5604 (1982)
(11) G. Ondrey, N. van Veen, J.Chem.Phys. 78, 3732 (1983)
(12) A. Jacobs, K. Kleinermanns, H. Kuge and J. Wolfrum, J.Chem.Phys., 79 3162 (1983)
(13) A. Rauk and J.M. Barriel, Chem.Phys. 25 409 (1977).

PHOTOPHYSICS OF SOME DOUBLY IONIZED MOLECULES : A STATE-TO-STATE STUDY OF THE DISSOCIATION OF CH_4^{++}

G. Dujardin, L. Hellner, S. Leach and D. Winkoun

Laboratoire de Photophysique Moléculaire du C.N.R.S.
Bâtiment 213, Université Paris-Sud - 91405 Orsay Cédex, France

Abstract

Doubly charged molecular cations are formed by photon excitation using a synchrotron excitation source. Various photophysical processes in these ions can be studied by a photoion-photoion coincidence (PIPICO) technique. The present report mainly concerns a state-to-state study of the dissociation of CH_4^{++} into the two channels $CH_3^+ + H^+$ and $CH_2^+ + H^+ + H$ in the excitation energy range 35-55 eV. Problems connected with the determination of parameters of importance in state-to-state unimolecular fragmentation studies, especially for doubly-charged ions, are raised and discussed.

I. Introduction

In the present study, double photoionization results from absorption of a single photon whose energy suffices for detaching two valence electrons. This process has to be distinguished from the Auger effect which occurs at much higher incident energies and in which core photoionization is followed by a radiationless process leading to the formation of two holes in the valence shell.

Electron correlation effects play an important role in the double photoionization (DPI) process as has been shown in the case of atoms *(1,2)*. Experimental evidence on many-body effects in the double photoionization of atoms is based on the variation of the total DPI cross-section as a function of excitation energy *(3)*. It would be more useful to obtain the DPI partial cross-sections corresponding to different final states. This information is very difficult to obtain for atoms, but we have shown that it is easier to

determine partial cross-sections for some final states in the case of molecules *(4)*.

The electronic states of doubly charged molecular cations produced by vertical transitions from the neutral ground state are well above the threshold energies for formation of the lowest dissociation products. The consequent instability or metastability of the doubly-charged photoions can lead to their rapid dissociation (Fig. 1). This propensity to dissociation results from the strong Coulomb repulsion forces between A^+ and B^+. We have used these

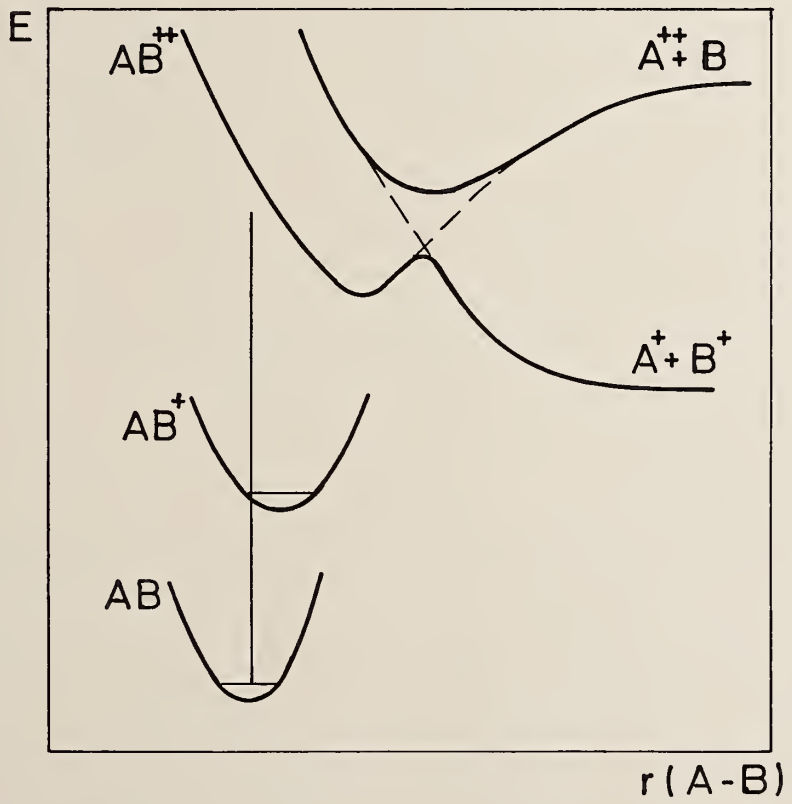

Fig. 1 - Schematic representation of potential energy surfaces of a neutral (AB), singly-ionized (AB^+) and doubly-ionized (AB^{++}) molecular species.

fragmentation properties, via photoion-photoion coincidence (PIPICO) measurements, as a specific tool for spectroscopic and dissociative relaxation studies on doubly-charged ions. The PIPICO technique has enabled us to study a number of photophysical processes in doubly charged cations. Among the species studied are SO_2 *(4)*, CH_4 *(5)*, CO_2 *(6)*, H_2O, NH_3, CH_3I and a number of diatomic species. The present report is principally concerned with electronic state-to-state dissociation processes in doubly charged methane. A fuller account of part of this work is reported elsewhere *(5)*.

II. Experimental

In the PIPICO technique we detect, with a single detector (microchannel plates), the two ionic fragments A^+ and B^+ resulting from the dissociation of a doubly-charged photoion AB^+ (Fig. 2). In the case of a polyatomic species ABC^{++} we detect the two ions resulting from various dissociation processes, e.g. $ABC^{++} \rightarrow A^+ + BC^+/AB^+ + C^+/A^+ + B^+ + C$/etc. Measurement is made, by delayed coincidence, of Δt the difference between the times of the two fragment ions. The Δt spectrum constitutes a PIPICO curve. Comparison of experimental and simulated PIPICO curves enables us to identify unambiguously the ionic fragments and the kinetic energy release in the fragmentation process. Simulation of the PIPICO spectrum is obtained by ion trajectory calculations on the basis of the ion optics conditions and as trial parameters the masses of A^+, B^+ and the kinetic energy release.

The general procedure is as follows. PIPICO spectra are measured as a function of photon excitation energy. The products of the dissociation processes are identified and the kinetic energy releases are measured . Energy thresholds for the various fragmentation processes are determined. The initial states of the doubly charged molecular ions and the final product states are identified for each process and, where possible, details of the dynamics of the dissociation are derived using all available relevant data. Before presenting results and discussion on methane, it is of interest

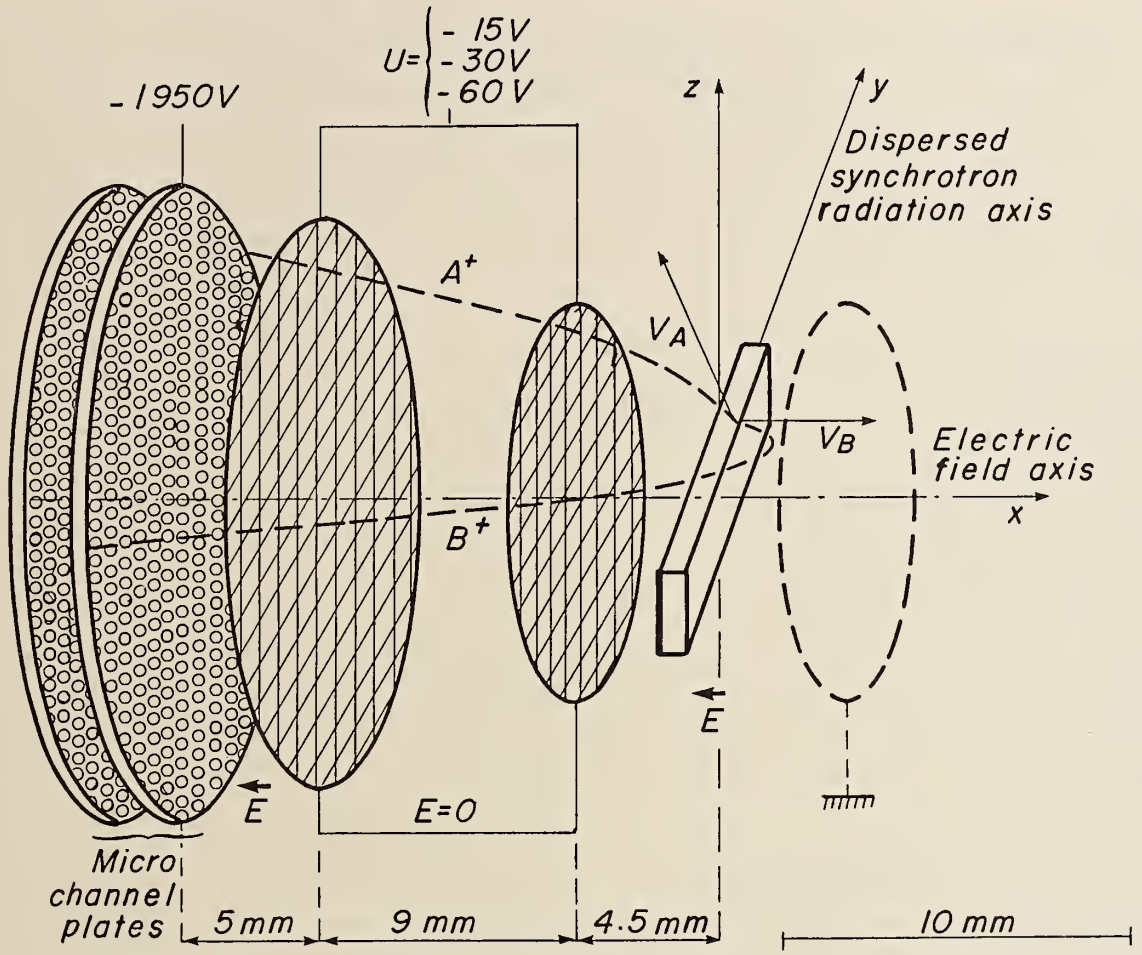

Fig. 2 - Schematic diagram of the photoion-photoion coincidence (PIPICO) apparatus. v_A and v_B are initial velocity vectors of the fragments A^+ and B^+ produced by the dissociation of a doubly charged cation.

to consider some general aspects of state-to-state studies of unimolecular processes and the problems which arise in the case of doubly-charged ions.

III. Unimolecular state-to-state reactions

The state-to-state study of the unimolecular dissociation of a photoexcited molecule requires a knowledge of the initial optically excited state - its total energy, internal energy, (ro)vibronic symmetry, etc ... - and a means of determining the nature of the fragment products, their internal energy states and corresding symmetries, and the kinetic energy release in the dissociative process. This information, coupled if possible with adequate theoretical descriptions (for which there are several different approaches and among which are trajectory calculations on the relevant potential energy surfaces), can provide detailed knowledge of the intramolecular dynamics leading to dissociation. If to these scalar properties are added vector properties (photofragment angular distributions, rotational alignment, orientation) deriving from polarisation and other studies *(7)*, a complete state-to-state study becomes theoretically available.

In such studies on neutral molecules, the characteristics of the optically excited initial state are determined from high resolution classical or laser spectroscopies, in conjunction with the appropriate theoretical models of molecular structure. Knowledge of the final, product, states is usually obtained from spontaneous infra-red or visible/ultraviolet fluorescence and/or by some form of laser probe (laser induced fluorescence, multiphoton ionization, continuum resonance Raman scattering, etc). Internal energy resolution is high in such studies, often a fraction of 1 cm^{-1}. One of the most difficult quantities to measure in the fragmentation of neutral species is the kinetic energy release, but this can be achieved using Doppler profile measurements *(8)* or time-of-flight techniques *(9)*.

Let us now consider the question of state-to-state studies of the unimolecular dissociation of singly-charged cations. If we start by photoionizing the neutral molecule, then initial state selection can be carried out, as for example in the case of SO_2^+, using coincidence techniques *(10)* such as photoelectron-photoion

coincidences (PEPICO) *(11)* at a fixed photon excitation energy or by threshold photoelectron -photoion coincidences (T-PEPICO) *(12)* at selected, variable incident photon energies. Energy resolution is no better than 20 meV in these techniques, so that the initial state can only be vibrationally defined, often not entirely unambiguously. Knowledge of the symmetries of the various electronic states in molecular ions is very often less well known than for neutral species since there is less optical spectroscopic information on molecular ions, although this area is advancing at a rapid rate *(13)*. State symmetry assignments usually rely on molecular orbital theoretical interpretations of photoelectron spectra ; this can lead to serious problems when several electronic states of the ion lie close together, as is the case for the SO_2^+ ion in the 16 eV region. Kinetic energy release distributions and product angular distributions can be fairly readily measured on singly-charged molecular ions and this provides some useful information for understanding the dissociation dynamics *(14)*.

Of course, the photon excitation of already formed singly-charged molecular ions gives the possibility of high resolution studies both in the initial state selectivity and in the determination of kinetic energy releases. Work of this kind, which makes use of laser excited ions in traps or ion beams and the kinematic compression effect, has mainly been on diatomic ions and a number of polyatomic ions *(15,16)*. Much of this work has had an emphasis on spectroscopy rather than on state-to-state dynamics *(17,18)*.

We turn now to the problem of state-to-state studies in <u>doubly-charged ions</u>. The field is only just beginning to develop. A number of special problems arise in assigning initial and final states. First of all information on the <u>initial states</u> is not immediately obtained. We note that because two electrons are ejected in double photoionization the corresponding photoelectron spectra would not give discrete lines but, for each ionization process, two broad photoelectron bands would be obtained. Chang and Poe have shown, in a theoretical study of the double photoionization of neon, that DPI probability is greatest for simultaneous ejection of a low-

kinetic-energy photoelectron and of a high-kinetic-energy photoelectron *(19)*. In our work the initial state is determined by the reasonable assumption that each separate fragmentation process observed occurs from a different electronic state. Determination of the threshold energy for a particular dissociation process then gives the vertical energy of the initial electronic state of the doubly-charged cation. This initial state vertical energy can be determined at best to within about 0.3 eV for polyatomic *(4-6)* and about 0.1 eV for diatomic species. Assignment of the symmetry of the various electronic states of doubly-charged molecular ions is hampered by the absence of independent spectroscopic information and by the fact that the density of electronic states would be much higher than for a neutral isoelectronic molecule because of the nuclear charge scaling factor. For the moment we determine electronic state symmetries of doubly charged ions by comparison of our experimentally determined energies with the energies and symmetries calculated by more-or-less sophisticated molecular-orbital methods *(5,6)* or from a simple Koopmans approximation approach *(4)*. There is an urgent need for more theoretical work on doubly-charged ion electronic states. Further information which aids in electronic state assignements can be obtained from the use of results on fragmentation dynamics from which geometrical aspects of the initial state can be estimated *(20)*.

Information on final states is obtained from the following equation :

$$E_{exc}(ABC^{++}) = E_{diss}(AB^{+} + C^{+}) + E_{int}(AB^{+}) + E_{t}(AB^{+} ; C^{+}) \qquad (1)$$

where the three measured or known parameters are $E_{exc}(ABC^{++})$, the excitation energy of photons incident on ABC, $E_{diss}(AB^{+} + C^{+})$, the thermodynamic onset for forming AB^{+} and C^{+} in states of specific internal energies, and $E_{t}(AB^{+} ; C^{+})$ the kinetic energy released in the fragmentation process $ABC^{++} \rightarrow AB^{+} + C^{+}$. The internal energy of the AB^{+} product, $E_{int}(AB^{+})$ can thus be determined from equation (1). This internal energy is usually rovibrational but can be electronic in content. From particular dynamic situations (based on assumed geometry of the initial state), one can surmise whether

the internal energy in the AB^+ product will mainly be in vibrational form or whether a rotational contribution is expected.

An example of our electronic state-to-state studies on doubly-charged molecular ions is provided by the case of CH_4^{++} discussed below.

IV. Results and Discussion

A. Methane

The double photoionization study of methane is reported in detail elsewhere *(5)*. Two dissociation processes were identified.

1) $CH_4^{++}(\tilde{X}^3T_1) \rightarrow CH_3^+(\tilde{X}^1A_1') + H^+$: the excitation onset for this process was found to be 35.0 eV (the energy origin is the vibrationless ground state of neutral CH_4). The thermodynamic threshold for this dissociation is at 27.8 eV. Measured kinetic energy release was 5.3 ± 1.1 eV at E_{exc} = 37 eV, with little apparent modification of the PIPICO spectrum over the excitation energy range 35.3 - 38.5 eV. From equation 1 we find that the CH_3^+ fragment is thus formed with internal energy of 3.9 ± 1.1 eV at E_{exc} = 37.0 eV. The amount of internal energy in CH_3^+ apparently increases from ≈ 2 to ≈ 5 eV between 35.0 and 38.5 eV excitation energy (based on the similitude between the PIPICO spectral shapes over this energy range). This internal energy can only be in the $\tilde{X}^1A_1'$ state of CH_3^+ over most of the E_{exc} range 35.0 - 38.5 eV. However, the thermodynamic threshold for the process $CH_4^{++} \rightarrow CH_3^+(\tilde{a}^3E') + H^+$ is at 32.7 eV *(5)*, so that at the upper end of this excitation range, the internal energy could be electronic in forming the $CH_3^+(\tilde{a}^3E')$ state.

The products $CH_3^+(^1A_1') + H^+(^1S)$ correlate not with the $\tilde{X}^3T_1$ ground state, but with the $\tilde{c}^1A_1$ excited state of CH_4^{++}. The latter should lie a few electron volts above the ground state and is expected to be the highest in energy of the four states ($\tilde{X}^3T_1$, $\tilde{a}^1E$, $\tilde{b}^1T_2$, $\tilde{c}^1A_1$) corresponding to the lowest electron configuration $(1a_1)^2(2a_1)^2(1t_2)^4$ of CH_4^{++}. Because we are concerned with vertical excitation processes, the electronic orbital and state symme-

tries are given in the T_d point group of the parent neutral methane molecule ; the ground state of CH_4^{++} is expected to be planar and have D_{4h} point-group symmetry *(21)*). Thus the dissociation of $CH_4^{++}(^3T_1)$ into electronically unexcited products must result from a predissociation and not a direct dissociative process. On the basis of the calculations of Siegbahn *(22)* on the $CH_3^+ + H^+$ dissociation channel, this predissociation process involves an electron transfer in going from the "covalent" $\tilde{X}^3T_1$ surface (which tends to dissociate to CH_3^{++} + H) to the Coulomb repulsion curve giving the $CH_3^+(^1A_1') + H^+(^1S)$ products.

Dissociation products $CH_3^+(\tilde{a}^3E') + H^+(^1S)$ could correlate with $CH_4^{++}(^3T_1)$ so that if this fragmentation channel is operative it could result from a direct dissociation process or a homogenous-type predissociation in the appropriate region(s) of the potential energy hypersurfaces.

It is of interest to compare E_t/E^*, the ratio of the total kinetic energy release E_t to the total available excess energy E^* above the dissociation limit for the process $CH_4^{++} \rightarrow CH_3^+ + H^+$, and the value for the corresponding neutral molecule process $CH_4 \rightarrow CH_3 + H$. For an identical value $E^* = 6.5$ eV, the doubly charged ion dissociation channel would correspond to $E_t/E^* \approx 0.8$ whereas for the neutral molecule a value of $E_t \approx 0.3$ eV was calculated for the maximum of the distribution of E_t *(23)*, giving a ratio $E_t/E^* \approx 0.04$ for the $CH_4 \rightarrow CH_3 + H$ process. We note that the neutral dissociation is endothermic by 4.58 eV so that the input energy of 6.5 eV is well above that for fragmentation. No experimental data appears to be available on the neutral system. The difference in the behaviour of the doubly-charged and neutral species reflects the quite different nature of the forces operative in the two cases.

2) $CH_4^{++}(\tilde{a}^1E) \rightarrow CH_2^+(\tilde{X}^2A_1) + H^+ + H(^2S)$: The corresponding thermodynamic threshold energy is 33.3 eV *(5)*. We find that the excitation threshold energy for this process is 38.5 eV. Dissociation into three products is more complex than the two products case previously discussed. Conservation of momentum and energy is no longer sufficient to determine the partition of the total momentum and kinetic

energy into the products. Simulations of the PIPICO spectra were therefore made on the basis of three different dynamic models (i) a simultaneous fragmentation statistical process based on the three-body fragmentation model of Baer et al *(24)* ; (ii) an impulsive model in which we assumed that the H^+ and H fragments have equal momenta, directed along the C-H bond directions ; (iii) a Coulomb repulsion model in which CH_2^+ and H^+ fly apart at 180° from each other and the H-atom carries off little or no kinetic energy. Fig. 3 shows : curve a, the experimental PIPICO curve at 42 eV photon excitation energy after subtraction of the contribution of the $CH_4^{++} \rightarrow CH_3^+ + H^+$ channel to the measured PIPICO curve at this energy ; curve b, the simulated PIPICO curve corresponding to the $CH_4^{++} \rightarrow CH_2^+ + H^+ + H$ dissociation channel, within the statistical model ; curve c, same dissociation channel but within the impulsive model ; curve d, for the same dissociation channel but within the Coulomb repulsion model. Good agreement

Fig. 3 - $CH_4^{++}(\tilde{a}^1E) \rightarrow CH_2^+ + H^+ + H$ dissociation. Experimental (curve a) and simulated (curves b, c, d) PIPICO spectra at E_{exc} = 42 eV. (see text for details)

with experimental PIPICO spectra was obtained only on the basis of the Coulomb repulsion model. This demonstrates the major role of Coulomb repulsion in the fragmentation process. The derived parameters at E_{exc} = 4 2 eV are as follows. The total kinetic energy release E_t = 5 eV, the kinetic energies taken up by H^+ and CH_2^+ are respectively $E_{kin}(H^+) = 0.93\ E_t$, $E_{kin}(CH_2^+) = 0.07\ E_t$, angle between the H^+ and CH_2^+ velocity vectors = 180°.

At E_{exc} = 42 eV we obtain a value of $E_{int}(CH_2^+)$ = 3.7 eV. This may be in vibrational energy but also in part in electronic energy since the channel $CH_4 \rightarrow CH_2^+(\tilde{A}^2B_1) + H^+ + H(^2S)$ lies only 1.7 eV above the nonexcited triple product channel *(5)*.

Finally we mention that the channels $CH_4 + h\nu \rightarrow CH_2^+ + H_2^+$, whose E_{diss} = 30.5 eV, and $CH_4 + h\nu \rightarrow CH^+ + H^+ + (H_2$ or 2 H) whose E_{diss} = 33.4 or 37.9 eV have been detected by Fournier et al *(25)* uisng the PIPICO technique at a fixed (HeII) excitation energy E_{exc} = 40.1 eV. These channels have branching ratios which are considerably smaller than for the two channels we observed in our synchrotron radiation source experiments. They would have been difficult to observe under our experimental conditions.

Concluding remarks

In the present report we have discussed how the PIPICO technique provides information on the state-to-state dissociation of doubly charged molecular ions and we have outlined the specific procedures and problems for determining initial and final states and fragmentation product internal and translational energies. Much theoretical work is called for on various aspects of the photophysics of doubly charged ions in order to clarify initial and final state assignments and the intramolecular dynamics of fragmentation. We remark that besides the study of electronic state-to-state dissociation processes, the PIPICO technique has enabled us to study the partial and total cross-sections for DPI, threshold behaviour in DPI, and electron correlation effects in DPI. The corresponding results are reported elsewhere *(4-6,26)*.

REFERENCES

1) F.W. Byron and C.J. Joachain, Phys. Rev. 164, 1 (1967).

2) T.N. Chang, T. Ishihara and R.T. Poe, Phys. Rev. Lett. 27, 838 (1971).

3) D.M.P. Holland, K. Codling, J.B. West and G.V. Marr, J. Phys. B12, 2465 (1979).

4) G. Dujardin, S. Leach, O. Dutuit, P.-M. Guyon and M. Richard-Viard, Chem. Phys. 88, 339 (1984).

5) G. Dujardin, D. Winkoun and S. Leach, Phys. Rev. A31, 3027 (1985).

6) G. Dujardin and D. Winkoun, submitted to J. Chemical Phys.

7) J.P. Simons, J. Phys. Chem. 88, 1287 (1984); C.H. Greene and R.N. Zare, Ann. Rev. Phys. Chem. 33, 119 (1982).

8) K.H. Welge and R. Schmiedl in Photoselective Chemistry Part 2 (ed. J. Jortner, R.D. Levine and S. Rice; Wiley, N.Y. 1981), p. 133; R. Vasudev, R.N. Zare and R.N. Dixon, J. Chem. Phys. 80, 4863 (1984).

9) G.E. Busch and K.R. Wilson, J. Chem. Phys. 56, 3626, 3638, 3655 (1972).

10) S. Leach, in Photophysics and Photochemistry above 6 eV (ed. F. Lahmani; Elsevier, Amsterdam, 1985), p. 113.

11) B. Brehm, J.H.D. Eland, R. Frey and A. Küstler, Int. J. Mass Spectrom. Ion Phys. 12, 197 (1973).

12) G. Dujardin, T. Govers, S. Leach and D. Winkoun in Photophysics and Photochemistry above 6 eV (ed. F. Lahmani, Elsevier, Amsterdam, 1985); p. 163.

13) D. Klapstein, J.P. Maier and L. Misev in Molecular Ions : Spectroscopy, Structure and Chemistry (ed. T.A. Miller and V.E. Bondybey; North-Holland, Amsterdam, 1983), p. 175.

14) J.H.D. Eland, Photoelectron Spectroscopy, 2nd edition (Butterworths, London, 1984), chap. 7.

15) R. Dunbar in Molecular Ions : Spectroscopy, Structure and Chemistry (eds. T.A. Miller and V.E. Bondybey; North-Holland, Amsterdam, 1983), p. 231.

16) F.M. Harris and J.H. Beynon in Gas Phase Ion Chemistry, Vol. 3 (ed. M.T. Bowers; Academic, N.Y., 1984), p. 100.

17) A. Carrington and T.P. Softley in Molecular Ions : Spectroscopy, Structure and Chemistry (eds. T.A. Miller and V.E. Bondybey; North-Holland, Amsterdam, 1983), p.49.

18) A. Carrington and R.A. Kennedy in Gas Phase Ion Chemistry, Vol. 3. (ed. M.T. Bowers, Academic, N.Y., 1984), p. 393.

19) T.N. Chang and R.T. Poe, Phys. Rev. A12, 1432 (1975).

20) S. Leach, unpublished work on CO_2^{++}.

21) A.F. Saturno, Theor. Chim. Acta 7, 273 (1967).

22) E.M. Siegbahn, Chem. Phys. 66, 443 (1982).

23) R. Viswanathan, L.M. Raff and D.L. Thompson, J. Chem. Phys. 80, 6141 (1984); 81, 3118 (1984).

24) T. Baer, A.E. De Pristo and J.J. Hermans, J. Chem. Phys. 76, 5917 (1982).

25) P.G. Fournier, J. Fournier, F. Salama, P.J. Richardson and J.H.D. Eland, unpublished results.

26) G. Dujardin, S. Leach and D. Winkoun in Photophysics and Photochemistry above 6 eV (ed. F. Lahmani; Elsevier, Amsterdam, 1985), p. 63.

THE ION-MOLECULE REACTION OF $O_2^+ + CH_4 \rightarrow CH_2OOH^+ + H$

Eldon E. Ferguson
Aeronomy Laboratory, National Oceanic and Atmospheric Administration, and Department of Chemistry, University of Colorado, Boulder, CO, U.S.A.

The reaction between O_2^+ and CH_4 to produce methylene hydroperoxy cation (CH_2OOH^+) and H atoms is one of the ion-molecule reactions which has been studied in most detail. The reaction has been studied in various flowing afterglow and flow-drift tube systems and to very low temperatures in a uniform gas expansion through a converging-diverging nozzle. The reaction has been studied for all of the H/D isotopic forms of methane. Extensive studies of the reactivity of the product ion have established its structure, and in conjunction with ab initio theory, its heat of formation. From this wealth of data a detailed reaction mechanism is deduced for this complex reaction. This is an outstanding example of the utility of bulk flow gas techniques to contribute to a detailed understanding of complicated reaction processes, an approach largely unexploited.

The first measurement reported for the reaction

$$O_2^+ + CH_4 \rightarrow CH_3O_2^+ + H \qquad (1)$$

was by Franklin and Munson[1], who found the reaction to be inefficient, occurring on about 1% of the collisions, and to have a definite isotope effect, CH_4 being more reactive than CD_4. Franklin and Munson believed the product ion was most likely protonated formic acid, $HC(OH)_2^+$.

Dotan et al.[2] found the reaction to increase drastically with increased relative kinetic energy, to 2×10^{-10} cm^3 s^{-1} at 1 eV, and they found CH_3^+ to be a major product at elevated energy. They also found the enhancement to be much greater in Ar buffer gas than in He buffer gas, which they suggested might be due to vibrational excitation of the O_2^+ in Ar buffer gas, followed by a vibrational enhancement of the rate constant. Several measurements[2]-[6] are in good agreement on the rate constant for (1) at 300K, about 6×10^{-12} cm^3 s^{-1}.

Both Nestler and Warneck[5] and Dotan et al.[6] found the reaction

$$O_4^+ + CH_4 \rightarrow O_2^+ \cdot CH_4 + O_2 \qquad (2)$$

to occur slowly.

There has recently been a revived interest in this reaction. Villinger et al.[7],[8] reported that the product ion of reaction (1) was protonated formic acid, $HC(OH)_2^+$. They deduced this by comparison of the threshold collisional break-up and the isotope exchange rates with D_2O of the $CH_3O_2^+$ product ion from (1) with known protonated acid. Recently Holmes et al.[9] reached the same conclusion based on high energy collisional breakup of isomeric $CH_3O_2^+$ ions.

These results stimulated us to study this reaction in greater detail, since the production of protonated formic acid, $HC(OH)_2^+$ in reaction (1) would require the breaking (and making) of four chemical bonds! Finding a mechanism for such a complex concerted reaction was an intriguing challenge.

Reaction (1) was measured[10] between 20K and 560K and found to exhibit a minimum in rate constant, $k_1 = 5.4 \times 10^{-12}$ cm^3 s^{-1} near 300K, increasing to 4.7×10^{-10} cm^3 s^{-1} at 20K and increasing to 7.4×10^{-12} cm^3 s^{-1} at 560K.

In detailed studies of the O_2^+ vibrational state dependence of (1) it has been found[11] that $O_2^+(v=1)$ ions are vibrationally quenched in about half the collisions with CH_4, $k_q = 6 \times 10^{-10}$ cm^3 s^{-1}, that $O_2^+(v=2)$ reacts rapidly, $k = 7 \times 10^{-10}$ cm^{3}s^{-1}, with CH_4 to give both CH_3^+ (77%) and $CH_3O_2^+$ (23%), while $O_2^+(v=3)$ reacts with CH_4 at near the collision frequency, ~ 10^{-9} cm^3 s^{-1}, primarily by charge-transfer to give CH_4^+.

Very recently, Tanaka et al.[12] have studied $O_2^+(v) + CH_4$, v = 0,1,2,3 at a fixed relative kinetic energy, 0.27 eV, by threshold electron-secondary ion coincidence technique, supporting the finding of vibrational enhancement for (1).

A breakthrough in understanding this reaction has recently occurred with the discovery that the product ion is not protonated formic acid, $HC(OH)_2^+$, but rather methylene hydroperoxy cation, H_2COOH^+[13]. This was deduced from the reactivity of the product $CH_3O_2^+$ ion. The ion reacts with many neutrals that protonated formic

acid does not react with, and indeed for which reaction with protonated formic acid would be quite endothermic. The reactions observed were hydride ion (H^-) abstraction from alkanes, proton transfer to neutrals of large proton affinity, and OH^+ transfer to several neutrals. The heat of formation is determined to be ~ 186 kcal mol^{-1}, compared to 97 kcal mol^{-1} for protonated formic acid. This deduction of $\Delta H_f(H_2COOH^+)$ is guided by theoretical calculations[14],[15] since the neutral products of H_2COOH^+ reactions with neutrals are not determined, leading to some ambiguity. Specifically, we infer that the product of H^- transfer to H_2COOH^+ yields H_3COOH, rather than the much more exothermic products $H_2CO + H_2O$. This assumption leads to a $\Delta H_f(H_2COOH^+)$ in excellent agreement with theory[14],[15], whereas the formaldehyde + water assumption would lead to disagreement far outside the uncertainty in the theoretical calculations. This makes the exothermicity of reaction (1) ~ 22 kcal mol^{-1}.

Another experimental result bearing on mechanism is the finding[16] that changes in relative kinetic energy of the reactants $O_2^+ + CH_4$ are about 1/8 as efficient in changing the reaction rate constant as is an equivalent change in kT, using the relationship KE = 3/2 kT. This suggests a long-lived complex in which the relative kinetic energy is randomized into approximately 8 internal modes prior to reaction.

One of the lines of investigation providing the most insight into the mechanism for reaction (1) is the study of the CH_4 isotope effects[17]. There is a primary kinetic isotope which gives a nearly linear increase of rate constant with number of H atoms, going from CD_4 to CH_4. Surprisingly, there is a nearly statistical distribution of product ions, e.g. $O_2^+ + CH_2D_2$ gives an equal number of $CH_2DO_2^+$ and $CHD_2O_2^+$ ions.

With all of this information on hand, we are in a position to delineate the mechanism of the reaction in some detail. Our proposed mechanism[17] is the following:

$$O_2^+ + CH_4 \underset{k_u}{\overset{k_c}{\rightleftarrows}} (O_2^+ \cdot CH_4)^* \xrightarrow{k_{H^-}} (C^+H_3 \cdot O_2H) \xrightarrow{k_H} H_2COOH^+ + H \quad (3)$$

A long-lived complex is formed at about the collision frequency, $k_c = 1.1 \times 10^{-9}$ cm^3 s^{-1}. This process is reversible, and at 300K

reverses most (99.5%) of the time. The unimolecular decomposition rate constant (or reciprocal lifetime) is ~ 10^9-10^{10} s^{-1}. This is inferred from the observed vibrational quenching rate constant of $O_2^+(v=1)$ by CH_4, $k_q = 6 \times 10^{-10}$ cm^3 s^{-1}, in conjunction with a recent model proposed[18] for the vibrational predissociation with a rate constant k_{vp} ~ 10^9-10^{10} s^{-1}.

Reaction to products is initiated by H^- transfer from CH_4 to O_2^+, leading to a complex of the form $H_3C^+ \cdot\cdot O_2H$. It is 5 kcal mol^{-1} endothermic for the CH_3^+ and HO_2 to separate, but of course this energy is much less than the electrostatic attraction between O_2^+ and CH_4, which is 9 kcal mol^{-1}[20], or than the electrostatic attraction between CH_3^+ and the very polar HO_2. This rate controlling reaction step has an isotope effect, $k_H-/k_D- = 3.0$, favoring H^- transfer. This accounts for the rate constant dependence of the reaction on H/D ratio of the deuterated methane. This also accounts for the relative number of OH and OD groups in an isotopically mixed H_2COOH^+ ion. For example, $O_2^+ + CH_2D_2$ gives three times as many product ions containing OH groups as OD groups, because of the factor three favoring H^- transfer over D^- transfer. The H^- (or D^-) transferred in this step is retained in the final ion product, hence favoring H enrichment in the product ion. The next, and final, reaction step is the ejection of one of the hydrogen atoms bonded to the carbon atom. H atom ejection is favored over D atom ejection, $k_H/k_D = 1.4$. This step is not rate controlling and hence does not affect the overall reaction rate constant. It does, however, affect the final $CH_3O_2^+$ isotopic composition. Since H is preferentially ejected, this step enriches the product ion in D. This D atom enrichment nearly offsets the H atom enrichment occurring in the hydride ion transfer step so that the product ion distribution is nearly statistical. The two isotope fractionation parameters, $k_H-/k_D- = 3.0$, $k_H/k_D = 1.4$ fit ten observable isotopic parameters, i.e. rate constants and composition to within the experimental uncertainties of about 5%. The ratio $k_H/k_D = 1.4$ is actually not a free parameter as we have used it to fit the composition data, but rather the high energy limit of the primary intermolecular isotope effect[19], $k_H/k_D = \sqrt{\mu_D/\mu_H} \approx 1.4$.

The well depth for $(O_2^+ \cdot CH_4)^*$ has been determined by Böhringer and Arnold[20] to be 9 kcal mol^{-1} from a study of the equilibrium between O_4^+ and $O_2^+ \cdot CH_4$ (reaction 2 and its reverse) as a function of temperature between 87 and 300K.

There is a barrier to hydride abstraction in this complex because the $O_2^+ \cdot CH_4$ product from reaction (2) is stable, i.e. CH_4 attached to O_2^+ without falling through the 9 kcal mol^{-1} attractive potential does not hydride ion transfer and thus lead to $CH_3O_2^+$. In fact, this barrier is very high, within a few kcal mol^{-1} of the dissociation limit to $O_2^+ + CH_4$. This can be inferred from the three-body association measurement of Böhringer and Arnold[20],

$$O_2^+ + CH_4 + He \rightarrow O_2^+ \cdot CH_4 + He \qquad (4)$$

who found $k_4 = 1.8 \times 10^{-29}$ cm^6 s^{-1} at 146K. Three-body association to produce $O_2^+ \cdot CH_4$ occurs by collisional stabilization of the $(O_2^+ \cdot CH_4)^*$ complex in collision with He. However, only a small average energy transfer occurs per collision, ~ kT, and the probability of an energy transfer larger than the average falls off exponentially so that the barrier to H^- transfer and thus reaction to $CH_3O_2^+$ must be very close to the dissociation limit, probably within one or two kcal mol^{-1}.

The ion H_2COOH^+ is thermodynamically unstable toward decomposition into $HCO^+ + H_2O$ (and also $H_3O^+ + CO$). This does not occur spontaneously but does occur[17] with an activation energy of 22 ± 6 kcal mol^{-1}. This suggests that the neutral products of proton transfer from H_2COOH^+ are $CO + H_2O$ and that a proton bound to carbon (and not to oxygen) is transferred. The mechanistically simpler transfer of the oxygen proton to leave H_2COO is very endothermic for the reactions observed[13]. This suggests that the "effective proton bonding energy" of H_2COOH^+ should be approximately equal to the proton affinity of CO (139 kcal mol^{-1}) plus the barrier height to produce $HCO^+ + H_2O$, 22 ± 6 kcal mol^{-1}, or 161 ± 6 kcal mol^{-1}. This is consistent with the rather broad limits deduced from observed proton transfers or their failure to occur[13].

The double minimum potential surface deduced for this reaction, and the relatively slow reaction rate constant with a negative temperature dependence, corresponds to a model developed over the years by Brauman and his colleagues, which has been recently reviewed by

Comita and Brauman[21]. A quantitative model leads to good agreement on the rate constant and its temperature dependence, and fair agreement on the magnitude of the isotope effect[17].

Our studies of this reaction are not yet complete, but already it appears that this reaction may stand as a milepost in the determination of reaction mechanisms using bulk gas flow techniques.

Acknowledgments: The support of the Defense Nuclear Agency of the Aeronomy Laboratory ion chemistry program is gratefully acknowledged. I am indebted to my colleagues listed in reference 17 for the results cited in this summary of that research, and to Drs. Böhringer and Arnold for supplying their results prior to publication.

References

(1) J.L. Franklin and M.S.B. Munson, Tenth International Symposium on Combustion (1965), Pittsburgh, PA, pp. 561-568.
(2) I. Dotan, F.C. Fehsenfeld, and D.L. Albritton, J. Chem. Phys. 68, 5665 (1978).
(3) B.R. Hollebone and D.K. Bohme, J. Chem. Soc. Faraday Trans. 269, 1569 (1973).
(4) D. Smith. N.G. Adams and T.M. Miller, J. Chem. Phys. 69, 308 (1978).
(5) V. Nestler and P. Warneck, Chem. Phys. Lett. 45, 96 (1977).
(6) I. Dotan, J.A. Davidson, F.C.Fehsenfeld and D.L. Albritton, J. Geophys. Res. 83, 4036 (1978).
(7) H. Villinger, R. Richter, and W. Lindinger, Int. J. Mass Spectrom. Ion Phys. 51, 25 (1983).
(8) H. Villinger, A. Saxer, R. Richter, and W. Lindinger, Chem. Phys. Lett. 96, 513 (1983).
(9) J.L. Holmes, A.A. Mommers, C. DeKoster, W. Heerma, and J.K. Terlouw, Chem. Phys. Lett. 115, 437 (1985).
(10) B.R. Rowe, G. Dupeyrat, J.B. Marquette, D. Smith, N. Adams, and E.E. Ferguson, J. Chem. Phys. 80, 241 (1984).
(11) M. Durup-Ferguson, H. Böhringer, D.W. Fahey, F.C. Fehsenfeld, and E.E. Ferguson, J. Chem. Phys. 81, 2657 (1984).
(12) K. Tanaka, T. Kato, and I. Koyano, Atomic Collision Research in Japan -Progress Report No. 9 (1983), p. 73; J. Chem. Phys. 84, 750 (1986).
(13) J.M. Van Doren, S.E. Barlow, C.H. DePuy, I. Dotan, and E. E. Ferguson, J. Phys. Chem. (to be submitted).
(14) T.K. Ha and M.T. Nguyen, J. Chem. Phys. 88, 4295 (1984).
(15) Michael Frisch, Sandia National Laboratories, Livermore, CA (private communication).
(16) N.G. Adams, D. Smith, and E.E. Ferguson, Int. J. Mass Spectrom. Ion Processes. 67, 67 (1985).
(17) S.E. Barlow, J.M. Van Doren, V. Bierbaum, C.H. DePuy, I. Dotan, E.E. Ferguson, M. Durup-Ferguson, D. Smith, N.G. Adams, B. Rowe, J.B. Marquette, and G. Dupeyrat (to be published).
(18) W. Federer, W. Dobler, F. Howorka, W. Lindinger, M. Durup-Ferguson, and E.E. Ferguson, J. Chem. Phys. 83, 1032 (1985).

(19) W. Forst, Theory of Unimolecular Reactions, Academic Press, NY (1973), p. 389.
(20) H. Böhringer and F. Arnold, J. Chem. Phys. Feb. 15, 1986.
(21) P. B. Comita and J. I. Brauman, Science 227, 863 (1985).

Thermochemistry, Structure and Reactivity of the Trifluoromethoxy Radical

J. S. Francisco and J. I. Steinfeld
Massachusetts Institute of Technology, Cambridge, Mass. 02139, U.S.A

I. H. Williams
University of Cambridge, U.K.

The importance of halomethanes in the chemistry of the atmosphere relates to their possible threat to the stratospheric ozone layer via photodissociation to $X^{\cdot}$ and $CX_3^{\cdot}$ (where X = F and Cl) radicals, but relatively little is known regarding the fate of the latter fragment. In order to investigate the role of CX_3 radicals in the chemistry of the atmosphere, thermochemical estimates [1] have been made for reactive intermediates which may be involved in the oxidation of $CX_3^{\cdot}$. In this study we consider the fate of the simplest trihalomethyl fragment, $CF_3^{\cdot}$. The reactions of $CF_3^{\cdot}$ with O_2 and O_3 yield species $CF_3O^{\cdot}$, $CF_3O_2^{\cdot}$ and $CF_3O_3^{\cdot}$ for which thermochemical estimates are given in Table 1. On the basis of these estimates, the important atmospheric catalytic cycles involving these species in the destruction of ozone are summarized below:

Cycle I

$$CF_3^{\cdot} + O_2 \rightarrow CF_3O_2^{\cdot} \qquad \Delta H = -37 \text{ Kcal/mol} \quad (1)$$

$$CF_3O_2^{\cdot} + O_3 \rightarrow CF_3O^{\cdot} + 2O_2 \qquad \Delta H = -41 \text{ Kcal/mol} \quad (2)$$

$$CF_3^{\cdot} + O_2 + O_3 \rightarrow CF_3O^{\cdot} + 2O_2$$

Cycle II

$$CF_3^{\bullet} + O_3 \rightarrow CF_3O_3^{\bullet} \qquad \Delta H = -58 \text{ Kcal/mol} \quad (3)$$

$$CF_3O_3^{\bullet} \rightarrow CF_3O^{\bullet} + O_2 \qquad \Delta H = -20 \text{ Kcal/mol} \quad (4)$$

$$CF_3^{\bullet} + O_3 \rightarrow CF_3O^{\bullet} + O_2$$

However, catalytic destruction of ozone would be possible only if O-atom abstraction (5) is faster than the more exothermic F• atom abstraction (6).

$$CF_3O^{\bullet} + O \rightarrow CF_3^{\bullet} + O_2 \qquad \Delta H = -15 \text{ Kcal/mol} \quad (5)$$

$$\rightarrow CF_2O + FO^{\bullet} \qquad \Delta H = -45 \text{ Kcal/mol} \quad (6)$$

Furthermore, the intermediate trifluoromethoxy radical is also a source of fluorine atoms (via reaction 7) which are involved in the catalytic ozone destruction:

$$CF_3O^{\bullet} \rightarrow CF_2O + F \qquad \Delta H = +23 \text{ Kcal/mol} \quad (7)$$

From these thermochemical considerations, it is apparent that $CF_3O^{\bullet}$ may be important in CF_3X oxidation.

There have been several experimental attempts to detect $CF_3O^{\bullet}$. Christe and Pilipovich [2] attempted to isolate $CF_3O^{\bullet}$ by trapping the products of a low-pressure pyrolysis of CF_3OOCF_3 in argon at 8 K, but found no evidence for the radical in the matrix. Chen and Kochi [3] studied the photolysis of CF_3OOCF_3 by electron spin resonance spectroscopy, but $CF_3O^{\bullet}$ could not be detected directly. Rossi et al. [4] studied the reaction of $CF_3^{\bullet}$ radicals with ozone, but again the $CF_3O^{\bullet}$ radical was not observed. Infrared multiphoton decomposition of CF_3OOCF_3 yields trifluoromethoxy radicals [5,6], but as yet these have eluded direct experimental observation. Consequently ab initio quantum-chemical methods have been used to predict the structure and

vibrational spectrum of this radical [7].

Ab initio calculations were performed using the Cambridge analytic derivative package (CADPAC) at the 3-21G level of open-shell theory. The optimized geometries for the low lying excited states of $CF_3O^{\bullet}$ are given in Table 2. The ground electronic state in C_{3v} is degenerate (^2E) and undergoes Jahn-Teller distortion. Geometry optimization in C_s symmetry yields stationary points for the $^2A'$ and $^2A''$ states, stabilized by 0.33 and 0.28 Kcal mol^{-1} respectively, relative to the C_{3v} symmetrical structure. Analytical determination of the second derivatives reveals that the $^2A'$ structure is at a true minimum, but the $^2A''$ structure is at a saddle point on the potential energy hypersurface. Furthermore, the $^2A'$ and $^2A''$ structures are connected by pseudo-rotational procession about C_3 axis of the ^2E structure. The $^2A'$ first excited state of C_{3v} symmetry is calculated to be 30937 cm^{-1} above the ground ^2E state at the RHF/3-21G level.

Vibrational frequencies and relative intensities for the $^2A'$ state are presented in Table 3. These results, along with predicted vibrational frequencies for difluorodioxane [8], now allow us to comment upon the previously published work concerning the formation of CF_3O from the low-pressure pyrolysis of bis-(trifluoromethyl) peroxide, CF_3OOCF_3 [2]. Two sets of infrared absorption bands were reported in Ref. 2. One set of bands was still present at 42 K in a controlled-diffusion experiment; these were reported at 1897, 899, 824, 389 and 336 cm^{-1}. Bands at 1592, 1025, 986, 319 and 268 cm^{-1} had disappeared and there was uncertainty as to whether bands at 1271, 1076 and 659 cm^{-1} had also disappeared. It was concluded that at least two different species were involved. The possibility that some of the

unassigned infrared absorptions observed by Christe and Pilipovich [2], following low-pressure pyrolysis of CF_3OOCF_3, might be due to trifluoromethoxy radicals may be discounted on the grounds that those frequencies bear no relation to those calculated for CF_3O. Some of the bands which disappeared at 42 K show a resemblance to those predicted for difluorodioxane, and thus suggest that these bands may be due to difluorodioxane, but the evidence is inconclusive. Nevertheless, one species which might account for the absorptions still present at 42 K is trifluoromethyl fluoroformate, which has strong absorptions at 1901 cm^{-1} [10]: this compound could be formed according to

$$CF_3O^{\bullet} + CF_2O \rightarrow CF_3OCFO + F^{\bullet} \qquad [8]$$

Chen and Kochi [3] studied the photolysis of CF_3OOCF_3 and though unable to detect $CF_3O^{\bullet}$ directly using ESR, found evidence for the presence of adducts of CF_3O with alkenes, as in the reaction

$$CF_3O^{\bullet} + CH_2{=}CH_2 \rightarrow CF_3OCH_2CH_2^{\bullet} \qquad [9]$$

These results lend support to the proposed reaction (8) and to the suggestion that $CF_3O^{\bullet}$ is highly reactive.

Acknowledgements

We are grateful to the Cambridge University Computing service for much assistance. JSF would like to thank St. Edmund's House at the University of Cambridge for a Research Fellowship and M.I.T. for a postdoctoral fellowship. IHW would like to thank the Royal Society for a Pickering Fellowship and Clare Hall of the University of Cambridge for a Research Fellowship. This work has also been supported by the Air Force Office of Scientific Research Grant 83-0007.

Table 1

Heats of formation (Kcal/mole) for $CF_3^{\bullet}$ and $CF_3O_x^{\bullet}$ radicals

Species	$\Delta H^{\circ}_{f,298}$
$CF_3^{\bullet}$	-112.4 ± 1.0
$CF_3O^{\bullet}$	-156.7 ± 2.3
$CF_3O_2^{\bullet}$	-149.9 ± 2.2
$CF_3O_3^{\bullet}$	-136.6 ± 3.0

Table 2

RHF/3-21G optimized geometries and energies for states of the trifluoromethoxy radical

Coordinate	$CF_3O^{\bullet}$			
	^2E (C_{3v})	$^2A'$ (C_s)	$^2A''$ (C_s)	$^2A_1$ (C_{3v})
CO (Angstroms)	1.385	1.383	1.383	1.442
CF′	1.332	1.332	1.333	1.316
CF	1.332	1.332	1.332	1.316
∢ (OCF)′ (degrees)	109.9	107.1	112.2	108.5
∢ (OCF)	109.9	111.3	108.7	108.5
∢ (FCF)′	109.1	109.5	108.6	110.5
∢ (FCF)	109.1	108.2	110.0	110.5

Table 3

Calculated vibrational frequencies and relative intensities for the $^2A'$ ground state of CF_3O·

symmetry	mode	description	Frequency (cm^{-1}) unscaled	Frequency (cm^{-1}) scaled[a]	relative intensity
a'	1	CF str., asym.	1444	1256	0.97
	2	CO str.	1397	1251	0.77
	3	CF str., sym.	932	855	0.03
	4	CF_2 wag	641	611	0.08
	5	CF_2 scissor	608	578	0.10
	6	OCF' def.	436	399	0.10
a"	7	CF str.	1470	1272	1.00
	8	CF_2 rock	636	584	0.02
	9	CF_2 twist	412	202	0.00

[a] Valence force constants scaled by factors determined for CF_2O and CF_3O^- (CO stretch 0.85, CF stretch 0.79, all bends 0.84); see reference [8].

References

[1] J. S. Francisco and I. H. Williams, submitted to J. Phys. Chem.

[2] K. O. Christe and D. Pilipovich, J. Am. Chem. Soc. 93, 51 (1971).

[3] K. S. Chen and J. K. Kochi, J. Am. Chem. Soc. 96, 1383 (1974).

[4] M. J. Rossi, J. R. Barker and D. M. Golden, J. Chem. Phys. 71, 3722 (1979).

[5] J. S. Francisco, M. A. Findeis, and J. I. Steinfeld, Intern. J. Chem. Kinetics 13, 627 (1981).

[6] Fumin Zhang, J. S. Francisco and J. I. Steinfeld, J. Phys. Chem. 86, 2402 (1982).

[7] J. S. Francisco and I. H. Williams, Chem. Phys. Lett. 110, 240 (1984).

[8] J. S. Francisco and I. H. Williams, Mol. Phys. 52, 743 (1984).

[9] J. S. Francisco and I. H. Williams, Chem. Phys. 93, 71 (1985).

[10] P. J. Aymonino, J. Chem. Soc. Chem. Commun. 241 (1965).
E. L. Varetti and P. J. Aymonino, J. Mol. Struct. 1, 39 (1967).

EXPERIMENTAL EVIDENCE FOR THE ROLE OF H_5^+ IN THE FORMATION OF RYDBERG LEVELS OF H_3 IN A HOLLOW CATHODE DISCHARGE

Gregory I. Gellene, Carl E. Krill, and Patrick E. Fleming

Department of Chemistry, University of Notre Dame, Notre Dame, Indiana 46556

J. L. Hardwick*

Radiation Laboratory, University of Notre Dame, Notre Dame, Indiana 46556

ABSTRACT

The effects of temperature and H_2 pressure on the efficiency of production of the H_3 Rydberg levels in a hollow cathode discharge cell were determined by monitoring the $3s^2A_1' \rightarrow 2p^2A_2''$ transition of H_3. Kinetic modeling of the ion-molecule reactions occurring in the discharge indicates that the rate of H_5^+/e^- recombination has a similar temperature and pressure dependency as that found for the intensity of H_3 emission. It is proposed that H_3 Rydberg levels arise from the dissociative recombination of H_5 with electrons. Anomalous Doppler broadening previously observed in the H_3 emission spectrum (I. Dabrowski and G. Herzberg, Can. J. Phys. 58, 1238 (1980)) is explained in terms of the kinetic energy released in the dissociation of H_5. Energy conservation considerations suggest that higher Rydberg levels, rather than the $3s^2A_1'$ state, are directly produced by H_5^+/e^- recombination thus predicting additional infrared and ultraviolet emission spectra of H_3 to be observable in a hollow cathode discharge.

*Present address: Department of Physics, University of Oregon, Eugene, Oregon 97403-1274

INTRODUCTION

Recently, several electronic transitions involving excited Rydberg levels of H_3 and D_3 have been observed and analyzed by Herzberg and co-workers.[1-4] These spectra, occurring in the visible and infrared regions, were obtained using a liquid nitrogen cooled hollow cathode discharge cell of a unique design which allowed the cathode and anode glows to be observed independently. This feature proved to be helpful in identifying triatomic hydrogen spectra which were found to occur only in the cathode glow. Further, production of H_3 and D_3 seemed to require a hollow cathode configuration as the spectra were not observed in other sources. Considering that ion-electron recombination is enhanced in the field-free region of a hollow cathode,[5] it seems likely that the spectra resulted from the recombination of an electron with a hydrogenic ion. While H_3^+ is certainly rapidly produced in the discharge, hydrogen cluster ions, $H_3^+ \cdot (H_2)_n$, are also produced with increasing efficiency as the temperature is decreased.[6] While the importance of cluster ions in the formation of Rydberg radicals has been suggested,[7,8] no direct experimental information addressing this question was available previously. In the present work the possible importance of these hydrogen cluster ions in the formation of H_3 radicals is investigated by a comparison of the dependence of the intensity of the 6025A band of H_3 on the discharge pressure and temperature with the results of kinetic calculations modeling the ion-molecule clustering reactions occurring in the discharge.

EXPERIMENTAL

A. Kinetic Modeling

The ion-molecule reactions occurring within the hollow cathode were modeled by the ion clustering reactions shown in Fig. 1. The scheme begins with the formation of H_3^+* which is known to be produced in excited vibrational levels.[9] This excitation is significant as recent experimental[7] and theoretical[10] results indicate that the efficiency of electron recombination with H_3^+ increases with increasing internal energy. Following vibrational quenching, H_3^+ ions enter into clustering equilibrium with H_5^+, eventually leading to H_7^+. As H_7^+ was the largest cluster ion considered, it should be interpreted as representing all hydrogen cluster ions larger than H_5^+. Simultaneously with the establishment of the ion cluster equilibria, each of the hydrogenic ions could be lost by either electron recombination or diffusion controlled wall collisions.

The rate constants used in the kinetic calculations are listed in Table I. Wall loss rate constants for the ions were calculated from their diffusion constants which in turn were determined from their reduced mobilities using the Einstein relation.[11] For H_3^+ and H_5^+ experimental values for their ionic mobility in hydrogen are available,[12] while the mobility of H_7^+ was estimated by scaling down the values for H_3^+ and H_5^+ according to the Langevin mobility theory in the polarization limit.[11]

Experimentally determined rates of electron recombination[7,13] were employed for H_3^+ (vibrationally excited and quenched) and H_5^+ with the assumption of the usual $T^{-0.5}$ temperature dependence.[14] While direct information on the rate of H_7^+ electron recombination is not currently available, it has been observed in other ion cluster systems that the electron

recombination rate increases dramatically with the addition of the first ligand and then remains fairly constant for larger clusters.[15,17] Thus the rate of electron recombination for H_7^+ was set equal to that of H_5^+.

Presently there is some controversy regarding the rate of vibrational relaxation of H_3^+ by H_2 collisions[9,18,19] with reported rate constants ranging from about 10^{-9} to 10^{-12} cm^3 $molecule^{-1}$ sec^{-1}. However, under the conditions investigated the low value of 10^{-12} cm^3 $molecule^{-1}$ sec^{-1} results in the rate of H_3^+ vibrational relaxation being fast compared with ion clustering and was thus used in the present calculation.

Both the forward and reverse rate constants (k_{35} and k_{53} respectively) with their temperature dependency have been experimentally determined for the H_3^+/H_5^+ clustering equilibrium.[20] Presently, no direct information is available on the rate of the individual forward and reverse reactions (k_{57} and k_{75} respectively) of the H_5^+/H_7^+ equilibrium. However, it can be estimated that under the conditions for which k_{35} was determined, k_{57} was at most 2% of k_{35}. In the present study it was found that the results of the kinetic modeling did not change significantly for k_{57} equal to 0.5-2% of k_{35}, and thus k_{57} was set at 1% of k_{35}. The reverse rate constant, k_{75}, was then determined using the known value of H_5^+/H_7^+ equilibrium constant.[6]

B. Spectral Intensity Measurements

The discharge cell used in this study was similar to that used by Herzberg which has been described in detail elsewhere.[3] Hydrogen gas, which had passed through a liquid nitrogen trap to remove condensible impurities, was flowed continuously through the discharge cell. It entered the cell through a copper coil attached to the bottom of the copper hollow cathode and exited past the tungsten anode. Spectra were obtained over the pressure range

of 0.35 to 3.5 Torr as measured by a baratron pressure transducer. The temperature of the cell was maintained by immersing it along with the preceeding copper coil in either liquid nitrogen (77 K), dry ice/methanol (195 K), or ice water (273 K). In order to minimize charge density variations over the pressure and temperature range investigated, the discharge current was held constant at the relatively low value of 50 mamp. Typical values of the discharge voltage and serial resistance were 750V and 1.8 kΩ respectively.

Spectra were taken in fourth order of a 7m asymmetric Czerny-Turner Spectrograph (reciprocal dispersion 0.37 Å/mm), recorded with Kodak 103aF photographic plates, and calibrated using a Fe/Ne hollow cathode discharge. H_3 lines were readily identified from the hydrogen discharge cathode glow using the previously reported spectra.[1] Under the mild discharge conditions employed in this work, exposure times of 3 to 6 hours were required to produce spectra of sufficient intensity for analysis. Integrated intensity measurements were obtained from photodensitometer traces with the intensity of a line being calculated as the full width at half maximum multiplied by the peak maximum. Intensity variations resulting from variations in the emulsion and/or developing were corrected for by normalizing the H_3 line intensities to the intensity of a 5962Å Fe line of the reference spectrum. This correction was never more than about 15%.

RESULTS

A. Kinetic Modeling

The kinetic equations represented schematically in Fig. 1 were solved for the relative amounts of the various hydrogenic neutrals produced by ion-electron recombination. The results are, of course, sensitive to the electron

density which, although not directly determined in these experiments, is expected to be on the order of 10^9 cm^{-3}.[21] Figure 2 graphically illustrates the results of these calculations with $[e^-] = 5 \times 10^9$ cm^{-3} over the hydrogen pressure and temperature range for which spectra were obtained. It can be seen that at the three temperatures investigated H_3 production is low, accounting for only a few percent of the electron recombination products. Alternatively, H_5 production demonstrates a strong temperature and pressure dependence as increasing pressure results in decreased production at 77 K and increased production at 195 K and 273 K. Finally, it can be seen that H_7 production is significant only at low temperature, accounting for less than 0.1% of the ion-electron recombination products at the higher temperatures investigated.

B. Spectral Intensity Measurements

The 6025Å band ($3s^2A_1' \rightarrow 2p^2A_2''$) of H_3 was monitored as an indication of the efficiency of production of H_3 radicals in the discharge. It has been shown[1] that the lower state of this transition undergoes a rapid heterogeneous predissociation into the repulsive ground state ($2p^2E'$) with an efficiency that increases with $N(N+1)-K^2$ (where N and K are the rotational quantum numbers of a symmetric top). This causes the R- and/or Q-branch lines to be generally narrower and thus integrable at lower intensity than the P-branch line resulting from a given upper level. For this reason the spectral investigations concentrated on the R- and Q-branch regions where the $R_0(0)$, $R_1(1)$, $R_1(2)$, $Q_1(1)$, and $Q_2(2)$ lines were observed. Although not extensively investigated, the P-branch region was examined where no evidence of transitions involving additional upper state rotational levels was found. The integrated intensities of the observed lines were multiplied by the

appropriate ratio of Honl-London factors[22] to account for the intensity of the unmeasured P-branch lines. These adjusted intensities, however, do not give directly a measure of the relative population of the upper state ($3s^2A_1'$) rotational levels because in addition to the parallel visible band observed, the $3s^2A_1'$ state also emits efficiently in the infrared giving rise to the 3600 cm^{-1} perpendicular band.[3] The intensity of this infrared transition is comparable to that of the visible band, as the emission probability decrease due to the ν^3 frequency dependency is offset by a nearly 100 fold increase in the transition moment.[23] The significance of this infrared band in the present context results from the fact that the branching ratio between a parallel and perpendicular transition is not identical for all rotational levels, but varies as the ratio of the sum of the Honl-London factors for the allowed transitions in these two types of emission bands. Thus, the measured line intensities were further adjusted by this ratio of parallel to perpendicular Honl-London factors to obtain the relative fraction of the population in the various rotational levels in the $3s^2A_1'$ state. These results are plotted as a function of discharge pressure and temperature in Fig. 3. It is interesting to note that at a similar hydrogen density, the relative population of a particular rotational level is similar for the three temperatures investigated. Increasing pressure is seen to have a rotational "cooling" effect as evidenced by a decrease in the (N,K) = (3,1) and (2,1) rotational levels and an increase in the (1,1) level. In sharp contrast to this trend, at a discharge temperature of 195 K the (3,1) and (2,1) levels are seen to increase in relative intensity while the (1,1) level decreases (i.e., a rotational "heating") over the hydrogen density range of 3-4 x 10^{16} cm^{-3}. It should be noted that even under these conditions, where the (3,1) level appeared to be the most populated rotational state, no emission was observed

from any N = 4 level. Finally, it can be seen that the relative population of the (1,0) level is relatively independent of pressure and temperature, accounting for less than about 10% of the observed rotational levels.

The relative total population of H_3 in the $3s^2A_1'$ can be obtained by simply summing over the observed rotational levels, and these results as a function of discharge pressure and temperature are represented by the points plotted in Figure 4. In agreement with earlier work,[1-4] the most intense H_3 emission was observed at low pressure and low temperatures with the intensity at T = 195 K and T = 273 K falling to approximately 50% and 20% respectively of the T = 77 K low pressure result. The effect of increasing hydrogen pressure on the band intensity depended dramatically on the temperature of the discharge. It can be seen that over a similar hydrogen density range the intensity of the $3s^2A_1' \rightarrow 2p^2A_2''$ transition falls by more than a factor of four at T = 77 K while the band slowly increases in intensity at T = 273 K. At the intermediate temperature of 195 K, the band intensity shows unusual behavior with increasing pressure causing an initial decrease in intensity followed by a slow increase.

Finally, the relative intensity of the undispersed cathode glow between 5600Å - 8100Å as a function of discharge pressure and temperature is shown in Fig. 5. It can be seen that while the discharge was somewhat more intense at T = 77 K, the decrease in the intensity of the cathode glow with increasing hydrogen pressure was similar at the three temperatures investigated.

Discussion

A comparison of the temperature and pressure dependence of the H_3 emission intensity in Fig. 4 with that of the cathode glow in Fig. 5 indicates that the observed changes in H_3 emission can not be accounted for simply by

changes in overall discharge intensity. Further, a comparison of Fig. 4 with the results of the kinetic modeling (Fig. 2) indicates that the calculated rate of H_5^+/e^- recombination has a qualitatively similar pressure and temperature dependence as that observed for the H_3 emission intensity. This similarity is emphasized by the curves plotted in Fig. 4 which represent the calculated relative intensity of H_5 neutral for $[e^-] = 2$ and 8×10^9 cm^{-3} (lower and upper curve in each plot respectively) scaled at each temperature to give quantitative agreement with the observed intensity of H_3 emission. Thus, with the exception of the low pressure measurement at T = 195 K, the pressure dependency of the H_3 emission can be explained by assuming that excited Rydberg states of H_3 result from the dissociative recombination of H_5^+ with electrons.

The quantitative agreement between calculated and observed intensity shown in Fig. 4 required a different scaling of the kinetic results at each temperature as the kinetic model appears to overestimate the H_3 emission at T = 195 K and 273 K by a factor of 2 and 7 respectively relative to the intensity observed at T = 77 K. It should be noted, however, that as a single emission band of H_3 was monitored as an indication of H_3 production, a direct comparison with the kinetic results would be valid only if the distribution of possible H_5^+/e^- recombination products was temperature independent. Although the possibility that dissociative recombination channels leading to production of $H_3(3s^2A_1')$ simply decrease in importance as temperature increases can not be ruled out, the observed temperature effects could also be adequately accounted for if the fraction of $H_3(3s^2A_1')$ produced in $N \geq 4$ rotational levels increases with temperature. Such an increase would be reasonable as the precursor H_5^+ would naturally populate higher rotational levels at elevated temperatures leading to increased rotational energy in the dissociative

recombination products. It has already been noted that even under discharge conditions where the population of the (3,1) level increases, no emission from $N \geq 4$ rotational levels is observed. This suggests the existence of some interaction resulting in dramatically decreased emission from the higher rotational levels of the $3s^2A_1'$ state and thus decreased total emission as these levels are increasingly populated. This explanation is consistent with the observed decrease in total H_3 intensity (Fig. 4) over the pressure range where the rotational "heating" was observed (Fig. 3). Further, it can be noted that the total H_3 intensity observed at low pressure and T = 195 K lies about a factor of 2 above the plotted curves. Thus, prior to the rotational "heating", the relative intensity of H_3 at T = 195 and 77 K scale as predicted by the temperature dependencies in the kinetic model.

The origin of this rotational "heating" can be understood as a conversion of translational energy of H_3 into rotational energy by collisions with H_2 molecules. Unusually broad line widths corresponding to a Doppler temperature of about 3000 K have been reported for H_3 transitions occurring in the visible and infrared regions.[1,3] In some cases the lower state of the transition is known to undergo emission, thus eliminating the possibility of lifetime broadening. While at first the occurrence of high translational energies in a liquid nitrogen cooled discharge was difficult to explain,[1] it can now be understood in terms of the kinetic energy released in the H_5^+/e^- dissociative recombination. With this viewpoint, line broadening results from a relatively narrow velocity distribution which is randomly oriented with respect to the optical axis. In the limit of a single velocity (v), the line shape would have a $\sin\theta$ dependence with a full width at half maximum ($\Delta\nu$) given by

$$\frac{\Delta\nu}{\nu_0} = \frac{\sqrt{3}\ v}{c} \qquad (1)$$

where ν_0 is the transition frequency and c is the speed of light. A photodensitometer trace of the $R_0(0)$ line obtained at a discharge pressure of 0.4 Torr and T = 77 K is shown in Fig. 6, where it can be seen that the line shape is well described by a sine curve (dotted line). From the observed width and equation 1, an H_3 velocity of 4.25×10^6 cm/s corresponding to a total kinetic energy release of 0.7 eV is calculated. By combining available experimental information from spectroscopic,[2,3] H_3 neutral scattering,[24] and H_3^+/H_5^+ equilibrium measurements,[6] the energy of $H_3(3s^2A_1') + H_2$ can be placed about 1.8 eV below that of $H_5^+ + e^-$. With about 0.7 eV appearing as kinetic energy, approximately 1.1 eV needs to be accounted for as internal energy. While the possibility that this energy is accounted for by H_2 vibration[25] with $v \simeq 3$ can not be ruled out, it would seem unlikely considering that theoretical calculations[26] for $H_3^+ \cdot H_2$ predict an H_2 bond length virtually unchanged from that of free H_2. However, this energy could be readily accounted for if H_3 is initially produced in higher Rydberg levels which subsequently radiate to the $3s^2A_1'$ state. Rydberg levels of H_3 are predicted to exist in this energy range[23] and their production in the hollow cathode discharge could be verified by the direct observation of infrared emission around 1.1 eV terminating in the $3s^2A_1'$ state or ultraviolet emission around 3.1 eV terminating in the $2s^2A_1'$ state.

It was noted earlier that as rotational "cooling" took place with increasing pressure, the relative intensity of individual levels seemed to depend mostly on the density of H_2 and was relatively independent of the discharge temperature. This effect can now be seen as a consequence of the high H_3 velocity which, being significantly greater than that of the thermalized H_2 molecules, causes the collision frequency to be relatively

temperature independent. The apparent exclusion of the (1,0) rotational level from rotational thermalization can be understood by noting that the rotational levels of H_3 exist in two different modifications (A_1 and E) as a consequence of nuclear spin. Of the observed rotational levels only the (1,0) is of species A_1 and hence does not readily interconvert with the other levels. However, the rotational levels of species E do readily interconvert, and as the discharge pressure is increased this subset of rotational levels is observed to approach thermal equilibrium. Using measurements from the highest pressure at each temperature, a log plot of the intensity of the E species rotational levels divided by their degeneracy vs. rotational energy was constructed (Fig. 7). It can be seen that for T = 77 K and 195 K the apparent rotational temperatures of 185 K and 255 K, respectively, scale roughly with the discharge temperature. Although the rotational temperature of 185 K was derived from only two points, it agrees well with a value of 200 K used to simulate observed H_3 emission spectra obtained under similar discharge conditions.[1] At T = 273 K, it would appear that the pressure was not increased sufficiently for the rotational distribution to be well-described by a temperature.

ACKNOWLEDGMENTS

Acknowledgment is made to the Donors of The Petroleum Research Fund, administered by the American Chemical Society, for partial support of this research (Grant 16836-G6). This work was supported in part by the Office of Basic Energy Science of the United States Department of Energy. This is document NDRL-2753 from the Notre Dame Radiation Laboratory. We are also grateful to the Notre Dame Computing Center for providing computer time.

References

1. I. Dabrowski and G. Herzberg, Can. J. Phys. 58, 1238 (1980).

2. G. Herzberg and J. K. G. Watson, Can. J. Phys. 58, 1250 (1980).

3. G. Herzberg, H. Lew, J. J. Sloan, and J. K. G. Watson, Can. J. Phys. 59, 428 (1981).

4. G. Herzberg, J. T. Hougen, and J. K. G. Watson, Can. J. Phys. 60, 1261 (1982).

5. A. von Engel, "Ionized Gases", (Oxford, London, 1965) pp. 161-163.

6. K. Hiraoka and P. Kebarle, J. Chem. Phys. 62, 2267 (1975).

7. N. G. Adams, D. Smith, and E. Alge, J. Chem. Phys. 81, 1778 (1984).

8. G. I. Gellene and R. F. Porter, J. Phys. Chem. 88, 6680 (1984).

9. J. J. Leventhal and L. Fiedman, J. Chem. Phys. 50, 2928 (1969).

10. H. H. Michels and R. H. Hobbs, Astrophys. J. 286, L27 (1984).

11. E. W. McDaniel in "Case Studies in Atomic Collision Physics, Vol. I" edited by E. W. McDaniel and M. R. C. McDowell (Wiley, New York, 1969) pp. 8-9.

12. M. T. Elford and H. B. Milloy, Aust. J. Phys. 27, 795 (1974).

13. M. T. Lev, M. A. Biondi and R. Johnsen, Phys. Rev. A 8, 413 (1973).

14. V. E. Golant, A. P. Zhilinsky, and I. E. Sakharov, "Fundamentals of Plasma Physics" (Wiley, New York, 1977) p. 68.

15. M. T. Leu, M. A. Biondi and R. Johnsen, Phys. Rev. 7, 292 (1973).

16. C.-M. Huang, M. A. Biondi, and R. Johnsen, Phys. Rev. A 14, 984 (1976).

17. C.-M. Huang, M. Whitaker, M. A. Biondi and R. Johnsen, Phys. Rev. A 18, 64 (1978).

18. J. K. Kim, L. P. Theurd, and W. T. Huntress Jr., Int. J. Mass Spectrom. Ion Phys. 15, 223 (1974).

19. C. R. Blakey, M. L. Vestral, and J. H. Futrell, J. Chem. Phys. 66, 2392 (1977).

20. K. Hiraoka and P. Kebarle, J. Chem. Phys. 63, 746 (1975).

21. W. B. Kunkel in "Plasma Physics in Theory and Application" edited by W. B. Kunkel (McGraw-Hill, New York, 1966) p. 323.

22. G. Herzberg, "Electronic Spectra of Polyatomic Molecules" (Van Nostrand Reinhold, New York, 1966) pp. 226-232.

23. H. F. King and K. Morokuma, J. Chem. Phys. 71, 3213 (1979).

24. G. I. Gellene and R. F. Porter, J. Chem. Phys. 79, 5975 (1983).

25. K. P. Huber and G. Herzberg, "Constants of Diatomic Molecules" (Van Nostrand Reinhold, New York, 1979).

26. R. Ahlrichs, Theoret. Chim. Acta (Berl.) 39, 149 (1975).

Table I. Values of Rate Constants Employed in Kinetic Modeling of the Hydrogen Hollow Cathode Discharge.

Rate Constant	Value	Reference
k_3^*	1×10^{-12} cm^3 molecule^{-1} sec^{-1}	9, 18, 19
k_{3d}	5.98×10^{16} cm^3 molecule^{-1} K^{-1} sec^{-1}	12
k_{5d}	5.55×10^{16} cm^3 molecule^{-1} K^{-1} sec^{-1}	12
k_{7d}	5.34×10^{16} cm^3 molecule^{-1} K^{-1} sec^{-1}	estimated
α_3^*	$3.99 \times 10^{-6}/\sqrt{T}$ cm^3 electrons^{-1} K$^{1/2}$ sec^{-1}	13
α_3	$1.94 \times 10^{-7}/\sqrt{T}$ cm^3 electrons^{-1} K$^{1/2}$ sec^{-1}	7
α_5	$5.15 \times 10^{-5}/\sqrt{T}$ cm^3 electrons^{-1} K$^{1/2}$ sec^{-1}	13
α_7	α_5	estimated
k_{35}	6.08×10^{-24} ($T^{-2.3}$) cm^6 molecules^{-2} sec^{-1}	20
k_{53}	$(8.7 \times 10^6)e^{-4227/T}$ cm^3 molecule^{-1} sec^{-1}	20
k_{57}	$0.01\ k_{35}$	estimated
k_{75}	$k_{57}\ (1.56 \times 10^{26})e^{-2063/T}/T$ cm^3 molecule^{-1} K sec^{-1}	6

(a) The rate constants are defined diagramatically in Fig. 1.

Figure Captions

Fig. 1. Schematic of reactions employed in the kinetic modeling of the hydrogen discharge.

Fig. 2. Calculated relative production of hydrogenic neutrals as a function of H_2 pressure and temperature for $[e^-] = 5 \times 10^9$ cm^{-3}.

Fig. 3. Relative population of the observed rotational levels of the $3s^2A_1'$ Rydberg state of H_3 as a function of discharge pressure and temperature. The rotational levels are denoted by (N,K) where N and K are the rotational quantum numbers of a symmetric top.

Fig. 4. Relative total population observed for the $3s^2A_1'$ state of H_3 (plotted points) as a function of discharge pressure and temperature. The curves represent the calculated production of H_5 for $[e^-] = 2$ and 8×10^9 cm^{-3} (lower and upper curve in each plot respectively) scaled at each temperature to give quantitative agreement with the observed results.

Fig. 5. Relative intensity of the undispersed cathode glow between 5600Å and 8100Å as a function of discharge pressure and temperature.

Fig. 6. Photodensitometer trace of the $R_0(0)$ line of the 6025 Å band of H_3 obtained at a discharge pressure and temperature of 0.4 Torr and 77 K respectively. The dotted line represents a fit of the observed line intensity (I) to the functional form I = Asin(bx) where A and b were adjusted to the amplitude and full width at half maximum of the line respectively.

Fig. 7. Logarithmic plot of the relative population of the observed rotational levels of symmetry species E divided by their degeneracy ($g_{N,K}$) vs. rotational energy. Points are taken from measurements at the highest pressure investigated for discharge temperatures of 77 K, 195 K and 273 K (denoted as triangles, squares, and circles respectively).

WALL COLLISIONS
$k_{3d}[H_2]^{-1}$
$k_3^*[H_2]$
$k_{3d}[H_2]^{-1}$
H_3^{++}
H_3^+
$k_{35}[H_2]^2$
$k_{53}[H_2]$
$k_{5d}[H_2]^{-1}$
H_5^+
$k_{57}[H_2]^2$
$k_{75}[H_2]$
$k_{7d}[H_2]^{-1}$
H_7^+
$a_3^*[e^-]$
$a_3[e^-]$
H_3
$a_5[e^-]$
H_5
$a_7[e^-]$
H_7

Fig. 1

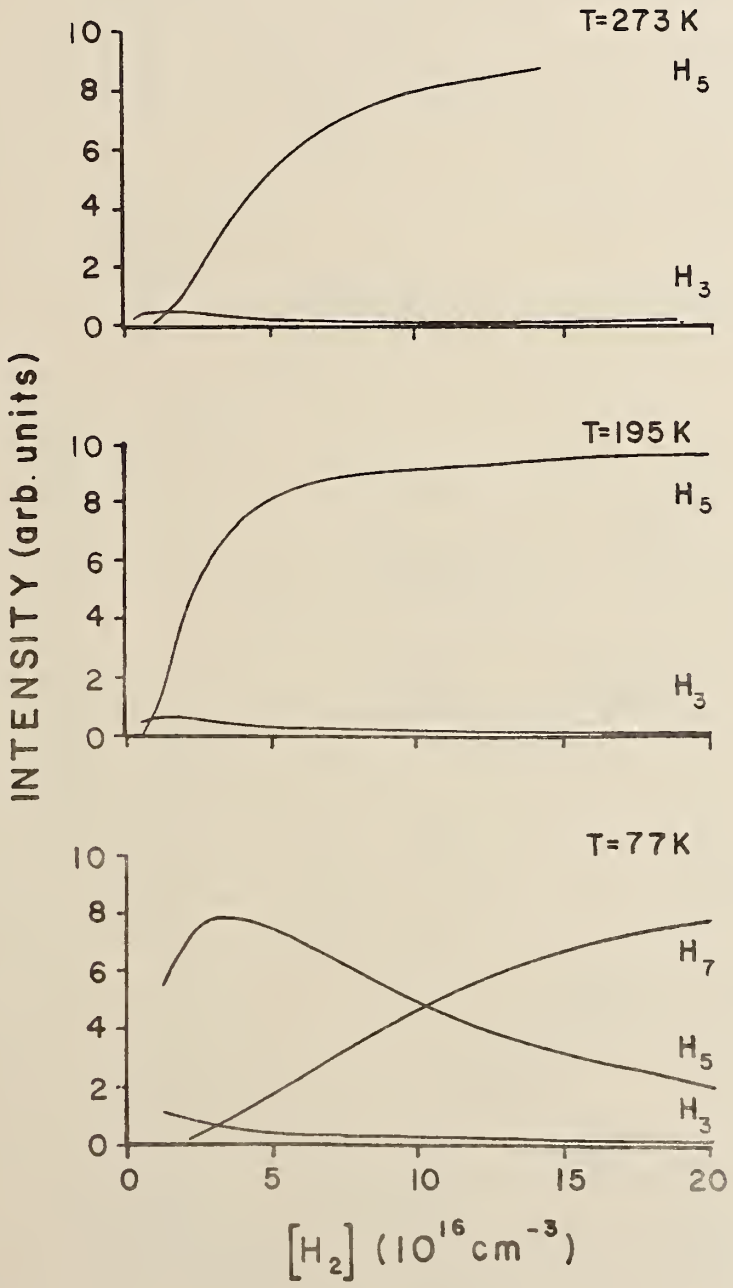
T=273 K
H5
H3
T=195 K
H5
H3
T=77 K
H7
H5
H3
INTENSITY (arb. units)
[H2] (10^16 cm^-3)
0
2
4
6
8
10
0
5
10
15
20

Fig. 2

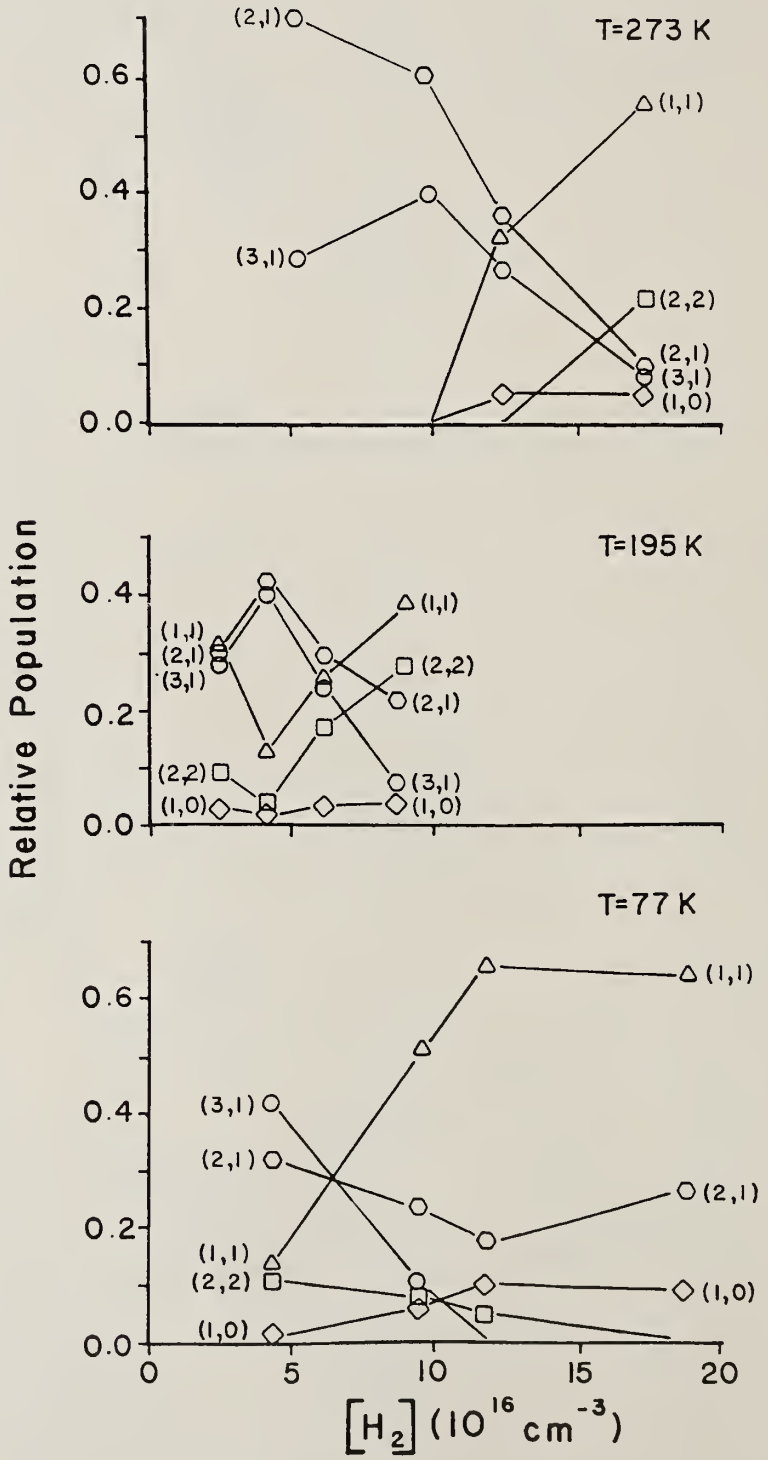
T=273 K
(2,1)
(1,1)
(3,1)
(2,2)
(2,1)
(3,1)
(1,0)
T=195 K
(1,1)
(2,1)
(3,1)
(2,2)
(1,0)
T=77 K
(1,1)
(3,1)
(2,1)
(2,1)
(1,1)
(2,2)
(1,0)
(1,0)
0.0
0.2
0.4
0.6
0
5
10
15
20
Relative Population
[H2] (10^16 cm^-3)

Fig. 3

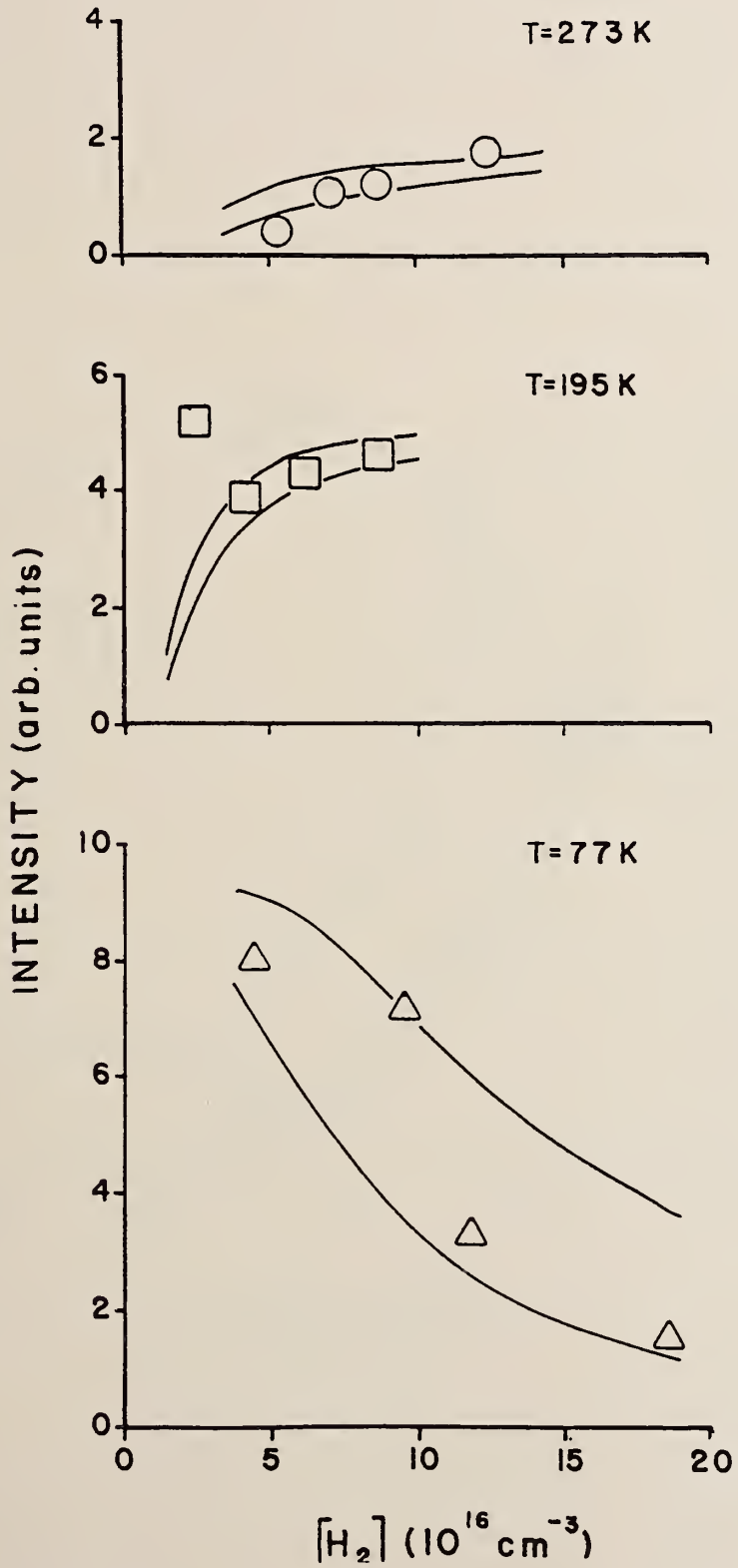
T=273 K
T=195 K
T=77 K
INTENSITY (arb. units)
[H2] (10^16 cm^-3)
0
2
4
6
8
10
0
5
10
15
20

Fig. 4

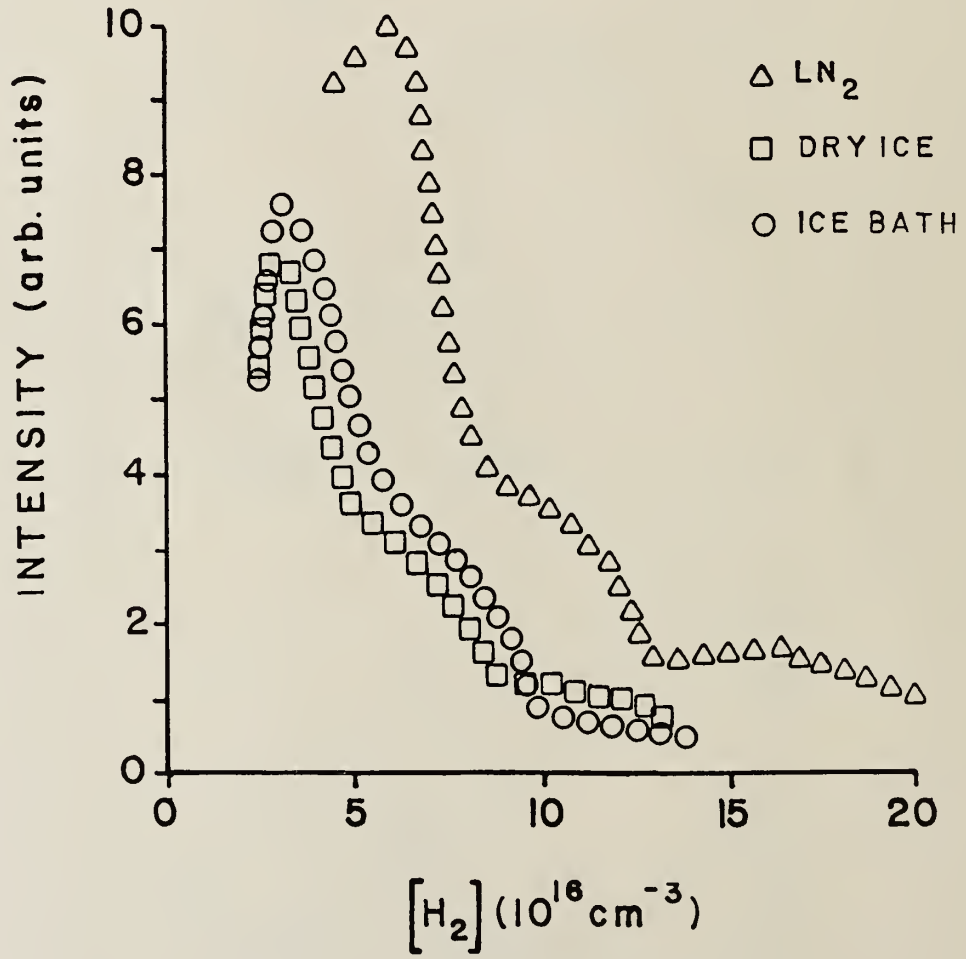
INTENSITY (arb. units)
10
8
6
4
2
0
0
5
10
15
20
[H2] (10^16 cm^-3)
LN2
DRY ICE
ICE BATH

Fig. 5

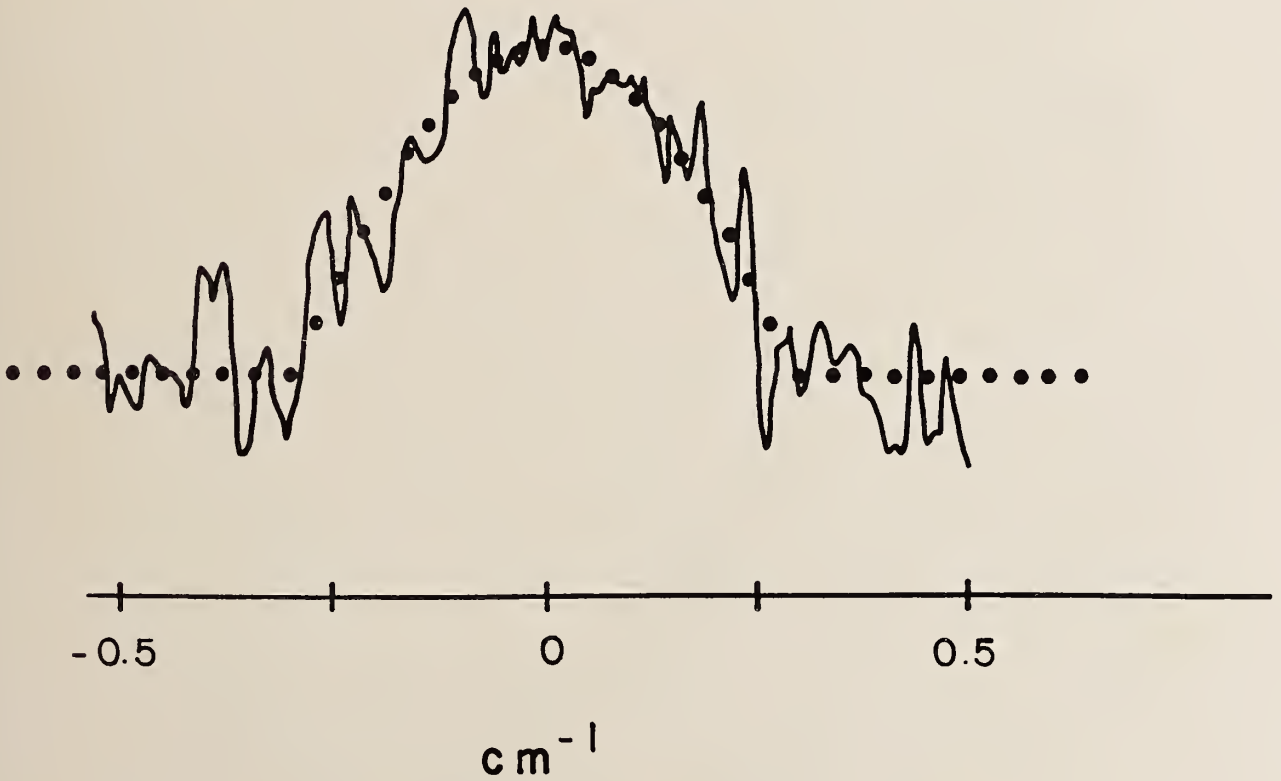

Fig. 6

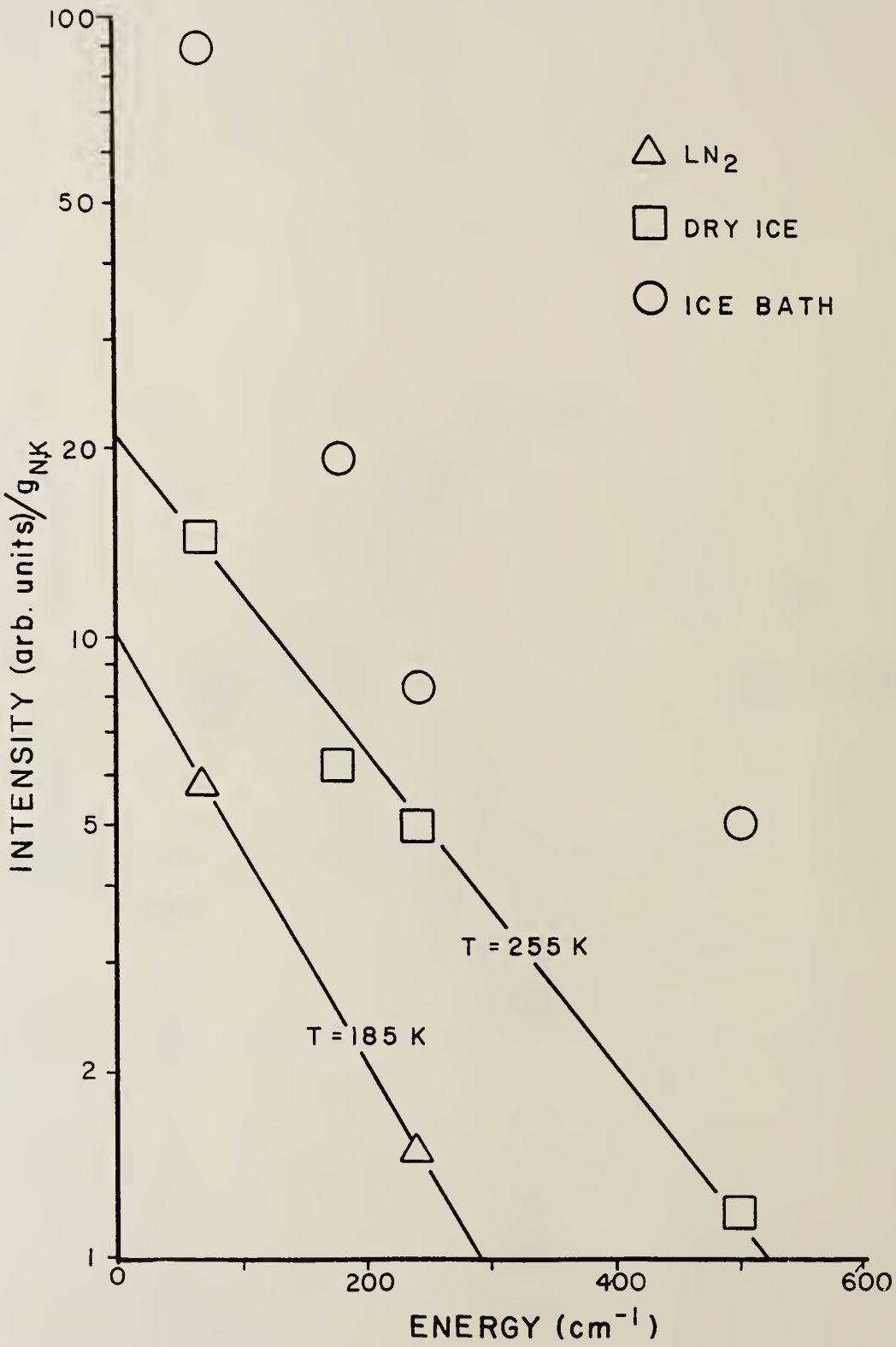
100
50
20
10
5
2
1
0
200
400
600
INTENSITY (arb. units)/g_{NK}
ENERGY (cm^{-1})
LN_2
DRY ICE
ICE BATH
T = 255 K
T = 185 K

Fig. 7

TIME-RESOLVED INTRACAVITY LASER SPECTROSCOPY OF FORMYL RADICAL PHOTOPRODUCT OF ACETALDEHYDE

N. Goldstein and G. H. Atkinson
University of Arizona, Department of Chemistry, Tucson, AZ, USA

The absorption spectra and kinetic behavior of the formyl radical formed in the 266 nm photolysis of gas phase acetaldehyde was investigated using time-resolved intracavity laser spectroscopy (ILS).[1-4] Rotationally-resolved absorption spectra of several vibronic bands were obtained at sufficient resolution to determine predissociative lifetimes of the individual rovibronic states from line broadening. Time resolution was accomplished by modulating the laser pumping to allow ILS detection for a controllable period of time at a variable delay after the photolysis event. Absolute absorbances of formyl radicals were obtained at number densities of 10^{11} cm^{-3}. The time evolution of populations in three vibrational levels were monitored via the (0,9,0) → (0,0,0), (0,9,1) → (0,0,1), and (0,13,0) → (0,1,0) transitions. Approximately one half of ground state population was formed by relaxation of vibrationally excited HCO. The kinetic properties of HCO (0,0,1) and HCO (0,1,0) were observed to be different although both are involved in relaxation from more highly excited vibrational levels of HCO. Removal of ground state HCO is consistent with previous measurements involving radical recombination.

References

(1) N. Goldstein, T. Brack, and G.H. Atkinson, Chem. Phys. Lett. (in press).
(2) F. Stoeckel and G.H. Atkinson, J. Chem. Phys. (submitted for publication).
(3) F. Stoeckel, M. Schuh, N. Goldstein, and G.H. Atkinson, Chem. Phys. (in press).
(4) F. Stoeckel, M.A. Melieres, and M. Chenevier, J. Chem. Phys. 76 (1982) 2191.

Figure 1; EXPERIMENTAL

Acetaldehyde is photolyzed within the cavity of a broad band dye laser defined by M_1, M_2, and M_3. AOM 1 serves to initiate laser activity and AOM 2 is used to send a portion of the laser output into a spectrometer after specified time delays. The dispersed spectral output of the laser shows absorbance losses proportional to an effective pathlength equal to the product of the speed of light and the generation time of the laser, t_g.

Figures 2-3; SPECTROSCOPY

The central portions of laser profiles containing (0,9,0)←(0,0,0) and (0,9,1)←(0,0,1) transitions are shown. All spectral features display predissociation broadening. Line positions and line widths are accurate within detector limits (absolute error = 1 cm^{-1}, relative error = 0.1 cm^{-1}).

Figure 4-6; ABSORPTION MEASUREMENT

The spectral features used for kinetic studies are shown in higher resolution: (0,9,0)←(0,0,0) P(8)-P(11), (0,13,0)←(0,1,0) QP bandhead, and (0,9,1)←(0,0,1) QP bandhead

Absorption coefficients are quantified using the Beer-Lambert relationship:

$$\log(I/I_0) = \alpha(\sigma)\ c\ tg \quad \text{where} \quad \alpha(\sigma) = \xi\ N(t)\ dt$$

Absorbance is proportional to the population density, N(t), integrated over the period of the ILS measurement,tg. Therefore maximum detection sensitivity is achieved for t_g greater than the lifetime of the transient absorber.(i. e. spectra A and B 2 torr, t_g= 10μs vide infra.)

Figures 7-8; EFFECT OF FINITE GENERATION TIME

The ILS signal observed at delay time, t_d, is the averaged absorption over the generation time, t_g. Kinetic profiles of HCO (0,0,0) obtained with different generation times are simulated using our model of the ILS process and consistent kinetic variables.(t_g = 0.9 and 6.4 μs, 2.3 torr).

Figure 7-8; (0,0,0) KINETICS

Time dependence of HCO (0,0,0) absorption coefficient (t_g=1μs, 0.5, 0.9, and 4.0 torr acetaldehyde, 7, 15, and 15 mJ 266 nm) is simulated using a two component population rise and known radical recombination rates. Free parameters:

A'_0 - product of 266 nm fluence and sum of all HCO population at t_d=0 (expressed in absorption units)

Φ - fraction of HCO formed with nonzero vibration

K_2 - pseudo first order vibrational relaxation rate

are plotted as a function of acetaldehyde pressure.

Figure 9; (0,0,1) AND (0,1,0) KINETICS

Signal rises and falls with characteristic times similar to the slow rise of (0,0,0). (Simulated curves assume rates 1.0 and 0.8 times k_2). Lower energy (0,1,0) is removed most rapidly.

CONCLUSIONS

Kinetic data indicate circa 1/2 of HCO photoproduct is formed with nonzero vibration. A substantial fraction is formed with V > 1 and is subsequently deactivated to (0,1,0), (0,0,1), and (0,0,0). The second order rate coefficient for formation of (0,0,0) is $K = 1.1 \pm 0.3 \times 10^{-11}$ molecules^{-1} cm^3 s^{-1}.

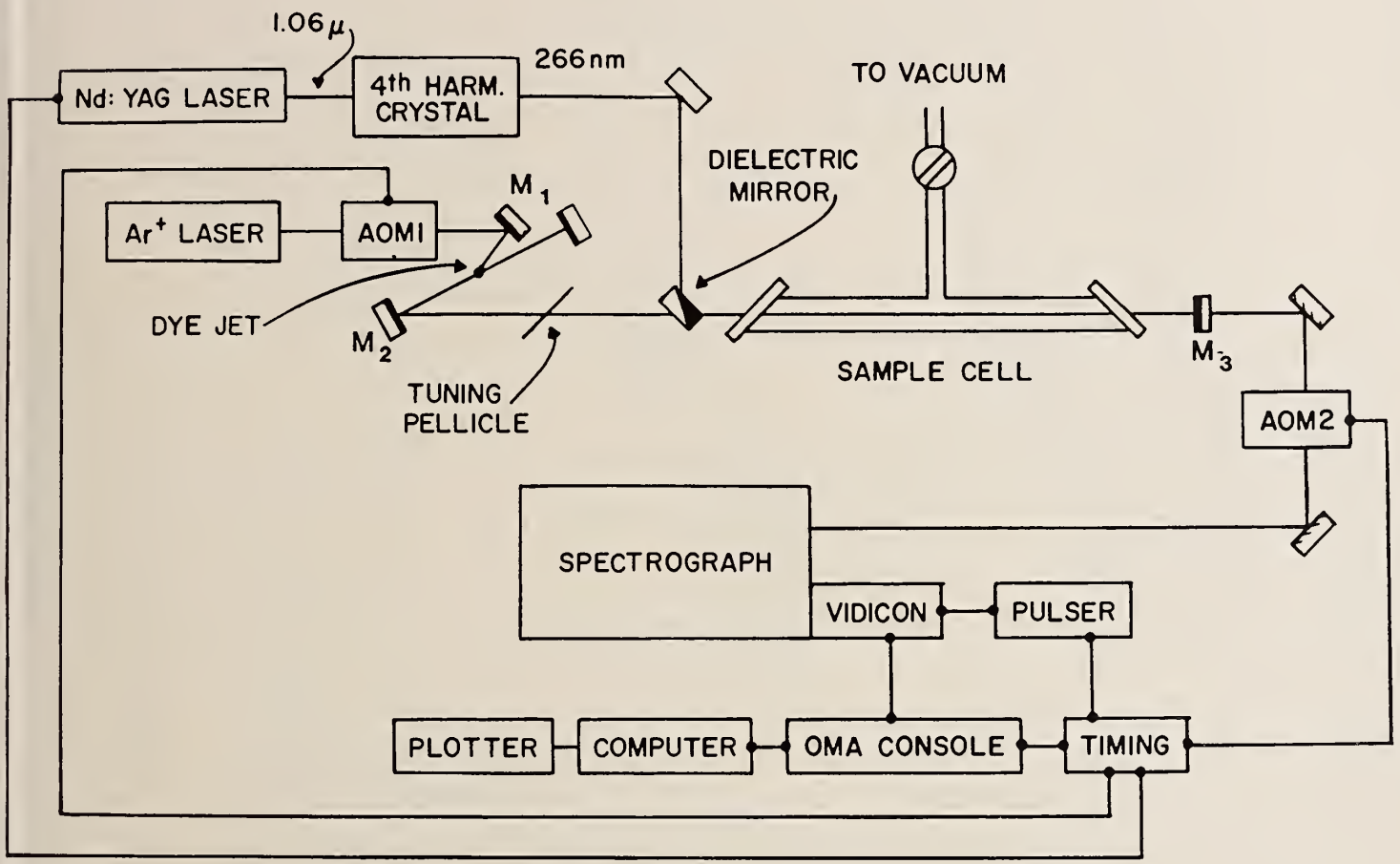
1.06μ
Nd: YAG LASER
4th HARM. CRYSTAL
266nm
TO VACUUM
DIELECTRIC MIRROR
Ar+ LASER
AOM1
M1
DYE JET
M2
TUNING PELLICLE
SAMPLE CELL
M3
AOM2
SPECTROGRAPH
VIDICON
PULSER
PLOTTER
COMPUTER
OMA CONSOLE
TIMING

figure 1.

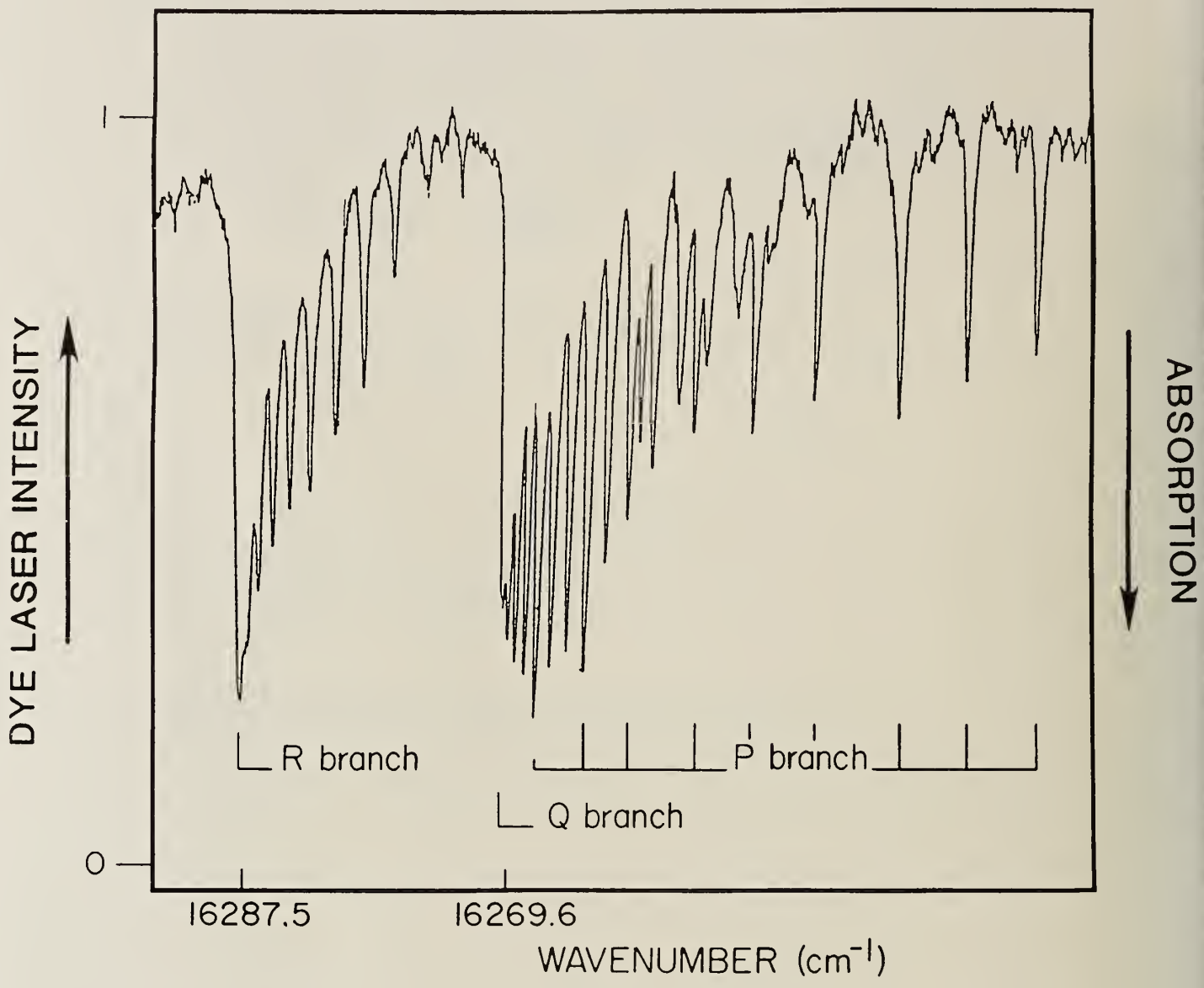
DYE LASER INTENSITY
1
0
ABSORPTION
R branch
P branch
Q branch
16287.5
16269.6
WAVENUMBER (cm⁻¹)

figure 2.

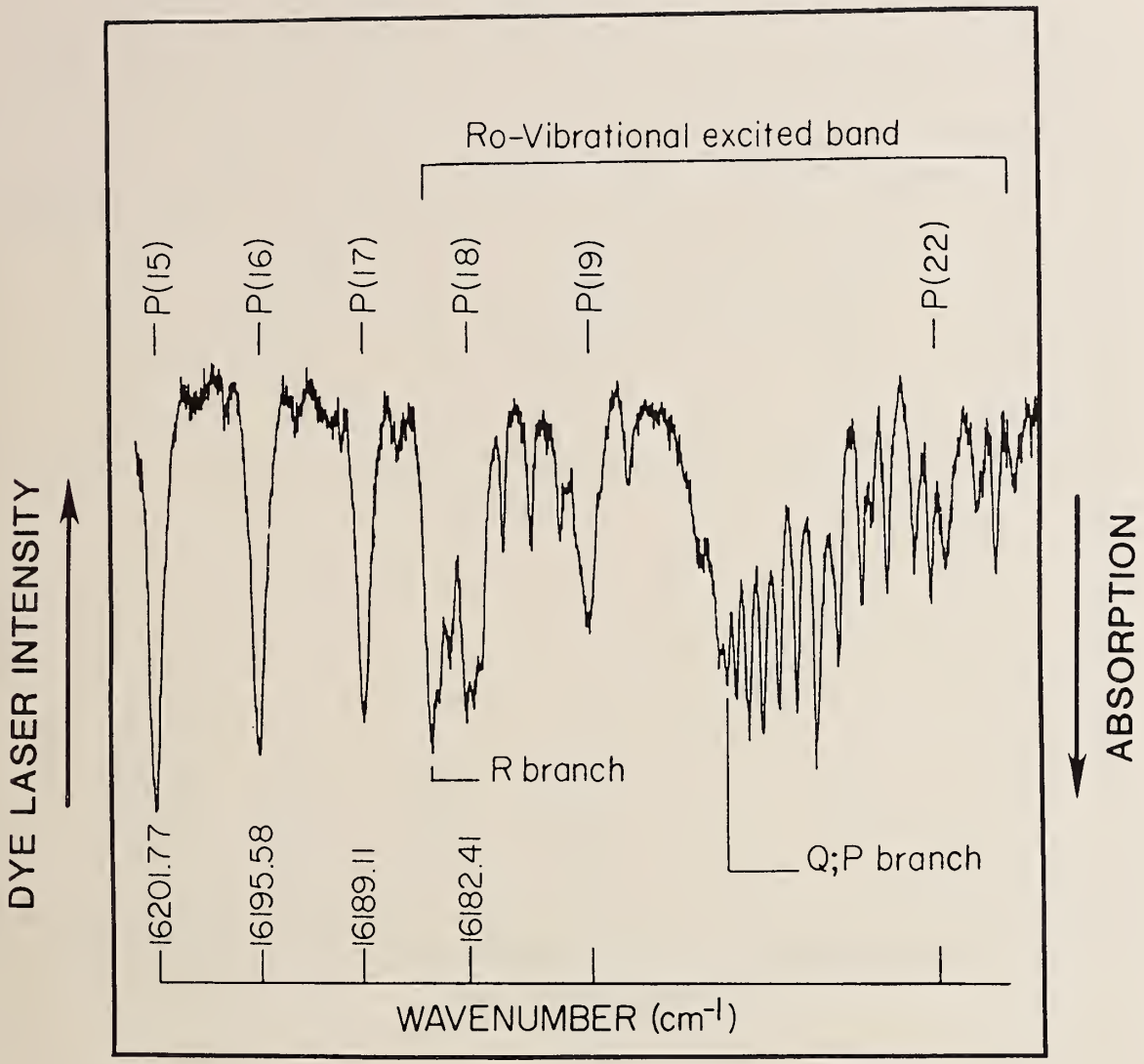
Ro-Vibrational excited band
P(15)
P(16)
P(17)
P(18)
P(19)
P(22)
DYE LASER INTENSITY
ABSORPTION
R branch
Q;P branch
16201.77
16195.58
16189.11
16182.41
WAVENUMBER (cm⁻¹)

figure 3.

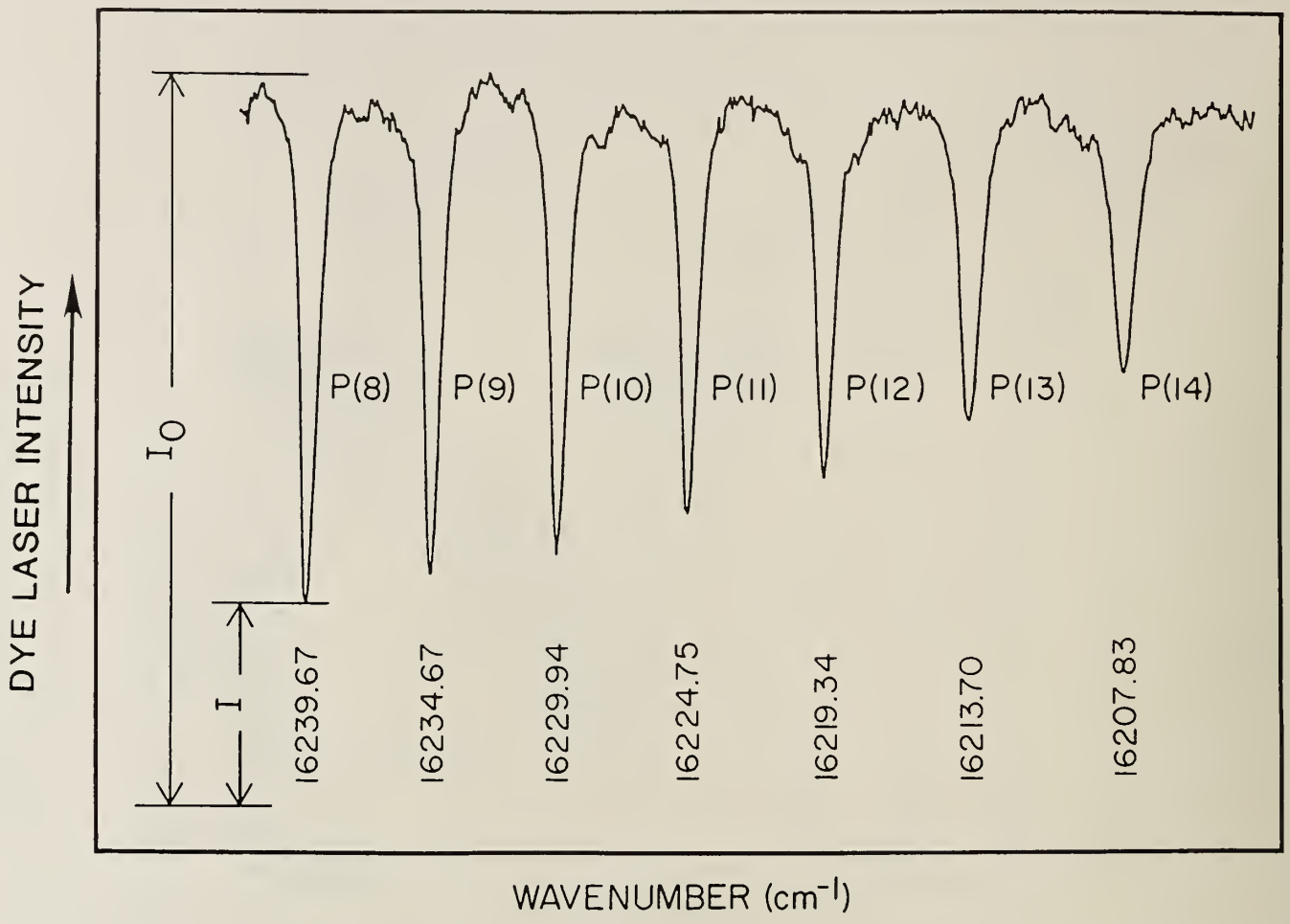
DYE LASER INTENSITY
ABSORPTION
I_0
I
P(8)
P(9)
P(10)
P(11)
P(12)
P(13)
P(14)
16239.67
16234.67
16229.94
16224.75
16219.34
16213.70
16207.83
WAVENUMBER (cm^{-1})

figure 4.

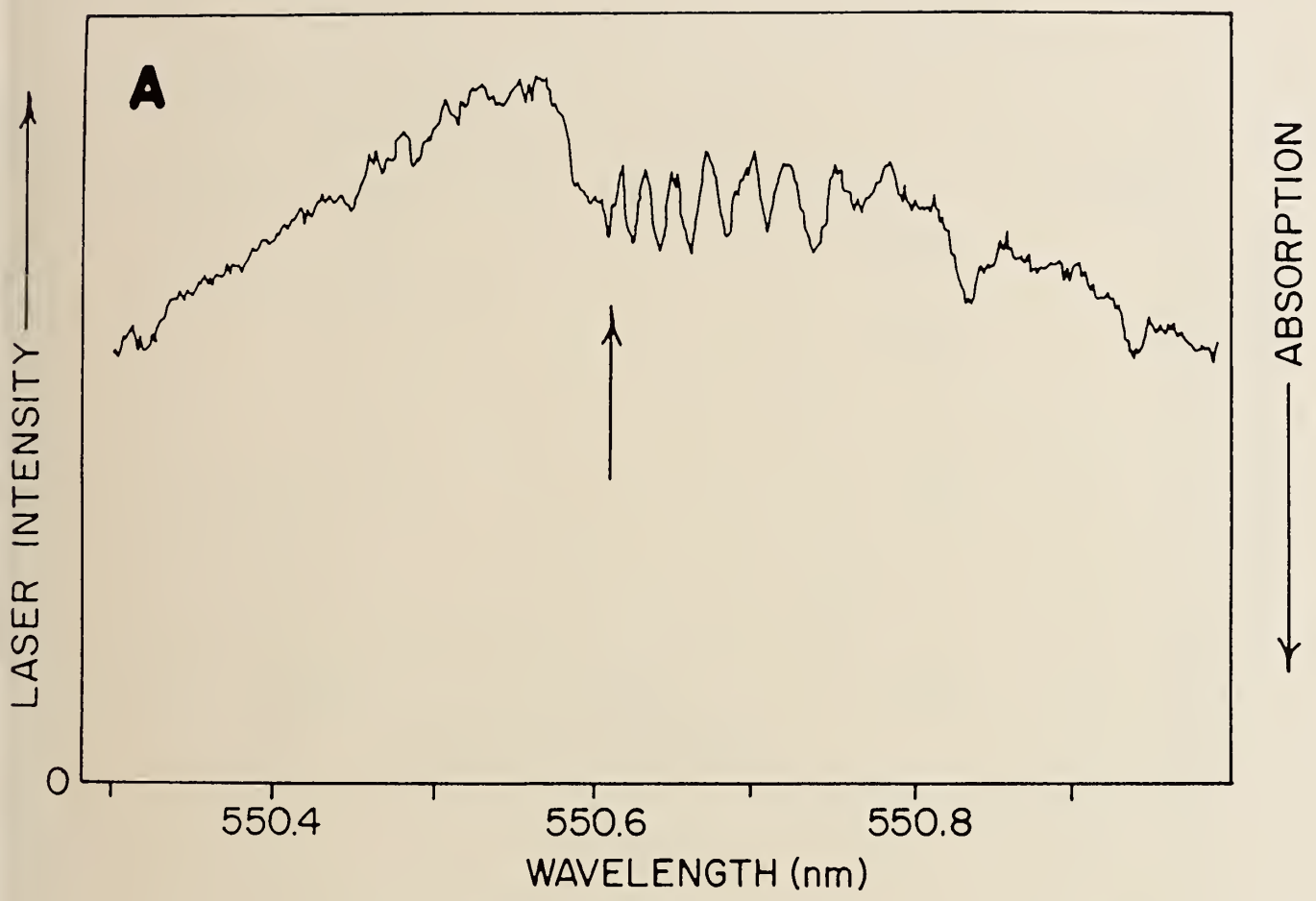
A
LASER INTENSITY
0
550.4
550.6
550.8
WAVELENGTH (nm)
ABSORPTION

figure 5.

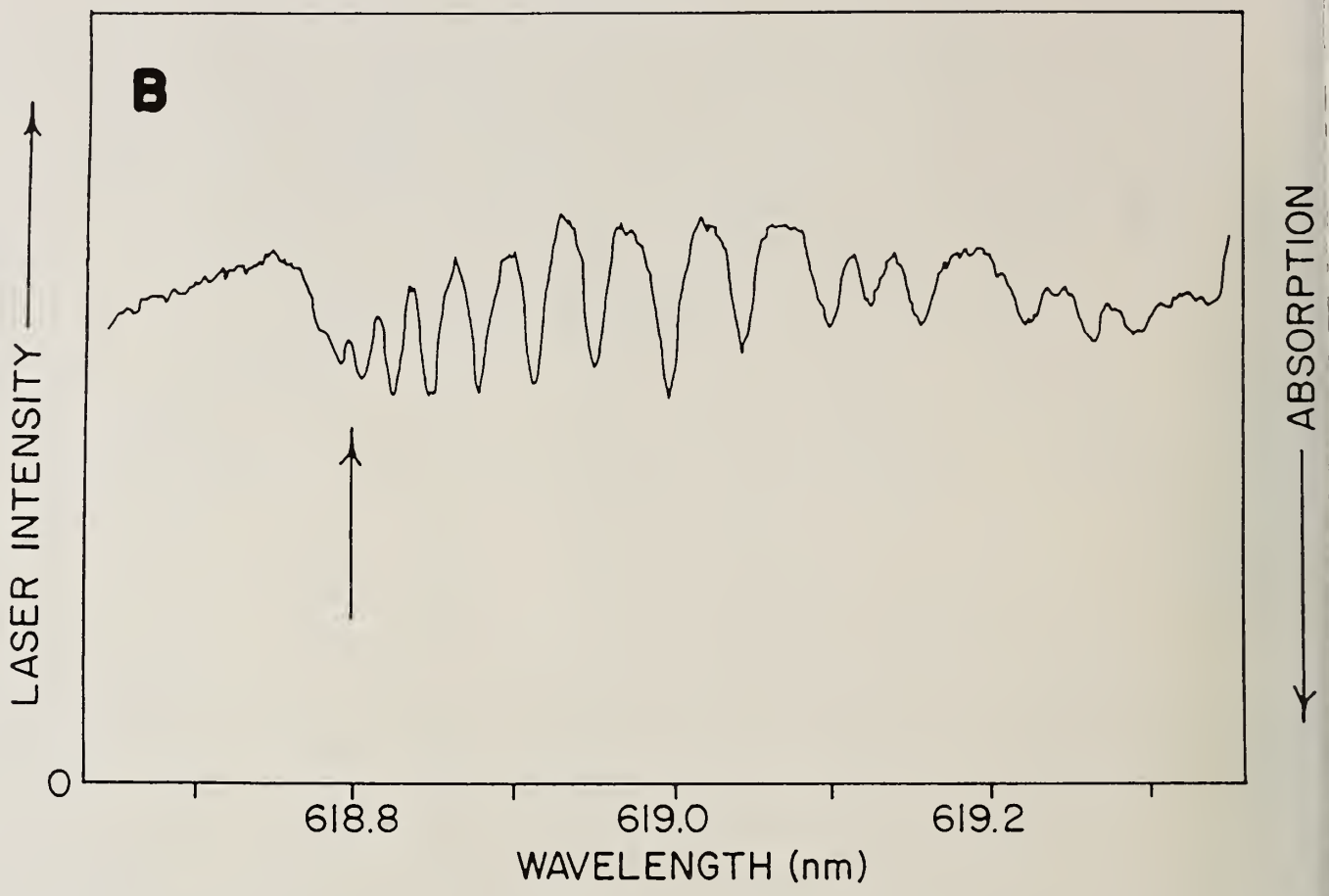
B
LASER INTENSITY
0
618.8
619.0
619.2
WAVELENGTH (nm)
ABSORPTION

figure 6.

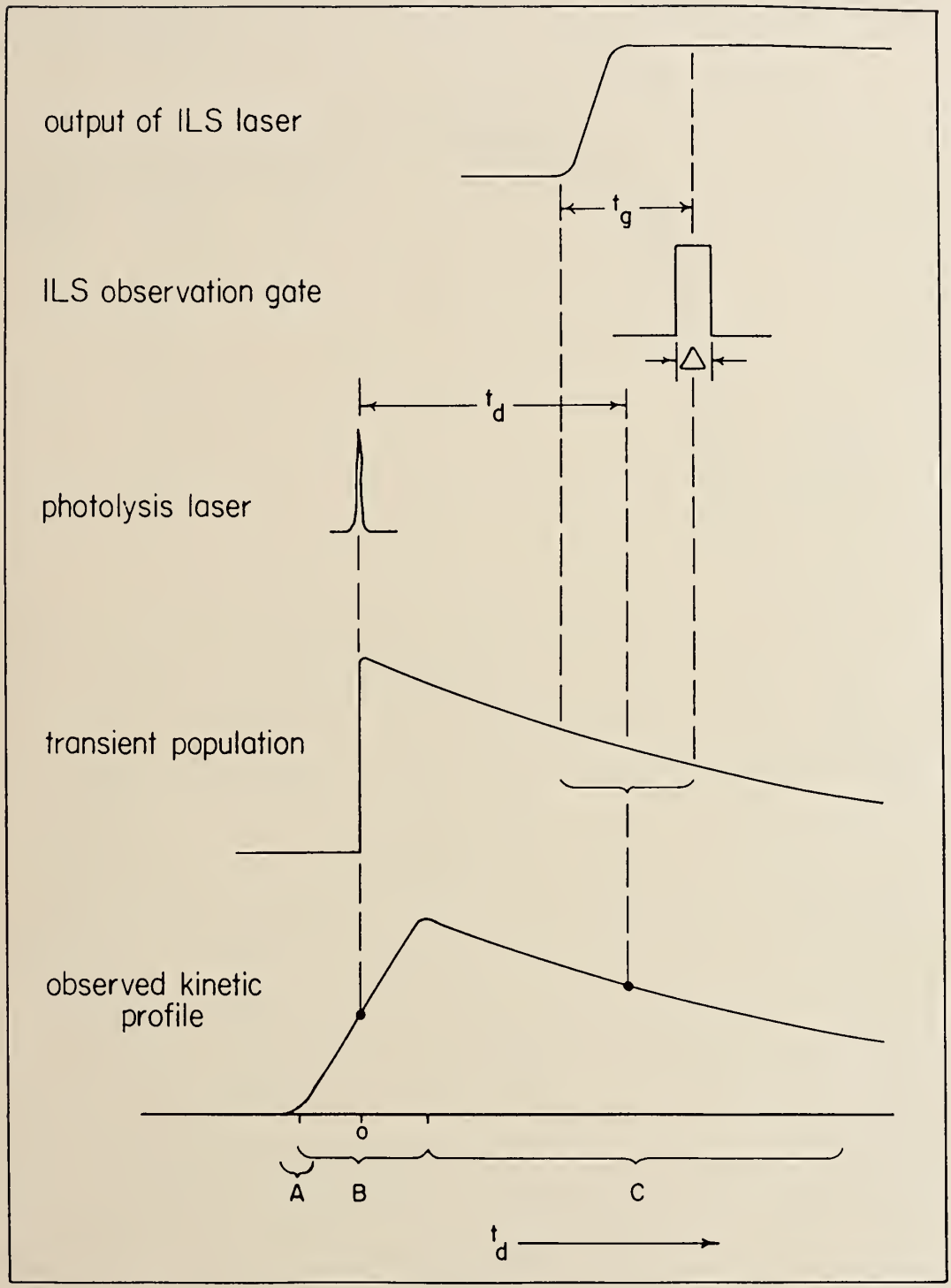
output of ILS laser
t_g
ILS observation gate
t_d
photolysis laser
transient population
observed kinetic profile
0
A
B
C
t_d

figure 7.

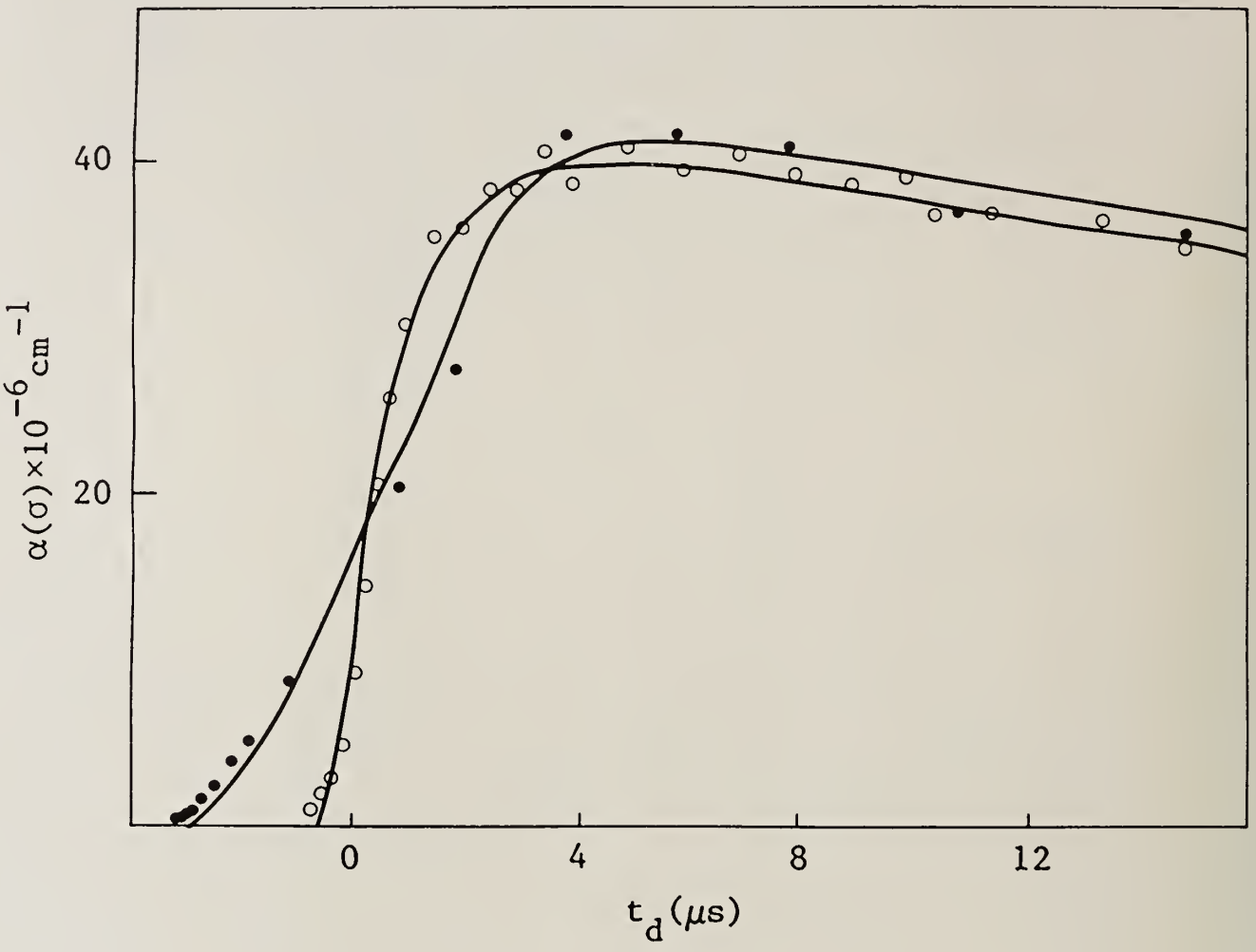

figure 8.

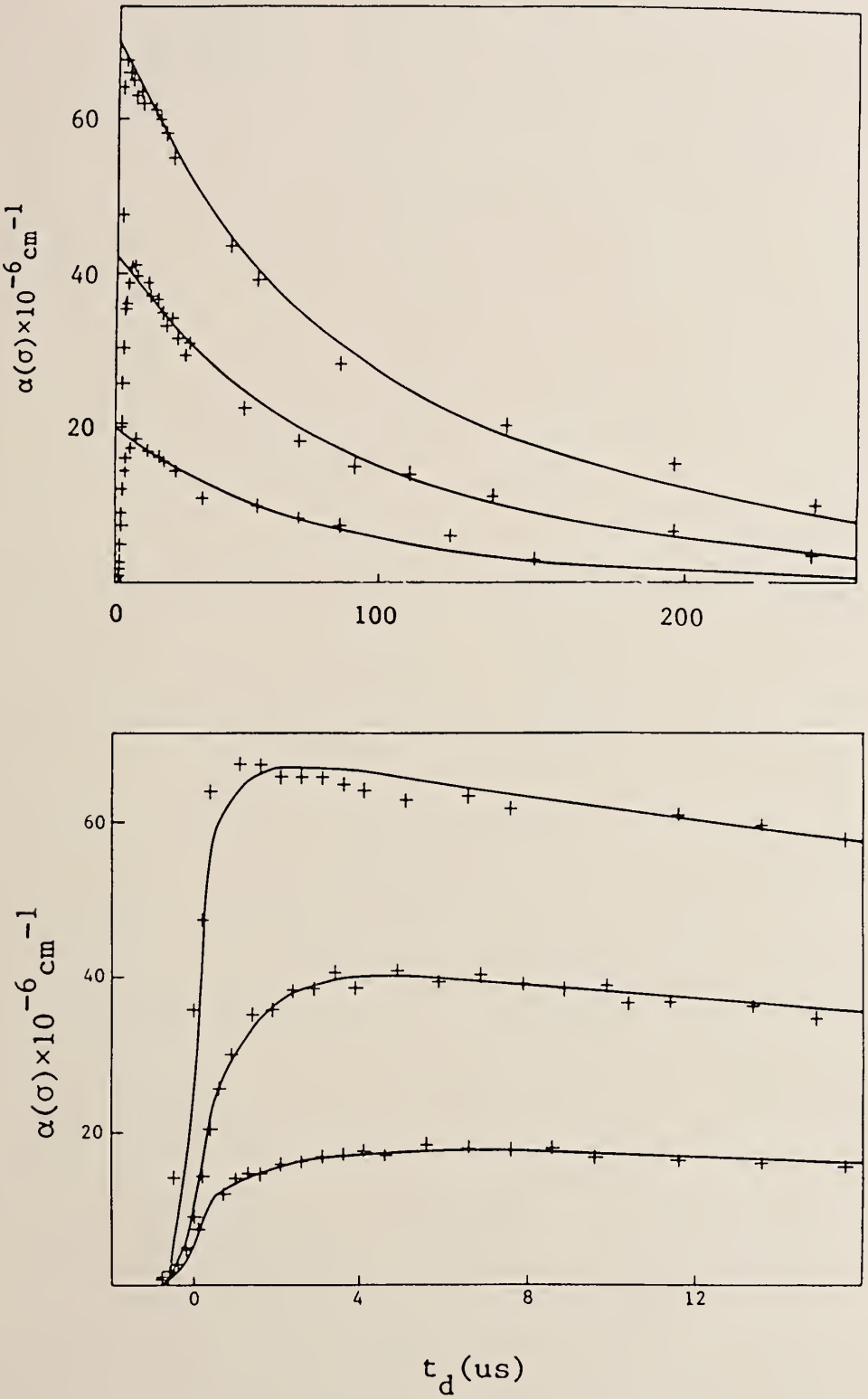

figure 9.

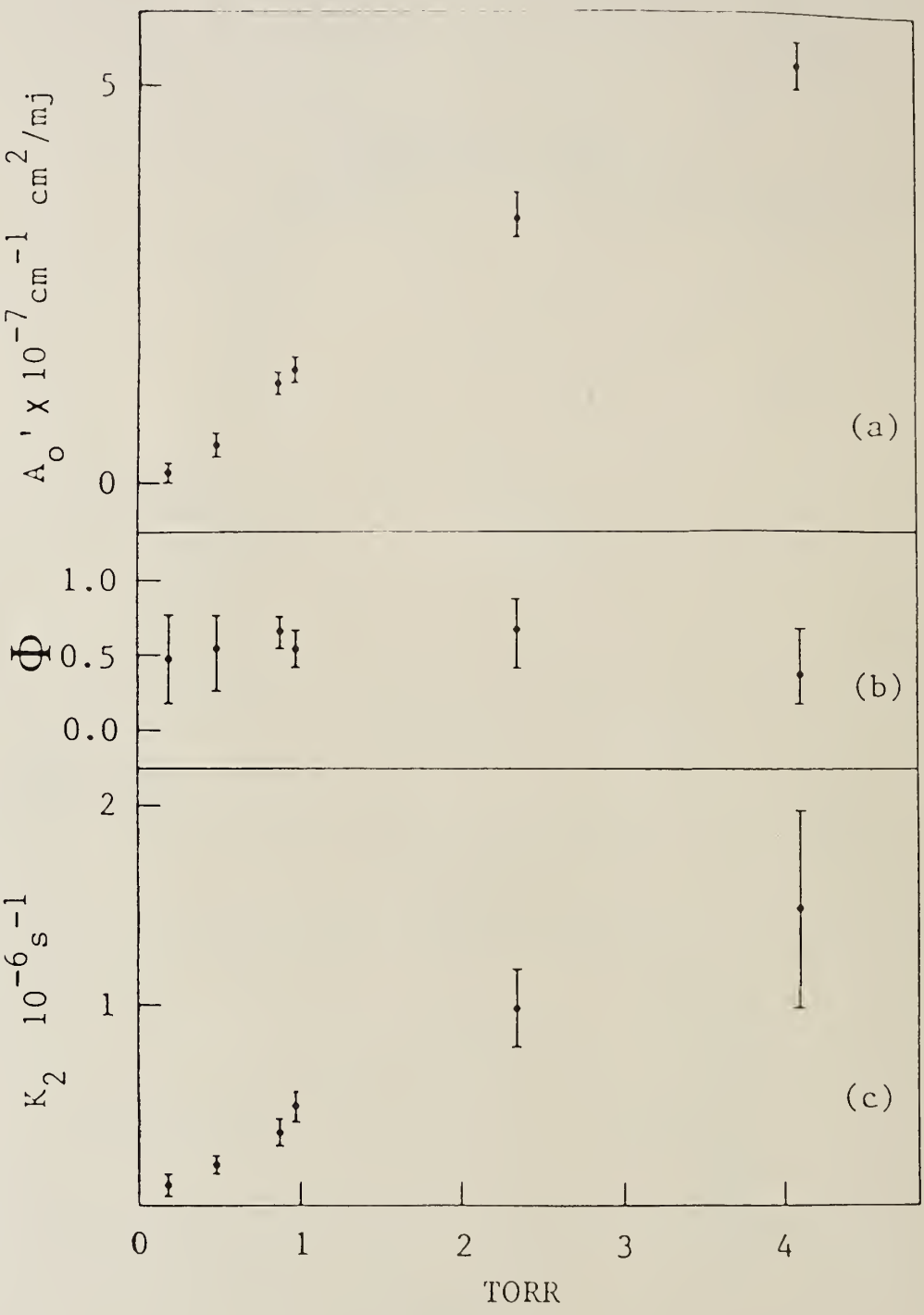
$A_o' \times 10^{-7}$ cm^{-1} cm^2/mj
5
0
(a)
Φ
1.0
0.5
0.0
(b)
K_2 10^{-6} s^{-1}
2
1
(c)
0
1
2
3
4
TORR

figure 10.

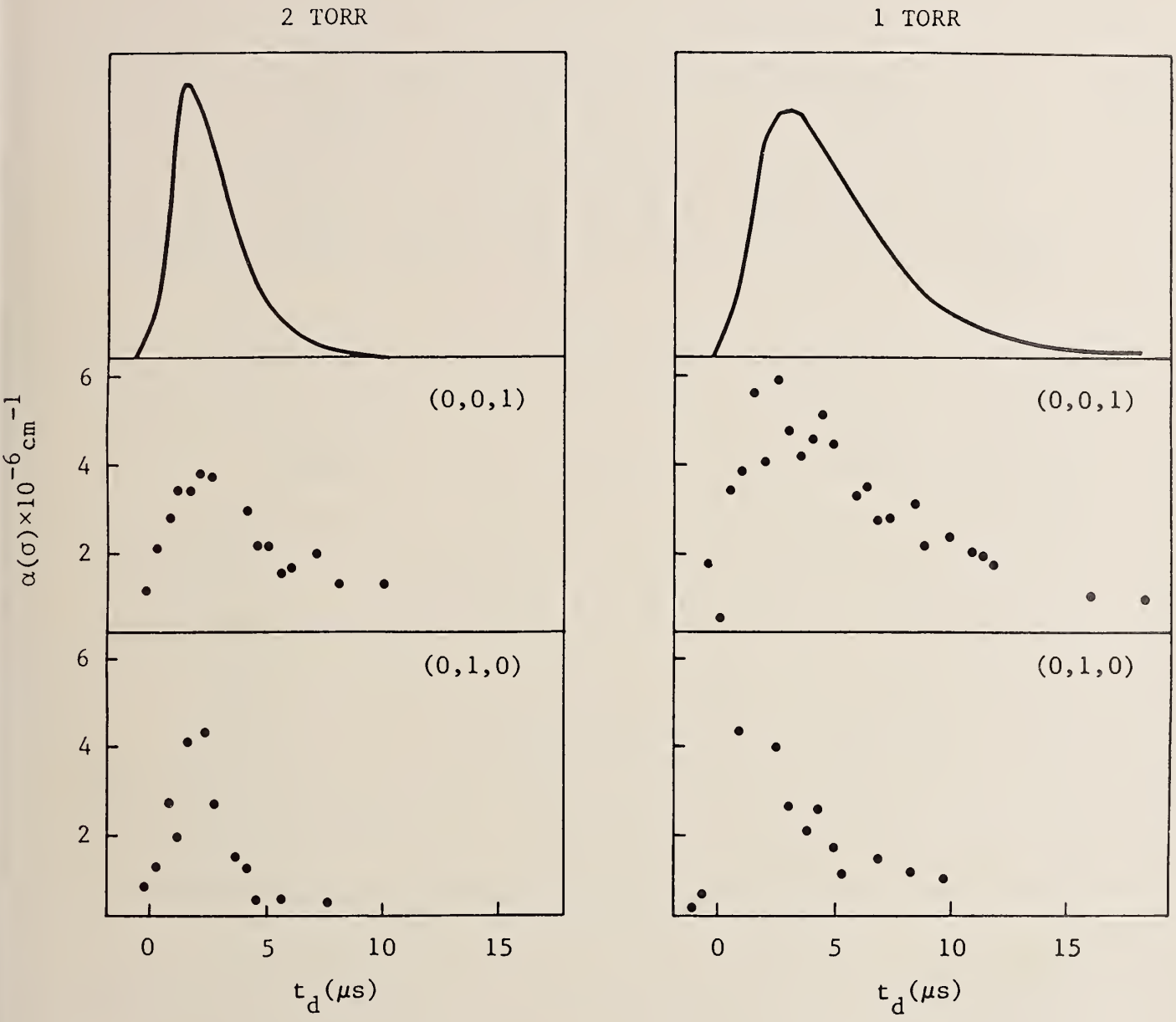
2 TORR
1 TORR
$\alpha(\sigma)\times10^{-6}cm^{-1}$
(0,0,1)
(0,1,0)
6
4
2
0
5
10
15
$t_d(\mu s)$

figure 11.

DETECTION OF CYCLOPROPENYLIDENE C_3H_2

C.A. Gottlieb, P. Thaddeus, and J.M. Vrtilek
Goddard Institute for Space Studies and Columbia University

The small planar carbene ring X^1A_1 cyclopropenylidene (Figure 1), the most stable molecule with the formula C_3H_2[1], was identified by combining frequencies of previously unidentified interstellar (U) lines with millimeter-wave rotational transitions measured in a laboratory glow discharge through He and C_2H_2.[2] The identification is based on the close agreement (to within 1.8%) of rotational constants derived from ab initio calculations[3] and from laboratory experiments, which verified that the carrier is not a molecular ion, does not have a magnetic moment, contains H and C but not N or O, and that the predicted 3:1 ortho-para ratio of line intensities is present. Secondary evidence for the identification is the close agreement of centrifugal distortion constants with cyclopropene[4] and the small inertial defect (0.083), which indicates that the molecule is planar as predicted.

Twenty-seven b-type rotational transitions have been observed, leading to a complete rotational assignment. Nineteen unblended laboratory lines between 82 and 218 GHz with $J \leq 9$ and two astronomical lines in TMC-1 were fitted to an rms deviation of 15 kHz with a standard Hamiltonian[5] containing eight parameters (Table 1), used to predict low lying radio

transitions of C_3H_2 (Table 2).

Cyclopropenylidene is the carrier of eleven U lines, including the intense ubiquitous lines at 18343 MHz[6] and 85338 MHz[7] identified as the lowest lying ortho transitions 1_{10}-1_{01} and 2_{12}-1_{01}. Only moderately abundant in the dense molecular sources such as Ori A and Sgr B2, C_3H_2 is conspicuous because of its large dipole moment of 3.3 D[3] and favorable partition function; in cold, diffuse molecular clouds it may be very abundant.

Laboratory spectroscopy of isotopically substituted species is anticipated.

REFERENCES

(1) W.J. Hehre, J.A. Pople, W.A. Lathan, L. Radom, E. Wasserman, and Z.R. Wasserman, J.A.C.S., 98, 4378 (1976).

(2) P. Thaddeus, J.M. Vrtilek, and C.A. Gottlieb, Ap.J. (Letters), in press.

(3) T.J. Lee, A. Bunge, and H.F. Schaefer III, J.A.C.S., 107, 137 (1985).

(4) W.M. Stigliani, V.W. Laurie, and J.C. Li, J. Chem. Phys., 62, 1890 (1975).

(5) W.H. Kirchhoff, J. Molec. Spectros., 41, 333 (1972).

(6) H.E. Matthews, and W.W. Irvine, Ap.J. (Letters), in press.

(7) P. Thaddeus, M. Guelin, and R.A. Linke, Ap.J. (Letters), 246, L41 (1981).

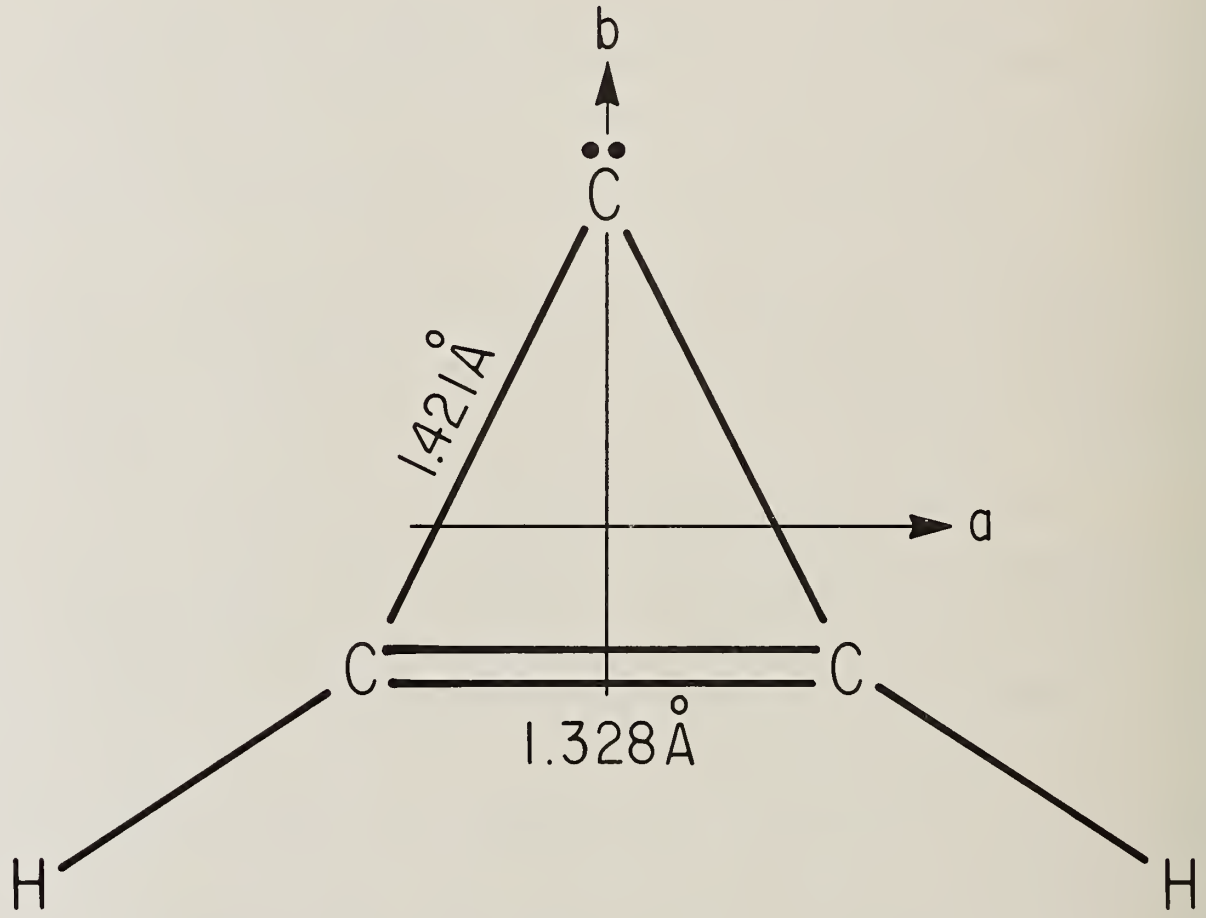

FIGURE 1

TABLE 1. MOLECULAR CONSTANTS OF C_3H_2

Parameter	Measured[a] (this work)	Expected[b]
Rotational and centrifugal distortion constants (in MHz)[c]:		
A	35092.5942 ± 0.0024	35094
B	32212.9292 ± 0.0024	32789
C	16749.3125 ± 0.0019	16951
τ_1	-0.6759 ± 0.0007	-0.7086
τ_2	-0.1626 ± 0.0002	-0.1910
τ_3[d]	15.3728 ± 0.0054	4.1925
τ_{aaaa}	-0.5899 ± 0.0002	-0.2692
τ_{bbbb}	-0.2980 ± 0.0003	-0.2208
τ_{cccc}	-0.0358 ± 0.0002	-0.0688
Inertial defect (in amu Å^2):		
Δ	0.083117 ± 0.000002	---
Bond lengths (in Å) and angle:		
r(C=C)	1.328[e]	1.314
r(C-C)	1.421[e]	1.418
r(C-H)	---	1.074
∢(HC=C)	---	149.6°

[a] Uncertainties: 1σ in least squares fit.

[b] Rotation constants from the ab initio structure of Lee et al. (1985, the DZ+P TCSCF I calculation). Centrifugal distortion constants from the stable three membered ring cyclopropene (Stigliani et al. 1975).

[c] Watson's (1967) determinable parameters.

[d] Not fit: calculated from the other τ's on the assumption of planarity (Kirchhoff 1972).

[e] Calculated from A and B, adopting for the C-H bond and angle the theoretical values (last column this table).

TABLE 2. PREDICTED LOW LYING RADIO TRANSITIONS OF C_3H_2

Frequency (MHz)	Transition	Sym	S	E/k (K)	Frequency (MHz)	Transition	Sym	S	E/k (K)
18343.14 (01)	$1_{1,0} \rightarrow 1_{0,1}$	O	1.50	0.9	122023.52 (02)	$2_{2,1} \rightarrow 1_{1,0}$	O	1.50	6.7
21587.40 (01)	$2_{2,0} \rightarrow 2_{1,1}$	P	2.28	9.7	145089.63 (03)	$3_{1,2} \rightarrow 2_{2,1}$	O	1.25	13.7
27084.34 (03)	$3_{3,0} \rightarrow 3_{2,1}$	O	2.76	17.1	150820.67 (02)	$4_{0,4} \rightarrow 3_{1,3}$	P	3.45	19.3
35360.90 (05)	$4_{4,0} \rightarrow 4_{3,1}$	P	1.11	32.5	150851.90 (02)	$4_{1,4} \rightarrow 3_{0,3}$	O	3.45	17.0
42231.26 (02)	$4_{3,1} \rightarrow 4_{2,2}$	P	3.25	30.9	151343.89 (05)	$5_{1,4} \rightarrow 5_{0,5}$	O	1.79	33.1
44104.79 (02)	$3_{2,1} \rightarrow 3_{1,2}$	O	2.09	15.8	151361.12 (06)	$5_{2,4} \rightarrow 5_{1,5}$	P	1.09	35.4
46755.62 (02)	$2_{1,1} \rightarrow 2_{0,2}$	P	1.05	8.7	155518.30 (02)	$3_{2,2} \rightarrow 2_{1,1}$	P	1.67	16.1
51841.41 (01)	$1_{1,1} \rightarrow 0_{0,0}$	P	1.00	2.5	183623.66 (02)	$4_{1,3} \rightarrow 3_{2,2}$	P	2.42	24.9
55027.77 (02)	$2_{2,1} \rightarrow 2_{1,2}$	O	0.83	6.7	184327.97 (03)	$5_{0,5} \rightarrow 4_{1,4}$	O	4.45	25.8
59557.89 (02)	$3_{3,1} \rightarrow 3_{2,2}$	P	1.37	19.0	184330.03 (03)	$5_{1,5} \rightarrow 4_{0,4}$	P	4.45	28.2
65674.68 (03)	$4_{4,1} \rightarrow 4_{3,2}$	O	1.76	29.9	185617.50 (02)	$4_{2,3} \rightarrow 3_{1,2}$	O	2.46	22.6
80723.20 (04)	$4_{2,2} \rightarrow 4_{1,3}$	P	1.82	28.8	193488.80 (03)	$3_{3,1} \rightarrow 2_{2,0}$	P	2.08	19.0
82093.55 (02)	$2_{0,2} \rightarrow 1_{1,1}$	P	1.37	6.4	204788.97 (05)	$4_{2,2} \rightarrow 3_{3,1}$	P	1.04	28.8
82966.21 (02)	$3_{1,2} \rightarrow 3_{0,3}$	O	0.98	13.7	216278.75 (03)	$3_{3,0} \rightarrow 2_{2,1}$	O	1.42	17.1
84727.70 (02)	$3_{2,2} \rightarrow 3_{1,3}$	P	0.96	16.1	217822.06 (06)	$6_{0,6} \rightarrow 5_{1,5}$	P	5.45	38.6
85338.90 (02)	$2_{1,2} \rightarrow 1_{0,1}$	O	1.50	4.1	217822.18 (06)	$6_{1,6} \rightarrow 5_{0,5}$	O	5.45	36.3
85656.42 (02)	$4_{3,2} \rightarrow 4_{2,3}$	O	1.75	26.7	217940.05 (03)	$5_{1,4} \rightarrow 4_{2,3}$	O	3.43	33.1
116770.81 (03)	$5_{2,3} \rightarrow 5_{1,4}$	O	2.45	38.7	218160.46 (03)	$5_{2,4} \rightarrow 4_{1,3}$	P	3.44	35.4
117151.18 (02)	$3_{0,3} \rightarrow 2_{1,2}$	O	2.44	9.7	227169.14 (04)	$4_{3,2} \rightarrow 3_{2,1}$	O	1.92	26.7
117530.69 (02)	$4_{1,3} \rightarrow 4_{0,4}$	P	1.27	24.9	249054.44 (03)	$5_{2,3} \rightarrow 4_{3,2}$	O	2.38	38.7
117546.23 (02)	$3_{1,3} \rightarrow 2_{0,2}$	P	2.45	12.1	265759.48 (03)	$4_{4,1} \rightarrow 3_{3,0}$	O	2.80	29.9
117731.82 (02)	$4_{2,3} \rightarrow 4_{1,4}$	O	0.99	22.6	282381.13 (03)	$4_{4,0} \rightarrow 3_{3,1}$	P	2.37	32.5

NOTE: Frequencies and 2σ errors (in parentheses) are calculated from the spectroscopic constants, taking into account correlation in the errors. Sym is the symmetry species, ortho (O) or para (P), S the asymmetric rotor line strength, E the energy of the upper level of the transition above the O or P ground state. Only O transitions with $S > 0.3$ and P transitions with $S > 0.9$, both with $E/k < 40$ K, are tabulated.

SPIN TRAPPING OF RADICALS IN TRITIATED ORGANIC MOLECULES *

A. Halpern

Institute of Chemistry 1, Nuclear Research Center Juelich, W. Germany

INTRODUCTION

Tritium decays to ^3He by β^--emission ($T_{1/2}$=12.3 y). If a decaying atom is a constituent of a molecule, this transmutation can be thought of as the annihilation of a hydrogen atom, leaving behind a singly-charged molecular ion: $RT \xrightarrow{-\beta^-} R^+ + {}^3He$, which in a condensed phase is likely to catch an electron to form a radical: $R^+ + e^- \longrightarrow R\cdot$.

Concomitantly, the emitted β^--particle (mean energy 5.7 keV) may cause internal radiolysis of the sorrounding molecules in much the same way as if X- or γ-rays passed through the system, yielding radicals. The question of the relative importance of both modes leading to a radical formation is crucial for the understanding of the molecular effects associated with the decay of incorporated radioisotopes.

In this paper, the radical formation upon the decay of tritium in benzene has been studied with the aim to draw conclusions as to the above question.

EXPERIMENT

The spin trapping ESR spectroscopy was utilized to determine the radical yield in two systems, C_6H_5T/CH_3OH (1%) and C_6H_6/CH_2TOH (1%), containing the same tritium activity. While in the first system both transmutation and internal radiolysis are operative, in the second only radiolysis is responsible for the production of phenyl radicals.

Note that the half-life of tritium is much longer than the duration of the experiment, therefore radicals are formed during the entire time at a constant rate.

RESULTS

Tritiated benzene containing nitrosodurene (ND) or phenyl-t-butyl nitrone (PBN) as spin traps exhibits ESR spectra which increase in amplitude, but

hfs remains unchanged during the entire storage of the sample. The spectra (Figs. 1 and 2a, respectively) are characteristic of the adducts with phenyl radicals only. They do not reveal the phenylcyclohexadienyl radical, which could be expected from the phenylation of benzene, consistently with the fact that Ph· react much faster with ND ($k = 5 \cdot 10^9$ $M^{-1}s^{-1}$) and PBN ($k = 2 \cdot 10^7$ $M^{-1}s^{-1}$) than with benzene ($k = 8 \cdot 10^4$ $M^{-1}s^{-1}$).

Fig. 2 b shows the spectrum observed when CH_2TOH was dissolved in non-radioactive C_6H_6 together with PBN, i.e. it served as an internal radiation source. Lines belonging to the PBN-Ph adduct are seen predominantly, and, at a small ratio, also lines of the PBN-CH_2OH adduct.

In Fig. 3 the relative concentration of Ph· trapped in the two systems under comparison, C_6H_5T/CH_3OH and C_6H_6/CH_2TOH, normalized to the same tritium activity, is plotted against the storage time. The concentration curve for the first system shows about 25 % more radicals than the curve for the second system at the same storage time, i.e. the same number of tritium atoms decayed. We conclude, therefore, that of four Ph· in tritiated benzen three are formed by internal radiolysis. From the nature of things, one Ph· is formed by the transmutation $T \xrightarrow{-\beta^-} {}^3He$. In addition, a ß-particle dissipating its mean energy of 5700 eV produces three Ph· radicals. Then, the radiation yield of Ph· upon tritium ß-particles is $G_{Ph}^{\beta} = \frac{3 \cdot 100 \text{ eV}}{5700 \text{ eV}} = 0.05$. This value agrees with the G_{Ph}-value in benzene irradiated with ^{60}Co γ-rays ($\bar{E} = 1.25$ MeV) what proves a lack of any significant LET effect between tritium ß-s and ^{60}Co γ-s in this system.

x Full paper is in press in Chem. Phys. Letters (1985)

Spin trapping : ND in T - C_6H_6

$A^N = 10.00\,G$

$A^H_o = A^H_p = 2.75\,G$

$A^H_m = 1.00\,G$

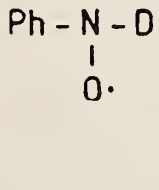

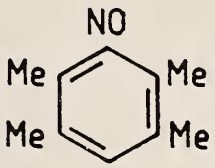

Fig. 1

Spin trapping : PBN in T-C_6H_6 (0.5M)

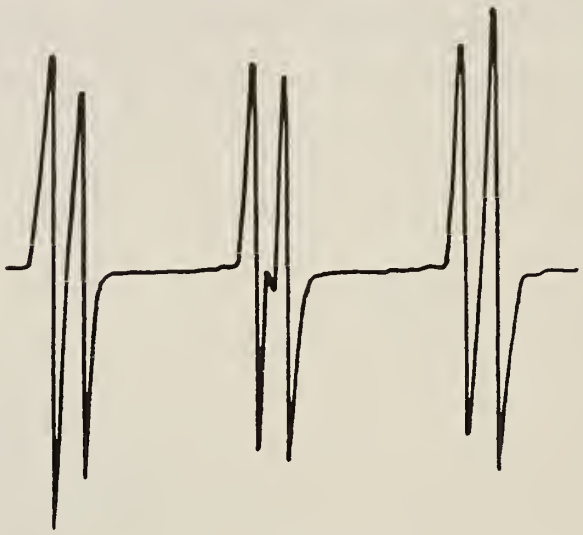

A^N = 14.38G
A^H = 2.25G

Fig. 2a

Spin trapping : PBN in $CH_2TOH + C_6H_6$ (1:100)

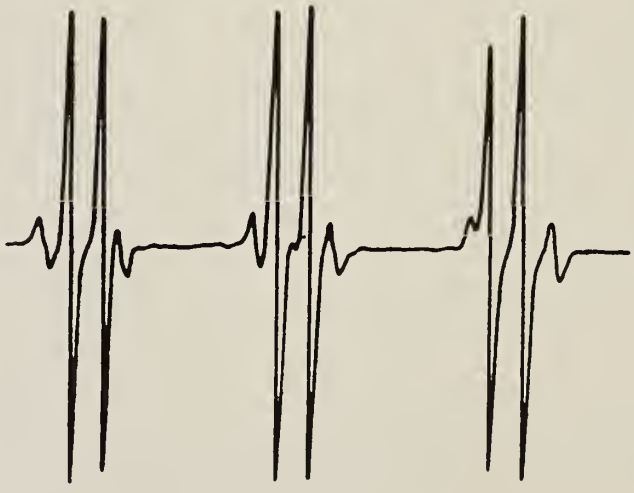

Fig. 2b

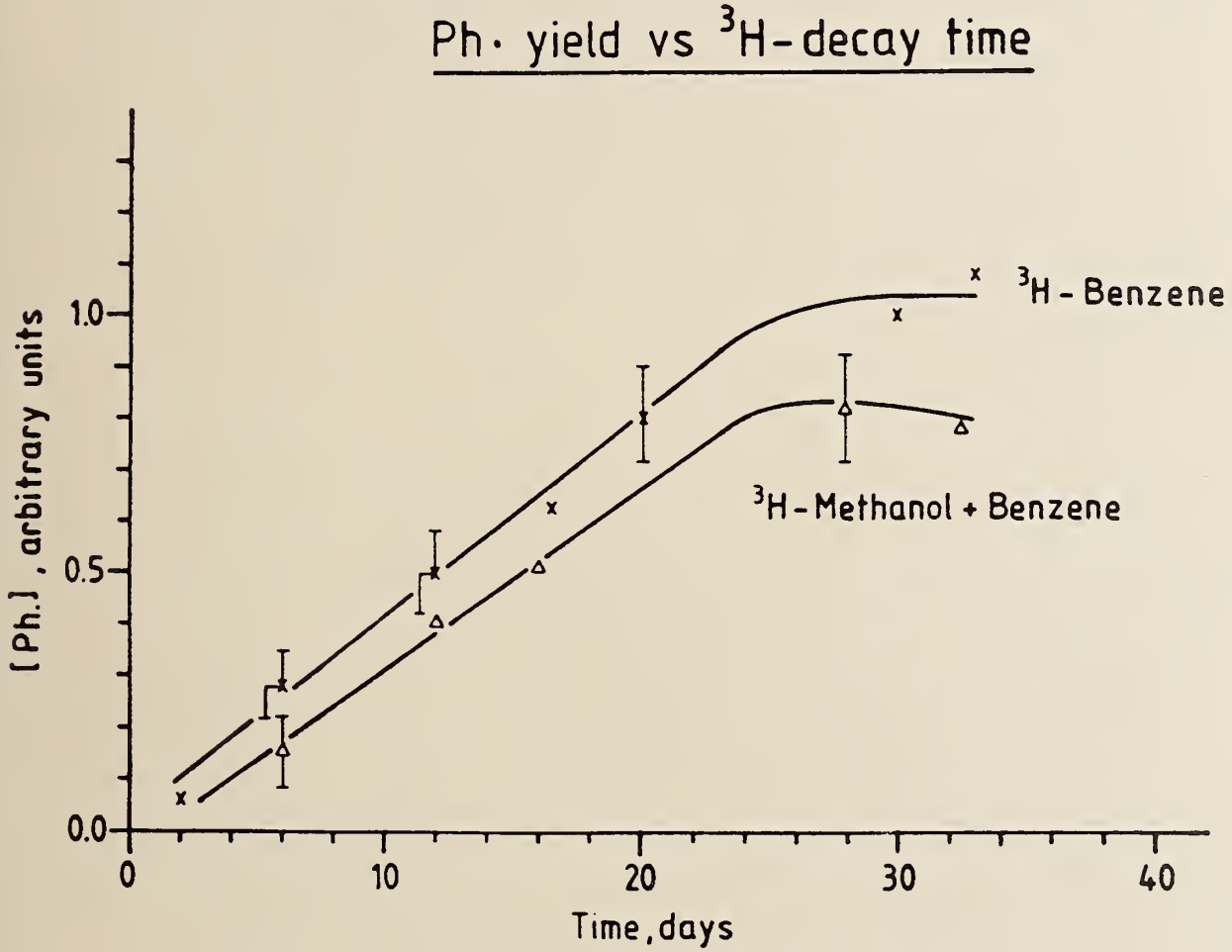
Ph· yield vs ^{3}H-decay time
[Ph.], arbitrary units
1.0
0.5
0.0
0
10
20
30
40
Time, days
^{3}H-Benzene
^{3}H-Methanol + Benzene

Fig. 3

SPIN TRAPPING OF RADICALS IN GAS-PHASE TOBACCO SMOKE *

A. Halpern and J. Knieper

Institute of Chemistry 1, Nuclear Research Center Juelich, W. Germany

INTRODUCTION

The laboratory of W.A. Pryor is presently the only research group carrying out systematic studies of radicals in tobacco smoke, both in the tar and the gas phase, by spin trapping (see a recent review, D.F. Church and W.A. Pryor, Environ. Health Perspect., 1985). Our results present an independent confirmation of those of Pryor et. al., and in certain respects offer new evidence.

EXPERIMENTAL

The manual smoking apparatus (Fig. 1) designed to smoke simultaneously three cigarettes was operated from a gas-tight syringe so that every 20 s a 25 ml puff of about 5 s duration (a total of 25 puffs per cigarette) was drawn through a cylindrical chamber (volume: 22 ml) with a paper filter on the porous glass support in the middle, and a 0.5 mm i.d. capillary, into a vessel containing spin trap solution. The total length from the cigarette holder to the solution was 550 mm. Commercial non-filtered cigarettes were used. The spin trap solution was then deoxygenated by flushing nitrogen, transferred to a ESR tube placed in the cavity, and the ESR spectra were recorded at room temperature.

RESULTS AND DISCUSSION

The ESR spectrum produced in 0.05 M PBN (N-t-butyl-α-phenyl nitrone) in benzene by smoke from three cigarettes, and the spectra recorded after 15 min and 90 min (Fig. 2 a, b and c) suggest the presence of two nitroxides, the dominant one with the coupling constants A^N = 13.63 G and A^H_β = 2.0 G, and the other (marked with arrows) with A^N = 10.25 G and no visible proton splitting. The relative intensities of the lines characteristic of the two adducts change with the storage time in favor of the simple triplet,

but it is clearly seen that the first one (with A^N = 13.63 G) always prevails. This triplet of doublets is likely to represent the superposition of lines due to different radical adducts having similar hfsc's, of which the PBN-RO is the prevailing adduct, but it may also include the alkyl adduct, PBN-R. However, since (i)alkyl radicals are trapped much less efficiently than alkoxy radicals, and (ii) alkyl radicals react exothermically with oxygen to form alkylperoxy radicals, it can be foreseen that that the contribution from PBN-R will be unimportant. The peroxy radicals can be trapped by PBN but the respective spin adducts are unstable toward light and are replaced by the alkoxy adducts.

The 10.25 G triplet does not seem to result from the oxidation of PBN, since such a signal was not observed when we let a stream of O_2, NO_2, or a mixture of NO and O_2 to pass through a 0.05 M PBN in benzene at room temperature. Recently, Pryor suggested that this adduct is a vinyl nitroxide.

In another series of experiments we employed DMPO (5,5-dimethyl-1-pyrroline-N-oxide), which is a convenient trapping agent for oxy-radicals. In the spectrum produced by smoke from three cigarettes in 0.05 M DMPO in benzene (Fig. 3) one set of reasonably sharp lines can be distinguished which indicate a triplet with A^N = 13.5 G, further split into secondary doublet due to a β-proton, A^H_β = 8.0 G, and another doublet by a γ-proton, A^H_γ = 2.2 G. This hfs is consistent with t-butoxy adduct. Moreover, a number of other lines which are superimposed and only partially resolved make the spectrum complex and its interpretation ambigous, even though they bear evidence to the presence of various radical species. The basic conclusion is that a mixture of several radicals, predominantly oxygen-centered, is obtained in the smoke. We did not observe any ESR signal in methanolic or aqueous solutions of PBN, presumably because the alkoxy radicals are unstable in polar media.

A comment on the origin of radicals trapped from tobacco smoke: The radicals in question are not expected to have lifetimes long enough to allow them to travel a substantial distance of 550 mm to the spin trap solution, including through a filter. Therefore, one has to assume that a radical-forming process is in operation in the smoke stream, in which radicals are continuously formed as the smoke proceeds toward the solution during the entire course of smoking. Pryor et al. provided evidence that this process depends on the slow oxidation of NO to NO_2, followed by reactions of NO_2 with smoke components such as olefins or dienes to give alkyl radicals R· which will be then oxidized to alkylperoxy radicals ROO· and eventually converted to alkoxy radicals RO· . Therefore, the radicals observed by the spin trapping, although initiated by the combustion pocess, are not those formed directly in the flame. A similar situation occurs in human smoking, i.e. these small radicals do not reach the lungs of a smoker.

* Full paper published in Z. Naturforsch. 40b, 850-852 (1985)

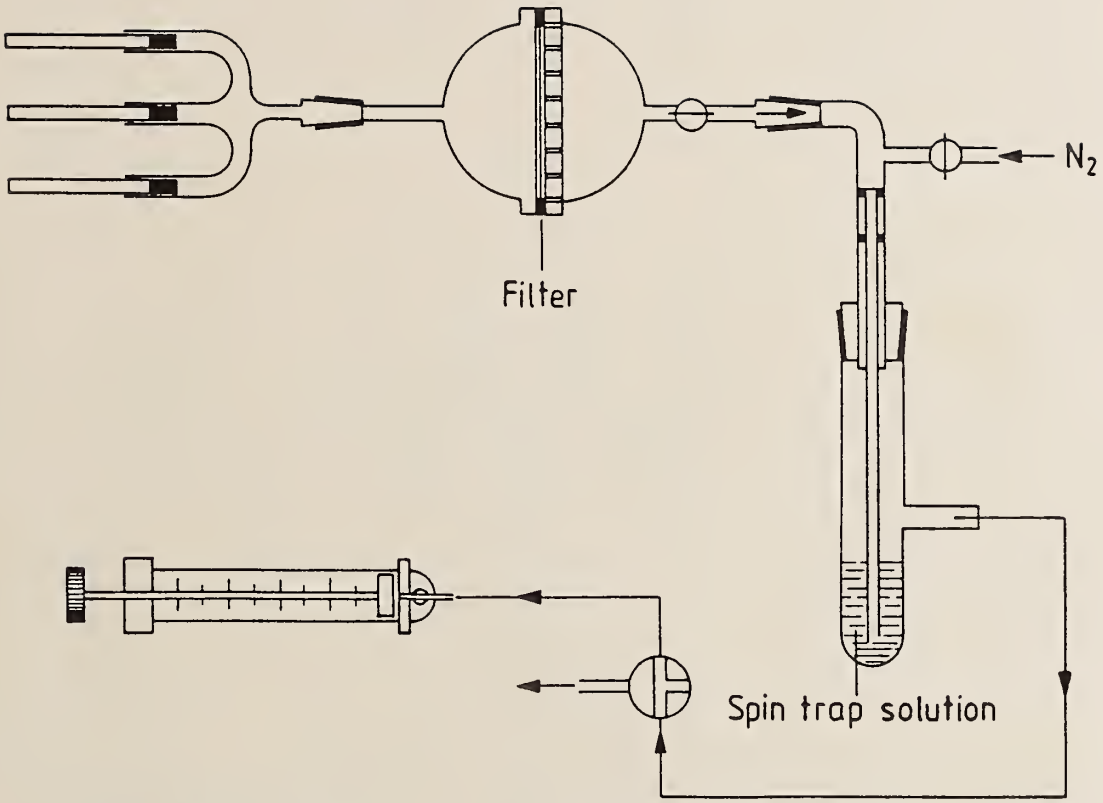

SKETCH OF THE MANUAL SMOKING DEVICE

Fig. 1

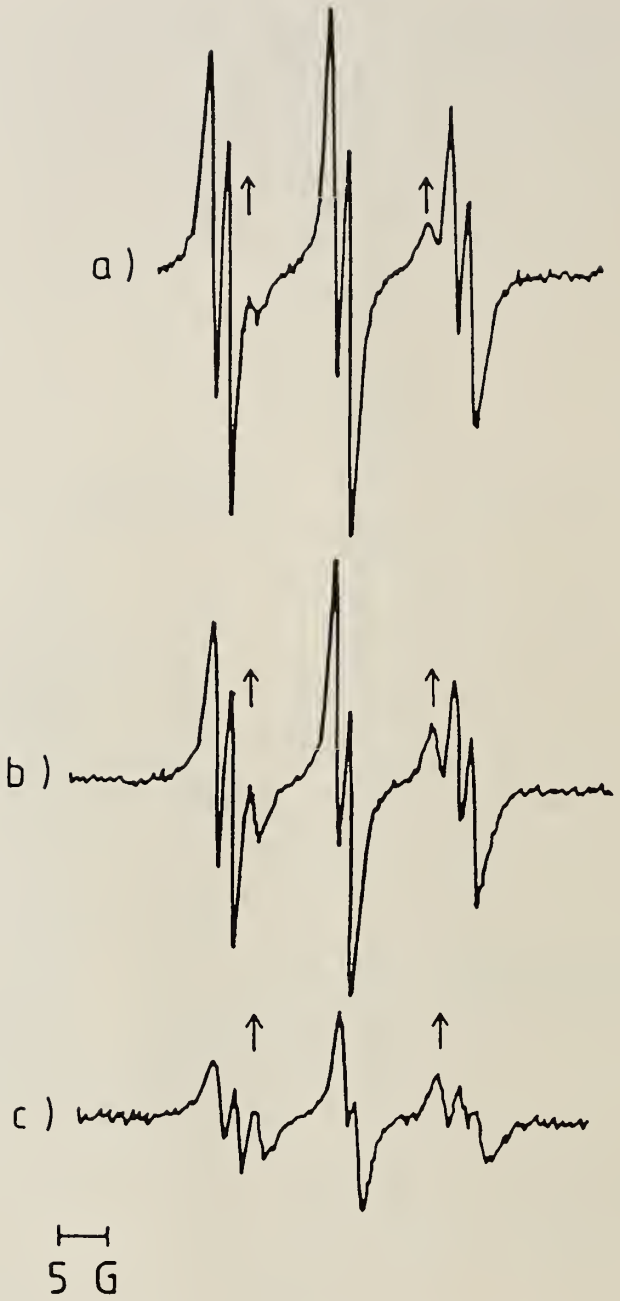

a) THE ESR SPECTRUM FROM CIGARETTE SMOKE IN 0.05 M PBN IN BENZENE

b) SAME SAMPLE, 15 MIN LATER

c) SAME SAMPLE, 90 MIN LATER

Fig. 2

THE ESR SPECTRUM FROM CIGARETTE SMOKE IN 0.05 M DMPO IN BENZENE.

Fig. 3

$HOSO_2$ and $HOS(O_2)O_2$ Radicals Studied by the Matrix Isolation FTIR Technique and ab initio Calculation

Satoshi Hashimoto and Hajime Akimoto
National Institute for Environmental Studies
P.O. Tsakubagakuen, Ibareki 305, Japan

Shigeru Nagase
Yokohama National University, Yokohama,
Kanagawa, Japan

Abstract. The infrared absorption bands at 3539.9 (3528.6), 1309.2 (1308.7), 1097.3 (1096.0) and 759.5 (735.1) cm^{-1} obtained in the Ar matrix have been assigned to the O-H st., $S(=O)_2$ asym. st., $S(=O)_2$ sym. st., and S-OH st. mode of the $H^{16}OS^{16}O_2$ ($H^{18}OS^{16}O_2$) radicals, respectively. Optimized geometries and fundamental vibrational frequencies for these radicals were given by the *ab initio* calculations with the 3-21G$^{(*)}$ basis function. The calculated frequencies for the $H^{16}OS^{16}O_2$ ($H^{18}OS^{16}O_2$), 3818 (3805), 1319 (1318), 1125 (1122) and 922 (889) cm^{-1} for the above vibrational modes, respectively, agree well with the observed values within 20% at the most and give the consistent isotope shift. All of the $HOSO_2$ band disappeared in the O_2 matrix suggesting that the radical does react with O_2 but the bands ascribed to either the $HOS(O_2)O_2$, SO_3 or HO_2 radical were not confirmed. The *ab initio* calculation gave the optimized geometry and expected vibrational frequencies of the $HOS(O_2)O_2$ radical.

INTRODUCTION

Hydroxysulfonyl radical, $HOSO_2$ is recognized as an important intermediate in the atmospheric oxidation of SO_2 initiated by the OH radicals,

$$OH + SO_2(+M) \rightarrow HOSO_2(+M) \quad (1)$$

and the fate of the $HOSO_2$ radical in the atmosphere is of particular concern[1]. Stockwell and Calvert[2] showed the evidence that the chain sustaining steps either by

$$HOSO_2 + O_2 \rightarrow HO_2 + SO_3 \quad (2)$$

or

$$HOSO_2 + H_2O \Longleftrightarrow HOSO_2 \cdot OH_2 \quad (3)$$

$$HOSO_2 + OH_2 + O_2 \rightarrow H_2SO_4 + HO_2 \quad (4)$$

should be of more significance than the recombination reaction,

$$HOSO_2 \cdot O_2(+M) \rightarrow HOS(O_2)O_2(+M). \quad (5)$$

Further evidence supporting the occurrence of reaction (2) has been reported in the kinetic studies[3-6].

In our attempt to characterize the intermediate radicals of atmospheric oxidation of SO_2, we attempted the infrared spectroscopic detection in the low temperature matrices and a part of the results in the argon matrix has been reported previously[7]. In the present study, *ab initio* calculations of the molecular geometries and vibrational fundamental frequencies for the ground state of the $HOSO_2$ and $HOS(O_2)O_2$ radicals using the 3-21G$^{(*)}$ basis set functions are reported as well as further experimental evidence in the $H/SO_2/Ar$ and

$OH/SO_2/O_2$ system in the matrices at 11K.

For the "hypervalent" sulfur-oxygen containing species, *ab initio* calculations have been studied by Boyed *et al.*[8] on sulfonyl radicals, XSO_2 (X = H, CH_3, NH_2, OH, F and Cl) and other related species by use of the STO-3G* basis set. Another series of sulfur-oxygen compounds, the S(IV) and S(VI) systems of stable molecules and ions have been studied by Baird and Taylor[9] using both the STO-3G* and 44-31G* basis set. In these studies, optimized geometries and total energies are given but no vibrational frequences were reported.

EXPERIMENTAL

Matrix isolation experiments were conducted by using the gas-phase photolysis of either H_2O_2/O_2 (1:250) at 185 nm or H_2O/O_2 (1:250) at 147 nm as the OH source. After mixing with SO_2/O_2 (1:250) the reaction mixture was deposited on the CsI cold surface at 11K. The details of the experimental setup used have been described previously[7]. In order to sort out the absorption bands of products from the $H + SO_2(+M)$ reaction, the matrix isolation experiments coupled with the discharge flow for the $H_2/SO_2/Ar$ system was also carried out. In this experiment, a microwave discharge lamp was substituted by a discharge flow tube with a sampling pinhole. The mixture of H_2/Ar was discharged through a microwave cavity and the SO_2/Ar mixture was added downstream, and a part of the reaction mixture was sampled to the cold finger through the pinhole.

Infrared spectra were measured by a Fourier transform infrared spectrometer (Nicolet, model 7199) under the conditions of 0.24 cm^{-1} resolution and 512 times

accumulation using a liquid N_2 cooled HgCdTe detector. The spectral region observed was 4000-700 cm^{-1}.

CALCULATION METHOD

Ab initio calculations for the $HOSO_2$ and $HOS(O_2)O_2$ radicals were performed using Gaussian 80 program provided at IMS (Institute for Molecular Science) with the 3-21G$^{(*)}$ basis function. In this basis set, polarization functions were included only for sulfur atoms. The Gaussian exponents given by Pietro *et al.*[10] were used for the calculation. Full optimization of geometries were performed for both of the radicals.

RESULTS AND DISCUSION

$HOSO_2$ Radical

Figure 1a and 1b represent the matrix infrared absorption spectra of reaction mixture obtained by the irradiation of the H_2O_2/Ar and SO_2/Ar mixture at 185 nm, and of the H_2O^{16}-$H_2{}^{18}O$ (1:1)/Ar and SO_2/Ar mixture at 147 nm, respectively. In our previous note[7], the bands at 3539.9 (3528.6), 1309.2 (1308.7), 1097.3 (1096.0) and 759.5 (735.1) cm^{-1} were assigned to the O-H st., $S(=O)_2$ asym. st., $S(=O)_2$ asym. st. and S-OH st. bands of $HO^{16}S^{16}O_2$ ($H^{18}OS^{16}O_2$) radicals, respectively. The bands at 1286.8 and 1285.4 nm were thought to be attributed to some other species which does not contain OH group since the isotope shift was not observed when the mixture of $H_2{}^{16}O$ and $H_2{}^{18}O$ was used and also the peak intensity varied independently from other peaks when the reaction

mixture was annealed. In the present study, discharged H_2/Ar was mixed with SO_2/Ar and the reaction mixture was deposited on the cold plate to take an infrared spectrum. Observed spectrum does show the two peaks at 1287.5 and 1285.5 cm^{-1} agreeing well with the unidentified peaks noted above, which confirms our previous assignment that these two peaks are not from the reaction of OH radical with SO_2 but from the reaction of H atom with SO_2.

Table 1 compares the observed vibrational frequencies of the $H^{16}OS^{16}O_2$ radical with the calculated values obtained by the *ab initio* calculation with the 3-21G$^{(*)}$ basis functions. As shown in Table 1, the calculated vibrational frequencies were 7.8, 0.7, 2.5 and 21.4% higher than the observed one for the H-O st., $S(=O)_2$ asym. st., $S(=O)_2$ sym. st. and S-OH st. mode, respectively. The uneven ratio of the calculated to observed frequencies for different vibrational modes and the ratio of larger than unity have been noted[10] in the *ab initio* calculations with the 3-21G$^{(8)}$ basis set for hypervalent sulfur compounds being consistent with the present result.

Further, values and trend of the ^{16}O-^{18}O isotope shift were reporduced satisfactorily for all the observed vibrational modes of the hydroxysulfonyl radicals as shown in Table 1. The H-O-S bending mode as calculated at 1181 and 1175 cm^{-1} for the $H^{16}OS^{16}O_2$ and $H^{18}OS^{16}O_2$, respectively, may be overlapped by the strong absorption of SO_2 centered at ca. 1150 cm^{-1}.

Figure 2 shows the optimized geometry, atomic spin densities, and net atomic charges of the $HOSO_2$ radical attained by the *ab initio* calculation. It

should be noted that the S=O bond length of the $HOSO_2$ radical (1.441A) is appreciably longer than that of SO_2 (the calculated value[10], 1.419A with the 3-21G(*) basis set, and the experimental value[11], 1.431A) giving the lower frequencies of the $S(=O)_2$ asym. and sym. stretching mode for the $HOSO_2$ as compared to SO_2 (1573 and 1341 cm^{-1} by the 3-21G(*) calculation[10], and 1356 and 1153 cm^{-1} in the Ar matrix[12]). It should also be noted in Figure 2 that the spin densities of the $HOSO_2$ radical is delocalized among the $S(=O)_2$ moiety rather than localized to the sulfur atom, and the net charges are polarized to give a large dipole moment for the radical.

$HOS(O_2)O_2$ RADICAL

When Ar was substituted by O_2 as the matrix gas both in the H_2O_2-SO_2 and H_2O-SO_2 system, all the bands shown in Figure 1 disappeared as depicted in Figure 3 indicating that $HOSO_2$ does react with O_2. However, no new distinct peak was recognized in the O_2 matrix in either of the reaction system in the wavenumber range of 4000-700 cm^{-1} except for the bands of O_3 at 1034 and 702 cm^{-1}. Since the band for the OH radicals in the matrix was clearly seen in the irradiation of the H_2O_2/O_2 or H_2/O_2 mixture during deposition, and the peak disappeared when the SO_2/O_2 mixture was codeposited, the reason for the invisibility of any new product peak is not clear. Formation of several products in the reaction of $HOSO_2$ in the O_2 matrix as expected from the delocalized spin density (see Figure 2) might be responsible to the weakness of each absorption band to

be observed. No band which can be ascribed to SO_3[12] and HO_2[13] was also observed.

Ab initio calculation of the $HOS(O_2)O_2$ radical gives the optimized geometry shown in Figure 4. It is to be noted that the S=O bond distance (1.414 and 1.406A) is appreciably shorter that that in the $HOSO_2$ radical (1.441A) and is closer to the value for SO_2 calculated[10] with the same basis set (1.419A). As shown in Figure 5, the atomic spin resides solely on the terminal oxygen atom giving the features of more common peroxy radical for the $HOS(O_2)O_2$. The electrons are highly polarized as in the case of the $HOSO_2$ giving the large dipole moment of 3.16 D. The calculated vibrational frequencies are given in Table 2 comparing with those for SO_2. As shown in Table 2, the expected frequencies of $S(=O)_2$ asym. and sym. stretching mode are very close to those for SO_2 corresponding to the close S=O bond distances for these species as noted above. From these results, while the invisibility of the $S(=O)_2$ stretching mode of the $HOS(O_2)O_2$ in the O_2 matrix might be due to the overlapping of the strong SO_2 band, the S-OH and S-OO stretching bands should be seen if the radical is formed in a signficant amount.

References

1. J. G. Calvert, and W. R. Stockwell, Acid precipitation: SO_2, NO and NO_2 oxidation mechanism: atmospheric considerations, Ann Arbor Science, Ann Arbor 1983 Ch. 1, and references therein.

2. W. R. Stockwell and J. G. Calvert, *Atmos. Environ.,* **17,** 2231 (1983).

3. J. J. Margitan, *J. Phys. Chem.,* **88,** 3014 (1984).

4. H. Bandow, and C. J. Howard, private communication.

5. K. H. Becker, private communication.

6. G. LeBras, private communication.

7. S. Hashimoto, and H. Akimoto, *Chem. Phys. Lett.,* **107,** 198 (1984).

8. R. J. Boyd, A. Gupta, R. F. Langler, S. P. Lownie, and J. A. Pinock, *Can. J. Chem.,* **58,** 331 (1980).

9. N. C. Baird, and K. F. Taylor, *J. Comput. Chem.,* **2,** 225 (1981).

10. W. J. Pietro, M. M. Francl, W. J. Hehre, D. J. DeFrees, J. A. Pople and J. S. Binkley, *J. Am. Chem. Soc.,* **104,** 5039 (1982).

11. Y. Morino, Y. Kikuchi, S. Saito, and E. Hirota, *J. Mol. Spectrosc.,* **13,** 95 (1964).

12. J. R. Sodeau, and E.K.C. Lee, *J. Phys. Chem.,* **84,** 3358 (1980).

13. H. Bandow and H. Akimoto, *J. Phys. Chem.,* **89,** 845 (1985).

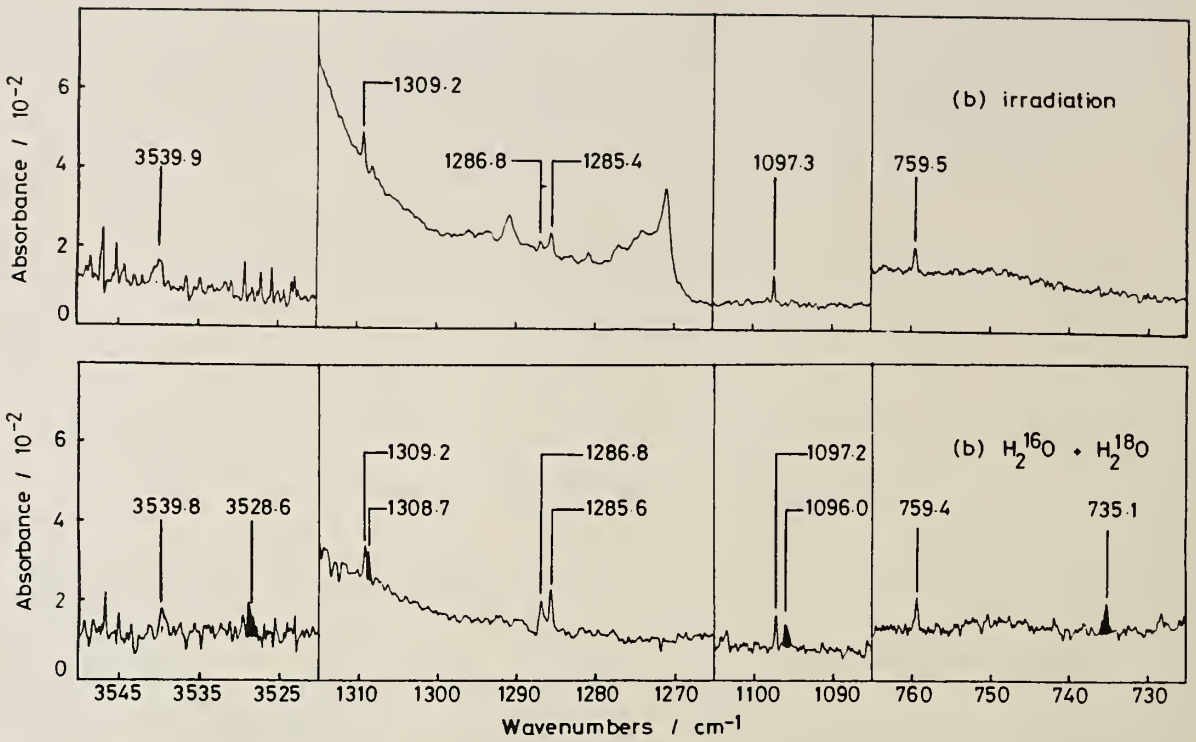

Figure 1. Infrared spectra of reactin mixtures of (a) H_2O_2/Ar and SO_2/Ar with the irradiation at 185 nm, and (b) $H_2{}^{18}O$-$H_2{}^{16}O$ (1:1)/Ar and SO_2/Ar with the irradiation at 147 nm.

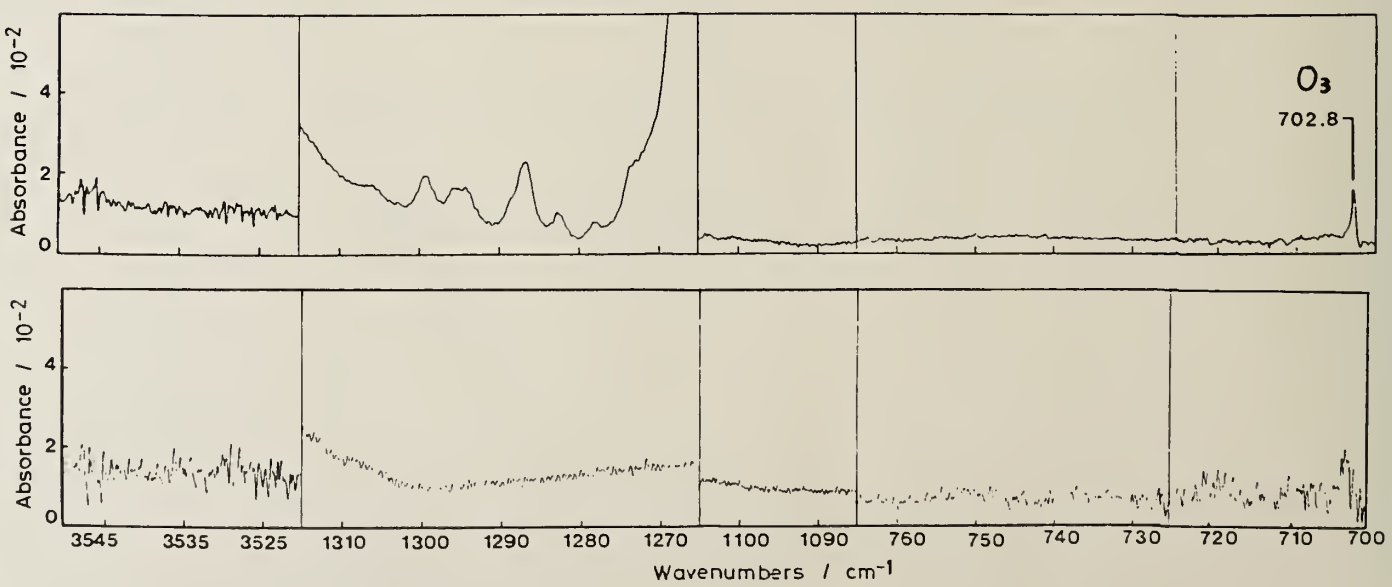

Figure 3. Infrared spectra of reaction mixtures of (a) H_2O_2/O_2 and SO_2/O_2 with the irradiation at 185 nm, and (b) H_2O/O_2 with the irradiation at 147 nm.

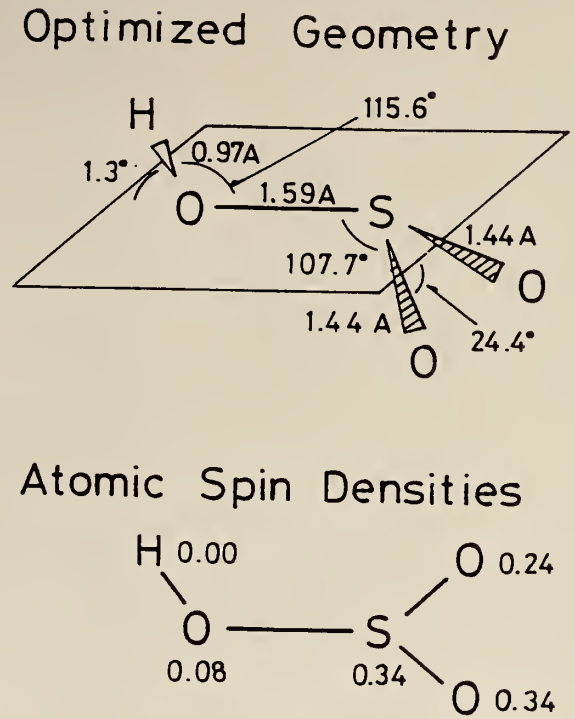

Figure 2. Optimized geometry, atomic spin densities, and net atomic charges of the $HOSO_2$ radical

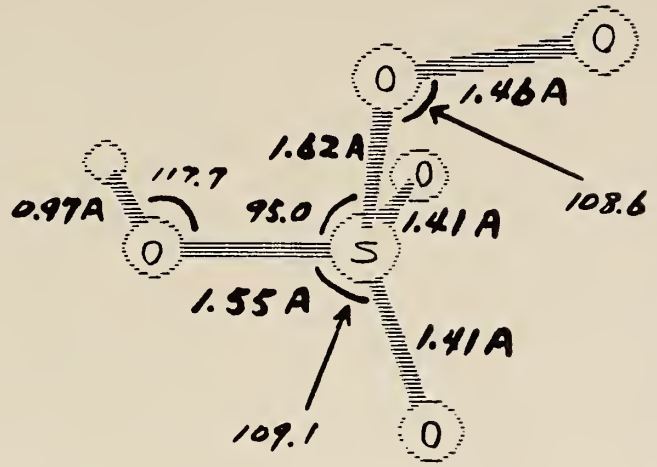

Figure 4. Optimized goemetry of the $HOS(O)_2O_2$ radical

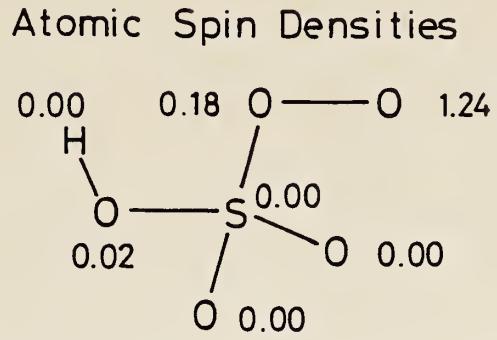

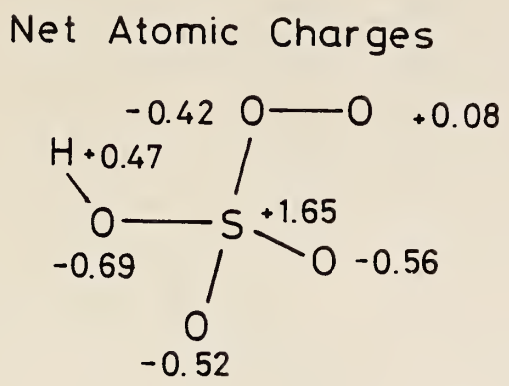

Figure 5. Atomic spin densities and net atomic charges of the $HOS(O)_2O_2$ radical

Table 1. Comparison of the experimental and calculated frequencies of $H^{16}OS^{16}O_2$ and $H^{18}OS^{16}O_2$.

	Calc.	Exp.	Calc./Exp.	
O-16	3818	3539.9	1.078	H-O st.
O-18	3805	3528.6	1.078	
	13	11.3		
O-16	1319	1309,2	1.007	$S(=O)_2$ asym. st.
O-18	1318	1308.7	1.007	
	1	0.5		
O-16	1125	1097.3	1.025	$S(=O)_2$ sym. st.
O-18	1122	1096.0	1.024	
	3	1.3		
O-16	921.9	759.5	1.214	S-OH st.
O-18	889.3	735.1	1.210	
	32.6	22.4		
O-16	1181	-	-	H-O-S bend.
O-18	1175	-	-	
	6			

Table 2. Calculated frequencies of $HOS(O_2)O_2$ and the comparison with SO_2 (see text).

	$HOS(O_2)OO$	c.f. SO_2
H-O st.	$3835cm^{-1}$	-
$S(=O)_2$ asym.st.	1588	1573(obs.1362)
$S(=O)_2$ sym.st	1349	1341(obs.1151)
H-O-S i.p. bend.	1184	-
HO-S st.	1025	-
S-OO st.	929	-
O-O st.	680	-

MEASUREMENTS OF H_2O_2 IN THE LOWER TROPOSPHERE

Brian G. Heikes
Allan L. Lazrus
Gregory L. Kok

The National Center for Atmospheric Research*
P.O. Box 3000
Boulder, Colorado 80307

*The National Center for Atmospheric Research
is sponsored by
The National Science Foundation.

Hydrogen peroxide is significant to gas and aqueous phase chemistry of the troposphere. In water droplets H_2O_2 is capable of oxidizing dissolved SO_2 to sulfuric acid at rates on the order of 100% per hour and is considered one of the principal acid rain precursors (Calvert *et al.*, 1985). Gas phase H_2O_2 is also important in characterizing the odd hydrogen free radical chemistry of the atmosphere (Crutzen and Fishman, 1977). Its formation results in the loss of two perhydroxyl radicals and, along with production of nitric acid, is a major sink for odd hydrogen.

The free-radical hydrogen-peroxide chemistry of the troposphere can be characterized simplistically by the following reactions;

$$O_3 + h\nu \ (\lambda < 310nm) \rightarrow O(D) + O_2 \quad (1)$$

$$O(^1D) + H_2O \rightarrow 2\,HO \quad (2)$$

$$HO + CH_4 \rightarrow H_2O + CH_3 \quad (3)$$

$$CH_3 + O_2 \rightarrow CH_3O_2 \quad (4)$$

$$CH_3O_2 + NO \rightarrow CH_3O + NO_2 \quad (5)$$

$$CH_3O + O_2 \rightarrow CH_2O + HO_2 \quad (6)$$

$$CH_2O + h\nu \ (\lambda \leq 320nm) \xrightarrow{+O_2} HO_2 + CHO \quad (7)$$

$$CH_2O + HO \rightarrow H_2O + CHO \quad (8)$$

$$CHO + O_2 \rightarrow HO_2 + CO \quad (9)$$

$$CO + HO \xrightarrow{+O_2} HO_2 + CO_2 \quad (10)$$

$$NO + HO_2 \rightarrow HO + NO_2 \quad (11)$$

$$NO_2 + HO \xrightarrow{+M} HNO_3 \quad (12)$$

$$HO_2 + HO_2 \rightarrow H_2O_2 + O_2 \quad (13)$$

$$CH_3O_2 + HO_2 \rightarrow CH_3OOH + O_2 \quad (14)$$

where, we have neglected higher order hydrocarbons which further react with light, HO and O_3 and contribute along with the listed reactions in defining HO, HO_2, RO and RO_2 radical levels (Greenberg and Zimmerman, 1984; Calvert and Stockwell, 1983). The last three reactions, 12-14, effectively remove odd hydrogen from the atmosphere. The relative abundances of nitrogen

oxides, CO and reactive hydrocarbons determine whether nitric acid, organo-nitrates, hydrogen peroxide or organic hydroperoxide production is the predominate radical sink. It should further be noted that these radicals determine the speciation and loss rates of other compounds within the atmospheric cycles of nitrogen, carbon and sulfur (NRC, 1984).

To date, few direct measurements of the odd hydrogen radical species are available. Measurements of HO are questionable. HO_2 measurements using chemical amplification (Cantrell, *et al.*, 1984) are subject to interference by organic peroxy radicals and have problems with calibration. Cryogenic trapping of HO_2 followed by ESR detection has been used to measure HO_2 in the stratosphere (Helten, *et al.*, 1984) and is under development for tropospheric analysis. Previous gas-phase hydrogen peroxide measurements are also tenuous (Heikes, *et al.*, 1982).

Pursuant to the need to measure HO and HO_2 radicals and the lack of sufficient techniques to make these measurements, we have undertaken a program of H_2O_2 instrument development and H_2O_2 field measurements. The gas-phase H_2O_2 system is presented first and is followed by our first set of aircraft measurements of H_2O_2 in conjunction with SO_2 and O_3. These measurements were made in Fall 1984 over the Eastern United States and extended from the surface to 3000 meters.

The gas-phase H_2O_2 technique developed at NCAR is detailed in Lazrus *et al.* (1985a). It involves the aqueous collection of H_2O_2 followed by its determination using the enzyme-fluorescence technique developed by Lazrus *et al.* (1985b). During collection, air containing H_2O_2 is passed through a helical coil in which a small volume of water is continually added. The air and water flow concurrently through the coil and are separated. The H_2O_2 collection water then enters the aqueous enzyme system. The collection system and analytical system are schematically shown in Fig. 1.

We have performed extensive interference testing of the gas-phase H_2O_2 instrument which is described fully in Lazrus *et al.* (1985a & b) and briefly here. 130 ppbv of NO caused a 0.016 ppbv reduction in H_2O_2 signal. H_2O_2 can be generated in the collecting coils by O_3. We find that O_3 concentrations of 40 and 100 ppbv give rise to H_2O_2 concentrations of 0.010 to 0.030 ppbv respectively. This effect is strongly dependent upon surface chemistry and we emphasize the need to maintain short sampling manifolds and high manifold flow rates. A slight loss of H_2O_2 signal is caused by reaction of H_2O_2 with HSO_3^- in the stripping coil. A 0.5% loss in H_2O_2 signal is caused by 10 ppbv of SO_2 and a 5% loss is caused by 100 ppbv of SO_2. Effects due to 15 ppbv of NO_2 and light-saturated or unsaturated hydrocarbons, 20 ppbv of HCHO, 10 ppbv of HNO_3 or 92 ppbv of NO were not detectable (< 0.010 ppbv).

The H_2O_2 instrument, a flame-photometric SO_2 instrument and a TECO O_3 instrument were flown aboard the NCAR Beechcraft Queen Air during October and November 1984. The aircraft was based at Springfield, Ohio and flew as far north as Watertown, N.Y. and as far south as New Orleans, LA. Local flights were flown normally near noon with a few flights ranging in time from 08:00 to 19:00 EST. A synopsis of the data is presented in Figures 2 and 3.

Figure 3 illustrates the variation in H_2O_2 with altitude under different synoptic categories of air mass origin. Four profiles are shown relative to surface meteorology. In general, the winds above 850 mb (5000 ft.) were from the southwest quadrant. Surface wind patterns are indicated by open black arrows. Note the lowest H_2O_2 values are post-cold frontal (Van Wert, OH; 10/17/84) and associated with air originating in "Central Canada." The highest H_2O_2 concentrations occur just ahead of the cold front (Lexington, KY; 11/1/84) in air coming up from the south.

All profiles indicate lower H_2O_2 concentrations in air near the earth's surface. This may arise through 1) deposition to the surface, 2) increased NO concentrations due to surface emissions causing a decrease in HO_2 (reaction 11) and subsequent decrease in H_2O_2 production (reaction 13), and 3) H_2O_2 heterogeneous loss due to haze aerosols. The latter process is suggested by measurements of relative humidity, SO_2 and H_2O_2 in which air high in humidity, SO_2 and observed haze is also low in H_2O_2.

The above observations of a northerly vs. southerly air mass difference in H_2O_2 and lower surface H_2O_2 concentrations, along with an expected latitudinal gradient in H_2O_2 (due to photochemistry) prompted us to carry out two flights under southerly flow ahead of two cold fronts. This data is presented in Fig. 4. It is interesting to compare the relative decrease in H_2O_2 above and below the boundary layer as the air moves up from the south. There is relatively little change in H_2O_2 from the Gulf of Mexico (4 ppbv) to the Pennsylvania-New York border (3 ppbv) above the boundary layer. In the boundary layer, H_2O_2 concentrations decrease from 3 ppbv (Gulf of Mexico) to less than 0.5 ppbv by Springfield, OH.

This phenomena is important to acid production incloud. It is these southerly flow patterns that are associated with most of the acid precipitation in the northeast. Clouds generally exist at the boundary layer--free troposphere interface and, depending upon atmospheric stability, exist in a region of vertical mixing. It is possible that within cloudy environments, H_2O_2 from aloft is mixed with SO_2 emissions from below and these then react in cloud. Consequently, long range transport of H_2O_2 in conjunction with localized mixing could lead to greater rates of acidification than would be predicted from local boundary layer SO_2-H_2O_2 measurements or free troposphere SO_2-H_2O_2 measurements alone.

Acknowledgements

The authors would like to thank the other members of our group who participated in the instrument development and field program: John A. Lind, James G. Walega, Richard E. Shetter, Sonia N. Gitlin and Bruce W. Gandrud. This work was funded, in part, by the Electric Power Research Institute through EPRI agreement RP1630-12.

References

Calvert, J.G., A.L. Lazrus, G.L. Kok, B.G. Heikes, J.G. Walega and J.A. Lind, *Nature*, in press (1985).

Calvert, J.G. and W.R. Stockwell, *Can. J. Chem.*, **61**, 983 (1983).

Cantrell, C., D.H. Stedman, and G.J. Wendel, *Anal. Chem.* **56**, 1496 (1984).

Crutzen, P.J. and J. Fishman, *Geophys. Res. Lett.*, **4**, 321 (1977).

Greenberg, J. and P. Zimmerman, *J. Geophys. Res.*, **89**, 4767 (1984).

Heikes, B.G., A.L. Lazrus, G.L. Kok, S.M. Kunen, B.W. Gandrud, S.N. Gitlin, and P.D. Sperry, *J. Geophys. Res.*, **87**, 3045 (1982).

Helten, M., W. Patz, M. Trainer, H. Fark, E. Klein, D.H. Ehhalt, *J. Atmos. Chem.*, **2**, 191 (1984).

Lazrus, A.L., B.W. Gandrud, S.N. Gitlin, B.G. Heikes, G.L. Kok, J.A. Lind, R.E. Shetter, and J.G. Walega, *Investigations on the Availability of H_2O_2 for In-Cloud Conversions of SO_2*, **Progress Report, EPRI-RP/630-12**, 7 August (1985a).

Lazrus, A.L., G.L. Kok, S.N. Gitlin, and J.A. Lind, *Anal. Chem.*, **57**, 917 (1985b).

National Research Council, *Global Tropospheric Chemistry: A Plan for Action*, National Academy Press, Washington, D.C., (1984).

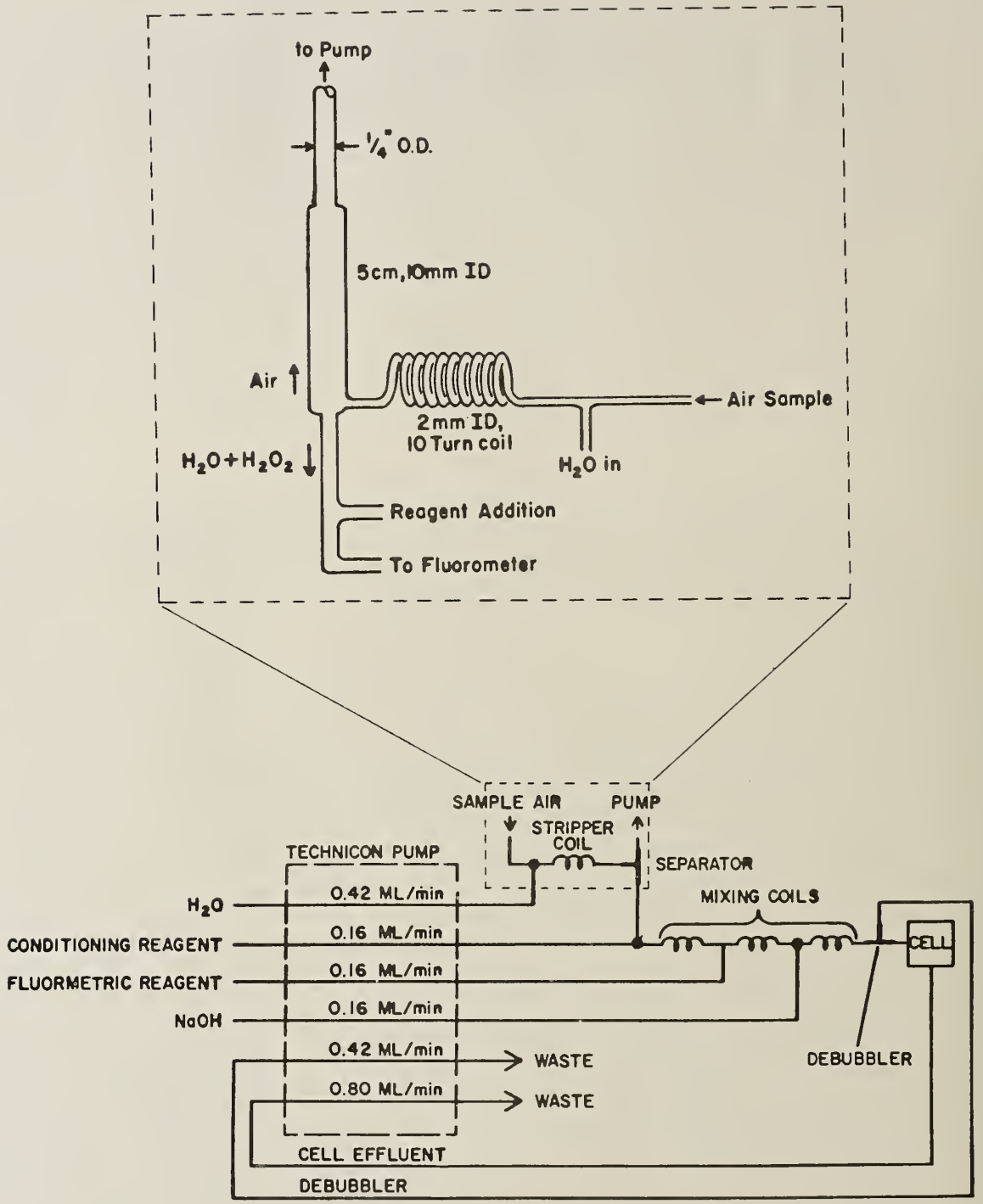

Figure 1: Schematic diagram of the H_2O_2 analytic system showing the aqueous collection coil with air water separator tube and the aqueous reagent manifold. Details can be found in Lazrus, et al, (1985a).

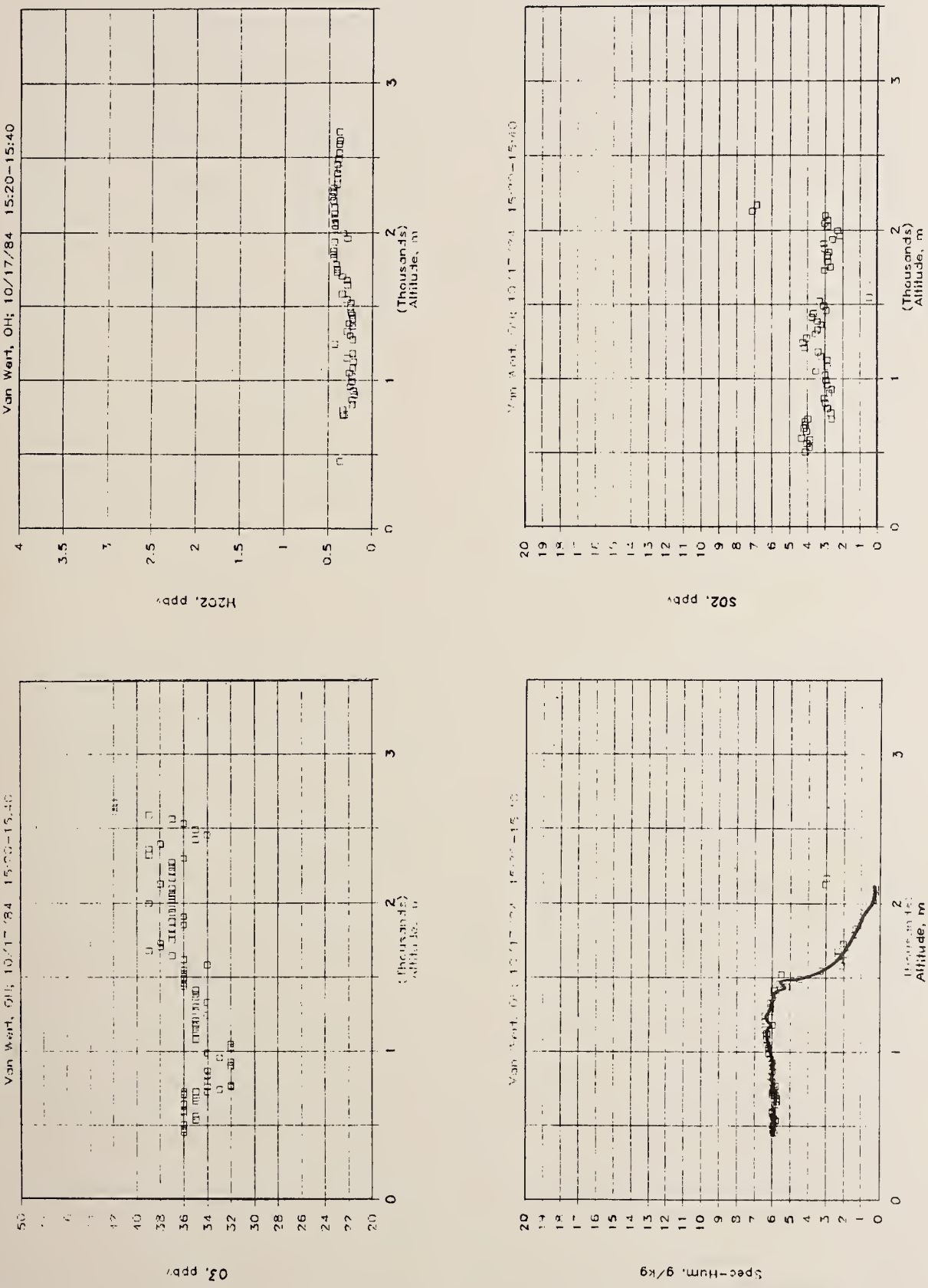

Figure 2a: H_2O_2, SO_2, O_3 and specific humidity vertical profiles under different synoptic conditions. Van Wert, OH 10/17/84 post cold front.

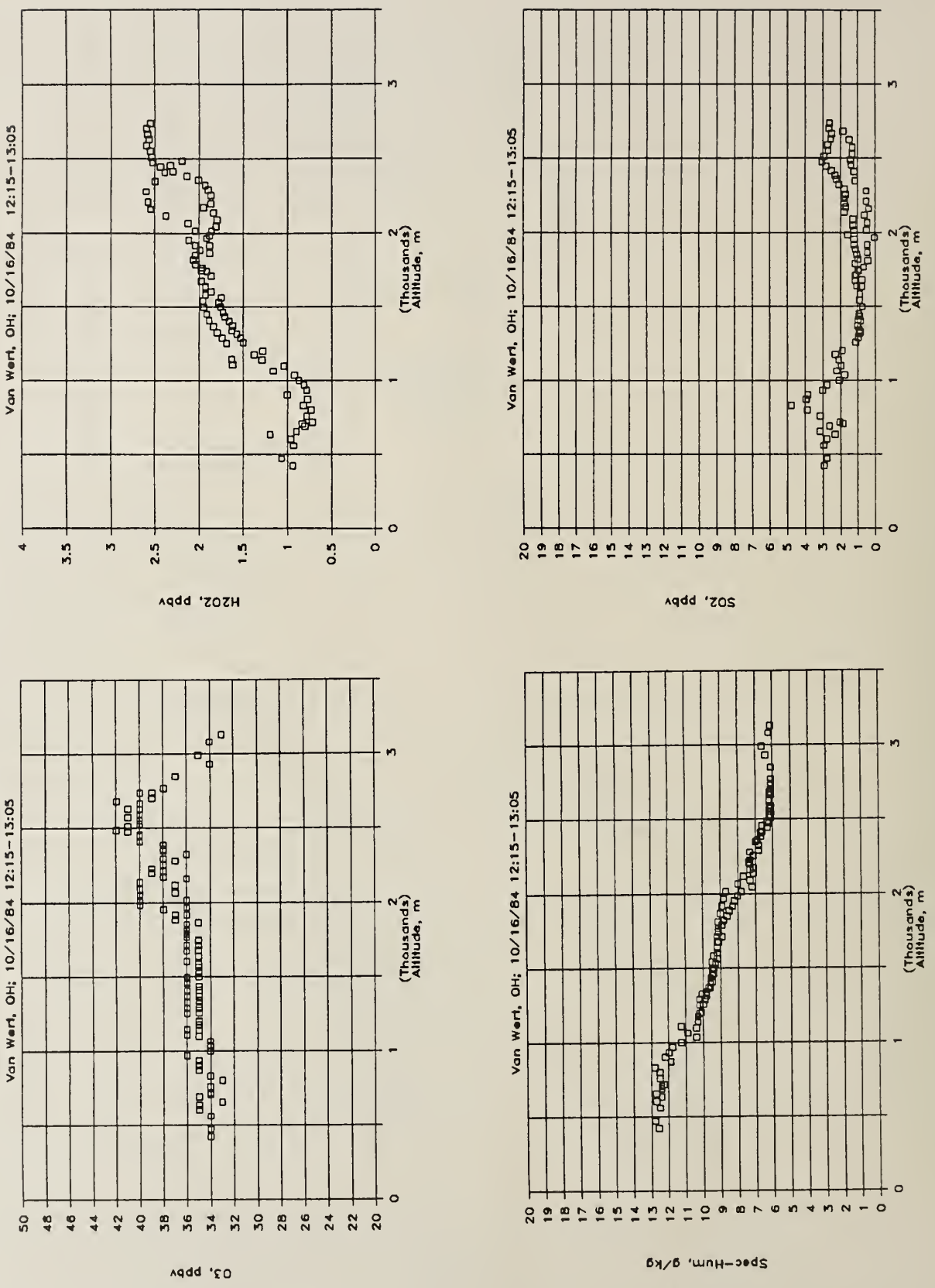

Figure 2b: As in Fig. 2a except samples were taken on 10/16/84 in air associated with a slowly moving high pressure system.

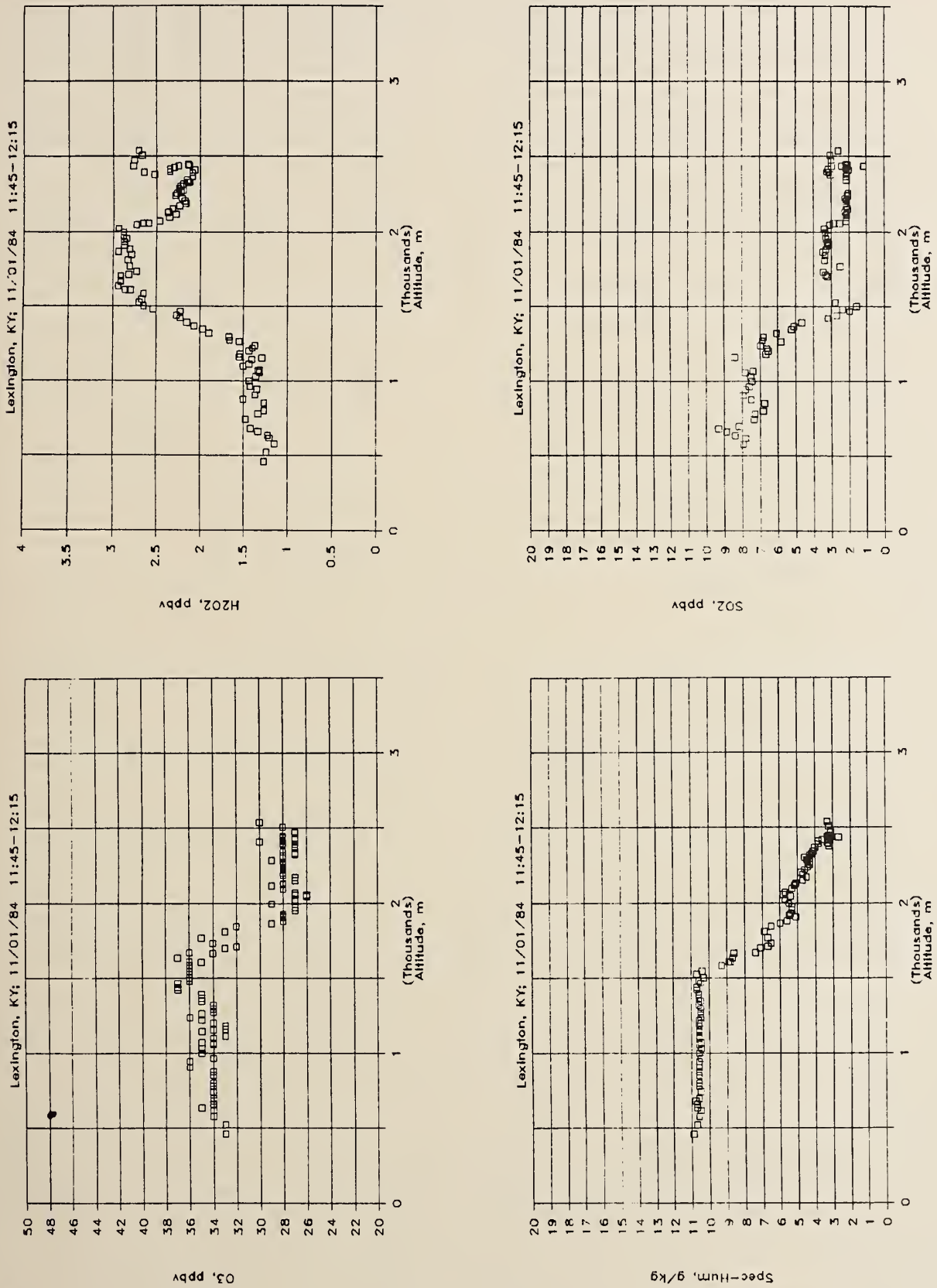

Figure 2c: As in Fig. 2a except samples were taken at Lexington, KY in air immediately preceding a surface cold front.

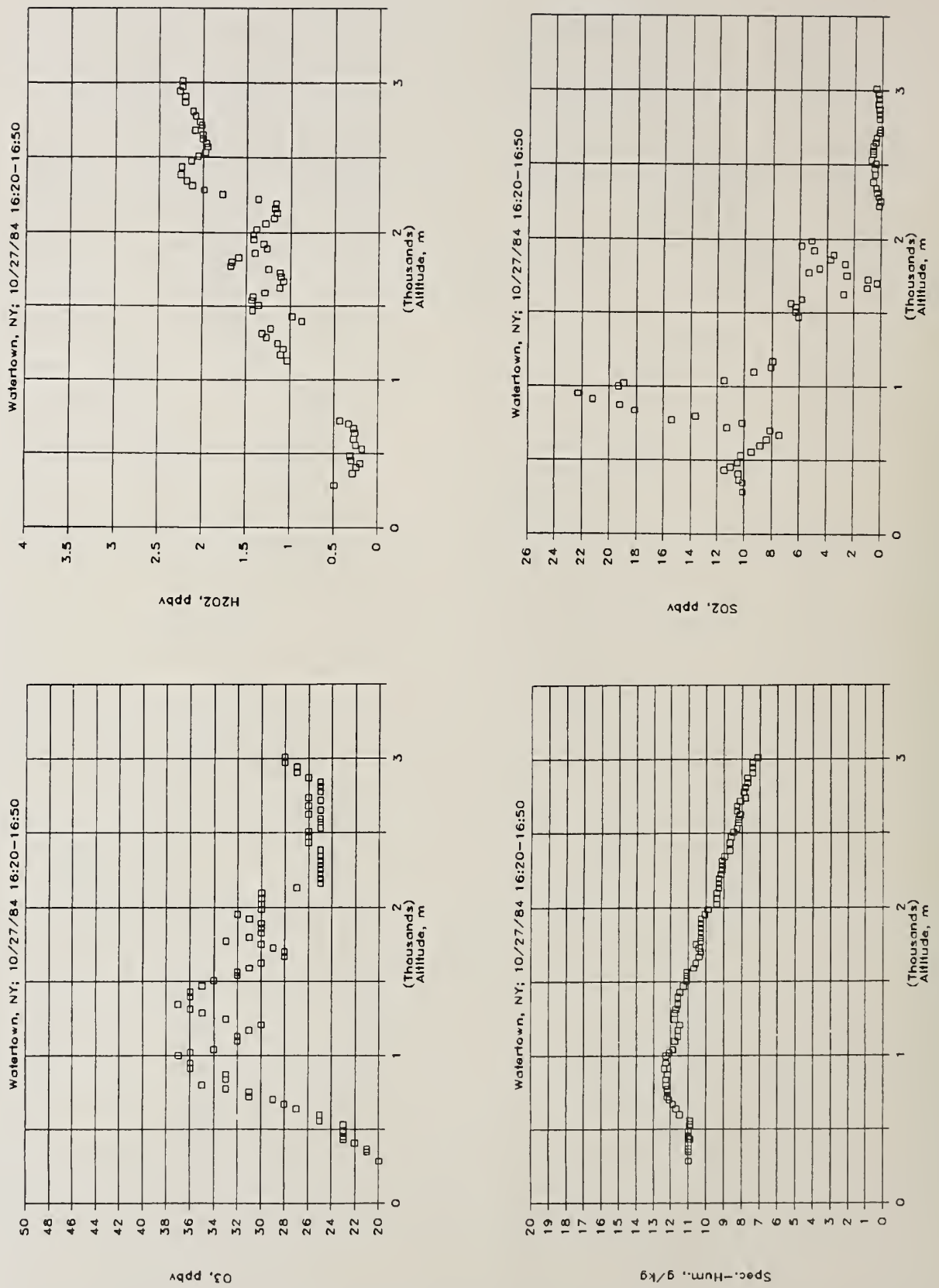

Figure 2d: As in Fig. 2a except samples were taken at Watertown, NY in air associated with a surface warm front. Air mass folding at the frontal interface can be seen in the vertical profiles of H_2O_2, SO_2 and O_3.

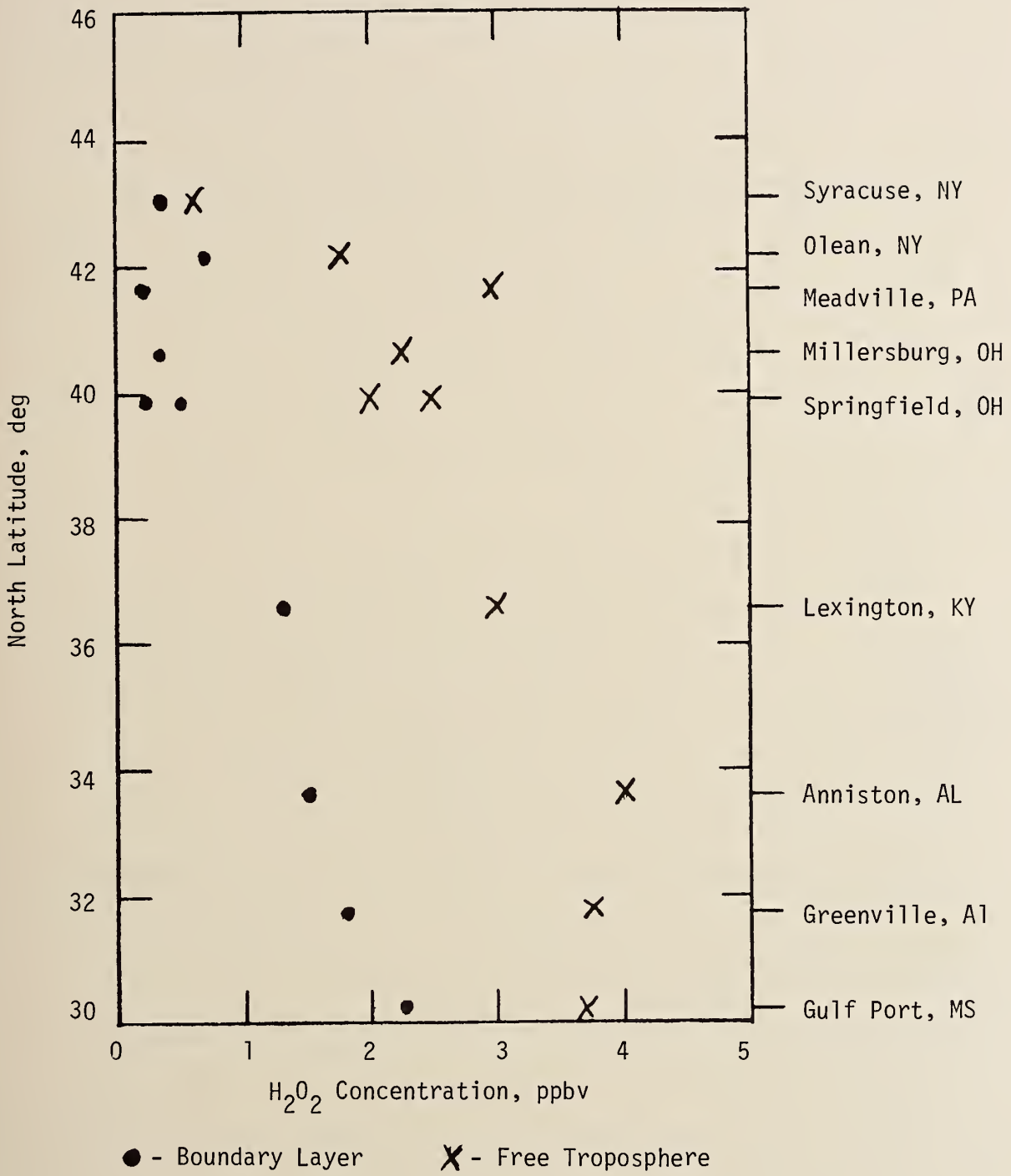

Figure 3: Latitudinal variation of H_2O_2 within the boundary layer and above the boundary layer. Airflow at all levels was predominately from the south-southwest. Measurements were made just ahead of two cold fronts as they moved in from the northwest.

SYMMETRY BEYOND POINT GROUPS IN MOLECULAR SPECTROSCOPY

Jon T. Hougen

Molecular Spectroscopy Division

National Bureau of Standards

Gaithersburg, MD 20899

ABSTRACT

An attempt is made to distill from the published literature a summary of some new uses of group theory in high resolution gas-phase spectroscopic studies of molecules with large amplitude and/or tunneling motions, paying particular attention to questions like: (i) When is a point group sufficient, and when is it not? (ii) What kind of information is easy, and what kind is difficult to extract from a permutation-inversion group treatment? (iii) What seem to be the advantages and disadvantages of various extended groups of the permutation-inversion group. While most spectroscopists would agree that a general group theoretical approach, suitable for application without modification to the majority of floppy molecules, has not yet been synthesized from the particular cases studied in the literature, some feeling for one direction of progress in the field can be obtained from the several examples presented.

1. Introduction

In this talk we shall attempt to present from a pedagogical point of view some opinions on the use of group theory in high resolution molecular spectroscopy. The scope of the discussion will be limited in two major ways. First, the ideas in the article will be expressed in words, rather than as mathematical equations. The advantage of words lies in the fact that the reader can quickly grasp the general outline of a problem and its solution. The disadvantage lies in the fact that no matter which words are chosen, they cannot unambiguously reflect the mathematics upon which any proof of legitimacy or any procedure for obtaining results is actually based. The serious student is therefore referred to the original literature citations, for which this article can serve only as an annotated table of contents.

There has been and still is ongoing controversy over how to extend symmetry treatments beyond point groups in molecular spectroscopy. This controversy, which is at times both heated and rancorous, flairs up primarily at the interface where the physical problem (i.e. measureable properties of the molecule) must be connected to pure mathematics (i.e. to group theory). An illustration of the importance of this connection is contained in the statement that the point groups C_{2h}, C_{2v} and D_2 are all isomorphic with the four-group, so that these point groups are all indistinguishable from a purely mathematical point of view. Nevertheless, because of the different way in which the mathematical operations are connected to the molecular model, the group C_{2h} leads to selection rules in which infrared active vibrations cannot be Raman active,

D_2 leads to selection rules in which infrared active vibrations must be Raman active, and C_{2v} leads to selection rules in which infrared active vibrations may or may not be Raman active.

In trying to make the connection between molecular model and group theory in a mathematically consistent way, it is the author's strong opinion that strict attention must be paid to the precise transformation of variables in the molecular wavefunction which is to be associated with a given symmetry operation. Readers who are comfortable with a position proposed to the author in an argument long ago that "group theory is so powerful that one does not need to specify exactly what the symmetry operations mean," should read no further, because as a second limitation to this article, no comprehensive review of such opposing viewpoints in the literature will be attempted.

The material below will be divided into three sections, one dealing with point groups, one with permutation-inversion groups, and one with extended groups. We shall try to consider questions like: What information can or cannot be obtained easily from the group theoretical formalism in a given section? How does the way of looking at things differ in different sections? What molecules provide good illustrations of the various concepts?

2. Point Groups

Point groups, which we shall assume to be well known to the reader (1,2), make the connection between group theory and molecular model through the shape of the molecule, and it is therefore not surprising that point groups are most useful when the molecule exists in a single well defined shape. To make the idea of shape more precise, and for future discussion, it is convenient to introduce the concept of a molecular framework (3), which can be thought of as a rigid ball and stick model with numbered atoms. Two frameworks are different if they cannot be superimposed with all atom labels coinciding. Using the concept of frameworks, we now describe two rather different cases for which point groups can usefully be employed.

The first case consists of molecules whose atoms always remain in the vicinity of their equilibrium positions, i.e. in the vicinity of a single framework. Examples of such molecules are: NO, HCN, SO_2, CH_3F and SF_6. We shall not consider this very familiar case (1,2) further in this article.

The second case in which point groups are useful is somewhat more subtle, and contains molecules whose atoms travel between two or more frameworks by means of some sort of large amplitude vibrational motion(s). In general, an uncertainty in molecular shape arising from large amplitude vibrational excursions leads to a corresponding uncertainty in the choice of point group. If, however, a reference configuration (not the equilibrium configuration) can be found for a molecule undergoing large amplitude vibrations, such that the point group associated with the

reference configuration contains all symmetry operations exhibited by the molecule during the course of its large amplitude motions, then it is the author's opinion that correct group theoretical conclusions can be obtained by the following two-step procedure. (While the correctness of this opinion seems almost obvious, it must be admitted that neither a careful mathematical proof, nor a careful search for counterexamples has been carried out.) (i) Set up the energy levels, symmetry labels, selection rules, etc. for the problem as if the molecule were carrying out small amplitude vibrations about a framework corresponding to the reference configuration, as illustrated in Fig. 1a. (ii) Introduce a set of potential humps at appropriate places in the harmonic oscillator wells associated with the reference configuration, as illustrated in Fig. 1b. The purpose of these humps from one point of view is to destroy the potential minimum at the reference configuration and create two or more equivalent potential minima at the actual equilibrium configurations. Their purpose from another point of view is to push the energy levels into positions close to those in the multiple minimum problem. The potential hump in the two-minimum problem illustrated in Fig. 1b has the well known effect of pushing up even vibrational levels more strongly than odd, since wavefunctions with odd v have a node at their center and do not sense the presence of the hump as efficiently as wavefunctions with even v and a local maximum at their center.

Perhaps the best known example of a molecule treated in this way is NH_3 (2), where the group D_{3h}, corresponding to the planar reference configuration, contains the subgroup C_{3v}, corresponding to the right and

left handed pyramidal equilibrium configurations. The coordinate Q along the abscissa in Fig. 1 then represents the planar (Q = 0) and pyramidal ($Q = \pm Q_o$) configurations of the umbrella vibration ν_2 of NH_3, and the group theoretical labels Γ represent symmetry species of D_{3h}.

More recent examples of such treatments are the molecules $(HF)_2$ (4) and H_2O_2 (5), each of which passes through a trans C_{2h} reference configuration at the midpoint of its tunneling motion. The group C_{2h} then contains as a subgroup C_s, which is the point group of the two equilibrium frameworks of $(HF)_2$, or contains as a subgroup C_2, which is the point group of the two equilibrium frameworks of H_2O_2. The coordinate Q in Fig. 1 represents a geared internal rotation angle for $(HF)_2$, and the traditional internal rotation angle for H_2O_2. Symmetry species Γ in Fig. 1 are from the point group C_{2h}. We note in passing that by carrying out the procedure in Fig. 1 in turn for the two hypotheses of trans tunneling (C_{2h} reference configuration) and cis tunneling (C_{2v} reference configuration), it is possible to show conclusively that trans tunneling, rather than cis tunneling, is responsible for the observed splittings in both $(HF)_2$ and H_2O_2.

A somewhat different example of this kind of treatment occurs in discussions of the Jahn-Teller effect (2). The reference configuration for H_3 in a degenerate electronic state, for example, would be taken as an equilateral triangle, with point group D_{3h}. The three lower symmetry configurations obtained after Jahn-Teller distortion occurs, correspond to isosceles triangles, with point groups C_{2v}. All elements of the latter groups are contained in D_{3h}, so that the subgroup criterion given above

is satisfied. Unfortunately, this example cannot be illustrated by the two-minimum potential curve of Fig. 1, since it requires a three-minimum potential surface (2). However, the principle of beginning with D_{3h} energy levels and symmetry species, and then pushing these levels about by the introduction of a Jahn-Teller interaction term, remains the same.

We now turn to a rather different question of interest in the present context, since it will lead us naturally into the next section: What is the relation betwen point group operations and permutations of identical nuclei in the molecule? As is well knonwn (1), point group operations are of four types: rotations C about an axis, reflections σ in a plane, the inversion i in a point, and rotation-reflections S. After performing a given rotation C of a molecular ball and stick model with labeled nuclei, one can easily determine which nuclear labels have been permuted. It has long been known (3) that the rotational subgroup of the point group of a molecule corresponds to the group of permutation operations determined in the above manner, and that this correspondence is the basis of Wilson's method (1,3) for determining nuclear statistical weights for the rovibronic levels of molecules.

The improper rotations σ, i and S applied to molecules with labeled nuclei, though they are not used in determining statistical weights, also give rise to configurations in which various nuclear labels have been permuted. (The treatment of improper rotations, particularly questions related to the effect of i on the molecule-fixed axis system, represent one area of sustained disagreement in the literature.) After performing a given improper rotation one can again compare the original ball and stick

model with the reflected (σ), inverted (i) or reflection-rotated (S) ball and stick model to determine which nuclear labels have been permuted. To yield a mathematically consistent treatment of the symmetry operations, however, these improper rotations must be associated with the nuclear permutation determined as above, followed by (or preceded by, or carried out simultaneously with) an inversion of the coordinates of all particles in the origin of the laboratory-fixed axis system (6). As an example, using a notation (7) where permutations are indicated as cycles, e.g. (123) $\equiv$ (1→2→3→1), and the laboratory-fixed inversion operation is denoted by a *, we find for an ethylene molecule with nuclei labeled as in Fig. 2 that $C_2(z)$ corresponds to the permutation (12)(34), whereas $\sigma(yz)$ corresponds to (12)(34)*. Somewhat more surprisingly, the molecule-fixed inversion operation i of the D_{2h} point group turns out to correspond to the permutation-inversion operation (ab)(14)(23)*; it is the reflection $\sigma(xz)$ which does not permute any nuclei and which therefore corresponds to the laboratory-fixed inversion operation E*.

The above rules can be summarized as: C → P; σ,i,S → P*, where C represents a proper rotation and P a permutation of identical nuclei, and where σ,i,S represent improper rotations, and P* a nuclear permutation followed by the laboratory-fixed inversion operation. By using the above rules, it can easily be seen that the point group operations are in a one-to-one correspondence with a set of permutation-inversion operations, and that the latter form a group isomorphic to the point group.

Several interesting observations can be made in connection with the preceeding two paragraphs: (i) The molecule-fixed inversion i and the

laboratory-fixed inversion E* are not the same, and are not even closely related to each other. (ii) The fact that Wilson's method (3) for determining statistical weights does not require consideration of improper rotations in the point group can be "understood" by noting that the improper rotations always correspond to a permutation followed by E*. Since Fermi-Dirac or Bose-Einstein statistics place no requirements on the effects of E*, they likewise place no requirements on the effects of E* when preceded by a nuclear permutation. (iii) All of the permutation-inversion operations defined from the point group operations as described above take a given framework into itself. Surprisingly, this is even true for the improper rotations. For example, the σ_v operation of a CH_3F molecule does not generate a new framework, since the corresponding permutation-inversion is, for example, (12)*, where (12) changes the original right-handed CH_3F framework into a left-handed one, but the following E* operation changes the left-handed framework back into the original right-handed one (6).

3. Permutation-Inversion Groups

In the previous section we let the operations of the point group play the primary role in our thinking, and treated their one-to-one correspondence with a set of permutation-inversion operations as a kind of mathematically curious afterthought. In this section, following Longuet-Higgins (7), we shall let the permutation-inversion operations play the primary role (8). Such an idea is not unappealing, since from the quantum mechanical hypothesis of not being able to distinguish

between identical particles, the symmetry in a molecule arises from the mere presence of identical nuclei, and not from the fact that some identical nuclei are accidentally found in chemically equivalent positions. Furthermore, such an idea will allow us to treat rather naturally large amplitude motions which take the molecule from one framework to another, and thus allow us to break away from the limitations of point groups. For example, the ethylene molecule labeled as in Fig. 2a might exhibit an internal rotation motion about the double bond. Such an internal rotation does not correspond to any operation of the point groups D_{2h}, D_2 or D_{2d}, which arise during the motion, and thus it cannot easily be included in a point group treatment. It does lead, however, to the exchange of the two hydrogens at one end of the molecule (e.g. (12)), and it thus fits naturally into a permutation-inversion group treatment. (Note that several ad-hoc but successful extensions of symmetry considerations to floppy molecules appeared well before Longuet-Higgins' paper; for brevity, these important early steps will not be reviewed here.)

One's first tendency when thinking about symmetry from the point of view of permuting identical nuclei might be to consider all permutations of identical nuclei in the molecule. Such a procedure for dimethylacetylene ($H_3C-C\equiv C-CH_3$), for example, would lead to a consideration of $4!6! = 17\ 280$ permutations. Such a procedure also leads to 2880 different rigid ball and stick models, or 960 different ball and stick models if free internal rotation of the methyl groups is permitted. The latter fact leads to the further conclusion that the lowest vibration-rotation-torsion state of a freely internally rotating dimethylacetylene molecule is still 960-fold degenerate. This large degeneracy, while actually correct, seems nevertheless to represent chemical and spectroscopic nonsense, since the effects of this degeneracy do not reveal themselves in any experiments of a type presently being performed.

To deal with this problem, Longuet-Higgins proposed (7) that only "feasible" permutation-inversion operations be considered, where a feasible operation is defined to be one which either does not generate a new framework (as is the case for point group operations), or generates a new framework which the molecule can easily reach from the original framework by some tunneling motion. Let us apply this criterion of feasibility to the $H_3C-C\equiv C-CH_3$ example above. Suppose first that the molecule cannot undergo internal rotation, and that it has a staggered equilibrium configuration of symmetry D_{3d}. The only feasible permutation-inversion operations are then those which do not generate a new framework, and we recover a permutation-inversion group of 12 elements which is isomorphic to the D_{3d} point group. Next suppose that the molecule does undergo internal rotation. The permutations (123) and $(123)^2$, corresponding to rotation of one of the methyl agroups by 120^o and 240^o, respectively, then become feasible (for the atom numbering in Fig. 2b), and the elements of the permutation-inversion group for this problem become the 36 products obtained when each of the 12 permutation-inversion operations from the group isomorphic with D_{3d} is multiplied by each of the three permutations E, (123) and $(123)^2$ (8,9). The remaining 34 524 elements of the full permutation-inversion group for C_4H_6 do not become feasible until we consider tunneling motions involving the breaking of chemical bonds, or racemization of the methyl groups.

We note in passing, that the molecules treated in this paper all contain large numbers of "chemical bonds," which are not permitted to break during the various large amplitude motions considered. This is a qualitatively different viewpoint from that which may be appropriate,

for example, when discussing clusters of metal atoms or rare gas atoms. For a cluster of n such atoms, it may well turn out that the full set of 2n! permutation-inversion operations must be considered to be feasible.

Several interesting remarks can be made concerning the criterion of feasibility. (i) For rigid molecules this criterion recovers the familiar point group treatment. (ii) For most nonrigid molecules, this criterion severely reduces the number of permutation-inversion operations admitted to the molecular symmetry group, but the obvious question arises as to what would happen if all possible permutation-inversion operations (in particular, large numbers of non-feasible operations) were included in the molecular symmetry group. From one point of view, no incorrect group theoretical answers would be obtained. However, each energy level would turn out to be described as a many-fold degenerate collection of states of different symmetry species, and the many-fold accidental degeneracies of these levels would never be split by any perceptible amount. Since it is a group theoretical axiom that accidental degeneracies will always be split by some small term in the Hamiltonian, it is inconvenient to use a group theoretical labeling scheme which describes unsplittable degeneracies (i.e. degeneracies with splittings millions of times smaller that the available resolution). (iii) The criterion of feasibility is flexible for both experimentalists and theoreticians. First, as the resolution of the experiment increases, new tunneling splittings become observable, and new tunneling motions must therefore be taken as feasible. Second, as various potential barriers are decreased in theoretical modeling calculations, new tunneling motions become feasible,

or as the masses of various atoms are increased (by deuterium substitution in the molecular model, for example) some tunneling motions become unfeasible. The fact that the criterion of feasibility is not defined in a mathematically "rigorous" way has generated significant discomfort and resistance in some workers in the field. It is the author's strong opinion, however, that the criterion of feasibility is in fact a particularly brilliant way of choosing the optimally useful connection between a given molecular model or given experimental measurements and the pure mathematics (i.e. the group theory) used to describe and understand the model or measurements.

Let us now turn to a discussion of what information is easy and what information is difficult to obtain from permutation-inversion groups. There are three kinds of easily accessible information: (i) Statistical weights are almost trivial to derive, since permutations of identical nuclei occur explicitly in the group theoretical symmetry operations. (ii) Selection rules on the overall vibration-rotation-tunneling levels are also trivial to derive, since the complete dipole moment operator (written as a function of the laboratory-fixed coordinates of the particles) must be invariant to exchanges of identical nuclei and must go into its negative under the laboratory-fixed inversion operation, i.e. the dipole moment operator must be invariant to all P operations and must go into its negative under all P* operations. (iii) The number of components, and their symmetry species, into which a given rotation-vibration energy level of a non-tunneling molecule will split, when various tunneling motions are permitted to occur, can easily be

determined by setting up a correlation table between the permutation-inversion group containing the newly feasible tunneling motions and the permutation-inversion group excluding those tunneling motions, and then "reading this correlation table backwards" (10).

There is, however, a large amount of group theoretical information which is extremely difficult to extract from permutation-inversion groups without significant additional work. For want of a better term, we will denote this as "approximate" group theoretical information, since it is valid to the extent that the various Born-Oppenheimer-like approximations involved in the separation of small amplitude vibrations, large amplitude vibrations, tunneling motions, rotations, etc. are valid. (Because of the significant additional work required to obtain this "approximate" information, graduate students in particular should not allow feelings of inadequacy to take root simply because repeated careful reading of Ref. (7) does not seem to permit them to answer the group theoretical questions they wish to ask.)

The additional work required can be described as follows (and this discussion will lead us naturally into the next section). In order to get selection rules for each of the separated motions mentioned above, several steps must be taken: (i) It is necessary to define in some way precisely what is meant by each type of separated motion. (ii) A set of coordinates must be found to describe the separated motions, together with corresponding zero order basis set wavefunctions of these coordinates which reasonably closely approximate the final eigenfunctions of the system. (iii) The approximate energy

levels, quantum numbers, symmetry species, etc. associated with the basis functions for each type of motion must be determined. (iv) The dipole moment operator must be rewritten as a function of the separated coordinates, and the symmetry species of the various parts of the dipole moment operator depending only on coordinates for one type of separated motion must be determined. (v) The symmetry species of the parts of the dipole moment operator must be used in conjunction with the symmetry species of the individual factors in the zeroth order basis functions to determine selection rules for each of the various types of molecular motion.

The level of difficulty of the above steps can be illustrated by the example of Berry pseudorotation in a gas phase $F\text{-}PF_3\text{-}F$ molecule (11,12). (In the pseudorotation of this trigonal bipyramid, the axial fluorines change places with the equatorial fluorines.) Exactly what angle or distance coordinate (in fact, how many angle or distance coordinates) should be used to describe the pseudorotation? What quantum numbers and approximate energy level expressions are appropriate? How should one write a zeroth order basis function in these coordinates, such that interactions between, for example, rotation and pseudorotation do not lead to so much mixing in the final eigenfunctions that any selection rules on the quantum numbers of the basis set are completely useless? As the reader may surmise, an understanding of even the gross features of the vibration-rotation spectrum of PF_5 requires far more than merely setting up the permutation-inversion group.

The situation in condensed phases is beyond the author's exeprience, but two limiting case conjectures can be imagined: (i) The situation in condensed phases will be far more complicated, because the intramolecular large amplitude motions and tunneling motions involve energies comparable to solvation interaction energies, and any isolated molecule treatment of the condensed phase spectrum will be hopelessly inadequate. (ii) The situation in condensed phases will be far simpler, because internal rotational motions, and other large amplitude motions, will all be quenched (just as the overall rotation is), and only the small amplitude vibrations in the molecule need be considered in detail.

4. Extended Groups

As indicated above, the next step after setting up the permutation-inversion group is to choose appropriate coordinates and zeroth order basis functions. As it happens, this procedure sometimes leads to the introduction of a group which is m times larger than the original permutation-inversion group, where m is some integer. We shall refer to this larger group as the m-fold extension of the permutation-inversion group, or simply as the m-fold extended group.

The most familiar illustration of such an extended group (though it is not usually viewed in this way) occurs for linear molecules (8,13), and we shall review the situation for acetylene to show how extended groups can arise and how they can be useful. The permutation-inversion group for H_1-$C_a \equiv C_b$-H_2 has four elements, i.e. E, (ab)(12), E* and (ab)(12)*, and it is isomorphic to the four-group. The four-group has four

nondegenerate representations, which for applications to linear molecules with a center of symmetry are often denoted by +s, -s, +a and -a (1), where the ± sign indicates the parity of the level, i.e. its character under E*, and the s,a labels indicate symmetry or antisymmetry with respect to interchange of all pairs of symmetrically equivalent nuclei, i.e. the character under (ab)(12). As is well known, these symmetry species of the four group are used to label the overall vibration-rotation levels in acetylene. Further, the dipole moment must be of symmetry -s, so that overall selection rules become + ↔ - and s ↔ s, a ↔ a. From the point of view of permutation-inversion groups, this is all that can be said about acetylene, and indeed, these results represent the only exact (ignoring hyperfine mixings) group theoretical symmetry species and selection rules for this molecule.

Nevertheless, it is also well known that after making the assumption of a linear equilibrium configuration, and after distinguishing between stretching and bending vibrational motions and rotational motions, it is convenient to discuss the energy levels of acetylene in terms of symmetry species of the group $D_{\infty h}$, i.e. in terms of Σ_g^+, Σ_g^-, Π_g, Δ_g, ... and Σ_u^+, Σ_u^-, Π_u, Δ_u, ... (1). In particular, basis set wavefunctions for each of the two bending vibrations in acetylene contain a factor of the form $e^{+i\ell\phi}$, where the quantum number ℓ = 0, 1, 2, ... corresponds to the symmetry species Σ, Π, Δ, ... (1). (Neither the quantum number ℓ, nor the symmetry species correspnding to it are exact; their goodness is destroyed by Coriolis interactions between the vibrational and rotational motions.)

It is in attempting to reconcile these two disparate treatments of the symmetry properties in acetylene that the concept of extended groups is useful. If one asks which permutation of identical nuclei corresponds to the infinitesimal rotation about the linear axis in acetylene, the intuitively obvious answer is that no atoms are interchanged. We thus say that the identity E of the permutation-inversion group must be "extended" to include not only the identity of $D_{\infty h}$, but also the infinite number of rotations about the linear axis. In similar fashion, E* must be extended to include the infinite number of planes of reflection containing the linear axis; (ab)(12) must be extended to include the infinite number of two-fold rotation axes perpendicular to the linear axis; and (ab)(12)* must be extended to include the infinite number of rotation-reflection operations (including the inversion $i \equiv S_2$). This procedure obviously leads to an ∞-fold extension of the original permutation-inversion four-group.

As a further complication, the concept of single-valued versus multiple-valued representation arises in attempting to deal with the different number of symmetry species produced by the two groups. Single-valued representations are those which correspond to valid symmetry species for both the original permutation-inversion group and the extended group. Clearly, if a symmetry species of $D_{\infty h}$ has the same character for the identity and for all rotations about the linear axis, then the character of that symmetry species for E in the permutation-inversion group is uniquely determined; this corresponds to a single-valued representation of the permutation-inversion group. If, on the other hand, a symmetry

species of $D_{\infty h}$ has characters for the identity and for the rotations about the linear axis which are not all the same, then there are several values from which the character for E in the permutation-inversion group must be chosen: this corresponds to a multiple-valued representation of the permutation-inversion group, i.e. to something which is in fact not a representation of the permutation-inversion group in the strict sense of the word. For the acetylene example under consideration, only Σ_g^+, Σ_g^-, Σ_u^+, and Σ_u^- of $D_{\infty h}$ are single-valued representations of the permutation-inversion group, and these symbols correspond to +s, -s, +a and -a, respectively.

Consider now the question of what kind of symmetry species are suitable for complete vibration-rotation wavefunctions. Since the complete functions contain all of the variables in molecular coordinate space (apart from the three coordinates of the center of mass), they can always be rewritten in terms of the laboratory-fixed Cartesian coordinates X_i, Y_i, Z_i of the particles i in the molecule (with the center of mass at the origin). These rewritten wavefunctions can then always be subjected to permutation-inversion operations simply by changing the atom labels i of the Cartesian coordinates and/or by changing their sign. Thus, the complete vibration-rotation wavefunctions must belong to true representations (i.e. to single-valued representations) of the permutation-inversion group.

Consider next the choice of symmetry species for the vibrational wavefunctions alone. Since a knowledge of the vibrational coordinates alone (without rotational, i.e. without orientational, information) is

not sufficient to locate the atoms in the laboratory, it is not possible to rewrite the vibrational functions alone in terms of laboratory-fixed Cartesian coordinates. Thus, a vibrational function by itself cannot in general be subjected in a mathematically unambiguous way to a permutation-inversion operation, and hence the requirement that such a wavefunction belong to a true representation of the permutation-inversion group is no longer necessary for mathematical consistency. In short, the conclusion of this paragraph is that each individual factor of a wavefunction, corresponding to only one kind of motion of the molecule, may belong to a multiple-valued representation of the permutation-inversion group, but the complete vibration-rotation wavefunction, i.e. the product of all the individual factors, must belong to a single-valued representation.

The reader should keep in mind, however, that extended groups do not always arise. Rigid molecules with shapes other than linear have permutation-inversion groups which are isomorphic with their point groups, and thus do not require extended group treatments.

We now turn to molecules with large amplitude motions for further illustration of the above considerations. In particular, we shall consider ethane (H_3C-CH_3) (14,15) and hydrogen peroxyde (HO-OH) (5,16-19), both of which exhibit internal rotation about the central bond, and both of which have been discussed in the literature using a double group of their permutation-inversion group. (Although certain formal group theoretical similarities exist, these vibration-rotation double groups are not related in any physical way to, nor are they necessarily isomorphic with, the double groups which arise in treatments of half-integral electron spin.)

The use of vibration-rotation double groups is intimately connected with the choice of coordinate system, a connection which we now discuss very briefly and superficially. Consider two possible ways of attaching a molecule-fixed axis system to the molecular model (i.e. two possible ways of defining the rotational variables). (These two ways are often referred to as the Principal-Axis-Method and the Internal-Axis-Method in the microwave literature (20).) In the first way, the axes are somehow firmly attached to one part of the molecule (often called the frame), and a torsional angle is introduced to allow for rotation of the other part (the top) about the frame. It turns out that if operations of the permutation-inversion group are applied to basis functions written in terms of these coordinates, then double groups do not arise. It is intuitively obvious, however (at least to the author), that such an axis system does not correspond to equal treatment for the two identical halves of C_2H_6 or H_2O_2. In the second way, we consider instead an axis system attached to the center of mass of the molecule, such that this axis system does not move if the two identical halves of the molecule are rotated by equal and opposite amounts about the central bond. It seems intuitively obvious that such an axis system does treat the two identical halves of the molecule in an equal fashion during the internal rotation motion. As it happens, when operations of the permutation-inversion group are applied to basis functions written in terms of coordinates corresponding to this axis system, double groups do arise. It further seems intuitively obvious (though this view is not shared by all workers in the field), that coordinate systems which treat the symmetrically equivalent parts of a

molecule in a symmetrically equivalent fashion will lead most directly to all symmetry related results for the problem, and that therefore the second coordinate system above is to be preferred in symmetry discussions (though not necessarily in numerical calculations) even if it requires the introduction of a double group of the permutation-inversion group. Given these biases, we now examine some results which I believe would not follow easily from a treatment without double groups.

Consider first the ethane example. As was first illustrated in an energy level diagram by Wilson (21), and later oberved both experimentally and calculationally by Susskind and others (14,15,22,23), there is a staggering in the rotational energy levels of H_3C-CH_3. This staggering, which is comparable in magnitude with the internal rotation splittings, manifests itself as a systematic and nearly constant displacement of all odd K rotational levels upward from the positions expected on the basis of a symmetric rotor fit (including the internal rotation splittings) of the even K levels. This even-odd staggering in K is at first surprising, since statistical weights in this molecule with a three-fold rotation axis about the C-C bond recur with a period of three in K.

Briefly, the double group explanation for the staggering is as follows. In one sense, the barrier to internal rotation in ethane is clearly three-fold, since if one methyl group is rotated while the other is held fixed, the rotating methyl group passes through three different minimum energy configurations before returning to its original position. As is well known (20), the torsional levels in a three-fold barrier problem split (for v = 0 in the torsional vibration) into a nondegenerate

A state and a doubly degenerate E state, with relative energies of -2 and +1, respectively. In another sense, however, namely in the spirit of equal treatment for identical halves, let us require that the two methyl groups rotate by equal and opposite amounts during the torsional motion. It can then be seen that six energy minima are traversed before the two methyl groups return to their original positions. This corresponds mathematically to a six-fold barrier to internal rotation. As is also well known (24) the torsional levels for a six-fold barrier split into an A, E, E, A set, with relative energies of -2, -1, +1, +2, respectively. The requirement that complete wavefunctions must belong to single-valued representations of the permutation-inversion group leads to the restriction that even K rotational levels must be associated with the first and third of these torsional levels (a result identical to that obtained from the three-fold barrier treatment), but that odd K rotational levels must be associated with the second and fourth of these torsional levels, thus causing all odd K levels to be shifted upward by an amount exactly (in the real world, nearly) equal to 1/3 of the even K torsional splitting, with the additional provision for odd K that the A levels must lie above the E levels. In the author's opinion, this simple and quantitative explanation of the internal rotation staggering and splitting pattern illustrates the power and beauty of the double group treatment in ethane.

Consider next hydrogen peroxide, which exists in two gauche equilibrium configurations connected by internal rotation tunneling through either a trans or a cis intermediate configuration. As pointed out in section 3, only the trans barrier is actually low enough to permit significant

tunneling penetration, and the symmetry properties of H_2O_2 can thus be treated using the C_{2h} point group of the trans intermediate configuration together with a potential curve like that of Fig. 1. Nevertheless, suppose that tunneling through both the trans and cis barriers were to occur to a comparable extent. Then a double group treatment (arising again from the desire to treat the two identical halves of the molecule in a symmetrical fashion during the internal rotation motion) leads to a four-fold barrier problem (two trans and two cis barriers), and to the result that trans and cis tunneling interfere constructively for even K rotational levels, i.e. the sum of the trans and cis tunneling splittings would be observed for even K, whereas trans and cis tunnelings interfere destructively for odd K rotational levels, i.e. their difference would be observed for odd K. (In fact, when the trans and cis barriers become identical, the odd K splittings go to zero.) It is again the author's opinion that this phenomenon of constructive and destructive interference of the two types of tunneling splitting illustrates (albeit only theoretically) the power and beauty of the double group treatment in hydrogen peroxide (5).

It is interesting to note in passing, that strong formal group theoretical similarities exist between the double group treatment of the internal rotation tunneling problem in HO-OH, and the double group treatment of the tunneling exchange of protons in the hydrogen bond in HF..HF (25).

Up to this point the reader has seen examples of m-fold extended groups with $m = \infty$ and $m = 2$. The general case, involving other values of m, has been discussed in the literature (26), but the formalism has not been applied sufficiently to assess its ultimate worth. Nevertheless, we shall close this section with a consideration of the molecule $D_3C\text{-}CH_3$, which would be treated using a 3-fold extension of its permutation-inversion group, i.e. using a triple group. Probably the first question to occur to the reader is how this value of 3 for m is arrived at. Clearly, the two halves of the $D_3C\text{-}CH_3$ molecule are not identical, and there is thus no symmetry argument for treating the two halves equally. Indeed, there is a "symmetry" argument for not treating them equally. However, an argument based on our intuitive notions of the Born-Oppenheimer-like separation of variables suggests how the two halves of this molecule should be treated. Suppose we seek a maximal separation of the internal and overall rotational motions. One way of accomplishing this is to require that only overall rotation generate angular momentum, i.e. that no net angular momentum be generated during the internal rotation motion. Since the moments of inertia for the $D_3C\text{-}$ and $\text{-}CH_3$ groups are in the ratio of 2:1, the elimination of angular momentum during an internal rotation requires that the $\text{-}CH_3$ group rotate through an angle of -2α when the $D_3C\text{-}$ group rotates through an angle of $+\alpha$. As a consequence, the molecule passes through nine energy minima during the internal rotation motion before the $\text{-}CH_3$ and $D_3C\text{-}$ groups return to their original positions. While all the details of the corresponding triple-group have not been worked out (27), it seems likely to the author that

various regularities in energy level splittings, selection rules, statistical weights, etc. will emerge which are related in some way to the integer 9. For other molecules, with two unequal parts rotating against each other, other values of m arise (26).

5. Discussion

One question which always seems to occur to molecular spectroscopists upon reading or hearing excerpts from the material above is: "Is group theory beyond point groups really necessary?" An eloquent answer to the general question of using or not using group theory is given in a few paragraphs towards the end of the introduction to Condon and Shortley's book on Atomic Spectroscopy (28), and that answer is applicable here also. In particular, it is even more possible today to obtain from numerical calculations results which are also derivable from symmetry considerations, if by results we mean the fact that some quantity is zero, or that two quantities are equal. The numerical calculations go even further, of course, and give us numerical values for the nonzero quantities. It should be added in favor of group theory, however, that important additional qualitative understanding, which is difficult to glean from tables of numbers, often emerges from a study of the pictures and diagrams associated with symmetry discussions.

A second question is: "What's next?" This is always difficult to speculate upon, but it seems clear that the new experimental data being acquired in a variety of laboratories on large amplitude and/or tunneling motions in van der Waals molecules, hydrogen-bonded species, and some protonated-molecule ionic species will require new methods of attack for the problem of energy levels, selection rules, etc. (i.e. for the spectroscopy) of such species. It is the author's opinion that group theory will play a contributing role in any increased understanding of such molecular systems.

References

1. G. Herzberg, Infrared and Raman Spectra, Van Nostrand, Princeton, 1945.
2. G. Herzberg, Electronic Spectra of Polyatomic Molecules, Van Nostrand, Princeton, 1966.
3. E. B. Wilson, Jr., J. Chem. Phys. 3, 276-285 (1935).
4. I. M. Mills, J. Phys. Chem. 88, 532-536 (1984).
5. J. T. Hougen, Canad. J. Phys. 62, 1392-1402 (1984).
6. J. T. Hougen, J. Chem. Phys. 37, 1433-1441 (1962), ibid. 39, 358-365 (1963).
7. H. C. Longuet-Higgins, Mol. Phys. 6, 445-460 (1963).
8. P. R. Bunker, Molecular Symmetry and Spectroscopy, Academic Press, New York, 1979.
9. J. T. Hougen, Canad. J. Phys. 42, 1920-1937 (1964).
10. J. K. G. Watson, Canad. J. Phys. 43, 1996-2007 (1965).
11. R. S. Berry, J. Chem. Phys. 32, 933-938 (1960).
12. B. J. Dalton, J. Chem. Phys. 54, 4745-4762 (1971).
13. P. R. Bunker and D. Papousek, J. Mol. Spectrosc. 32, 419-429 (1969).
14. J. Susskind, J. Mol. Spectrosc. 49, 1-17 (1974).
15. J. T. Hougen, J. Mol. Spectrosc. 82, 92-116 (1980).
16. R. H. Hunt, R. A. Leacock, C. W. Peters and K. T. Hecht, J. Chem. Phys. 42, 1931-1946 (1965).
17. H. Dreizler, Z. Naturforschg. 21a, 1628-1632 (1966).
18. G. Dellepiane, M. Gussoni and J. T. Hougen, J. Mol. Spectrosc. 47, 515-530 (1973).

19. K. Yamada, T. Nakagawa and K. Kuchitsu, J. Mol. Spectrosc. 51, 399-421 (1974).

20. C. C. Lin and J. D. Swalen, Revs. Mod. Phys. 31, 841-892 (1959).

21. E. B. Wilson, Jr., J. Chem. Phys. 6, 740-745 (1938).

22. J. Susskind, D. Reuter, D. E. Jennings, S. J. Daunt, W. E. Blass, and G. W. Halsey, J. Chem. Phys. 77, 2728-2744 (1982).

23. L. Henry, A. Vanentin, W. J. Lafferty, J. T. Hougen, V. Malathy Devi, P. P. Das and K. Narahari Rao, J. Mol. Spectrosc. 100, 260-289 (1983).

24. A. A. Frost and B. Musulin, J. Chem. Phys. 21, 572-573 (1953).

25. J. T. Hougen and N. Ohashi, J. Mol. Spectrosc. 109, 134-165 (1985).

26. J. T. Hougen and B. J. DeKoven, J. Mol. Spectrosc. 98, 375-391 (1983).

27. An investigation of the nuclear hyperfine Hamiltonian in molecules of the type D_3C-CH_3, H_3C-SiF_3, etc. is presently being carried out by the author, using m-fold extensions of the permutation-inversion group.

28. E. U. Condon and G. H. Shortley, The Theory of Atomic Spectra, Cambridge University Press, Cambridge, 1964.

FIGURE CAPTIONS

Fig. 1

Schematic illustration of one way of treating a double-minimum vibrational problem. (a) A harmonic oscillator well in the coordinate Q, with energy levels and symmetry species Γ_v shown explicitly for v = 0,1,2,3. (b) The "same" set of levels, as perturbed by the presence of a potential hump centered at Q = 0. This hump gives rise to a potential curve with two minima, at $Q = \pm Q_o$. Furthermore, even v vibrational levels are strongly raised by the potential hump from their original positions (dashed lines) to positions nearly degenerate with the next higher odd v level. Symmetry species from Fig. 1(a) can be carried over to 1(b). The vibrational numbering could also be carried over, and v would then give the total number of nodes in each vibrational wavefunction. However, it is more common to count only the nodes occuring in one potential minimum, leading to the vibrational numbering shown on the right. For this type of numbering, the superscript + or - indicates no nodes or one node, respectively, occuring under the potential hump.

Fig. 2

Schematic structures and the atom numbering schemes used in this paper for ethylene and dimethylacetylene. (a) With a z axis along the C=C bond, and a y axis out of plane, the point group rotation $C_2(z)$ corresponds to the permutation (12)(34), whereas the reflection $\sigma_v(yz)$ corresponds to (12)(34)*. The reflection $\sigma_v(xz)$ corresponds to the laboratory-fixed inversion E*, whereas the molecule-fixed inversion i corresponds to (ab)(14)(23)*. (b) Rotation of the upper methyl group only, through angles of 120^o and 240^o, corresponds to the permutations (123) and $(123)^2 = (132)$.

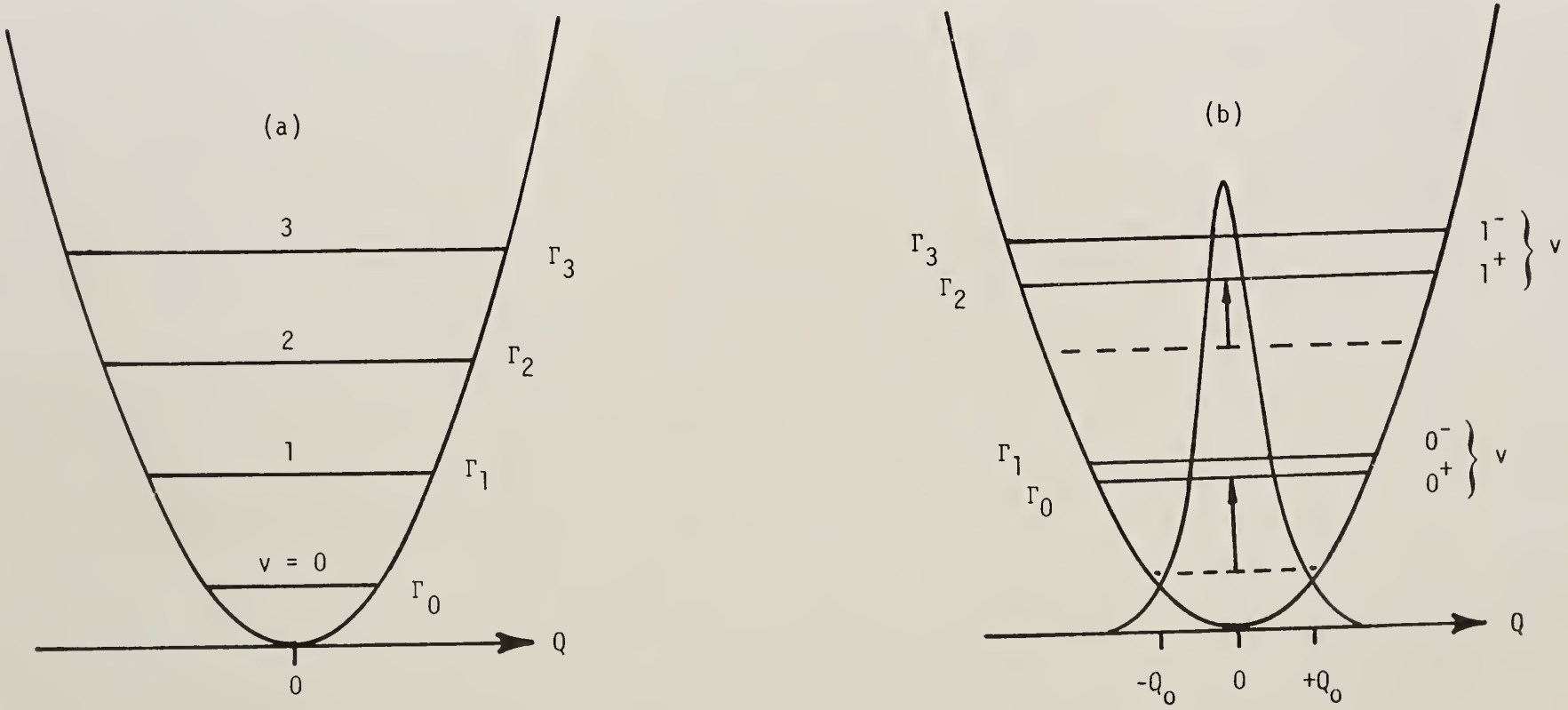
(a)
3
2
1
v = 0
Γ_3
Γ_2
Γ_1
Γ_0
Q
0
(b)
Γ_3
Γ_2
Γ_1
Γ_0
1^-
1^+
v
0^-
0^+
v
Q
$-Q_o$
0
$+Q_o$

Figure 1

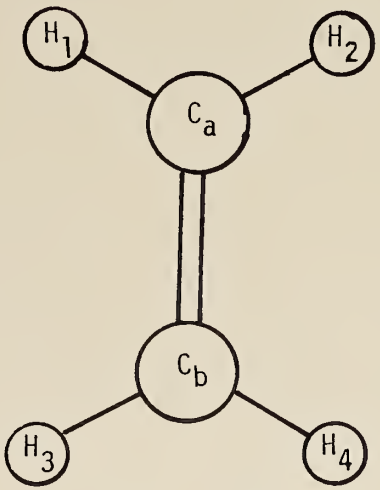

(a)

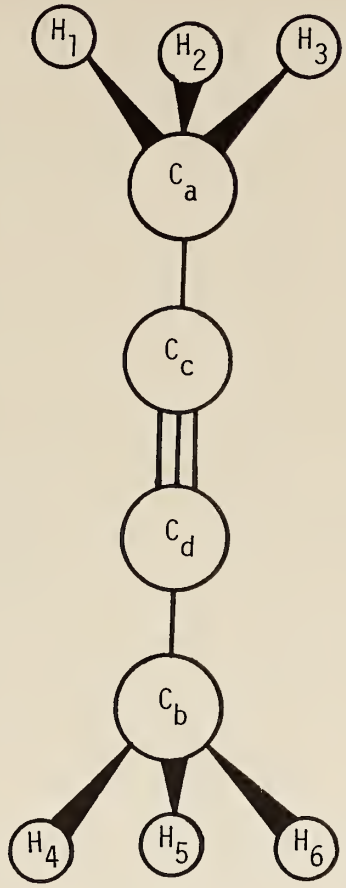

(b)

Figure 2

METASTABLE RADICALS AND HYPERVALENT CLUSTERS BY NEUTRALIZED ION BEAM TECHNIQUES

J.S. Jeon, A.B. Raksit, G.I. Gellene* and R.F. Porter

Department of Chemistry, Cornell University

and

W.P. Garver, C.E. Burkhardt and J.J. Leventhal

Department of Physics, University of Missouri - St. Louis

ABSTRACT

A number of metastable radicals have been generated by neutralizing a fast beam of positively charged ions in electron transfer collisions with metal target atoms. We will present results of studies to identify the dissociative, metastable and radiative states of H_3 following the reaction $H_3^+ + K_g \rightarrow H_3^* + K^+$. We will also present and discuss results for other metastable radicals, including ND_4, and a new series of hypervalent cluster radicals of the type $NH_4(NH_3)_n$.

---

*Department of Chemistry, University of Notre Dame, Notre Dame, Indiana, 46556

Introduction

In this paper we discuss the use of neutralized ion beam techniques[1] to generate and study a variety of radicals not usually observed in conventional chemical systems. We are investigating process of the general type

$$X^+ + M(g) \rightarrow X^* + M^+ \qquad (1)$$

in which a fast projectile ion, X^+, is neutralized by electron transfer from a metal target atom. The product molecule X^*, can be ground or excited states of X. Cross sections for resonant electron transfer when I.P.(M) = I.P.(X^*), are generally large and the yields of X^* states will vary with electron donors having different ionization potentials. Non-resonant processes also occur with lower probabilities. Since electron transfer occurs on a very short time we can view reaction 1 as a vertical process dominated largely by Franck-Condon factors. The states of X^* are classified as dissociative (or predissociative), metastable or radiative. We will discuss results for the radicals, H_3, NH_4 and the hypervalent clusters, $NH_4(NH_3)_n$.

Experimental

The apparatus and the experimental procedures were described in detail previously[2]. The primary ions were produced by chemical ionization of the appropriate gas mixture in a high pressure ion source. The ions were then accelerated through 6 keV, mass resolved, and focussed into a neutralization chamber containing a few mTorr of metal vapor. The chamber is 0.5 in. thick and has a knife edge entrance slit of 0.025 x 0.200 in. and

an exit slit of 0.025 x 0.250 in. The resulting neutral species are permitted to continue undeflected toward the channeltron electron multiplier located 40 cm from the center of the neutralization chamber while the remaining ions are removed from the beam by means of electrostatic deflector plates. After traversing the electrostatic field, a fraction of the neutral beam along the beam axis was re-ionized by charge stripping. For this purpose, a collisional ionization chamber, 4.25 in. long with 0.020 x 0.280 in. entrance and exit slits was positioned between the detector and the neutralization chamber. This second chamber was pressurized with N_2 or NO_2 gas at approximately 50 mTorr. The collisionally re-ionized beam ($\sigma \sim 10^{-18}$ cm^2) was deflected electrostatically off axis and detected by translating the detector normal to the beam axis. Since an ion is deflected a distance ΔX proportional to the reciprocal of its kinetic energy, a resolved mass spectrum can be obtained from the deflected secondary ion beam. Further, the mass resolution of the apparatus can be increased by floating the collisional ionization chamber at a negative potential to reduce the kinetic energies of the secondary ions by a constant amount.

Discussion

H_3^*

Molecules of H_3 are generated through the reaction sequence

$$H_2^+ + H_2 \rightarrow H_3^+ + H \qquad (2)$$

$$H_3^+ + M(g) \rightarrow H_3^* + M^+ \qquad (3)$$

H_3^* and H_3^+ have D_{3h} symmetries and united atom-group theoretical symbols will be used as state designations for H_3^*. This is a model system for illustrating several modes of product excitation.

Dissociative States

When K or Mg is used as the electron donor in reaction 3, the majority of H_3 states formed undergo rapid dissociation (fragmentation) to H_2 + H which scatter isotropically from the point of neutralization[3]. By analysis of the angular dependence of scattered particles (beam profiles) the maximum kinetic energy release in the products can be calculated. The widths of the beam profiles (figure 1A) show that more kinetic energy is released in the K/H_3^+ reaction than in the Mg/H_3^+ reaction and that different states of H_3 are accessed in the two cases. This enables us to place the $2s,^2A_1'$ state, which is known to undergo heterogeneous predissociation[4], and the dissociative $2p,^2E'$ ground state on a vertical energy scale with respect to H_3^+ (figure 2).

Metastable State ($2p,^2A_2''$, N=K=O level)

In 1967 Devienne[5], using a combination of neutralization and charge stripping techniques found evidence for a long-lived state of H_3. However, Gray and Tomlinson[6] using a similar approach were unable to confirm the existence of a metastable state and concluded that an impurity, HD, was possibly responsible for the re-ionized mass 3 peak. Beam profiles from our K/H_3^+ experiment

reveal a central peak that is too intense to be due to naturally occurring HD but the absence of a central peak in profiles from K/D_3^+ experiments requires additional consideration. Recent charge stripping experiments clearly confirm the existence of metastable forms of H_3 and D_3 but show a disproportionately high ratio of H_3/D_3 in neutralized H_3^+ and D_3^+ beams of equivalent flux (figure 1c). Herzberg and collaborators[4] have shown that the $2p,{}^2A_2''$ state of H_3 undergoes efficient heterogenous rotational predissociation. However the process is forbidden for the N=K=0 level which we believe accounts for the metastablility. The $2p,{}^2A_2''$ and $2s,{}^2A_1'$, states of H_3 are both near resonant products of the K/H_3^+ reaction (figure 2) but the allowed transition $2p,{}^2A_2'' \rightarrow 2s,{}^2A_1'$ has a low oscillator strength. The radiative life-time of the $2p,{}^2A_2''$ state is estimated[7] to be about 90 μsec. Much of the controversy surrounding the earlier literature on metastable H_3 can be resolved by recognizing that the state can not be formed from any ro-vibrational level of the precursor H_3^+. For H_3^* we have the predominant process

$$H_3^+(N=1,\ K=0) + K \rightarrow H_3^*(N=K=0) + K^+$$

In a thermalized H_3^+ beam the population of the precursor state can be calculated from statistical considerations. However H_3^+ ions generated by reaction 2 will, in general, carry excess ro-vibrational energies unless they are collisionally quenched before exiting the ion source. This effect on the production of metastable H_3 is illustrated in figure 1b. As the precursor ions are relaxed at high source pressures of H_2, the intensity ratio of re-ionized H_3^+ to H_2^+ reaches a plateau showing that the den-

sity of metastables in the beam has reached maximum value. The lower abundance of metastable D_3 molecules for equivalent ion beam fluxes can be understood by the reduced population of the N=1, K=0 precursor levels in D_3^+ in accordance with the Pauli principle when nuclear spin is considered[3,7].

Radiative States

Herzberg and collaborators[4] have obtained and analysed emission spectra for a number of visible transitions between upper Rydberg levels of H_3. The $3p,{}^2A_2'' \rightarrow 2s,{}^2A_1'$ and $3p,{}^2E' \rightarrow 2s,{}^2A_1'$. transitions occur in the spectral region near 560 and 710 nm, respectively. Other visible transitions originate from the 3d levels. Figger and co-workers[8] also observed many of these bands following the processes:

$$H_3^+ + M(g) \rightarrow H_3^* + M^+ \quad (M = \text{alkali metal}) \qquad (5)$$

$$H_3^* \rightarrow H_3^\dagger + h\nu \qquad (6)$$

Transitions involving the ground repulsive state have not been observed previously. The intense emission predicted[9,10] for the $2s,{}^2A_1' \rightarrow 2p,{}^2E^1$ transition is not observed due to strong predissociation of the upper state. The $2p,{}^2A_2'' \rightarrow 2p,{}^2E'$ transition is forbidden by electronic selection rules and the $3p,{}^2E' \rightarrow 2p,{}^2E'$ transition is expected to be weak in the united atom approximation.

We have recently observed[11] a low resolution UV continuum attributed to D_3 with $\lambda_{max} \approx 230$ nm (figure 1d). The luminescence is observed following D_3^+/K charge transfer collisions

(reactions 4 and 5). Since the spectrum is structureless, its identification is indirect. the possiblity that it arises from (D_2 $a^3\Sigma_g^+$) formed by collisional dissociation of D_3 was considered in detail. Several experimental factors taken together rule this possibility out. First, the spectra of H_2 and D_2 obtained from H_2^+(or D_2^+)/K collisions show both the $B^1\Sigma_u^+ \rightarrow X^1\Sigma_g^+$, (Lyman bands), and the $a^3\Sigma_g^+ \rightarrow b^3\Sigma_u^+$ continuum. Note there is no spin restriction on the electron transfer process but the Lyman bands are absent in the D_3 spectrum. Secondly, the spectral intensities of the UV and visible bands in $H_3(D_3)$ diminish proportionately if the precursor $H_3^+(D_3^+)$ ions are not collisionally relaxed prior to charge transfer. This is contrary to expectations that the probability of forming excited H_2 or D_2 would increase if the precursor ions have excess vibrational energy. The effect of ion relaxation on the D_2^+/K spectrum (figure 1d) is to shift the continuum to longer wave lengths corresponding to transitions from lower vibrational states of D_2 ($a\ ^3\Sigma_g^+$). The band at $\lambda \approx 225$ nm most probably occurs from $\nu' = 1$.

King and Morokuma[9] calculated transition moments for a number of transitions originating in excited Rydberg levels in H_3 and terminating on the $2p,^2E'$ ground state. The strongest transition is predicted to be $3d,^2E' \rightarrow 2p,^2E'$, but transitions from higher levels can also occur. There appears to be only one band in the spectrum but this is a tentative judgment until higher resolution spectra are recorded.

NH_4

In 1981 Herzberg[13] published high resolution spectra of the so-called Schuster and Schüler bands in emission and attributed the spectra to NH_4 (and ND_4). He also made tentative assignments of the electronic states involved in the transitions. About the same time Williams and Porter[14] obtained direct experimental data related to the thermodynamic stabilities of the radicals from neutralized ion beam studies. It was shown that ND_4 formed by ND_4^+/K or ND_4^+/Na collisions could be detected as an isolated species in a beam but that NH_4 fragmented in transit to the detector. Later Gellene, et al.[15] studied the complete series of isotopic NH_nD_{4-n} molecules and showed that the metastability was related to a tunnel barrier accounting for the rapid loss of H compared to D. The dramatic difference in kinetic stabilities of NH_4 vs ND_4 is further illustrated by the charge stripping spectra of neutralized NH_4^+ and ND_4^+ in figure 3. With NO_2 as collisional ionization gas, NH_4^+ is not observed on reionization but ND_4^+ is a prominent mass peak.

The NH_4 molecule is an interesting model for testing theoretical methods. The existence of a tunnel barrier on the ground potential surface was not addressed in the earliest calculations[16] but recently several groups[17-19] have calculated barrier heights and ionization potentials in reasonable agreement with experimental values.[15]

Kaspar and co-workers[19] calculated tunnel rates for loss of H and D from NH_4 and ND_4 and found, rather surprisingly, that the lifetime of NH_4 was substantially greater than expected from pre-

vious experimental work. Their result has interesting implications since it would predict that NH_4 is kinetically stable in its ground state for observation by absorption spectroscopy and other physical techniques. Two research groups[20,21] using different innovative techniques were able to observe the absorption spectrum of ND_4 (Schuler band) but, thus far, there is no report of an absorption spectrum of any of the partially deuterated species. Kaspar and co-workers[19] calculated dissociative lifetimes for individual rotational levels in NH_4 and found τ as high as 40 μsec for J=7. It is difficult to reconcile this result with that of the beam work which can easily detect a metastable with a microsecond lifetime. The issue can only be resolved by studies of the absorption spectrum of NH_4 (negative or positive results) or by further refined calculations.

Hypervalent Clusters, $NH_4(NH_3)_n$

Cluster radicals of the type $NH_4(NH_3)_n$ are generated through the sequence of steps:

$$NH_3^+ + NH_3 \rightarrow NH_4^+ + NH_2 \qquad (6)$$

$$NH_4^+ + nNH_3 \xrightarrow{NH_3} NH_4(NH_3)_n^+ \qquad (7)$$

$$NH_4(NH_3)_n^+ + M \rightarrow NH_4(NH_3)_n + M^+ \qquad (8)$$

The conditions for forming precursor ions in a high pressure source have been investigated extensively by Kebarle and co-workers[22] and ion structures of have been calculated theoretically[23]. Beam scattering profiles for $NH_4 \cdot NH_3$ and $ND_4 \cdot ND_3$ are compared with those for NH_4 and ND_4 in figure 3. For $ND_4 \cdot ND_3$ there

is clear evidence for a stable peak near θ=0 as there is for ND_4. For $NH_4 \cdot NH_3$ there is also clear evidence of a stable peak near θ=0 in contrast to the situation for NH_4. Charge stripping mass spectra also confirm these conclusions. The wings on the profiles show that a sizable fraction of $NH_4 \cdot NH_3$ molecules undergo decomposition prior to detection. The charge stripping mass spectra reveal that NH_3 is a major product from $NH_4 \cdot NH_3$ but that $ND_4 \cdot ND_3$ fragments partially to $ND_4 + ND_3$. As the degree of clustering increases fragmentation dominates for n>2.

For the process $NH_4 \rightarrow NH_3 + H$, $\Delta E \approx -0.1$ e.v.[15] The exothermicity of the association reaction is apparently sufficient to stabilize $NH_4 \cdot NH_3$ with respect to $2NH_3 + H$, indicating that the cluster is slightly stable thermodynamically. The binding energy between NH_4 and NH_3 can not be obtained directly from the beam results but Cao and co-workers[24] have calculated a value of -0.38 e.v. This is substantially larger in magnitude than that found for H-bonding in $(NH_3)_2$.[25] The nature of the interaction between NH_4 and NH_3 molecule is a subject for further theoretical analysis.

Vertical electron transfer in reaction 8 will lead to cluster radicals in the geometry of the precursor ion. Since the equilibrium configuration of the radical and ion are expected to differ significantly, the radical is probably formed in a state of vibrational excitation. This can affect the branching ratio for fragmentation, expecially if the ions are not collisionally relaxed in the source.

Estimated ionization energies for these cluster radicals are

exceptionally low and fall off as n increases (see Table I). Values were calculated through the cycle:

$$NH_4^+ + nNH_3 \rightarrow NH_4(NH_3)_n^+ \qquad \Delta H_1$$

$$NH_4 \rightarrow NH_4^+ + e \qquad \Delta H_2$$

$$NH_4(NH_3)_n \rightarrow NH_4 + nNH_3 \qquad \Delta H_3$$

which gives

$$\text{I.P. } [NH_4(NH_3)_n] = \Delta H_1 + \Delta H_2 + \Delta H_3$$

where ΔH_1 values are taken from the literature,[22] ΔH_2 is the ionization potential[15] of NH_4 and ΔH_3 is estimated as to be 0.38 e.v. per NH_3 unit[24].

Acknowledgment

The work at Cornell University was supported by N.S.F. Grants No. CHE-8215184 and CHE-8314501. The work at UMSL was supported by U.S. D.O.E., Division of Chemical Sciences, under Grant No. DE-FG02-84ER13237.

Table I. Ionization Energies

Species	I.P. (e.V.)
NH_4	4.7[a]
N_2H_7	4.0 ± 0.2
N_3H_{10}	3.5 ± 0.2
CH_3NH_3	4.4 ± 0.1[b]
$CH_3N_2H_6$	3.9 ± 0.2

a) Value for NH_4 taken from Ref. 15.

b) Value for CH_3NH_3 taken from Ref. 26.

Reference

1. G.I. Gellene and R.F. Porter, Accts. Chem. Res. 16, 200 (1983).
2. G.I. Gellene and R.F. Porter, Inter. J. Mass Spectr. and Ion Proc. 64, 55 (1985).
3. G.I. Gellene and R.F. Porter, J. Chem. Phys. 79, 5975 (1983).
4. G. Herzberg and J.K.G. Watson, Can. J. of Phys. 58, 1250 (1980); I. Dabrowski and G. Herzberg, Can. J. of Phys 58, 1238 (1980).
5. F.M. Devienne, Entropie 24, 35 (1968).
6. J. Gray and R.H. Tomlinson, Chem. Phys. Lett. 4, 251 (1969).
7. S.J. Jeon, A.B. Raksit, G.I. Gellene and R.F. Porter, J. Chem. Phys. 82, 4916 (1985).
8. H. Figger, M.N. Dixit, R. Maier, W. Schrepp, H. Walther, I.R. Peterkin and J.K.G. Watson, Phys. Rev. Lett. 52, 906 (1984).
9. H.F. king and K. Morokuma, J. Chem. Phys. 71, 3213 (1979).
10. R.L. Martin, J. Chem. Phys. 71, 3541 (1979).
11. A.B. Raksit, R.F. Porter, W.P. Garver and J.J. Leventhal, Phys. Rev. Lett. 55, 378 (1985).
12. G.I. Gellene, D.A. Cleary, R.F. Porter, C.E. Burkhardt and J.J. Leventhal, J. Chem. Phys. 77, 1354 (1982).
13. G. Herzberg, Faraday Discuss. Chem. Soc. 71, 165 (1981).
14. B.W. Williams and R.F. Porter, J. Chem. Phys. 73, 5598 (1980).
15. G.I. Gellene, D.A. Cleary and R.F. Porter, J. Chem. Phys.

77, 3471 (1982).

16. W.A. Lathan, W.J. Hehre, L.A. Curtis and J.A. Pople, J. Am. Chem. Soc. 93, 6377 (1971).

17. H. Cardy, D. Liotard, A. Dargelos and E. Poquet, Chem. Phys. 77, 287 (1983).

18. S. Havriliak, T.R. Furlani and H.F. King, Can. J. of Phys. 62, 1336 (1984).

19. J. Kaspar, V.H. Smith and B.N. McMaster, Chem. Phys. 96 (1985).

20. E.A. Whittaker, B.J. Sullivan, G.C. Bjorklund, H.R. Wendt and H.E. Hunziker, J. Chem. Phys. 80, 91 (1984).

21. F. Alberti, K.P. Huber and J.K.G. Watson, J. Mol. Spectr. 107, 133 (1984).

22. J.D. Payzant, A.J. Cunningham, P. Kebarle, Can. J. Chem. 51, 3242 (1973).

23. K. Hirao, T. Fujikawa, H. Konishi, and S. Yamabe, Chem. Phys. Lett. 104, 184 (1984).

24. H.Z. Cao, E.M. Evleth, E. Kassab, J. Chem. Phys. 81, 1512 (1984).

25. The values range between 0.16 and 0.20 e.V., see S.T. Ceyer, P.W. Tiedemann, B.H. Mahan and Y.T. Lee, J. Chem. Phys. 70, 14 (1979) and K.D. Cooke and J.W. Taylor, Int. J. Mass Spectrum Ion Phys. 30, 345 (1979).

26. S.J. Jeon, A.B. Raksit, G.I. Gellene and R.F. Porter, J. Am. Chem. Soc., July issue (1985).

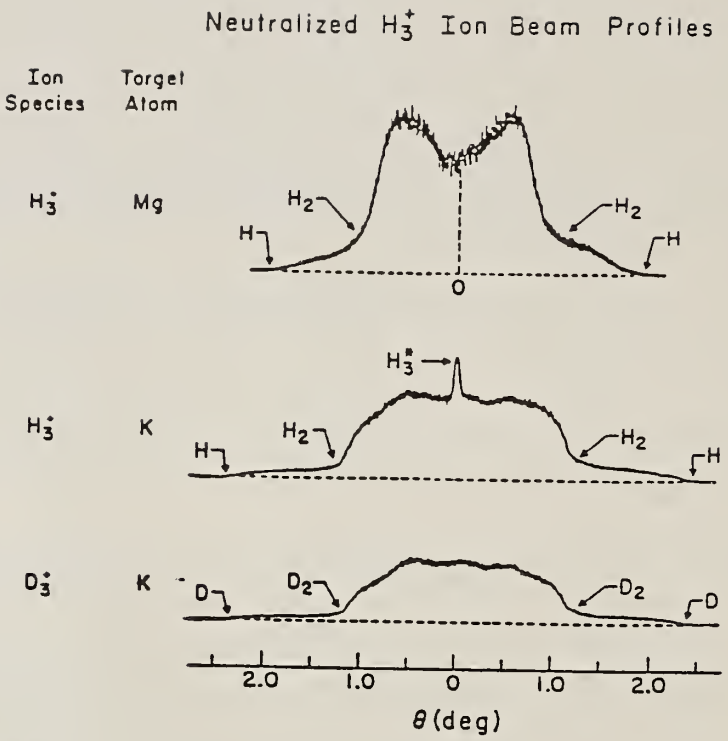

Figure 1a

H_3 beam scattering profiles following $H_3^+(D_3^+)$/K and H_3^+/Mg collisions.

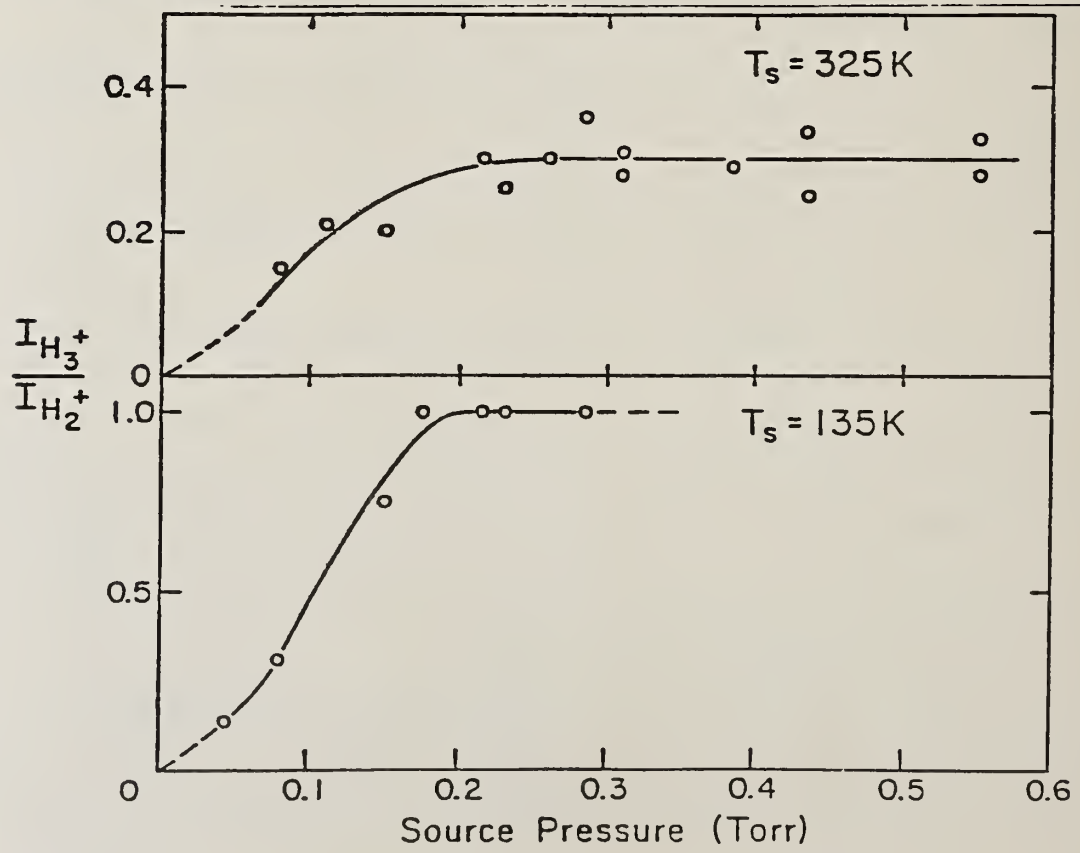

Figure 1b

Effect of H_2 source pressure and temperature on the relative beam intensities of H_3^* and D_3^* as monitored by charge stripped ion signals.

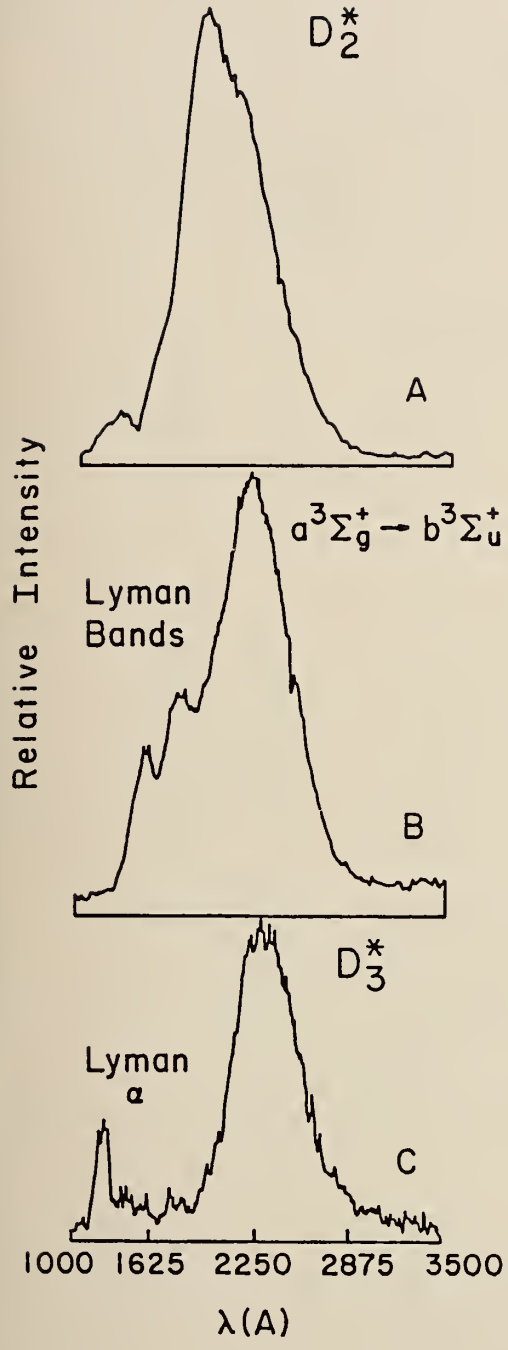

Figure 1d

UV spectra following D_2^+/K and D_3^+/K collisions.

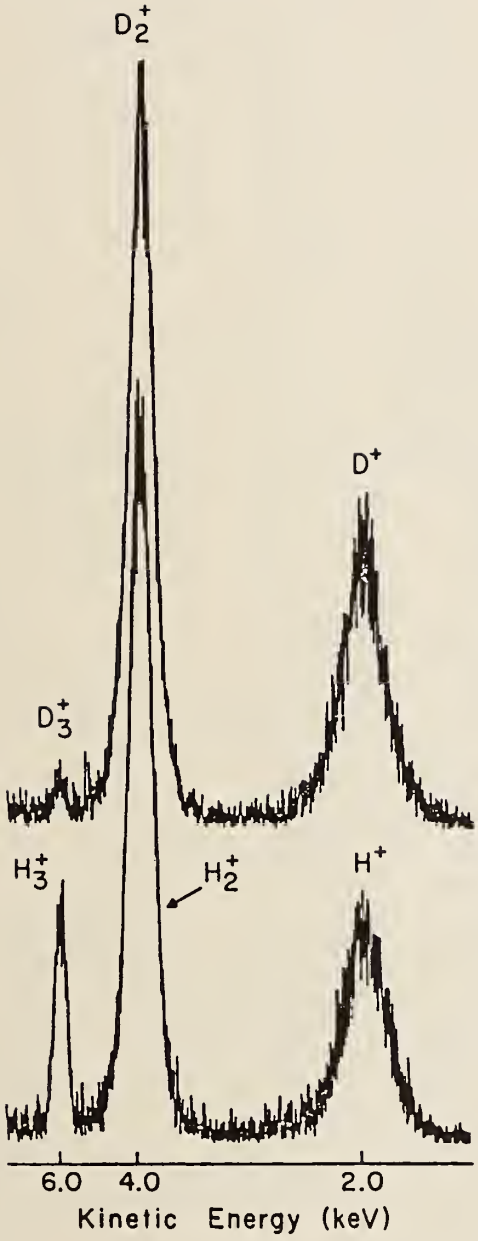

Figure 1c

Charge stripped mass spectra of H_3 and D_3.

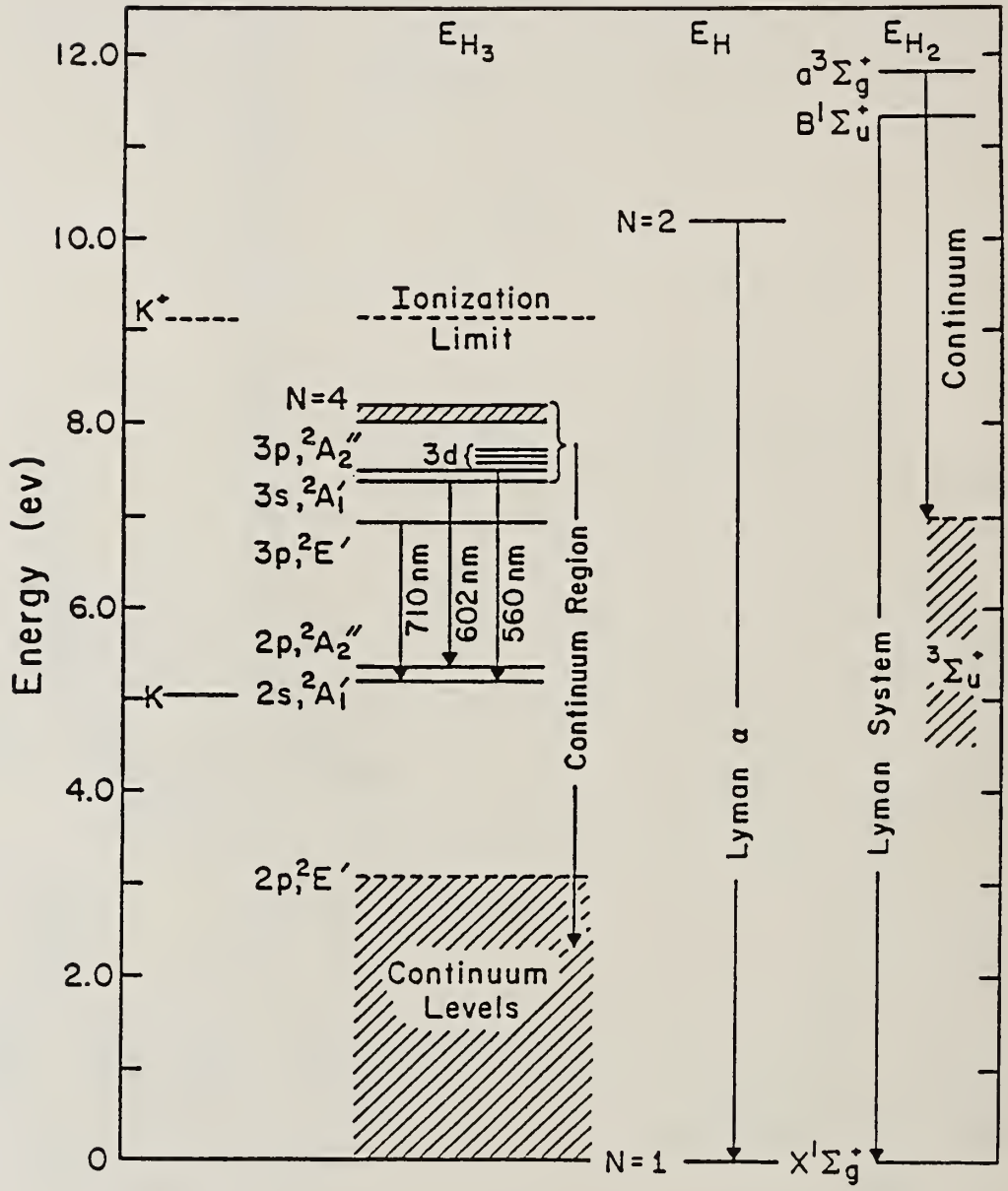

Figure 2

Energy level diagram showing many of the known states of H_3 and the region of the UV continuum.

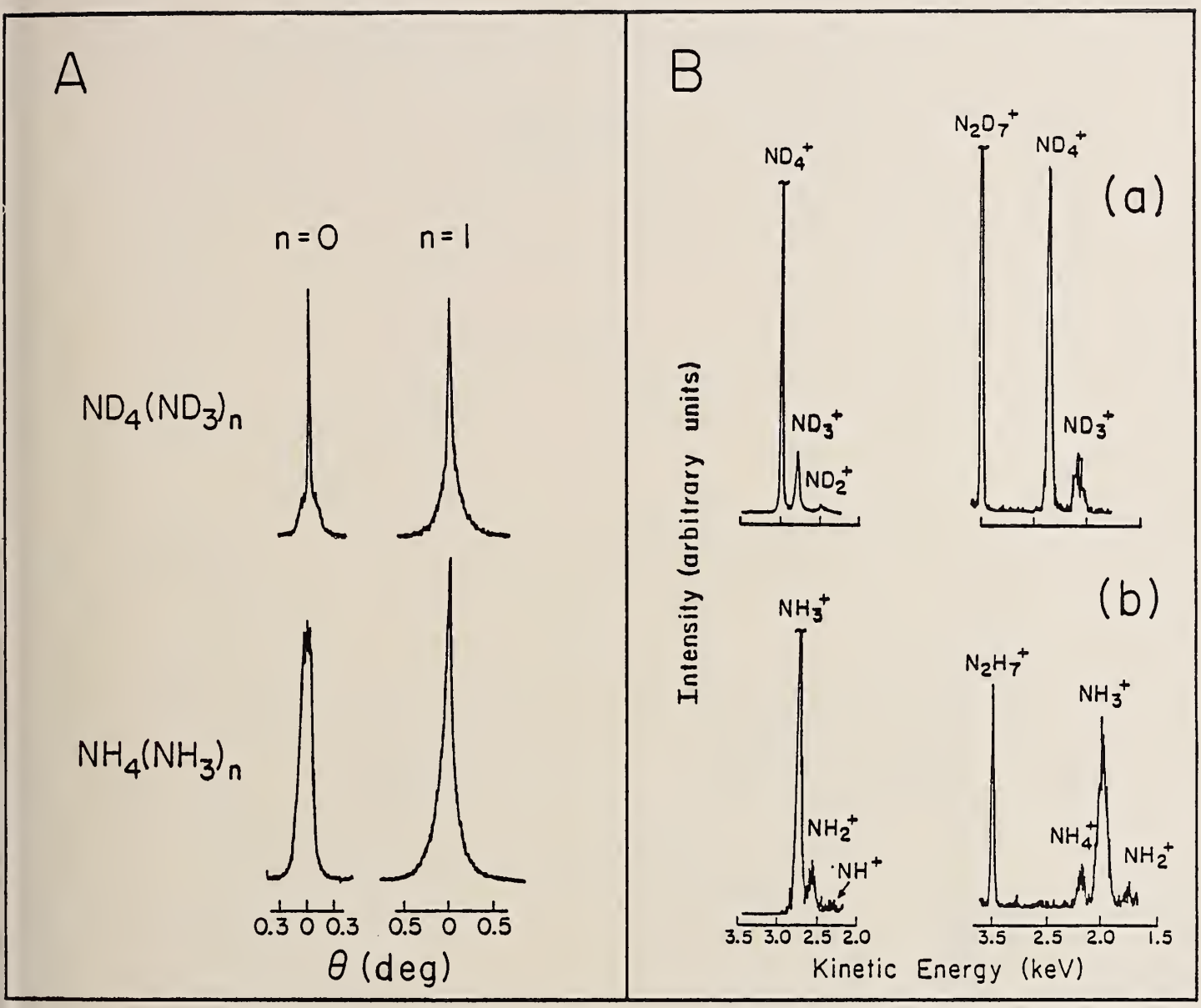

Figure 3

A. Neutral beam profiles following charge transfer from K to NH_4^+, ND_4^+, $N_2H_7^+$ and $N_2D_7^+$.
B. Charge stripped mass spectra of NH_4, ND_4, N_2H_7 and N_2D_7.

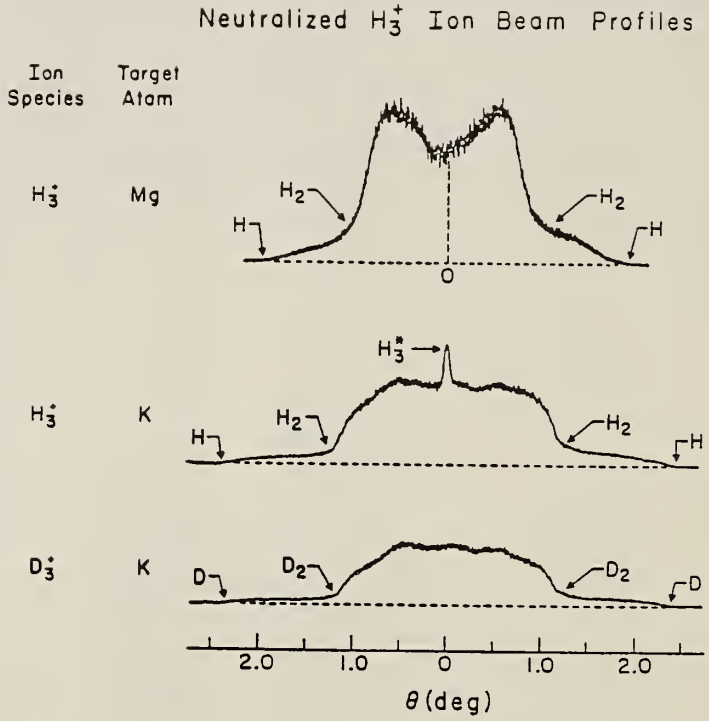

Figure 1a

H_3 beam scattering profiles following $H_3^+(D_3^+)/K$ and H_3^+/Mg collisions.

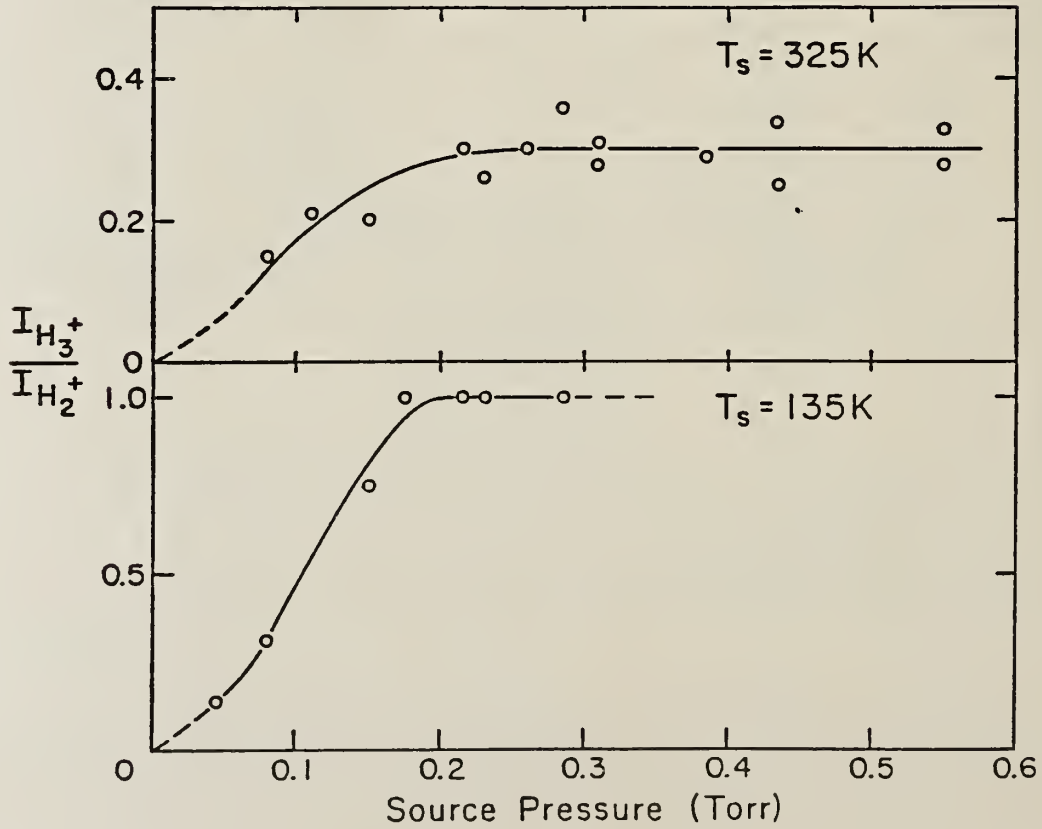

Figure 1b

Effect of H_2 source pressure and temperature on the relative beam intensities of H_3^* and D_3^* as monitored by charge stripped ion signals.

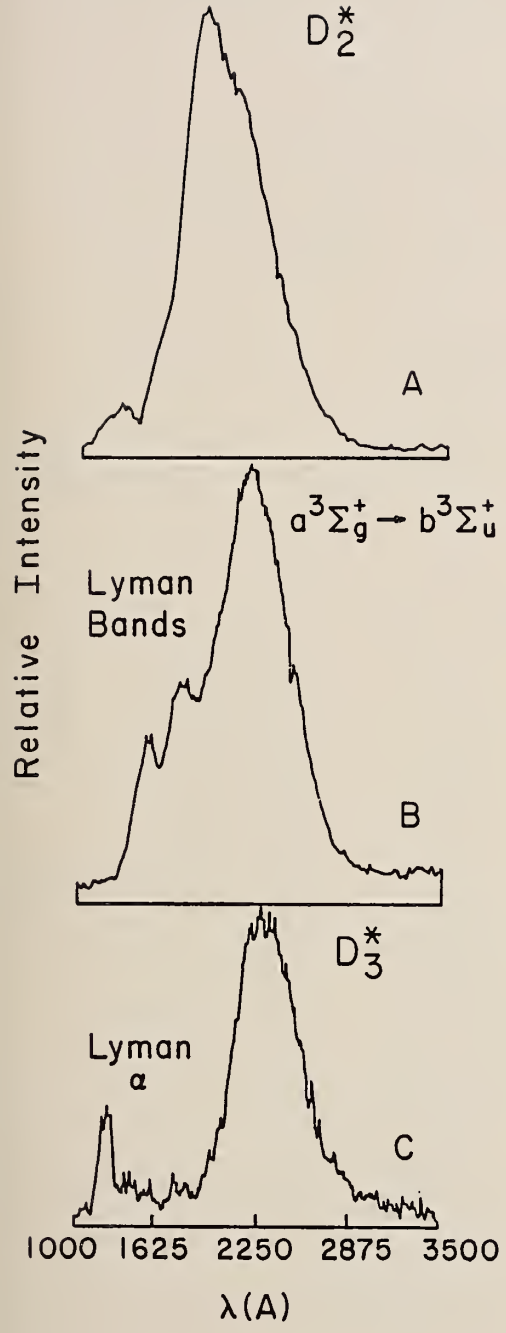

Figure 1d

UV spectra following D_2^+/K and D_3^+/K collisions.

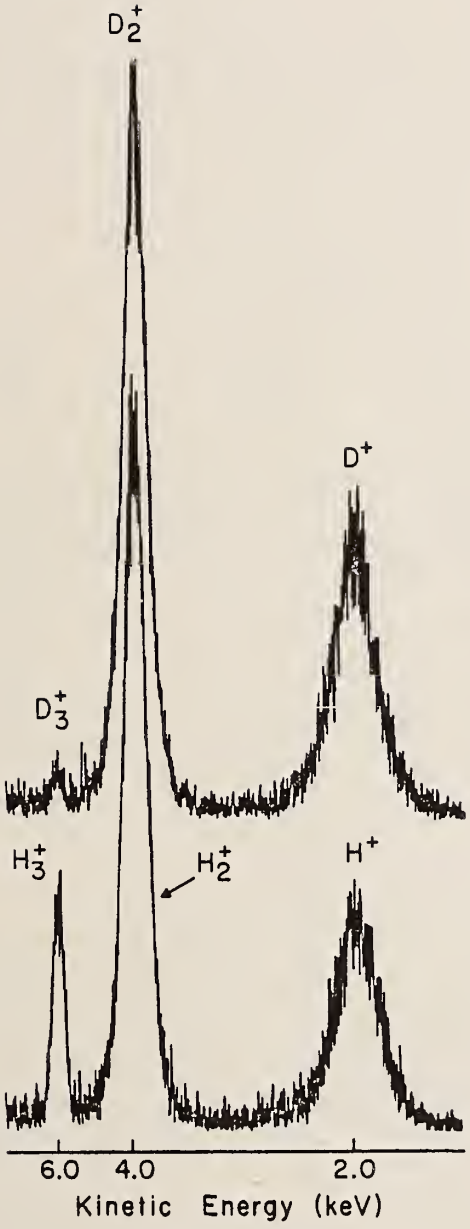

Figure 1c

Charge stripped mass spectra of H_3 and D_3.

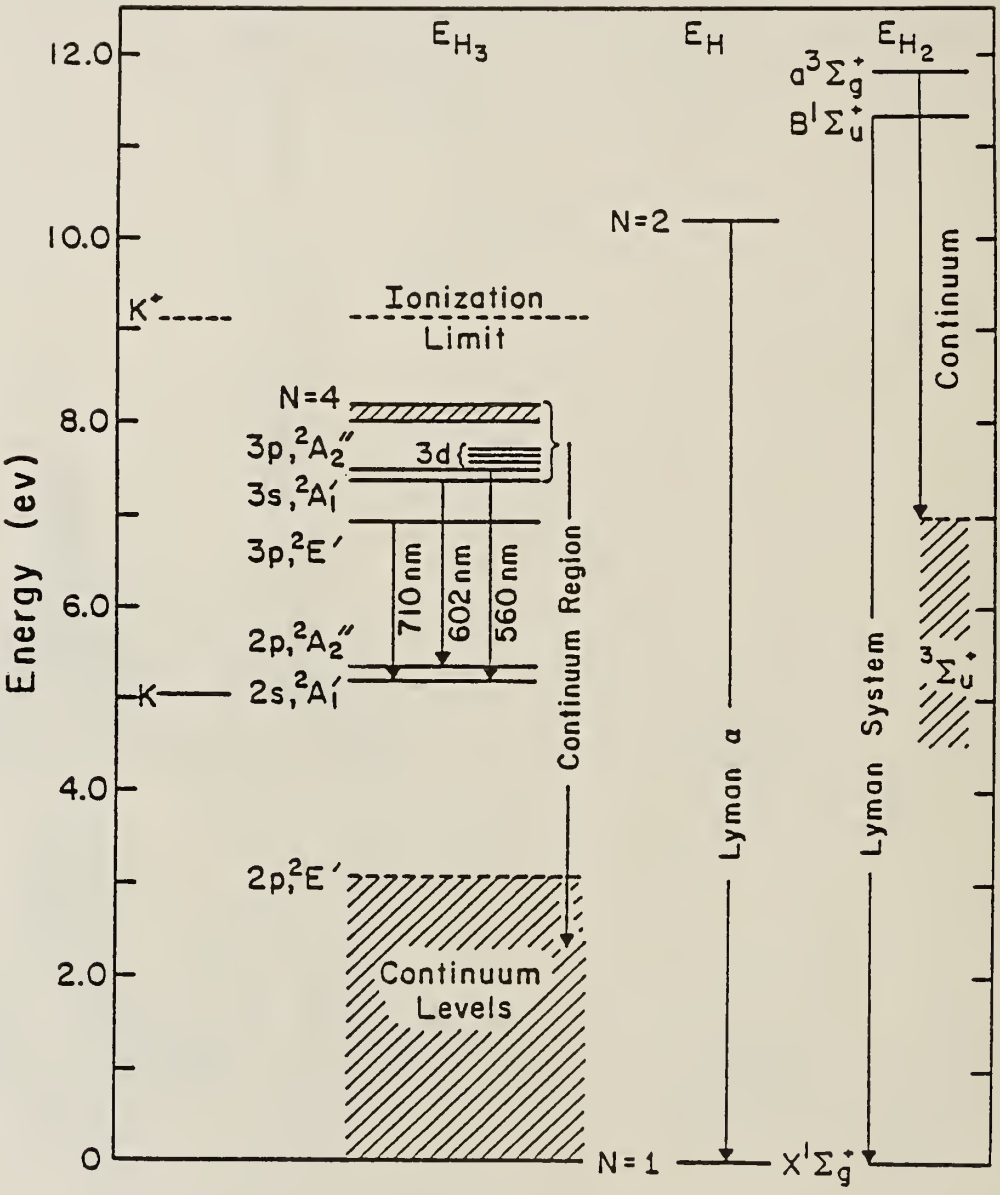

Figure 2

Energy level diagram showing many of the known states of H_3 and the region of the UV continuum.

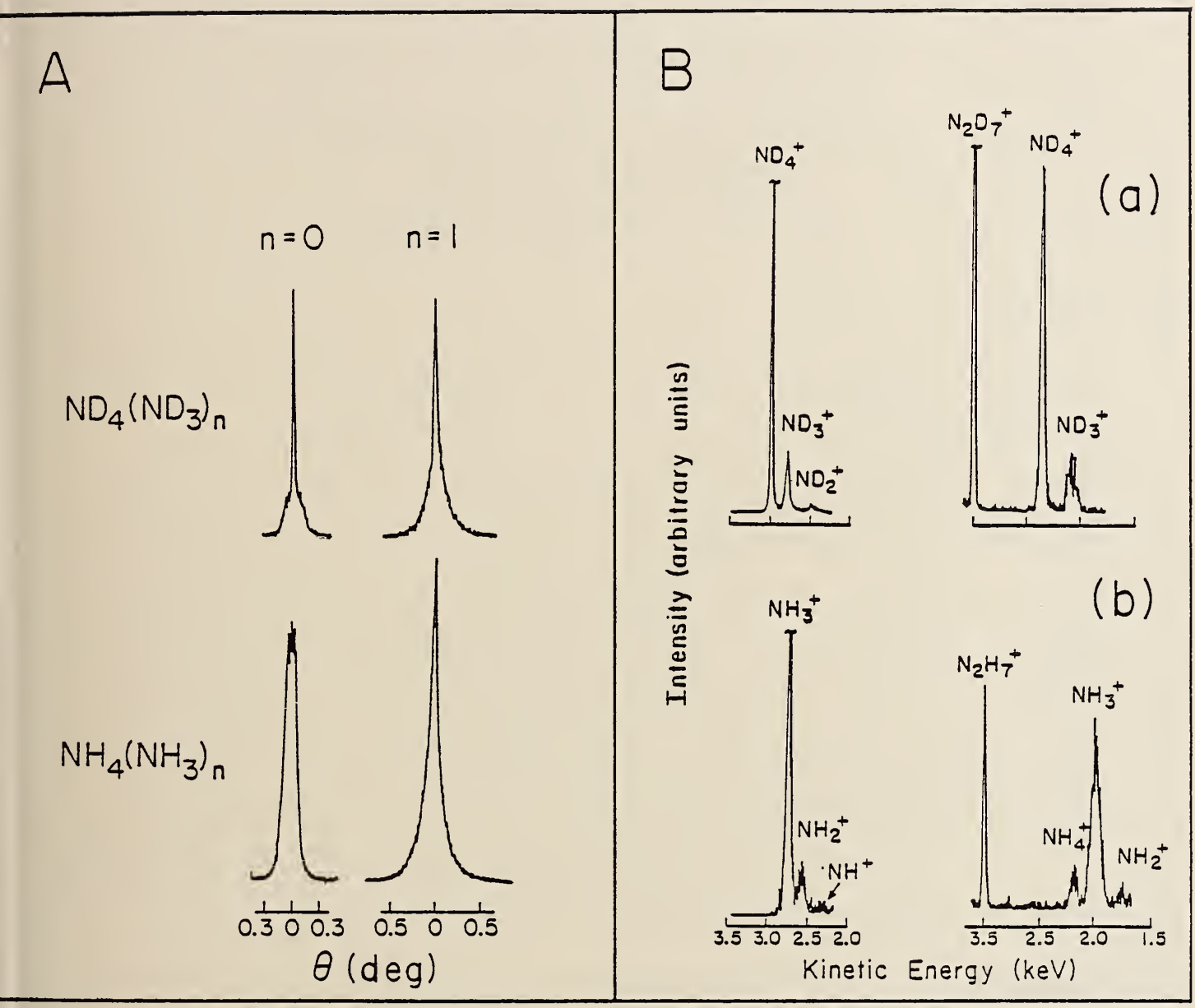

Figure 3

A. Neutral beam profiles following charge transfer from K to NH_4^+, ND_4^+, $N_2H_7^+$ and $N_2D_7^+$.
B. Charge stripped mass spectra of NH_4, ND_4, N_2H_7 and N_2D_7.

Optogalvanic Studies with a CO_2 Laser

W.E. Jones, B.A. Collings and M.Verpoorte
Department of Chemistry
Dalhousie University
Halifax, Nova Scotia, Canada
B3H 4J3

ABSTRACT:

The optogalvanic effect has been observed in several gases when emission from a low power continuous wave CO_2 laser is passed through a discharge containing the test gas. The laser was tunable across the $(00^{o}1) - (02^{o}0)$ and $(00^{o}1) - (10^{o}0)$ bands of CO_2. A very low power radio frequency oscillator was used to excite the discharge. Transitions occurring as a result of the optogalvanic effect have been assigned in the molecules CO_2, NH_3, N_2O, $CHClF_2$, CCl_2F_2, $CClF_3$, $CBrF_3$ and $C_2Cl_2F_4$. Details of these are presented. Some interesting pressure effects have been observed in CO_2 and NH_3 and may be explained on the basis of the dynamics of the energy levels involved.

INTRODUCTION:

The optogalvanic effect (OGE) in gas discharges - the change in plasma impedance by absorption of radiation - results when a change in the populations of the various energy states occurring as a consequence of resonant absorption of radiation causes a shift in the ionization processes in the discharge.

The performance, mechanism and application of OGE, as induced by absorption of resonant laser radiation (LOGE) has been extensively studied using visible and near IR lasers, especially for atomic systems [1-3]. Experiments in the far infra-red

region have made use of the CO_2 laser and LOGE at 10.6 μm; to measure laser output power [4-6], to automatically align the resonator [5], to stabilize the laser frequency [7-11] and to measure vibrational relaxation [12,13]. The LOGE has been used to study electronic transitions in atomic and molecular systems using DC[1] and RF[14-18] discharges and visible and ultra-violet lasers. The first observation of the effect in molecular systems in the infra-red was demonstrated by Webster and Menzies [19] when they observed strong LOGE signals for NH_3 at 10 μm and NO_2 at 6 μm using a DC discharge and tunable diode laser. More recently, G.W. Hills and co-workers [20,21] have used a low pressure RF discharge and an isotopic CO_2 laser to study the LOGE in the gases D_2O, H_2CO, NH_3, SO_2, H_2S and H_2O_2.

Studies in an RF cell with off-axis laser excitation provided support for a V->T acoustic wave mechanism to explain the effect in the infra-red region.

This communication describes the results obtained using a low power RF oscillator as the discharge source and a line-tunable CW CO_2 laser operating on the gases CO_2, NH_3, N_2O, $CHClF_2$, CCl_2F_2, $CClF_3$, $CBrF_3$ and $C_2Cl_2F_4$. The RF discharge has been found to be particularly suitable for these studies because of its uniformity along the axis of the discharge tube and low background noise level. The effect of gas pressure on the LOGE of CO_2 and NH_3 is discussed. Several off axis experiments further confirm the observations of Hills and Co-workers which point to the existence of a V->T wave mechanism. However, it has been necessary to introduce other processes into the mechanism to

fully account for the changes in magnitude and polarity of the LOGE signals observed in CO_2 and NH_3.

EXPERIMENTAL:

The experimental apparatus is shown schematically in Fig. 1. The CO_2 laser consisted of a pyrex discharge tube 130 cm in length and 2 cm in diameter surrounded by a water jacket for cooling. The windows of the discharge tube were made from sodium chloride set at Brewster's angle. The laser cavity was enclosed by a total reflecting gold mirror with a 10 meter radius and a diffraction grating for discrete wavelength selection, giving a cavity length of 190 cm. The diffraction grating contained 150 lines/mm blazed at 6 μm. Scanning was accomplished by a motorized micrometer drive which was scanned at a rate of .24 μm/minute over the 9.4 μm and 10.6 μm bands of CO_2 . The CO_2 laser provided a maximum output power of 2 watts from a flowing mixture of CO_2: N_2: He in the ratio 5:12:2 at 10 Torr, when operating at 7000 V and 25 ma.

Laser radiation extracted from the cavity was modulated by a mechanical chopper at a frequency of approximately 500 Hz. The laser beam, 6 millimeters in diameter, passed through the optogalvanic cell, (20 cm in length, 1 cm diameter), and into a Scientech 361 Laser Power Meter which detected radiation not absorbed by the gas in the optogalvanic cell. Several experiments were also performed in a T shaped cell such that the discharge was off axis of the laser beam.

The polyatomic gases were continuously pumped through the optogalvanic cell at pressures which ranged from 250 to 2000

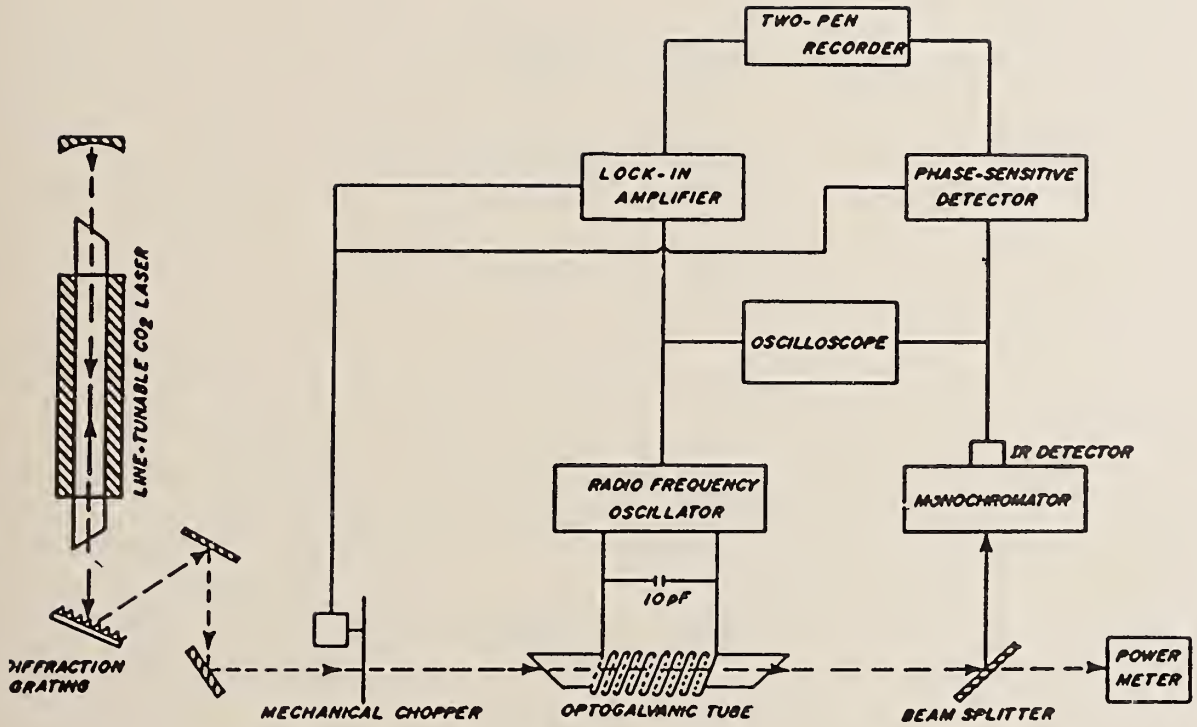

Figure 1: Schematic of apparatus used for LOGE.

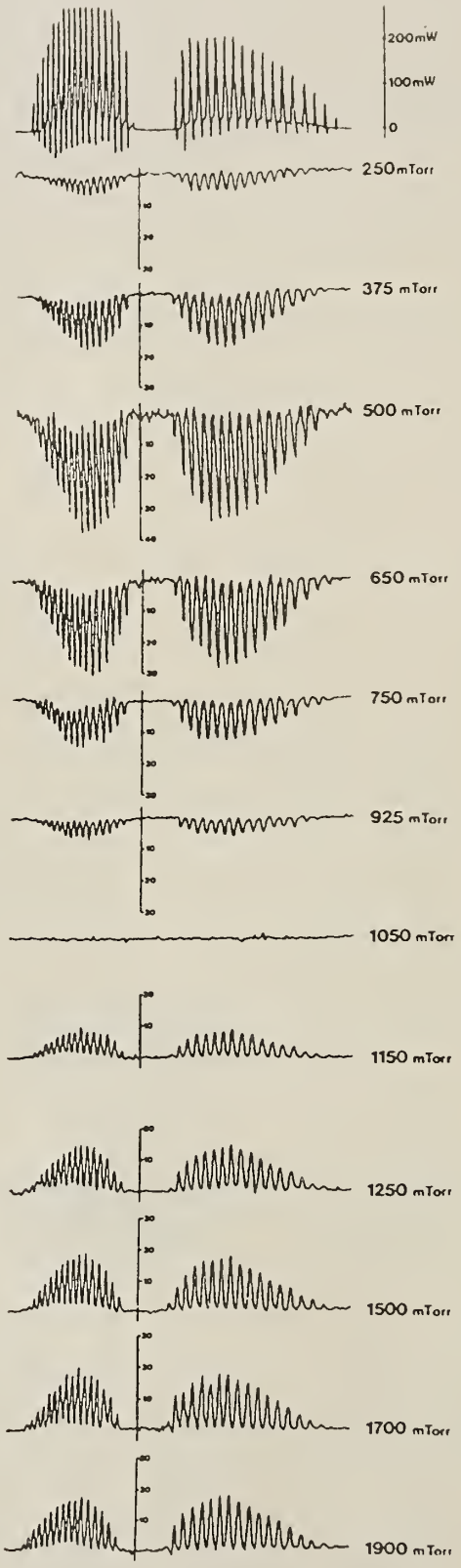

Figure 2: Post absorption and LOGE signal for CO_2 at various pressures.

mTorr. The dishcarge was excited by a Colpitts regenerative oscillator similar to that of Lyon's [22]. The oscillatory circuit consisted of a 10 pF capacitor and a 3.4 μH inductor consisting of 13 turns and a diameter of 1 cm. and produced a frequency of 50 MHz. To maintain the dishcarge, voltages from 200-325V and currents from 18 ma - 33 ma were required depending on the gas being studied.

The optogalvanic signal was observed as the change in voltage across the 7.8 kΩ load resistor. The signal was processed by a PAR model 128 lock-in amplifier with a time constant of 0.3 seconds. The output was then recorded simultaneously with the output from the laser power meter.

RESULTS:

Carbon Dioxide

In CO_2, LOGE signals were observed for all branches available in the $00^{\circ}1 - 02^{\circ}0$ and $00^{\circ}1 - 10^{\circ}0$ bands of the CO_2 laser. The total pressure of CO_2 in the OGE cell ranged from 250 to 1900 mTorr and the maximum laser power was 300 mwatts over the $00^{\circ}1 - 10^{\circ}0$ band (Fig. 2). Input power used to maintain the RF discharge was set at 1.6 watts. The LOGE signal ranged from +20 to -38 μvolts (R branch maximum) (Fig. 3). In Fig. 2 the negative peaks represent a decrease in the impedance of the discharge. The positive peaks from 1150 to 1900 mTorr represent an increase in the discharge impedance. For CO_2 the maximum intensity of the LOGE signal is at approximately 500 mTorr. At 1050 mTorr the discharge impedance appears not to be affected by the absorption of laser radiation. As pressure increases above

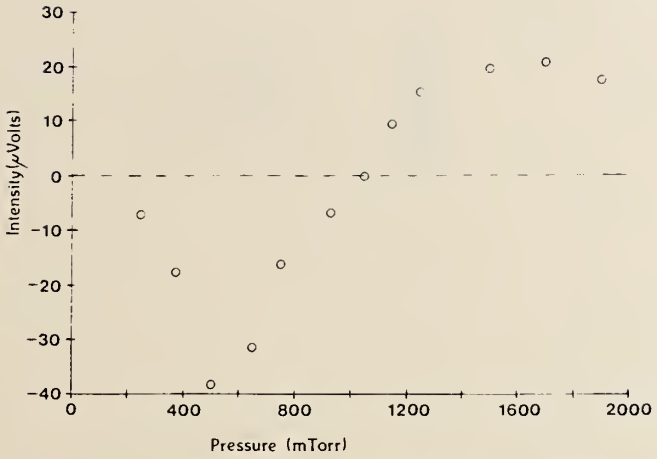

Figure 3: Variation of intensity of LOGE signal for CO_2 as a function of pressure.

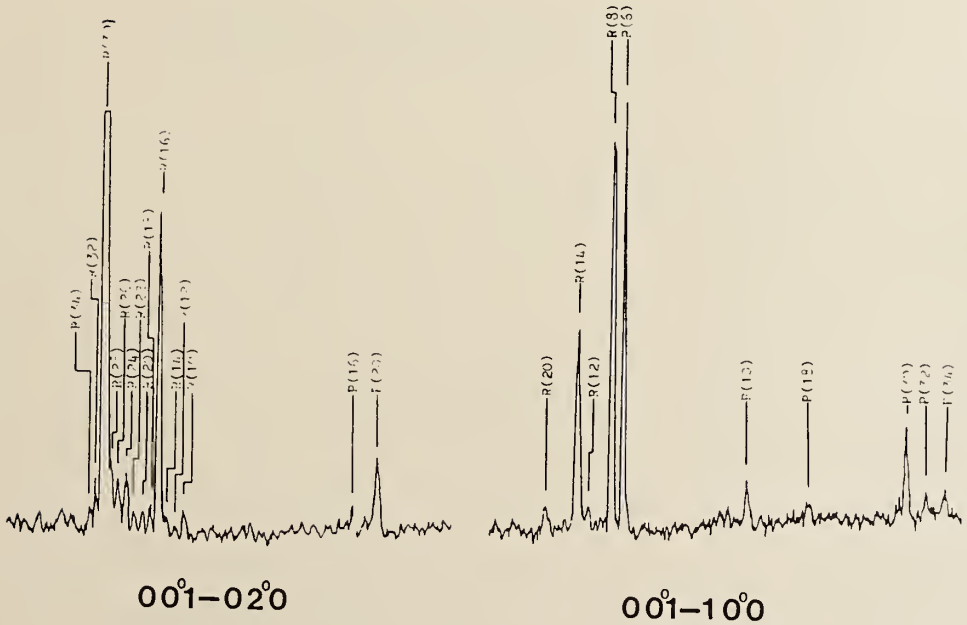

Figure 4: LOGE signal from NH_3 for the 00°1 - 02°0 and 00°1 - 10°0 bands of the CO_2 laser.

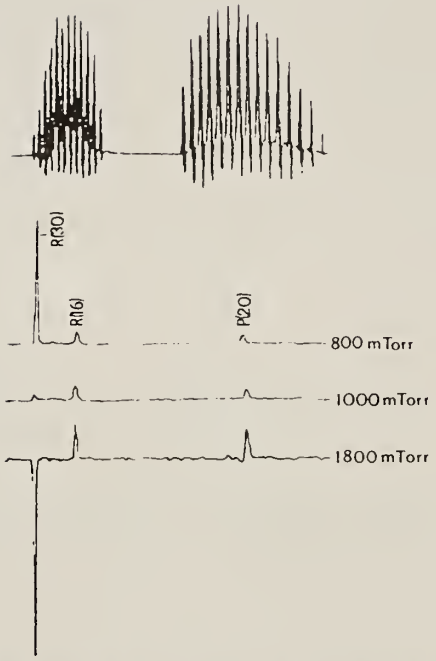

Figure 5: Post absorption and LOGE signals in NH_3 at 800,1000 and 1800 mTorr., for the R30, R16 AND P(20) laser lines of the $00^0 1 - 02^0 0$ CO_2 Band.

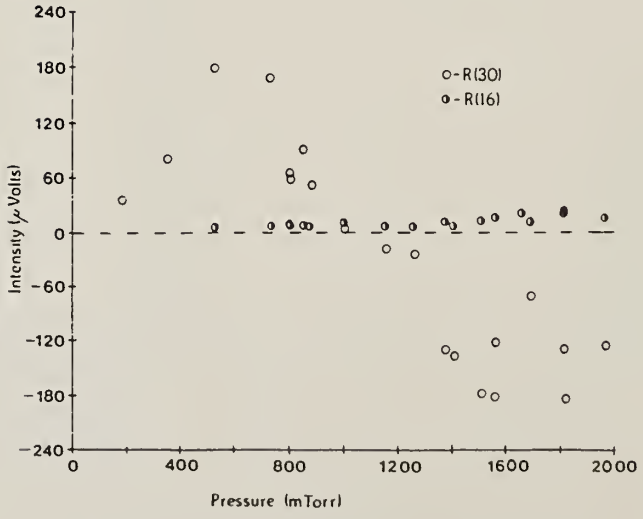

Figure 6: Variation in intensity of R(30) and R(16) over the pressure range 200 to 2000 mTorr NH_3.

1050 mTorr the LOGE signal indicates an increase in discharge impedance, and then levels off at approximately 15-20 μVolts above 1250 mTorr. There is some indication that the discharge impedance might be decreasing again but the high pressure quenched the discharge making further measurements impossible. Although the figures present the observation for the $00^{o}1 - 10^{o}0$ band, similar results were obtained on the $00^{o}1 - 02^{o}0$ band.

In off-axis studies with CO_2, we obtained LOGE signals as much as 1 meter from the axis of the laser beam. At each position measured, the signal appeared to increase regularly with pressure and did not show changes (other than constant increase) in magnitude or polarity as in the on-axis experiments.

Ammonia

LOGE signals were observed on 15 lines of the $00^{o}1 - 02^{o}0$ band and 10 lines of the $00^{o}1 - 10^{o}0$ band of the CO_2 laser. (Fig. 4) The lines and the corresponding NH_3 transitions [23] are identified in Table 1. LOGE signals for the $00^{o}1 - 02^{o}0$ band were recorded at 1000 mTorr and for the $00^{o}1 - 10^{o}0$ band at 1100 mTorr. The discharge was maintained with an input power of 0.9 watts. The intensities of the LOGE signals in NH_3 as excited by the R(30), R(16) and P(20) lines of the $00^{o}1 - 02^{o}0$ band of CO_2 were measured at many pressures between 200 - 2000 mTorr. Fig. 5 presents the observed signals at 800, 1000 and 1800 mTorr. A plot of the intensity of the LOGE signal from absorption of R(30) and R(16) is shown in Fig. 6. For R(30) absorption the signal (and discharge impedance) initially increases (opposite to effect in CO_2) and then decreases. At the same time the signal from

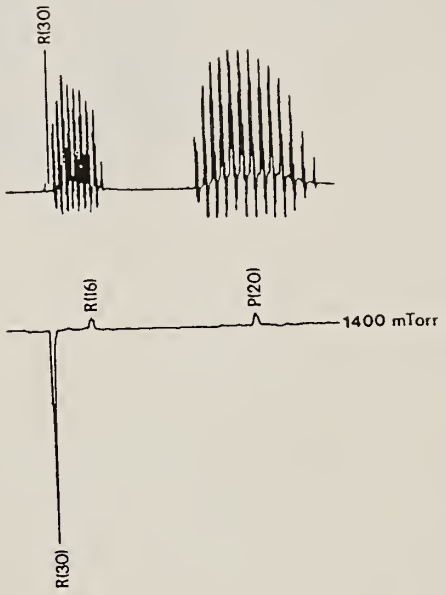

Figure 7: Post absorption and LOGE signals showing the unique situation at 1400 mTorr NH_3 where the CO_2 R(30) line has been completely absorbed.

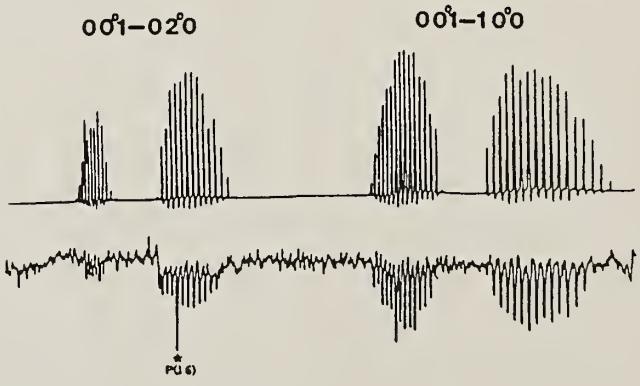

Figure 8: Post absorption and LOGE signals for N_2O at 700 mTorr. Resonance with P(16) of CO_2.

R(16) absorption appears to increase regularly with pressure.

The situation for the absorption of the R(30) line is unique in that the laser line is totally absorbed by the gas above 1250 mTorr (Fig. 7).

Although off-axis studies of NH_3 are not complete, we have observed the effect as far as 1 meter from the axis of the laser. Further, over the pressure range 200 to 1600 mTorr the signal on all lines appears to change regularly and not to undergo the change in polarity as above.

Nitrous Oxide

N_2O has many resonances with the CO_2 laser lines and a complete spectrum taken with 700 mTorr N_2O in the discharge is presented in Fig. 8. One striking feature is the strong resonance at P(16) of the $00^01 - 02^00$ band of CO_2.

Halogenated Methanes and Ethanes

Several halogenated methanes and one halogenated ethane have been found to give strong LOGE responses. These include $CHClF_2$, CCl_2F_2, $CClF_3$, $CBrF_3$ and $C_2Cl_2F_4$. In each case the signal obtained from the $00^01 - 10^00$ CO_2 laser band excitation was very similar. A typical set of observations is given in Fig. 9, for $CHClF_2$. Although there appears to be interaction at most of the CO_2 lines, the strongest signals resulted from R(20), R(12), P(22), P(34) and P(36). It is interesting to note that in this case these major coincidences did not alter uniformly with pressure. At low pressure (80 mTorr), only R(20), R(12) and P(22) gave LOGE signals. As pressure increased the LOGE signals from other lines increased more rapidly than the original three

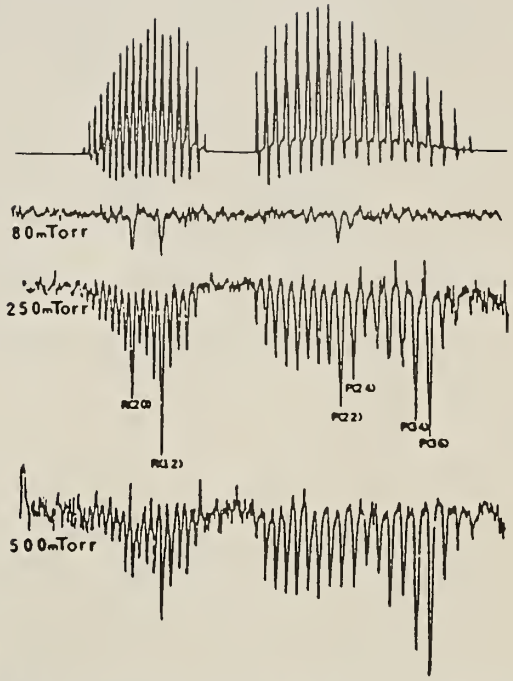

Figure 9: Post absorption and typical LOGE signals for the halocarbon. The example shown here is $CHClF_2$.

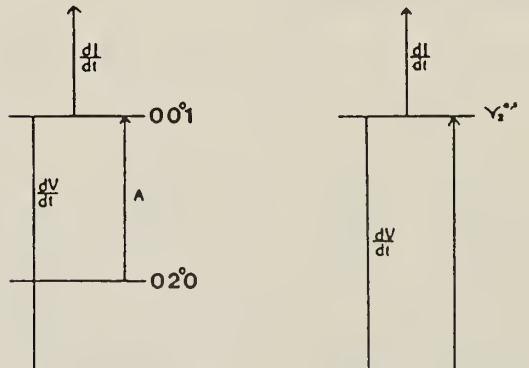

Figure 10: Active processes in the discharges of the polyatomic gases CO_2 and NH_3. dI/dt represents the rate of ionization from excited levels. dV/dt represents the rate of collisional vibrational relaxation.

lines. At 500 mTorr, the LOGE signal from P(34) and P(36) were more pronounced while that from P(22) had decreased to a level equal to intensity of the other lines nearby.

DISCUSSION:

The magnitude and polarity of the LOGE signal from polyatomic RF discharges has been observed to change upon interaction with the CO_2 laser lines as pressure is varied over the range 200 to 2000 mTorr in CO_2, and NH_3, when the discharge is on-axis of the laser beam. Similar effects have not been observed when the optogalvanic discharge is off-axis of the laser beam.

From off-axis studies Hills and coworkers [20,21] and from our own off-axis measurements, where the OGE was observed as far as 1m from the axis of the laser beam, there is little doubt that conversion of the absorbed rovibrational energy into translational motion of the gas molecules produces a pressure wave analogous to the transfer mechanism in the opto-acoustic effect (V->T wave mechanism). A similar effect has been observed in an iodine discharge using visible lasers [24,25]. This pressure wave will affect the impedance of the discharge by altering diffusion and recombination rates [24] and thus cause the off-axis LOGE.

Since changes in pressure affect the LOGE signal magnitude and polarity in on-axis but not in off-axis configuration, it is reasonable to suggest that some different or additional mechanism to the V->T wave mechanism is active in the on-axis configuration. To suggest a possible mechanism we assume, as did

Kerecman et. al., [26] in their study of photon-induced current changes in a CO_2 laser amplifier, that molecules in the excited state (e.g. 00^01 for CO_2) are more easily ionized than molecules in lower levels. Kindl, Leeb and Schiffern [27] also found this assumption valid in their explanation of the dependence of CO_2 laser discharge current on laser action.

The pressure effects in the on-axis configuration in CO_2 can thus be explained by considering the two processes: (a) the rate of ionization from a particular energy level (dI/dt), and (b) the rate of collisional vibrational relaxation of the excited levels (dV/dt). These two processes are illustrated for CO_2 and NH_3 in Fig. 10. If the variables of laser power and discharge power are held constant, the rates of ionization and relaxation will be affected by variables which depend only on the pressure of the gas. With an increase in pressure of the polyatomic gas under study the number of molecules absorbing radiation and thus the population of excited levels will increase until the laser line is completely absorbed (saturation) assuming no excited state loss mechanism. Thus the rate of ionization (dI/dt) will be dependent on pressure. The rate of collisional vibrational relaxation (dV/dt) will increase as pressure increases. As pressure increases the rate of collisional vibrational relaxation becomes the dominant process due to the larger number of collisions, while the rate of ionization will not increase as rapidly due to quenching of the excited levels.

In addition to quenching of the excited levels an increase in pressure should enhance the V->T wave and will thus have an

additional effect on the discharge. In fact off-axis studies show a strong increase in the LOGE signal with increased pressure of the polyatomic gas. Hills et. al., [21] found that the impedance of the discharge increased when they irradiated D_2O with the 9P(24) line of the $^{12}C^{18}O_2$ laser line. They suggested as a likely explanation, that the increased kinetic energy of the molecules caused by the V->T process is transferred by collisions to the electron gas and the electrons increase their rate of loss by faster diffusion to the walls.

In carbon dioxide, as pressure increases, the impedance first decreases (see Fig. 2 and 3) presumably the result of an increased population of excited levels. At about 500 mTorr the process of collisional vibrational relaxation becomes the dominant process and the impedance begins to increase and return to normal for that pressure. At 1050 mTorr the impedance begins to increase over the normal impedance. This increase in impedance may be explained by suggesting that the V->T process is now becoming the most important process and increasing impedance in the manner described above by Hill et. al. [21].

The situation in NH_3 is quite different from that for CO_2 . As shown in Fig. 6 variation of impedance depends on the particular transition being studied. Further, the impedance initially increases from its normal value and in the case of the R(30) excited signal, returns to normal and then decreases. A further observation is the complete absorption of the R(30) laser line above 1400 mTorr (Fig. 7).

Although possibly unsatisfactory, the same processes can be used to explain the NH_3 results. The major difference between

CO_2 and NH_3 is that in NH_3 absorption of the laser radiation occurs within the ground vibronic state [28-30] where as has been found in strongly hydrogen bonding systems such as H_2O and HF, the V->T,R rate is quite fast [30]. Thus the V->T process may cause the initial increase in impedance as the pressure of NH_3 increases. In the case of the R(16) resonance, where absorption is weak, this process continues to cause a small increase in the impedance throughout the pressure range studied. For the R(30) resonance, however, where absorption is much stronger, ultimately absorbing all of the intensity of the R(30) CO_2 line, the population of the excited state by absorption becomes more important as pressure increases, whereby the rate of ionization overcomes the vibrational relaxation and V->T wave processes at about 500 mTorr. This effect continues to increase until saturation at about 1400 mTorr.

Detailed pressure studies for other gases have not been made, however, there is an indication in the LOGE signals from $CHClF_2$ that here also there is a difference in how various coincidences depend on pressure. Before a truly clear picture of these effects and the processes which cause them can be obtained, it will be necessary to do further pressure studies on these and other gases. There is little doubt, however, that the effect of pressure on the laser optogalvanic signals depends on the character of the absorbing transition.

ACKNOWLEDGEMENTS:

We thank the National Sciences and Engineering Research Council of Canada for financial assistance in the form of an operating grant to W.E.J. We are also extremely grateful to B. Millier for his patience, perseverance and helpful advice with regard to the RF oscillator and other electronics.

REFERENCES

1. Goldsmith, J.M. and Lawler, J.E., Contemp. Phys., 22, 235 (1981), and references therein.

2. Ferguson, A.I., Phil. Trans. R. Soc. Lond. (A), 307, 645 (1982).

3. Travis, J., Turk, G. and Green, R., Anal. Chem., 54, 1006A (1982).

4. Jacobs, H., Kerecman, A.J. and Schmacher, J., J. Appl. Phys., 38, 3412 (1967).

5. Stefenov, V.J., J. Phys., (E) 3, 1027 (1970).

6. Scholtz, A.J. and Schiffner, G., Appl. Phys., 21, 407 (1980).

7. Skolnick, M.L., IEEE J. Quant. Electron., QE-6, 139 (1970).

8. Thomason, W.H. and Elbers, D.C., Rev. Sci. Instrum., 46, 409 (1975).

9. Smith, A.L.S. and Moffatt, S., Opt. Commun., 30, 213 (1979).

10. Moffatt, S. and Smith, A.L.S., Opt. Commun., 37, 119 (1981).

11. Kavaya, M.J., Menzies, R.T. and Oppenheim, U.P., IEEE J. Quant. Electron., QE-18 19 (1982).

12. Grower, M.C. and Carswell, A.I., Appl. Phys. Lett., 22, 321 (1973).

13. Grower, M.C. and Carswell, A.I., J. Appl. Phys., 45, 3922 (1974).

14. Stanciulescu, C., Bobulescu, R.C., Surmeian, A., Popescu, D., Popescu, I., and Collins, C.B. Appl. Phys. Lett. 37. 888, (1980).

15. Lyons, D.R., Schawlow, A.L., and Yan, G.Y., Optics Comm. 38, 35 (1981).

16. Suzuki, T., Optus. Comm. 38, 364 (1981).

17. Vasudev, R., and Zare, R.N., J. Chem. Phys. 76, 5267 (1982).

18. Suzuki, T. and Kakimoto, M., J. Mol. Spectrosc., 93, 423 (1982).

19. Welster, C.R. and Menzies, R.T., J. Chem. Phys. 78, 2121 (1983).

20. Hills, G.W., May, R.D., McCoy, W.J. and Muenchausen, R.E., Proceedings Int. Conf. Lasers, S.F. December 1983.

21. Muenchausen, R.E., May, R.D. and Hills, G.W., Optics Comm. 48, 317 (1984).

22. Lyons, D.R., Schalow, A.L. and Yan, G.Y., Optics Comm., 38, 35 (1981).

23. Garing, J.S., Nielsen, H.H. and Rao, K.N., J. Mol. Spectrosc. 3, 496 (1959).

24. Haner, D.A., Webster,C.R., Flamant, P.H. and McDermid, I.S., Chem. Phys. Lett., 96, 302 (1983).

25. Rettner, C.T., Webster, C.R. and Zare, R.N., J. Phys. Chem., 85, 1105 (1981).

26. Kerecman, A.J., Jacobs, H., LoCascio, C. and Brand, F.A., IEEE J. Quant. Elec., QE-5, 474 (1969).

27. Kindl, H., Leeb, W. and Scheffner, G., Proc. IEEE (Letters), 56, 781 (1968).

28. Herzberg, G. "Molecular Spectra and Molecular Structure II Infrared and Raman Spectra of Polyatomic Molecules, D. Van Nostrand Co., New York, (1945).

29. Starov, V., Steel, C. and Harrison, R.G., J. Chem. Phys., 71, 3304 (1979).

30. Hovis, F.E. and Moore, C.B., J. Chem. Phys., 69, 4947 (1978).

PHOTODISSOCIATION OF METAL HALIDES

Kazuo Kasatani, Masahiro Kawasaki and Hiroyasu Sato
Chemistry Department of Resources, Faculty of Engineering,
Mi'e University, Tsu 514, Japan

Abstract

Photodissociation of IIB metal halides CdI_2, HgI_2 and $HgBr_2$ was studied at 308 and 337 nm. The nascent vibrational distribution of $CdI(X^2\Sigma)$ on the photodissociation of CdI_2 at 308 nm was determined by the laser-induced fluorescence (LIF) technique. The ratio for $v'' = 0$, 1, and 2 was 1.00 : 0.85 : 0.80. The LIF technique has also been used to monitor the temporal density variation of $CdI(X^2\Sigma)$ radicals following the dissociation of CdI_2 by an N_2 laser, and it was shown that the second-order recombination reactions were important for the regeneration of CdI_2 under our experimental conditions. Highly excited states of cadmium atoms were generated in more than four-photon absorption of CdI_2 when the XeCl laser beam was tightly focused. In the case of the mercury halides, strong $B \rightarrow X$ transitions of HgI and HgBr were observed by the near UV two-photon dissociation. Several atomic transitions of Hg were also observed.

Introduction

The photodissociation of many triatomic group IIB metal halides continues to attract current attention because it provides an efficient laser transition of atomic and molecular species. Previously, lasing has been reported for the mercury halides HgCl, HgBr, and HgI. Pumping of the upper laser level ($B^2\Sigma$ state) was accomplished by ultraviolet photodissociation of HgX_2 (X=Cl, Br, or I).[1-3] Dissociative excitation of these dihalide molecules in a fast transverse discharge[4,5] and relativistic electron beam irradiation of gas mixture containing Hg and the desired halogen donor[6-8] were also attempted. The first two pumping methods (photo or electrical dissociation of HgX_2) have an advantage over the third in that they involve a cyclical production scheme for the excited species. That is, the HgX_2 molecules are regenerated efficiently after lasing. These and other attractive features of the Hg halides (such as the Franck-Condon shift between the B and X states) are also embodied by the zinc- and cadmium-halide diatomic radicals.

Cadmium is the second element of the same group in the periodic table. Photodissociation of CdI_2 by an excimer (KrF or ArF) laser has led to Cd atomic laser lines along with molecular laser transitions in cadmium monoiodide.[9,10]

In the present paper, the study of the photodissociation of metal halides, mainly CdI_2, with a 308 nm XeCl laser or 337 nm N_2 laser is reported. A spectroscopic study on CdI C-X, D-X transitions, a kinetic study on CdI_2 regeneration, and observation of atomic lines of the metal by multiphoton dissociation of metal halides are presented.

Experimental

The optical cells used in these experiments were made of quartz and were 40 mm in length, 25 mm in diameter, and had a sidearm which served as a sample reservoir. After several milligrams of CdI_2 (Wako), HgI_2 (Nakarai), or $HgBr_2$ (Nakarai) were introduced into each cell, it was evacuated to $\sim$ 1 mTorr and sealed under vacuum. The cell was placed in an oven, and chromel-alumel thermocouples were used to monitor the temperature of the oven and the separately heated sidearm. The vapor pressure of metal halides in the cell was estimated from the temperature of the sidearm, which was lower than that of the oven.

The experimental setup for the measurement of the laser-induced fluorescence (LIF) spectra is given in Figure 1. A pulsed XeCl laser (Lambda Physik EMG 103MSC, $\sim$ 100 mJ/pulse) was used as a photolysis light source and as a pump laser of a dye laser (Lambda Physik LF2002) at the same time. After a delay of ten nanoseconds, $CdI(X^2\Sigma)$

radical produced was excited by the dye laser. LIF was detected by a photomultiplier (Hamamatsu Photonics 1P28) through a 25 cm monochromator (Nikon P-250 or G-250). The signal was fed to a Boxcar integrator (PAR 162/164) through a preamplifier (PAR 115) and was recorded by a strip chart recorder. The spectral response of the detection system was corrected by using a standard tungsten lamp.

In the measurement of the temporal variation in the density of $CdI(X^2\Sigma)$ radicals, a home-made N_2 laser

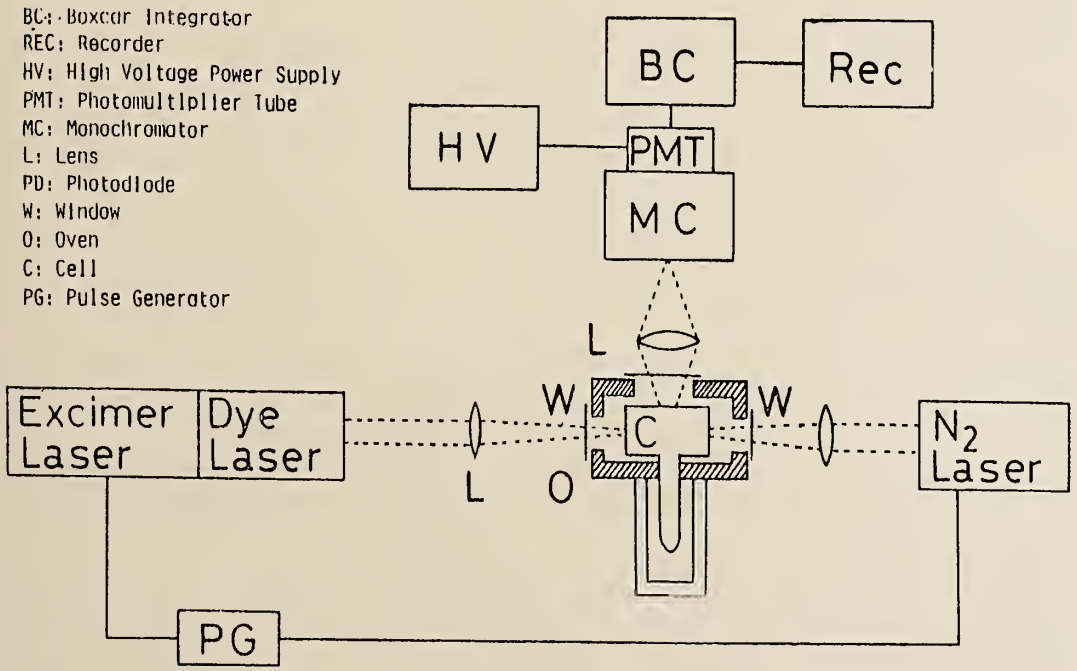

Fig. 1. Experimental setup for the measurement of the LIF spectra. About 30 % of the output of the 308 nm XeCl laser was used to dissociate CdI_2, and the rest was used to pump the dye laser.

(∿ 1mJ/pulse) was used to dissociate CdI_2. An XeCl-laser-pumped dye laser (Lumonics TE-430 + Molectron DL14, ∿ 0.1 mJ/pulse) was timed to probe the sample at selected delay times following the dissociation pulse. Intensity measurements of LIF from CdI($C^2\Pi_{1/2}$, v'=0 $X^2\Sigma$, v"=0 or 1) band gave a measure of the instantaneous density of CdI ground-state radicals.

Results

Emission spectra of CdI radical

Figures 2 (a) and (b) show the emission spectra from the v' = 0 levels of the $C^2\Pi_{1/2}$ and $D^2\Pi_{3/2}$ states, respectively. From the relative intensity we

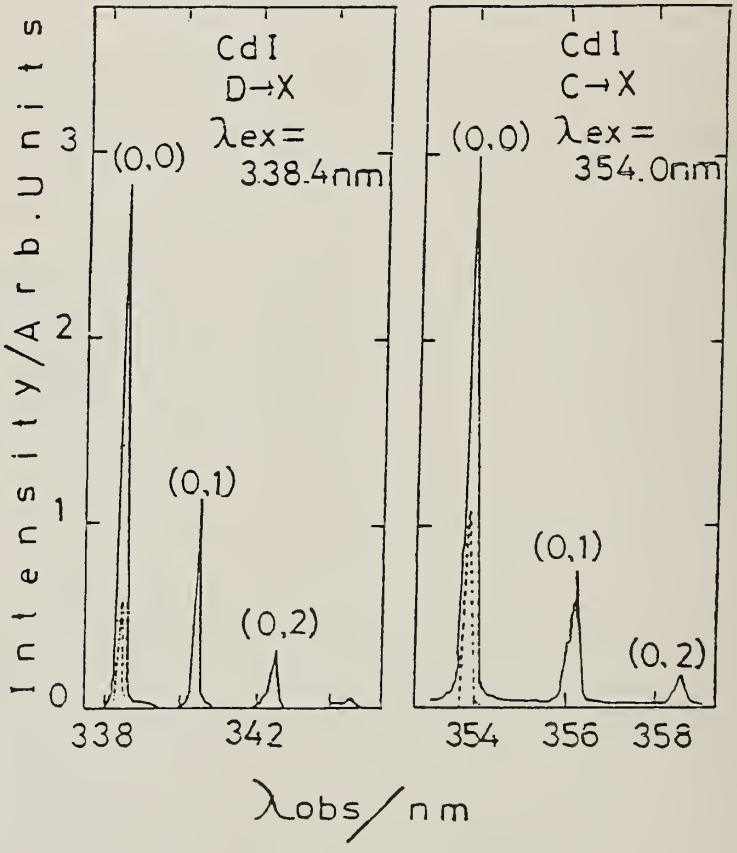

Fig. 2. LIF spectra of CdI radical.
(a) λ_{ex} = 354.03 nm ($C^2\Pi_{1/2} \leftarrow X^2\Sigma$ (0, 0) band).
(b) λ_{ex} = 338.40 nm ($D^2\Pi_{3/2} \leftarrow X^2\Sigma$ (0, 0) band).

can obtain the Franck-Condon factors as tabulated in Table 1. Since the Franck-Condon factors are sensitive to the relative location of two potential curves, we have calculated the Franck-Condon factors with the value of $\Delta r_e = r_e' - r_e''$, the deviation of the equilibrium internuclear distance of each $^2\Pi$ state from that of the ground state, as a parameter, and compared them with the experimental values. The potential curves of the ground, C, and D states were approximated by Morse functions. ω_e and $\omega_e x_e$ of these three states of CdI radical are given by Huber and Herzberg.[11)]

Since bands of both C - X, and D - X transitions have P heads, Δr_e's have negative values. We found the observed values of the Franck-Condon factors were reasonably consistent with the calculated ones for Δr_e = -0.051 Å for C-X transition, and for Δr_e = -0.055 Å for C-X

Table I. Franck-Condon factors of CdI $C^2\Pi_{1/2}$-$X^2\Sigma$ and $D^2\Pi_{3/2}$-$X^2\Sigma$ transitions

	C - X		D - X	
(v', v")	expt.	calcd.(Δr_e =-0.051 A)	expt.	calcd.(Δr_e =-0.055 A)
(0, 0)	0.65 ± 0.02	0.66	0.61 ± 0.01	0.60
(0, 1)	0.26 ± 0.02	0.26	0.29 ± 0.02	0.29
(0, 2)	0.08 ± 0.01	0.07	0.08 ± 0.01	0.08

transition. These calculated values are also tabulated in Table I.

Vibrational population of the CdI($X^2\Sigma$) radicals photodissociated by an XeCl laser

Figure 3 shows the LIF excitation spectrum for the D ← X transition of CdI radical obtained by observing the fluorescence of the D → X transition with low resolution (∿ 5 nm) of the monochromator. This spectrum shows that several vibrational states are excited in the ground state of CdI radical.

Figure 4 shows the LIF excitation spectra for the D ← X transition obtained by observing the D → X (0,0) emission. From the relative intensity of each band in this spectrum and the Franck-Condon factors obtained above, the relative population of the CdI ground state produced

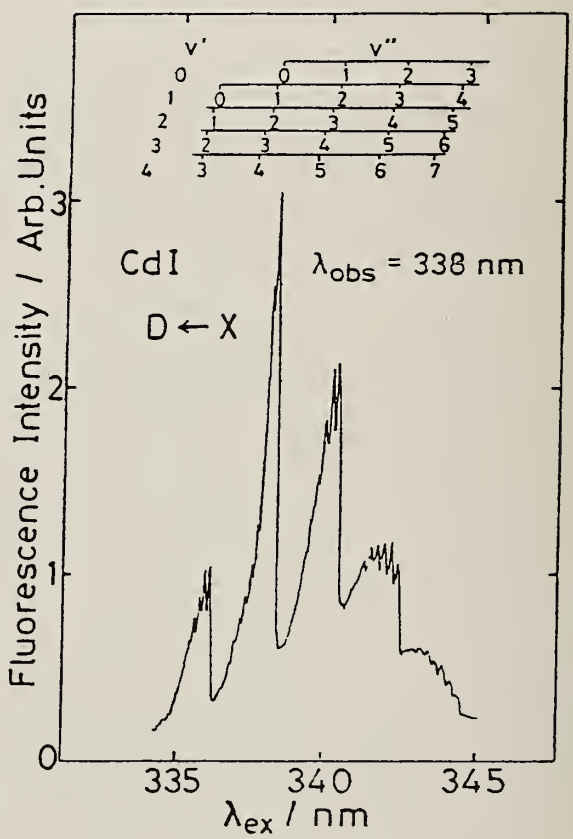

Fig. 3. LIF excitation spectra for the D ← X transition of CdI radical generated by photo-dissociation with 308 nm XeCl laser. λ_{obs} = 338.4 nm. Resolution of the monochromator is ∿ 5 nm.

by photodissociation of CdI_2 with a 308 nm XeCl laser was determined to be 1.00:0.85:0.80 for v" = 0, 1, 2 levels, respectively.

We could separate only three transitions (0,0), (0,1), (0,2) because of spectral congestion. Isotopically pure CdI_2 molecule should be used to eliminate this problem.

Changes in the density of $CdI(X^2\Sigma)$ radicals

The temporal decay of CdI radical density was monitored as a function of time after the dissociation pulse. Figure 5(a) shows an example of the temporal

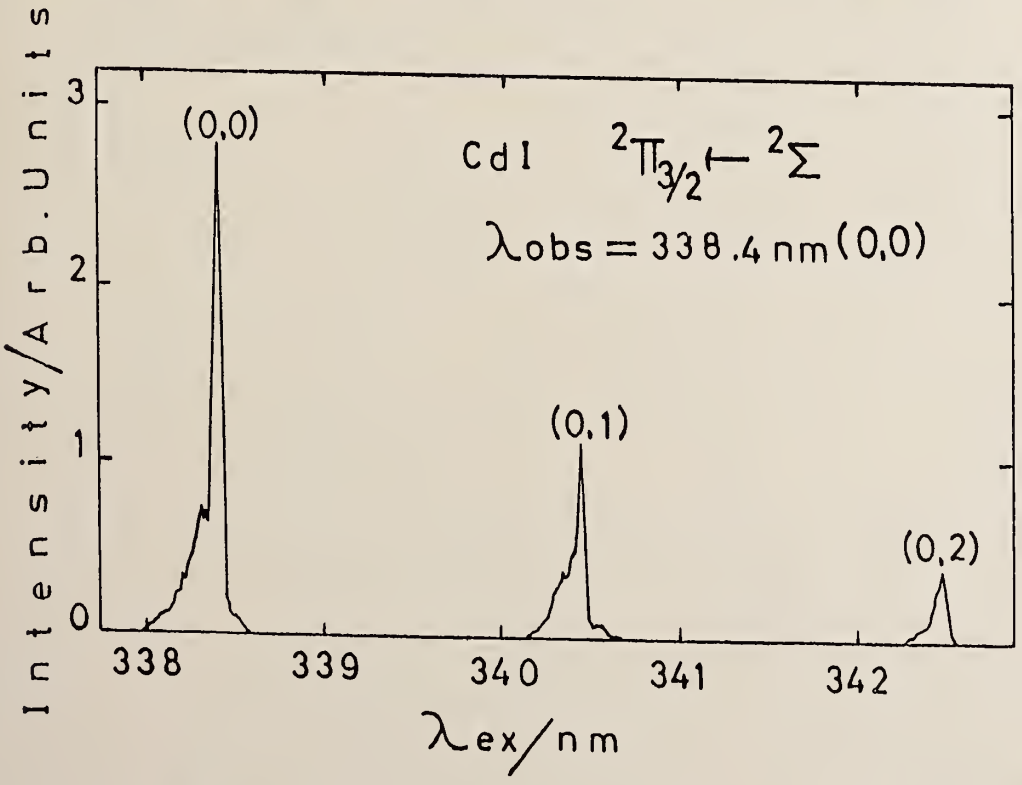

Fig. 4. LIF excitation spectra for the D ← X transition of CdI radical. λ_{obs} = 338.4 nm ($D^2\Pi_{3/2} \rightarrow X^2\Sigma$ (0, 0) band).

variation of the density of CdI($X^2\Sigma$ v"=0) radicals following dissociation of CdI_2. An N_2 laser was used as a photolysis light source and an XeCl-laser-pumped dye laser was used as an LIF probe laser.

The concentration of CdI($X^2\Sigma$, v"=0) radical decayed after the initial very fast (within ~ 1 μs) increase due to vibrational relaxation. The decay curves were not exponential. Figure 5(b) shows the reciprocal plot of the relative CdI ($X^2\Sigma$) radical concentration vs. time, and it turned out that the concentration of CdI($X^2\Sigma$) radical decayed following a

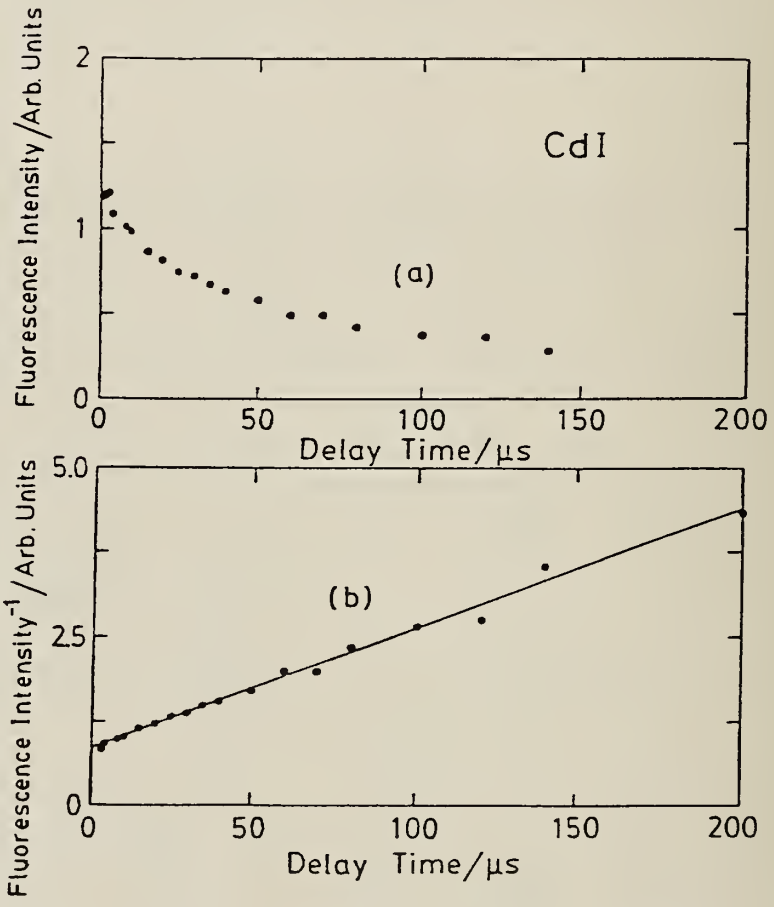

Fig. 5. (a) An example of the temporal variation of the density of CdI($X^2\Sigma$) radicals following dissociation of CdI_2 with a 337 nm N_2 laser. λ_{ex} = 354.03 nm (C ← X (0, 0) band). λ_{obs} = 356.25 nm (C → X (0, 1) band). (b) the reciprocal plot of (a).

second-oder kinetics.

Multiphoton dissociation of metal halides

When the XeCl laser beam was focused at the CdI_2 cell, many atomic transitions of cadmium were observed. Figure 6 shows the emission spectra of the cadmium atom produced by the photodissociation of CdI_2. Fluorescence due to the B → X transition of CdI radical was very weak compared with the atomic emission.

In the case of the mercury halides, the tightly focused UV (λ = 290 nm) laser light produced the strong B → X transitions of HgI and HgBr given by the two-photon dissociation, together with several atomic transitions of Hg. However, on the irradiation by a 340 nm dye laser, only B → X transition are observed. Atomic lines of mercury atom were very weak.

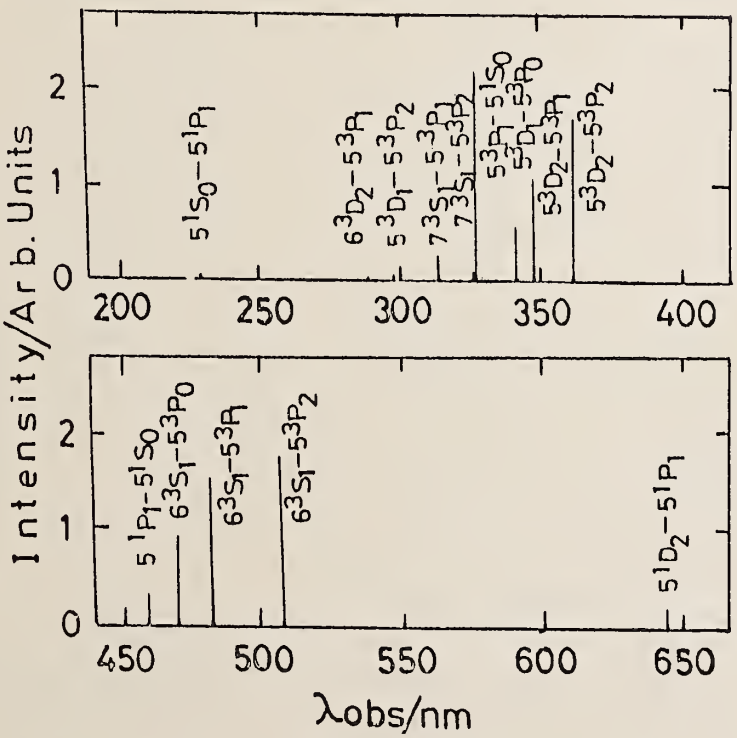

Fig. 6. Emission spectra of the cadmium atom produced by the photo-dissociation of CdI_2 with 308 nm XeCl laser.

In the case of the zinc bromide, the (λ = 290 nm) laser irradiation gave only atomic transitions of Zn.

Discussion

Potential curves of CdI radical

Since no band of CdI radical has been thoroughly analyzed, r_e's, equilibrium internuclear distances, of any states have not been known so far. Figure 7 shows the semiquantitative potential energy level diagram for CdI radical drawn after Greene and Eden.[12] In this diagram, r_e's for X and B states were assumed to be similar to those for HgI.

The B states of the group IIB metal-halide diatomic molecules are ionic in character. In the case of $^{200}Hg^{127}I$ radical, r_e's are 2.18 Å and 3.30 Å for the X and B states, respectively.[13] Therefore, r_e of the B state of the CdI

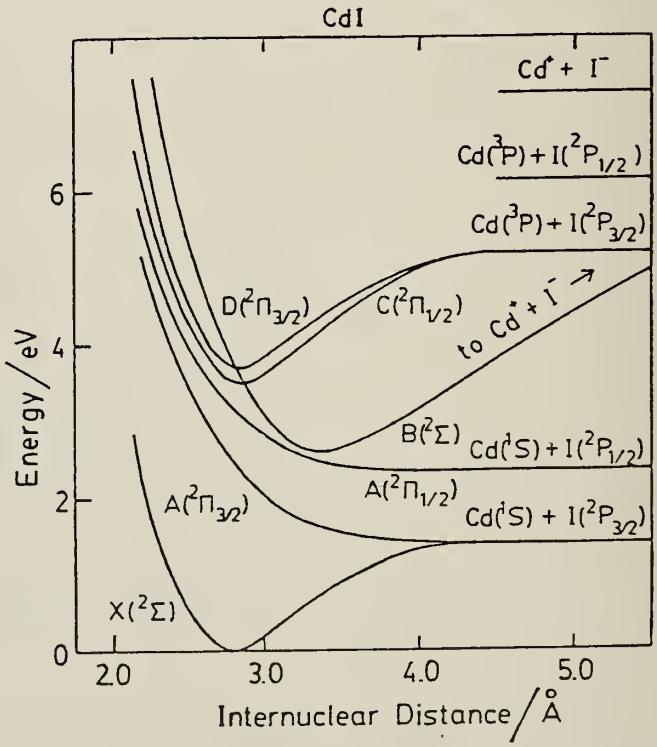

Fig. 7. A semiquantitative potential energy level diagram for CdI radical drawn after Greene and Eden.[12]

radical must be larger than that of the ground state.

Contrary to the B state, r_e's of both $^2\Pi$ excited covalent states, $C^2\Pi_{1/2}$ and $D^2\Pi_{3/2}$ states, of CdI radical are shorter than that of the ground state, because bands in both C-X and D-X transitions are degraded toward the violet.[14] Our results of the Franck-Condon factors show that r_e varies little among the X, C, and D states.

Vibrational population of $CdI(X^2\Sigma)$ radical

Our results on the vibrational distribution of $CdI(X^2\Sigma)$ showed that the population is nearly equal in the lowest three vibrational levels. Figure 3 suggests the other upper vibrational levels are also populated.

Possible dissociation processes of CdI_2 with the one-photon energy of 308 nm XeCl laser (388.4 kJ mol^{-1}) are

$$CdI_2(^1\Sigma) \xrightarrow{h\nu} CdI(X^2\Sigma)+I(^2P_{3/2}) \quad E_0=239.8 \text{ kJ mol}^{-1} \quad (1),^{15}$$

$$CdI_2(^1\Sigma) \xrightarrow{h\nu} CdI(X^2\Sigma)+I(^2P_{1/2}) \quad E_0=330.7 \text{ kJ mol}^{-1} \quad (2),$$

$$CdI_2(^1\Sigma) \xrightarrow{h\nu} Cd(^1S)+2I(^2P_{3/2}) \quad E_0=389.6 \text{ kJ mol}^{-1} \quad (3).^{15}$$

If the dissociation follows equation (1), $CdI(X^2\Sigma)$ produced is expected to be excited to high vibrational levels.

With the spectator model one can obtain

$$\frac{E_V}{E_{AVL}} = 0.28,$$

where E_V is vibrational energy, E_{AVL} is available energy,

which equals photon energy minus dissociation energy. With this model average vibrational quamtum number of $CdI(X^2\Sigma)$ is expected to be about 20 for the first equation, about 8 for the second equation.

Kawasaki et al.[16] suggested that the first absorption band of CdI_2 was a superposition of a parallel band dissociating to $I^*(^2P_{1/2})$ atoms and $CdI(X^2\Sigma)$ radicals and a perpendicular band dissociating to $I(^2P_{3/2})$ and $CdI(X^2\Sigma)$, and concluded that about half of the available energy was distributed as vibrational energy of CdI radicals in the photodissociation with 300 nm laser radiation, based on the results of a photofragment TOF experiment. More data are necessary to elucidate the photodissociation dynamics.

Regeneration mechanism of CdI_2

One of the advantages of metal-halide laser is the remarkable ability of the laser gas mixture to support thousands of laser pulses with essentially complete regeneration of metal halides on a very short time scale between laser pulses. This feature is important for applications of metal-halide laser since it permits efficient pulsed operation at high repetition rates and relatively long lifetimes for the laser gas fill.

Erlandson and Cool[17] reported that the fast bimolecular reaction

$$HgBr + Br_2 \longrightarrow HgBr_2 + Br$$

is responsible for the observed rapid and efficient regeneration of $HgBr_2$ in cyclic operation of the repetitively pulsed HgBr laser. The decay of HgBr radicals they observed was nearly exponential and its rate was independent of diluent species and diluent pressure for He, Ar, and N_2 diluents at pressures ranging from 20-700 Torr. They concluded that the three-body recombination process

$$HgBr + Br + M \longrightarrow HgBr_2 + M$$

and

$$HgBr + HgBr + M \longrightarrow (HgBr)_2 + M$$
$$\longrightarrow HgBr_2 + Hg + M$$

were not important.

On the contrary, the decay of $CdI(X^2\Sigma)$ radicals we observed followed the second-order decay kinetics. This indicates that the bimolecular reaction

$$CdI + I_2 \longrightarrow CdI_2 + I \quad \Delta H = -25.5 \text{ kJ mol}^{-1}$$ 18)

is not important for the regeneration of CdI_2. The similar reaction

$$HgBr + Br_2 \longrightarrow HgBr_2 + Br \quad \Delta H = -113 \text{ kJ mol}^{-1}$$ 17)

is about 4 times more exothermic than that for CdI_2.

Possible process for the regeneration of CdI_2 is the three-body recombination process,

$$CdI + I + M \longrightarrow CdI_2 + M$$

or

$$CdI + CdI + M \longrightarrow (CdI)_2 + M$$
$$\longrightarrow CdI_2 + Cd + M$$

or radical-radical disproportionation reaction

$$CdI + CdI \longrightarrow CdI_2 + Cd.$$

In the case of the $HgBr_2$, the radical-radical disproportionation reaction

$$HgBr + HgBr \longrightarrow HgBr_2 + Hg$$

is reported to be very slow (reaction rate constant is less than 5×10^{-16} $cm^3 molecule^{-1} s^{-1}$).[19] The corresponding rate constant for CdI has not been known.

The relative second-order rate constant obtained was independent of the CdI_2 pressure within the experimental error at pressures ranging from 0.3 - 1.1 Torr (653 - 693 K). Though this result supports the radical-radical disproportionation reaction, the possibility that the steady-state concentration of I_2 generated by thermal decomposition of CdI_2 is larger than the that of CdI_2, and that I_2 acts as a third body M, could not be denied.

Multiphoton dissociation of metal halides

When XeCl laser beam was focused at the CdI_2 cell, atomic emission from highly excited Cd atom was observed. Figure 8 shows the energy level diagram for CdI_2, CdI, and Cd. 5^3P states can be generated by two-photon absorption. Other atomic lines correspond three- or four-photon absorption.

Though the production of the B, C, and D states of CdI radical is energetically possible by the two-photon absorption of 308 nm laser photon, only very weak $B \rightarrow X$

transition was observed. CdI ($B^2\Sigma$) generated by a photo-dissociation with 193 nm ArF laser can lase. CdI_2 may dissociate to $Cd(^1S, ^3P) + 2I$ rapidly instead of CdI(B) + I by 308 nm two-photon absorption.

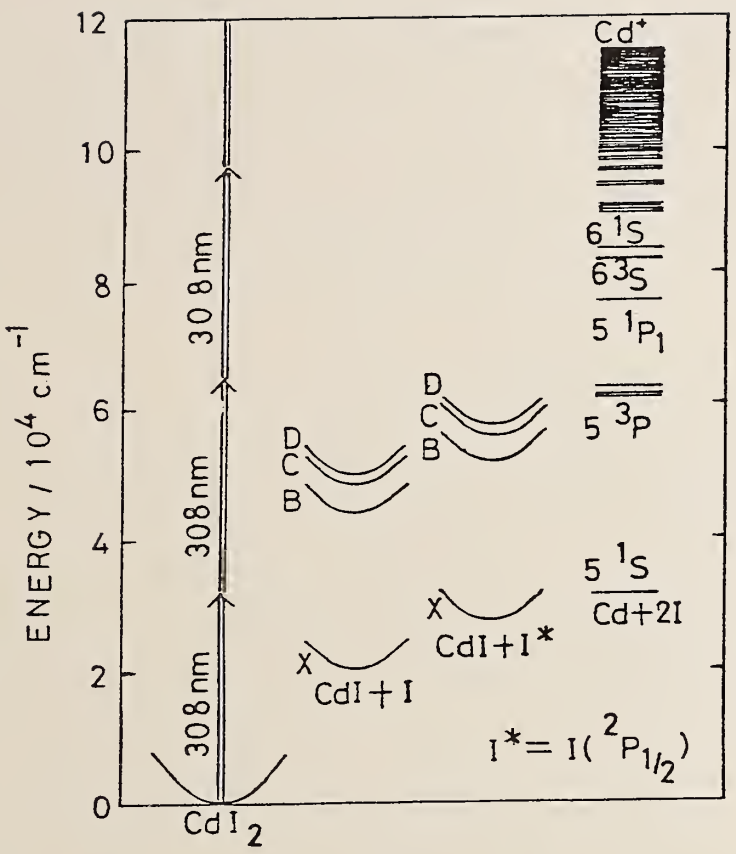

Fig. 8. Energy level diagram for CdI_2, CdI, and Cd.

In the case of mercury halides, strong B → X transitions of HgBr and HgI were observed by the near UV (290 - 340 nm) two-photon dissociation. However, in this case, $HgBr(X^2\Sigma)$ or $HgI(X^2\Sigma)$ produced by one-photon absorption of UV photon might absorb another UV photon.

Aknowledgments

The authors are grateful to K. Nakane and K. Mori for their help in the experimental work. They thank Dr.

Nagata, Tokyo University, for the help in early stage of the experiment. They are also grateful to the Center of Instruments, Institute for Molecular Science, Okazaki National Research Institute, for the use of the laser.

References

1) E.J. Schimitschek, J.E. Celto, and J.A. Trias, Appl. Phys. Lett., **31**, 608 (1977).

2) E.J. Schimitschek and J.E. Celto, 10th International Quantum Electronics Conference, Atlanta, 1978 (unpublished).

3) J.G. Eden, Appl. Phys. Lett., **33**, 495 (1978).

4) E.J. Schimitschek and J.E. Celto, Opt. Lett., **2**, 64 (1978).

5) R. Bernham, Appl. Phys. Lett., **33**, 156 (1978).

6) J.H. Parks, Appl. Phys. Lett., **31** 192 (1977); ibid. **31**, 297 (1977).

7) W.T. Whitney, Appl. Phys. Lett., **32**, 239 (1978).

8) J.G. Eden, Appl. Phys. Lett., **31**, 448 (1977).

9) E. Gerk and E. Fill, IEEE J. Quant. Electr. **QE-17**, 2140 (1981).

10) S.G. Dinev, H.-U. Daniel, and H. Walter, Opt. Commun., **41**, 117 (1982).

11) K.G. Huber and G. Herzberg, "Molecular Spectra and Molecular Structure. IV. Constants of Diatomic Molecules", (Van Nostrand Reihold, New York, 1978).

12) D.P. Greene and J.G. Eden, J. Chem. Phys., **82**, 702 (1985).

13) J. Tellinghuisen, P.C. Tellinghuisen, S.A. Davies, P. Berwanger, and K.S. Viswanathan, Appl. Phys. Lett., **41**, 789 (1982).

14) B. Rosen "Tables Internationales de Constantes Selectionnees. 17. Donnees Spectroscopiques Relatives aux Molecules Diatomiques", (Pergamon Press, Oxford, 1970).

15) K. Wieland, Helv. Phys. Acta, 2, 46 (1929).

16) M. Kawasaki, S.J. Lee, and R. Bersohn, J. Chem. Phys., 71, 1235 (1979).

17) A.C. Erlandson and T.A. Cool, Chem. Phys. Lett., 96, 685 (1983).

18) The enthalpy change for this reaction was calculated from the anthalpy of formation of I atom, $\Delta H = 107.16 \pm 0.04$ kJ mol^{-1}, M.W. Chase, J.L. Curnutt, H. Prophet, R.A. McDonald, and A.N. Syverud, JANAF Thermochemical Tables, 1975 Supplement, J. Phys. Chem. Ref. Data, 4, 1 (1975).

19) A.M. Schilowitz and J.R. Wiesenfeld, Chem. Phys. Lett., 89, 438 (1982).

SPECTROSCOPIC CHARACTERIZATION OF MOLECULAR RADICAL CATIONS: THE $\tilde{A}\,^2\Pi_{\Omega,g} \leftrightarrow \tilde{X}\,^2\Pi_{\Omega,u}$ TRANSITION OF $X\text{-}C{\equiv}C\text{-}X^+$, X = Cl, Br, I

D. Klapstein
Department of Chemistry, St. Francis Xavier University, Antigonish, N.S., Canada B2G 1C0

J.P. Maier, Institut für Physikalisch Chemie, Klingelbergstrasse 80, CH-4056 Basel, Switzerland

1. INTRODUCTION

Ions are important species in atmospheric, plasma and chemical processes, both terrestrial and extraterrestrial. Spectral characterization of such species is an important step towards understanding their structure and role in such processes. With the advent of new experimental techniques the study of such species has accelerated rapidly in recent years. Work at Basel has been centered on molecular radical cations, using spectroscopic techniques to probe the cationic ground and lowest excited electronic doublet states [1]. This has been based on valence-shell photoelectron spectroscopy which provides a direct energy mapping of the accessible doublet states.

One of the techniques employed is emission spectroscopy of the radical cations excited by electron impact:

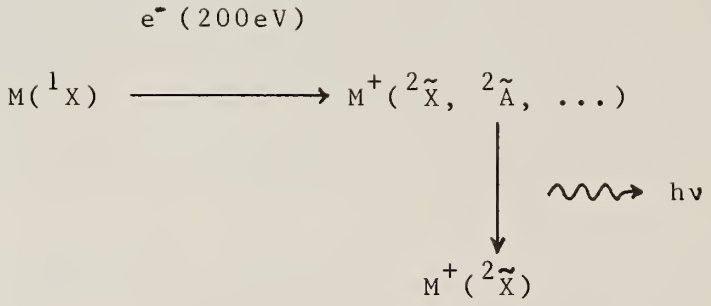

It should be noted that here the cation electronic states will be labelled with a tilde (e.g. $\tilde{X}$) to distinguish them from those of the neutral molecule. While the electron beam excitation is rather nonspecific, its intensity and energy-control make it preferable to photon sources.

A second technique used is that of laser-excited fluorescence. Cations are generated in the ground electronic state by Penning ionization with rare gas metastables and collisional deactivation, followed by laser excitation and detection of the fluorescence:

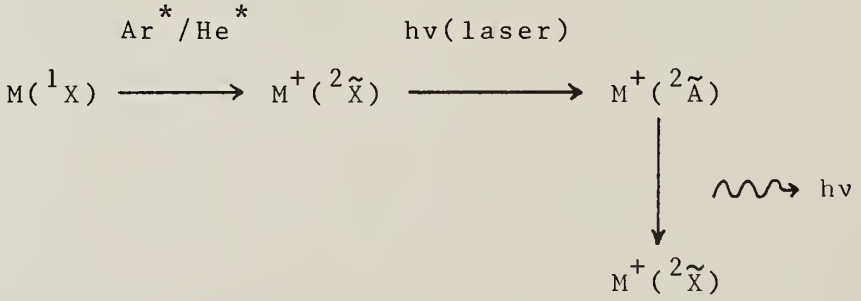

The emission and laser-excited fluorescence spectroscopies are based on the radiative decay of the lowest excited states of the cations. This has been detected for well over one hundred molecular radical cations. Table 1 lists the main types of cations which exhibit the radiative decay and have been studied by these methods [1].

Table 1

Main Types of Molecular Cations

Which Exhibit Radiative Decay

$X-C\equiv C-H^+$
$X-C\equiv C-X^+$ } X = Cl, Br, I
$X-C\equiv N^+$

$X-C\equiv P^+$, X = H, F

$X-(C\equiv C)_2-H^+$, X = Cl, Br, I, CN, CH_3, C_2H_5

$X-(C\equiv C)_2-X^+$, X = F, Cl, Br, I, CN, CF_3, C_2H_5

$CH_3-C\equiv C-X^+$, X = Cl, Br, CN

$CH_3-(C\equiv C)_2-X^+$, X = Cl, Br, CN, CH_3

$H-(C\equiv C)_n-H^+$, n = 2, 3, 4

Conjugated $Polyenes^+$

$Halobenzenes^+$

$Fluorophenols^+$

Recent experimental advances have led to an improvement in the quality of the gas-phase emission and laser-excited fluorescence spectra. This has been accomplished by the production of rotationally cooled cations using a seeded supersonic free jet in the case of emission spectroscopy; for the LEF technique considerable rotational and vibrational cooling can be achieved by surrounding the Penning ionization source with a liquid nitrogen bath. The new information forthcoming from such experiments has led to the vibrational interpretation of spectra which were previously incomprehensible using room temperature samples.

An additional technique employed is the direct absorption spectroscopy:

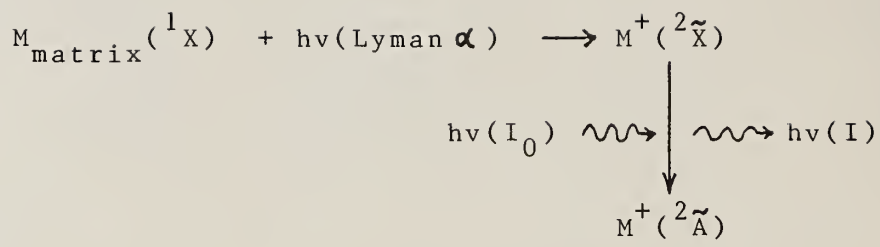

Obviously this can also be applied to species which do not exhibit fluorescence from the excited states.

Typical spectra from these three techniques and the information which can be deduced from them will be illustrated here by recent results obtained for the $\tilde{A}\ ^2\Pi_{\Omega,g} \leftrightarrow \tilde{X}\ ^2\Pi_{\Omega,u}$ transition of the dihaloacetylene cations, $X\text{-}C\equiv C\text{-}X^+$, X = Cl, Br, I.

2. EXPERIMENTAL

The emission spectra of rotationally cold molecular cations were obtained using a crossed supersonic free jet - electron beam apparatus [2]. A schematic representation of the apparatus is shown in Figure 1. The sample was held in a cryostated metal bubbler through which helium gas was passed, the resultant gas mixture having a sample concentration of 1 - 5%. The gas mixture, at a backing pressure of 1 bar, was then expanded through a 70 or 100 μm nozzle into the main vacuum chamber where the pressure was $\lesssim 10^{-3}$ mbar. Ionization-excitation was achieved by crossing the free jet expansion, 5 - 7 mm downstream from the nozzle, with a well-collimated 200 eV electron beam of 3 - 6 mA collected current. Radiated photons were collected at right angles to both the free jet and electron beam and wavelength-dispersed by an f/9.5, 1.26m monochromator. The photomultiplier signal was fed into a single-photon counting system and

acquired on-line by an LSI 11/03 computer which also controlled the monochromator stepping motor.

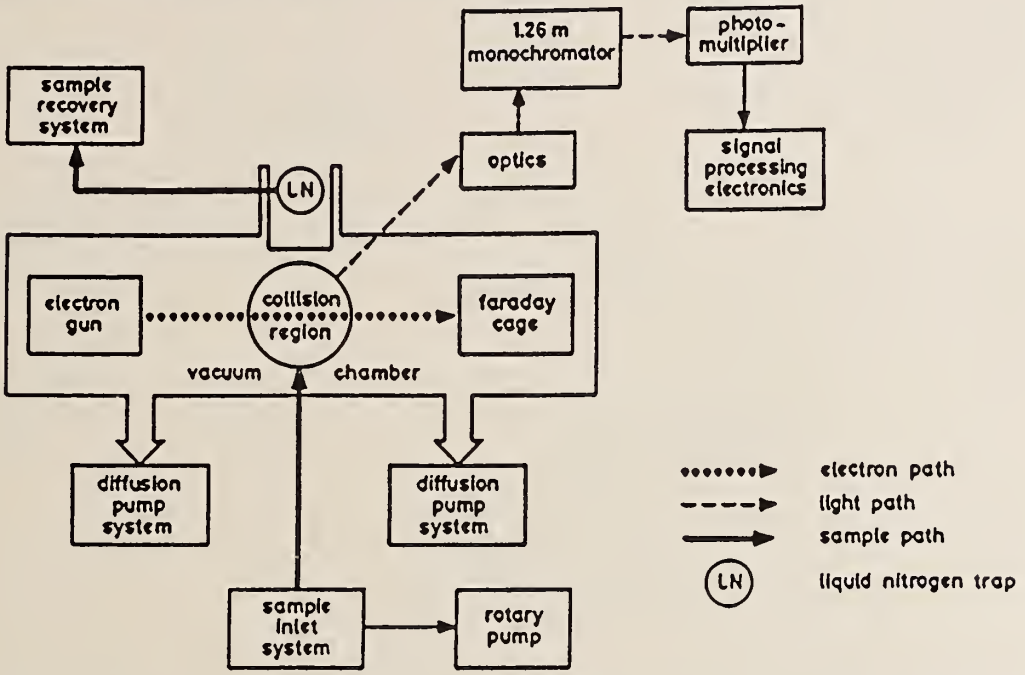

FIG.1. Schematic of the apparatus for gas-phase emission spectroscopy of cations excited by electron beam impact.

The laser-excited fluorescence apparatus has been described in detail [2]. Figure 2 shows the basic arrangement of the apparatus. Cations were produced by Penning ionization of the neutral precursors with helium or argon metastables produced in a d.c. discharge flow system. Rotational and vibrational cooling of the cations was achieved by collisions with the carrier gas, the entire discharge system being surrounded by a liquid nitrogen-cooled jacket [3]. The thermalized ground state cations were then optically pumped with a pulsed tunable dye laser and the resulting fluorescence detected by a photomultiplier tube. The signal was fed through a transient digitizer to an LSI 11/23 computer which corrected the signal for laser intensity and stored it as a function of the dye laser wavelength.

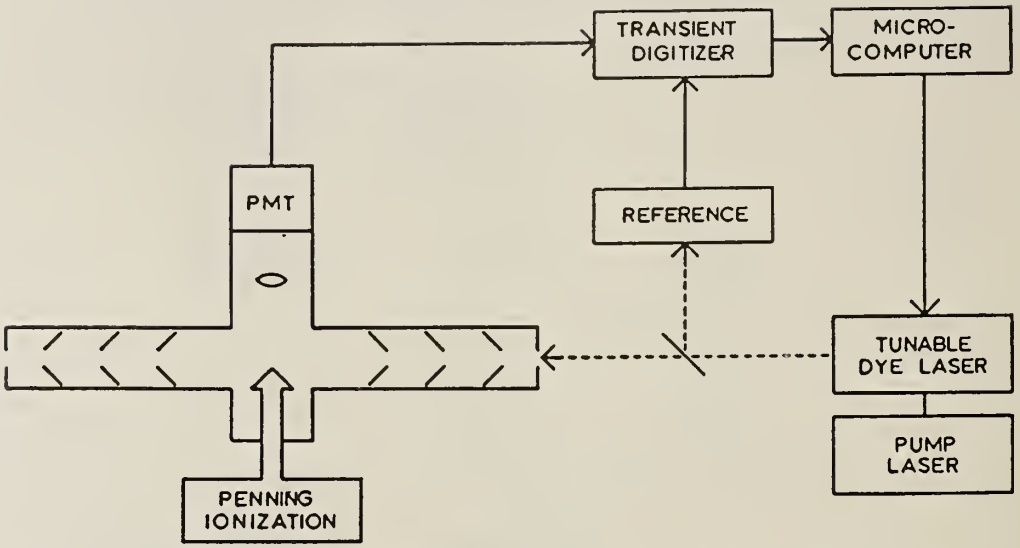

FIG.2. Schematic of the apparatus for laser-excited fluorescence spectroscopy of gas-phase cations.

The apparatus for obtaining the electronic absorption spectra of cations in inert gas matrices has been described elsewhere [4]. Figure 3 is a schematic of the experimental arrangement. Gas mixtures of sample-to-neon ratios of approximately 1:5000 were deposited onto a rhodium-coated copper block cooled to 4.5 K, to a total thickness of about 120 um. Light from a tungsten-halogen lamp was passed through a 0.5 m monochromator, mechanically chopped and focused onto the input slot coupler of the matrix. A thin-film total internal reflection technique [5] was employed to give a total absorption length of 10 mm. The transmitted light was detected by a photodiode using phase-sensitive detection, the signal then being accumulated by an LSI 11/03 computer which also controlled the monochromator stepping motor. Molecular cations in the ground electronic state were generated by irradiating the matrix for about 60 s with Lyman α photons (121.6 nm) from a microwave discharge lamp.

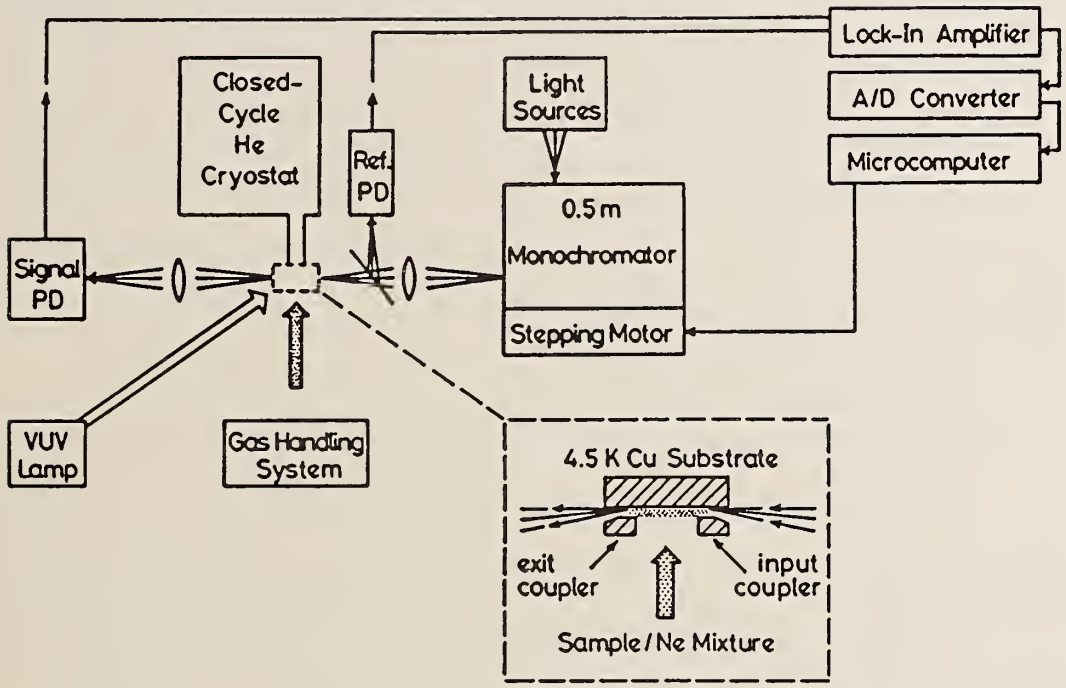

FIG.3. Schematic of the apparatus for optical absorption spectroscopy in a matrix.

3.1 GENERAL REMARKS

The $\tilde{A}\,^2\Pi_g \leftrightarrow \tilde{X}\,^2\Pi_u$ transition of the dihaloacetylene cations is composed of the two spin-orbit components, $\Omega = 3/2$ and $1/2$. On the basis of the photoelectron spectroscopy data [6] the two spin-orbit subsystems are expected to be well-separated for the diiodo- species but overlap for the dibromoacetylene cation and more extensively for the dichloroacetylene cation. For all three species the spin-orbit splitting is larger in the excited state [7], so that the respective vibronic bands of the $\Omega = 1/2$ subsystem should lie to higher energy of the corresponding bands of the $\Omega = 3/2$ subsystem.

A few remarks are in order concerning the methods used for production of the molecular cations in the three techniques. For emission spectroscopy the cations are formed in the first excited state by excitation-ionization from the ground state of the rotationally cooled molecule; thus population of both spin-orbit levels of the $\tilde{A}$ state occurs to about the same extent and the emission spectrum consists of the two transitions to the respective spin-orbit levels of the cationic ground state. In the laser excitation experiment, on the other hand, the cations produced by Penning ionization collide with the large excess of helium carrier gas which has been cooled to liquid nitrogen temperature. Thus, not only the rotational and vibrational but also the electronic level populations will be governed by the Boltzmann distribution of ca. 100 -150 K: the lowest vibrational levels of the two spin-orbit components of the cationic ground state will be populated according to this temperature and the magnitude of the spin-orbit splitting. Depending on this latter quantity, the $\Omega = 1/2$, $\tilde{A} \leftarrow \tilde{X}$, transition will either be partially or totally discriminated against in the laser excitation spectrum. This same argument applies for the matrix absorption technique where the matrix temperature of 4.5 K ensures that the energetically higher lying $\Omega = 1/2$ substate of the $\tilde{X}$ state has negligible population and the corresponding transition is absent.

The linear symmetric dihaloacetylenes, $D_{\infty h}$ symmetry, have five fundamental vibrational modes: two of Σ_g^+ symmetry (ν_1 : ν(C≡C), ν_2 : ν(C-X)), one of Σ_u^+ symmetry (ν_3 : ν_a(C-X)) and two bending modes Π_g (ν_4) and Π_u (ν_5) [8].

3.2 EMISSION SPECTROSCOPY: The $\tilde{A}\ ^2\Pi_{\Omega,g} \rightarrow \tilde{X}\ ^2\Pi_{\Omega,u}$ Transition of $I\text{-}C{\equiv}C\text{-}I^+$

The $\tilde{A}\ ^2\Pi_{\Omega,g} \rightarrow \tilde{X}\ ^2\Pi_{\Omega,u}$ emission spectrum of diiodoacetylene cation was reported some time ago using electron-beam impact on an effusive sample beam [7]. Even though the two spin-orbit subsystems were expected to be well-separated, no specific vibrational assignments could be made, not even for the origin bands, due to the numerous overlapping bands. A similar situation applied to the emission spectra of the other dihaloacetylene cations. Figure 4 shows the main part of the emission spectrum of diiodoacetylene cation which had been rotationally cooled in a seeded helium supersonic free jet [9]. The intensities of the detected bands appear to decrease toward lower energy because the efficiency of the photomultiplier falls rapidly in this wavelength region. Compared with that obtained with an effusive beam the spectrum is of much higher quality and allows resolution of the many bands as a result of the greatly reduced widths of the rotational line envelopes of the vibronic bands. Similar improvements were realized for the corresponding emission spectra of the dibromo- and dichloroacetylene cations, where also the vibrational isotope effect of the naturally occuring isotopes of bromine and chlorine could be resolved for certain modes. This information, and comparison with the laser excitation and matrix absorption spectra, allows a vibrational analysis of the spectra.

Comparison of the emission spectrum with the absorption spectrum in a neon matrix [10] unambiguously locates the origin of the $\Omega = 3/2$ subsystem at 12 971 ± 1 cm^{-1}. The $\overline{0_0^0}$ band (all bands belonging to the $\Omega = 1/2$ subsystem will be denoted throughout with a horizontal bar) is found at 14 276 ± 1 cm^{-1}. Bands lying to the red of the respective origin bands correspond

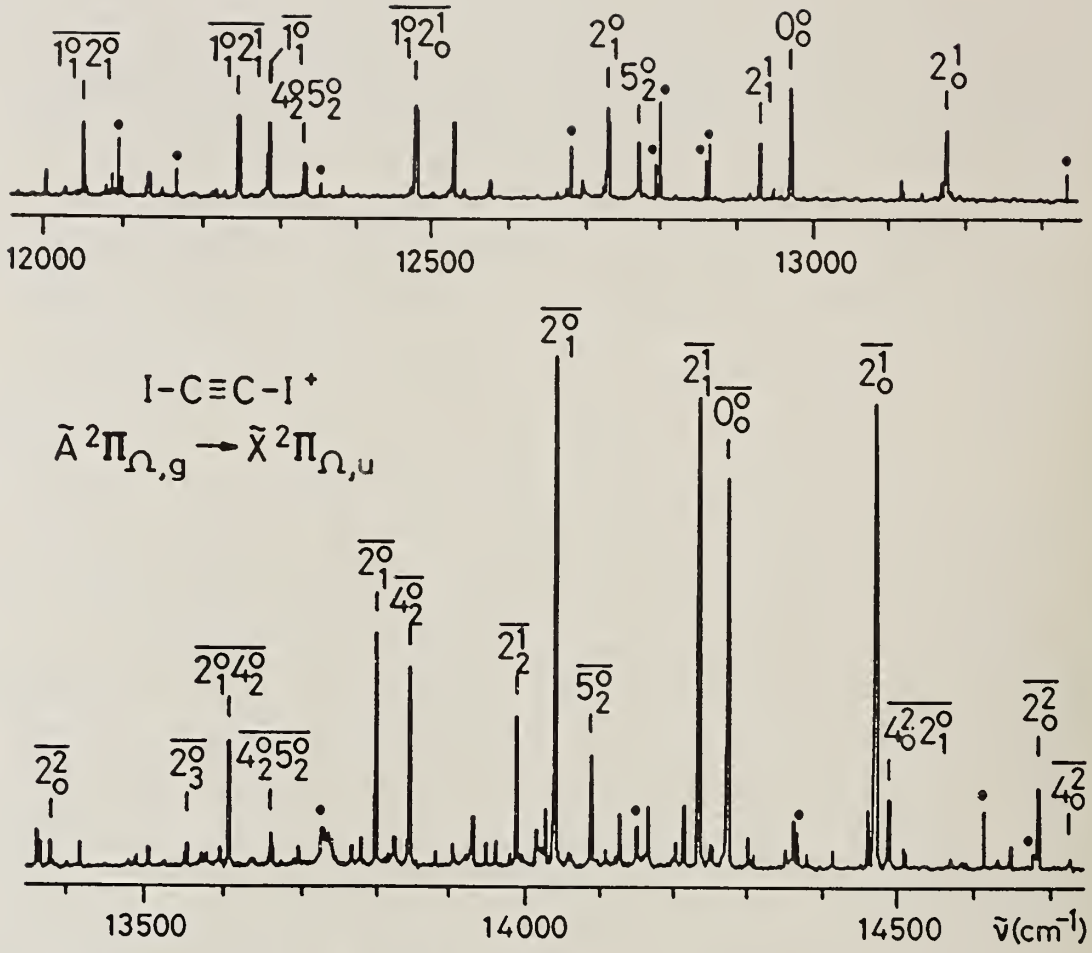

FIG.4. Part of the $\tilde{A}\,^2\Pi_{\Omega,g} \rightarrow \tilde{X}\,^2\Pi_{\Omega,u}$ (Ω= 3/2,1/2) gas-phase emission spectrum of I-C≡C-I^+ in a seeded helium supersonic free jet, resolution 0.03 nm. Some of the vibrational assignments are indicated; a horizontal bar indicates the Ω= 1/2 system. Helium lines are marked with a dot.

mainly to transitions from the lowest vibrational level of the $\tilde{A}$ state to the accessible vibrational levels of the cationic ground state. The most intense vibrational progression in the $\tilde{X}$ state corresponds to excitation of the ν_2, symmetric C-I stretching, mode. Bands are also observed corresponding to excitation in the $\tilde{X}$ state, in double quanta, of the two bending modes, ν_4 and ν_5. These latter transitions probably gain intensity through Fermi resonance with the near-lying transitions of the ν_2 progression.

Bands lying to higher energy of the respective origin bands correspond to transitions from vibrational levels in the excited state. These are populated according to the selection rules and Franck-Condon factors of the ionization process from the molecular ground state. The main activity observed in the emission spectrum is a short progression in the excited state ν_2 mode.

Analysis of the emission spectrum yields some of the vibrational frequencies of the cationic electronic states, mainly of the ground state and to a lesser extent of the first excited state. The energy difference between the $\Omega = 3/2$, $1/2$ origin bands gives the difference in the magnitudes of the spin-orbit splitting constants in the upper and lower states; this can be used in conjunction with the photoelectron data to determine more accurate ionization energies for the ground cationic state.

3.3 LASER EXCITATION SPECTROSCOPY: The $\tilde{A}\ ^2\Pi_{\Omega,g} \leftarrow \tilde{X}\ ^2\Pi_{\Omega,u}$ Transition of $Br-C\equiv C-Br^+$

The laser excitation spectrum [11] of the dibromoacetylene cation in the gas phase is shown in figure 5. The photoelectron spectroscopy data has shown that the spin-orbit splitting in the cationic ground state, $\tilde{X}\ ^2\Pi_{\Omega,u}$, is of the order of 1400 cm^{-1} [7]; thus, following collisional thermalization, the zeroth level of the $\tilde{X}\ ^2\Pi_{1/2}$ component has a negligible population. All of the bands observed in the spectrum of figure 5 must thus belong to the $\Omega = 3/2$ transition.

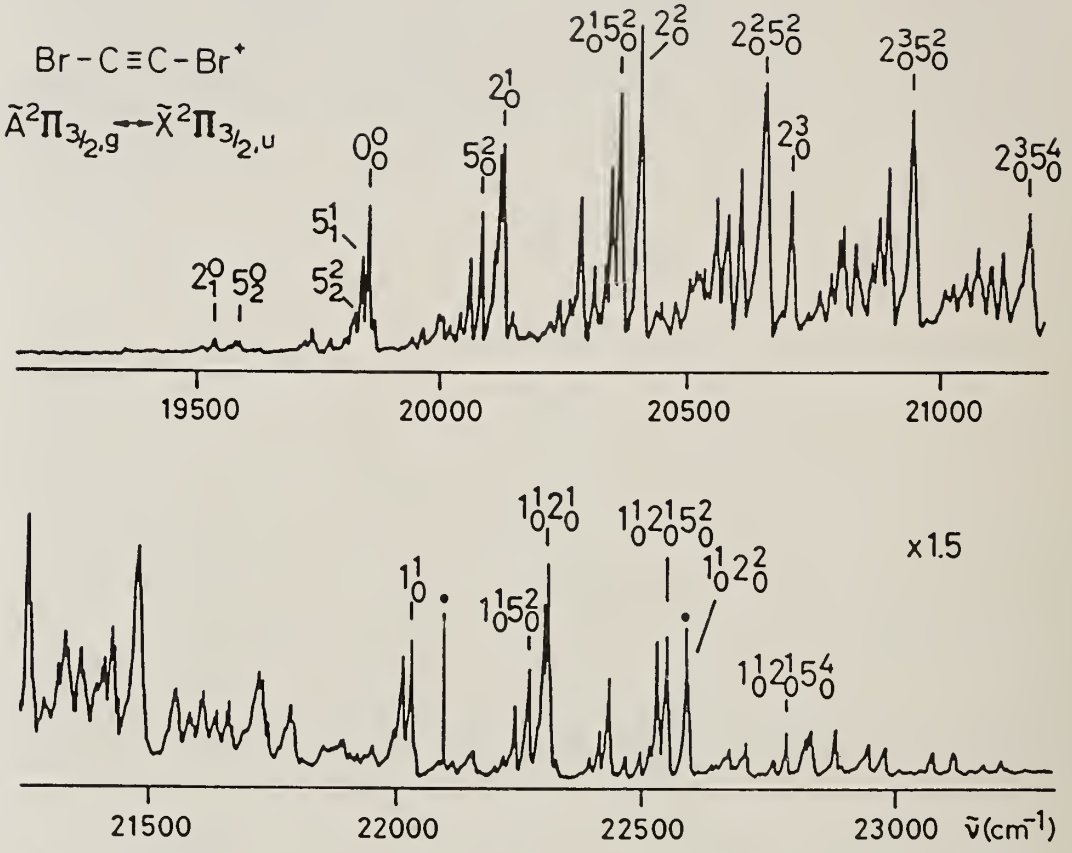

FIG.5. Part of the laser excitation spectrum of the $\tilde{A}\ ^2\Pi_{3/2,g} \leftarrow \tilde{X}\ ^2\Pi_{3/2,u}$ transition of $Br-C\equiv C-Br^+$ in the gas-phase, resolution 0.02 nm. Atomic lines are marked with a dot.

The location of the origin band is confirmed by comparison with the emission and matrix absorption data. The main vibrational progressions observed in the excited electronic involve the v_2 and v_5 modes; the latter is excited in double quanta and the transitions probably gain intensity via a Fermi resonance interaction with the energetically near-lying and intense transitions involving the v_2 progresssion. Many of the bands show splitting due to the effects of the bromine 79 and 81 isotopes on the vibrational

frequencies; the magnitude of the splitting can be followed within a progression and help to confirm the location of the system origin.

Bands lying to lower energy of the origin band correspond to transitions from excited vibrational levels of the cationic ground state. At the sample temperature of 100 - 150 K only the lowest energy mode levels have any significant population, and transitions from such levels are of low intensity.

The vibrational analysis of the laser excitation spectrum leads to the frequencies of three of the five fundamental modes in the first excited electronic state [11] and complements the data from the emission spectrum.

3.4 ABSORPTION SPECTROSCOPY: The $\tilde{A}\ ^2\Pi_{\Omega,g} \leftarrow \tilde{X}\ ^2\Pi_{\Omega,u}$ Transition of $Cl-C\equiv C-Cl^+$ in a Neon Matrix

The technique of direct optical absorption spectroscopy of cations embedded in rare gas matrices [4] has been applied to the $\tilde{A} \leftarrow \tilde{X}$ transition of the dihaloacetylene cations [10]. Neon was used as the host matrix due to it low polarizability: weak sample-matrix interactions keep the band positions and sample vibrational frequencies close to those observed in the gas phase.

A portion of the $\tilde{A} \leftarrow \tilde{X}$ absorption spectrum of dichloroacetylene cation in a neon matrix is shown in figure 6. At the low matrix temperature the spectrum is exclusively that of the $\Omega = 3/2$ spin-orbit subsystem. The spin-orbit splitting of the cationic ground state is of the order of 240 cm^{-1} [7] so that even in the laser excitation experiment, at liquid nitrogen temperature, the $\Omega = 1/2$ transition has appreciable intensity. The laser excitation and emission spectra are also complicated by the fact that the difference in the spin-orbit splittings in the $\tilde{X}$ and $\tilde{A}$ states is relatively

small, 296 ± 1 cm^{-1} [9], so that the two subsystems overlap considerably. Thus a great simplification is obtained in the matrix absorption experiment.

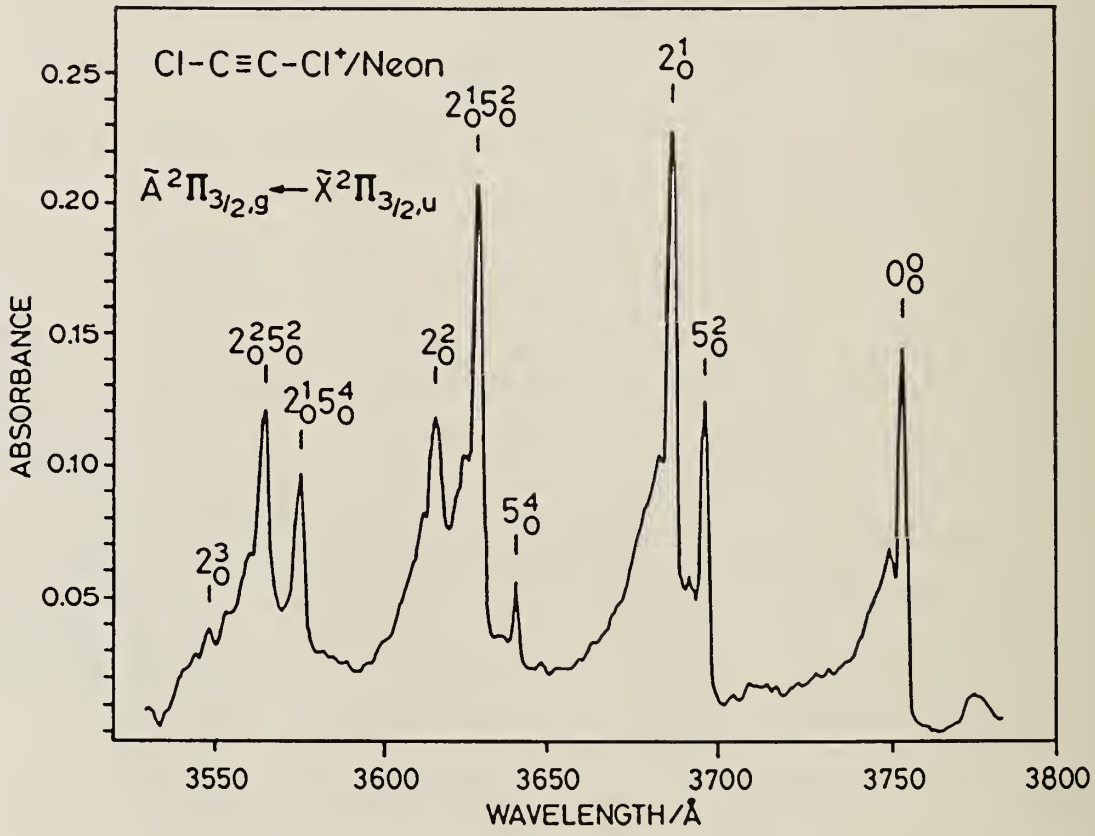

FIG.6. Part of the $\tilde{A}\,^2\Pi_{3/2,g} \leftarrow \tilde{X}\,^2\Pi_{3/2,u}$ absorption spectrum of $Cl\text{-}C{\equiv}C\text{-}Cl^+$ in a neon matrix, optical resolution 0.1 nm.

The vibrational excitations observed in the first excited electronic state involve mainly the ν_2 and ν_5 modes, as indicated in figure 6. Excitation of ν_1 is also observed to higher energy. Thus the absorption spectrum yield three of the five fundamental frequencies in the $\tilde{A}$ state, with an uncertainty of ± 5 cm^{-1}.

3.5 GENERAL TRENDS

Vibrational analysis of the abovementioned spectra leads to vibrational frequencies of the observed modes in the cationic ground and first excited electronic states. Consideration of which modes are observed, their relative energies in the two cationic states, and comparison with the molecular values can be rationalized in terms of the molecular orbital description of the electronic structure [6]. Figure 7 gives, for the example of the dibromoacetylene cation, the prominent vibrational excitations observed in the $\tilde{A} \leftrightarrow \tilde{X}$ transitions, their frequencies, the molecular values [8] and the nodal characteristics of the highest occupied and penultimate molecular orbitals [6].

	Σ_g^+		Π_u	
	$\nu_1: \nu(C\equiv C)$	$\nu_2: \nu_s(C-Br)$	$\nu_5: \delta(BrCCBr)$	
$X\ ^1\Sigma_g^+$	2185	267	137	
$\tilde{X}\ ^2\Pi_u$	2067	321	136	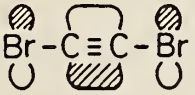
$\tilde{A}\ ^2\Pi_g$	2188	280	119	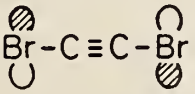

FIG.7. Some of the molecular and cationic vibrational frequencies (cm^{-1}) of dibromoacetylene and nodal characteristics of the appropriate molecular orbitals.

The highest occupied molecular orbital has bonding characteristics in the C≡C internuclear region but is C-Br antibonding. Thus, removal of an electron from this orbital, giving rise to the $\tilde{X}\ ^2\Pi_{\Omega,u}$ cationic electronic state, should result in a weakening of the C≡C bond and a strengthening of

the C-Br bonds. This is reflected in the reduced ν_1 and increased ν_2 values of the cationic ground state compared to those of the neutral. On the other hand, the penultimate occupied molecular orbital is essentially localized on the bromine atoms ("lone pairs") so that removal of an electron from this orbital, giving rise to the $\tilde{A}\ ^2\Pi_{\Omega,g}$ state, results in very little change to the bond strengths and vibrational frequencies. Strong excitation of the ν_5 mode is observed in double quanta, as this results in a totally symmetric component; the observed strength of these transitions is believed to arise from Fermi resonance with near-lying intense transitions involving ν_2. The gas-phase spectral bands are shaded to the red, indicating the relative magnitudes of the rotational constants: $B(\tilde{X})>B(\tilde{A})$. Assuming linearity is retained, this implies that the C-Br bond is shorter in the $\tilde{X}$ state compared to the $\tilde{A}$ state. Similar trends can be deduced from the spectra of the dichloro- and diiodoacetylene cations.

4. SUMMARY

The three techniques, gas-phase emission and laser excitation spectroscopies and absorption spectroscopy in a matrix, can be used to study the transitions between the ground and lower excited states of molecular radical cations. The first two techniques are, however, limited to those species which exhibit radiative decay from the excited states. Such species have also been studied by other techniques such as photon-photoelectron coincidence spectroscopy [1][12] which gives useful quantitative information concerning the relaxation dynamics of the cationic excited states.

Analysis of the spectra leads to many of the vibrational frequencies in the ground and excited electronic states of the cations. A considerable

improvement in the data from the gas-phase spectra can be accomplished by rotational and vibrational cooling of the cations. As an example, many of the stronger bands in the emission spectra of the dihaloacetylenes have been examined under higher resolution so that the vibrational frequencies of the individual isotopic species can be determined to ± 0.3 cm^{-1} [13]. These may be useful for theoretical force-field calculations or experimental high-resolution tunable laser studies.

The three techniques discussed here are complementary. While the emission spectra provide information concerning the vibrational energy levels of the cationic ground state, the laser excitation and matrix absorption spectra provide the corresponding information for the lowest excited states. As well, the techniques generate the cations by quite different methods so that if a certain species is not amenable to one method it can be studied by alternate methods.

ACKNOWLEDGEMENTS

Co-workers: R. KUHN, S. LEUTWYLER, L. MISEV, M. OCHSNER, U. SPITTEL, F. THOMMEN, W. ZAMBACH

Work at Basel funded by the Schweizerischer Nationalfonds zur Förderung der wissenschaftlichen Forschung. D.K. acknowledges partial support by the Natural Sciences and Engineering Research Council of Canada.

REFERENCES

1. J.P. Maier, O. Marthaler, L. Misev and F. Thommen, in J. Berkowitz and K.-O. Groeneveld (Eds.), Molecular Ions, Plenum, New York, 1983, and refs. cited therein.

2. D. Klapstein, J.P. Maier, L. Misev, in T.A. Miller and V.E. Bondybey (Eds.), Molecular Ions: Spectroscopy, Structure and Chemistry, North-Holland, New York, 1983, p.175.

3. T.A. Miller and V.E. Bondybey, J. Chim. Phys. 77 (1980) 695.

4. S. Leutwyler, J.P. Maier, U. Spittel, Chem. Phys. Lett. 96 (1983) 645.

5. R. Rosetti, L.E. Brus, Rev. Sci. Instrum. 51 (1980) 467; V.E. Bondybey, T.A. Miller, J.H. English, J. Chem. Phys. 72 (1980) 2193.

6. E. Heilbronner, V. Hornung, E. Kloster-Jensen, Helv. Chim. Acta 53 (1970) 331.

7. M. Allan, E. Kloster-Jensen, J.P. Maier, J. Chem. Soc. Faraday II 73 (1977) 1417.

8. P. Klaboe, E. Kloster-Jensen, D.H. Christensen and I. Johnsen, Spectrochim. Acta 26A (1970) 1567; D.H. Christensen, T. Stroyer-Hansen, P. Klaboe, E. Kloster-Jensen and E.E. Tucker, Spectrochim. Acta 28A (1972) 939.

9. D. Klapstein, J.P. Maier, W. Zambach, Chem. Phys. 77 (1983) 463.

10. S. Leutwyler, J.P. Maier, U. Spittel, Mol. Phys. 51 (1984) 437.

11. J.P. Maier, L. Misev, Int. J. Mass Spectrom. Ion Processes 58 (1984) 243.

12. J.P. Maier and F. Thommen, Chem. Phys. 70 (1982) 325.

13. D. Klapstein, R. Kuhn, J.P. Maier, J. El. Spectrosc. Rel. Phenom. 35 (1985) 171.

MELANIN FREE RADICALS AND THE PHOTODYNAMIC EFFECTS OF MELANINS

P. J. Lea and A. Pawlowski

Electron Microscopy Laboratory and Department of Medicine, University of Toronto, Toronto, Ontario, Canada.

S. Persad, I. A. Menon and H. F. Haberman

Department of Medicine, Clinical Science Division, University of Toronto, Toronto, Ontario, Canada.

INTRODUCTION

Melanins are of two types: (a) eumelanin - the melanin present in black hair and in skin of people with black hair and (b) pheomelanin - the melanin present in red hair and in skin of people with red hair (1). Eumelanin is derived from 3,4-dihydroxyphenylalanine (dopa) and pheomelanin from cysteinyldopa (1). These two types of melanins also differ in their physical and chemical properties (2-7).

Melanins contain stable free radicals, which can be detected by electron spin resonance (ESR) (8). Eumelanin and pheomelanin give one common signal. Pheomelanin also gives an additional ESR signal (5, 6).

Irradiation of Ehrlich ascites carcinoma (EAC) cells in the presence of red hair melanin (RHM) produces lysis of the cells to a larger extent, than irradiation in the presence of black hair melanin (9-11).

It is conceivable, that the lysis of cells could represent

the final phase of a series of cytotoxic events. Hence the possible changes produced in the cells prior to lysis, were investigated. This paper reports the ultrastructural changes produced in EAC cells by irradiation in the presence of RHM.

MATERIALS AND METHODS

EAC was maintained in mice. The cells were isolated and suspended in Medium 199 as previously described (9). RHM was isolated from human red hair according to Menon et al (2).

7.5×10^6 EAC cells were suspended in 3.0 ml of Medium 199 contained in 30 ml beakers. In the specified samples listed below, 600 ug of RHM were added. The suspensions were irradiated using a Westinghouse 400W mercury vapor lamp, placed 14 cm above the surface of the cell suspensions. The detailed specifications of the radiation source and the radiation emitted are given in a previous paper (4).

In the present study, three sets of samples were employed. 1. EAC-0: suspensions of EAC cells with no melanin. 2. MEAC-60D: suspensions of EAC cells and RHM incubated in the dark for 60 min. 3. MEAC-60L: suspensions of EAC cells and RHM irradiated for 60 min.

The cells were sedimented by centrifugation at 200 x g for 10 min, and the pellets fixed in universal fixative (12) for 60 min. The pellets were post-fixed in osmium tetroxide for 60 min and embedded in Epon B12 epoxy resin. Thin serial sections were cut and placed on slotted, formvar/carbon coated grids. The sections were stained with lead citrate and examined with a Philips EM 300 transmission electron microscope.

The cells were photographed at magnifications of 16000 and 32000 diameters.

RESULTS

The cells in the control group (EAC-0), not treated with melanin or irradiated, were used as basis for comparison to the cells treated with melanin and or exposed to radiation (Table 1).

TABLE 1

Summary of the findings on the effects of irradiation of EAC in the presence of RHM on the ultrastructure of these cells

Twenty cells in each group were examined. The ultrastructural features of each component were classified as normal (N) and abnormal (A). The numbers of the cells having N or A features are given in the table.

Sample	Membrane		Cytoplasm		Mitochondria		Nucleus	
	N	A	N	A	N	A	N	A
1. EAC-0	19	1	19	1	17	1	19	1
2. EAC-60D	2	18	4	7	6	9	14	6
3. EAC-60L	0	20	0	20	0	20	3	17

The membrane of the cells in the control group was complete, including the occasional pseudopod. The cytoplasm appeared to be of normal density and contained the usual organelles. Lipid

droplets were abundant. They varied in size and number from cell to cell (Fig.1). All the cells observed, in the three groups, contained single or grouped lipid droplets.

In the control group, 20 mitochondria per cell section was the average number counted. Numerous mitochondria were well circumscribed by double membrane. Most of the cristae were continuous with the double membrane and appeared uniformly spaced (Fig.2).

The nucleoplasm was evenly distributed and the nucleoli were prominent. The nuclear membrane was not distended (Fig.3). The nuclei occupied approximately one third of the cell section in the three groups observed.

In the group treated with melanin and incubated in the dark (MEAC-60D), 90 percent of cells showed some abnormality, whereas 10 percent of cells were comparable to the control group. Thirty percent of cells showed breaks. Many pseudopodia were observed in the section plane.

The cytoplasm was markedly more dense in this group (Fig. 4) than in the control group (Fig.1).

Mitochondria were found in 55 percent of cells observed. Thirty six percent of these cell sections contained mitochondria comparable to those in the control group. On average, 12 mitochondria were counted per cell section. In the remaining 64 percent of these cell sections, the average number of mitochondria per cell section was 5. The abnormal mitochondria were much smaller and had a dark, dense matrix. The cristae appeared to be close to each other (Fig. 5).

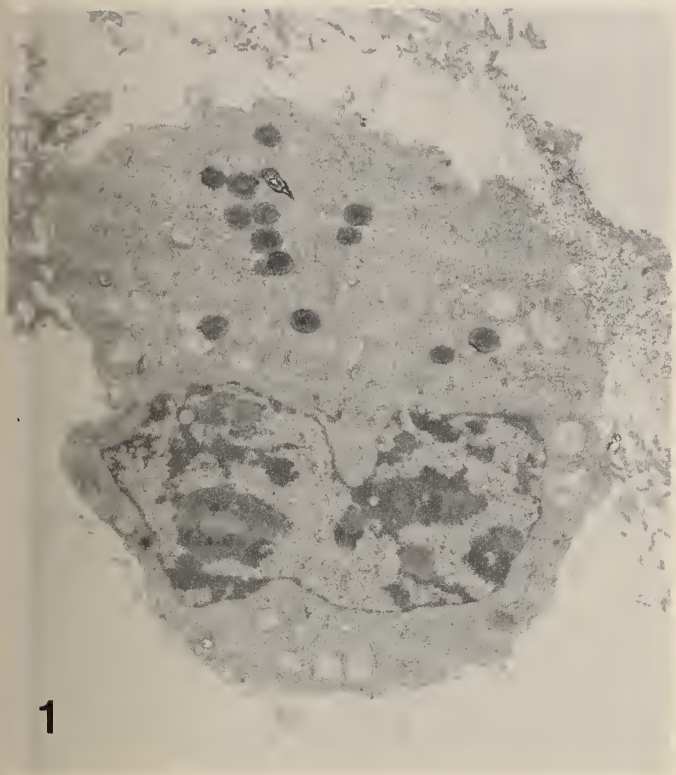

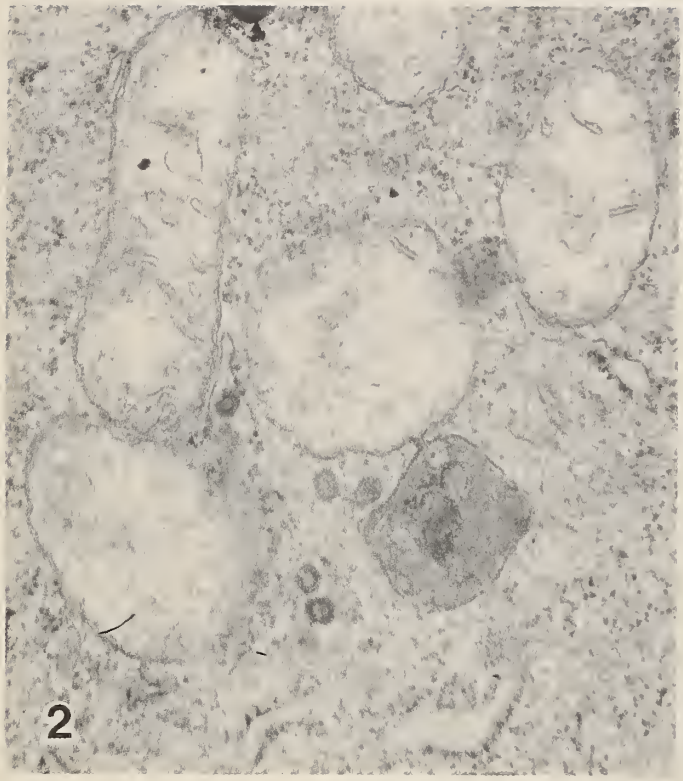

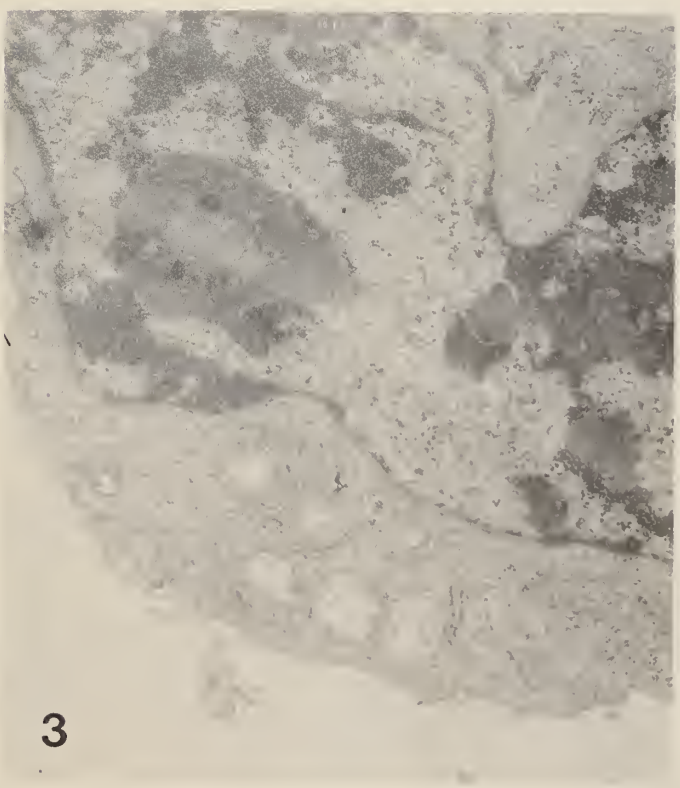

LEGEND
Fig.1. EAC-0. Untreated.
Mag. X 9400

Fig.2. EAC-0. Mitochondria.
Mag. X 54000

Fig.3. EAC-0. Nucleoplasm and nucleoli. Mag. X 21000

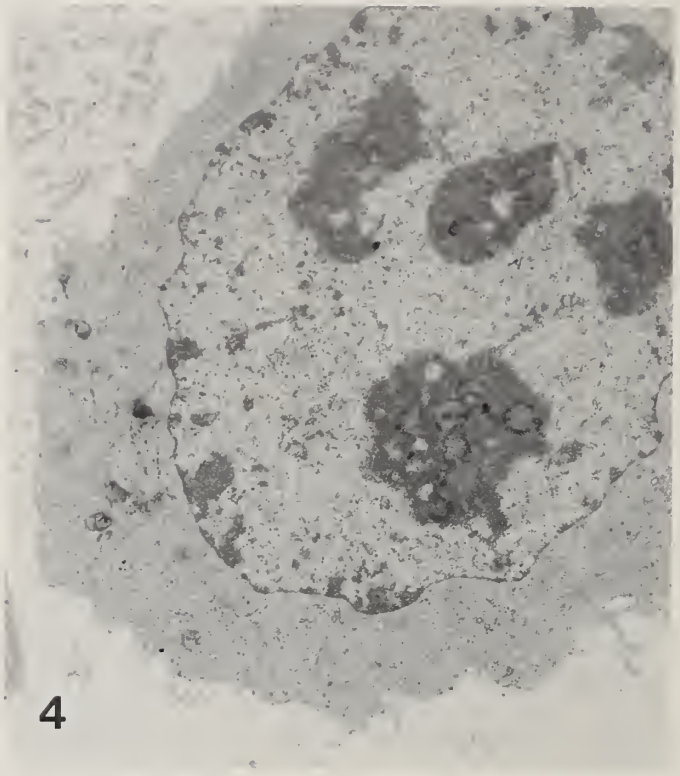

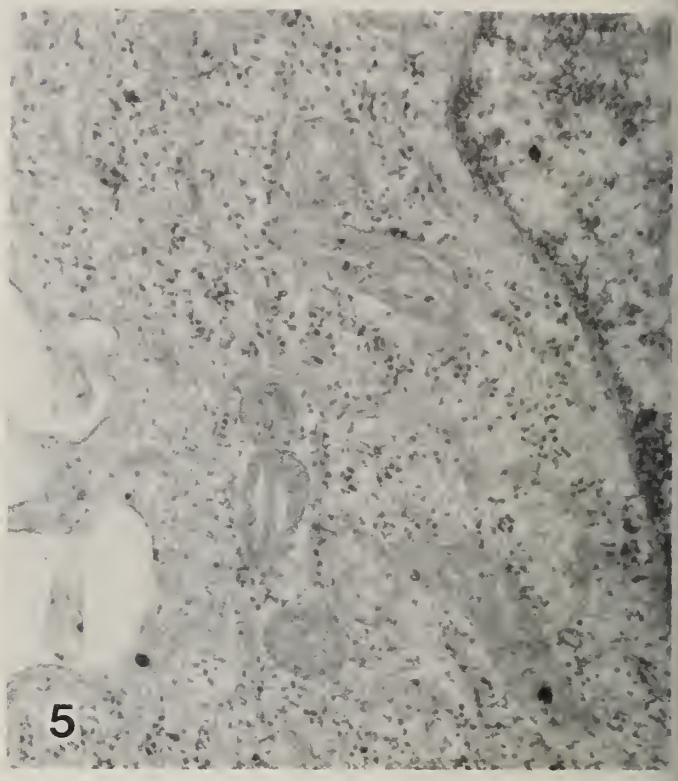

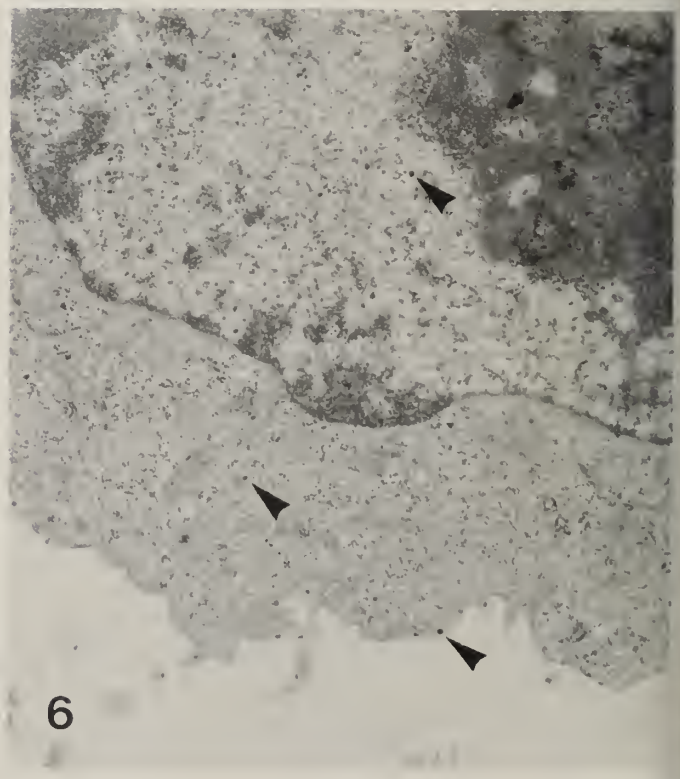

LEGEND

Fig.4. MEAC-60D. Many pseudopodia and dense cytoplasm. Mag. X 9400

Fig.5. MEAC-60D. Small mitochondria with a dense matrix. Nuclear membrane is distended. Mag. X 54000

Fig.6. MEAC-60D. Melanin particles (arrows), in the cytoplasm and nucleus. Some melanin external to the cell. Mag. X 21000

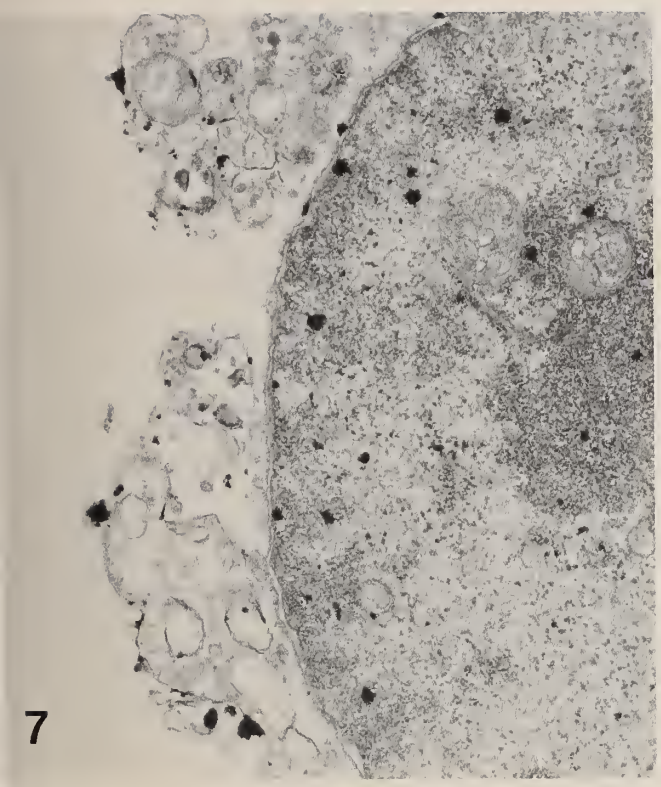

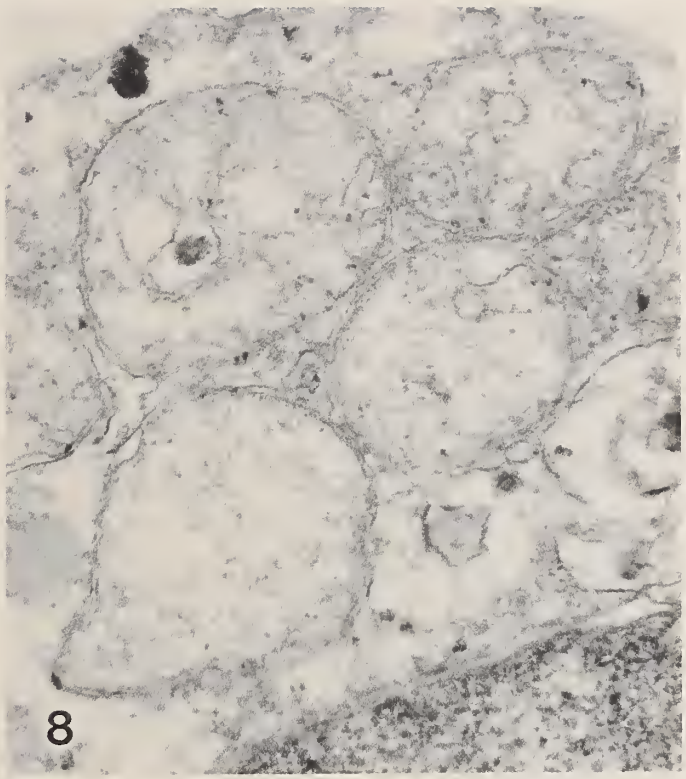

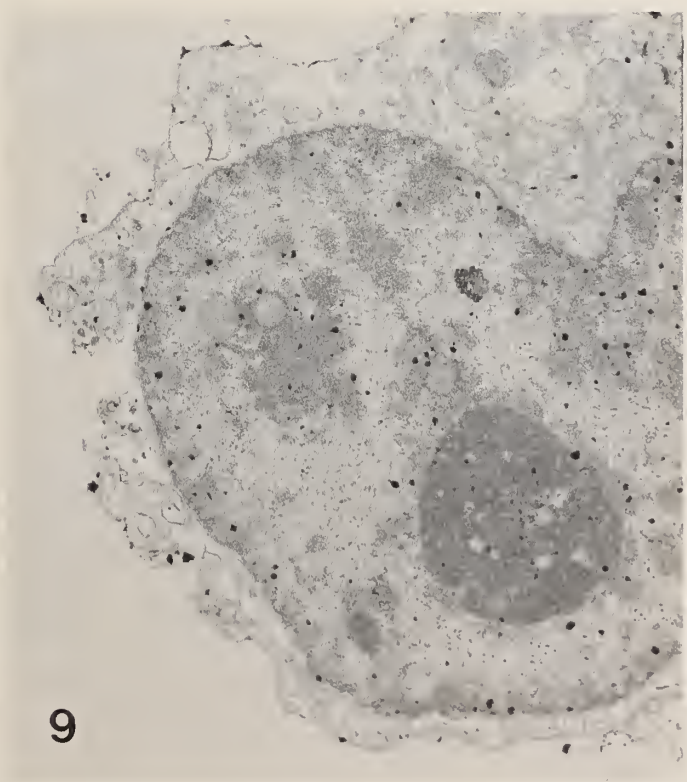

LEGEND

Fig.7. MEAC-60L. Broken cell membrane, swollen vacuolated cytoplasm. Mag. X 21000

Fig.8. MEAC-60L. Distended mitochondria with ruptured cristae. Mag. X 54000

Fig.9. MEAC-60L. Melanin particles distributed throughout the nucleus and cytoplasm. Mag. X 9400

Eighty percent of cell sections observed contained nucleus. Of these, 56 percent had distended nuclear membrane (Fig. 5).

Melanin was found mainly around the periphery of the cell, at the cell membrane, and in the cytoplasm. Some melanin particles were observed in the nucleus (Fig. 6).

In group 3 (MEAC-60L), the cells were irradiated in the presence of melanin. Most of the cells observed were necrotic. In 85 percent of cells, the cell membrane was broken. The cytoplasm was swollen and vacuolated, and the organelles difficult to identify (Fig. 7). The mitochondria were distended and many cristae were ruptured (Fig. 8). The nuclei were also distended and the nuclear membranes dilated (Figs. 7 and 8). Many melanin granules were observed in the cytoplasm and throughout the nucleus (Fig. 9).

DISCUSSION

Ultrastructural observations clearly showed that, if melanin is added to cell suspensions, it penetrates into the cells. Melanin particles penetrated the cell membrane immediately, without apparent structural damage to the cell or the cell membrane.

The process of particle penetration appeared to have no destructive effect on the cells. Changes in ultrastructure became apparent after 30 min in both dark and light treated samples. Effects on cells treated in the dark, were expressed as structural, mainly cytoplasmic changes. Most of the cells exposed to light were lysed.

It would appear that irradiation of the cells in the presence of melanin produces phototoxic effects within the cells, even before the membrane is lysed.

Effects observed in the dark, could be due to the presence of melanin, and/or due to hydrogen peroxide formed by the reaction of melanin with sulfhydryl compounds (11).

In cells irradiated in the presence of the melanin, the observed changes could be due to action of free radicals produced by irradiation of melanin (10, 11, 13).

Normal melanocytes are difficult to grow in tissue culture. Malignant melanoma cells can be cultured and several lines of human and animal melanomas are available. There is no published data if these cell lines contain eumelanin or pheomelanin. The present findings that EAC cells readily take up RHM, may serve as an in vitro model to provide cells containing eumelanin or pheomelanin. In vitro studies using cells containing these melanins may provide information relevant to the effects of UV radiation on human skin.

UV radiation on human skin may result in sunburn and cancer. The lysis or killing of cells in vitro, may be compared to sunburn. Cell lysis however, cannot account for carcinogenic effects. To make a cell malignant, it is necessary to alter the cell without killing it.

The findings reported here, show that UV irradiation of cells in the presence of pheomelanin, produced ultrastructural changes in the cytoplasm, as well as the nucleus, prior to cell lysis. This indicates the possibility of mutations without cell killing, which is also supported by the observation, that

irradiation under similar conditions produced alkali- sensitive lesions in DNA (14). Such changes in DNA may result in initiation of carcinogenesis. Therefore, it is possible that photosensitive effects of pheomelanin in human skin may positively contribute to photodestructive and carcinogenic effects of UV radiation.

ACKNOWLEDEGMENTS

This work was supported by a grant (MT-5043) from the Medical Research Council of Canada. H.F. Haberman is an Associate of the Ontario Cancer Treatment and Research Foundation.

REFERENCES

1. G. Prota, J Invest. Dermatol. 75: 122-27. 1980.

1. I.A. Menon, S. Persad, H.F. Haberman and C.J. Kurian, J. Invest. Dermatol. 80: 202-06, 1983.

3. I.A. Menon, S. Persad, H.F. Haberman, C.J. Kurian and P.K. Basu. Exp. Eye Res. 34: 531-37, 1982.

4. S. Persad, I.A. Menon, H.F. Haberman. Photochem. Photobiol. 37: 63-68, 1983.

5. R.C. Sealy, J.S. Hyde, C.C. Felix, I.A. Menon, G. Prota, H.M. Swartz, S. Persad, H.F. Haberman. Proc. Natl. Acad. Sci. USA, 79: 2885-89, 1982.

6. R.C. Sealy, J.S. Hyde, C.C. Felix, I.A. Menon and G. Prota. Science 217: 545-47, 1982.

7. S. Ito and K. Jimbow, J. Invest. Dermatol. 80: 268-72, 1983.

8. R.C. Sealy, C.C. Felix, J.S. Hyde and H.M. Swartz, Free Radicals in Biol, Vol IV, Edited by W.A. Pryor, New York, Academic Press, 1980, pp. 209-59.

9. I.A. Menon, S. Persad, N.S. Ranadive and H.F. Haberman, Cancer Res. 43: 3165-69, 1983.

10. I.A. Menon, S. Persad, N.S. Ranadive and H.F. Haberman, Oxygen radicals in Chemistry and Biology, edited by W. Bors, M. Saran, D. Tait. Walter de Gruyter & Co, Berlin, 1984. pp. 673-679.

11. I.A. Menon, S. Persad, N.S. Ranadive and H.F. Haberman, Canadian J. Biochem. Cell Biol. 63: 278-83, 1985.

12. E.M. McDowel and B.F. Trump, Arch. Path. Lab. Med. 100: 405-414, 1976.

13. T.Sarna, I.A. Menon and R.C. Sealy, Photochem. Photobiol. 39: 805-809, 1984.

14. I.A. Menon, S. Persad and H.F. Haberman, Proc. Amer. Assoc. Cancer Res. 25: 104, 1984.

Far Infrared Spectroscopy of NH(D) ($a\ ^1\Delta$) and NaH($X\ ^1\Sigma^+$)

K.R. Leopold, L.R. Zink, K.M. Evenson, and D.A. Jennings
National Bureau of Standards
Boulder, CO 80303 U.S.A.

J.M. Brown
Physical Chemistry Laboratory
Oxford University
Oxford, England OX1 3QZ

Rotational spectroscopy provides one of the most accurate means with which to determine molecular spectroscopic constants relating to geometry, potential curves, and electronic structure. Particularly amenable to theoretical studies of these properties are light diatomic hydrides, whose rotational spectra fall in the far infrared (FIR). Observation of such species at FIR frequencies can therefore provide valuable data with which to test computational methods. In addition, the far infrared region is well suited to the astrophysical observation of molecules under a wide range of conditions, and the laboratory detection of new FIR spectra can thus increase the number of processes which may be studied in interstellar space. In this paper, we present the results of far infrared spectroscopic studies of the excited ($a\ ^1\Delta$) state of the NH and ND radicals, and of the ground ($X\ ^1\Sigma^+$) state of the sodium hydride molecule. The NH work has been performed using the technique of far infrared laser magnetic resonance (LMR) spectroscopy, and spectra of the non-magnetic NaH molecule have been recorded using a new tunable far infrared spectrometer.

A. Laser Magnetic Resonance Detection of NH(D) ($a\ ^1\Delta$)

In the far infrared LMR experiment, transitions of a paramagnetic species are Zeeman tuned into resonance with a fixed frequency far infrared laser. The optically pumped far infrared laser consists of a far infrared gain

cell which is separated from the intracavity sample region by a polypropylene beam splitter. A small 45° copper mirror reflects a portion of the circulating laser power out a window in the side of the laser so that it may be monitored by a helium cooled bolometer detector. When the magnetic field has the correct value to bring a molecular transition frequency into resonance with the laser frequency, an intracavity absorption is detected at the bolometer output.

NH radicals were produced by the reaction of fluorine atoms with ammonia. Figure 1 shows a single Zeeman component in the lowest rotational transition of $NH(^1\Delta)$, as observed on the 102 μm lasing line of CH_2DOH The spectrum shows clearly resolved magnetic hyperfine structure due to the ^{14}N (I=1) and H(I=1/2) nuclei. In the case of a $^1\Delta$ state, a single hyperfine parameter per nucleus is necessary to completely characterize the magnetic hyperfine structure, and the hyperfine constant for the nucleus i, a_i, is directly proportional to the quantity $\langle 1/r^3 \rangle$. Here, r is the distance between the nucleus in question and the electron(s) carrying the angular momentum. Thus the observed splittings give in a very direct manner, detailed information about the electronic structure of the radical. By studying the $J = 3 \leftarrow 2$ transition of NH and the $J = 3 \leftarrow 2$ and $J = 5 \leftarrow 4$ transitions of ND, we have determined the magnetic hyperfine constants a_N, a_H, and a_D for the nitrogen, hydrogen, and deuterium nuclei respectively. In addition, the spectra provide accurate rotational and distortion constants, as well as the orbital and rotational g-factors for the radical. Table I gives the parameters determined from a fit to the observed LMR spectra.

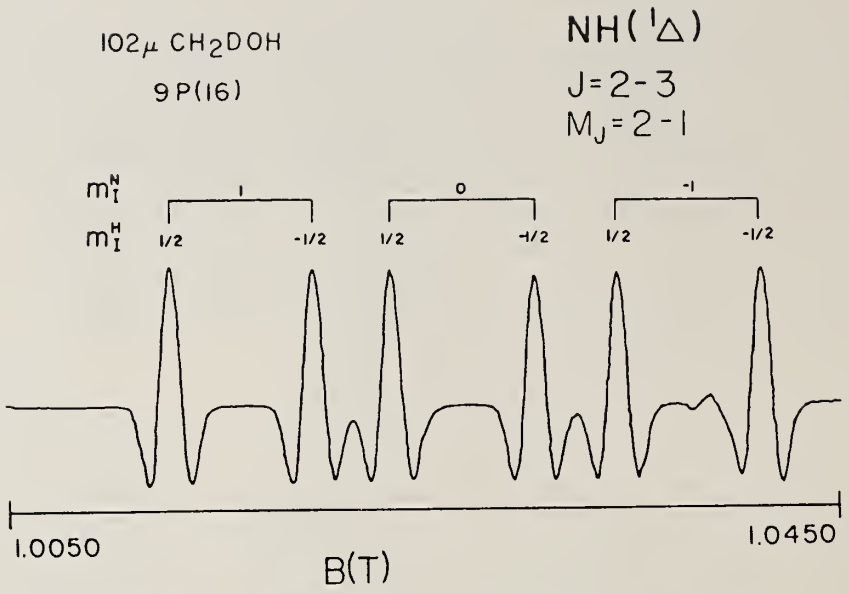

Fig. 1. The J = 2 ← 3, M_J = 2 ← 1 transition of NH($a^1\Delta$).

Table I

Spectroscopic Constants of NH(D) ($a\ ^1\Delta$) [a]

	NH($^1\Delta$)	ND($^1\Delta$)
B_0 (MHz)	492622.12(10)	264635.237(30)
D_0 (MHz)	48.6[b]	14.37606(90)
a_N (MHz)	109.7(9)	109.6(2)
$a_{H(D)}$ (MHz)	70.7(15)	11.0(2)
g_r	-0.00158(6)	-0.00086(10)
g_L	1.00105[c]	1.000515(17)

(a) Quoted uncertainties are one standard deviation in the fit.
(b) Constrained to value from optical spectra (M. Shimauchi, Sci. Light, 13,53 (1961)).
(c) Scaled from the value for ND($^1\Delta$).

Table II provides a comparison of the electronic structure of the NH and ND ($^1\Delta$) radicals with a number of other related systems. Values of $\langle 1/r^3 \rangle$ for the $^3\Sigma$ states were determined from the electron spin-nuclear spin dipole-dipole interaction constants determined from previous LMR work on these states, assuming the angular expectation value for a p orbital, viz. $\langle 3\cos^2\theta - 1 \rangle = -2/5$. It is readily seen from the table that for both NH and PH the values of $\langle 1/r^3 \rangle$, for the N or P atoms are nearly the same in

the $^1\Delta$ and $^3\Sigma$ states, and that the values are slightly less than the corresponding ab initio values for the nitrogen or phosphorus atoms. In addition, the value of $\langle 1/r^3 \rangle_N$ is the same in NH and NF $^1\Delta$. These observations are clearly consistent with the expectation that the electrons carrying the angular momentum in these two states are in p-type orbitals on the nitrogen or phosphorus atoms. It is perhaps counter-intuitive that the value of $\langle 1/r^3 \rangle$ is larger for phosphorus than for nitrogen. Such intuition, however, is based on $\langle r \rangle$, which is not expected to be a reliable indicator of $\langle 1/r^3 \rangle$. It is gratifying, however, to see that the experimental trend for the hydrides parallels the ab initio trend for the atoms. Finally, we note that the values of $\langle 1/r^3 \rangle_H$ for the $^1\Delta$ states of NH and PH are very nearly equal to the inverse cube of the known bond lengths for these species (1.044 A and 1.431 A, respectively). Here, the $\langle 1/r^3 \rangle$ values are more intuitive since the distance between the proton and the orbitally degenerate electrons is relatively insensitive to the radial electron distribution about the nitrogen or phosphorus atom.

Table II

Comparison of $\langle r^{-3} \rangle$ for related systems.

	$\langle r^{-3} \rangle_{N,P}$	$\langle r^{-3} \rangle_{H,F}$
N[(a)]	24.3 A^{-3}	
NH($^3\Sigma$)[(b)]	20.1	
NH($^1\Delta$)[(c)]	19.3	0.89
P[(a)]	28.7	
PH($^3\Sigma$)[(d)]	23.7	
PH($^1\Delta$)[(d)]	24.0	0.35
NF($^3\Sigma$)	-	
NF($^1\Delta$)[(e)]	19.1	

(a) *ab initio* value from J.R. Morton and K.F. Preston J. Mag. Res., 30 , 1407, (1976)
(b) F.D. Wayne and H.R. Radford, Mol. Phys., 32 , 1407 (1976)
(c) This work.
(d) P.B. Davies, D.K. Russell, D.R. Smith, and B.A. Thrush, Can. J. Phys., 57 , 522 (1979)
(e) P.B. Davies and F. Temps , J. Chem. Phys., 74 , 6556 (1981)

B. Tunable Far Infrared Spectroscopy of NaH ($X^1\Sigma^+$)

The laser magnetic resonance experiment operates within two important constraints. The first is that the species under investigation must be paramagnetic. The second is that the species must have zero field transitions which are sufficiently close to known far infrared lasing lines that they may be tuned into resonance using laboratory magnetic fields. While much can be learned within these constraints, it would clearly be desirable to have a tunable source of far infrared radiation. We have been generating tunable far infrared radiation between 100 GHz and 6 THz from the difference frequency between two CO_2 lasers using a tungsten-nickel point contact diode as the non-linear mixing device. Figure 2 shows a schematic diagram of the spectrometer. CO_2 laser I is stabilized using the saturated fluorescence technique, and its radiation is mixed on the diode with that of the waveguide CO_2 laser. The waveguide laser, which is cavity tuned to provide the tunable FIR difference frequency, is frequency offset locked to a third stabilized laser (CO_2 laser II). The FIR radiation emitted from the diode is collected by a parabolic mirror, sent through a Pyrex absorption cell, and then monitored with a bolometer detector. The many combinations of CO_2 isotopes and lasing lines provides nearly complete coverage of the far infrared. A more detailed description of the spectrometer has been published elsewhere [1].

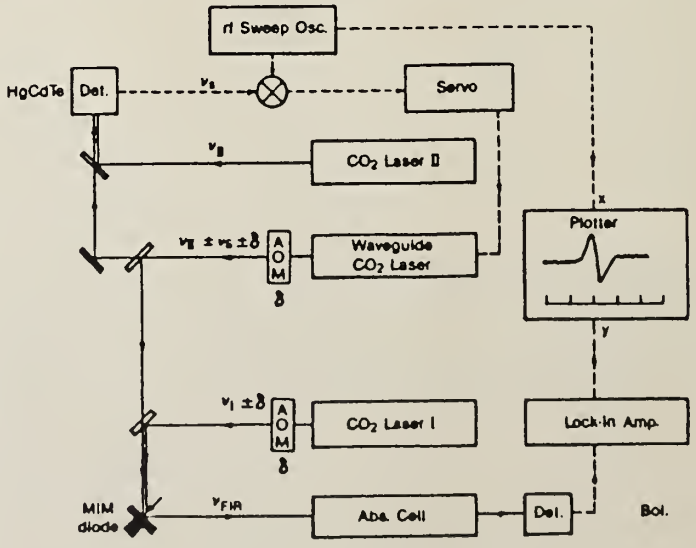

Fig. 2. Diagram of the Tunable Far Infrared Spectrometer

The wide frequency coverage of the spectrometer permits many transitions of a given species to be measured. In addition, the species under investigation need not be paramagnetic. We have demonstrated these features by measuring a total to twelve rotational transitions in both v=0 and v=1 of the ground $^1\Sigma$ state of the sodium hydride molecule. Figure 3 shows the J = 6 ← 5 transition in the v=0 state, and is a single sweep using a 400 ms instrumental time constant. NaH was produced in a dc discharge of H_2 over sodium, as suggested by Sastry, Herbst, and De Lucia [2] who also measured the lowest rotational transition in v=0, 1, 2, and 3. In their work, a fit to Dunham's expansion for the molecular levels was possible only after judicious borrowing of constants from optical data, and the use of isotopic scaling relations. We have measured rotational transition as high as the J = 7 ← 6 transition in v=0 and the J = 8 ← 7 transition in v=1, and have obtained a new set of Dunham coefficients which are independent of optical data or isotopic scaling laws. The constants obtained, which are in generally good agreement with those of previous work, are given in Table III. The high signal-to-noise ratio obtained for NaH demonstrates the utility of the technique for the study of elusive species.

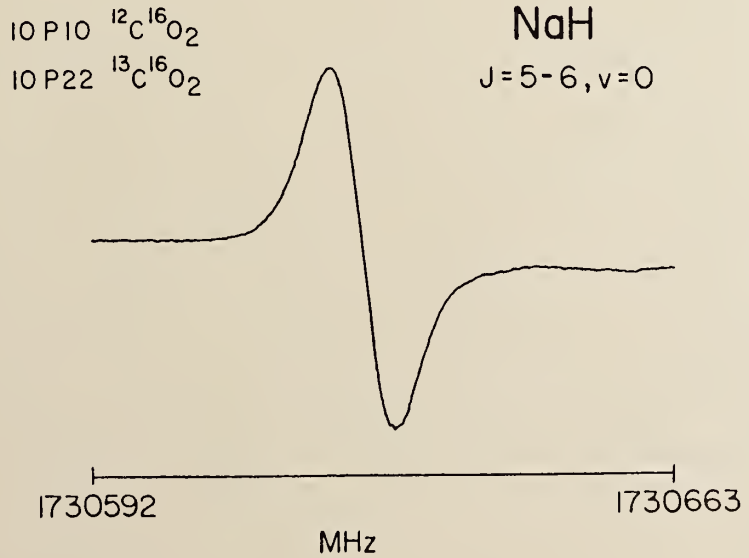

Fig. 3. The J = 5 ← 6, v=0 transition of NaH.

Table III. Dunham Coefficients for NaH

Y_{01}(MHz)	146999.33(30)
Y_{02}	-10.294(2)
Y_{03}	$6.32(20)\times10^{-4}$
Y_{11}	-4110.29(80)
Y_{12}	0.1417(12)
Y_{21}	33.56(54)
Y_{31}	-1.077(96)

References

(1) K.M. Evenson, D.A. Jennings, and F.R. Peterson, Appl. Phys. Lett. 44(6), 576 (1984)

(2) K.V.L.N. Sastry, E. Herbst, and F.C. De Lucia, J. Chem. Phys. 75, 4753 (1981)

A SIMPLE MOLECULAR ORBITAL DESCRIPTION OF RADICAL-MOLECULE REACTIONS

L.M. Loewenstein* and J.G. Anderson
Department of Chemistry and Center for Earth and Planetary Physics, Harvard University, Cambridge, MA, 02138

ABSTRACT

A qualitative application of frontier orbital theory explains the observed correlation of thermal rate constants and activation energies of radical-halogen reactions with the ionization potentials of halogens and the electron affinities of radicals. In the initial interaction of the two species, electrons in the highest occupied orbital of the halogen interact with the lowest unoccupied (or partially unoccupied) orbital of the radical, in effect, exchanging charge. Since electrons may also move in the opposite direction through another orbital interaction, the relative energies of the two processes determines their final importance. The specific dynamical implications of the described orbital interactions are supported by the results of crossed molecular beam experiments.

INTRODUCTION

The reactions of free radicals with gaseous halogen and interhalogen molecules provide an excellent set of data for developing and testing a theory of chemical reactivity that relates the physical properties of the reactants to observed rate constants and scattering behavior. A wide body of measurements - made by thermal methods such as discharge flow and flash photolysis, as well as, recently, by crossed molecular beams - have shown that these gas phase reactions occur with rate constants spanning many orders of magnitude, and with a variety of scattering behaviors. In addition, the properties of the halogens vary in a systematic way. Most simply, fluorine is markedly electronegative, while iodine is only slightly so, with the other halogens in between. We correlate the electronic nature of the halogens to their observed reactivity with radicals.

---

* Current address: Materials Science Laboratory, Texas Instruments Incorporated, P.O. Box 225936, MS 147, Dallas, TX, 75265

THERMAL RATE CONSTANTS

The comparison of room temperature rate constants of halogens with a great number of radicals shows that their reactions with fluorine are usually very slow. For a given radical, as we progess down the halogen column of the periodic chart the rate constant generally increases,[1] so that, for instance, the reaction of a radical with iodine is virtually gas kinetic, as is evidenced by the OH + I_2 reaction.[2] The interhalogens also fit the same trend, when the halogens and interhalogens are all ordered according to their ionization potentials, as is shown in Fig. 1. The increase in reactivity appears to arise largely from a decrease in the activation energy.

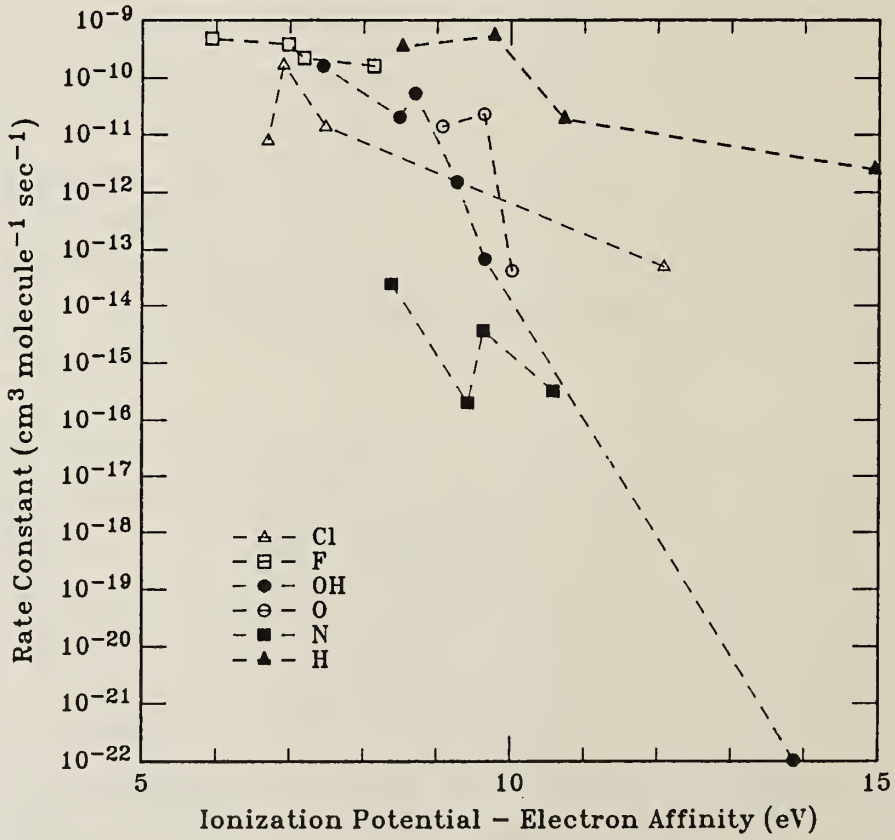

Figure 1. Rate constants at 298K vs.
I.P. (halogen) - E.A. (Radical).

A given halogen's reactivity toward different radical species also varies tremendously. For instance, halogen atoms react very rapidly with halogen molecules, while S, O, and OH reactions are generally slower, and those of N

much slower; the reactions of F and N with bromine, for example, differ by four orders of magnitude. To a large extent, the variation correlates very well with the electron affinity of the radical. The ordering of reaction rates generally follows the same ordering of electron affinities:[1] Cl > Br > F > S > OH > O > N > H. The thermal rate constants of O and OH, which have similar electron affinities, are quite similar. Exceptions to this rule are H and F, which react much more rapidly with halogen molecules than their positions in the electron affinity list imply.

FRONTIER ORBITAL THEORY

A qualitative application of frontier orbital theory[3] explains the observed rate constant correlations with the ionization potential of the halogen molecules, and the electron affinities of the free radicals.[4] During the course of a chemical reaction, the orbitals of the colliding species must be altered to form new molecular orbitals. The energetically most significant interaction is between the frontier orbitals: the highest occupied molecular orbital (HOMO) of one molecule and the lowest unoccupied orbital (LUMO) of the other. In fact, there are two interactions, since both molecules have a HOMO and a LUMO; however, only the less energetic interaction is likely to be important.

In these interactions, electronic charge can be considered to be donated from the HOMO to the LUMO. Consequently, the energetics of charge transfer will be important in determining the courses of the reaction. A type (i) interaction is defined to be one where the halogen accepts an electron from a radical, and a type (ii) where the halogen donates charge to the radical. The interaction of specific orbitals often also implies certain symmetry requirements, since for any transfer of charge to take place, the orbitals must have a net overlap.

We consider two cases: (1) the radical's interacting orbital is spherically symmetric, e.g., the 1s orbital of $H(^2S)$; and (2) the radical's interacting orbital is axially symmetric with an inversion center, e.g., the 2p orbital of $O(^3P)$.

The HOMO-LUMO interactions of H with a halogen, e.g., Cl2, may either be $s(H)\text{-}\sigma_u^*(Cl_2)$ or $s(H)\text{-}\pi_g^*(Cl_2)$ - types (i) and (ii), repectively. Orbital symmetry requires that the type (i) interaction be end-on (Fig. 2), while type (ii) implies

that the interaction is more angular, since the π_g^* orbital extends in wings off of the molecular axis (Fig. 3). Ionization energetics will determine the dominant mechanism; the difference between the adiabatic IP's and EA's should be good indicators of this. Trends in reactivity will result from variations of the IP's and EA's of the reactants.

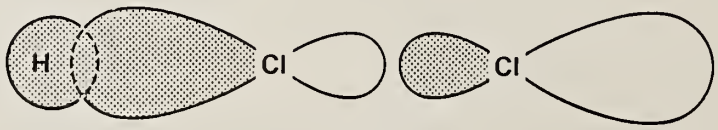

Fig. 2. Type (i) interaction: s(H) - σ^*_u (Cl_2).

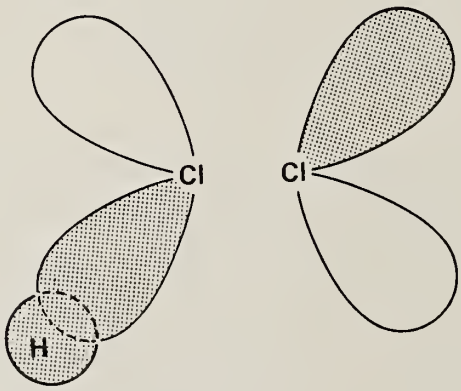

Fig. 3. Type (ii) interaction: s(H) - π^*_g (Cl_2).

The reaction of O(3P) with Cl_2 can be analyzed in the same way. The type (i) interaction is p(O)-σ_u^*(Cl_2): still likely to favor an end-on approach, although symmetry does not rigidly require this. The type (ii) interaction again supports a sideways approach for the same reasons as above; in addition, a second interaction of p(O) with σ_u^*(Cl_2) (Fig. 4) favors a perpendicular approach. The structure in Fig. 4 represents an interaction which may be favored energetically, yet does not lead to products without further molecular rearrangement.

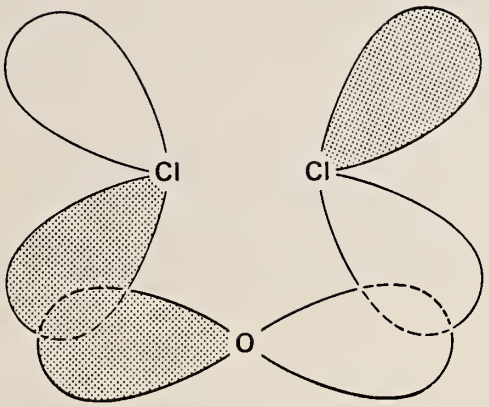

Fig. 4. Type (ii) interaction: $p(O)-\sigma^*_u\ (Cl_2)$.

INTERPRETATION OF EXPERIMENTAL RESULTS

The qualitative frontier orbital model presented here accounts for the observed thermal rate behavior. O and OH, for instance, with similar electron affinities and ionization potentials, have similar rate constants. The addition of the H atom does not much affect the energy of the $2p_x$ or $2p_y$ orbital of O. Moreover, the second unpaired orbital of O is orthogonal to the interacting orbitals, and its effect on the reaction should be minimal.

Scattering behavior, obtained from crossed molecular beam experiments, also supports the model. For instance, the trend in lifetimes of long-lived intermediates[5],

$$\tau OCl_2 < \tau OBr_2 < \tau OI_2, \tau OIC\ell,$$

agrees with the trend that the frontier orbital model predicts for a type (ii) interaction. While the angular distribution of the HCl product of H + Cl_2 reaction is strongly in the backward direction, the Br_2 and I_2 reactions with H have product distributions which peak more and more toward the side. Interpreted as a change in the preferred angle of attack of H on X-X,[6] the results are in concordance with a shift from a type (i) interaction to type (ii), as the electron exchange energetics of the species change.

CONCLUSION

We have presented an interpretation of the observed patterns in the reactivity of halogens with free radicals. While qualitative, the model provides a picture of chemical reactivity that describes both thermal measurements and dynamical observations. The reactions of radicals with other radicals and with unsaturated hydrocarbons may also fit the frontier orbital model. "The goal ... is not kinetics as an end in itself, but it is rather to understand reactivity."[7]

REFERENCES

1. L.M. Loewenstein and J.G. Anderson, J. Phys. Chem. 88, 6277 (1984).
2. L.M. Loewenstein and J.G. Anderson, J. Phys. Chem., submitted.
3. R.G. Pearson, Accts. Chem. Res. 4, 152 (1971).
4. L.M. Loewenstein and J.G. Anderson, J. Phys. Chem., in preparation.
5. R. Grice, Accts. Chem. Res., 14, 37 (1981).
6. D.R. Herschbach, Faraday Disc., 55, 233 (1973).
7. H. Taube, Chem. & Eng. News (May 6, 1985), p. 41.

FREE RADICAL EXCHANGE REACTIONS BETWEEN VITAMIN E AND VITAMIN C IN PEROXIDIZING LIPIDS

J. Löliger, P. Lambelet, M.-C. Savoy and F. Saucy
NESTEC LTD., Research Laboratories
Avenue Nestlé 55, CH-1800 Vevey (Switzerland)

Abstract

Free radical exchange reactions between peroxidizing lipids, Vitamin E and Vitamin C have been evidenced by ESR spectroscopy. In peroxidizing lipids sequential consumption of first Vitamin C and then Vitamin E has been observed using polarography. These free radical exchange reactions have been measured in an homogenous lipid phase as well as in reversed phase evaporation vesicles made using a fraction of soya lecithin.

Introduction

In a great number of vital biological processes, free radical species are involved. The predominant origin of radicals is certainly linked to the reduction of dioxygen during respiration processes (Boschke, 1983 & Gilbert, 1981). Only a minor slipping in one of the numerous defence reactions can have disastrous effects. Superoxide dismutase (Friedovic, 1978), glutathione peroxidase (Willson, 1983), catalase (Wittig, 1980), Vitamin E (Tappel, 1968), Vitamin C (Cort, 1982), Uric acid (Ames, 1981), β-carotene (Burton, 1984), etc., have been claimed to be involved in one or several of these defence mechanisms against oxygen toxicity. A number of diseases and age-related problems have been linked with reactions involving free radicals. For cancer induction (Crary, 1984, Willson, 1984) and ageing (Pryor 1984; Walton, 1980), e.g. radicals seem to play an important role.

A number of authors have proposed experiments showing mechanisms involving the function of the most widely available biological antioxidants, i.e. Vitamin E and Vitamin C, during *in vivo* autoxidation of polyunsaturated lipids of cellular membranes. Experiments and speculations have been published to show the importance of radical exchange reactions during biological lipid peroxidations. A regeneration scheme (Tappel, 1968) has been proposed whereby the primary radical of lipid peroxidation is intercepted by Vitamin E, which is then captured by Vitamin C, etc. (Fig. 1).

Fig. 1 – *Regeneration scheme of antioxidants involved in lipid peroxidation (Tappel 1968).*

A number of authors have been providing experimental proof for this scheme (Packer, 1979; Bascetta, 1983; Niki, 1984 and Barclay, 1984) generating the radicals of Vitamin E and Vitamin C by various initiators.

The inhibition of autoxidation reactions of the highly unsaturated polar lipids encountered in cell membranes of all aerobic organisms is of utmost importance for the survival of aerobic species. Experimental proof available for radical interactions between autoxidizing polyunsaturated lipids and the important biological antioxidants Vitamin E and Vitamin C is already very convincing. It has however not yet been possible to show that these types of radical reactions actually occur in the living cell. It is the aim of this presentation and in part of an earlier paper (Lambelet, 1985) to show results of radical exchange reactions between autoxidizing polyunsaturated lipids, Vitamin E and Vitamin C in systems more closely related to cell membranes.

Materials and methods

Purified phosphatidylcholin (PPC) of isolated soya phospholipids was obtained from Lucas-Meyer, D-2000 Hamburg 28, FRG (with the trade name of Epikuron 200). PPC was composed of 93% phosphatidylcholine, 5% other phospholipids, 2% moisture and triglyerides. About 0.23 mM of Vitamin E was detected in PPC by polarography. PPC had a peroxide value of 14 meq O_2/kg. Chicken fat liquid fraction (CFLF) was prepared according to a procedure already described (Lambelet, 1984). Ascorbyl palmitate (AP) was obtained from Hoffmann-La Roche, CH-4000 Basel, Switzerland and Vitamin E (dl-α-tocopherol) from E. Merck, D-Darmstadt, FRG.

The polarographic determination of AP and Vitamin E were run according to known procedures (Löliger, 1980).

First derivative ESR spectra were recorded at ambient temperature on a Varian E-109 Century series Mark III spectrometer (× band) with 100 kHz magnetic field modulation.

Reverse-phase-evaporation vesicles (REV) containing 3% w/w PPC were prepared according to known procedures (Konings, 1984). As organic solvents methanol and dichloromethane were used. The indicated quantities of Vitamin E (in the organic solvent) and Vitamin C (in water) were added according to the preparations.

Results

An equimolar mixture of Vitamin E and AP (about 2.4 mM each) in oxidizing CFLF gave three different types of ESR spectra, according to the time the reaction was allowed to proceed. At the onset, shortly after mixing (about 15 minutes), the ESR spectrum reported in Fig. 2a was observed.

Fig. 2 – *Behaviour of Vitamin E and AP in autoxidizing CFLF. ESR spectra of CFLF containing AP (2.3 mM), and Vitamin E (2.4 mM).*

a) shortly after mixing,

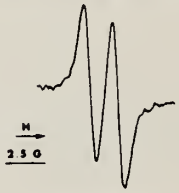

b) 10 days after mixing,

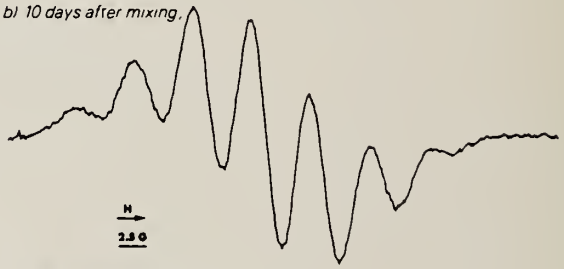

c) 6 days after mixing,

d) determination of residual AP (●) and Vitamin E (■) during autoxidation of CFLF.

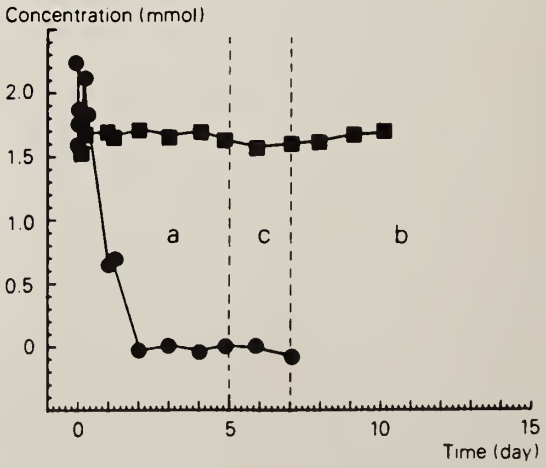

It could be unambiguously attributed to the radical of AP (Lambelet, 1985). After this solution was left at room temperature for about 10 days, the ESR signals completely changed and the ESR spectrum depicted in Fig. 2b was observed. It was assigned to the radical of Vitamin E (Lambelet, 1984). In between, about 6 days after starting the experiment, the badly resolved ESR spectrum represented in Fig. 2c was obtained. During several days, the residual quantities of Vitamin E and AP were determined by polarography (Fig. 2d). It could be seen that the concentration of AP was rapidly decreasing (no longer detectable after more than 7 days) whereas the concentration of Vitamin E stayed almost constant.

REVs (containing 116 mM of Vitamin E and 116 mM Vitamin C) showed by ESR spectroscopy the typical doublet of the radical of Vitamin C (Fig. 3) for about 1/2 hour. Later,

Fig. 3 – *ESR spectrum of the Radical of Vitamin C in REV*

the ESR signal was no longer observed unless the liposomes were brought in close contact with air (bubbling of air for several minutes). The same type of signal (Fig. 3) could then be detected. When the liposomes were formed without adding Vitamin C in the aqueous phase, containing apart from 3% PPC only 116 mM Vitamin E in the lipid phase, one observed the very weak ESR signal reproduced in Fig. 4.

Fig. 4 – *ESR spectrum of the Radical of Vitamin E in REV*

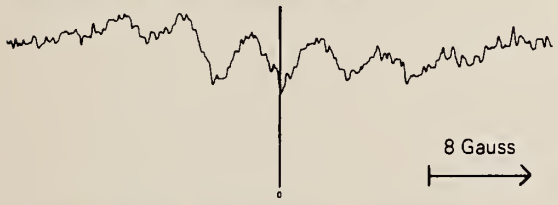

It could tentatively be associated with the radical of Vitamin E (Fig. 2a). After having adjusted the liposomes to 116 mM of Vitamin C, the familiar doublet associated with the radical of Vitamin C appeared.

Discussion

The reactions described above proceeded just as well with many other oxidizing lipids such as trilinoleate, methyllinoleate, etc. CFLF was a source of a highly unsaturated lipid (about 75% unsaturation) which was readily available for this study. AP, with respect to most chemical properties identical to Vitamin C (Pongracz, 1981; Cort, 1982), was chosen for obvious solubility considerations. It was reported earlier (Lambelet, 1985) that CFLF oxidized to a peroxide value of approximately 130 meq. O_2/kg generates radicals of Vitamin E in concentrations high enough to be easily detected by ESR spectroscopy. Since then it was established that also much lower concentrations of hydroperoxides (down to peroxide levels of 15 meq. O_2/kg) induced sufficiently high concentrations of radicals of Vitamin E to be detected by ESR spectroscopy.

The interactions between peroxidizing lipids (CFLF), AP and Vitamin E are summarized in Fig. 2. During a first period, the radical of AP could be observed exclusively. Later on, the only radical detected was the one of Vitamin E (for more than 100 days). The ESR spectrum taken in between is reproduced in Fig. 2c. It could only be speculated that it represented a superimposition of both the signals observed from Vitamin E and AP (with different intensities). Peroxidizing lipids containing Vitamin E only showed the typical signal pattern of the Vitamin E radical. Upon addition of AP it was replaced by the characteristic doublet of the AP radical.

Free radical exchange reactions between oxidizing PPC, Vitamin E and Vitamin C in REV preparations showed in many respects similar behaviour patterns as those of the monophase lipid system. The radical of Vitamin C (Fig. 3) was detected in REVs prepared with Vitamin E and Vitamin C, irrespective of the degree of oxidation of PPC within the limits tested from 15 to 250 meq. O_2/kg. This radical could be observed in liposomes containing concentrations of Vitamin E ranging from about 0.23 to 116 mM, and Vitamin C from 12 to 116 mM. The radical of Vitamin E (Fig. 4) also seemed to be quenched when Vitamin C was added to the already formed REVs. However, a number of important differences were observed between liposomes and the homogeneous lipid system. For example, the radical of Vitamin C could only be observed for approximately half an hour in REVs, whereby it could be observed for several days in the homogeneous system. It could be regenerated in REVs by vigorous aeration of the liposomes too. These free radical exchange reactions in liposomes are not yet fully studied A great number of questions remain open and are still under active investigation.

It could be seen however that the formation of radicals as described here opens up a wide field of interesting possibilities for studying autoxidation damage caused in biological material.

References

Ames, B.N., Cathcart, R., Schwiers, E., Hochstein, P., 1981 Uric acid provides an antioxidant defence in humans against oxidant, and radical-caused ageing and cancer. A hypothesis Proc natl Acad Sci USA 78, 6858-6862

Barclay, L.R.C., Locke, S.J., MacNeil, J.M., Van Kessel, J., Burton, G.W., Ingold K.U., 1984 Autoxidation of micelles and model membranes Quantitative kinetic measurements can be made by using either water-soluble or lipid-soluble initiators with water-soluble or lipid-soluble chain-breaking antioxidants J Am Chem Soc 106, 2479-2481

Bascetta, E., Gunstone, F.D., Walton, J.C., 1983 Electron spin resonance study of the role of Vitamin E and Vitamin C in the inhibition of fatty acid oxidation in a model membrane Chemistry and Physics of Lipids, 33, 207-210

Boschke, F.L., 1983 Radicals in biochemistry Springer, Berlin

Burton, G.W., Ingold, K.U., 1984 β-Carotene an unusual type of lipid antioxidant Science 224, 569-573

Cort, W.M. 1982 Antioxidant properties of ascorbic acid in Foods. in Ascorbic Acid Chemistry, metabolism and uses pp 533-550 Eds P Seib and B.M Tolbert, American Chemical Society, Washington

Crary, E.J., McCarty, S., McCarty, G., McCarty, M.F., 1984 Potential clinical applications for high-dose nutritional antioxidants Medical Hypothesis 13, 77-98

Friedovic, I., 1978 The Biology of oxygen radicals Science 201, 875-880

Gilbert, D.L., 1981 Oxygen and living processes. An Interdisciplinary Approach. Springer, New York

Konings A.W.T., 1984 Lipid peroxidation in liposomes. in Liposome Technology, Vol I, Preparation of liposomes, pp 129-161, Gregoriadis, G., Ed., CRC Press, Boca Raton, Florida

Lambelet, P., Löliger, J. 1985 Chemical Evidence for Interactions between Vitamin E and Vitamin C, Experientia, in Press

Lambelet, P., Löliger, J. 1984 The Fate of antioxidant radicals during lipid autoxidation I The Tocopheroxyl radicals Chemistry and Physics of Lipids, 35, 185-198

Löliger, J., Saucy, F. 1980 Rapid determination of antioxidants with an electrochemical flow-through detector Z. Lebensm Unters Forsch 170, 413-416

Niki, E., Yamamoto, Y., Kamiya, Y., 1984 Oxidation of phosphatidylcholine and its inhibition by Vitamin E and Vitamin C, in Oxygen radicals in chemistry and biology, pp 273-280 Eds W Bors, M Saran, D Tait, Walter de Gruyter & Co., Berlin

Packer J.E., Slater, T.F., Willson, R.L., 1979 Direct observation of a free radical interaction between Vitamin E and Vitamin C Nature 278, 237-738

Pryor, W.A., 1984 Free Radicals in autoxidation and in ageing, in Free Radicals in molecular biology ageing and disease, pp 13-41, Armstrong, O., Ed., Raven Press, New York

Pongracz, G., Klaui, H., 1981 Ascorbic acid and its derivatives as antioxidants in oils and fats, in Vitamin C Ascorbic Acid pp 139-166 Eds J.N Counsell, O.H Horning, Applied Science Publishers, London

Tappel, A.L., 1968 Will antioxidant nutrients slow ageing processes? Geriatrics 23, 97-105

Walton, J.R., Packer L., 1980 Free radical damage and protection Relationship to cellular ageing and cancer, in Vitamin E, a comprehensive treatise, pp 495-517 Eds L.J Machlin, Oekker, Basel

Willson, R.L., 1983 Free radical protection Why Vitamin E, not Vitamin C, β-Carotene or glutathione? In Biology of Vitamin E, Ciba Foundation Symposium, 101, pp 19-44, Pitman, London

Willson, R.L., 1984 Peroxy free radicals and enzyme inactivation in radiation injury and oxygen toxicity protection by superoxide dismutase and antioxidants Lancet, 804

Wittig, L.A., 1980 Vitamin E and lipid antioxidants in free radical initiated reactions. in Free radicals in Biology, Vol IV, pp 295-319, Ed., W.A Pryor, Academic Press New York

UV LASER-INDUCED RADICAL ETCHING OF INTEGRATED CIRCUIT MATERIALS

G. L. Loper and M. D. Tabat
Chemistry and Physics Laboratory
The Aerospace Corporation
P. O. Box 92957
Los Angeles, CA 90009

ABSTRACT

Atomic fluorine, generated by the 193 nm ArF laser photolysis of carbonyl difluoride or nitrogen trifluoride vapor, can provide practical etch rates and selectivities for removing polycrystalline Si deposited on SiO_2 substrates, and the refractory metals W, Mo, or Ti from SiO_2. These atomic fluorine generation processes have been demonstrated to etch substrates with a spatial resolution as good as 0.3 μm. SiO_2 substrates can be efficiently etched by difluoromethylene radicals produced by the KrF laser photolysis of CF_2Cl_2. This method should allow the selective etching of SiO_2 over Si or Al. The results obtained indicate the possibility of developing similar rapid and specific laser etching processes for the different substrate combinations used in fabricating integrated circuits.

I. Introduction

Localized chemical reactions on surfaces can be efficiently promoted by lasers. Laser-induced surface processes such as chemical etching, chemical vapor deposition, semiconductor doping, and metal alloying are thus being examined for use in integrated circuit fabrication. As reviewed by Chuang,[1] efficient etching processes have been demonstrated with infrared and visible lasers for selected materials. However, these lasers cannot pattern surfaces with submicrometer linewidths unless nonlinear chemical processes are employed. Ultraviolet (UV) laser enhanced etching processes are thus being increasingly investigated as methods to pattern materials with linewidths below 1 μm.[2-7]

We are investigating the use of an UV laser-induced, radical-etching technique as a means of simultaneously patterning and etching, with submicrometer resolution, the various materials used in electronic devices.[3,6,7] By this technique, photodissociation processes involving one or more UV photons generate radical etchants from precursor compounds near a gas/substrate interface. The substrate may undergo etching reactions with radicals with lifetimes sufficiently long to collide with it. The substrate is removed in the localized regions exposed to light by the formation of volatile compounds containing the substrate elements. Excessive broadening of the patterned lines due to diffusion of the radicals from the irradiation zone can be controlled by buffer and radical scavenging gases.[2] The proper choice of radical species permits high etch selectivities between various substrates.

Integrated circuits are built up in multiple layers by successively depositing and patterning thin semiconductor, insulator, or metal films on a substrate. Before the laser etching technique can be used to fabricate devices, efficient and selective, submicrometer-resolution etching processes need to be developed for the substrate combinations used in silicon devices. This paper reviews our work toward developing atomic fluorine generation processes, based on the

ArF laser photolyses of carbonyl difluoride (COF_2) or nitrogen trifluoride (NF_3), that can rapidly and specifically etch the important substrate combinations: polycrystalline (poly)-Si over SiO_2,[3,6] and the refractory metal electrode materials W,[3] Mo,[6] and Ti[6] over SiO_2. These fluorine atom generation processes are shown to produce features as small as 0.3 μm on substrates.[7] SiO_2 is also shown to be efficiently etched by difluoromethylene radicals produced by the KrF laser photolysis of CF_2Cl_2.[3]

The results obtained indicate that it should be possible to develop similar laser etching processes for other substrate combinations. The technique is being developed for use with UV excimer lasers which, due to their short wavelength, high average power,[8] and low spatial coherence[9] would be well-suited for practical fabrication applications. The method could greatly simplify the processing of submicrometer-linewidth devices by eliminating photoresist patterning and acid or plasma etching steps.

II. Background

Several criteria must be considered in designing efficient UV laser etching processes. (1) The elements that comprise the material to be etched must readily form species upon reaction with the etchant that volatilize at the surface temperatures achieved during processing. (2) The precursor compounds used must decompose to form the desired radicals in high yield upon absorption of one or more UV photons. (3) These compounds must efficiently absorb radiation at the laser wavelengths and intensities used.

On the basis of previous RF-discharge plasma etching studies,[10] either or both trifluoromethyl radical ($\cdot CF_3$) and difluoromethylene radical ($:CF_2$) have been postulated as the active etchants in fluorocarbon plasmas for the efficient and selective removal of SiO_2 layers deposited on either Si or Al. SiO_2 removal results from the formation of volatile fluorides of silicon and oxides of carbon. Plasma etching studies have also shown that atomic fluorine can

remove poly-Si or certain metals (W, Mo, Ta, Te, Ti) deposited on SiO_2.[11] These materials are removed by the formation of volatile fluorides.

III. Experimental

Etching efficiency and selectivity studies[3,6] were performed by placing the wafer to be etched in a photolysis cell containing radical precursor and helium buffer gases and successively exposing various small regions of the wafer surface with pulsed (10 Hz) ArF (193 nm) or KrF (248 nm) laser light for different exposure times. The laser output was collimated with a lens system to the desired fluence before it was passed into the photolysis cell through a Suprasil fused silica window. The wafer was mounted 8.5 mm behind the cell window. An aperture was placed in front of the cell window to define the wafer exposure region. The surface profiles of the exposed regions on the wafer were determined with a Sloan Dektak mechanical stylus profilometer.

A simple proximity exposure experiment was performed to examine the spatial resolution of the laser etching processes.[7] The near-field diffraction pattern produced by a single slit, when illuminated with laser output, was used to induce radical etching of a wafer surface. This slit was held close to the wafer surface inside the photolysis cell. The etch pattern produced was then examined by scanning electron microscopy (SEM) and compared with the predicted intensity profile for the diffraction pattern.

In these experiments a continuous flow of precursor gas was maintained across the wafer surface by a convection mixing loop on the photolysis cell. Laser fluences were kept sufficiently low that material was not removed from the wafer surface in the absence of precursor gas. A Scientech A38-0103 power meter was used to measure average laser powers.

The cell could be attached to a mercury-free, greaseless vacuum line for evacuation and pressurization with various gases. Gas pres-

sures were measured on the vacuum line with either an MKS Instruments, Inc. type 77 pressure meter with a 10-Torr full range differential pressure head, a 0-50 Torr Wallace and Tiernan pressure gauge, or a 0-800 Torr Wallace and Tiernan pressure gauge.

Radical precursor compounds of purity 98% or greater were used. Samples were deaerated at liquid nitrogen temperature prior to use. High purity helium (99.999%) was used as the buffer gas. UV absorption spectra of the precursor compounds were measured in the gas phase on a Cary 14 spectrophotometer. Compound purities were confirmed by the good agreement between these spectra and standard literature spectra. The various wafer substrate combinations employed were obtained from Thin Film Technology and CVD Systems and Services, Inc.

IV. Results and Discussion

Etching of Poly-Si and W by 193 nm COF_2 Photolysis Process

Figure 1 shows the results of experiments carried out to determine the feasibility of using fluorine atoms, generated by the COF_2 photolysis process of Eq. 1, to remove poly-Si or W from SiO_2.[3,6]

$$F-\overset{O}{\overset{\|}{C}}-F + h\nu\ (193\ nm) \rightarrow 2\cdot F + C\equiv O \qquad (1)$$

Wafers with a 4000 Å thick poly-Si layer deposited on silicon SiO_2 and a 4600 Å thick layer of W deposited on (100) p-type Si were irradiated with ArF laser output (surface fluence 85 mJ/cm^2) for various exposure times in 260 Torr COF_2/500 Torr helium mixtures. The average etch depths at the different exposure locations on these wafers are plotted in Fig. 1 versus the total number of photons incident on the wafer surfaces at each location.

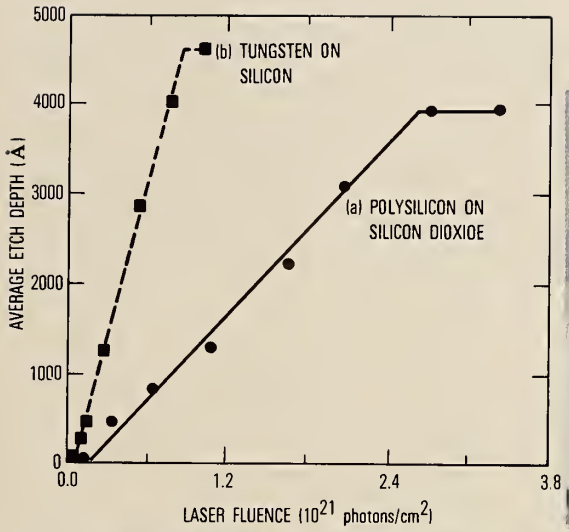

FIG. 1. Laser-generated ·F atom etching results for (a) a wafer containing a 4000 Å thick layer of poly-Si deposited on SiO_2, and (b) a wafer containing a 4600 Å thick layer of tungsten on (100) p-type Si.

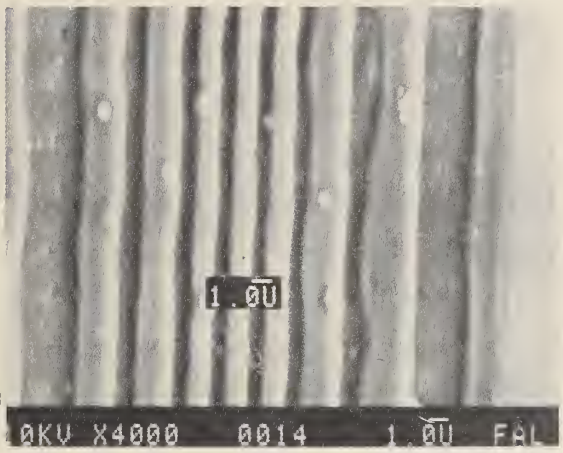

FIG. 2. Submicrometer-resolution etching of poly-Si surface by ArF laser photolysis of COF_2.

The average etch depth for the poly-Si wafer can be observed to increase linearly with exposure time to 4000 Å where the underlying SiO_2 layer is reached and where etching proceeds with very poor efficiency. The marked decrease in etching efficiency observed here for SiO_2 compared to poly-Si indicates that the COF_2 photolysis process can be used to remove poly-Si deposited on SiO_2 with high selectivity. The process also efficiently removes poly-Si. Poly-Si etch rates of 0.13 Å/laser pulse were obtained under the modest fluence conditions employed. Etch rates of this magnitude would be suitable for fabrication applications where high average power excimer lasers are used. For example, with available 200 W excimer lasers, it would be possible under the fluence conditions employed here to remove poly-Si from a 9 cm^2 area of a wafer at the rate 2,000 Å/min. This etching rate is equal to removal rates typically obtained in RF-discharge plasma etching applications.

Figure 1b shows that even more efficient etch rates are obtained for W under the same conditions used in the poly-Si etching experiment. The average etch depth can be observed to increase

linearly at an etch rate of 0.48 Å/pulse until the underlying silicon substrate is reached where etching is a factor of four less efficient. This etch rate difference would be suitable for practical etching processes. From the poly-Si over SiO_2 etching results shown in Figure 1a, it can also be concluded that this process will allow the highly selective removal of W from SiO_2. The W etch rate observed in Figure 1b corresponds to the removal of one W atom for every 280 incident photons. Under the fluence conditions employed here, it would be possible to remove tungsten from a 9 cm^2 are of a wafer at the rate of 7,500 Å/min with a 200 W excimer laser.

Besides providing practical etch efficiencies and selectivities for poly-Si or W deposited on SiO_2, the fluorine atom generation process based on the ArF laser photolysis of COF_2 can etch surfaces with submicrometer linewidths.[7] This was demonstrated by illuminating a poly-Si surface with the Fresnel diffraction pattern produced by a single slit to induce etching by this process.

In the Fresnel limit, a series of fringes appear within the image of the slit on the wafer. The number of these fringes increase as a dimensionless parameter $\Delta\nu = d(2/\lambda r)^{1/2}$ increases, where d is the slit width, λ is the illumination wavelength, and r is the distance between the slit and wafer.[12] Under the proper conditions (e.g. the $\Delta\nu = 7.9$ case when d = 30 μm and r = 150 μm), the widths of intensity peaks at their half-heights can be made to be less than 1μm in portions of the diffraction pattern.

An SEM micrograph of a portion of the Fresnel pattern etched into the poly-Si surface by the COF_2 photolysis process is shown in Fig. 2. Here etching was carried out under the same fluence and pressure conditions as employed in the etch efficiency and selectivity studies above. The dark areas in Fig. 2 are due to grooves that have been etched into the surface by the laser generated fluorine atoms. The bright areas are due to the remaining surface ridges. The groove and ridge positions correspond to regions of intensity maxima and minima in the incident intensity profile.

Careful examination of the etched pattern showed that it reproduced the incident profile predicted by diffraction theory with good fidelity. In addition, the widths of some of the more narrow grooves in Fig. 2 are observed to be close to 0.5 μm. These results lead to the important conclusion that the fluorine atom etching process based on the ArF laser photolysis of COF_2 does not limit the production of etched features with submicrometer linewidths on surfaces.

Etching of Mo and Ti by 193 nm NF_3 Photolysis Process

Although Mo, like Si and W, can form volatile fluorides, Mo etching by the COF_2 photolysis process in Eq. 1 was found to be inefficient.[6] This may be due to the formation of molybdenum carbonyls of low voltatility that inhibit molybdenum fluoride formation. As shown in Fig. 3a, however, the efficient and selective etching of Mo deposited on SiO_2 was obtained by the photolysis process described by Eq. 2.

$$NF_3 + h\nu\ (193\ nm) \rightarrow n \cdot F + NF_{3-n} \qquad (2)$$

where n is 1,2, or 3

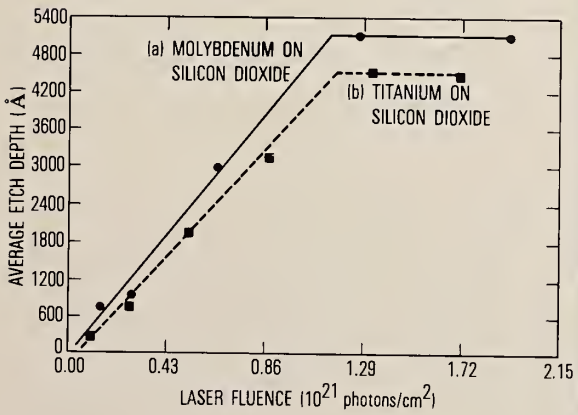

FIG. 3. Laser-generated ·F atom etching results for (a) a wafer containing a 5000 Å thick layer of Mo deposited on SiO_2, and (b) a wafer containing a 4500 Å thick layer of Ti on SiO_2.

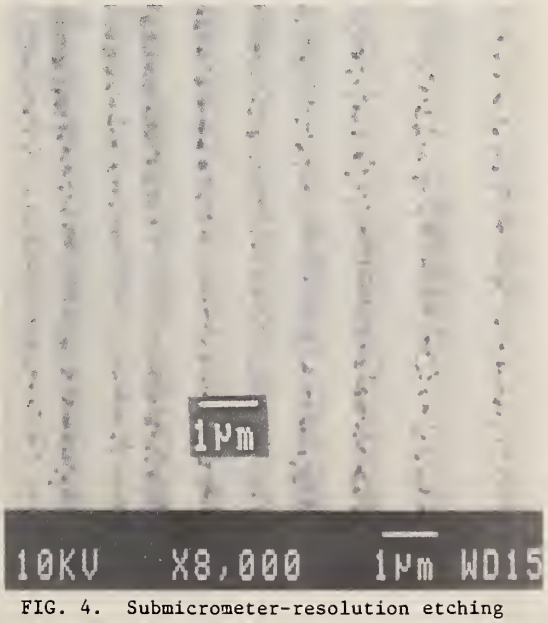

FIG. 4. Submicrometer-resolution etching of Mo surface by ArF laser photolysis of NF_3.

A wafer with a 5000 Å thick Mo layer deposited on SiO_2 was irradiated in various regions with ArF excimer laser output (surface fluence 57 mJ/cm^2) in the presence of 750 Torr of NF_3. Here, the average etch depth can be observed to increase linearly at an etch rate of 0.22 Å/laser pulse until the SiO_2 substrate is reached and etching is inefficient. This Mo etch rate corresponds to the removal of one Mo atom for every 390 incident photons. With a 200 W excimer laser it would be possible under the fluence conditions employed here to remove Mo over a 9 cm^2 area of a wafer surface at the rate of about 6000 Å/min or three times faster than practical plasma etching rates.

The photolysis process described by Eq. (2) is also capable of efficiently and specifically removing Ti from SiO_2.[6] The results of etching studies performed on wafer with a 4500 Å thick Ti layer deposited on SiO_2 are shown in Fig. 3b. When irradiated in the presence of 750 Torr of NF_3 at an ArF laser surface fluence of 115 mJ/cm^2, Ti was removed from the wafer in a linear manner at a rate of 0.29 Å/laser pulse until the SiO_2 substrate was reached where etching was again inefficient. The Ti etch rate obtained corresponds to the removal of one Ti atom for every 670 incident photons. Under these fluence conditions a 200-W laser could remove Ti from a 9 cm^2 area of wafer at the rate of 2400 Å/min.

The fluorine atom etching process based on the ArF laser photolysis of NF_3 also does not limit the production of submicrometer linewidths on surfaces.[7] A single slit Fresnel diffraction pattern, with submicrometer dimension fringes ($\Delta\nu = 7.9$ case when d = 30 μm and r = 70 μm) was used to induce etching by the NF_3 photolysis process in a Mo substrate. An SEM micrograph of a portion of the pattern etched into the Mo surface is shown in Fig. 4. The same etching conditions were employed as used above for Mo. The etched pattern in Mo accurately replicated the predicted incident intensity profile. Etched grooves with widths as small as 0.3 μm can be observed in Fig. 4.

Etching of SiO_2 by 248 nm CF_2Cl_2 Photolysis Process

Experiments have been performed to compare the etching efficiencies of silicon dioxide by $\cdot CF_3$ and $:CF_2$ radicals produced from various precursor compounds.[3] Under our test conditions, as described below, the photolysis processes designed to produce $\cdot CF_3$ radicals were found to etch SiO_2 with poor efficiency. However, efficient silicon dioxide etching was achieved with a process designed to produce $:CF_2$ radicals.

Two different methods were examined to produce $\cdot CF_3$ by the KrF laser-induced photodecomposition of hexafluoroacetone. These included the direct photolysis of hexafluoroacetone (Eq. 3) and the sensitized photodecomposition of hexafluoroacetone as the result of collisional singlet electronic energy transfer processes from monofluorobenzene (Eq. 4).

$$CF_3\overset{O}{\overset{\|}{C}}CF_3(S_o) + h\nu \ (248\ nm) \rightarrow CF_3\overset{O}{\overset{\|}{C}}CF_3(S_1) \qquad (3)$$

$$CF_3\overset{O}{\overset{\|}{C}}CF_3(S_1) \rightarrow \cdot CF_3 + \cdot\overset{O}{\overset{\|}{C}}CF_3(\nu)$$

$$\rightarrow 2\cdot CF_3 + C{\equiv}O$$

$$C_6H_5F(S_o) + h\nu \ (248\ nm) \rightarrow C_6H_5F(S_1) \qquad (4)$$

$$C_6H_5F(S_1) + CF_3\overset{O}{\overset{\|}{C}}CF_3(S_o) \rightarrow C_6H_5F(S_o) + CF_3\overset{O}{\overset{\|}{C}}CF_3(S_1)$$

$$CF_3\overset{O}{\overset{\|}{C}}CF_3(S_1) \rightarrow \text{products as in Eq. 3}$$

The sensitized decomposition process was investigated since hexafluoroacetone absorbs weakly at 248 nm. Monofluorobenzene was selected as the sensitizer because it efficiently absorbs 248

nm light and its singlet emission profile possesses good spectral overlap with the hexafluoroacetone $S_1 \rightarrow S_o$ absorption profile. In each case the SiO_2 etching was found to be inefficient under the conditions employed. Mechanical stylus traces of the SiO_2 surface profiles revealed significant photopolymer deposition. This photopolymer may have formed as the result of reactions of trifluoroacetyl radical with hexafluoroacetone.

Photolysis processes were also examined to produce $\cdot CF_3$ from trifluoromethyliodide (Eq. 5), trifluoromethylbromide (Eq. 6), and trifluoronitrosomethane (Eq. 7).

$$CF_3I + h\nu\ (248\ nm) \rightarrow \cdot CF_3 + \cdot I \qquad (5)$$

$$CF_3Br + h\nu\ (193\ nm) \rightarrow \cdot CF_3 + \cdot Br \qquad (6)$$

$$CF_3NO + h\nu\ (193\ nm) \rightarrow \cdot CF_3 + \cdot NO \qquad (7)$$

Although photopolymer deposition was substantially reduced in these processes compared to that observed in the hexafluoroacetone processes, minimal SiO_2 etching was observed in each case for the conditions used. It is possible that involatile species form to inhibit silicon dioxide etching. In addition, it was found that the SiO_2 etching efficiency did not improve when hydrogen was added to the photolysis mixtures containing trifluoromethyliodide or trifluoromethylbromide to scavenge $\cdot I$ and $\cdot Br$ atoms. Further work, including spectroscopic studies to determine the $\cdot CF_3$ concentrations formed under our experimental conditions, will be carried out in an attempt to determine whether $\cdot CF_3$ is inherently inefficient as an etchant for silicon dioxide. These results strongly suggest that $\cdot CF_3$ etches silicon dioxide with poor efficiency. These conclusions have been corroborated by Brannon in a recent study.[14]

Efficient etch rates of silicon dioxide were obtained by the process designed to produce $:CF_2$ through the KrF laser photolysis of dichlorodifluoromethane (Eq. 8).

$$CF_2Cl_2 + 2h\nu\ (248\ nm) \rightarrow :CF_2 + 2\cdot Cl \text{ or } 2\ Cl \qquad (8)$$

A feature etched into a silicon dioxide layer by this process had an etch depth of about 650 Å when only 5100 laser pulses (0.13Å/ pulse) were used at a laser fluence of 270 mJ/cm^2. In this case, a 100 Torr dichlorodifluoromethane/660 Torr helium photolysis mixture was used. SiO_2 removal rates equal to practical plasma etching rates (2000Å/ min) should be possible by this process over a 3 cm^2 wafer area with a 200 W excimer laser.

Work is being carried out to determine the efficiencies of etching Si and Al by this process. If silicon and aluminum etching by $:CF_2$ radical is inefficient, as suggested by RF-discharge plasma etching studies, then this process will be useful for the efficient and selective removal of SiO_2 over either Si or Al substrates.

V. Conclusions

Atomic fluorine can be efficiently generated by the ArF laser photolysis of COF_2 and NF_3. Etching methods based on the COF_2 photolysis process can rapidly and specifically remove poly-Si from SiO_2, and W from SiO_2 dioxide or Si. Etching methods based on the NF_3 photolysis process can efficiently and selectively remove Mo or Ti from SiO_2. These processes will be capable of etching various substrates that can readily form volatile fluorides. The processes can also etch surfaces with linewidths well below 1 μm. This was demonstrated by illuminating Mo and poly-Si surfaces with submicrometer-dimension Fresnel fringes to induce etching by these processes. The narrow linewidths produced on these substrates indicate that the laser photolysis processes and resulting surface etch chemistry take place with a spatial resolution as good as 0.3 μm.

$:CF_2$ radical can be generated by the KrF laser photolysis of CF_2Cl_2. This process can efficiently etch SiO_2 and should allow its selective removal of from Si or Al substrates. Our studies suggest $:CF_2$ radical is a more effective SiO_2 etchant than $\cdot CF_3$ radical.

The results obtained indicate that it should be possible to develop similar etching processes for all the substrate combinations used in complex integrated circuits.

Acknowledgment

This work was supported by Aerospace Sponsored Research.

References

1. T. J. Chuang, J. Vac. Sci. Technol. 21 798 (1982); Mater. Res. Soc. Symp. Proc. 17. 45 (1983).

2. D. J. Ehrlich, R. M. Osgood, Jr., and T. F. Deutsch, Appl. Phys. Lett. 36, 698 (1980).

3. G. L. Loper and M. D. Tabat, Proceedings International Conference on Lasers '83, San Francisco, CA, December, 12-16 1983; Proc. Soc. Photo-Opt. Instrum. Eng. 459, 121 (1984).

4. P. Brewer, S. Halle, and R. M. Osgood, Jr., Appl. Phys. Lett. 45, 475 (1984).

5. D. J. Ehrlich, J. Y. Tsao, and C. O. Bozler, J. Vac. Sci. Technol. B 3, 1 (1985).

6. G. L. Loper and M. D. Tabat, Appl. Phys. Lett. 46, 654, 1985.

7. G. L. Loper and M. D. Tabat, J. Appl. Phys., to appear 15 Oct. 1985.

8. T. S. Fahlen, IEEE J. Quantum Electron QE-16, 1260 (1980); R. R. Butcher, R. A. Tennant, G. F. Erickson, S. L. Swisher, and W. L. Willis, AIP Conf. Proc. 100, 66 (1983).

9. K. Jain, C. G. Willson, and B. J. Lin, IBM J. Res. Dev. 26, 151 (1982); IEEE-Electron Device Lett. EDL-3, 53 (1982).

10. R. A. H. Heinecke, Solid State Electron. 18, 1146 (1975).

11. R. G. Poulsen, J. Vac. Sci. Technol. 14, 266 (1977).

12. M. Born and E. Wolf, Principles of Optics, fifth edition (Pergamon, New York, 1975); E. Hecht and A. Zajac, Optics (Addison, Wesley, Reading, MA, 1974).

13. G. L. Loper and E. K. C. Lee, J. Chem. Phys. 63, 264 (1975).

14. J. H. Brannon, to appear J. Phys. Chem.

KINETICS AND MECHANISMS OF THE GAS PHASE REACTIONS OF THE NO_3 RADICAL WITH A SERIES OF REDUCED SULFUR COMPOUNDS

Hélène Mac Leod, Sara M. Aschmann, Roger Atkinson,
Ernesto C. Tuazon, Janet A. Sweetman
Arthur M. Winer and James N. Pitts, Jr.

Statewide Air Pollution Research Center
University of California
Riverside, California 92521

Abstract. The gas phase reactions of the NO_3 radical with the reduced sulfur compounds COS, CS_2, CH_3SH, C_2H_5SH and CH_3SSCH_3 have been investigated. Using a relative rate technique and long pathlength Fourier transform infrared (FT-IR) absorption spectroscopy, rate constants for these reactions have been determined, at 297 ± 2 K in one atmosphere of air, to be (in units of 10^{-13} cm^3 $molecule^{-1}$ s^{-1}): COS, <0.0004; CS_2, <0.008; CH_3SH, 10 ± 3; C_2H_5SH, 12 ± 3; and CH_3SSCH_3, 0.42 ± 0.09. A number of products from these reactions were determined using FT-IR absorption spectroscopy and combined gas chromatography-mass spectrometry (GC-MS). Atmospheric implications of these kinetic and product data are discussed.

INTRODUCTION

The biogenic emissions of reduced sulfur compounds such as hydrogen sulfide (H_2S), carbon disulfide (CS_2), carbonyl sulfide (COS), methanethiol (CH_3SH), ethanethiol (C_2H_5SH), dimethyl sulfide (CH_3SCH_3) and dimethyl disulfide (CH_3SSCH_3) are considered to be the most important sources of sulfur in the troposphere.[1-4]

Until recently it has been believed that reaction with the OH radical is the most important atmospheric loss process for H_2S,[5] CS_2[6] and the sulfur-containing organics.[5] However, we have recently shown that for CH_3SCH_3 the nighttime reaction with the NO_3 radical may dominate over the daytime reaction with OH radicals.[7,8] The NO_3 radical has been recognized as an important reactive species of nighttime atmospheres[9-15] and may also react rapidly with the other sulfur containing compounds.

In this work we have determined the rate constants, and investigated the reaction products and mechanisms, of the gas-phase reactions of the

NO_3 radical with COS, CS_2, CH_3SH, C_2H_5SH and CH_3SSCH_3 in air at atmospheric pressure and 297 ± 2 K.

EXPERIMENTAL

Kinetic Measurements

The experimental technique used for the determination of NO_3 radical reaction rate constants was a relative rate method which has been described in detail previously.[7,16] This technique is based upon monitoring the relative decay rates of the sulfur compound being studied and a reference organic, whose NO_3 radical reaction rate constant is reliably known, in the presence of NO_3 radicals.

NO_3 radicals were generated by the thermal decomposition of N_2O_5 in air.

$$N_2O_5 \xrightarrow{M} NO_2 + NO_3 \qquad (1)$$

$$NO_2 + NO_3 \xrightarrow{M} N_2O_5 \qquad (2)$$

Providing that the sulfur compound and the reference organic react negligibly with N_2O_5 and NO_2 (see below), then under the experimental conditions employed the sole chemical loss process of these organics was due to their reaction with the NO_3 radical:

$$NO_3 + \text{sulfur compound} \rightarrow \text{products} \qquad (3)$$

$$NO_3 + \text{reference organic} \rightarrow \text{products} \qquad (4)$$

Additionally, small amounts of dilution occurred from the incremental additions of N_2O_5 to the reactant mixture. Thus

$$\ln\left\{\frac{[\text{sulfur compound}]_{t_o}}{[\text{sulfur compound}]_t}\right\} - D_t = \frac{k_3}{k_4} \ln\left\{\frac{[\text{reference organic}]_{t_o}}{[\text{reference organic}]_t}\right\} - D_t \qquad (I)$$

where $[\text{sulfur compound}]_{t_o}$ and $[\text{reference organic}]_{t_o}$ are the concentrations of the sulfur compound and the reference organic, respectively, at time

t_o, [sulfur compound]$_t$ and [reference organic]$_t$ are the corresponding concentrations at time t, and k_3 and k_4 are the rate constants for reactions (3) and (4), respectively. D_t is the dilution factor and was typically 0.004 per N_2O_5 addition. Hence, plots of [ln([sulfur compound]$_{t_o}$/[sulfur compound]$_t$)-D_t] against [ln([reference organic]$_{t_o}$/[reference organic]$_t$)-D_t] should yield straight lines of slope k_3/k_4 and zero intercept.

Rate constant determinations were carried out in a ~2400 liter all-Teflon environmental chamber or a 5800-liter evacuable, Teflon-coated environmental chamber at room temperature (297 ± 2 K) and atmospheric pressure (~740 torr), with the diluent gas being dry purified air. These chambers were equipped with in-situ multiple-reflection White-type optical systems interfaced to FT-IR absorption spectrometers. CS_2, COS, CH_3SH, C_2H_5SH and CH_3SSCH_3 were monitored by FT-IR absorption spectroscopy, using pathlengths of 62.9 or 95.8 m and a resolution of 1 cm^{-1} (unapodized), at the following frequencies: CS_2, 1530 cm^{-1}; COS, 2071.7 cm^{-1}; CH_3SH, 2947.3 cm^{-1}; C_2H_5SH, 2988.8 cm^{-1}; and CH_3SSCH_3, 2927.5 cm^{-1}. CH_3SSCH_3 was also monitored by gas chromatography with flame ionization detection (GC-FID).

The initial concentrations of the sulfur compounds were ~2.4 x 10^{13} molecule cm^{-3} for CS_2 and COS, ~2.4 x 10^{14} molecule cm^{-3} for C_2H_5SH and CH_3SSCH_3, and ~5 x 10^{14} molecule cm^{-3} for CH_3SH. The reference organic, propene or trans-2-butene, was present at an initial concentration of ~2.4 x 10^{13} molecule cm^{-3} and was monitored by GC-FID.

Up to six incremental amounts of N_2O_5 [(7-14) x 10^{13} molecule cm^{-3} per addition] were added to the reactant mixtures during an experiment. In order to extend the reaction times beyond the mixing time, NO_2 [(1.2-2.4) x 10^{14} molecule cm^{-3}] was also included in the reaction mixtures to drive the equilibrium between NO_3 radicals, NO_2 and N_2O_5 toward N_2O_5. Varying this initial NO_2 concentration also allowed checks to be made that the reaction observed was between the sulfur compound and the NO_3 radical, and not between the sulfur compound and N_2O_5.

Product Analyses

In-situ long pathlength FT-IR absorption spectroscopy, GC-FID and combined GC-MS were employed to identify and quantify the products formed

from the reactions of CH_3SH, C_2H_5SH and CH_3SSCH_3 with NO_3 radicals. These experiments were conducted in the 5800-liter evacuable Teflon-coated environmental chamber under similar experimental conditions to the kinetic experiments. For each of these sulfur compounds, two experiments were carried out, one in an atmosphere of 80% N_2 + 20% O_2, and the other in an atmosphere of N_2. Each experiment involved the addition of three incremental amounts of N_2O_5 (~1.2 x 10^{14} molecule cm^{-3} each) to the reactant mixture.

RESULTS

Kinetic Measurements

Using the relative rate technique described above, rate constants for the reactions of the NO_3 radical with COS, CS_2, CH_3SH, C_2H_5SH and CH_3SSCH_3 were determined, with propene as the reference organic for COS and CS_2 and trans-2-butene for CH_3SH, C_2H_5SH and CH_3SSCH_3. Prior to each experiment it was verified that the dark decays of the sulfur compound and the reference organic were negligible in the presence of NO_2.

The experimental data obtained for CH_3SH, C_2H_5SH and CH_3SSCH_3 are plotted according to equation (I) in Figure 1. Least squares analyses of these data yield the rate constant ratios k_3/k_4 given in Table 1. The data obtained for COS and CS_2 yield upper limits to the rate constant ratios k_3/k_4, also given in Table 1.

The rate constant ratios k_3/k_4 obtained from the plots in Figure 1, and the upper limits of k_3/k_4 calculated for COS and CS_2, can be placed on an absolute basis by using rate constants k_4 for the reactions of NO_3 radicals with trans-2-butene and propene of (3.80 ± 0.43) x 10^{-13} and (7.6 ± 1.6) x 10^{-15} cm^3 $molecule^{-1}$ s^{-1}, respectively.[17] The rate constants k_3 so obtained for the reduced sulfur compounds studied are listed in Table 1.

Product Analyses

Features of the product spectra, in each case obtained after the second injection of N_2O_5, are shown in Figures 2-4. These spectra were obtained after substraction of the features due to the unreacted sulfur compound, NO_2, HNO_3 and, when present as reaction products, HCHO, SO_2 and CH_3ONO_2.

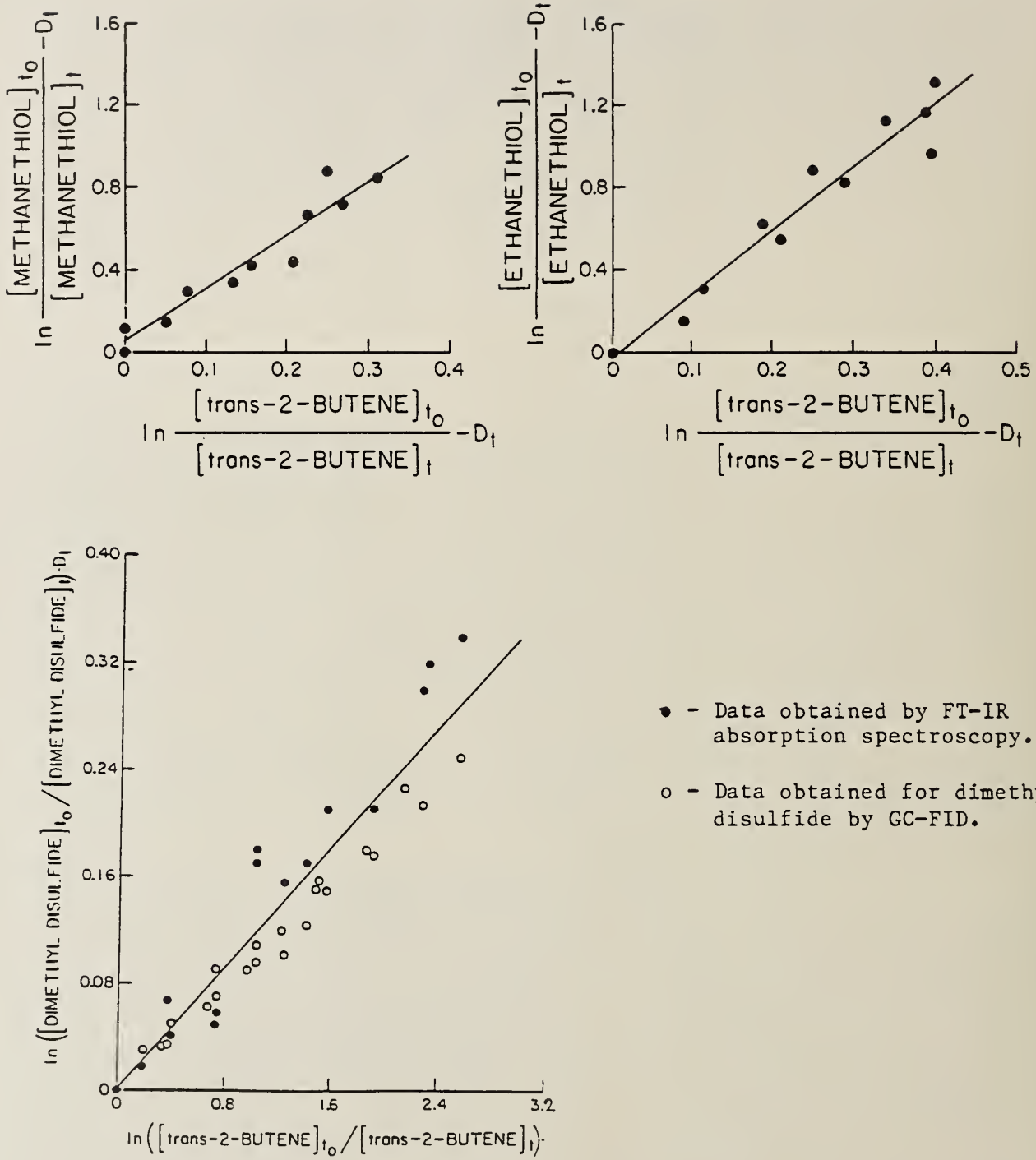

Figure 1. Plot of equation (I) for methanethiol (CH_3SH), ethanethiol (C_2H_5SH) and dimethyl disulfide (CH_3SSCH_3).

TABLE 1. Relative Rate Constant Ratios k_3/k_4 and Rate Constants k_3 for the Reactions of NO_3 Radicals with COS, CS_2, CH_3SH, C_2H_5SH and CH_3SSCH_3 at 297 ± 2 K

Sulfur Compound	k_3/k_4[a] Relative to Propene	k_3/k_4[a] Relative to trans-2-Butene	$10^{13} \times k_3$[a,b] (cm^3 $molecule^{-1}$ s^{-1})
COS	<0.0048		<0.0004
CS_2	<0.11		<0.008
CH_3SH		2.57 ± 0.55	10 ± 3
C_2H_5SH		3.11 ± 0.72	12 ± 3
CH_3SSCH_3		0.11 ± 0.02	0.42 ± 0.09

[a]Indicated error limits are two least-square standard deviations.

[b]Placed on an absolute basis using rate constants k_4 for propene and trans-2-butene of 7.6×10^{-15} cm^3 $molecule^{-1}$ s^{-1} and 3.8×10^{-13} cm^3 $molecule^{-1}$ s^{-1}, respectively.[17]

$CH_3SH + NO_3$ (Figure 2). CH_3ONO_2 and SO_2 were identified as reaction products by FT-IR absorption spectroscopy both in the presence and absence of oxygen. CH_3SSCH_3 and HCHO were identified as products only in the experiment conducted in a matrix of 80% N_2 + 20% O_2. Confirmation that CH_3SSCH_3 was a product was obtained by GC-FID analyses of gas phase samples and by GC-MS and GC-FID analyses of gas samples collected on Tenax GC adsorbent. Infrared absorption bands at 820, 1258 and 1562 cm^{-1} were observed both in the presence and absence of oxygen (Figures 2A and 2B). These bands are virtually identical to those suggested by Niki et al.[18] as being due to CH_3SNO_2.

The products responsible for the other infrared absorption bands in the presence of oxygen (Figure 2A) at 778, 1203, 1302, 1413, 1437, 1535 and 1768 cm^{-1}, and in the absence of oxygen (Figure 2B) at 1190, 1300, 1330, 1415 and 1535 cm^{-1}, remain unidentified at present.

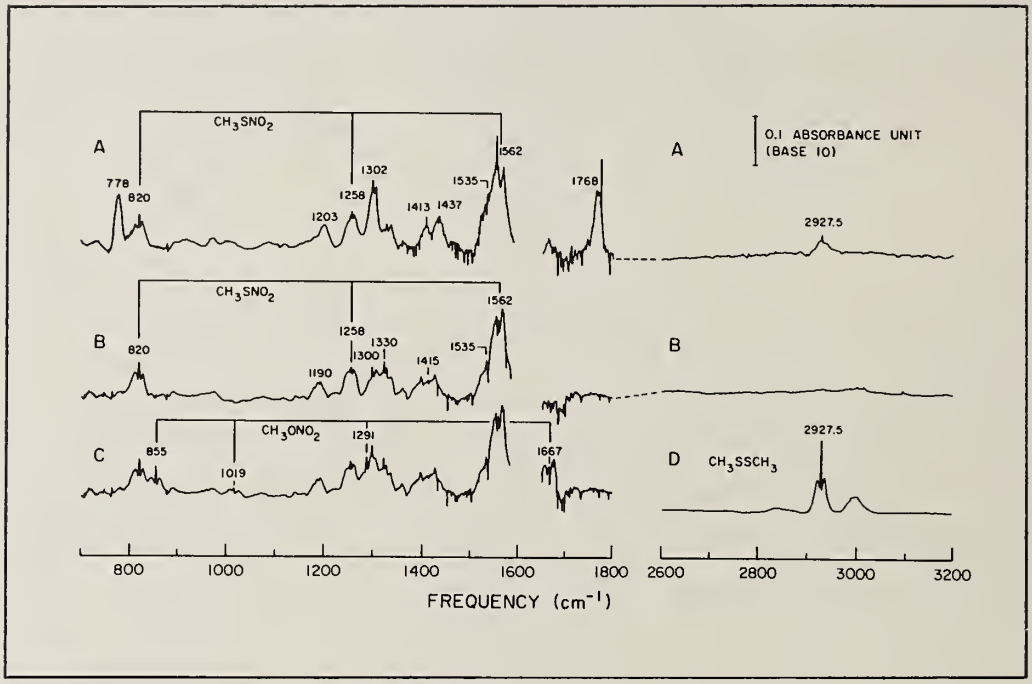

Figure 2

In the experiment conducted in the presence of oxygen, the yields of HCHO, SO_2, CH_3SSCH_3 and CH_3ONO_2 were ~8%, ~15%, ~11% and ~5%, respectively (secondary reactions of these products with the NO_3 radical are significantly slower than the NO_3 radical reaction with CH_3SH, and hence corrections due to secondary reactions were negligible). In the experiment conducted in the absence of oxygen, the yield of SO_2 was ~15%, identical to that in the presence of O_2, while CH_3SSCH_3 and HCHO were not observed in measurable quantities. CH_3ONO_2 and CH_3SNO_2 were again formed, with the CH_3ONO_2 yield being ~11%.

$C_2H_5SH + NO_3$ (Figure 3). In this reaction SO_2 was identified by FT-IR absorption spectroscopy both in the presence and absence of oxygen. By analogy with the formation of CH_3SNO_2 from the reaction of NO_3 radicals with CH_3SH, $C_2H_5SNO_2$ was also tentatively identified as a product in the presence and absence of O_2 from the infrared absorption bands at 820, 1254, and 1557 cm^{-1} (Figure 3A and 3B). $C_2H_5ONO_2$ was a product in the experiment conducted in the absence of oxygen, as identified by comparison with the published spectrum of Erley and Blake.[19] HCHO was not observed as a product from this reaction either in the presence or absence of oxygen.

The products responsible for the other infrared absorption bands in the presence of oxygen (Figure 3A) at 761, 1190, 1302, 1426, 1735 and 1760 cm^{-1} and in the absence of oxygen (Figure 3B) at 1190, 1360 and 1720 cm^{-1} remain unidentified at present.

The SO_2 yield was ~36% in the presence of O_2 and ~46% in the absence of O_2.

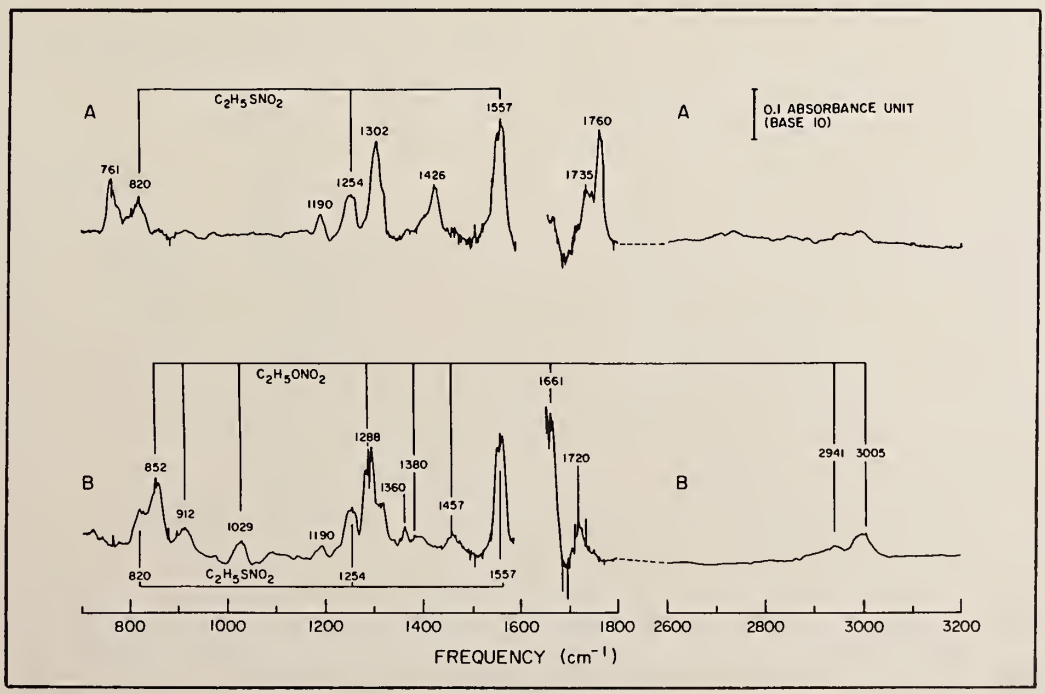

Figure 3

$CH_3SSCH_3 + NO_3$ (Figure 4). The products HCHO, SO_2 and CH_3ONO_2 were identified by FT-IR absorption spectroscopy from this reaction both in the presence and absence of oxygen. CH_3SNO_2 was tentatively identified in both runs from its infrared absorption bands at 820, 1258 and 1562 cm^{-1}. In the experiment conducted in the absence of oxygen (Figure 4B), the absorption band at 820 cm^{-1} is overlapped by other features from an unidentified product.

Remaining unidentified are the products responsible for the absorption features at 778, 1190, 1302 and 1768 cm^{-1} observed in the experiment conducted in the presence of oxygen (Figure 4A) and those at 820, 970, 1035, 1190, 1292, 1363, 1403 and 1683 cm^{-1} observed in the experiment conducted in the absence of oxygen (Figure 4B).

The SO_2 yield, on a molar basis, was ~60-70% in both the presence and absence of O_2. On a molar basis, the HCHO yield was ~55% in the presence of O_2 and ~30% in the absence of O_2. The CH_3ONO_2 yield was ~13% in the absence of O_2, and ~9% in the presence of O_2.

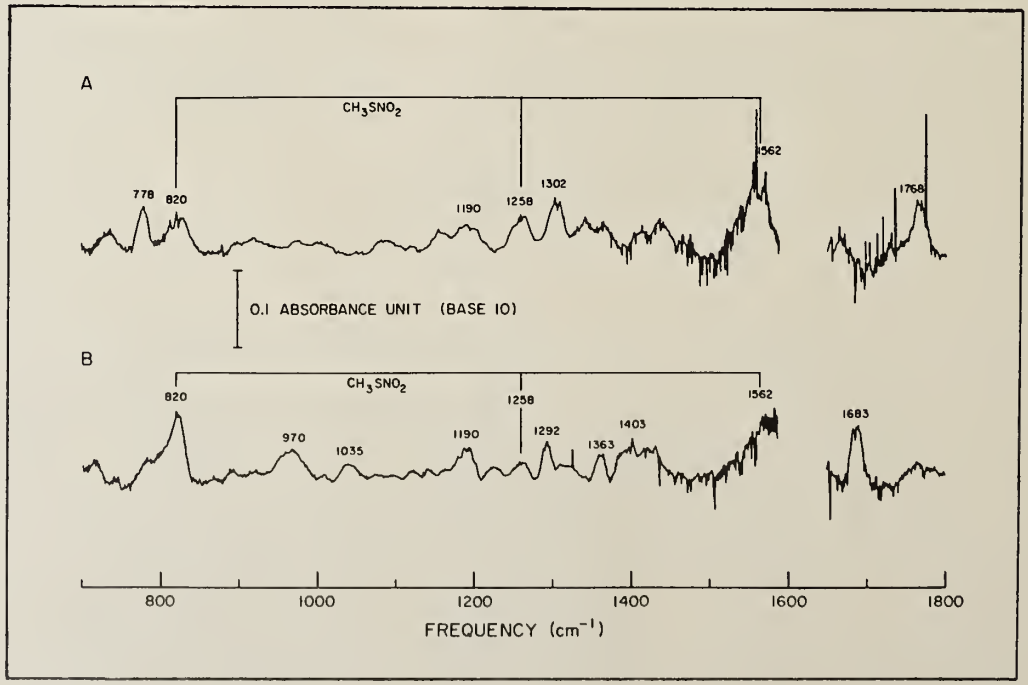

Figure 4

DISCUSSION

Kinetics

The sulfur-containing organic compounds CH_3SH, C_2H_5SH and CH_3SSCH_3 were observed to react relatively rapidly with the NO_3 radical, with measured rate constants at room temperature of ~1 x 10^{-12} cm^3 $molecule^{-1}$ s^{-1} for CH_3SH and C_2H_5SH and ~4 x 10^{-14} cm^3 $molecule^{-1}$ s^{-1} for CH_3SSCH_3.

These rate constants k_3 for CH_3SH, C_2H_5SH and CH_3SSCH_3 allow their atmospheric lifetimes due to reaction with NO_3 radicals to be calculated. Using an NO_3 radical concentration appropriate to the "clean" troposphere of 2.4 x 10^8 cm^{-3},[13] we obtain lifetimes of 1.2, 1.0 and 28 hours for CH_3SH, C_2H_5SH and CH_3SSCH_3, respectively. These atmospheric lifetimes can be compared to those due to reaction with OH radicals under similar "clean" conditions which are equal to 8.4, 5.9 and 1.3 hours for CH_3SH, C_2H_5SH and CH_3SSCH_3, respectively.[20] Clearly, nighttime reaction with the NO_3 radical is a dominant atmospheric loss process over the daytime reaction with the OH radical for CH_3SH and C_2H_5SH, as it is for CH_3SCH_3.[7] For COS and CS_2, only upper limit rate constants have been determined in this work, corresponding to lifetimes due to NO_3 radical reaction >60 day for CS_2 and >4 year for COS.

Products and Mechanisms

The product data obtained from the reactions of NO_3 radicals with CH_3SH, C_2H_5SH and CH_3SSCH_3 are not sufficient to allow the reaction mechanisms to be elucidated. All three reaction systems were observed to produce SO_2 in yields which ranged from ~15% to ~60%. The CH_3SH and CH_3SSCH_3 reaction systems also yielded CH_3ONO_2 and probably CH_3SNO_2 as products in both the presence and absence of O_2. In addition, HCHO was observed in the presence of O_2 from CH_3SH and in both the presence and absence of O_2 (though in enhanced yield in the presence of O_2) from CH_3SSCH_3.

That SO_2 is formed from CH_3SH in essentially identical yield in both the presence and absence of O_2 suggests that a direct reaction pathway leading to SO_2 must exist. However, the relatively minor yield of SO_2 and the observation of CH_3SSCH_3 and CH_3SNO_2 shows that other reaction pathways involving the formation of CH_3S radicals also exist, possibly via

intermediate formation of an NO_3-CH_3SH addition adduct. Thus, a possible reaction scheme for CH_3SH is as follows:

$$NO_3 + CH_3SH \rightarrow \left[CH_3\overset{ONO_2}{\underset{|}{S}}H \right] \rightarrow CH_3S + HNO_3 \qquad (5a)$$

$$\left[CH_3\overset{ONO_2}{\underset{|}{S}}H \right] \rightarrow SO_2 + \text{other products} \qquad (5b)$$

$$CH_3S + CH_3S \xrightarrow{M} CH_3SSCH_3 \qquad (6)$$

$$CH_3S + NO_2 \xrightarrow{M} CH_3SNO_2 \qquad (7)$$

$$CH_3S + O_2 \rightarrow [CH_3SO_2] \rightarrow CH_3 + SO_2 \qquad (8a)$$

$$[CH_3SO_2] \rightarrow \text{other products} \qquad (8b)$$

$$CH_3 + O_2 \xrightarrow{M} CH_3O_2 \qquad (9)$$

$$2\ CH_3O_2 \rightarrow 2\ CH_3O + O_2 \qquad (10)$$

$$CH_3O + O_2 \rightarrow HCHO + HO_2 \qquad (11)$$

$$CH_3O + NO_2 \xrightarrow{M} CH_3ONO_2 \qquad (12)$$

The formation of HCHO and CH_3ONO_2 strongly suggests that CH_3O radicals are intermediate species. As shown above [reactions (9)-(12)], CH_3O radicals can be formed from CH_3 radicals in both the N_2 and $N_2 + O_2$ atmospheres [the ultrahigh purity N_2 typically has O_2 concentrations of ~50-100 parts-per-million, quite sufficient for reaction (9) to dominate as a loss process for CH_3 radicals]. The relative yields of HCHO versus CH_3ONO_2 in N_2 and $N_2 + O_2$ atmospheres, for both the CH_3SH and CH_3SSCH_3 reaction, are then consistent with the sequence of reactions (9)-(12), with the yield of HCHO being higher in the $N_2 + O_2$ atmosphere, and the yield of CH_3ONO_2 being higher in the N_2 atmosphere. Indeed, the combined yields of HCHO and CH_3ONO_2 from CH_3SH are virtually identical in both N_2 and $N_2 + O_2$ atmospheres at ~12%.

The invariance of the SO_2 yield with the O_2 concentration and the observation of CH_3SSCH_3, formed by recombination of CH_3S radicals,[18] in the presence of O_2 suggests that reaction (8a) is of minor importance, and that a direct reaction such as (5b) must be operative. Thus the source of CH_3 (or CH_3O) radicals leading to the observed products HCHO and CH_3ONO in this reaction system is not presently known.

For the reaction of NO_3 radicals with C_2H_5SH, and CH_3SSCH_3 analogous reaction schemes may be expected, and indeed SO_2, $C_2H_5ONO_2$ and probably $C_2H_5SNO_2$ were observed from C_2H_5SH and SO_2, HCHO, CH_3ONO_2 and CH_3SNO_2 were observed from CH_3SSCH_3.

Acknowledgements

The authors gratefully acknowledge the financial support of the National Science Foundation through NSF Grant No. ATM-8410795.

References

1. Graedel, T. E., Rev. Geophys. Space Phys., 15, 421-428, 1977.

2. Nguyen, B. C., A. Gandry, B. Bonsang, and G. Lambert, Nature, 275, 637-639, 1978.

3. Cullis, C. F., and M. M. Hirschler, Atmos. Environ., 14, 1263-1278, 1980.

4. Adams, D. F., S. O. Farwell, E. Robinson, M. R. Pack, and W. L. Bamesberger, Environ. Sci. Technol., 15, 1493-1498, 1981.

5. Wine, P. H., N. M. Kreutter, C. A. Gump, and A. R. Ravishankara, J. Phys. Chem., 85, 2660-2665, 1981.

6. Jones, B. M. R., R. A. Cox, and S. A. Penkett, J. Atmos. Chem., 1, 65-86, 1983.

7. Atkinson, R., J. N. Pitts, Jr., and S. M. Aschmann, J. Phys. Chem., 88, 1584-1587, 1984.

8. Winer, A. M., R. Atkinson, and J. N. Pitts, Jr., Science, 224, 156-159, 1984.

9. Platt, U., D. Perner, A. M. Winer, G. W. Harris, and J. N. Pitts, Jr., Geophys. Res. Lett., 7, 89-92, 1980.

10. Noxon, J. F., R. B. Norton, and E. Marovich, Geophys. Res. Lett., 7, 125-128, 1980.

11. Platt, U., D. Perner, J. Schroder, C. Kessler, and A. Toennissen, J. Geophys. Res., 86, 11965-11970, 1981.

12. Noxon, J. F., J. Geophys. Res., 88, 11017-11021, 1983.

13. Platt, U. F., A. M. Winer, H. W. Biermann, R. Atkinson, and J. N. Pitts, Jr., Environ. Sci. Technol. 18, 565-569, 1984.

14. Pitts, J. N. Jr., H. W. Biermann, R. Atkinson, and A. M. Winer, Geophys. Res. Lett., 11, 557-560, 1984.

15. Perner, D., A. Schmeltekopf, R. H. Winkler, H. S. Johnston, J. G. Calvert, C. A. Cantrell, and W. R. Stockwell, J. Geophys. Res., 90, 3807-3812, 1985.

16. Atkinson, R., C. N. Plum, W. P. L. Carter, A. M. Winer, and J. N. Pitts, Jr., J. Phys. Chem., 88, 1210-1215, 1984.

17. Atkinson, R., S. M. Aschmann, A. M. Winer, and W. P. L. Carter, Environ. Sci. Technol., 19, 87-91, 1985.

18. Niki, H., P. D. Maker, C. M. Savage, and L. P. Breitenbach, J. Phys. Chem., 87, 7-9, 1983.

19. Erley, D. S., and B. H. Blake, Infrared spectra of gases and vapors, vol. II, Grating Spectra, Dow Chemical Company, 1965.

20. Atkinson, R., Chem. Rev., in press, 1985.

LASER INDUCED FLUORESCENCE SPECTROSCOPY OF CHEMICAL INTERMEDIATES IN A SUPERSONIC FREE JET EXPANSION

Terry A. Miller
Department of Chemistry, 140 W. 18th Ave., The Ohio State University, Columbus, Ohio 43210

I. Introduction

The concept of a chemical, or reactive, intermediate is an old one in chemistry, dating back at least 100 years. As with many older concepts, it has undergone refinement with time. Generally speaking, we would now call any atomic or molecular species that is produced during the detailed mechanism of an overall chemical reaction, but is not an isolable end product of that reaction, a chemical intermediate. Such intermediates will generally be chemically unstable, i.e. highly reactive, but physically stable, i.e. not susceptible to spontaneous decomposition.

For many years the detection and characterization of chemical intermediates has provided a significant challenge to spectroscopists. Because of their highly reactive nature, the production of chemical intermediates in sufficient concentration to allow high resolution spectroscopy has proved difficult. For simple, particularly diatomic, intermediates, the relentless improvement in sensitivity of spectroscopic techniques has yielded considerable recent success in their detection and characterization. However, more complex intermediates pose a stiffer challenge, because of the large number of low-lying energy levels typically populated. Such dilution of the population lessens the number of molecules available in any particular quantum level for study by high resolution spectroscopic techniques. Moreover, even if signals can be detected, the plethora of levels guarantees a highly congested spectrum.

One obvious solution to this problem is to try and cool reactive intermediates in low temperature matrices. The wide application of matrix isolation spectroscopy to the study of

reactive intermediates is ample testimony to the soundness of this approach. However, significant problems remain. In particular, even in inert gas matrices, there is still a significant possibility, or at least question, of the perturbation of the host spectra by the matrix.

The introduction of supersonic free jet expansions, such as shown in Fig. 1, to spectroscopy offers an attractive alternative to matrix isolation for cooling complex molecules to low temperatures. In most experiments a gas mixture containing mostly inert gas with a small percentage of the molecule to be studied is

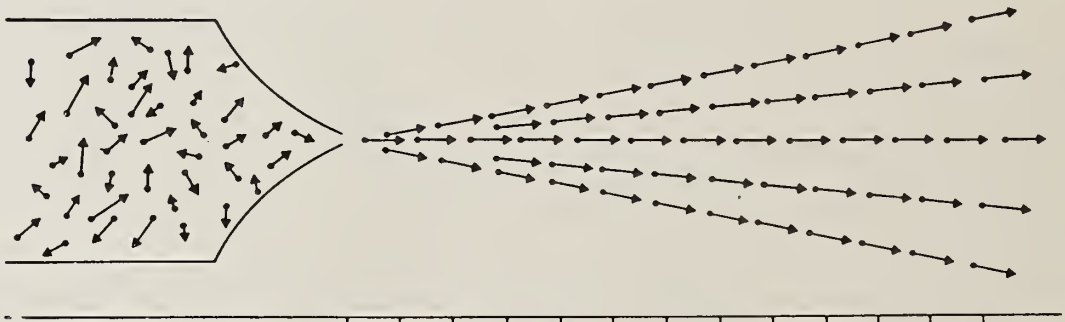

DISTANCE (X/D)	10	20	30	40	50	60
MACH NUMBER	15	24	32	38	44	50
TEMPERATURE (K)	4.0	1.6	0.9	0.6	0.5	0.4
DENSITY (S.T.P. Torr)	15	3.7	1.6	0.9	0.6	0.4
PRESSURE (mTorr)	150	15	3.5	1.5	0.7	0.4
COLLISIONS (5→X)	80	106	112	115	117	119

Fig. 1. Schematic diagram of a free jet expansion. Shown below the expansion is a scale measuring distance (X/D) downstream in units of the nozzle diameter (D). Given at various positions downstream are the Mach number, the temperature, the density [in torr at standard temperature and pressure (S.T.P.); 1 S.T.P. torr = 3.54×10^{16} molecules per cubic centimeter], the pressure (in millitorr), and the number of collisions between X/D = 5 and the indicated point. It is assumed that the stagnation pressure behind the nozzle is 10 atm. of He at 300 K; for the collision calculation, D = 0.15 mm, and a collision cross section of 50 A^2 is assumed.

contained in a reservoir and expanded through a small nozzle orifice yielding extensive cooling (to a few degrees Kelvin) of both the translational and internal degrees of freedom of the guest molecule. Spectroscopic studies can be performed on the cold guest molecule downstream in the expansion by crossing it with a laser beam and collecting laser induced fluorescence or, in some cases, ions produced by multi-photon ionization.

However as presently described, the technique is inadequate for the study of reactive species. Even if one possesses the means for injecting them into the reservoir, they would surely react with themselves, the walls, etc. before they could pass through the nozzle and be cooled by the expansion. To remedy this difficulty, we have turned to the in situ production of neutral free radicals and ions by crossing with a laser (or sometimes an electron) beam the inert gas expansion suitably doped with precursor molecules.

By such a technique we have been able to generate reactive intermediates and cool them to very low temperatures for downstream study by laser spectroscopy. We have produced and spectroscopically characterized four general categories of reactive intermediates: (i) isolated ions, (ii) ionic clusters, (iii) small neutral free radicals, (iv) neutral organic free radicals. In the following we will briefly overview our work on each of these species.

II. Isolated Ions

Ion-molecule reactions, as a class, are considered the fastest in all of chemistry. Therefore it is easy to understand why it has been difficult to obtain high resoltuion spectra of reactive molecular ions. However we have found it relatively straight-forward to produce cold organic radical cations in our free jet expansion. The technique has utilized 2 photons from an ArF laser to ionize the parent molecule. Fig. 2 shows a section of the laser excitation spectrum of $C_6F_6^+$ produced in this manner. Also shown for comparison are the laser excitation spectrum of $C_6F_6^+$ at higher temperatures and isolated in a Ne

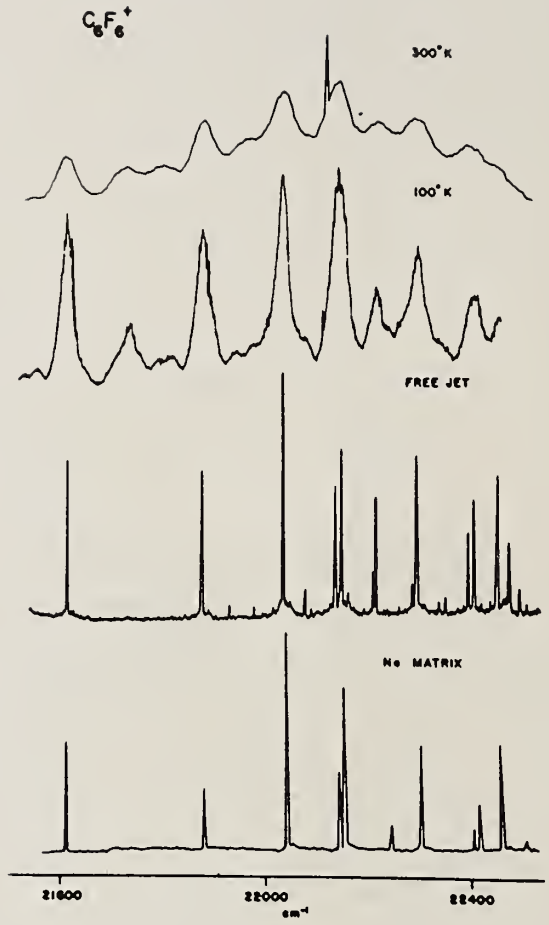

Fig. 2. Laser Excitation Spectra of $C_6F_6^+$. In the top two traces the $C_6F_6^+$ was produced by Penning ionization in a flow system at room temperature (uppermost) and cooled by liquid N_2 (penultimate upper). For the prepenultimate upper trace the $C_6F_6^+$ was produced by two photon photoionization through the use of an ArF laser interacting with C_6F_6 dilutely seeded in a free jet expansion. The lowest trace corresponds to an excitation spectrum of $C_6F_6^+$ isolated in a Ne matrix at 4°K. The entire matrix spectrum has been shifted to the blue to eliminate the matrix-gas-phase solvent shift.

matrix at 4°K. In Fig. 3 we show the laser excited wavelength resolved emission spectrum of the same ion.

The most remarkable fact about Fig. 3 is that it establishes at a glance that the $C_6F_6^+$ does not correspond to a regular hexagon (more specifically does not retain D_{6h} symmetry) in both states involved in the electronic transition. For if that were so, only two vibronic transitions could be observed in the pictured region of the spectrum. These are marked in Fig. 3 with arrows and correspond to the vibrationless transition and the one (to lower frequency) to the v"=1 level of the totally symmetric "ring-breathing" mode.

A detailed investigation[1] of the spectra in Figs. 2 and 3 shows that the ground state of $C_6F_6^+$ is distorted, at its

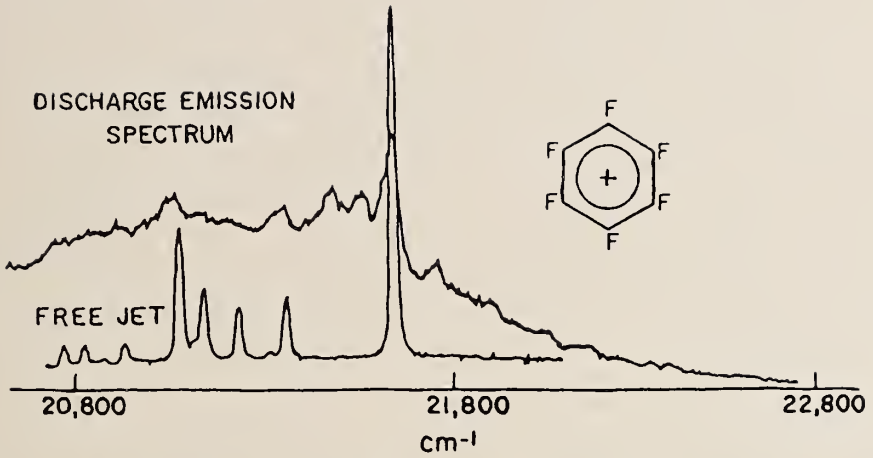

Fig. 3. Wavelength Resolved Emission Spectra of $C_6F_6^+$. The top spectrum was obtained by electron impact ionization and excitation of C_6F_6 in a cell at roughly 100 millitorr pressure. The lowest trace was obtained from $C_6F_6^+$ in a supersonic jet, laser excited.

equilibrium configuration, from D_{6h} symmetry by the Jahn-Teller effect. Based upon these studies, Fig. 4 shows in some detail the form and magnitude of the distortion for $C_6F_6^+$. In the center of each of the benzene rings in Fig. 4 is the value, ε, of the Jahn-Teller stabilization energy. As is evident from Fig. 4, the majority (>80%) of the stabilization energy is achieved for the two modes involving predominantly distortion of the ring. Similar spectra have been obtained, and analyses performed, for a number of related Jahn-Teller active ions, sym-$C_6F_3H_3^+$, sym-$C_6F_3Cl_3^+$, sym-$C_6Cl_3H_3^+$, sym-$C_6F_3Br_3^+$. In all cases similar conclusions are reached. The ring modes are the most important in the distortion. Typically C-C-C bond angles differ by 3-4° and the C-C bond lengths differ by 0.03-0.04 Å. In all cases the total stabilization energies are in the range of 500-1000 cm^{-1}.

III. Ionic Clusters

Referring to Fig. 1, it is apparent that by positioning the photo-ionization event relatively near the nozzle, the newly-created ion can be forced to undergo a number of collisions before it is characterized by the probe laser downstream. If the conditions are precisely chosen, these collisions can lead to the

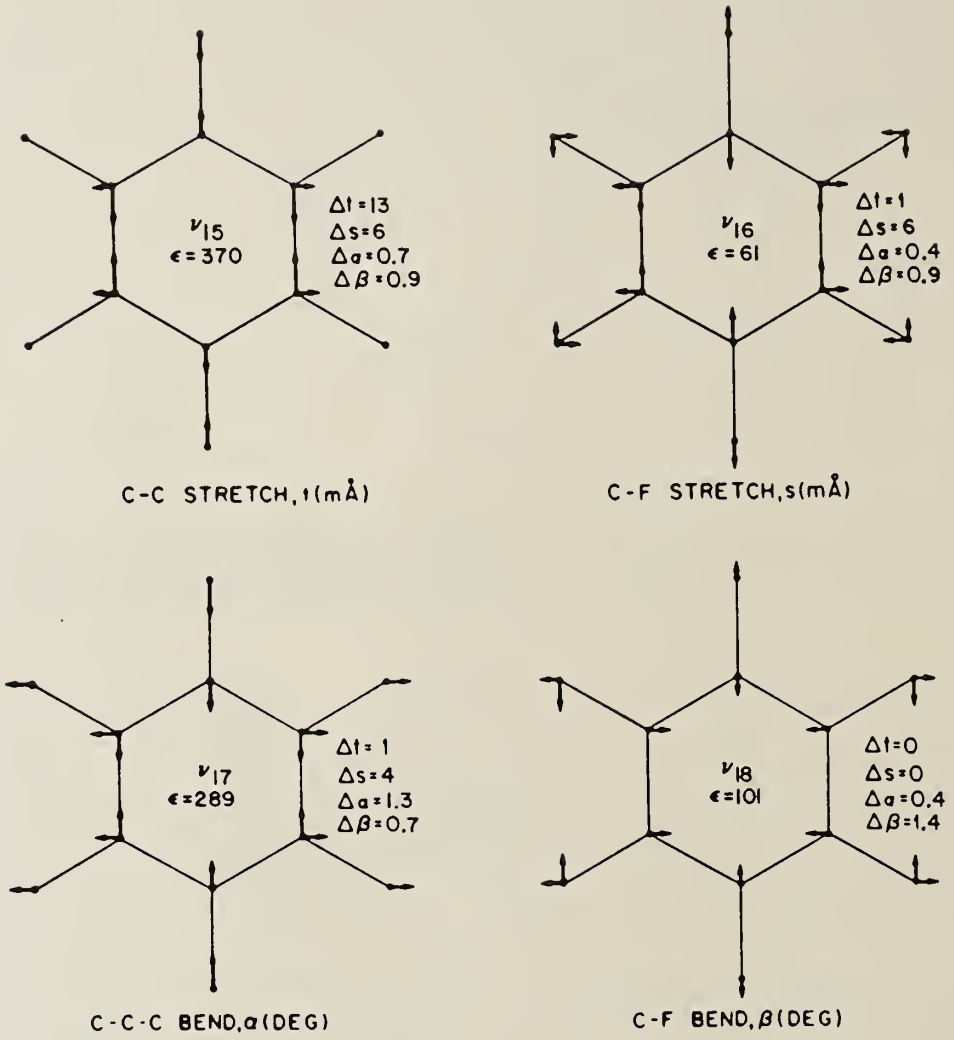

Fig. 4. Schematic Representation of the Four Jahn-Teller Active e_{2g} Modes of $C_6F_6^+$. The value of the Jahn-Teller stabilization energy, ε, is given within each ring. Beside each ring are given the changes at the minimum of the potential, from their equilibrium D_{6h} configuration, of each of the internal coordinates: α, C-C-C bond angle (degrees), β, C-C-F bond angle (degrees), t, C-C bond length (milliangstroms), and s, C-F bond length (milliangstroms).

formation of ionic clusters, in which a chromophore ion will have clustered to it, a number of neutral molecules, just as one believes most ions in solution do. The advantage of the jet

experiment is that individual cluster ions, $M^+ \cdot X_N$, with N taking on several distinct values, can be studied[2,3] and their electronic properties determined. In this way the transition from isolated ion to condensed phase ion can be chronicled.

Fig. 5 shows a portion of the $C_6F_6^+$ excitation spectrum near the origin as the backing pressure is varied. At the lowest pressure only one line is visible, the origin band of the isolated ion. At the highest backing pressure recorded there are at least six different ionic species present. By examining the remainder of the spectrum and noting its similarity with that of isolated $C_6F_6^+$, it is clear that the carrier of each spectrum

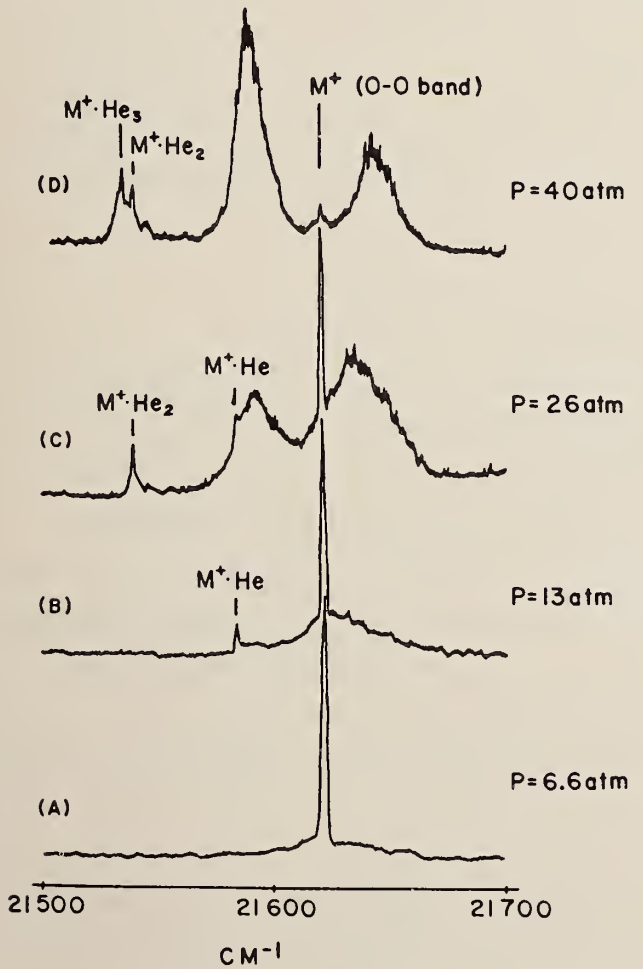

Fig. 5. Laser Excitation Spectra of $C_6F_6^+$ (= M^+) Expanded in Pure He. The relevant stagnation pressure (P) is indicated on each trace.

contains a $C_6F_6^+$ chromophore. At this point the identities of the broad line spectra in Fig. 5 are uncertain. However, a number of sharp line features can be assigned to $C_6F_6^+ \cdot He_N$ with

N = 1-3. One notes that as N, the number of He atoms complexed to the ion, increases, the red shift of the electronic spectrum increases.

Clearly if N becomes large enough, the observed red shift might be expected to reach the "solvent" shift of the condensed phase. In the case of Ar direct comparisons with the condensed phase are possible, i.e. a $C_6F_6^+$ ion isolated in an Ar matrix. The gas phase complex does indeed reach the matrix limit as expected. However as is often the case, it is not the destination but the journey that is most interesting. Our data[3] clearly show that $C_6F_6^+ \cdot Ar_N$ goes through a maximum red shift which is approximately twice as large as its final limiting value. What changes in electronic or nuclear structure are required to account for this behavior is unclear at present. However, it suggests that clusters of intermediate size may well have properties that neither isolated ions nor bulk material possess.

IV. Small Neutral Free Radicals

There is obviously no reason why one should be restricted to the production of ionized reactive species in the jet. Given the appropriate molecules and photons, photodissociation of a precursor into neutral free radical fragments is obviously a distinct possibility. While the production of neutral free radicals should be straightforward, it is not nearly so obvious that the radicals produced in the jet by photodissociation will be cold.

The case of photo-ionization producing the parent ion can be described as follows,

$$R + nh\nu \rightarrow R^+ + e^- \qquad (1)$$

The precursor molecule R is typically cooled to a low temperature by the initial stages of the expansion. Because the electron cannot carry much angular momentum, R^+ will be nearly as rotationally cold as R. The vibrational state of R is not so well defined. However, in many cases the removal of only one electron will not greatly effect the potential felt by the

nuclei. Thus transitions with little or no change in the vibrational quantum number are favored. Therefore if R is vibrationally cold, there is a propensity for R^+ to be vibrationally cold also.

If one is dealing with photodissociation rather than photoionization, the event is better described as follows,

$$R\text{-}R' + h\nu \rightarrow R\cdot + R'\cdot \qquad (2)$$

In general, even though the molecule R-R′ may be cold, there is no reason that the free radical fragments R· and R′· need be. The net conservation of angular momentum is quite possible even if both R· + R′· contain considerable rotational energy. Similarly, the breaking of a chemical bond gives ample opportunity for vibrational excitation of one or both fragments.

These effects are clearly illustrated in Fig. 6. The figure shows[4,5] excitation spectra of the CN radical formed from the photodissociation of cold BrCN in a jet by an ArF excimer laser. In the top trace, the probe laser's position and timing were arranged so that approximately nascent CN radicals are sampled. The spectrum shows high rotational levels populated. While not quite a Boltzmann distribution, the rotational population is fairly well described by a temperature of ≈4000°K. Similarly the populations observed in the lowest two vibrational levels require a temperature of nearly 2000°K. Clearly the nascent CN is internally "hot".

It may then seem pointless to perform such experiments in jets if cold precursor molecules give rise to only hot radicals. However the lower trace in Fig. 6 revels this not to be the case. If the probe laser is delayed in time ≈10μsec and moved ≈5.7 mm downstream of the photolysis laser, then the hot CN radicals have an opportunity (see Fig. 1) to suffer numerous collisions with the inert gas and cool towards its temperature. While equilibrium is yet to be established at this time and pressure, it is clear that the hot CN has been dramatically "cooled".

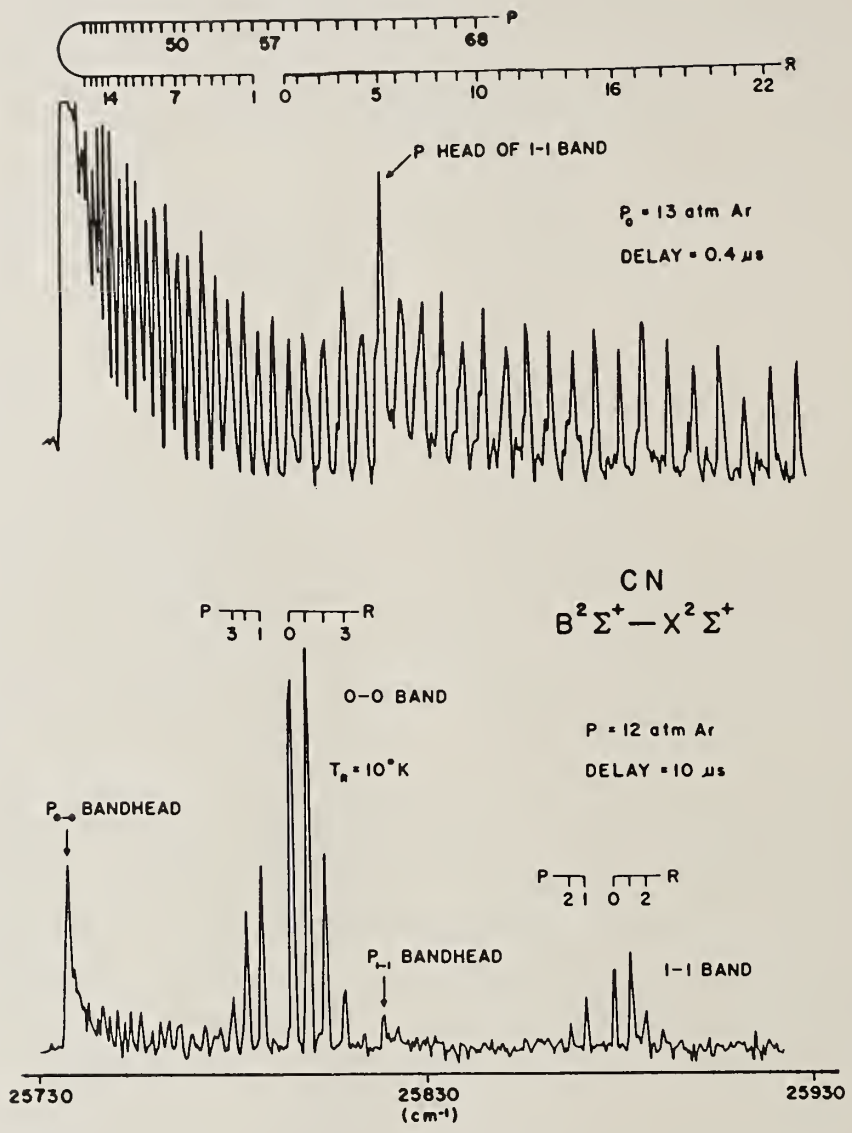

Fig. 6. Laser-induced fluorescence spectra of the CN free radical produced by the ArF laser photolysis of BrCN in an Ar free jet expansion. In the upper trace, the probe and photolysis laser are nearly overlapped in space and time, and the CN distribution detected is nascent or near nascent. In the lower trace, the probe laser has been displaced downstream by 10 μsec in time and 6 mm in distance. Large redistributions in rotational populations are clear. The rotational assignments for the R and P branches are as indicated.

Fig. 7 reveals that if one raises the Ar backing pressure, the number of collisions is increased and the CN rotational distribution can be described by a Boltzmann temperature of about 8°K.

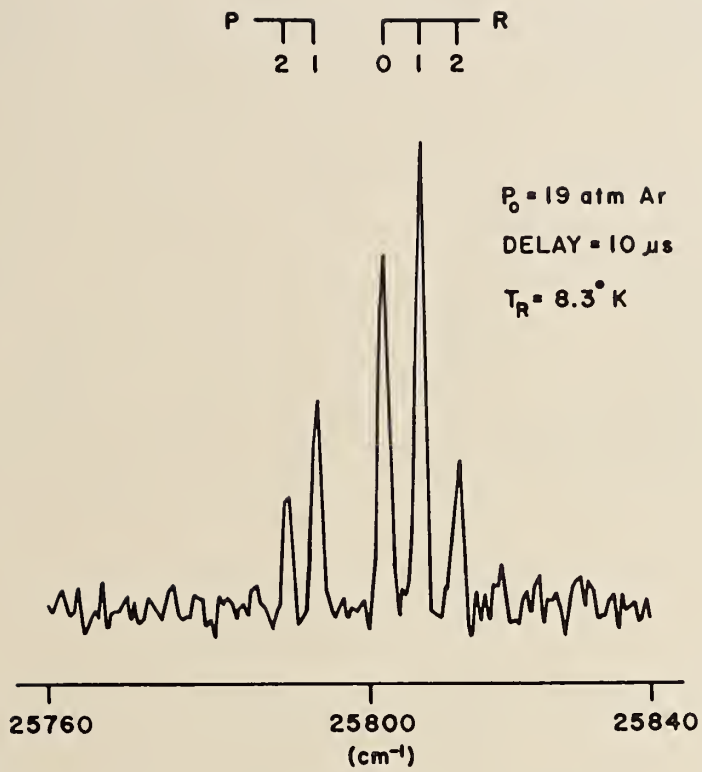

Fig. 7. Laser Induced Fluorescence Spectrum of CN. Conditions the same as in Fig. 6 except the backing pressure has been increased.

While the collisions involved in the CN experiment are non-reactive, this need not be case.[6] Fig. 8 reveals the excitation spectra of the photo-dissociation products of H_2S. The upper trace again corresponds to a nearly nascent distribution of products, i.e., SH radicals. The lower trace is delayed and shows cooler SH radicals. However most interestingly, there is now revealed in addition the spectrum of the S_2 molecule. We believe that S_2 arises because of reactive collisions in the jet following the mechanism,

$$H_2S + h\nu \rightarrow SH + H \quad (3)$$

$$SH + H \rightarrow H_2 + S \quad (4)$$

$$S + SH \rightarrow S_2 + H \quad (5)$$

Perhaps the most exciting thing about the CN and SH experiments is the possibility that they hold for doing novel chemistry. The CN spectra show that depending upon the sampling position and backing pressure, etc., highly reactive radical

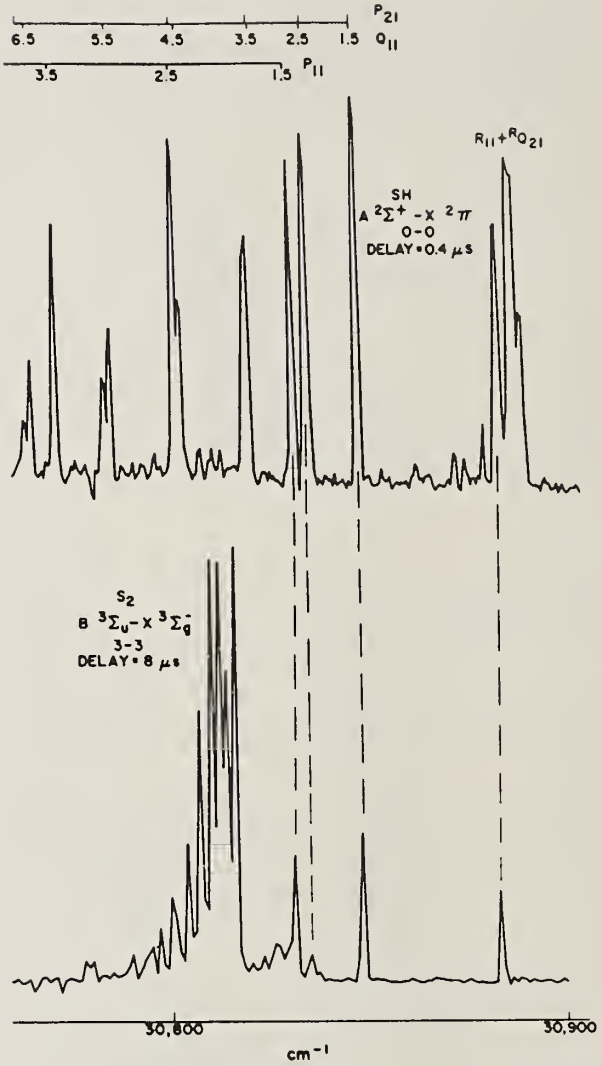

Fig. 8. Laser induced fluorescence spectrum of the products of an ArF laser photolysis of H_2S seeded in an Ar free jet expansion. In the upper trace, the probe and photolysis lasers are nearly overlapped. The spectrum observed is for the SH free radical with a nearly nascent population distribution. The rotational assignments of the lines are as indicated. In the lower trace, the probe laser is delayed about 8 μsec in time and moved 5 mm downstream. The SH is considerably colder than above, and the new, denser spectrum can be attributed to the S_2 molecule.

with various amounts of internal energy content can be obtained. The SH experiment shows that chemical reactions can occur in the jet itself. Since the conditions within the jet are quite unusual, roughly corresponding to a few-degree-Kelvin, gas-phase reaction, it is likely that unique chemical processes may occur in this environment.

V. Neutral Organic Free Radicals

While the dynamical processes occurring within the jet for the small free radicals are very interesting, the cooling of these radicals for spectroscopic purposes is not particularly useful. These molecules are small enough that even at room

temperature their spectra are relatively simple and they can be easily analyzed. Indeed the decrease in the number of spectral transitions incurred with extreme cooling often limits the information content of the spectrum.

However if we turn to radicals containing several atoms, the situation is totally altered. At room temperature their spectra are so congested that they are virtually impossible to analyze. The spectra of most organic free radicals fall into this category. However if they are cooled to within a few degrees of absolute zero, only a few levels are populated and their spectral analyses become quite tractable.

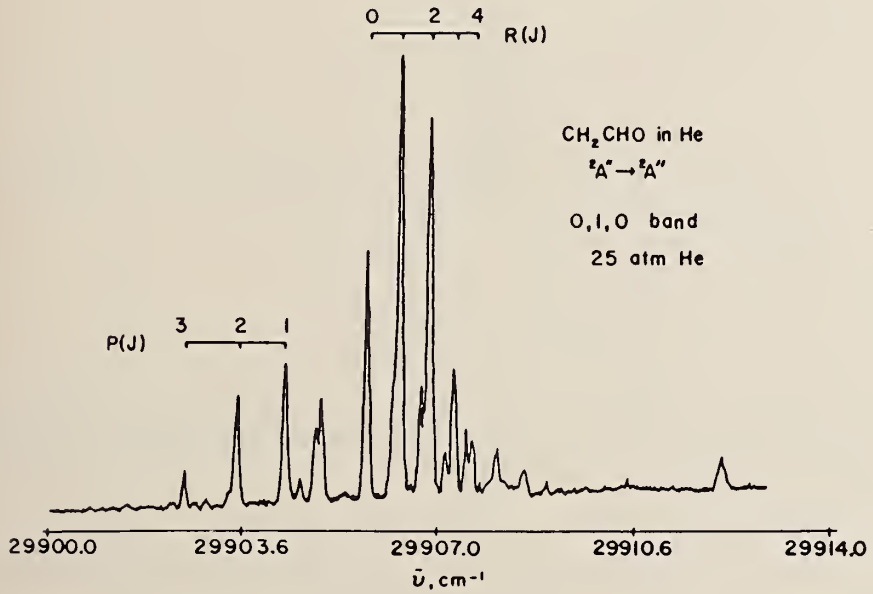

Fig. 9. Section of rotationally resolved spectrum of vinoxy in the region of the parallel transitions. The rotational temperature is between 2-3 K for the K=0, *N* states. The relative populations of the different *K* levels must be described by a slightly higher temperature ≈5 K.

Fig. 9 shows the spectrum[7] of the vinoxy free radical, $CH_2CHO\cdot$, taken at an approximate temperature of 3°K. As is indicated in the figure, a rotational assignment and analysis is quite straightforward. Using the molecular constants obtained from this analysis, it is possible to predict the spectrum at higher temperatures. Fig. 10 shows the spectrum at ≈10°K. While

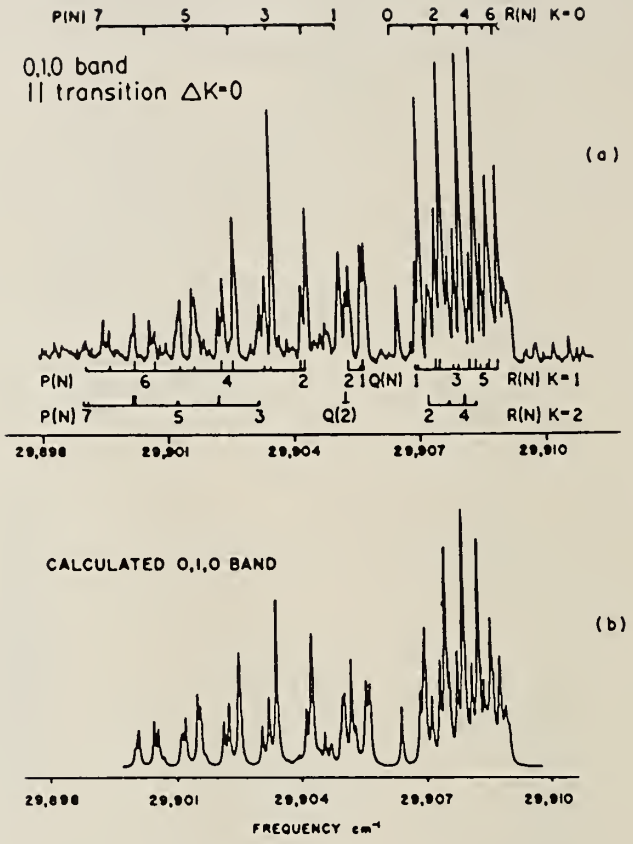

Fig. 10. (a) Spectrum of vinoxy covering approximately the same frequency region as Fig. 9, but with the rotational temperature now approximately 10°K, (b) a simulation of spectrum in (a) based upon the molecular constants.

it is much more complicated, it is readily predicted from refined values of the molecular constants obtained from the spectrum of Fig. 9. It is, however, clear that if the temperature were raised much above 10°K, the spectral congestion would become impossible. The spectrum in Fig. 10 has yielded good molecular constants for both the ground and excited electronic states involved in the transitions. These constants have allowed the determination of the bond lengths and angles of the C-C-O skeleton of the vinoxy radical.

We have observed several other organic free radicals in similar experiments.[8,9] Fig. 11 shows the rotationally resolved spectrum of the monomethylsulfide radical, $CH_3S\cdot$.

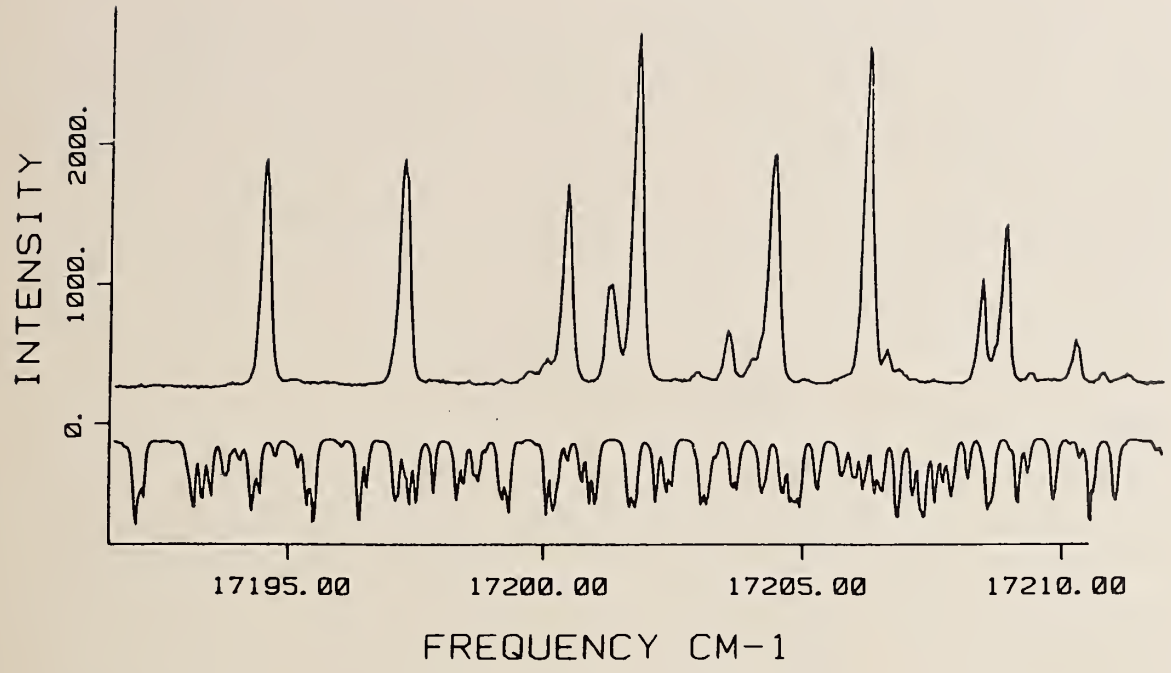

Fig. 11. Rotationally resolved spectrum of CH_3S. The electronic transition is $^2A-^2E_{3/2}$.

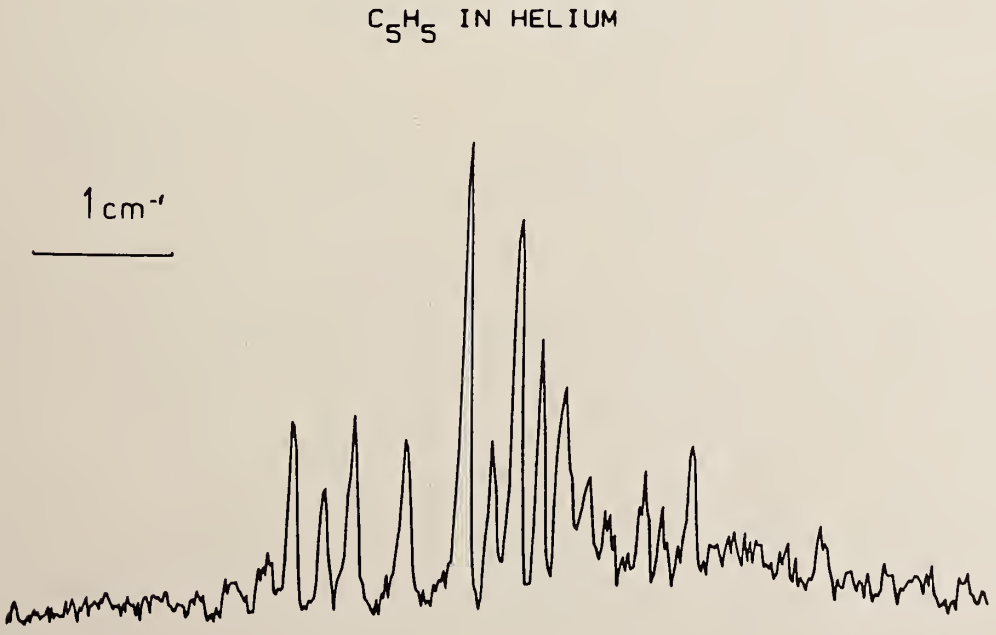

Fig. 12. Rotationally resolved spectrum of C_5H_5. Shown is the 0-0 band of the electronic transition, $\tilde{A}^2A_2''-\tilde{X}^2E_1''$.

Fig. 12 shows a similar spectrum for the cyclopentodienyl radical, $C_5H_5\cdot$. Fig. 13 shows a lower resolution spectrum for the benzyl radical, $C_6H_5CH_2\cdot$. Spectral analyses for all these radicals are now in progress and should yield detailed structural information on these important chemical intermediates.

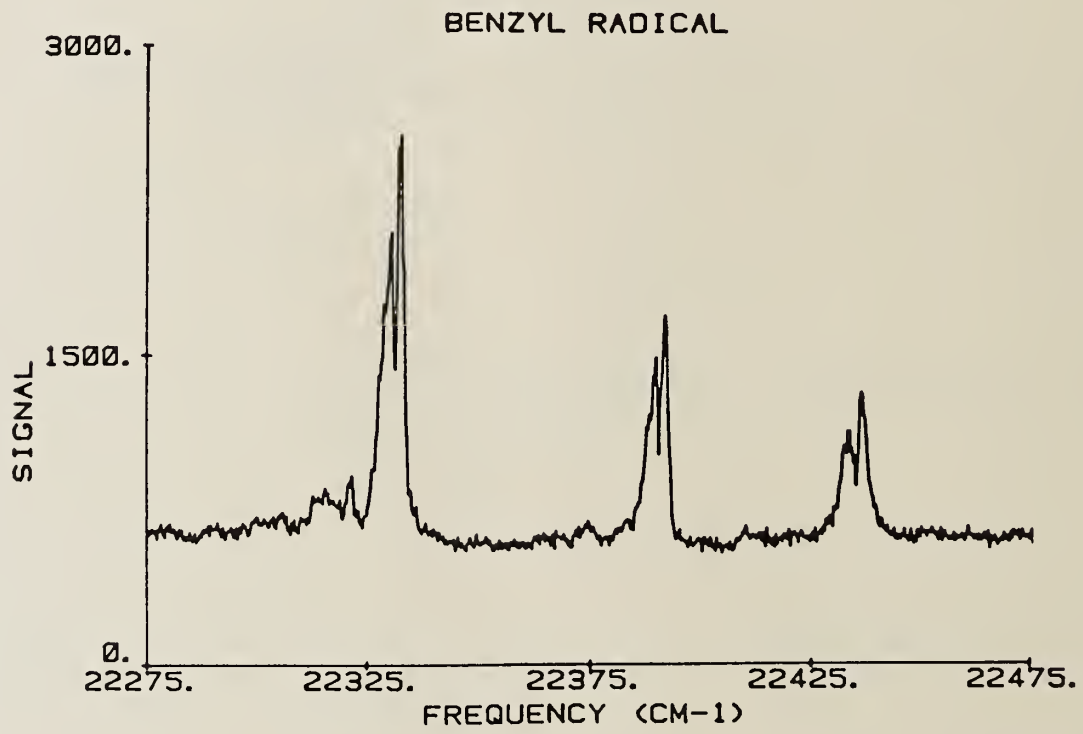

Fig. 13. Laser excitation spectrum of the $C_6H_5CH_2$ free radical showing three vibronic bands of the $\tilde{A}^2A_2$-$\tilde{X}^2B_2$ electronic spectrum.

Acknowledgement: The author gratefully acknowledges the partial support of this work by the National Science Foundation under grant CHE-8507537. He also acknowledges the many contributions of his colleagues, particularly V. E. Bondybey, M. Heaven, and L. DiMauro, to the portion of this work done at A.T.& T. Bell Laboratories.

Spectrokinetic Studies of HO_2 and OH involved in the Chain Reactions (2) $H + O_2 + M \rightarrow HO_2 + M$; (3) $H + HO_2 \rightarrow 2\ OH$; and (8) $OH + H_2 \rightarrow H_2O + H$; under experimental Conditions where (7) $OH + HO_2 \rightarrow H_2O + O_2$ is the predominant Termination Reaction for OH.

Jette Munk, O.J. Nielsen A. Sillesen and P.Pagsberg.
Chemistry Department, Risoe National Laboratory,
DK-4000 Roskilde, Denmark.

ABSTRACT

The yield of H-atoms produced by pulse radiolysis of 10% H_2 in Ar at 1 atm and 298 K was determined by monitoring the transient absorption at 215 nm due to the formation of HO_2 radicals via reaction (2) in the presence of 0.2-10 mbar O_2. OH radicals are formed via reaction (3) and the kinetics was studied by monitoring the transient absorption at 3090 A. The OH decay was near exponential, $(OH)=(OH)_o exp(-k^*t)$, and with a ten-fold variation of k^* in the range of $p(O_2)$=0.2-10 mbar. A strong correlation with the yield of the long-lived HO_2 radicals indicates that $k^* = k_7(HO_2)$, i.e. that the OH decay is primarily controlled by reaction (7). A computer model including eight elementary reactions accounts for all of the experimental observations when $k_2 = 4.5 \times 10^8$, $k_3 = 6.5 \times 10^{10}$, $k_8 = 4.0 \times 10^6$, and $k_7 = 6.0 \times 10^{10}$ $M^{-1}s^{-1}$.

INTRODUCTION

The kinetics and mechanism of the reaction

(7) $OH + HO_2 \rightarrow H_2O + O_2$; $\Delta H_{298} = -69.6$ kcal/mol

have been studied in many laboratories employing different experimental techniques.[1-17] This reaction plays an important role in the termination of free radical chain reactions in the atmosphere and in combustion systems. Experimental values of k_7 at T = 298 K and a pressure of 1 atm average 6.5×10^{10} $M^{-1}s^{-1}$. It has been argued that this value is higher than would be expected for a direct H-abstraction reaction. The observation of a slight pressure dependence and "negative activation energy" has been taken as evidence for a more complex mechanism involving an adduct, H_2O_3. A mechanism proceeding via H-O-O-O-H seems to be ruled out, however, by a recent $^{18}O/^{16}O$ isotope experiment.[16] Of particular interest to atmospheric chemistry modelling is the question whether the rate of reaction (7) depends on the partial pressure of water in a similar way as observed for the combination of HO_2 radicals.[18]. In the present investigation we have studied the kinetics of HO_2 and OH by pulse radiolysis of $Ar/H_2/O_2$ mixtures at T = 298 K and p = 1 atm. The rates of formation and decay of HO_2 and OH were studied by monitoring the transient absorption signals at 215 nm and 309 nm, respectively. The observed large changes in the relative yields and kinetics of HO_2 and OH with varying oxygen concentrations shows that the decay rate of OH is mainly controlled by reaction (7) while competing reactions are of minor importance because of a high HO_2/OH ratio.

EXPERIMENTAL

The experimental set-up for pulse radiolysis combined with transient UV-spectrophotometry has been described earlier.[19] Gas mixtures were prepared by admitting one component at a time to the sample cell and measuring the corresponding pressures with a MKS Baratron Model 170 membrane manometer. A platinum thermometer was used to measure the temperature near the center of the cell. The analyzing light beam from

a pulsed 150 W Xe-lamp enters the sample cell through a suprasil window and a set of internal mirrors provides optical path lengths of 40, 80 or 120 cm. A one meter grating spectrometer with a reciprocal dispersion of 8 A/mm is used to select a suitable spectral band pass of the analyzing light. The modulated light intensity is monitored with a fast photomultiplier and the signals are captured with a transient digitizer controlled by a minicomputer which is used for on-line data processing and display of absorbance versus time curves or derived functions, 1/A or lnA. High yields of H-atoms were obtained when mixtures of Ar and H_2 were irradiated with single pulses of 2 MeV electrons with a pulse length of 30 nsec. In the presence of 0.1-2% oxygen we observed the formation and decay of HO_2 by monitoring the transient absorption at 215 nm. OH radicals were monitored at 3090 A with a spectral band pass of 0.8 A which was chosen as the best compromise between spectral resolution and S/N ratio. With a band pass far wider than the OH line width the apparent extinction coefficient depends on the spectral band pass employed and the absorbance was found to be a non-linear function of the optical path length. However, plots of log(A) versus log(L) were found to be linear within the experimental uncertainties. Thus, to calculate concentration versus time profiles for OH we have used the expression $A = (\varepsilon LC)^n$ with a value of $n = d\log(A)/d\log(L) = 0.70 \pm 0.04$. The experimental results were transferred to a large central computer for analysis and comparison with the model kinetics.

RESULTS and DISCUSSION

The yield of HO_2 obtained by pulse radiolysis of $Ar-H_2-O_2$ mixtures was studied as a function of $p(O_2)$ by monitoring the transient absorption at 215 nm. As shown in Fig.1 the yield approaches a maximum value at high oxygen concentrations corresponding to a complete conversion of H-atoms via reaction (2).

(1) $H + H + M \rightarrow H_2 + M$

(2) $H + O_2 + M \rightarrow HO_2 + M$

(3) $H + HO_2 \rightarrow OH + OH$

(4) $HO_2 + HO_2 \rightarrow H_2O_2 + O_2$

(5) $OH + OH + M \rightarrow H_2O_2 + M$

(6) $H + OH + M \rightarrow H_2O + M$

(7) $OH + HO_2 \rightarrow H_2O + O_2$

(8) $OH + H_2 \rightarrow H_2O + H$

The reduced yields observed at the lower oxygen concentrations are due to losses of H-atoms via the reactions (1) and (3). Since $k_3 >> k_1$ the major part of the H-atoms are consumed in reaction (3) which gives rise to a significant yield of OH radicals with a maximum at $p(O_2)$ = 2 mbar as shown in Fig. 2. HO_2 radicals were observed to build up with a rate proportional to $p(O_2)$ in accordance with reaction (2). The subsequent second order decay with a typical half life of 400 usec is governed mainly by the recombination reaction (4). The yield of OH goes through a maximum at low oxygen concentrations as shown in Fig.2. The decreasing yields obtained at higher oxygen concentrations reflect the competition between (2) and (3). The decay of OH was governed by first order kinetics, i.e. $(OH) = (OH)_o \exp(-k^*t)$ and the corresponding experimental half-lives are shown in Fig. 3. The prevailing first order kinetics indicates that the OH radicals react with a large excess of reactant molecules. A comparison of Fig.1 and Fig.2 shows that the half live of OH is long when the yield of HO_2 is low, and vice versa. Thus, the reciprocal half life is nearly a linear function of the HO_2 yield, i.e. $k^* = \ln 2/\tau = -d\ln(OH)/dt = k_7(HO_2)$. Using this expression we estimated $k_7 = 6 \times 10^{10}$ $M^{-1}s^{-1}$ which was used as a first trial value in the subsequent computer simulations. A value of $k_2 = 5 \times 10^8$ $M^{-1}s^{-1}$ was calculated from the rate of HO_2 formation observed at $p(O_2)$ = 10 mbar where the high yield of HO_2 implies that most H-atoms are consumed in (2) and the effect of the competing reaction (3) is small. Likewise, a value of $k_4 = 6 \times 10^9$ $M^{-1}s^{-1}$ was estimated from the derivative $d(1/A)/dt = 2k_4/\varepsilon L$ using a consensus value of the extinction coeffici-

ent, ε_{215} = 1170 $M^{-1}cm^{-1}$.[20] Finally we have estimated a value of k_3 assuming that the yield of HO_2 obtained at low oxygen concentrations is governed by (2) and (3), i.e. $d(H_2O_2)/dt = k_2(H)(O_2) - k_3(H)(HO_2)$ neglecting minor losses of HO_2 via (4) and (6). Using the value of k_2 above we obtained a linear plot of $k_2(O_2)/(HO_2)_{max}$ with an extrapolated value of $k_3 = 6.5 \times 10^{10}$ $M^{-1}s^{-1}$ at $p(O_2)=0$. The trial values of (k_2,k_3,k_4,k_7) were used to start up the computer modelling with a realistic set of rate constants not far from the final set corresponding the best fit between the kinetics obtained with the model and the experimental results. The strategy employed in our computer simulations is outlined in Table 1 which summarises the stepwise evaluation of the rate constants obtained by studying the response of the complete model to changes in the rate constants k_1 - k_8 in comparison with the experimental results. The initial yield of H-atoms employed in the model was calculated from the limiting yield of HO_2 obtained at high oxygen concentrations which serves as a basis for the evaluation of absolute rate constants for the radical-radical reactions involved. Thus, the estimated 10% uncertainty in the value of the extinction coefficient of HO_2 at 215 nm contributes to the total error limits quoted in Table 1. The formation and decay kinetics of HO_2 observed at high oxygen concentrations could be accounted for with model values of k_2 and k_4 as quoted in Table 1. The error limits were estimated by sensitivity studies, i.e. the partial derivatives of the model halflives with respect to k_2 and k_4 were compared with the uncertainties in the experimental half-lives corresponding to the actual signal-to-noise ratio. As expected the yields of HO_2 obtained with the model were very sensitive to the value of k_3 while changes in the value of k_7 had a ten-fold smaller effect. The experimental yield curve shown in Fig.1 could be reproduced only with the high value of k_3 listed in Table 1. The yield of OH is controlled mainly by the rates of (3) and (7) in competition with (2). Experimental formation and decay curves are shown in Fig.4. By curve fitting with the model we have studied the sensitivities with respect to all of the rate constants. The decay rate of OH was found to be governed by reaction (7) and the low sensitivities with respect to k_5 and k_6 must be due to

a high HO_2/OH ratio which makes the losses via (5) and (6) relatively unimportant. Interestingly, while the rate of reaction (8) is high the sole effect of this reaction is a fast feed-back of H-atoms to maintain a short chain reaction which is terminated by reaction (7). This is true only at low temperatures where the chain branching reaction $H + O_2 \rightarrow OH + O$ is unimportant because of the high activation energy. The model seems to be adequate in reproducing all of the experimental results including shape of the yield curve shown in Fig.2 and the decay half-lives in Fig.3. It should be noted, however, that we have not tried to determine the absolute yield of OH. To do this we would need a value of the apparent extinction coefficient of OH corresponding to the spectral band pass. Work is in progress to achieve this goal by studies of the consecutive reactions $H + NO_2 \rightarrow OH + NO$ and $OH + NO_2 \rightarrow HNO_3$ where the yield of OH can be determined relative to the initial yield of H-atoms. However, for the purpose of obtaining a reliable value of k_7 from the actual experimental results there is no need to determine the absolute yield of OH as long as the HO_2/OH ratio is high enough to ensure that reaction (7) proceeds under pseudo-first order conditions. Since this has been verified for all of the experimental OH decay curves we believe that the best-fit value of k_7 quoted in Table 2 may be taken with confidence. In estimating the error limits we have taken into account a ± 10% uncertainty in the absolute yield of HO_2 as well as the effect of noise in the determination of the experimental decay rates, dlnA/dt. Table 2 contains a summary of reported rate parameters for the reaction (7) $OH + HO_2 \rightarrow H_2O + O_2$.The pressure dependence of the rate constant seems marginal in the range of 1-1200 torr. Also, while the two high temperature studies [12,13] indicate a negative temperature coefficient the rate constant obtained in the range of 288-348 K was found be independent of of the temperature.[11] Thus, the present data base cannot be considered sufficient to settle the question whether or not reaction (7) proceeds via a complex, H_2O_3. It is of interest to compare our results with an earlier pulse radiolysis study [10] where the decay of OH and HO_2 in approximately equal amounts were studied in the presence of water vapor. The reported value of k_7 is identical with the

value obtained in the present study with a high HO_2/OH ratio and in the absence of water vapor except for the very small amounts produced in the the reactions. Thus, it seems fair to state that the rate of reaction (7) is independent of water vapor. At present there is no convincing vidence against the assumption that (7) is a direct H-abstraction reaction without activation energy which is compatible with the strong exothermicity.

References

(1) W. Hack, A.W. Preuss and H.Gg. Wagner Ber. Buns. Phys. Chem., 82, 1167 (1978)
(2) J.P. Burrows, D.I. Cliff, G.W. Harris, B.A. Thrush and J.P.T. Wilkinson, Proc. Roy. Soc. (London), 368A, 463 (1979)
(3) J.P. Burrows, G.W. Harris and B.A. Thrush, Nature, 267, 233 (1977)
(4) B.A. Thrush, and J.P.T. Wilkinson, Chem. Phys. Lett., 81, 1 (1981)
(5) U.C. Stridharan, L.X. Qui and F. Kaufman, J. Phys. Chem., 85, 3361 (1981)
(6) L.F. Keyser, J. Phys. Chem. 85, 3667 (1981)
(7) W.B. DeMore and E. Tschuikow-Roux J. Phys. Chem., 78, 1447 (1974)
(8) W.B. DeMore, J. Phys. Chem., 83, 1113 (1979)
(9) C.J. Hochanadel, T.J. Sworski and P.J. Ogren, J. Phys. Chem., 84, 3274 (1980)
(10) R.-R. Lii, R.A. Gorse, Jr., M.C. Sauer, Jr. and S. Gordon, J. Phys. Chem., 84, 819 (1980)
(11) J.P. Burrows, R.A. Cox and R.G. Derwent, J. Photochem., 16, 147 (1981)
(12) N.J. Friswell and M.M. Sutton, Chem. Phys. Lett., 15, 108 (1972)
(13) K. Glanzer and J. Troe Ber. Buns. Phys. Chem., 79, 465 (1975)
(14) R.A. Cox, J.P. Burrows and T.J. Wallington, Chem Phys. Lett., 84, 217 (1981)
(15) W.B. DeMore J. Phys. Chem., 86, 121 (1982)
(16) M.J. Kurylo, O. Klais and A.H. Laufer J. Phys. Chem., 85, 3674 (1981)
(17) F. Temps and H.Gg. Wagner Ber. Buns. Phys. Chem. 86, 119 (1982)
(18) E.J. Hamilton, Jr., and C.A. Naleway, J. Phys. Chem., 80, 2037 (1976)
(19) P.B. Pagsberg, J.Eriksen and H.C. Christensen, J. Phys. Chem., 83, 582 (1979)
(20) T.T. Paukert and H.S. Johnston, J. Phys. Chem., 56,2824 (1972)
(21) O. Lang Rasmussen and E. Bjergbakke, Risø Report, Risø-R-395. January 1984.
(22) Handbook of Bimolecular and Termolecular Gas Reactions. Editors: J. Alister Kerr and Stephen J. Moss

TABLE 1: Rate constants obtained by fitting the computer model (1)-(8) to experimental yields and kinetics.

Reaction	$M^{-1}s^{-1}$	Model fitted to	Note
1	5.0×10^7		1
2	$4.5 \pm 0.5 \times 10^8$	Rate of HO_2 formation	2
3	$6.5 \pm 0.8 \times 10^{10}$	Yields of HO_2 and OH	3
4	$2.0 \pm 0.6 \times 10^9$	Tail end of HO_2 decay	4
5	4.0×10^9		1
6	1.0×10^{10}		1
7	$6.0 \pm 1.0 \times 10^{10}$	OH yield and kinetics	5
8	4.0×10^8		1

Notes

(1) Value adopted from compilation of rate constants. [22]

(2) Contribution from k_3 only at low oxygen concentrations.

(3) The yield of HO_2 is very sensitive to variations of k_3 at low oxygen concenmtrations. Losses of HO_2 via (7) were observable, but less important.

(4) The tail end of the HO_2 decay where OH has disappeared is entirely controlled by k_4.

(5) The rates of formation and decay of OH are governed mainly by k_3 and k_7 while the sensitivities with respect to k_5, k_6 and k_8 were found to be small. The decay is nearly exponential because of the long life time of HO_2 which is present in a large excess of OH.

TABLE 2: Rate Constants for the OH + HO_2 Reaction (7)

10^{-10} k_7 $M^{-1}s^{-1}$	T(K)	p(torr)	Method	Ref.
4.3-1.3 [a]	293	1.3-2.4	DF-LMR	1
6.1 [a]	298	2.0	DF-LMR	2,3
3.5 ± 0.5	298	2.0	DF-LMR	4
4.5 ± 0.7	296	3.0	DF, OH by res. fluoresc.	5
3.9 ± 0.9			DF, OH by res. fluoresc.	6
7.2 [b]	298	700	Steady-state photolysis	7
7.2-9.6 [b]	298	755	Steady-state photolysis	8
7.0	296	760	FP-UV absorption	9
6.0	308	1200	PR-UV absorption	10
3.7 [c]	288-348	760	Modulated photolysis	11
1.2	2130	760	Flame studies	12
1.8	1500	760	Shock tube and review	13
6.0 ± 1.5	308	760	Modulated photolysis	14
7.2 ± 2.4	298	75-730	Steady-state photolysis	15
9.0 ± 3.0	296	760	Steady state photolysis	16
6.0 ± 1.0	298	760	PR-UV abs. Present work	

[a] Reported values corrected using a recommended value of k(OH + H_2O_2).[6]

[b] Recalculated using recommended rate constants.[6]

[c] Independent of temperature at 288-348 K

FIGURE CAPTIONS

Fig.1

Yields of HO_2 obtained by pulse radiolysis of $Ar-H_2-O_2$. $p(H_2) = p(Ar) = 0.5$ atm. T = 298 K. Maxima of the transient absorption signals were monitored at 215 nm with an optical path length of 120 cm. Absolute yields were calculated using the most recent consensus value of $\varepsilon_{215} = 1170\ M^{-1}cm^{-1}$.

Fig.2

Yields of OH monitored at 3090 A with an optical band pass of 0.8 A and L = 120 cm. $p(H_2) = p(Ar) = 0.5$ atm. T = 298 K.

Fig.3

Half-lives of OH-decay. Experimental conditions as in Fig.2.

Fig.4

Kinetics of OH radicals monitored at 3090 A. $p(H_2) = p(Ar) = 0.5$ atm. T = 298 K. Upper curves: $p(O_2) = 0.2$ mbar. Lower curves: 0.5 mbar.

Fig.1. Yield of HO_2 versus $p(O_2)$

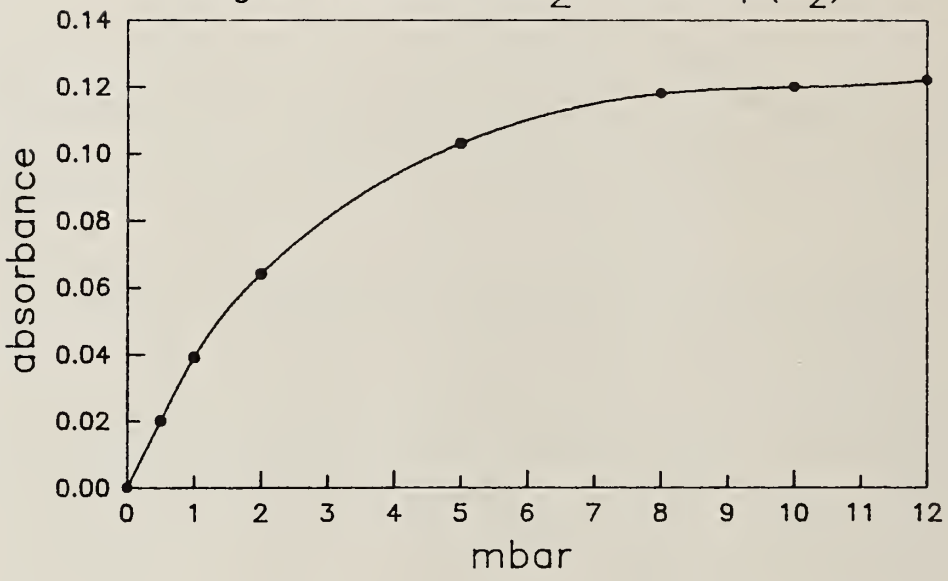

Fig.2. Yield of OH versus $p(O_2)$

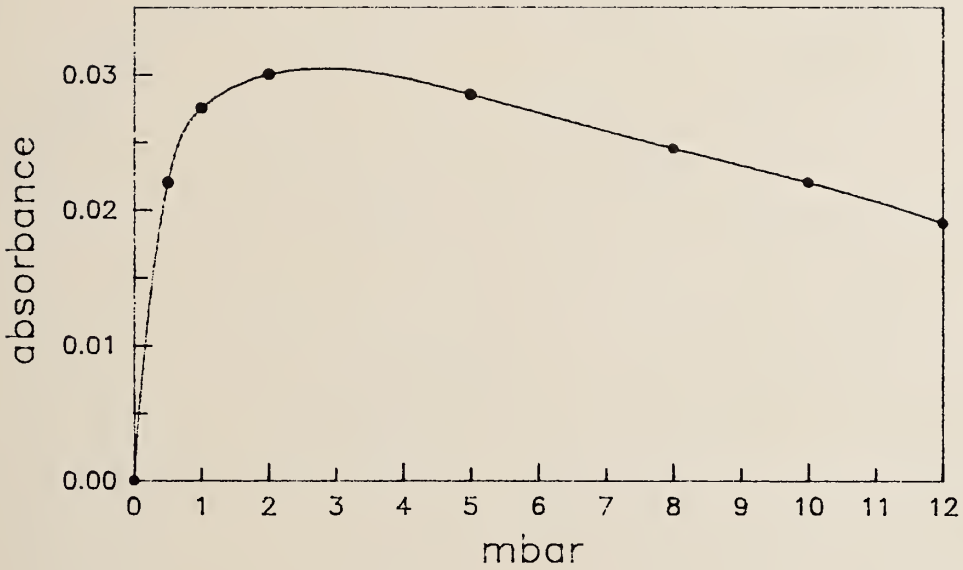

Fig.3. Half--life of OH versus $p(O_2)$

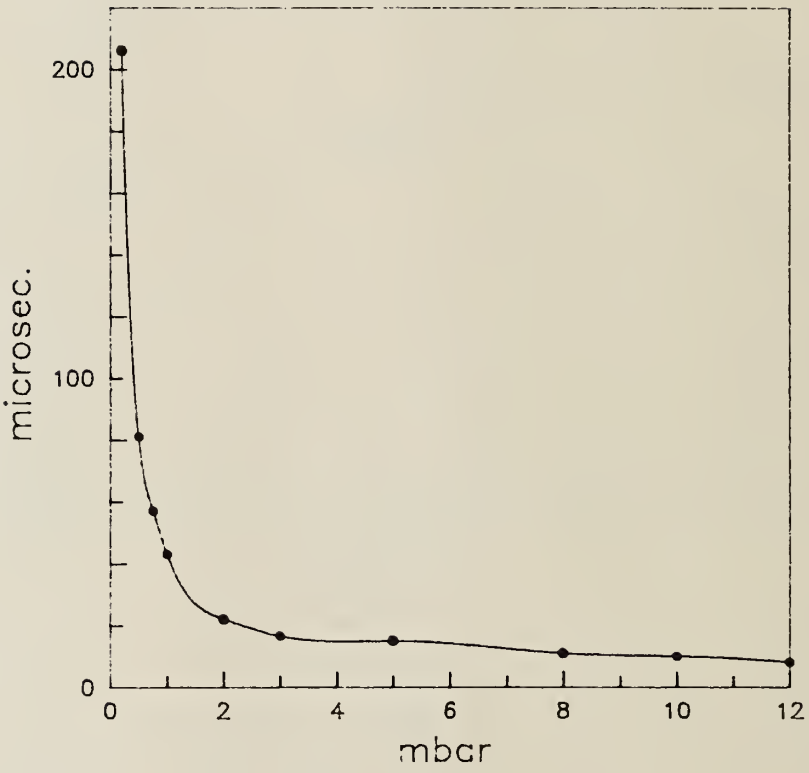

Fig.4.

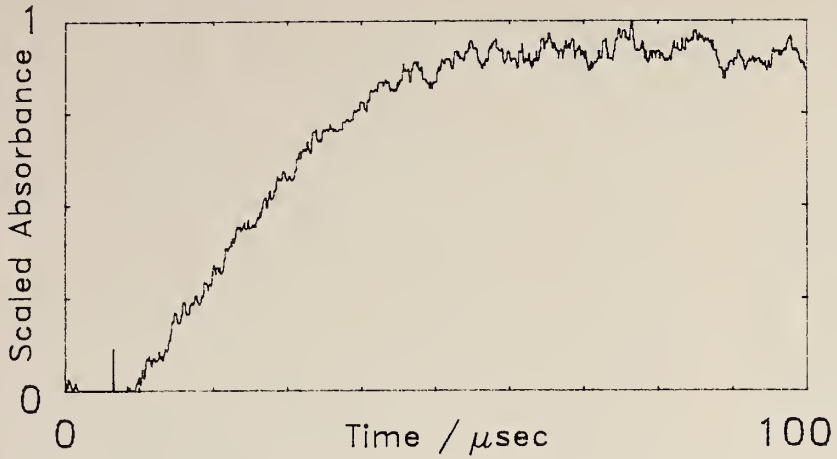
Scaled Absorbance
1
0
0
Time / μsec
100

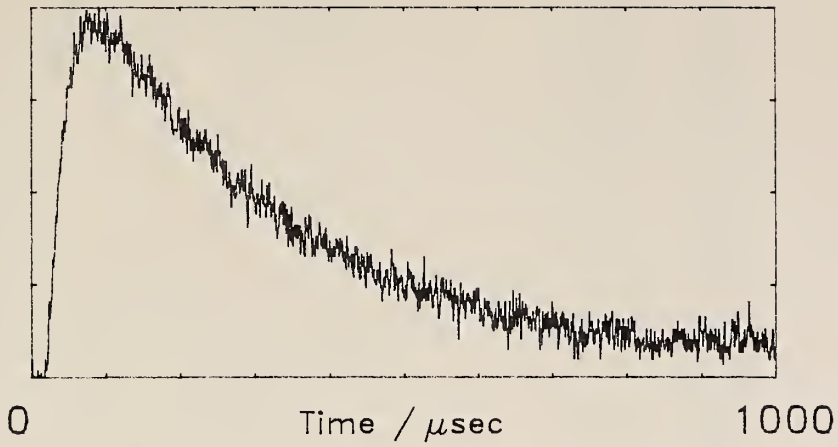
0
Time / μsec
1000

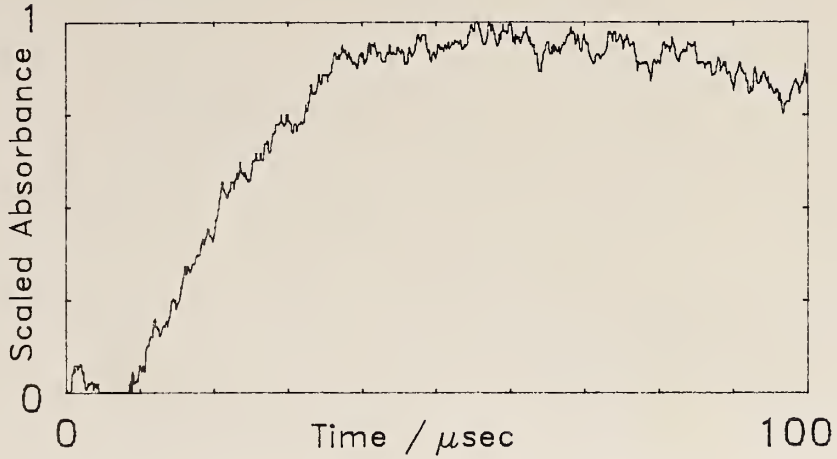
Scaled Absorbance
1
0
0
Time / μsec
100

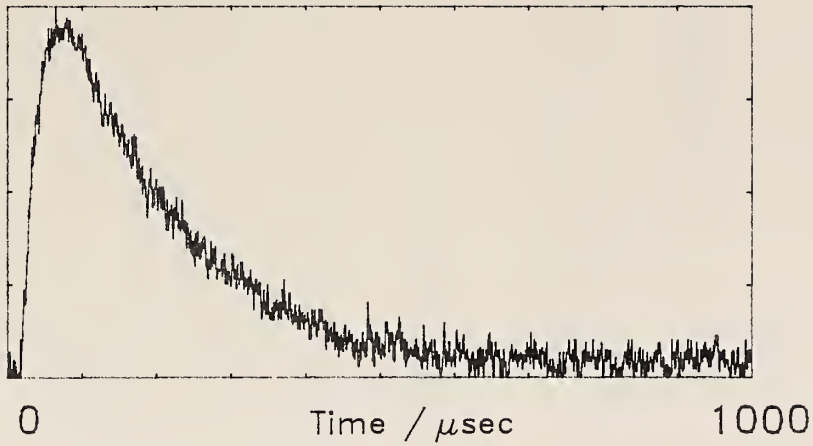
0
Time / μsec
1000

TEMPERATURE DEPENDENCE OF THE ABSOLUTE RATE CONSTANT FOR THE REACTION OF H ATOMS WITH C_4H_2

David F. Nava, Mark B. Mitchell, and Louis J. Stief
Astrochemistry Branch, Laboratory for Extraterrestrial Physics, NASA-Goddard Space Flight Center, Greenbelt, MD, U.S.A.

INTRODUCTION

One of the hydrocarbon species which is an important intermediate in the photodecomposition of methane in Titan's atmosphere in diacetylene (C_4H_2 butadiyne). Reaction with atomic hydrogen and photodissociation are probably the most important loss processes for C_4H_2 in this atmospheric system.

$$H + C_4H_2 \rightarrow \text{Products} \quad (1)$$

$$C_4H_2 + h\nu \rightarrow C_4H + H \text{ and } 2C_2H \quad (2)$$

Diacetylene has not only been suggested as a catalyst in processes converting H atoms into molecular hydrogen, it has been postulated to be the major pathway for this conversion[1] via the following reaction scheme:

$$C_4H_2 + H + M \rightarrow C_4H_3 + M \quad (3)$$

$$C_4H_3 + H \rightarrow C_4H_2 + H_2 \quad (4)$$

This gives diacetylene an important role in both the formation and survival of the unsaturated species in the atmosphere of Titan.

The reaction kinetics of $H + C_4H_2$ are also of importance in incomplete combustion processes that form higher unsaturated hydrocarbons from acetylene and its radicals in the C_2H_2/O/H system.[2] The early formed hydrocarbons in this system include diacetylene. The experimental studies reported by Homann and Schweinfurth[2] showed that hydrogen atoms have a strong positive influence on formation rates of the unsaturated hydrocarbons and that the formation and

concentration of polyacetylenes produced in this chemical system necessitates consideration of reaction steps which form as well as consume diacetylene:

$$C_2H + C_2H_2 \rightarrow C_4H_2 + H \quad (5)$$

$$O + C_4H_2 \rightarrow C_3H_2 + CO \quad (6)$$

$$H + C_4H_2 \rightarrow \text{Products} \quad (1)$$

The chemical kinetics of $H + C_4H_2$ and the photochemistry of diacetylene are poorly understood. Only a room temperature reaction rate measurement at 0.75-7.5 Torr total pressure has been published[3] and only recently has a quantitative study of the photodissociation of C_4H_2 been presented.[4] Because of the importance of understanding the potential of this molecule's role in the atmospheric chemistry of Titan and in the low temperature combustion of C_2H_2 and due to the paucity of kinetic data concerning reactions of this molecule, we have measured the absolute rate constant for the reaction of $H + C_4H_2$ as a function of temperature and pressure.

EXPERIMENTAL

The present kinetic experiments were performed by the technique of flash photolysis coupled with time resolved detection of atomic hydrogen by resonance fluorescence (FP-RF). The apparatus and experimental procedures employed have been described previously[5-7] as well as details specific to the study of H atom reactions.[8,9] Thus only the procedural modifications and details specific to the study of the present reaction are described here.

Flash photolysis of both diacetylene and methane was the source of atomic hydrogen. The low diacetylene concentrations [$(1.32\text{-}13.8) \times 10^{14}$ molecules cm^{-3}] required by the kinetics of this reaction, necessitated the use of three-component mixtures with argon, and in some cases nitrogen, diluent including methane (57-300 mTorr) to

enhance the photolytic production of sufficient hydrogen atoms. Methane was selected as the additional hydrogen atom source because of the slow rate of the H + CH_4 reaction.[10,11] Photolysis occurred at wavelengths above 110 nm (MgF_2 cutoff) to produce $[H]_0 \leq 10^{11}$ atoms cm^{-3}. Lyman-α resonance fluorescence followed directly the exponential decay of atomic hydrogen and was independent of the presence or absence of methane.

Experiments were carried out at five temperatures from 210-423 K over substantial ranges of $[C_4H_2]$, total pressure, and flash intensity (i.e., initial [H]). The pseudo-first-order rate constants obtained from the hydrogen atom decays are composite, including a contribution due to diffusional loss of hydrogen atoms out of the reaction zone analytically viewed by the photomultiplier. Therefore, the diffusion correction k_d was measured independently in identical experiments at each of the various conditions of the reactant kinetic measurements, except that $[C_4H_2] = 0$. We purified the diacetylene, obtained from H. Okabe by preparation according to the method of Jones,[12] by a series of high vacuum degassing and bulb-to-bulb distillation procedures. Analysis by mass spectrometry showed the diacetylene to be more than 99% pure with C_2H_2 (~0.3%) and a constituent (~0.4%) at mass peak 86 (probably CH_2=CCl-C≡CH)[13] being the only measurable impurities.

Argon (Cryogenic Rare Gas Labs. Inc., 99.9995%), helium (Ideal Gas Products, 99.9999%), methane (Matheson, UHP 99.97%), and nitrogen (Scientific Gas Products, UHP 99.999%) were all used without further purification.

RESULTS

The reported experiments measuring the reaction rate of hydrogen atoms with diacetylene were carried out under pseudo-first-order conditions with $[C_4H_2] \gg [H]$. Therefore, the decay of atomic H is represented by

$$\ln[H] = -k_{observed}t + \ln[H]_0 \quad (7)$$

where [H] is proportional to fluorescent counts. Linear least squares analysis of plots of the logarithm of accumulated fluorescent counts against time is used to obtain values of $k_{observed}$. Decay plots are shown in Figure 1 for typical experiments performed at 210, 298, and 423 K. The linearity of these plots over several decay lifetimes confirms the pseudo-first-order conditions of the experiments. The pseudo-first-order decay constant, $k_{observed}$, is given by

$$k_{observed} = k_1 [C_4H_2] + k_d \quad (8)$$

where k_1 is the bimolecular rate constant for reaction (1) and k_d is the first order rate constant for H atom loss by diffusion out of the reaction detection zone. The values of the diffusion correction, k_d, were generally less than 5% of the $k_{observed}$ values for experiments at 210, 247, and 363 K, and in most instances were less than 10% at 298 and 423 K.

Rate data for the reaction of H atoms with C_4H_2 obtained at the five temperatures under the experimental conditions employed are presented in Table 1. These results indicate that at any one temperature, the derived rate constant k is independent of flash energy (i.e., initial [H]), total pressure, or composition of the gas mixture. This further suggests that the data obtained are free of any kinetic complications due to secondary reactions involving species formed in the initial photolytic flash[4] or formed in the primary reaction. Rate constant data yield the Arrhenius expression

$$k_1 = (1.39 \pm 0.25) \times 10^{-10} \exp(-1184 \pm 44/T) \text{ cm}^3 \text{ molecule}^{-1} \text{ s}^{-1} \quad (9)$$

over the temperature range $210 \leq T \leq 423$ K, where the uncertainties are at the one standard deviation level. This temperature dependence is shown graphically in Figure 2.

DISCUSSION

There is only one previous measurement of the reaction rate of H + C_4H_2 with which our result can be compared. Schwanebeck and Warnatz[3] reported a room temperature study of the reaction over a total pressure range of 0.75-7.5 Torr by the technique of discharge flow-mass spectrometry. Their k value of 2.2×10^{-12} cm^3 $molecule^{-1}$ s^{-1} is in substantial agreement with our value for 298 K of $(2.63 \pm 0.23) \times 10^{-12}$ cm^3 $molecule^{-1}$ s^{-1}. Since the mechanism for H + C_4H_2 must be an addition reaction yielding the pressure stabilized C_4H_3 radical, $H + C_4H_2 \underset{\leftarrow}{\overset{\rightarrow}{}} C_4H_3^* \overset{M}{\rightarrow} C_4H_3$, the absence of an observed pressure effect indicates that within experimental error the high pressure limit has been reached at even our lowest pressure studied (5 Torr). In conjunction with results from the earlier room temperature work,[3] the high pressure limit appears to have been reached even at 0.75 Torr.

CONCLUSIONS

The present chemical kinetic study of the reaction of atomic hydrogen with diacetylene enables better understanding of the role of diacetylene in rapidly catalyzing H atom combination to molecular hydrogen via the sequence of reactions:

$$C_4H_2 + H \overset{M}{\rightarrow} C_4H_3 \qquad (3)$$

$$C_4H_3 + H \rightarrow C_4H_2 + H_2 \qquad (4)$$

In conjunction with results from the recent photochemical study of diacetylene,[4] and in light of the slower, less effective rate for H atom removal by analogous reaction with C_2H_2,[8] consideration of the reaction H + C_4H_2 does indeed appear to be important for accurate modeling and understanding of Titan's atmosphere.

The present flash photolysis-resonance fluorescence study, in addition to confirming the only published measurement of the room temperature reaction rate, has

extended direct measurements to higher pressures and to other temperatures. The low temperature data is especially relevant for the atmosphere of Titan.

The present temperature study also provides more comprehensive kinetic information from which to more accurately model the effect of H + C_4H_2 in low temperature combustion mechanisms for hydrocarbon formation in the C_2H_2/O/H system.

ACKNOWLEDGMENTS

This work was supported by the NASA Planetary Atmospheres Program. M. B. M. acknowledges support by NASA under Grant NSG 5173 to the Catholic University of America. We sincerely thank Hideo Okabe for providing the diacetylene; Sol Glicker for advice concerning purification procedures for diacetylene and for mass spectrometric analysis of the purified compound; and Stephanie Myers for patiently typing this paper.

References

(1) Yung, Y. L., M. Allen, and J. P. Pinto, Astrophys. J. Suppl. 55, 465, 1984.
(2) Homann, K. H., and H. Schweinfurth, Ber. Bunsenges. Phys. Chem., 85, 569, 1981.
(3) Schwanebeck, W., and J. Warnatz, Ber. Bunsenges Phys. Chem., 79, 530, 1975.
(4) Glicker, S., and H. Okabe, paper presented at the International Conference on Chemical Kinetics, Nat. Bur. of Stds., Gaithersburg, MD, June 17-19, 1985.
(5) Klemm, R. B., and L. J. Stief, J. Chem. Phys., 61, 4900, 1974.
(6) Michael, J. V., and J. H. Lee, J. Phys. Chem., 83, 10, 1979.
(7) Stief, L. J., D. F. Nava, W. A. Payne, and J. V. Michael, J. Chem. Phys., 73, 2254, 1980.
(8) Payne, W. A., and L. J. Stief, J. Chem. Phys., 64, 1150, 1976.
(9) Whytock, D. A., W. A. Payne, and L. J. Stief, J. Chem. Phys., 65, 191, 1976.
(10) Kurylo, M. J., G. A. Hollinden, and R. B. Timmons, J. Chem. Phys., 52, 1773, 1970.

(11) Sepehrad, A., R. M. Marshall, and H. Purnell, J. Chem. Soc. Faraday Trans. I., 75, 835, 1979.
(12) Jones, A. V., Proc. R. Soc. London, Ser A 211, 285, 1952.
(13) Georgieff, K. K., and Y. Richard, Can. J. Chem., 36, 1280, 1958.

TABLE 1. Rate Data for the Flash Photolysis - Resonance Fluorescence Study of the Reaction H + C_4H_2

T (K)	[Ar] (Torr)	[CH_4] (mTorr)	[C_4H_2] (10^{14} cm^{-3})	Flash Energy (J)	No. of Expts.	k_1[c] 10^{-12} cm^3 $molecule^{-1}$ s^{-1}
210	30	75	5.14	20,36	2	0.53 ± 0.01
	40	57	5.52	20-36	3	0.56 ± 0.02
	50	125	8.57	20,36	2	0.58 ± 0.02
	60	86	8.28	20-56	4	0.53 ± 0.03
	60	150	10.28	20-56	3	0.53 ± 0.02
	85	121	11.70	20-56	4	0.53 ± 0.01
	100	143	13.80	20-56	4	0.54 ± 0.02
					22	0.54 ± 0.02[d]
247	30	112	3.79	20-56	3	1.20 ± 0.13
	40	150	5.05	20-56	3	1.17 ± 0.08
	50	71	4.75	14-36	3	0.78 ± 0.01
	50	187	6.31	20-56	3	0.98 ± 0.02
	75	107	7.12	14-36	3	0.97 ± 0.03
	100	143	9.50	20-36	3	1.08 ± 0.03
					18	1.03 ± 0.15[d]
298	5	100	1.62	36-81	3	2.58 ± 0.16
	5[a]	100	2.59	36-81	3	2.51 ± 0.02
	10[a]	100	2.59	36-81	4	2.54 ± 0.17
	10	200	3.24	36,56	2	2.33 ± 0.06
	10	200	3.24	36-81	3	2.43 ± 0.13
	20	160	1.94	20-110	5	2.72 ± 0.15
	35	280	3.40	9-110	6	2.62 ± 0.21
	50[b]	105	1.62	36,36	2	2.47 ± 0.04
	50[b]	111	1.62	56-81	3	3.18 ± 0.03
	70[b]	147	2.27	36-81	4	2.59 ± 0.18
	70[b]	156	2.27	56-81	3	2.85 ± 0.25
	90[b]	189	2.92	56-110	4	2.66 ± 0.13
	90[b]	200	2.92	68,81	2	2.64 ± 0.06
					44	2.63 ± 0.23[d]
363	5[a]	100	1.87	36,56	2	5.30 ± 0.11
	10[a]	200	3.74	36-81	3	5.39 ± 0.07
	20	250	3.97	36-81	4	5.43 ± 0.06
	25	125	1.32	36-81	3	5.72 ± 0.25
	35	175	1.88	36-81	3	5.45 ± 0.18
	40	200	2.12	36-81	3	5.51 ± 0.14
	50	250	2.69	36-81	3	5.23 ± 0.08
					21	5.44 ± 0.19[d]
423	10[a]	100	1.60	36-81	4	8.74 ± 0.39
	20	120	1.37	81-110	3	8.93 ± 1.50
	35	210	2.40	81-110	3	8.72 ± 0.80
	70	233	1.51	36-81	3	9.15 ± 0.53
	90	300	1.94	36-81	3	8.88 ± 0.41
					16	8.88 ± 0.70[d]

[a]Experiments under static conditions; all others flowing.

[b]Diluent was nitrogen instead of argon.

[c]Error limit is one standard deviation.

[d]Mean value of reaction rate at that temperature.

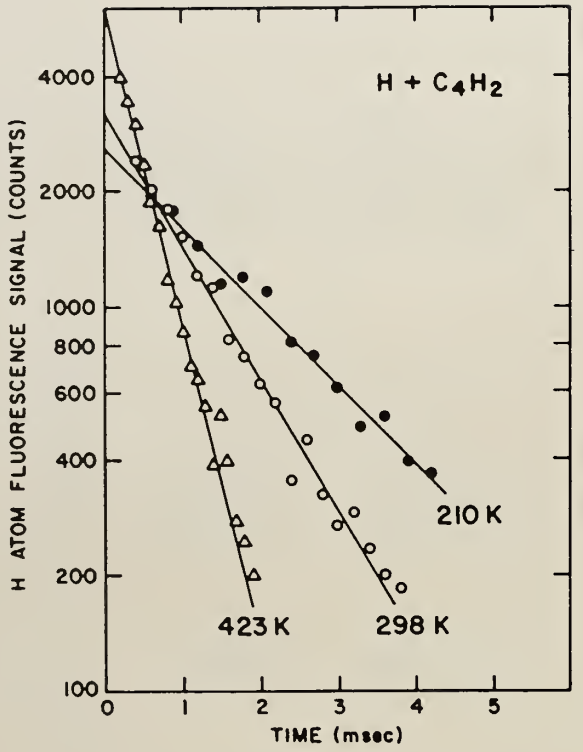

FIGURE 1. FIRST ORDER DECAY PLOTS OF THE LOGARITHM OF H ATOM FLUORESCENT COUNTS MINUS BACKGROUND VS. TIME AT THREE TEMPERATURES. ●: T = 210 K, $[C_4H_2]$ = 8.28 X 10^{14} CM^{-3}, $[CH_4]$ = 86 mTORR, [Ar] = 60 TORR, K_{OBS} = 469 S^{-1}, K_d = 14 S^{-1}; ○: T = 298 K, $[C_4H_2]$ = 2.92 X 10^{14} CM^{-3}, $[CH_4]$ = 189 mTORR, [Ar] = 90 TORR, K_{OBS} = 793 S^{-1}, K_d = 35 S^{-1}; △: T = 423 K, $[C_4H_2]$ = 2.40 X 10^{14} CM^{-3}, $[CH_4]$ = 210 mTORR, [Ar] = 35 TORR, K_{OBS} = 2078 S^{-1}, K_d = 56 S^{-1}.

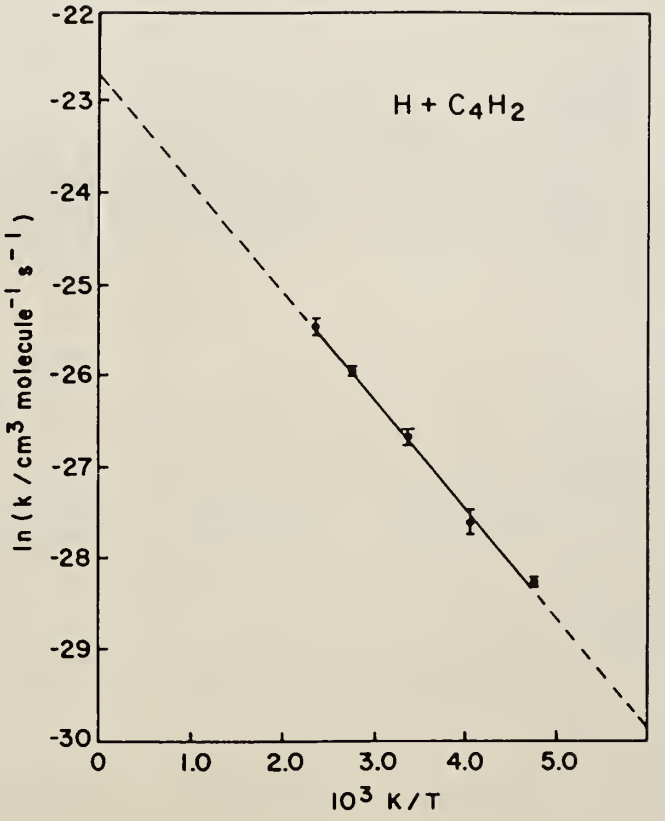

FIGURE 2. ARRHENIUS PLOT OF THE REACTION RATE FOR H + C_4H_2. THE LINEAR LEAST-SQUARES LINE IS GIVEN BY (1.39 ± 0.25) X 10^{-10} exp (-1184 ± 44/T) CM^3 $MOLECULE^{-1}$ S^{-1} WHERE THE UNCERTAINTIES ARE ONE STANDARD DEVIATION.

Photoabsorption Cross Sections of Free Radicals in Vacuum Ultraviolet

J. B. Nee and L. C. Lee
Department of Electrical and Computer Engineering
San Diego State University
San Diego, CA 92182

The molecular formation and destruction processes in the various interstellar clouds are interested in astrophysics.[1,2] It is well recognized that free radicals play important roles in the interstellar molecular processes, because their chemical reactions determine the abundances of interstellar species. The radicals also play an important role in the Earth's atmosphere.

The photoabsorption cross sections of free radicals in the vacuum ultraviolet wavelengths have been investigated in this laboratory in the last few years. A pulsed-discharge and time-resolved method has been employed to measure the photoabsorption cross sections of OH, OD, CN and SO. Very limited data so far are available. Most cross sections used in the modeling of interstellar chemistry relied on theoretical calculations.[3]

II. EXPERIMENTAL

The experimental apparatus has been described in detail elsewhere.[4] Free radicals were produced from pulsed-discharge of a trace amount of parent gas (e.g. H_2O, HCN, or SO_2) mixed with several torr of Ar. The free radicals produced by the pulsed-discharge will exist in a short time period of about a

millisecond. The photoabsorption caused by the transient radicals is differentiated from those caused by stable molecules using a time-resolved technique.

A H_2 lamp was used as the light source. The wavelength was selected by a 0.2 m monochromator (Acton VM-502) with an 0.5 nm resolution. A multichannel analyzer (Canberra Model 35) was used to process the optical signals detected by a solar-blind photomultiplier tube.

III. RESULTS AND DISCUSSION

The experiment was done under the condition that the Ar concentration was much greater than the parent molecules (such as H_2O or SO_2) that produces radicals. The radicals are produced by the chemical processes:

$$e^- + Ar \longrightarrow Ar^* (^3P_{o,2}) \quad (1)$$

$$Ar^* + H_2O \longrightarrow Ar + OH + O \quad (2)$$

$$\text{or} \quad Ar^* + SO_2 \longrightarrow Ar + SO + O \quad (3)$$

The OH or SO radical in (2) or (3) has been shown to be the major product of the reaction.[7] The $Ar^* (^3P_{o,2})$ are metastable states whose energies are 11.73 eV for J=0 and 11.55 eV for J=2. The radiative lifetimes of these excited states are about seconds.[5] Quenching of Ar^* by H_2O or SO_2 is very fast with rate constants[6] greater than 10^{-10} cm^3 sec^{-1}. Thus, the chemical lifetime of Ar^* was about a millisecond after the discharge was turned off. This is consistent with the observation that the photoabsorption occurs in a period of about 1 ms after the discharge being turned off as shown in the time-resolved spectrum of Fig. 1.

Using H_2O as a source, we have measured[4] the photoabsorption cross section of OH, which absorbs light at wavelengths shorter than 183 nm as shown in Fig. 2. Several discrete structures were observed. In addition to the well-known $D^2\Sigma^-$ state at 122.2 nm, we also observed bands at 120.5 and 124.5 nm. The two later bands presumably result from two $^2\Pi$ states.[8] A similar spectrum was obtained by using D_2O as an OD source.[9]

We also used HCN as the source for the photoabsorption measurement of CN. The photoabsorption cross section[10] of this radical in the VUV region is small whose upper limit is shown in Fig. 3.

Recently, we also studied the SO radical using SO_2 as the parent molecule. Photoabsorption of this radical in the 190-230 nm region has been investigated by Phillip.[11] In this wavelength region, the photoabsorption is caused by the $B^3\Sigma^- - X^3\Sigma^-$ transition joining to an absorption continuum at 190 nm. The photoabsorption caused by these transitions were repeatedly observed in our experiment. In addition, we observed strong photoabsorption at wavelengths shorter than 135 nm as shown in Fig. 4. Preliminary results showed that the peak VUV photoabsorption cross section is in the order of 10^{-16} cm^2.

IV. CONCLUSION

Using a pulsed-discharge technique, we have measured the photoabsorption cross sections of several free radicals in the VUV region. These data are needed for determining the photodissociation rates of these radicals in the interstellar

medium. Since the interstellar VUV radiation is very intense, photodissociation is the major source for the destruction of interstellar radicals. The photoabsorption cross section are thus useful for understanding the photochemistry processes occurring in the interstellar medium. The photoabsorption data are also useful for understanding the photochemistry of the Earth's upper atmosphere.

REFERENCES

1. W. W. Duley and D. W. Williams, Interstellar Chemistry, (Academic Press, New York, 1984).

2. A. Dalgarno and J. H. Black, Rep. Prog. Phys. 39, 573, (1976).

3. P. M. Solomon and W. Klemperer, Astro. Phys. J. 178, 389, (1972).

4. J. B. Nee and L. C. Lee, J. Chem. Phys. 81, 31, (1984).

5. J. H. Kolts and D. W. Setser in Reactive Intermediates in the Gas Phase, edited by D. W. Setser, (Academic Press, New York, 1979).

6. J. E. Velazco, J. H. Kolts, and D. W. Setser, J. Chem. Phys. 69, 4357, (1978).

7. J. Balamuta and M. F. Golde, J. Chem. Phys. 76, 2430, (1982).

8. E. F. van Dishoeck, S. R. Langhoff and A. Dalgarno, J. Chem. Phys. 78, 4552, (1983), E. F. van Dischoeck, M. C. van Hemert, A. C. Allison, and A. Dalgarno, J. Chem. Phys. 81, 5709, (1984).

9. J. B. Nee and L. C. Lee, J. Chem. Phys. 81, 3811, (1984).

10. J. B. Nee and L. C. Lee, Astrophys. J. 291, 202, (1985).

11. L. F. Phillips, J. Phys. Chem. 85, 3394, (1981).

*This work is supported by NASA under Grant No. NAGW-319 and by NSF under Grant No. ATM-8412618.

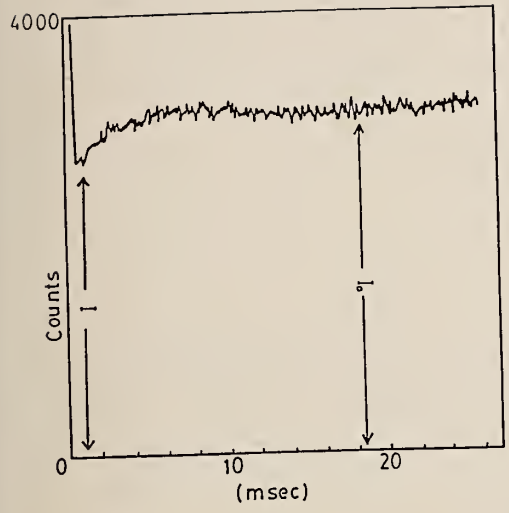

Fig. 1 Photoabsorption of OH at 122.2 nm of the $D^2\Sigma^-$ state (Ref. 4).

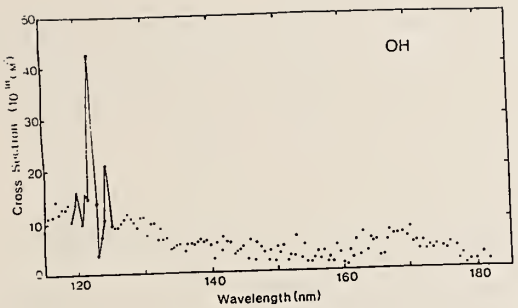

Fig. 2 A spectrum of photoabsorption cross sections of OH; peaks are at 120.5, 122.2, and 124.5 nm (Ref. 4).

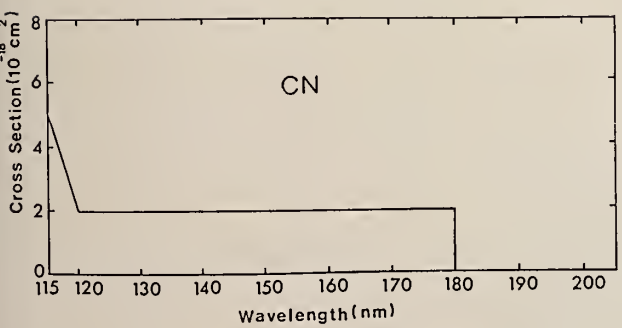

Fig. 3 The upper limit of photoabsorption cross sections of CN radicals (Ref. 10).

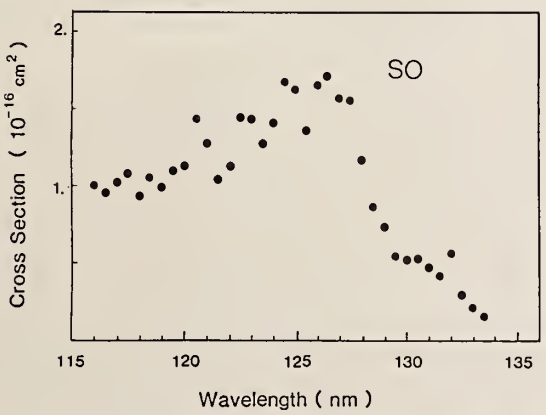

Fig. 4 Photoabsorption cross sections of SO radicals

Infrared Spectroscopy of Molecular Ions

Takeshi Oka

Department of Chemistry and
Department of Astronomy and Astrophysics
The University of Chicago
Chicago, IL. 60637

Following is a brief summary of infrared spectroscopy of molecular ions since June 1984 when I gave a talk at the Columbus Meeting. I limit myself to works done in our laboratory and other works closely related to them.

1. H_3^+

A detailed analysis of the ν_2 vibration-rotation band has been completed by Watson et al.[1] in which the originally reported 15 lines[2] and the subsequently reported 15 lines[3] were added with another 16 lines of higher rotational levels and lower frequency P branch transitions to determine accurate molecular constants of this fundamental ion. Because of the large vibration-rotation constants of H_3^+, the Pade approximation has proved useful. The determined constants are shown on the following page.

Amano and Watson[4,5] observed and analyzed the ν_1 fundamental band of H_2D^+ which enabled them to accurately predict the H_2D^+ rotational lines in the millimeter wave region. Following their predictions, the rotational transitions $1_{10} \leftarrow 1_{11}$[6,7] and $2_{11} \leftarrow 2_{12}$[8] have been detected. Based on this laboratory data a possible detection of the $1_{10} \leftarrow 1_{11}$ transition of H_2D^+ in the giant molecular cloud NGC 2264 has been reported[9]. The ν_2 and ν_3 band of H_2D^+ which was initially reported by Shy et al.[10] without assignment has been studied more extensively and analyzed[11]. Because of the large molecular constants and the Coriolis coupling between the two states, supermatrix approach was used to eliminate ambiguity in assignment. Doubly deuterated species HD_2^+ has been studied (ν_1 band[12], and ν_2 and ν_3 band[13]). Rotational spectrum of this species should also be observable in the millimeter wave region.

Vibration–rotation parameters for the ν_2 band of H_3^+ (cm^{-1})

Parameter i*	Value (SD)†	Correlation κ_i‡	*Ab initio*§	*Ab initio*‖
		Ground state		
B_0	43.564570(1553)	163.2	43.668	43.520
C_0	20.605147(2993)	167.7	20.675	20.579
$10^2 D_0^{JJ}$	4.17537(1900)	2 248.5	3.72	4.22
$10^2 D_0^{JK}$	−7.60626(4096)	3 332.9	−6.70	−7.76
$10^2 D_0^{KK}$	3.74107(3683)	1 797.7	3.29	3.85
$10^5 h_3$	−1.056(100)	5.7		−0.9
$10^3 d_J$	1.7325(1529)	348.6		2.0
$10^3 d_K$	−4.1003(4428)	190.4		−4.6
		ν_2 state		
ν_2	2521.30817(925)	18.2	2516	2494.4
B_2	44.225698(3011)	242.1	43.839	
C_2	19.339581(6389)	1 000.8	19.735	
$C\zeta_2$	−18.65110(384)	49.7	−18.516	
$10^2 \eta_2^J$	−14.0319(858)	691.4		
$10^2 \eta_2^K$	16.7714(1937)	2 659.1		
$10^2 D_2^{JJ}$	5.27821(3051)	7 814.5		
$10^2 D_2^{JK}$	−10.87796(9077)	36 917.6		
$10^2 D_2^{KK}$	6.07921(6385)	12 807.9		
$10^3 \beta_2$	−3.1598(363)	3.3		
q_2	−5.37192(254)	33.8	−4.87	
$10^5 h_3$	−1.056(100)	5.7		
$10^3 d_J$	2.0467(1481)	691.2		
$10^3 d_K$	−1.8823(3657)	1010.0		
$10^3 e_J$	4.0396(307)	263.6		
$10^3 e_K$	−7.1747(1467)	1772.6		

An exciting development was the observation of strong H_3^+ emission spectrum by Majewski et al.[14] using a Fourier Transform spectrometer. A calculation of distortion induced rotational transitions of H_3^+ has been completed[15].

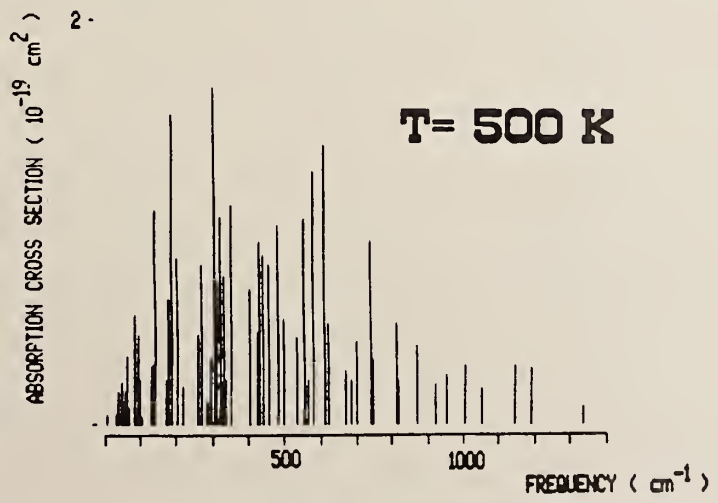

Calculated rotational spectrum of H_3^+

2. $HCNH^+$

Based on the molecular constants of $HCNH^+$ determined from the infrared spectrum[16] of $HCNH^+$, Bogey et al.[17] have observed rotational spectrum of the ion in the millimeter wave region. The radio astronomical detection of this ion has not been successful yet. Amano has studied several isotopic species and hot bands of this ion and determined the molecular structure accurately[18,19].

3. H_3O^+

A systematic diode laser spectroscopy of the ν_2 vibration-inversion bands of H_3O^+ has led to an accurate determination of the ground state inversion doubling of this important ion.

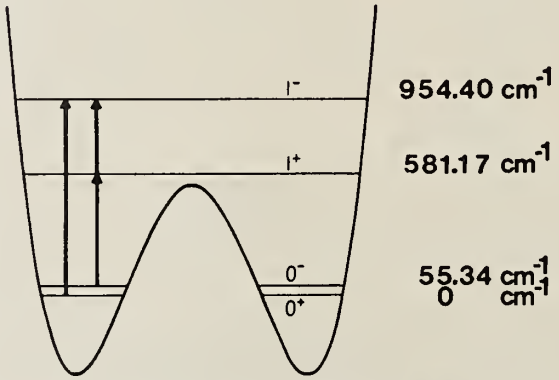

FIG. 1. The double minimum potential and the vibration-inversion energy levels of the ν_2 bending mode of H_3O^+. The three infrared bands $1^- \leftarrow 0^+$, $1^+ \leftarrow 0^-$, and $1^- \leftarrow 1^+$ shown by the bold arrows appear at 10.5, 19, and 27 μm, respectively. The ground-state inversion splitting has been determined from the measurement of the $1^- \leftarrow 1^+$ band, reported in this paper, and our previous measurements of the other two bands (Ref. 4).

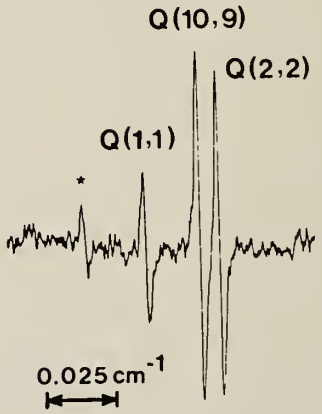

FIG. 2. The group of lines close to the origin of the $1^- \leftarrow 1^+$ band. The derivative shape is due to velocity modulation (Ref. 14). The line with the asterisk is most likely the ground-state inversion-rotation transition $R(15, 9)$. Time constant of detection is 3 sec.

Following the initial study of the $1^- \leftarrow 0^+$ transition in the 10μ region (ν_0 = 954.40 cm^{-1})[20], the $1^+ \leftarrow 0^-$ transition in 19μ (ν_0 = 525.83 cm^{-1})[21] and the $1^- \leftarrow 1^+$ transition in 27μ (ν_0 = 373.23 cm^{-1})[22] have been observed and analyzed. This enabled us to calculate four submillimeter rotation-inversion lines of H_3O^+. Based on this prediction the $0^- \leftarrow 0^+$ P(2,1) transition[23] and the three $0^- \leftarrow 0^+$ P(3,K) transition (K = 2,1,0)[24] have been measured. It is anticipated that these laboratory measurements will lead to radio astronomical detection of this ion which is predicted to be abundant in dense clouds.

The infrared spectroscopy of 10μ band was also reported by Lemoine and Destombes[25] and that of 19μ by Davies et al.[26] Sears has measured more R-brand lines of the $1^- \leftarrow 1^+$ transition[27]. Simultaneously analyzing these results, accurate molecular constants for the ν_2 vibration inversion levels have been determined[28]. The prediction of millimeter wave and far infrared transitions related to metastable levels of H_3O^+ are listed below.

Predicted inversion and inversion-rotation spectrum of H_3O^+ related to the metastable rotational levels (in cm^{-1})

Transition	Predicted	Observed
R(3,3)	143.8060(77)[a]	---
R(3,0)	141.1839(68)	---
R(2,2)	121.5437(47)	---
R(1,1)	99.4255(34)	---
Q(3,3)	55.4912(63)	---
Q(2,2)	55.2791(39)	---
Q(1,1)	55.2312(31)	---
P(1,0)	32.8454(30)	---
P(2,1)	10.2468(34)	10.24682[c]
P(3,2)	-12.1678(49)[b]	-12.16831[d]
P(3,1)	-12.9576(47)[b]	-12.95757[d]
P(3,0)	-13.2186(47)[b]	-13.21821[d]

[a]Numbers in the parenthesis are uncertainties of the prediction.
[b]For those transitions the 0^+ level is above the 0^- level.
[c]Experimental observation by Plummer, Herbst and De Lucia.
[d]Experimental observation by Bogey, Demuynck, Denin and Destombes.

The detection of far-infrared direct inversion transitions in H_3O^+ is an exciting possibility.

4. CH_3^+ and Hydrocarbon Cation

Our search for hydrocarbon cations revealed a very rich group of spectral lines in the area of 3250 cm^{-1} - 2950 cm^{-1}. The most dense group of lines show spacings of $\sim$2 cm^{-1} and is likely due to protonated acetylene. The pattern is basically that of an asymmetric rotor but deviates from it in detail. This may be due to the interconversion between the two theoretical predicted structures, the classical (formaldehyde shape) and the non-classical (bridged) which are predicted to have very close energy[29,30,31].

The other group of lines were much widely spaced and this was obviously due to hydrocarbon cations containing one carbon atom. Initially protonated methane CH_3^+ was suspected to be the carrier of this spectrum but the analysis revealed that it is CH_3^+. With hindsight, the abundance of CH_3^+ in the methane discharge is not surprising because it does not react with H_2 to form CH_4^+.

About 150 lines were measured and assigned to the ν_3 fundamental band of CH_3^+. The molecular constants of this ion are shown in the following table[32].

Molecular constants of CH_3^+ (in cm^{-1})[a]

$\nu_o - (1-\zeta)\zeta C' = 3107.8527\ (70)$	
$C' - C'\zeta - B' = -5.2244\ (18)$	$(C'-B')-(C''-B'') = 0.0530\ (16)$
$B' = 9.2691\ (13)$	$B'' = 9.3600\ (15)$
$D'_J = 6.57\ (29) \times 10^{-4}$	$D''_J = 7.25\ (34) \times 10^{-4}$
$D'_{JK} = 13.46\ (85) \times 10^{-4}$	$D''_{JK} = 14.5\ (11) \times 10^{-4}$
$D'_K - \eta_K/4 = 5.36\ (57) \times 10^{-4}$	$D''_K = 4.98\ (73) \times 10^{-4}$
$\eta_J = -7.3\ (17) \times 10^{-4}$	
$q = 9.94\ (99) \times 10^{-3}$	$r_o = 1.09151\ (9)$ Å

[a] the numbers in parentheses are one standard deviation.

More detailed analysis of the CH_3^+ spectrum and other hydrocarbon cations are in progress.

5. Plasma Diagnosis Using Infrared Spectroscopy.

Possibility of observing infrared absorption lines of molecular ions makes it possible to analyze plasma conditions in detail. Thus we should be able to study concentrations of various ions (and free radicals), their vibrational, rotational, and translational temperatures, the drift velocity of ions, concentration distributions of ions and so on. The advantage of this method is that it is in-situ and non-intrusive unlike traditional methods. We also have quantum mechanical information and a reasonable space resolution. Some such work will be discussed.

References.

1. J.K.G. Watson, S.C. Foster, A.R.W. McKellar, P. Bernath, T. Amano, F.S.Pan, M.W. Crofton, R.S. Altman and T. Oka, Can. J. Phys. 62, 1875 (1984).

2. T. Oka, Phys. Rev. Lett. 45, 531 (1980).

3. T. Oka, Phil. Trans. Roy. Soc. London Ser. A. 383, 543 (1981).

4. T. Amano and J.K.G. Watson, J. Chem. Phys. 81, 2869 (1984).

5. T. Amano, J. Opt. Soc. Amer. B2, 790 (1985).

6. M. Bogey, C. Demuynck, M. Denis, J.L. Destombes, and B. Lemoine, Astron. Astrophys. 137, L15 (1984).

7. H.E. Warner, W.T. Conner, R.H. Petrmichl and R.C. Woods, J. Chem. Phys. 81, 2514 (1984).

8. S. Saito, K. Kawaguchi and E. Hirota, J. Chem. Phys. 82, 45 (1985).

9. T.G. Phillip, G.A. Blake, J. Keene, R.C. Woods and E. Churchwell, Ap. J. Lett. 294, L45 (1985).

10. J.T. Shy, J.W. Farley and W.H. Wing, Phys. Rev. A24, 1146 (1981).

11. S.C. Foster, A.R.W. McKellar, J.R. Peterkin, J.K.G. Watson, F.S. Pan, M.W. Crofton, R.S. Altman and T. Oka, J. Chem. Phys., submitted.

12. K.G. Lubic and T. Amano, Can. J. Phys. 62, 1886 (1984).

13. S.C. Foster, A.R.W. McKellar and J.K.G. Watson, Symposium on Molecular Spectroscopy, Columbus, Ohio (1985).

14. W.A. Majewsky, J.K.G. Watson and J.W.C. Johns, Symposium on Molecular Spectroscopy, Columbus, Ohio (1985).

15. F.S. Pan and T. Oka, to be published.

16. R.S. Altman, M.W. Crofton and T. Oka, J. Chem. Phys. 80, 3911, 81, 4255 (1984).

17. M. Bogey, C. Demuynck and J.L. Destombes, J. Chem. Phys., in press.

18. T. Amano, J. Chem. Phys. 81, 3350 (1984).

19. T. Amano and k. Tanaka, Symposium on Molecular Spectroscopy, Columbus, Ohio (1985).

20. N.N.Haese and T. Oka, J. Chem. Phys. 80, 572 (1984).

21. D.J. Liu, N.N. Haese and T. Oka, J. Chem. Phys. 82, 5368 (1985).

22. D.J. Liu and T. Oka, Phys. Rev. Lett. 54, 1787 (1985).

23. G.M. Plummer, E. Herbst and F.C. De Lucia, J. Chem. Phys. 83, 1428 (1985).

24. M. Bogey, C. Demuynck, M. Denis and J.L. Destombes, Astron. Astrophys. (1985).

25. B. Lemoine and J.L. Destombes, Chem. Phys. Lett. 111, 284 (1984).

26. P.B. Davies, P.A. Hamilton and S.A. Johnson, J. Opt. Soc. Amer. B2, (1985) in press.

27. T. Sears, private communication.

28. D.J. Liu, T. Oka and T. Sears, to be published.

29. W.A. Lathan, W.J. Hehre and J.A. Pople, J. Am. Chem. Soc. 93, 808 (1971).

30. J. Weber, M. Yoshimira and A.D. McLean, J. Chem. Phys. 64, 4159 (1976).

31. G.P. Raine and H. Schaeffer III, J. Chem. Phys. 81, 4034 (1984).

32. M.W. Crofton, W.A. Kreiner, M.-F. Jagod, B.D. Rehfuss and T. Oka, J. Chem. Phys., in press.

THE REACTION OF MUONIUM WITH HYDROGEN PEROXIDE IN AQUEOUS SOLUTION

Paul W. Percival, Jean-Claude Brodovitch, and Kenneth E. Newman*
Department of Chemistry and TRIUMF, Simon Fraser University,
Burnaby, B.C., Canada V5A 1S6

There are two pathways for the reaction of H atoms with hydrogen peroxide in the gas phase:

$$H + H_2O_2 \rightarrow H_2O + \cdot OH \qquad (1)$$

and

$$H + H_2O_2 \rightarrow H_2 + \cdot OOH \ , \qquad (2)$$

but there is ambiguity as to which one dominates in aqueous solution. The exotic atom muonium (Mu $\equiv \mu^+e^-$) is a light isotope of hydrogen, and its reactions with H_2O_2 and D_2O_2 have been studied by the μSR technique at TRIUMF. The results include determination of isotope effects, pH dependence and temperature dependence.

INTRODUCTION

The results of many gas-phase studies indicate that hydrogen atoms react with hydrogen peroxide in two distinct ways:

$$H + H_2O_2 \rightarrow H_2O + \cdot OH \qquad (1)$$

$$H + H_2O_2 \rightarrow H_2 + \cdot OOH \ . \qquad (2)$$

Unfortunately, there is little agreement on the absolute values of the rate constants k_1 and k_2 [1], or even which dominates at a particular temperature. Some of the discrepancies can undoubtedly be ascribed to the indirect nature of many of the early determinations, and later work [2] has shown that k_1 and k_2 have markedly different temperature dependencies. However, the conclusion of [2] is that $k_1 >> k_2$ at room temperature, and this is not in accord with two other studies, which

*Present address: Département de Chimie, Université de Sherbrooke, Québec.

find $k_1/k_2 = 1.86 \pm 0.14$ [3] and $k_1/k_2 = 1.3$ [4]. The situation is anything but clear.

Since the outcome of the H + H_2O_2 reaction is so finely balanced in the gas phase, it is interesting to consider whether one reaction pathway dominates in liquid solution. Individual rates can change by more than an order of magnitude [5], so differential effects of solvation might serve to tip the balance. Since H and H_2O_2 are both produced in the radiolysis of water, their reaction is of great importance in the field of radiation chemistry, and it is consequently listed in all the standard texts and reviews, e.g. [6]. Invariably the mechanism is stated to be that of reaction (1), with no mention of (2). On the other hand, a noted authority on H atom chemistry states [5]: "The reaction with H is hydrogen abstraction resulting in the formal oxidation of H_2O_2 to HO_2", i.e. reaction (2).

Muonium (Mu) is a single-electron hydrogen-like atom with a short-lived elementary particle, the positive muon, as nucleus. From a chemical point of view it is a light (0.11 amu) isotope of hydrogen, and as such is expected to undergo analogous reactions [7]. In the early days of muonium chemistry (just over a decade ago!) it was suggested that muonium reacts with hydrogen peroxide in aqueous solution to give the MuO• radical [8]:

$$Mu + H_2O_2 \rightarrow H_2O + {\cdot}OMu \ . \qquad (3)$$

While this has a formal similarity to reaction (1) consideration of the points of attack of H (or Mu) on H_2O_2 suggests otherwise:

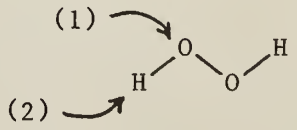

Attack of Mu at the oxygen site would result in the products MuOH + •OH. Further atomic rearrangement would be necessary to achieve MuO•, so this seems less likely than mechanism (1) and (2), which place Mu in a diamagnetic molecule. The distinction between (1) and (3) demonstrates the value of isotopic species as tracers; the muon nucleus is a unique label.

The study that led to the suggestion of (3) was carried out prior to the direct detection of muonium in water [9]. The reaction mechanism and rate constants were inferred from the dependence on H_2O_2 concentration of the muon polarization in the diamagnetic reaction products (the MuO• radical was supposed to react further). Nowadays, the direct measurement of muonium reaction rates is routine, but the older indirect method of studying the "residual polarization" in the reaction products provides complementary information, as will be demonstrated below.

EXPERIMENTAL

Experiments were performed at the TRIUMF cyclotron facility, using low-momentum ("surface") muon beams. These are sufficiently penetrating to pass through the muon detector and the front windows of the sample cell, so that all the muons stop in the liquid sample. The samples were continuously bubbled with an inert gas to remove dissolved oxygen. Sample temperature was controlled by circulating the liquid from a constant temperature bath through the back of the sample cell. The stopped muons were detected by the muon spin rotation (μSR) technique [7,10]. In some experiments a longitudinally spin polarized beam was used, in others the polarization was rotated until transverse to the beam momentum. In both cases a magnetic field was applied to the sample in a direction perpendicular to the spin polarization, so that the muonic species could be identified by their characteristic precession signals. Two signals are present in water and aqueous solutions of hydrogen peroxides: muonium, which was detected at 14 MHz in the 10 G applied field, and a "diamagnetic" signal due to MuOH (and any other diamagnetic molecules), which precesses at 13.55 kHz/G of applied field. Of relevance to the work described here are the initial amplitude and decay rates of the precession signals. These were extracted from computer fits to μSR histograms as described elsewhere [11].

Stock solutions were made by dilution of commercially available stabilizer-free H_2O_2 solutions. D_2O_2 solutions were made simply by dilution of stock H_2O_2 solution with D_2O. Since only millimolar D_2O_2 solutions were studied, the protons in the peroxide would have exchanged with the large excess of deuterons, with negligible contamination of the

solvent. To ensure stability, stock solutions were stored in polyethylene bottles, glassware and plasticware were thoroughly cleaned before used, and samples were made up from stock immediately prior to their use in experiments. Sample pH was adjusted by addition of calculated amounts of sulphuric acid or sodium hydroxide, and measured after the experiments. It was found necessary to purify the commercially available sodium hydroxide to remove trace amounts of transition metals.

MUONIUM DECAY RATES

Since no more than 10^8 muons are stopped in the sample in a typical μSR experiment, there is negligible effect on the concentration of reactive solutes, so the muonium decay rate is pseudo-first-order:

$$\lambda_M = \lambda_o + k_M[S] \ , \qquad (4)$$

where λ_o is the decay rate in the pure solvent and k_M is the second-order rate constant for the reaction between Mu and S. Typical muonium precession signals are shown in fig. 1, where the effect of increasing H_2O_2 concentration is evident. Variation of pH was also found to have an

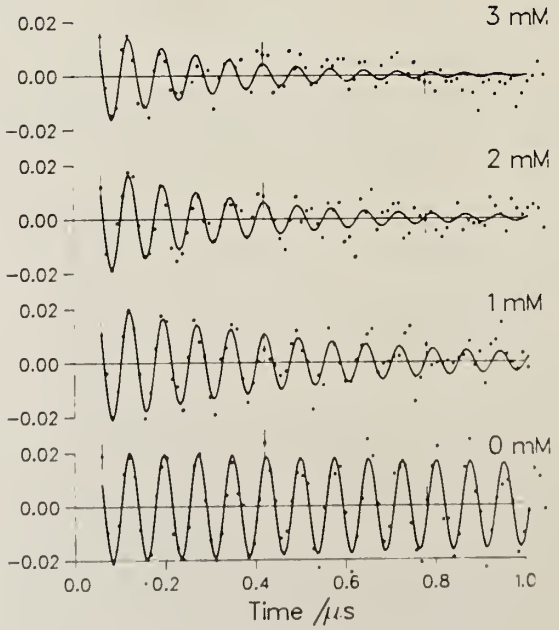

Fig. 1. Muonium precession signals in aqueous solutions of H_2O_2 at pH 11. The solid line indicates the best fit of the theoretical function for an exponentially decaying muonium signal. An additional slow precession from diamagnetic muon species has been removed in the interest of clarity.

effect, as demonstrated in fig. 2. This is only partly due to the reaction [12]

$$Mu + OH^- \rightarrow MuOH + e^-_{aq} \ . \qquad (5)$$

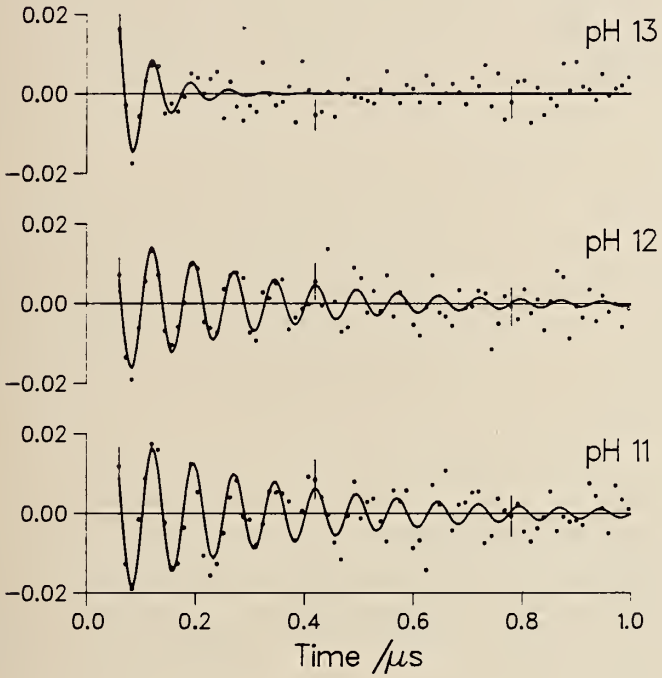

Fig. 2. Muonium precession signals in 2 mH H_2O_2 at various pH's.

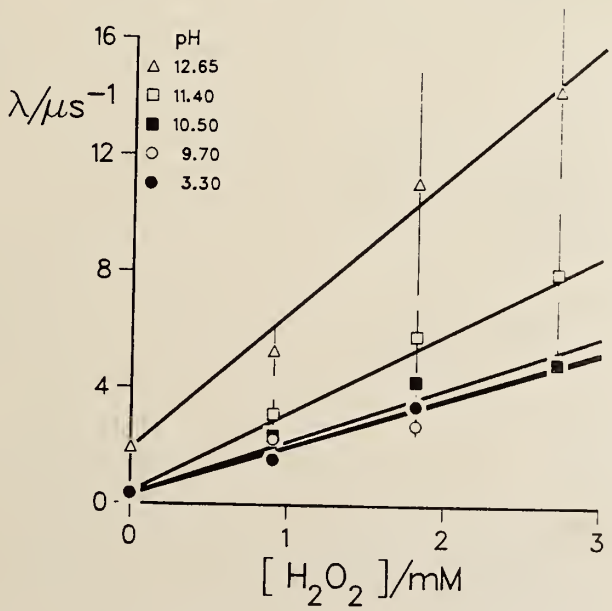

Fig. 3. The pH dependence of muonium reaction rates in aqueous solutions of H_2O_2 at room temperature.

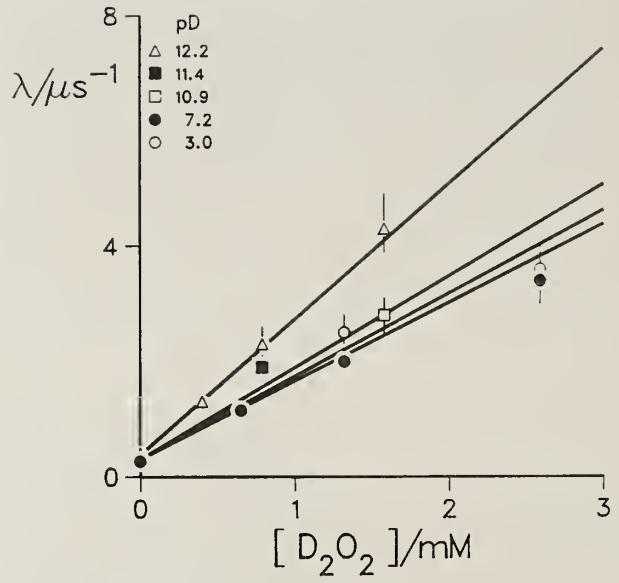

Fig. 4. The pD dependence of muonium reaction rates in aqueous solutions of D_2O_2 at room temperature.

Plots of λ_M versus peroxide concentration (figs. 3 and 4) reveal that the effective rate constant (calculated from the slope of the best straight line through the points) increases with pH. Reaction (5) affects only the intercept of the plots.

The pH dependence is most marked in the region of pH close to the pK_a of H_2O_2. It is therefore attributed to a difference in rate constants for the two reactions

$$Mu + H_2O_2 \rightarrow \text{products} \qquad (6)$$

and

$$Mu + HO_2^- \rightarrow \text{products} \; . \qquad (7)$$

Combination of the rate equations for reactions (5), (6) and (7) with the relations

$$K_a = \frac{[HO_2^-][H^+]}{[H_2O_2]} \qquad (8)$$

$$K_w = [H^+][OH^-] \qquad (9)$$

and

$$[H_2O_2]_{tot} = [H_2O_2] + [HO_2^-] \qquad (10)$$

leads to an expression for the muonium decay rate in terms of the total peroxide concentration and acidity:

$$\lambda_M = \frac{k_6[H^+] + k_7 K_a}{[H^+] + K_a} [H_2O_2]_{tot} + \frac{k_5 K_w}{[H^+]} + \lambda_o \ . \qquad (11)$$

The H_2O_2 and D_2O_2 data were separately fitted to this expression to determine values of k_5, k_6 and k_7. K_a for H_2O_2 is known from the literature (2.4×10^{-12} [13]), but the value for D_2O_2 had to be estimated from the isotope effect on K_w. The fit results are given in Table 1.

Table 1. Rate Constants for Reactions of Muonium

reactant	k/1 mol^{-1} s^{-1} a)	reactant	k/1 mol^{-1} s^{-1} b)
H_2O_2	$1.65(6) \times 10^9$	D_2O_2	$1.36(6) \times 10^9$
HO_2^-	$5.0\ (6) \times 10^9$	DO_2^-	$4.5\ (4) \times 10^9$
OH^-	$3.6\ (4) \times 10^7$	OH^-	$4.2(1.4) \times 10^7$

a) at ~22 °C, b) at 25 °C.

The temperature dependence of each rate constant was also investigated, but the analysis is not yet complete. Some of the data is displayed in fig. 5.

RESIDUAL POLARIZATION

When muonium reacts, the muon is placed in a different electronic environment. The consequent change in precession frequencies in a transverse magnetic field results in a loss of some or all of the original muon spin polarization. The loss depends on the rate of reaction and the amount of change in muon precession frequency, and can be calculated [14-16]. The fraction retained in the reaction product is termed the residual polarization. Since it depends on the nature and lifetime of the muonic species involved in each elementary reaction step it can be used to test a proposed reaction mechanism. Variable field studies are particularly valuable, since they facilitate the separation of any prompt signal from that which appears as a result of muonium reaction. Accordingly, the muon polarization of the diamagnetic signal (P_D) was measured as a function of magnetic field for various concentrations of H_2O_2. Solutions of both natural pH and pH 12 were studied,

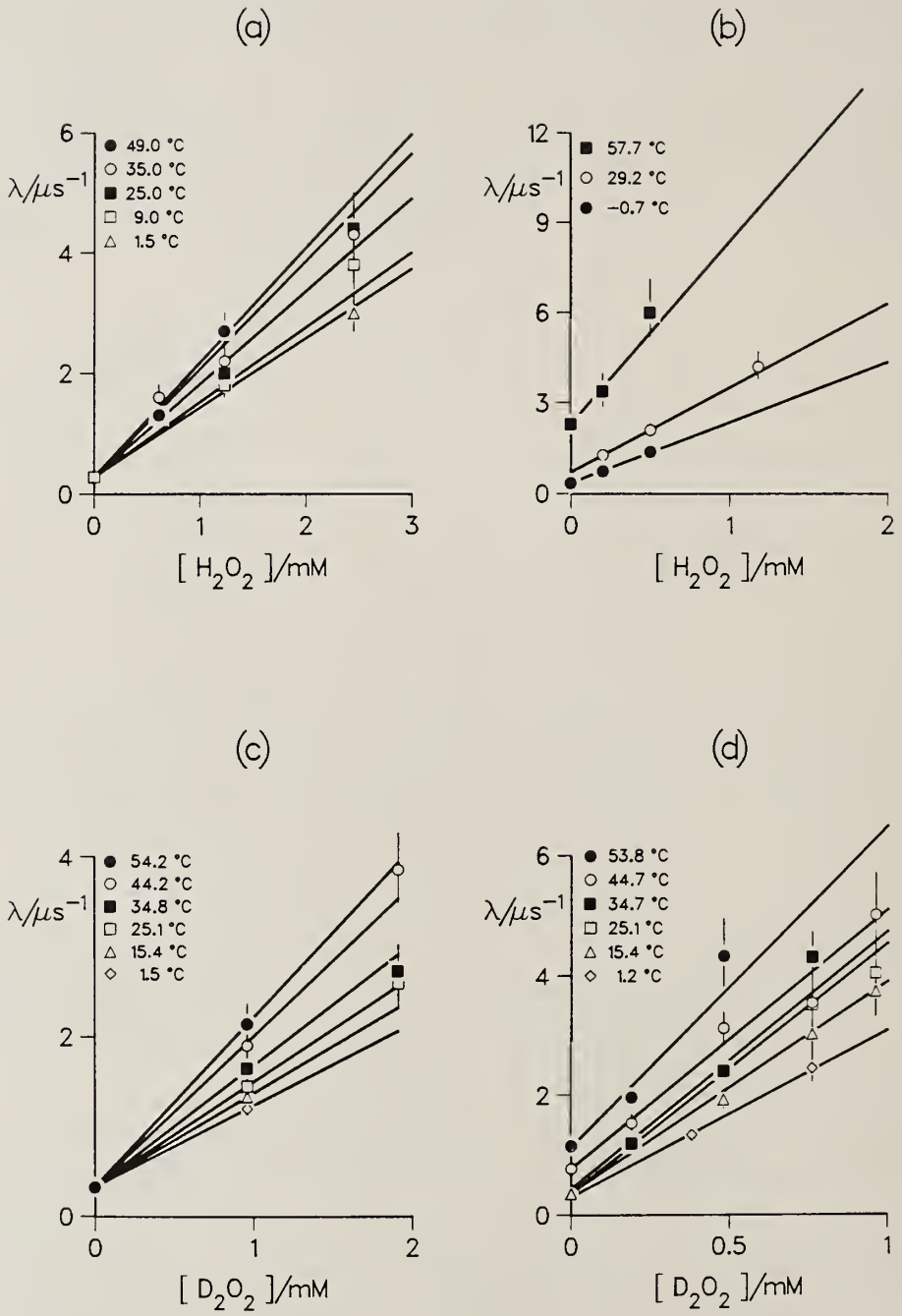

Fig. 5. The temperature dependence of muonium reaction rates in aqueous solutions of (a) H_2O_2 at pH 3, (b) H_2O_2 at pH 12.4, (c) D_2O_2 at pH 2.6, (d) D_2O_2 at pH 12.5.

and a temperature of 2°C was chosen to minimize the risk of peroxide decay. The results are shown in fig. 6 and 7. The uncertainty is similar for all points and amounts to ±0.004. The curves represent the best fits of calculations of P_D assuming a single-step mechanism:

$$Mu + H_2O_2 \text{ (or } HO_2^-) \rightarrow \text{diamagnetic products} . \qquad (12)$$

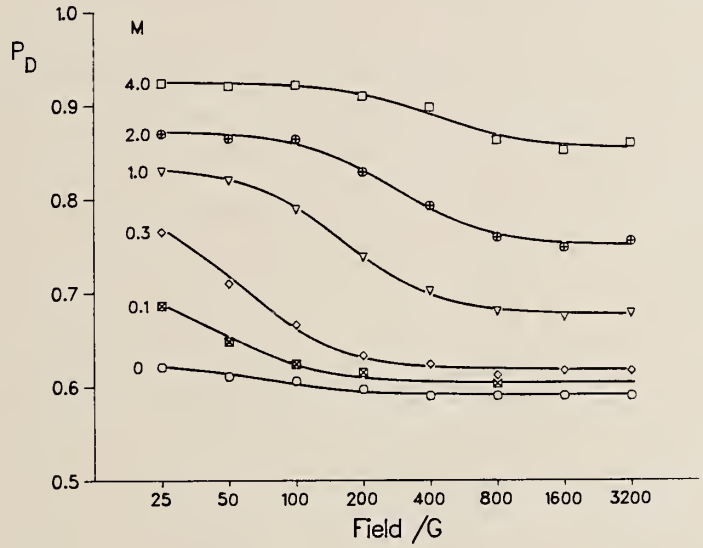

Fig. 6. Muon polarization as a function of magnetic field for concentrated H_2O_2 solutions of natural pH at 2°C.

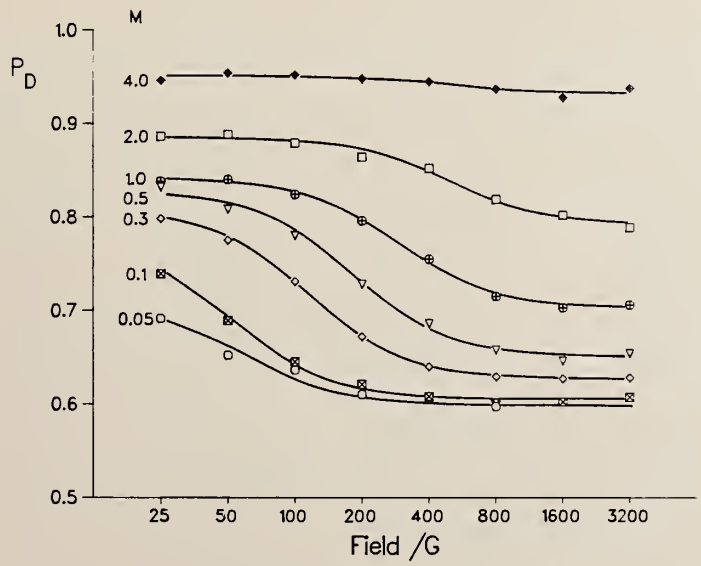

Fig. 7. Muon polarization as a function of magnetic field for concentrated H_2O_2 solutions at pH 12 and 2°C.

Each curve is characterized by three fit variables: (1) The shape of the curve is determined by the rate constant k_M; (2) the extent of the field variation is determined by P_M, the spin polarization of the muonium fraction at the moment of reaction; and (3) a field-independent contribution is accommodated by the prompt fraction, h_D. The optimum values of these parameters are given in Tables 2 and 3.

Table 2. Best Fit of the Residual Polarization in H_2O_2 Solutions at natural pH

$[H_2O_2]$/mol l^{-1}	log k_M	P_M	h_D
0.00	8.94(15)	0.06(1)	0.590(2)
0.106	9.57(7)	0.22(2)	0.604(2)
0.319	9.19(3)	0.35(2)	0.617(2)
1.063	9.13(3)	0.32(1)	0.672(3)
2.125	9.10(3)	0.26(1)	0.739(4)
3.80	9.08(6)	0.17(1)	0.835(8)

Table 3. Best Fit of the Residual Polarization in H_2O_2 Solutions at pH 12

$[H_2O_2]$/mol l^{-1}	log k_M	P_M	h_D
0.052	10.05(6)	0.21(1)	0.597(2)
0.103	9.67(4)	0.32(2)	0.604(2)
0.371	9.51(2)	0.36(1)	0.624(2)
0.538	9.45(2)	0.36(1)	0.647(3)
1.052	9.42(3)	0.30(1)	0.690(4)
1.92	9.45(6)	0.24(2)	0.76(1)
3.84	a)	0.09(2)	0.90(1)

a) Parameter fixed at 9.42.

In all except pure water and the lowest concentrations of H_2O_2 the sum of h_D and P_M is very close to 1.00. This means that all the muon

polarization is accounted for by the fit model. Furthermore, the average rate constants found for the higher concentrations (1.3×10^9 l mol^{-1} s^{-1} at natural pH and 2.8×10^9 l mol^{-1} s^{-1} at pH 12) are in good agreement with the values found from the muonium decay measurements under similar conditions of pH and temperature. The exceptional behaviour at the low concentrations can be attributed to the interaction of muonium with hydrated electrons produced in the muon track [17]. The increase in h_D with H_2O_2 concentration is likewise due to radiolysis effects, which are not relevant to the reaction kinetics under consideration, and which are therefore not discussed further.

DISCUSSION

The pH dependence of the muonium reaction rates is nicely explained by different rate constants for reaction of muonium with H_2O_2 and HO_2^- (and similarly for the deuterated peroxides). The H/D isotope effect is small and in the same direction for H_2O_2 and HO_2^-, which suggests that there is no change of reaction mechanism on ionization of the peroxide. If H (D) abstraction were the dominant reaction mode, then on statistical grounds HO_2^- would be expected to react slower than H_2O_2, and not as found.

The recommended literature value of the rate constant for $H + H_2O_2$ in aqueous solution is 6×10^7 l mol^{-1} s^{-1} [18]. It applies to neutral and acidic solutions. There is no data on alkaline solutions, nor is it possible to obtain, since the hydrogen atom is readily converted into the hydrated electron at high pH ($k = 1.5 \times 10^7$ [18]). For reaction with H_2O_2 the Mu/H kinetic isotope effect is substantial (~30), and is in the wrong direction for the effect of zero-point vibration in the transition state of a hydrogen atom abstraction reaction. Such an isotope effect is instead consistent with the dominance of tunnelling, which could apply to either of reactions (1) and (2).

Preliminary analysis of the temperature dependence data suggests activation energies around 10 kJ mol^{-1}, consistent with that found for H in the gas phase near room temperature [2]. Values closer to 40 kJ mol^{-1} have been determined at higher temperatures, for both reactions (1) and

(2). This is also consistent with a much increased contribution from tunnelling at room temperature.

The residual polarization studies show that the muonic products are diamagnetic and are formed at the same rate as muonium decays. Reaction (3) is therefore ruled out. Unfortunately μSR results cannot distinguish between MuH and MuOH. However, if Mu attacks the O atom of HO_2^- there are two possible products:

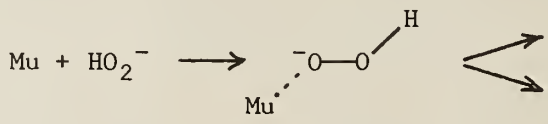

(13)

(14)

Reaction (13) would give rise to a loss of polarization, and is completely inconsistent with the residual polarization study of the alkaline solutions. Perhaps H abstraction is the correct mechanism after all? Theoretical study of the reaction dynamics is desirable to provide tests of isotope and temperature dependencies.

References

[1] CRC Handbook of Bimolecular and Termolecular Gas Reactions, J.A. Kerr, and S.J. Moss, eds. CRC Press, Boca Raton, Florida.
[2] R.B. Klemm, W.A. Payne and L.J. Stief, Int. J. Chem. Kin. Symp. 1, 61 (1975).
[3] R.A. Gorse and D.H. Volman, J. Photochem. 3, 115 (1974).
[4] J.F. Meagher and J. Heicklen, J. Photochem. 3, 455 (1974/5).
[5] P. Neta, Chem. Rev. 72, 533 (1972).
[6] I.V. Draganić and Z.D. Draganić, The radiation chemistry of water (Academic Press, New York, 1971).
[7] P.W. Percival. Radiochim. Acta 26, 1 (1979).
[8] J.H. Brewer, K.M. Crowe, F.N. Gygax, R.F. Johnson, D.G. Fleming and A. Schenck, Phys. Rev. A9, 495 (1974).
[9] P.W. Percival, H. Fischer, M. Camani, F.N. Gygax, W. Rüegg, A. Schenck, H. Schilling and H. Graf, Chem. Phys. Lett. 39, 333 (1976).
[10] J. Chappert and R.I. Grynszpan (eds.), "Muons and Pions in Materials Research", North-Holland, 1984.
[11] P.W. Percival, J.C. Brodovitch and K.E. Newman, Far. Disc. Chem. Soc. 78, (1984) 315.
[12] P.W. Percival, E. Roduner, H. Fischer, M. Camani, F.N. Gygax and A. Schenck, Chem. Phys. Lett. 47, 11 (1977).
[13] CRC Handbook of Chemistry and Physics, 59th Edition, R.C. Weast and M.J. Astle, eds., CRC Press, West Palm Beam, Florida.
[14] P.W. Percival and H. Fischer, Chem. Phys. 16, 89 (1976).

[15] P.W. Percival and J. Hochmann, Hyperfine Interactions 6, 421 (1979).

[16] P.F. Meier, Phys. Rev. A25, 1287 (1982).

[17] P.W. Percival, J.C. Brodovitch and K.E. Newman, Chem. Phys. Lett. 91, 1 (1982).

[18] M. Anbar, Farhartaziz and A.B. Ross, Selected specific rates of reactions of transients from water in aqueous solution. II Hydrogen Atom, NSRDS-NBS 51, Washington, 1975.

FREE RADICAL PROPERTIES OF EYE MELANINS AND OCULAR PHOTOTOXICITY

S. Persad and I.A. Menon
Clinical Science Division, University of Toronto, Toronto, Ontario, Canada
P.K. Basu and M. Avaria
Department of Ophthalmology, University of Toronto, Toronto, Ontario, Canada
C.C. Felix and B. Kalyanaraman
National Biomedical ERS Centre, Medical College of Wisconsin, Milwaukee, WI. U.S.A.

INTRODUCTION

The melanin present in the black hair and in the skin of people with black hair is called eumelanin, whereas the melanin present in the red hair and in the skin of people with red hair is termed pheomelanin[1]. These melanins differ in their chemical and physical properties as well as in their biosynthetic pathways. Eumelanin is synthesized from dopa and pheomelanin from cysteinyldopa. Eumelanin contains little or no sulfur, in contrast to pheomelanin which contains approximately 10% sulfur[2-5]. Various natural melanins are however neither pure eumelanin nor pure pheomelanin. These have sulfur contents and other chemical and physical properties intermediate between pure eumelanin and pure pheomelanin[4,6-10]. Melanins contain stable free radicals, which can be detected by electron spin resonance (ESR). Both eumelanin and pheomelanin give one common ESR signal; but pheomelanin gives another ESR signal which is not seen in the case of eumelanin. The above difference in the ESR signal is observed with melanins isolated from human black and red hair[8,11]. Certain other differences in the photochemical and photobiological properties of melanins from black hair and red

hair have also been reported by us[12-15]. Our previous studies [7,16] have shown that there are some qualitative differences in the physical and chemical properties of melanins isolated from human eyes having blue and brown irises (designated as blue and brown eyes respectively). These differences were observed in the oxidation properties of these melanins and the binding of some metabolites and drugs (e.g. protoporphyrin, chlorpromazine, and paraquat) to these melanins. The oxidation of NADH by the melanin-protoporphyrin complexes was also different for these two melanins from human eyes.

Popular and semiscientific beliefs indicate a correlation between eye, hair and skin colours. However, there are no scientific data to prove or disprove the apparent relationship. The present study was therefore undertaken to investigate whether the melanins from human blue and brown eyes would have characteristics similar to that of the melanins from human black and red hair with respect to cell lysis and ESR signals. Another question - whether or not the various pigmented tissues of the eye, viz. iris, ciliary body, choroid and retinal pigment epithelium contain the same type of melanin or not, was also investigated in the course of this study.

MATERIALS AND METHODS

Human donor eyes having blue and brown irises were dissected and the melanins were prepared from the iris, ciliary body, choroid and retinal pigment epithelium according to the method described previously[7].

The methods for the maintenance of Ehrlich ascites carcinoma cells in mice, the preparation of these cell suspensions, the

labelling of the cells with ^{51}Cr, irradiation of the cells and the determination of ^{51}Cr release following cell lysis were carried out by the methods described previously[4,13,14].

The formation of superoxide was determined by measuring the reduction of nitroblue tetrazolium chloride (NBT)[13]. Hydrogen peroxide (H_2O_2) was determined by the method of Wang and Nixon[17].

The ESR measurements on melanins extracted from eye tissues were carried out using a Varian E-109 spectrometer operating at X-band (9.1 GHz) and employing 100 kHz field modulation. Measurements of magnetic field (H) and microwave frequency (ν) were made using a Radiopan MJ110-R gaussmeter and an EiP model 548 frequency counter respectively. g-Values were calculated to $\pm$ 0.0001 from $g=h\nu/\beta H$ where h is Planck's constant and β is the Bohr magneton. Spectra were recorded on melanins previously incubated for 30 minutes in a solution of zinc sulfate (3mM) at pH ca. 5. This procedure serves to increase free radical concentrations and to accentuate any pheomelanin signals that are present.[8] Samples were maintained at -196°C in a dewar flask inside the ESR cavity. For all ESR measurements the modulation amplitude was 4 G and the microwave power was 20μW.

RESULTS

The release of the ^{51}Cr from labelled Ehrlich ascites carcinoma cells during incubation in the dark and irradiation in the presence of blue or brown eye melanin.

Ehrlich ascites carcinoma cells labelled with ^{51}Cr were irradiated in the presence of blue or brown eye melanin. The amount of ^{51}Cr released under each of the above conditions was

compared with the ^{51}Cr released from the cells which were frozen and thawed[14]. Cells which were incubated in the dark or irradiated in the presence of either the blue or brown eye melanin did not produce any greater ^{51}Cr release as compared to the control cells (Table 1).

TABLE I

RELEASE OF ^{51}Cr FROM LABELLED EHRLICH ASCITES CARCINOMA CELLS DURING INCUBATION IN THE DARK OR IRRADIATION IN THE PRESENCE OF BLUE EYE MELANIN (BlEM) OR BROWN EYE MELANIN (BrEM)

Reagents added*	^{51}Cr release (%) Mean ± SEM	
	Incubation	Irradiation
None	2.3 ± 0.5	1.0 ± 0.6
BlEM	2.5 ± 0.6	4.5 ± 0.6
BlEM, cysteine	3.3 ± 0.3	5.5 ± 0.6
BlEM, catalase	2.8 ± 0.3	3.3 ± 0.5
BlEM, cysteine, catalase	3.0 ± 0.0	3.5 ± 0.5
BrEM	2.0 ± 0.4	2.7 ± 2.0
BrEM, crysteine	5.3 ± 1.0	11.7 ± 1.0
BrEM, catalase	2.3 ± 0.3	3.0 ± 0.6
BrEM, cysteine, catalase	2.8 ± 0.3	2.7 ± 0.4

* Concentrations: BlEM and BrEM, 200 µg/ml; cysteine, 1.0 mM; catalase, 3,500 units/ml. The Mean ± SEM were calculated from the results of four experiments, done in duplicates.

Since 1.0 mM cysteine was found to enhance the ^{51}Cr release during irradiation of labelled carcinoma cells in the presence of

the red hair melanin[12,15] the effect of cysteine upon the ^{51}Cr release in the presence of the blue or brown eye melanin was investigated. Cysteine slightly increased the ^{51}Cr release during incubation in the presence of the blue eye melanin. However the increase was much larger in the presence of the brown eye melanin. The ^{51}Cr release under both of the above conditions was completely abolished by catalase. Incubation of the cells in the presence of the blue eye melanin with or without cysteine did not release ^{51}Cr in an amount greater than that released by the control cells in the absence of melanin. Irradiation of the cells in the presence of the blue eye melanin with or without cysteine released small amounts of ^{51}Cr. This release was inhibited by catalase. Irradiation of the cells in the presence of brown eye melanin produces a relatively large extent of cell lysis; this also was inhibited by catalase.

Reduction of NBT during incubation in the dark or irradiation in the presence of the blue or brown eye melanin.

Incubation or irradiation of either blue or brown eye melanin did not show any reduction of NBT.

Formation of hydrogen peroxide during incubation in the dark or irradiation in the presence of blue or brown eye melanin.

Incubation in the dark or irradiation of either blue or brown eye melanin showed the formation of only a small amount of H_2O_2 (Table II).

TABLE II

FORMATION OF HYDROGEN PEROXIDE DURING INCUBATION IN THE DARK OR IRRADIATION IN THE PRESENCE OF BLUE EYE MELANIN (BIEM) OR BROWN EYE MELANIN (BrEM).

Reagents added*	H_2O_2 formed (uM) Mean ± SEM	
	Incubation	Irradiation
None	0.0	0.0
BlEM	0.7 ± 0.3	2.4 ± 0.2
BlEM, cysteine	12.7 ± 0.3	11.2 ± 0.5
BlEM, catalase	1.1 ± 0.3	1.3 ± 0.0
BlEM, cysteine, catalase	0.9 ± 0.1	0.4 ± 0.0
BrEM	0.7 ± 0.3	3.3 ± 0.1
BrEM, cysteine	10.1 ± 0.4	12.4 ± 0.4
BrEM, catalase	0.7 ± 0.1	0.8 ± 0.0
BrEM, cysteine, catalase	0.9 ± 0.1	0.7 ± 0.0

* Concentrations: BlEM and BrEM, 200 µg/ml; cysteine, 1.0 mM; Catalase, 3,500 units/ml.

Addition of 1.0 mM cysteine considerably enhanced the formation of H_2O_2. Irradiation of the cells in the presence of the blue or brown eye melanin produced H_2O_2 in amounts significantly larger than that produced during the incubation of the cells in the dark. When mixtures consisting of 1.0 mM cysteine and either of the two melanins were irradiated, the amounts of H_2O_2 formed were of the same order as that formed during incubation of these mixtures. When catalase was present

during incubation or irradiation of the melanin, only very small amounts of H_2O_2 were present.

Electron Spin Resonance

ESR spectra were obtained for melanins extracted from the iris, ciliary body, choroid and retinal pigment epithelium of brown and blue eyes. Representative spectra are shown in Figure 1. For each spectrum the magnetic parameters of linewidth and g-value were measured and are reported in Table III.

TABLE III

MAGNETIC PARAMETERS FOR EYE MELANINS[a]

Sample		linewidth, G[b]	g[c]
Blue eye	1, iris	5.50	2.0042
	2, iris	5.50	2.0041
	1, ciliary body	5.50	2.0040
	2, ciliary body	5.50	2.0041
	1, choroid	5.50	2.0043
	2, choroid	5.50	2.0042
	1, pigment epithelium	5.75	2.0042
	2, pigment epithelium	5.75	2.0040
Brown eye	1, iris	5.75	2.0041
	2, iris	5.50	2.0041
	1, ciliary body	5.50	2.0042
	2, ciliary body	5.50	2.0043
	1, choroid	5.50	2.0042
	2, choroid	5.75	2.0042
	1, pigment epithelium	5.50	2.0042
	2, pigment epithelium	5.50	2.0041

a Measured in 3 mM zinc sulfate solution at pH 5. Temperature = - 196°C.
b ± 0.25 G; c ± 0.0001.

These spectral parameters (linewidth ca. 5.5 G, g ca. 2.004) are for the most part characteristic of eumelanins derived from dopa[18]. However, slight spectral wings (Figure 1) indicative

Fig. 1 ESR spectra of melanins extracted from brown eye iris (left) and blue eye iris (right). Spectra were recorded at -196°C on samples incubated in 3 mM zinc sulfate solution at pH 5.

of units derived from cysteinyldopa[8] were evident with samples extracted from brown eyes. These spectral wings, although slight, were distinct in the original recordings and were consistently observed; however they are not distinct in the reduced size of Figure 1. Estimated values of r for brown eye and blue eye melanins were ca. 14 (similar to our earlier report)[11] and > 20 respectively. These data are consistent with the brown eye melanins having a slightly greater cysteinyldopa content, i.e. having weak pheomelanin-like spectral properties. In terms of the ESR spectroscopy melanins from the different eye tissues were indistinguishable.

DISCUSSION

Our results show that irradiation of carcinoma cells in the presence of blue or brown eye melanin did not produce any detectable amounts of superoxide, as tested by the reduction of

NBT. Although irradiation of the carcinoma cells in the presence of blue eye melanin did not produce any cell lysis, irradiation of these cells in the presence of brown eye melanin however, produced cell lysis to a small extent. These results indicate that the blue eye melanin is essentially eumelanin, whereas the brown eye melanin is almost like eumelanin with small, but distinct presence of pheomelanin. These conclusions are supported by the difference observed in the ESR signals produced by these melanins. The blue eye melanin gave only one signal characteristic of eumelanin, whereas the brown eye melanin gave not only the same signal, but it also gave a small, but distinct signal characteristic of pheomelanin. That the blue and brown eye melanins may differ in quality was also suggested in one of our previous experiments where we studied the sulfur contents of these melanins[7]. Although the sulfur content was found to be low for both melanins, the brown eye melanin had a larger amount of sulfur as compared to the blue eye melanin.

The ESR signals further suggested that with respect to the quality of the blue and brown eye melanins in the individual eye tissues, the iris, ciliary body, choroid and retinal pigment epithelium did not differ.

ACKNOWLEDGEMENTS

This research was funded by grants from the Medical Research Council of Canada, Lion's International District A-16 Ophthalmological Research Foundation and Independent Order of Odd Fellows and Rebekahs of Ontario and grants from NIH (AM-26950 and DR-01008). We also wish to thank Dr. R.C. Sealy for consultations in the ESR studies.

REFERENCES

1. Prota, G.: Invest Dermatol, 75, 122-127 (1980)

2. Dryja, T.P., O´Neil-Dryja, M. and Albert, D.M. Invest. Ophthalmol. Vis. Sci. 18,231-6. (1979)

3. Ito, S., Novellino, E., Chioccara, F., Misuraca, G. and Prota, G. Experientia. 36,822-3. (1980)

4. Menon, I.A., Persad, S., Haberman, H.F. and Kurian, C.J. J. Invest. Dermatol. 80,202-6 (1983 a).

5. Rorsman, H., Agrup, G., Hansson, C., Rosengren, A. M and Rosengren E. In: Pigment Cell, Vol. 4 (Ed. SN Klaus). Pp. 244-252. Basel, S. Karger (1979).

6. Ito, S. and Jimbow, K. (1983). J. Invest. Dermatol. 80,268-72.(1983).

7. Menon, I.A., Persad, S., Haberman, H.F., Kurian, C.J. and Basu, P.K. Exp. Eye Res. 34:531-7 (1982).

8. Sealy, R.C., Hyde, J.S., Felix, C.C., Menon, I.A. and Prota, G. Science, 217: 545-7. (1982 a)

9. Jimbow, K., Ishida, O., Ito, S., Hori, Y., Witkop, C.J. and King, R.A. J. Invest. Dermatol., 81:506-11 (1983).

10. Jimbow, K., Miyake, Y., Homma, K., Yasuda, K., Izumi, Y., Tsutsumi, A. and Ito, S. Cancer Res. 44: 1128-34 (1984).

11. Sealy, R.C., Hyde, J.S., Felix, C. C., Menon, I.A., Prota, G., Swartz, H.M., Persad, S. and Haberman, H.F. Proc. Natl. Acad. Sci. USA, 79: 2885-9 (1982b).

12. Menon, I.A., Persad, S., Ranadive, N.S. and Haberman, H.F. In: Oxygen Radicals in Chemistry and Biology, Ed. W. Bors, M. Saran and D. Tait, Walter de Gruyer, Berlin, Pp. 673 (1984).

13. Persad, S., Menon, I.A. and Haberman, H.F. Photochem. Photobiol. 37: 63-8 (1983).

14. Menon, I.A., Persad, S., Ranadive, N.S. and Haberman, H.F. Cancer Res. 43: 3165 (1983b).

15. Menon, I.A., Persad, S., Ranadive, N.S., and Haberman, H.F.: Can. J. Biochem. Cell Biol. 63, 278-283 (1985)

16. Menon, I.A., Persad, S., Haberman, H.F., Kurian, C.J. and Basu, P.K. In: Pigment Cells, ed. M. Seiji, University of Tokyo Press. Pp. 17-22 (1981).

17. Wang. R. and Nixon. B.T. In Vitro 14, 715-22 (1978).

18. Sealy, R.C. Methods in Enzymology. (Ed. L. Packer) Academic Press, New York, Vol. 105: 479-483 (1984).

KINETICS OF THE REACTION OF OH WITH ClO

G. Poulet, G. Laverdet and G. Le Bras
C.N.R.S., C.R.C.C.H.T., 45045 Orleans Cedex, France.

The inclusion of the reaction OH + ClO in stratospheric modeling has shown that the reduction of ozone due to chlorofluorocarbon emissions may significantly depend on the importance of channel (1b) of this reaction :

$$OH + ClO \longrightarrow HO_2 + Cl \quad (1a)$$
$$\longrightarrow HCl + O_2 \quad (1b)$$

since some disagreement still exists between the published kinetic results [1-4], measurements of the rate constant and the HCl product were performed in a discharge flow reactor at 298 K and at low pressure (0.5 - 1.0 torr).

OH radicals, produced from $H + NO_2 \longrightarrow OH + NO$, were monitored via the laser induced fluorescence technique. ClO radicals, generated from either $Cl + ClO_2$ or $Cl + O_3$, were detected by a quadrupole mass spectrometer using a modulated molecular beam sampling with synchronous detection. Absolute measurements of ClO concentrations were done systematically from the calibration of NO_2 resulting from the titration reaction $ClO + NO \longrightarrow Cl + NO_2$.

k_1 was first measured relatively to the rate constant of the reaction $OH + ClO_2 \longrightarrow$ prod.[2] , ClO_2 being the precursor of ClO radicals via $Cl + ClO_2 \longrightarrow 2\ ClO$ in the presence of an excess of Cl over ClO_2. Using a correction in the data analysis (due to a partial reformation of OH via $HO_2 + Cl \longrightarrow OH + ClO$) and the value obtained in a preliminary determination of $k_2 = (6.9 \pm 0.4) \times 10^{-12}$ cm^3 molecule^{-1} s^{-1} at 298 K, the relative experiments gave : $k_1 = (1.77 \pm 0.33) \times 10^{-11}$ cm^3 molecule^{-1} s^{-1}.

Two series of absolute measurements of k_1 were done under pseudo-first order conditions, $(ClO) \gg (OH)$, with (ClO) ranging from 0.2 to 2.2 10^{13} cm^{-3} : i) with an excess of Cl over ClO_2 or O_3 and making the same correction as above from a computer simulation of each

experiment : ii) with a slight excess of O_3 over Cl where the value of k_1 was directly measured. These two measurements led to a mean value of $k_1 = (1.94 \pm 0.38) \times 10^{-11}$ cm^3 molecule^{-1} s^{-1}, which is in good agreement with the recent value obtained in ref. 3.

The branching ratio to channel (1b) was measured from the calibration of HCl detected by mass spectrometry in experiments where O_3 was the precursor of ClO. The method involved two measurements of HCl formed when Cl or O_3 was successively used in excess in the same experiment. The computer model was also used to account for the secondary reactions and to fit the HCl measured in both conditions. It was found : $k_{1a}/k_1 = 0.98 \pm 0.12$ at 298 K. This value is largely higher than the lower limit 0.65 estimated in ref. 1 and can be compared with the two other determinations recently obtained from the product analysis of channel (1a) : (0.86 ± 0.14)[3] and (0.85 ± 0.07)[4]. This confirms that the four centre reaction (1b) is unlikely to occur at low temperature.

In relation with the stratospheric ozone chemistry, this result indicates that reaction (1b) is an insignificant channel of converting OH and ClO active radicals into the reservoir species HCl.

References

(1) M.T. Leu and C.L. Lin, Geophys. Res. Lett. 6, 425 (1979).
(2) A.R. Ravishankara, F.L. Eisele and P.H. Wine, J. Chem. Phys. 78, 1140 (1983).
(3) A.J. Hills and C.J. Howard, J. Chem. Phys. 81, 4458 (1984).
(4) J.P. Burrows, T.J. Wallington and R.P. Wayne, J. Chem. Soc. Faraday Trans. 2 80, 957 (1984).

Infrared Fourier transform emission spectroscopy of CuH and NeH^+

R. S. Ram,* P. F. Bernath* and J. W. Brault**

*Department of Chemistry, University of Arizona, Tucson, AZ 85721

**National Solar Observatory, National Optical Astronomy Observatories, Tucson, AZ 85726

Abstract

The vibration-rotation spectra of CuH and NeH^+ were detected by infrared emission from a copper hollow cathode lamp with the Kitt Peak Fourier transform spectrometer. The (1,0), (2,1) and (2,0) bands of ^{63}CuH and ^{65}CuH were found as well as the (1,0), (2,1) and (3,2) bands of NeH^+. The Ne and H_2 pressures in the lamp were 2 torr and 30 mtorr, respectively. By replacing the H_2 with D_2 the (1,0) and (2,1) bands of NeD^+ were observed. CuH is the first metal hydride for which a vibration-rotation emission spectrum has been detected. Dunham coefficients, including the effects of Born-Oppenheimer breakdown, were extracted from the data.

Introduction

The fundamental bands of $^{20}NeH^+$ and $^{22}NeH^+$ were found in the difference frequency laser experiments of Wong, Bernath and Amano.[1] It was noted, however, by one of the authors (J. W. B.) that NeH^+ occurred as an impurity in a titanium hollow cathode discharge in neon, suggesting that infrared Fourier transform techniques had the required sensitivity to detect NeH^+. Titanium is a well-known hydrogen absorber. Using a copper hollow cathode and an neon discharge with a small amount of added hydrogen and deuterium, we were able to find the several bands of $^{20}NeH^+$, $^{22}NeH^+$ and NeD^+. In our NeH^+ spectra we were able to pick out vibration-rotation lines of CuH.

Although the Fourier transform emission experiments lack the sensitivity of laser experiments, there are certain advantages. The obvious one is that the entire spectrum can be recorded quickly at full resolution without a wavelength search. Another advantage, not unique to Fourier transform methods, is that emission work usually provides more bands than absorption so that the potential energy surface of CuH and NeH^+ can be more thoroughly characterized.

Experimental

The CuH and NeH^+ spectra were excited in a water-cooled copper hollow cathode lamp at a current of 330 mA. A continuous flow of 2.0 torr of neon and 30 mtorr of H_2 (D_2) was maintained through the lamp. A similar experiment was carried out with D_2 instead of H_2 and NeD^+ (but not CuD) was detected.

The spectrum was recorded with the Fourier transform spectrometer associated with the McMath Solar Telescope of the National Solar Observatory located at Kitt Peak. The 1800-5000 cm^{-1} interval was recorded at 0.05 cm^{-1} resolution using liquid nitrogen cooled InSb detectors with wedged Ge filter. The lower wavenumber is determined by the red limit of the detector while the upper limit is set by the Ge filter. Sixty-four scans were co-added in two hours of integration.

Results and Discussion

The fundamental band of NeH^+ was identified and assigned with the aid of the previous laser work.[1] Additional transitions up to J = 19 were found. The (2,1), (3,2), and (4,3) and (2,0) bands of $^{20}NeH^+$ were all searched for but only the (2,1) and (3,2) bands were found. The (4,3) band was too weak to observe and the (2,0) band lies higher than the 5000 cm^{-1} cut-off of the Ge filter. Since ^{22}Ne has an abundance of 8.8%, only the fundamental band of $^{22}NeH^+$ had a high enough signal-to-noise ratio to be recorded. When H_2 was replaced by D_2 the (1,0) and (2,1) bands of $^{20}NeD^+$ were found. Unfortunately, the signal-to-noise ratio was not as high for $^{20}NeD^+$ as for $^{20}NeH^+$, preventing observation of $^{22}NeD^+$. The InSb detector allowed only lines with frequencies greater than 1800 cm^{-1} to be detected, so P lines of the (2,1) band of $^{20}NeD^+$ were not detected.

The (1,0) band of CuH was noted and easily identified during our NeH^+ work because of its characteristic spectral pattern. A regularly spaced branch with each line doubled and split by about 0.5 cm^{-1} was found. The doublets had a 2:1 intensity ratio characteristic of ^{65}Cu and ^{63}Cu in natural abundance. Ringström's molecular constants[2] allowed the lines to be unambiguously identified. Once the (1,0) band had been picked out and fit, the (2,1) and (2,0) bands were predicted and found.

The observed line positions were fit using the customary[3] rotational energy level expression for $^1\Sigma$ states. All of the transition frequencies

for each isotopic species were simultaneously fit using a non-linear least squares procedure. Tables 1 and 2 list the molecular constants for CuH and $^{20}NeH^+$, respectively. Complete line lists, fits for other isotopes, Dunham parameters and equilibrium constants will be published elsewhere.[4]

The molecular constants for NeH^+ are in good agreement with ab initio theoretical estimates.[5] For instance, our r_e = 0.991795 Å compares with the computed[5] r_e = 0.996 Å.

The first emission observation of a metal hydride vibration-rotation spectrum opens up a number of interesting possibilities. Not only might the alkali and alkaline earth hydrides be observed in their v = 2 sequence but additional transition metal hydrides may be detected. The transition metal hydrides have complicated visible transitions, largely because of extensive perturbations among the numerous excited states. The infrared vibration-rotation spectra and infrared electronic transitions may be relatively unperturbed and amenable to analysis.

Acknowledgments

We thank Rob Hubbard for expert technical support during our data run. Acknowledgment is made to the donors of the Petroleum Research Fund, administered by the ACS, for partial support of this research. The research was also supported by grants NSF CHE-8306504 and ONR N00014-84-K-0122.

References

1. Wong, M., Bernath, P., and Amano, T., J. Chem. Phys., Vol. 77, pp. 693-696 (1982).
2. Ringström, U., Arkiv for Fysik, Vol. 32, pp. 211-239 (1966).
3. Herzberg, G., Spectra of Diatomic Molecules, Van Nostrand-Reinhold (1950).
4. Ram, R. S., Bernath, P. F., and Brault, J. W., submitted J. Molec. Spectrosc.
5. Rosmus, P. and Reinsch, E. A., Z. Naturforsch, Vol. 35a, pp. 1066-1070 (1980).

Table 1. Molecular constants (in cm^{-1}) for the $X^1\Sigma^+$ states of the ^{63}CuH and ^{65}CuH molecules.

Molecular Constants[a]	v = 0		v = 1		v = 2	
	^{63}CuH	^{65}CuH	^{63}CuH	^{65}CuH	^{63}CuH	^{65}CuH
T_v	0.0	0.0	1866.4048(19)	1865.9757(23)	3658.4682(25)	3657.6531(34)
B_v	7.81745(22)	7.81356(25)	7.56472(24)	7.56075(25)	7.31425(25)	7.31021(23)
$10^4 D_v$	5.341(40)	5.166(30)	5.276(45)	5.133(25)	5.217(42)	5.097(19)
$10^8 H_v$	8.8(37)	8.8[b]	7.4(31)	7.4[b]	6.5(23)	6.5[b]

a: The numbers in the parentheses are one standard deviation in the last digit.
b: Fixed values.

Table 2: Molecular constants (in cm^{-1}) for the ground state of $^{20}NeH^{+}$.

Molecular[a] Constants	v = 0	v = 1	v = 2	v = 3
T_v	0.0	2677.8565(5)	5131.2741(29)	7361.7726(35)
B_v	17.338053(74)	16.255055(56)	15.17667(10)	14.09358(14)
$10^3 D_v$	2.68550(83)	2.66071(51)	2.65233(79)	2.6723(15)
$10^8 H_v$	8.94(34)	7.80(13)	2.99(17)	-3.38(40)
$10^{11} L_v$	4.38(48)	-	-	-

a: The values in parentheses represent one standard deviation in the last digit.

Time-resolved LIF detection of silylene in the IR MPD of ethylsilane.

D.M. Rayner, R.P. Steer[‡] and P.A. Hackett

Laser Chemistry Group
Division of Chemistry
National Research Council Canada
100 Sussex Drive
Ottawa, Ontario K1A 0R6
Canada

and

C. L. Wilson and P. John
Department of Chemistry
Heriot-Watt University
Riccarton, Currie
Edinburgh EH14 4AS
Scotland

[‡]On sabbatical leave 1984-1985 from
Department of Chemistry
University of Saskatchewan
Saskatoon, Saskatchewan

Abstract

Silylene has been observed in the collisionless IR MPD of ethylsilane via LIF. A mechanism for the unimolecular dissociation of ethylsilane which is consistent with known shock-induced dissociation and IR MPD data is advanced.

Introduction

The widespread use of chemical vapour deposition of amorphous silicon has led to a renewed interest in the chemistry of silanes. Despite this increased activity the primary dissociation pathways of these molecules remains a controversial topic [1-3]. As usual, this is in large part due to the complications introduced by secondary and/or heterogeneous reactions. Infrared multiphoton dissociation (IR MPD) combined with time resolved product detection provides a powerful method of initiating and following homogeneous gas phase reactions and we have applied these techniques to the dissociation of ethylsilane.

Francisco, Joyce and Steinfeld have determined the final products following IRMPD of alkylsilanes and infer that silylene, SiH_2, is an important intermediate [4]. The visible absorption of this transient is well known from the work of Dubois [5] and it has recently been detected via LIF following the 193 nm photolysis of phenylsilane [6]. In this letter we report upon the detection of silylene following IR MPD of ethylsilane and discuss the relevance of these results to the mechanism of alkylsilane dissociation.

Experimental

Our pump-and-probe apparatus for time-resolved IR MPD studies is described in detail elsewhere [7]. Briefly, the pump laser was a Lumonics 820 CO_2 laser operated in TEM_{00} and single longitudinal modes and employing an optional plasma shutter to remove the tail of the pulse. The probe was a modified Molectron DL16 dye laser pumped by a Lumonics 860 XeCl excimer laser. The beams from the two lasers counterpropagated in a colinear arrangement and were mildly focussed at the centre of the reaction cell, the infrared with a 1 m Ge lens to a

beam radius of 0.55 mm and the probe with a 600 mm quartz lens. This arrangement ensured that the probe sampled only a region of well defined IR flux, with no spatial averaging.

LIF was observed orthogonally through suitable filters (Schott 610 for λ (probe) < 573 nm, Schott 630 for λ (probe) > 573 nm) using a cooled Hamamatsu R446 photomultiplier. Scanning of the probe laser wavelength and the delay between the two lasers was controlled by a Tektronix 4052 system which also recorded the LIF signal, the pulse energy of each laser and the interpulse delay on each firing of the system.

Ethylsilane (Petrarch Systems Inc.) was degassed several times and used without further purification. It was flowed through the reaction cell neat or buffered in either helium or nitrogen.

Results and Discussion

The LIF spectrum of silylene was observed following IR MPD of ethylsilane with the 10P(24) CO_2 laser line whose wavelength is close to the centre of the absorption band of the molecules. A portion of the LIF spectrum covering the (020)-(000) band of the SiH_2 $\tilde{A}(^1B_1) - \tilde{X}(^1A_1)$ transition is shown as figure 1. The agreement with the rovibronic assignment due to Dubois [5] is apparent as is the fact that many unassigned lines are observed. However there is no evidence for vibrationally excited SiH_2 ($\tilde{X}$) at wavelengths predicted by Dubois [5]. At short interpulse times (0-0.8 μs) the spectrum is unaffected by pressures of up to 1 torr of nitrogen or helium.

These measurements support the contention that SiH_2 plays a role in IR MPD of alkylsilanes [4] but give no indication of the relative importance of the silylene producing channel. However the fluence

dependence of the silylene yield, figure 2, mimics that for final product yield [4] and it is not unreasonable that silylene plays a role in the major decomposition pathway.

The dependence of the LIF signal on the interpulse delay is detailed in figure 3. The major conclusion to be drawn from these data is that SiH_2 is produced only in the presence of the IR pulse and hence by photolysis not via secondary chemistry. There are two likely photolytic sources of SiH_2, either the three-centred elimination

$$CH_3CH_2SiH_3 \xrightarrow{nh\nu} C_2H_6 + SiH_2 \qquad (1)$$

or secondary photolysis of a hot primary product. Ring, O'Neal et al have studied the shock-induced decomposition of n-propylsilane and reject reactions similar to (1) [8]. Moreover, only a 1% yield of ethane was observed in IR MPD of ethylsilane [4]. Thus, either the majority of silyene is not formed via reaction (1) or silylene is a minor product in which case it may all be formed via (1).

Primary products which may undergo secondary photolysis to silylene are SiH_4 formed via a four centered elimination.

$$CH_3CH_2SiH_3 \xrightarrow{nh\nu} C_2H_4 + SiH_4 \qquad (2)$$

$$SiH_4 \xrightarrow{nh\nu} SiH_2 + H_2 \qquad (2a)$$

and CH_3CH_2SiH produced via the 1,1 elimination

$$CH_3CH_2SiH_3 \xrightarrow{nh\nu} CH_3CH_2SiH + H_2 \qquad (3)$$

$$CH_3CH_2SiH \xrightarrow{nh\nu} C_2H_4 + SiH_2 \qquad (3a)$$

We favour reactions (3) and (3a) as this is congruent with the major channel observed by Ring, O'Neal et al for shock-induced decomposition of alkylsilanes larger than methylsilane [8,9] and because the activation energy of (3a) is estimated as low as 31 ± 2

kcal mol^{-1} [9]. It is possible that CH_3CH_2SiH is produced with sufficient internal energy to undergo reaction (3a).

The observation of SiH_4 as a major product in IR MPD of alkylsilanes appears at odds with this preference [4]. However, these product studies were carried out at pressures, 1-25 Torr which could support a silylene chain reaction of the type proposed by Ring, O'Neal et al [9].

$$SiH_2 + C_2H_5SiH_3 \longrightarrow [C_2H_5SiH_2SiH_3]^* \quad (4)$$

$$[C_2H_5SiH_2SiH_3]^* \longrightarrow C_2H_5SiH + SiH_4 \quad (5)$$

$$[C_2H_5SiH_2SiH_3]^* \longrightarrow C_2H_5SiH_2SiH + H_2 \quad (6)$$

This mechanism implies a $[C_2H_4]/[SiH_4]$ ratio which is independent of pressure and reflects the rates of reactions (5) and (6). Ring, O'Neal et al's value $k_6 > 3k_5$ which implies $C_2H_4/SiH_4 \sim 4$ is in reasonable agreement with Steinfeld et al's value of 3. In this regard, we should like to mention the interesting possibility that the chain may be driven by the IR pulse via reaction (3a).

Conclusions

We have observed prompt production of silylene in the collisionless IR MPD of ethylsilane. We interpret these results in terms of secondary photolysis of CH_3CH_2SiH formed from the primary dissociation of ethylsilane. This interpretation and our interpretation of the $[SiH_4]/[C_2H_4]$ ratio observed by Steinfeld et al [4] derives from and is consistent with shock tube data of Ring, O'Neal et al [8,9] and differs from the mechanism (2 + 2a) proposed by Steinfeld et al [4].

Acknowledgement

We would like to acknowledge discussions with Professor J. Steinfeld who has recently observed SiH_2 by LIF following IR MPD of $n\text{-}C_4H_9SiH_3$ and phenylsilane. We also acknowledge the assistance provided to this project from a NATO grant for international collaboration in research.

References

1. J.H. Purnell and R. Walsh, Chem. Phys. Letters 110 (1984) 330.
2. H.E. O'Neal and M.A. Ring, Chem. Phys. Letters 107 (1984) 442.
3. R. Robertson, D. Hils and A. Gallagher, Chem. Phys. Letters 103 (1984) 397.
4. J.S. Francisco, S.A. Joyce and J.I. Steinfeld, J. Phys. Chem. 88 (1984) 3098.
5. I. Dubois, Can. J. Phys. 46 (1968) 2485.
6. G. Inoue and M. Suzuki, Chem. Phys. Letters 105 (1984) 641.
7. D.M. Rayner and P.A. Hackett, J. Chem. Phys. 79 (1983) 5414.
8. B.A. Sawrey, H.E. O'Neal, M.A. Ring and D. Coffey Jr., Int. J. Chem. Kinetics 16 (1984) 801.
9. M.A. Ring, H.E. O'Neal, S.F. Rickborn and B.A. Sawrey, Organometallics 2 (1983) 1891.

Figure Captions

1. LIF excitation spectrum of SiH_2 in the region of the (020)-(000) band of the $\tilde{A}(^1B_1) - \tilde{X}(^1B_1)$ transition observed at an interpulse delay of 400 ns following the IR MPD (10P(24), 6 Jcm^{-2}) of $C_2H_5SiH_3$ (30m Torr) in N_2 buffer (0.5 Torr).
2. Fluence dependence of the relative SiH_2 yield as determined from LIF intensities in the IR MPD (10P(24)) of $C_2H_5SiH_3$ (20 mTorr) in He buffer (0.7 Torr).
3. Timescales of SiH_2 production in the IR MPD (10P(24)) of $C_2H_5SiH_3$ (20 mTorr) in He buffer (0.7 Torr) as monitored by the dependence of LIF intensity on the interpulse delay.
   (a) using the full infrared pulse and (b) using a truncated infrared pulse obtained with a plasma shutter. Infrared pulse profiles are shown as solid lines.

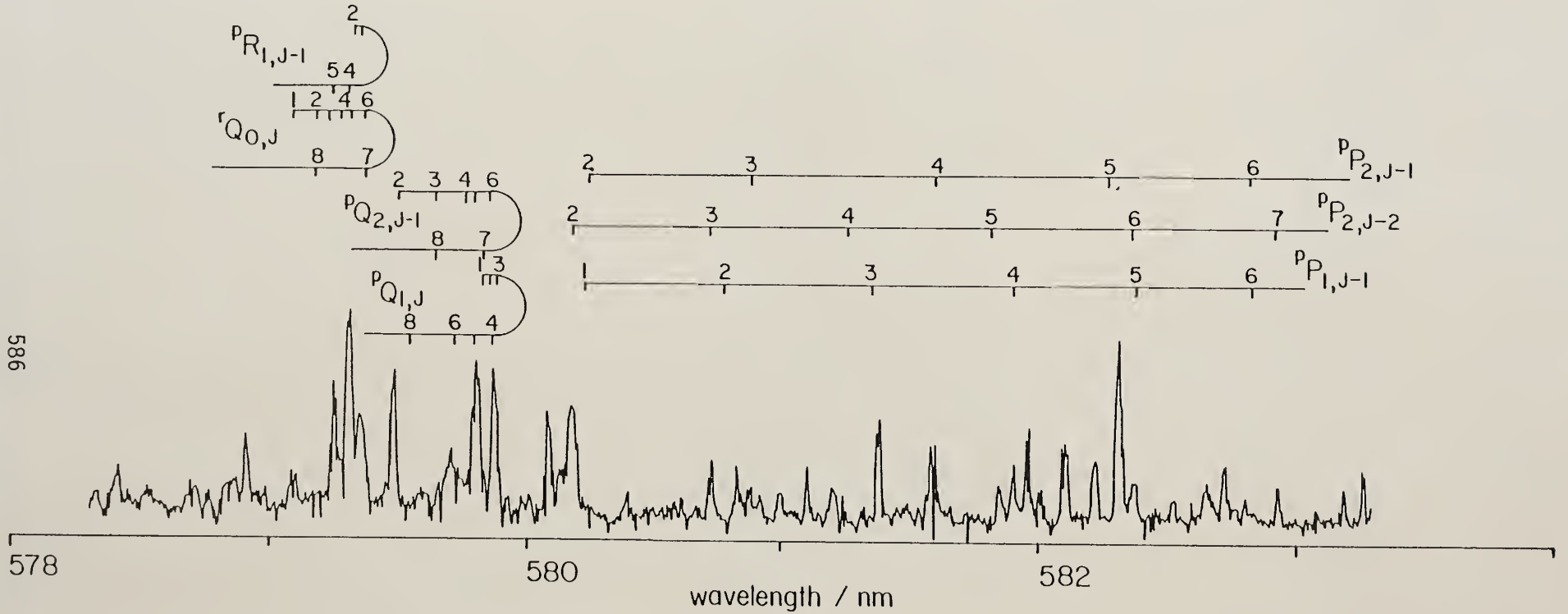
$^{P}R_{1,J-1}$
$^{r}Q_{0,J}$
$^{P}Q_{2,J-1}$
$^{P}Q_{1,J}$
$^{P}P_{2,J-1}$
$^{P}P_{2,J-2}$
$^{P}P_{1,J-1}$
586
578
580
582
wavelength / nm

FIGURE 1

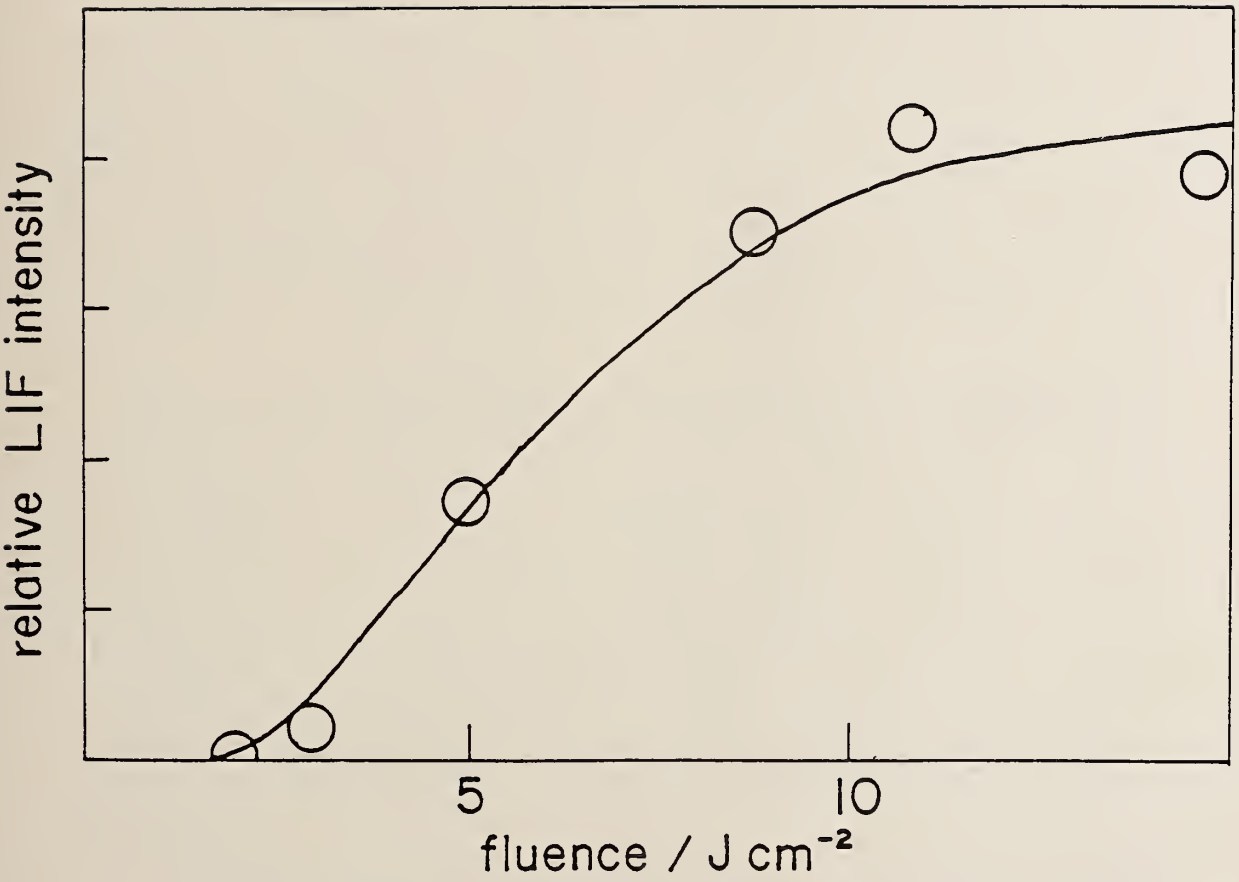

FIGURE 2

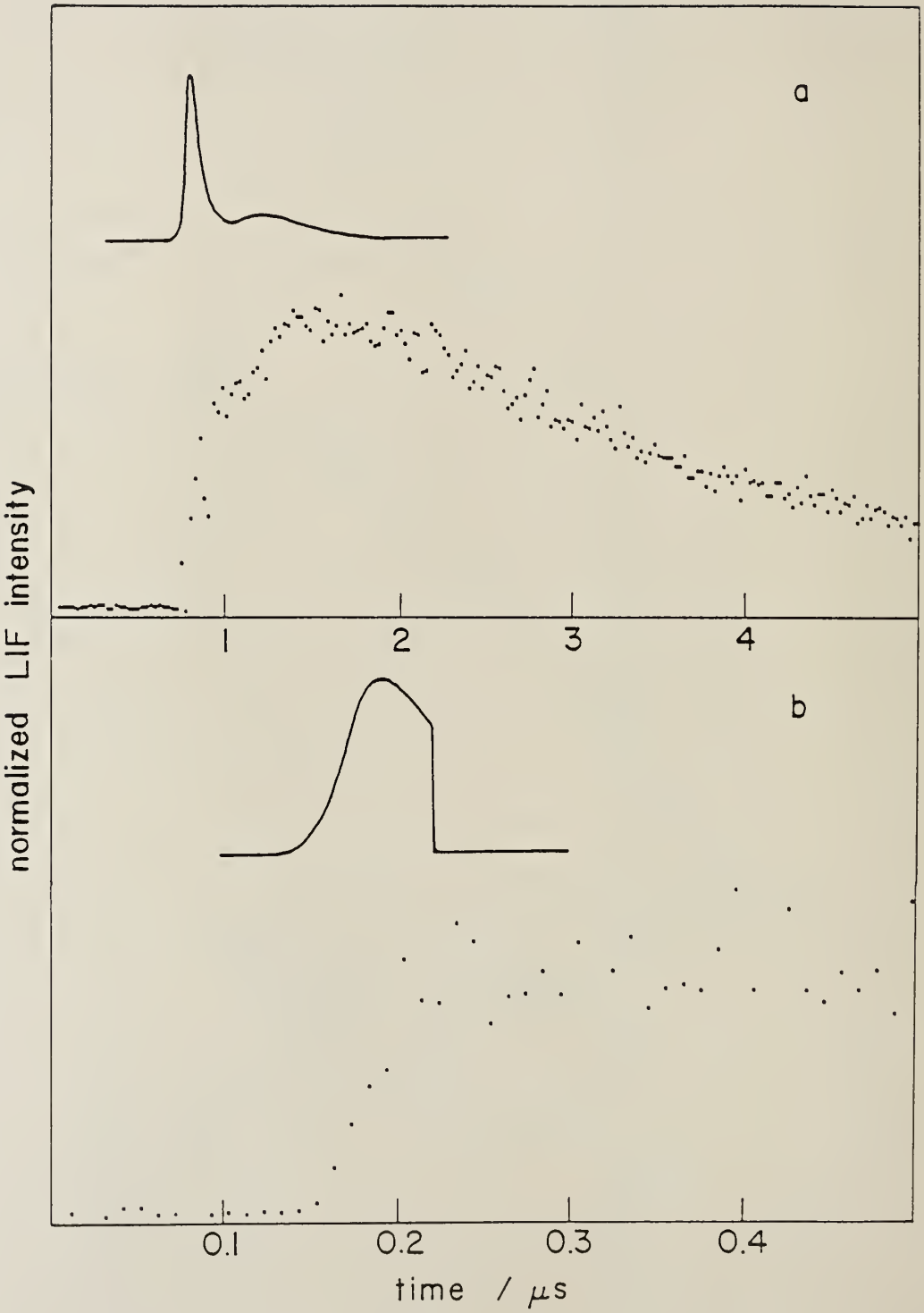

FIGURE 3

REACTIONS OF LASER-GENERATED FREE RADICALS AT SILICON SURFACES

B. Roop, S. Joyce, J.C. Schultz, J.W. Thoman, Jr., K. Suzuki [a], and J.I. Steinfeld
Department of Chemistry, Massachusetts Institute of Technology, Cambridge, MA 02139

Introduction

Fluorocarbon free radicals are thought to play an important role in the reactive etching of silicon and other semiconductor materials[1]. These reactions are typically carried out in high-frequency plasmas, in which ions, electrons, and deep-U.V. radiation are present, in addition to free radicals. In order to elucidate the specific interactions of the neutral radical species with silicon surfaces, we have studied these reactions under low-pressure conditions in which the radicals are generated *in situ* by infrared multiple photon dissociation (IRMPD) of the parent fluorocarbons.

Laser-induced dissociation reactions provide a clean, controllable way of producing specifically desired reactive species at a precisely known concentration, location, and time. Fortunately, most of the fluorocarbon gases used in plasma etching can be readily dissociated by high-power CO_2 laser pulses[2]. F atoms, CF_2, or CF_3 can be individually produced from specific precursors; other species of importance in etching, such as Cℓ atoms, CFCℓ, etc., can also be generated. In favorable cases, the translational or rotational energy content of the fragments can be varied by controlling the laser pulse characteristics.

For detection of the gas-phase species, laser-induced fluorescence (LIF) is the preferred method. In contrast to total emission measurements from the plasma, which (a) are not sensitive to the presence of electronic ground states and (b) probe the discharge region, not the vicinity of the surface, LIF is both species-and state-specific, sensitive, and permits spatial resolution to the dimensions of mm or less. In addition to optical diagnostics, we have found that it is essential to carry out measurements of surface properties as well. Both kinds of information are required for a complete understanding of the surface chemistry and the gas-surface interactions.

1. Chemisorption of CF_3 Radicals on Single Crystal Silicon

We have studied the chemisorption of CF_3 free radicals generated by IRMPD of fluorocarbons at a silicon surface. The IRMPD of C_2F_6 appears[3]-[6] to be selective for production of CF_3, at least below fluences of ~ 50 J/cm^2. Si(111)7x7 p-type crystals (resistivity 1.5 ohm-cm) were used in most of these experiments. X-ray photoelectron spectroscopy and thermal desorption spectrometry were the principal measurement techniques employed.

The experimental apparatus[7] is a two stage system with a base pressure of 2 x 10^{-10} Torr. The upper chamber is the high pressure cell which can be separated from the lower chamber by a gate valve. After exposing the crystal to relatively high pressures, the upper chamber can be evacuated to 1 x 10^{-8} Torr, the gate valve opened and the crystal lowered to the bottom chamber by a long-travel manipulator. The upper chamber incorporates two differentially pumped ZnSe windows for admitting the laser beam. Rotation of the crystal is provided by a two-stage differentially pumped rotary seal. The silicon crystal is held by two Ta wires, which also serve as leads for resistive heating of the material.

The bottom chamber has capabilities for ion sputtering, LEED, Auger, X-ray photoelectron spectroscopy (XPS), ultraviolet photoemission spectroscopy (UPS), and thermal desorption spectrometry (TDS). A cylindrical mirror analyzer (CMA) is used as the detector for the photoemission and Auger techniques.

The beam from a 20-Hz TEA-CO_2 laser (Tachisto 550G) is introduced into the upper chamber through ZnSe windows. The beam is focussed parallel to and approximately 1-2 mm away from the crystal surface. The fluorocarbon precursors (C_2F_6 or CF_3I) are flowed through the upper chamber at a pressure of approximately 10 mTorr. At this pressure the mean free path is 2-3 mm. Therefore radicals generated by IRMPD could intercept the adjacent surface without undergoing more than 1 or 2 collisions with background molecules. The 9R(30) CO_2 laser line [1084.64 cm^{-1}] was used to dissociate C_2F_6.

No C(1s) or F(1s) XPS peaks were detectable on the Si(111)7x7 surface after exposure to 10 mTorr of C_2F_6 for periods up to one hour.

Background chemisorption of C_2F_6 therefore does not contribute to the signals observed following laser irradiation. CF_3I, however, was found to undergo spontaneous dissociative chemisorption on this surface in the absence of infrared excitation. C(1s) and F(1s) peaks are observed after IRMPD of C_2F_6 at pressures of a few mTorr.

In addition to CF_3 radicals, the infrared excitation process produces a high concentration of vibrationally excited C_2F_6 molecules above the surface. Some of these "hot" molecules may interact with the silicon surface to produce the observed features. The possibility of enhanced chemisorption for vibrationally excited species has been suggested in a few recent studies[8]-[12], but little firm evidence is available on whether such vibrationally excited molecules contribute to chemisorption.

In order to assess the possible role of vibrationally excited C_2F_6, a series of measurements on the F(1s) peak was carried out at varying infrared fluences. The area of each peak was determined by subtracting a baseline and subsequently adding all the counts contained within the peak. The resulting curve of F atom coverage *vs.* infrared fluence shows a threshhold at a 2 J/cm^2, and reaches a constant value above 15 J/cm^2. This behavior mirrors the dissociation yield dependence on infrared fluence found for many similar molecules[2,13,14]. The threshold of 1-2 J/cm^2 is also consistent with available data[3]. Currently accepted models for IRMPD[2,13,14] suggest that, at the infrared fluences required for dissociation of molecules such as C_2F_6, most of the molecules in the beam path have acquired a substantial degree of vibrational excitation. The mean vibrational energy content [as measured, for example, by photoacoustic spectroscopy[14,15]] is a nearly linear function of infrared fluence, and does not display threshold behavior. For these reasons, we feel that the chemisorption is due to CF_3 radicals, and that vibrational excitation of the parent molecules does not substantially enhance chemisorption in this system.

In order to verify that the fluence dependence represents the dissociation yield and not saturation of the surface, a series of measurements was performed in which the exposure (number of laser pulses) was varied at a constant laser fluence of 15.5 J/cm^2. Although

the resulting curve of coverage vs. exposure begins to level off after approximately 20,000 laser pulses, the coverage (as measured by the F(1s) peak intensity) continues to increase slowly, even after 72,000 laser pulses. This indicates that saturation coverage has not been fully attained. This is perhaps surprising, given the amount of radicals impinging on the surface. Under these irradiation conditions, approximately 10% of the C_2F_6 molecules will be dissociated in a critical reaction volume[16] of 0.024 cm^3, yielding about 2×10^{12} CF_3 radicals per laser pulse. About 10% of these may reach the surface; the rest will either miss the crystal or be lost by gas-phase recombination[17]. We thus estimate that 72,000 laser pulses at the highest infrared fluence used in these experiments correspond to approximately 10^{16} radicals impinging on the silicon surface. For comparison, the density of surface sites is 7×10^{14} cm^{-2} for unreconstructed Si(111).

There are several possible explanations for this behavior. One might be adatom-adatom interactions, i.e., the CF_3 radicals may be inhibited from binding due to steric interactions after the initial chemisorption of the radicals has occupied readily available surface sites. Another possible mechanism could be polymerization of the CF_x species on the surface[18]. However, the position of the F(1s) XPS peak is not observed to shift to the binding energy expected[19] for $(CF)_n$ polymer. It is also possible that fluorine is reacting with silicon, i.e., etching is occurring. In experiments previously reported[20] using XeF_2, we found that the F(1s) peak intensity increased with dose well beyond the amount necessary for monolayer coverage. This was interpreted as a facile diffusion of fluorine into the bulk of the crystal. If the chemisorption of CF_3 is at least partly dissociative, as these results suggest, then some of the fluorine could penetrate to bulk sites, as was the case with XeF_2. Additional measurements at much higher CF_3 doses will be required to distinguish between these possible mechanisms.

From the shifts observed in the C(1s) and F(1s) XPS peaks, we have inferred that the CF_3 radical undergoes a partial dissociation at the Si(111)7x7 surface, with CF and C being the most likely stable surface

species. This dissociative chemisorption is suppressed by the presence of coadsorbed hydrocarbons. Full details are given elsewhere[21].

2. Measurements of CF_2 Concentration Profiles by LIF

In favorable cases, laser-excited fluorescence (LIF) can be used as a sensitive probe for gas-phase species interacting with surfaces. CF_2 is such a case. The apparatus assembled for this part of the research consists of a high-vacuum stainless-steel chamber suitable for generation of active species either in a discharge-flow configuration, or by infrared or ultraviolet photodissociation. The species so generated can be monitored either in the unperturbed gas flow or in the proximity of a substrate to be investigated, using a movable stage to position the substrate. Detection is by laser-excited fluorescence, using a frequency-doubled excimer-pumped tunable dye laser as the source. Either total or dispersed fluorescence can be measured using a fast boxcar integrator interfaced to a laboratory computer.

Initial experiments have been carried out using CF_2interacting with Si(100) and SiO_2 surfaces. The CF_2 is generated by a DC glow discharge in CF_4. Excitation of the $\tilde{A}\ ^1A_1(020) \leftarrow \tilde{X}\ ^1A_1(000)$ vibronic transition at 261.70 nm produces a well-resolved single-vibronic-level (SVL) fluorescence spectrum. CF_2 can be conveniently monitored via the strong (020)→(020) peak at 270.96 nm. The estimated lower limit of single-quantum-level detectivity is 10^9~10^{10} molecules/cm^3; since the excitation-detection region is only about $(0.2mm)^2$ x (1 cm), this corresponds to an absolute detection of ~10^6 molecules. This sensitivity should be sufficient for monitoring products of surface reactions as well.

A simple analytic form for the species concentration can be derived for steady flow near the surface of a substrate. In this case,

$$\frac{\partial n}{\partial t} = \mathcal{D}\frac{\partial^2 n}{\partial z^2} + G - R \qquad (1)$$

where n is the density of active species (e.g., CF_2), $\mathcal{D}$ is its diffusion

coefficient in the gas, G is the gas-phase generation rate and R is the gas-phase reaction rate of the active species. In steady-state, $\frac{\partial n}{\partial t} = 0$ and $G = R$. Thus $\frac{\partial^2 n}{\partial z^2} = 0$ with the boundary condition at the surface,

$$\mathscr{D} \frac{\partial n}{\partial z}\Big|_{z\to 0} = \frac{1}{4} \alpha_r \langle v_r \rangle n(z)\Big|_{z\to 0} \tag{2}$$

with α_r the net reaction probability on the surface and $\langle v_r \rangle$ the mean thermal velocity. The solution, for $z \ll L$ (the linear dimension of the substrate), is

$$\tilde{N}(z) = \frac{n(z)}{n(z\to 0)} = \frac{1}{4} \frac{\alpha_r \langle v_r \rangle}{\mathscr{D}} z + 1 \tag{3}$$

and, since

$$\mathscr{D} = \frac{1}{3} \langle v_r \rangle \lambda_r \tag{4}$$

for ideal gases (λ_r is the mean free path of the active species in the gas),

$$\tilde{N}(z) = \frac{3}{4} \frac{\alpha_r}{\lambda_r} z + 1 \tag{5}$$

The CF_2 concentration profiles found in our preliminary measurements show the linear dependence on z (for small z) predicted by Eq. (5); for $z\to L$, n(z) approaches the bulk (unperturbed) gas-phase concentration. From the limiting slopes, we have estimated $\alpha_r \cong 1.4 \times 10^{-2}$ for CF_2 on Si(100), and $\alpha_r \cong 3 \times 10^{-3}$ on SiO_2. The value of α_r for CF_2 is comparable with that found for F atoms [22] and XeF_2[23], using very different techniques; values of α_r as high as 0.75 have been estimated[1], for CF_3 on Si. Further measurements on these systems are currently in progress.

3. LIF Detection of SiH_2 Produced in IRMPD of Organosilanes

The IRMPD of organosilanes has been observed[24] to yield olefins, silane, and a deposit on adjacent surfaces identified as amorphous silicon (a:Si-H). The low silane:olefin product ratios found in those experiments, and the accompanying deposition of a:Si-H, were attributed to secondary IRMPD of the vibrationally hot silane produced in the

initial photolysis steps to yield silylene (SiH_2). In order to verify this proposed mechanism, we have used LIF to detect the SiH_2 produced in this reaction. The organosilanes were photolyzed with a TEA CO_2 laser at 0.5 -5 J/cm^2. SiH_2 was detected via its $\tilde{A}^1B_1(020) \leftarrow \tilde{X}^1A_1(000)$ transition at 580 nm, using an XeCl excimer-pumped dye laser (Lambda Physik EMG 101E + FL 2002) as the excitation source. The delay between the IR (photolysis) and visible (probe) lasers was varied, as was the delay between the probe laser pulse and the boxcar detection gate. The materials (n-butylsilane and phenylsilane, Silar Industries) were slowly flowed through the reaction chamber at a pressure of 5 to 20 mTorr.

SiH_2 was observed as a product in the IRMPD of both n-butylsilane and phenylsilane, either under collision-free conditions (10-25 mTorr) or with added buffer gas (0.4-0.8 Torr He). The LIF signals from phenylsilane are a factor of 30-50 weaker than with butylsilane, indicating that significantly less SiH_2 is produced in the former system. Since the IRMPD of phenylsilane is considerably more facile than for butylsilane or other n-alkylsilanes[24], the production of SiH_2 (via $SiH_4^{\ddagger}$) must be a relatively minor channel in the decomposition of the phenyl system.

By delaying the visible LIF excitation laser pulse with respect to the IR photolysis pulse, we can monitor the formation and decay kinetics of SiH_2. The fluorescence signal rises rapidly to a maximum (< 1 μsec), indicating that SiH_2 production occurs during the IR pulse under collision free conditions, in accordance with the mechanism suggested in Ref. (24). The rapid decay of the SiH_2 density, as measured by the LIF signal under collision-free conditions, is due to kinetic transport out of the volume probed by the excitation pulse[25]. The observed 1/e time (~3 to 4 μsec) is consistent with a thermal velocity distribution, i.e., the SiH_2 species are not translationally hot. In the presence of buffer gas, this transport process is slowed by collisions to the diffusion limit. There is no indication of a homogeneous gas phase reaction removing SiH_2; this species thus appears to be sufficiently long lived to provide efficient transport of silicon to a nearby surface in the deposition process.

The LIF excitation spectra of SiH_2 in the He buffer gas taken at delay times of 30-40 μsec following the IR photolysis pulse show a considerable reduction in the number of intense lines, which implies extensive rotational cooling relative to the initial distribution and efficient collisional relaxation by He.

If the fluorescence detection gate is set to a delay of 60-260 nsec following the LIF excitation pulse, most of the features have disappeared, indicating that the radiative lifetime in $\tilde{A}\ ^1B_1$ is less than 25-30 nsec. A few features remain in the spectrum, however, corresponding to anomalously long-lived excited rovibronic states. Based on the assignments available for this transition[26], the long-lived states in this spectral region all have low values of K_a' (= 0 or 1), but there is no clear pattern to the J' values, which range from 1 to 7. The rotational-state dependence of radiative lifetimes has been studied for a few systems, most extensively in formaldehyde[27,28]. Measurements of collision-free single-rovibronic level lifetimes in H_2CO and D_2CO show a considerable variation with rotational state. These variations arise from a K'-dependent radiationless decay rate on which is superimposed a random variation arising from energy mismatches between the excited-state levels and nearby levels in the S_0 manifold. The SiH_2 system evidently shows the same type of behavior; a more complete study of the lifetimes is in progress and will be reported in subsequent publication[29].

Acknowledgments

This work has been supported by National Science Foundation Industry-University Cooperative Grant CHE81-21472 and Air Force Office of Scientific Research Grant 83-0007. Various aspects of this work have benefited from helpful discussions and technical assistance from Drs. J.S Francisco, A.E.W. Knight, D. Rayner, P. Vaccaro, F. Walsh, and C. Zarowin. We also thank the M.I.T. Laser Research Center for the loan of a Tachisto 550G CO_2 laser, and the Lyons foundation for fellowship support (S.J.).

Notes and References

(a) Present address: Central Research Laboratory, Hitachi Ltd.,

Tokyo, Japan
(1) H.F. Winters, J. Appl. Phys. 49, 5165 (1978).
(2) J.I. Steinfeld, Laser-Induced Chemical Processes (Plenum Press, New York, 1981), pp. 243-267.
(3) G.A. Fisk, Chem. Phys. Letts. 60, 11 (1978)
(4) A.B. Horwitz, J.M. Preses, R.E. Weston, Jr., and G. Flynn, J. Chem. Phys. 74, 5008 (1981).
(5) S. Arai, T. Watanabe, Y. Ishikawa, and T. Oyama, Chem. Phys. Letts. 112, 224 (1984).
(6) Aa. S. Sudbo, P.A. Schulz, E.R. Grant, Y.R. Shen, and Y.T. Lee, J. Chem Phys. 70, 912 (1979).
(7) B. Roop, Ph.D. Thesis, Massachusetts Institute of Technology (1985).
(8) A. Gelb and M.J. Cardillo, Surf. Sci. 64, 197 (1977).
(9) J.T. Yates, J.J. Zinck, S. Sheard, and W.H. Weinberg, J. Chem. Phys. 70, 2266 (1979).
(10) S.G. Brass, D.A. Reed, and G. Ehrlich, J. Chem. Phys. 70, 5244 (1979).
(11) C.T. Rettner, H.E. Pfaur, and D.J. Auerbach, Surf. Sci. (in press).
(12) T.J. Chuang, J. Chem. Phys. 74, 1453, 1461 (1981).
(13) M. Quack, Adv. Chem. Phys. 50: Dynamics of the Excited State (K. Lawley, ed.), pp. 395-473 (J. Wiley Ltd., Chichester, 1982).
(14) J.S. Francisco, Zhu Qingshi, and J.I. Steinfeld, J. Chem. Phys. 78, 6339 (1983).
(15) F.M. Lussier, J.I. Steinfeld, and T.F. Deutsch, Chem. Phys. Letts. 58, 227 (1978).
(16) C. Reiser and J.I. Steinfeld, Opt. Eng. 19, 2 (1980).
(17) The gas-phase recombination rate for CF_3 radicals is given as 3.2 x 10^{-11} cm^3 $molecule^{-1}$ sec^{-1} [S.W. Benson, The Foundations of Chemical Kinetics, p. 302 (McGraw-Hill Book Co., New York, 1960)]. The half-life of the CF_3 radicals in the gas phase is thus approximately 0.3 msec, so that the loss due to recombination is comparable to that at the surface.
(18) E. Kay, J. Coburn, and A. Dilks, in Plasma Chemistry III - Topics in Current Chemistry (S. Veprek and M. Venugopalan, eds.), pp. 1-42, Fortschritte der Chem. Forschung, vol. 94 (Springer-Verlag, Berlin, 1980).
(19) T.J. Chuang, H.F. Winters, and J.W. Coburn, Appl. Surf. Sci. 2, 514 (1979).
(20) B. Roop, S. Joyce, J.C. Schultz, N.D. Shinn, and J.I. Steinfeld, Appl. Phys. Letts. 46, 1187 (1985).
(21) B. Roop, S. Joyce, J.C. Schultz, and J.I. Steinfeld (to be published).
(22) Flamm, Donnelly, and Mucha [J. Appl. Phys. 52, 5633 (1981)] find α_r = 0.0017 for F on Si while Vasile and Stevie [J. Appl. Phys. 53, 3799 (1982)] report α_r = 0.005. There is an ambiguity in the definition of α_r in the latter work, however, so the actual value could be as high as 0.08. In the case of Flamm's work, neglect of surface layer depletion above the substrate may require the reported result to be corrected upward, to as much as 0.05 [K. Suzuki, unpublished results]. It is just these kinds of problems in the determination of α_r that has been one of the strong

incentives to developing the present technique.
(23) H.F. Winters and J.W. Coburn, Appl. Phys. Letts. 34, 70 (1979).
(24) J.S. Francisco, S.A. Joyce, J.I. Steinfeld, and F. Walsh, J. Phys. Chem. 88, 3098 (1984).
(25) S.E. Bialkowski, D.S. King, and J.C. Stephenson, J. Chem. Phys. 72, 1156 (1980).
(26) (a) I. Dubois, Can. J. Phys. 46, 2485 (1968);
(b) National Research Council of Canada, Depository of Unpublished Data, File No. 18-9D-764 (1968).
(27) J.C. Weisshaar and C.B. Moore, J. Chem. Phys. 72, 5415 (1980).
(28) K. Shibuya, P.W. Fairchild, and E.K.C. Lee, J. Chem. Phys. 75, 3397 (1981).
(29) J.W. Thoman, Jr., and J.I. Steinfeld (to be published).

MICROWAVE SPECTROSCOPY OF FREE RADICALS AND MOLECULAR IONS

Shuji Saito
Institute for Molecular Science, Okazaki 444, Japan

Essential points in the microwave spectroscopy of transient molecules such as free radicals and molecular ions are sensitivity of the spectrometer, production of molecules and prediction of their transition frequencies.[1] A good combination of these three points makes it easy to detect spectral lines of transient molecules by overcoming their very low concentration attained in laboratory conditions. When we examine the points, we see that there is a slight difference in nature between sensitivity of the spectrometer and the other points. Monitoring of a transient species by optical emission or absorption, mass spectrometry, or matrix methods can be used to find the optimum production for the species. The transition frequencies of a molecule can be predicted with an accuracy in accordance with the resolutions of such methods as optical spectroscopy, LMR spectroscopy, EPR spectroscopy, or ab initio calculations. Thus these two points require support from other methods, especially other spectroscopic methods. On the other hand, sensitivity is self-supporting. If the sensitivity of the spectrometer is much improved, it will be possible to look for a transient species even under conditions of non optimized production and/or poorly predicted frequency region. The high sensitivity may partly cover deficiencies in the other points: wide frequency searching in shorter time.

We have developed a millimeter-wave spectrometer suitable for observations of free radicals and molecular ions. The main features of our spectrometer are summarized in Table I. We examined the sensitivity of our spectrometer at 122 GHz, because source noise of a klystron in this region is small. We observed the J=11-10 transition of $^{18}O^{13}C^{34}S$ in natural abundance of 0.96 ppm as shown in Fig.

Table I. Summary of the Millimeter-Wave Spectrometer at IMS.

Power source	OKI klystrons for 8 - 200 GHz	
	Harmonic generators for 200 - 400 GHz	
Absorption cell	3.5 m free space cell	30 GHz-
	1 or 2 m free space cell with the hollow cathode for ions	50 GHz-
	40 cm parallel plate cell	-150 GHz
Detector	GaAs Schottky barrier diode	-160 GHz
	InSb detector at 4.2 K	100 GHz-
Modulation	Stark or source	
Assisted by a minicomputer		

Fig. 1. The J = 11 - 10 transition of $^{18}O^{13}C^{34}S$ in natural abundance (0.96 ppm) observed by an integration of 50 s with the 3.5 m free space cell and source moduration.

1. The calculated peak absorption intensity of this line is 5.24×10^{-9} cm^{-1}.(2) Therefore the minimum detectable peak absorption intensity is 1.1×10^{-9} cm^{-1} at 122 GHz. This means that the minimum detectable density in the cell is 1.8×10^{7} molecules $/cm^{3}$. This high sensitivity is achieved by a combination of low noise and high power source, low noise detector, and low loss cell in the high frequency region assisted by a minicomputer.

We have studied various free radicals and a molecular ion as listed in Table II. Detections of most of the molecules given in Table II were helped by imformation from other spectroscopic

Table II. Transient Molecules Studied by Microwave Spectroscopy at IMS.

CF, CCl, SiF, SiCl, GeF, SF, PO,
SiN, NCl, PF, PCl, FeO,
NCO, HCCN, CCO, CCCO,
HO_2, DO_2, HSO, FSO, ClSO,
PH_2, PF_2, PO_2, HPO,
CF_3, CH_2F, CH_2Cl, CH_2CHO, SiF_3,
CH_3O, CD_3O, CH_3S, CH_3CO,
H_2D^+

methods, but several species such as HCCN and PF_2 were detected without any previous spectroscopic information from the gas phase. In the lecture some recent results on individual molecules will be given in detail and their significances in the fields of molecular structural study, chemical kinetics, photochemistry, and radioastronomy will be discussed.

The author would like to thank A. R. W. McKellar for a critical reading of the manuscript.

References

(1) S. Saito, Pure and Appl. Chem., 50, 1239 (1978).
(2) Z. Kiziel and D. J. Millen, J. Phys. Chem. Ref. Data, 11, 101 (1982).

THE OPTICAL SPECTRUM OF NbO

U. Sassenberg and A.J. Merer
Dept of Chemistry, U. of British Columbia, Vancouver, B.C., Canada

G. Cheval, J.-L. Fémênias and R. Stringat
Laboratoire d'optique atomique et moléculaire, Université de Nice, 06034 Nice, France

The optical spectrum of niobium monoxide, NbO, is still poorly understood, although the ground state is now known to be $^4\Sigma^-$, following the e.s.r. work of Brom, Durham and Weltner[1]. Among the puzzling features are the very considerable differences between the gas-phase emission spectrum[2] and the rare gas matrix absorption spectrum[1].

Most of the puzzles in the spectrum are resolved by the present work. An intense microwave discharge emission source of NbO has been developed, and the transitions at 4700 Å and 6500 Å have been photographed at high resolution using a 7 m Ebert spectrograph. The discharge emission source has been adapted for laser-induced fluorescence work, and extensive laser studies have been carried out in the wavelength region covered by the dye DCM. Various sub-bands have been recorded at a resolution of about 50 MHz, using the sub-Doppler technique of intermodulated fluorescence.

The principal results are as follows. The ground $^4\Sigma^-$ state of NbO turns out to have a second-order spin-orbit splitting of 62 cm^{-1} between the $^4\Sigma_{3/2}$ and $^4\Sigma_{1/2}$ components. As a result the $B^4\Pi(a)$-$X^4\Sigma^-(a)$ transition near 6500 Å, although very complex in the gas phase, reduces to just two sub-bands in matrix absorption (where only $^4\Sigma_{1/2}$ is populated) because the transitions to $^4\Pi_{5/2}$ and $^4\Pi_{-1/2}$ are case (a) forbidden. The 4700 Å system is now seen to be $^4\Sigma^-(a)$-$^4\Sigma^-(a)$, with $\lambda' \sim \lambda'' \sim 15$ cm^{-1}, even though it looks like a case (b)-case(b) transition[3]. Every band in the spectrum shows fantastic hyperfine effects resulting from the I=9/2 spin of Nb and the large Fermi contact

interaction of the $5s\sigma$ electron in the ground electronic state. Some very surprising hyperfine structure results from the unusual case (a) nature of the ground $^4\Sigma^-$ state, and its transition to case ($b_{\beta J}$) coupling with increasing rotation. The $^4\Pi$ excited state at 6500 Å has comparatively small hyperfine splittings, indicating a configuration $(4d\delta)^2\,(5p\pi)^1$, although its hyperfine Λ-doubling effects are quite sizeable.

References

(1) J.M. Brom, C.H. Durham and W. Weltner, J. Chem. Phys. 67, 903 (1974).
(2) V.K. Rao and D. Premaswarup, Ind. J. Phys. 27, 399 (1953).
(3) U. Uhler, Ark. Fys. 8, 265 (1954).

STUDY OF THE SPECTRA AND STRUCTURE OF THE SiC_2 RADICAL AT 8 K

Richard A. Shepherd and W.R.M. Graham

Department of Physics, Texas Christian University

Fort Worth, TX 76129, U.S.A.

The products from the evaporation of silicon carbide have been trapped in argon at 8 K and studied using FTIR and optical spectroscopy. Using the two fundamentals occurring at 1741.1 and 824.4 cm^{-1}, frequencies for SiC_2 singly and doubly substituted with carbon-13 were calculated for linear and bent geometries. Comparison with the spectra observed on isotopic substitution shows conclusively that SiC_2 is a C_{2v} radical, in agreement with a recent rotational analysis of the 500 nm band. Derived force constants suggest that the carbon atoms are doubly bonded. Calculation of the relative amplitudes of the vibrations at 1741.1 and 824.4 cm^{-1} indicates that they are ν_1 and ν_2, respectively, and leads to revised vibrational assignments for the transition observed at 500 nm in an Ar matrix. Possible implications of the present results for the assignment of the ν_3 vibration are also discussed.

INTRODUCTION

The SiC_2 radical was first identified by means of its electronic spectrum in the atmospheres of certain N-type stars[1], and more recently has been detected by its microwave spectrum in the envelope of the carbon star IRC +10216 [2]. Because it is isoelectronic with C_3, SiC_2 was for a long time thought to be linear; however, it was concluded from a recent rotational analysis of a

band in the optical spectrum at 500 nm that the molecule is cyclic [3]. A preference for the cyclic structure was also supported by the results of *ab initio* calculations [4].

Matrix studies have provided useful information on both the infrared and optical spectra of this radical. Weltner and McLeod [5] made assignments for the three fundamentals in the ground and excited states of the 500 nm transition of SiC_2 trapped in a Ne matrix. Bondybey [6], in an extensive laser fluorescence study in a Ne matrix observed ground state vibrations at 1746, 836, and 344 cm^{-1} which he assigned to ν_3, ν_1, and an overtone $2\nu_2$, respectively, under the assumption that SiC_2 was linear. Corresponding vibrations were identified for the upper state of the 500 nm band system at 1466, 1011, and 462 cm^{-1}.

The present work was undertaken with the objective of studying the effects of carbon-13 isotopic substitution on the ground state vibrations of the molecule in order to independently determine the ground state geometry, to correctly assign the fundamental vibrations, and to examine the possible implications for the vibrational analysis of the upper state of the 500 nm transition.

EXPERIMENTAL PROCEDURE

The SiC_2 radical is easily formed in matrices by trapping the products from the evaporation of silicon carbide powder

from a tantalum cell lined with graphite; however, in order to facilitate isotopic substitution an alternate procedure was used in which equal weights of silicon and graphite (either carbon-12 or 99 at % carbon-13) were heated for 4 h at 1670 K prior to deposition. The vapor was co-deposited with argon onto a CsI or LiF window maintained at 8 K in a Displex closed cycle refrigerator. Spectra were recorded on a McPherson 0.5 m spectrometer and a Nicolet 5DXE FTIR instrument.

RESULTS AND DISCUSSION

Strong absorptions were observed in the infrared at 1741.1 and 824.4 cm^{-1} corresponding to bands of SiC_2 previously observed in the gas phase and in a Ne matrix (see Table I).

TABLE I. Observed ground state vibrations of SiC_2

	$\nu_1(cm^{-1})$	$\nu_2(cm^{-1})$	Reference
Gas Phase	1742	852	6
Ne matrix	1746	836	5, 6
Ar matrix	1741.1	824.4	Present work

Fig. 1(a) shows the spectrum observed for a silicon/carbon-12 mixture and 1(b), for silicon/carbon-13. The appearance of the 1741 and 824 cm^{-1} bands in Fig. 1(b) indicates that silicon reacted with the graphite liner of the evaporation cell.

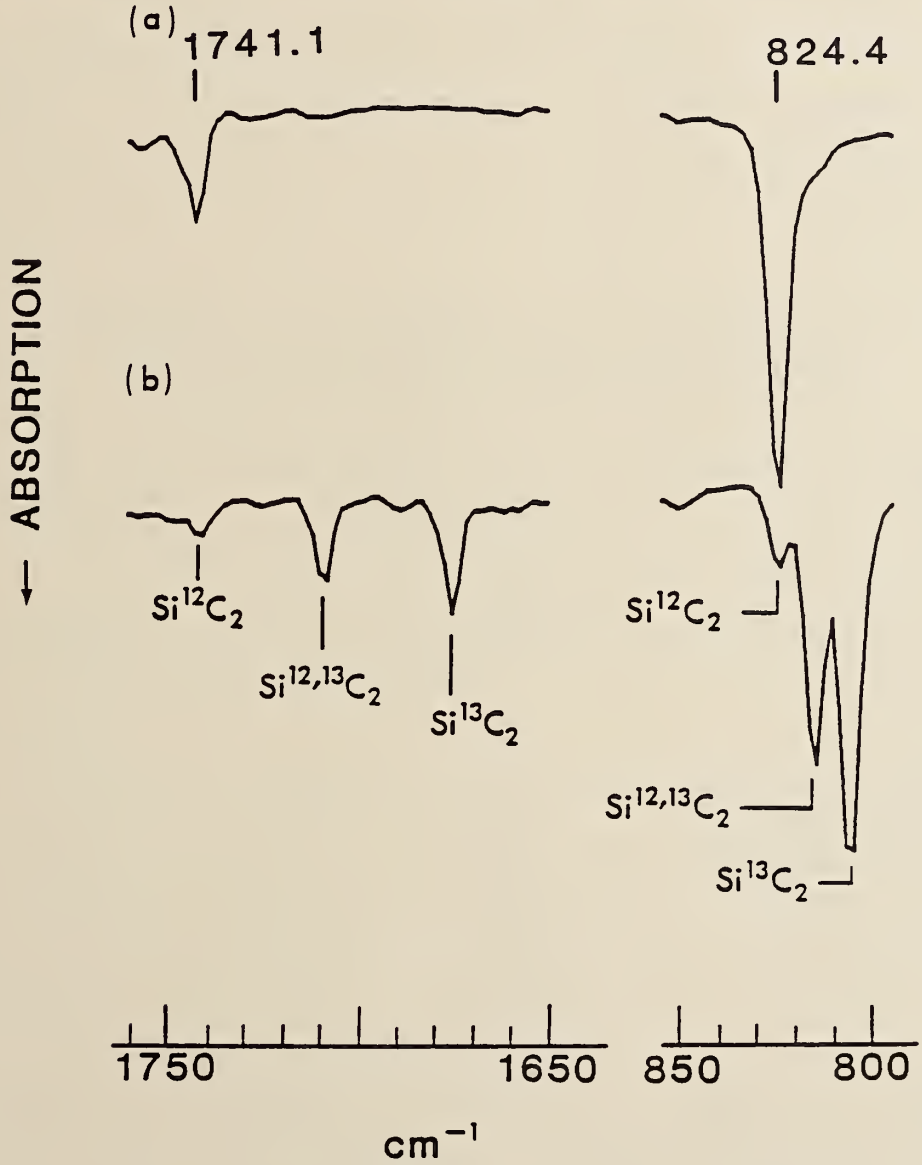

FIG. 1. FTIR spectra obtained using (a) silicon/carbon-12 and (b) silicon/carbon-13 mixtures.

Two strong, new features to the low frequency side of the original bands result from single and double carbon-13 substitution, and immediately suggest equivalent carbon atoms in SiC_2, with either $D_{\infty h}$ or C_{2v} symmetry. Using the observed vibrations at 1741.1 and 824.4 cm^{-1} frequencies for single and double substituted SiC_2 were calculated [7,8] for $C_{\infty v}$, $D_{\infty h}$, and C_{2v} geometries, with the results shown in Table II. Comparison of the results with the observed bands, which are reproducible to 0.2 cm^{-1}, shows clearly that the geometry is C_{2v}.

Table II. The effect of ^{13}C substitution on two SiC_2 fundamentals compared with the spectrum calculated for various geometries.

Species	Calculated			Observed
	$C_{\infty v}$ (cm^{-1})	$D_{\infty h}$ (cm^{-1})	C_{2v} (cm^{-1})	(cm^{-1})
$Si^{12}C_2$	---	---	---	1741.1
$Si^{12,13}C_2$	1722.2[a] 1695.0[b]	1723.2	1707.2	1708.2
$Si^{13}C_2$	1675.4	1704.7	1673.0	1674.2
$Si^{12}C_2$	---	---	---	824.4
$Si^{12,13}C_2$	808.4[a] 821.4[b]	815.8	815.5	814.7
$Si^{13}C_2$	805.9	807.1	807.0	805.3

[a] $Si-^{12}C-^{13}C$

[b] $Si-^{13}C-^{12}C$

The three normal vibrations of a C_{2v} molecule are ν_1, the symmetric "breathing" vibration; ν_2, the symmetric deformation vibration in which the legs of the triangle expand while the base contracts; and ν_3, the antisymmetric vibration. Assignment of either of the frequencies observed in the infrared to the ν_3 vibration leads to inconsistencies between the vertex angle and the force constants calculated from the observed isotopic shifts. Assignment of the two absorptions to the symmetric, a_1 vibrations together with the observed isotopic shifts leads to a C-C force constant of ~10 mdyn/A, and a Si-C constant of ~3 mdyn/A, which indicate that the bonds are double and single, respectively. The vertex angle of 40.5 $\pm$2.5° resulting from this model is consistent with 40.36° derived from the rotational analysis recently carried out for a band of the 500 nm transition.

In order to correctly identify which of the observed vibrations is ν_1 and ν_2 the relative amplitudes of the atoms for each frequency were calculated. Fig. 2 illustrates the results which show unambiguously the correct assignments. The form of ν_3, the only b_2 vibration for a C_{2v} molecule, is specified independently of its actual value. As was the case in previous matrix work, the third vibration was not observed in the infrared in the present study. A vibration at 344 cm^{-1} observed by Bondybey [6] in the laser-induced fluorescence

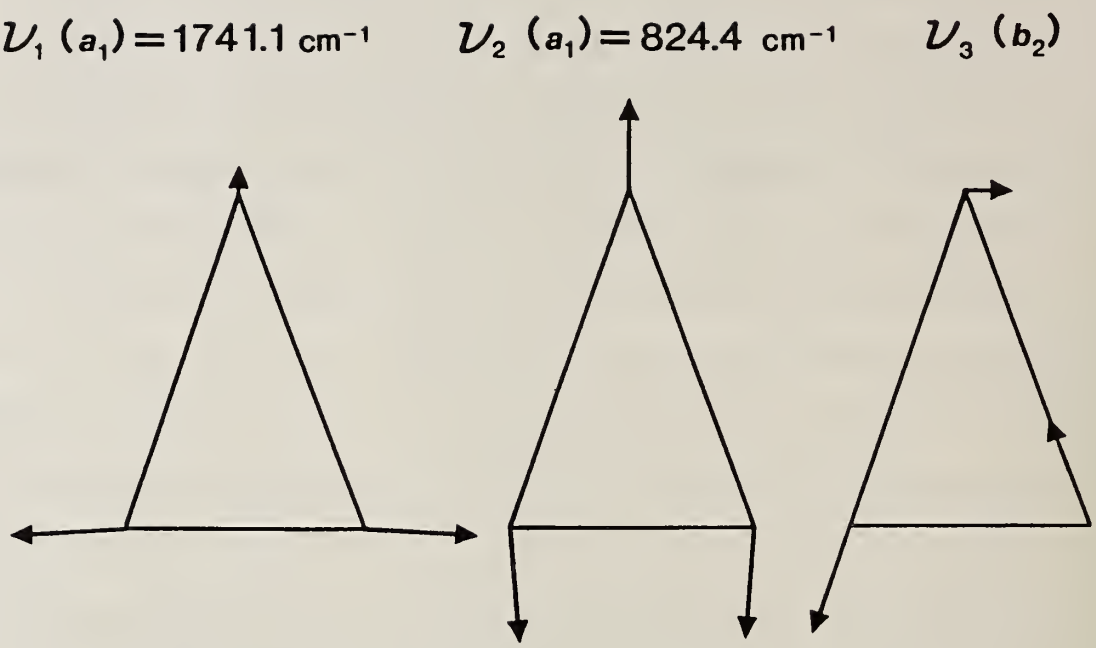

FIG. 2. Normal vibrations of SiC_2.

spectrum of SiC_2 was interpreted as an overtone of ν_2 since the excitation of single modes of the antisymmetric vibration is forbidden for the linear geometry then assumed. Under C_{2v} geometry excitation of single modes of the antisymmetric vibration is similarly forbidden for the transition at 500 nm, which on the basis of the recent rotational analysis [3] has been identified as $\tilde{A}\ ^1B_2 \leftarrow \tilde{X}\ ^1A_1$. A careful search for the third vibration in the infrared down to 225 cm^{-1} under conditions when the symmetric vibrations were very strong, failed to reveal another band; therefore, the evidence continues to point to a third vibration of ~180 cm^{-1}. Such a low vibration however, would tend to favor a T-shaped molecule in which there is an ionic bond between Si^+ and C_2^-. It has been pointed out [9] that the ν_1 = 1741.1 cm^{-1} fundamental

of SiC_2 which, as Fig. 2 indicates, is essentially a C-C stretching mode, is close to the 1758 cm^{-1} frequency observed for C_2[10]. Additional support for this view is provided by data derived from rotational spectra indicating that the C-C bond length is 1.27 A for both molecules. Finally, calculations predicting a large dipole moment of 3.2 D are consistent with the T-shaped structure.[2] In C_{2v} symmetry the isotopic shifts predicted for the T-shaped structure are not significantly different from those predicted for the cyclic structure.

Fig. 3 shows the vibrational analysis of the 500 nm system recorded for SiC_2 trapped in Ar, incorporating the revised identifications of the fundamentals.

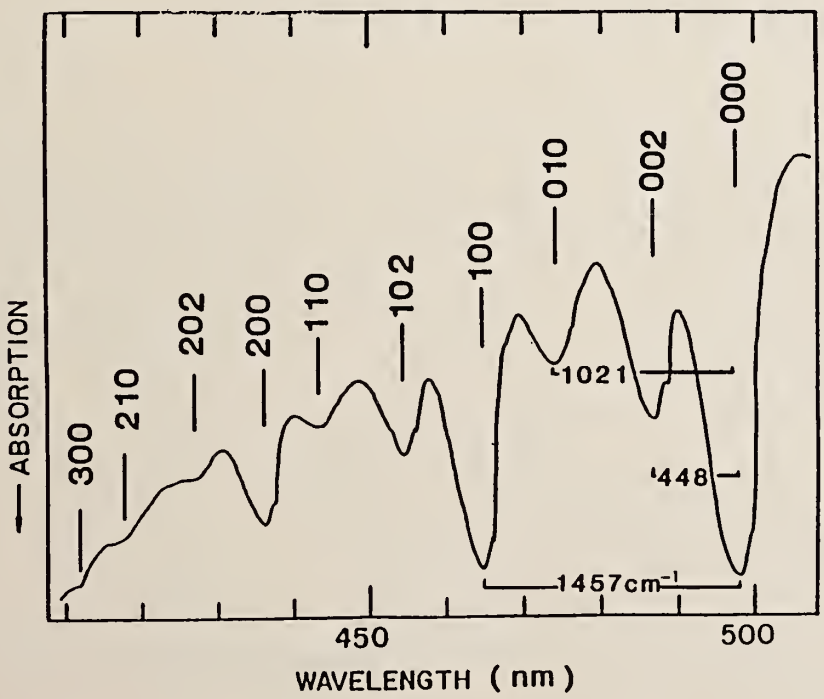

FIG. 3. Revised vibrational assignments for the 500 nm transition.

CONCLUSIONS

The results of the isotopic FTIR studies verify that SiC_2 is a C_{2v} molecule with small vertex angle of ~40°, in agreement with the theoretical predictions and the recent rotational analysis. The bands at 1741.1 and 824.4 cm^{-1} have been identified as ν_1 and ν_2, respectively. Derived force constants suggest that the carbons are doubly bonded. The present work indicates the reassignment of the $\tilde{X}\ ^1A_1$ ground and $\tilde{A}\ ^1B_2$ excited state vibrations summarized in Table III for both an Ar matrix and the gas phase. The observation of ν_3 and in particular, confirmation of the low frequency (~180 cm^{-1}) would tend to favor a T-shaped rather a cyclic structure for SiC_2.

Table III. Revised Vibrational Assignments

State		ν_1 (cm^{-1})	ν_2 (cm^{-1})	$2\nu_3$ (cm^{-1})
$\tilde{X}\ ^1A_1$	Gas phase	1742	852	354
	Ar matrix	1741.1	824.4	
$\tilde{A}\ ^1B_2$	Gas phase	1464	979	455
	Ar matrix	1457	1021	448

ACKNOWLEDGMENT

Support of this work by the Robert A. Welch Foundation under Grant P-786 and the TCU Research Fund is gratefully acknowledged.

REFERENCES

1. R. Kleman, Astrophys. J. 123, 162 (1956).

2. P. Thaddeus, S. E. Cummins, and R. A. Linke, Astrophys. J. 283, L45 (1984).

3. D. L. Michalopoulos, M. E. Geusic, P.R.R. Langridge-Smith- and R. E. Smalley, J. Chem. Phys. 80, 3556(1984).

4. R. S. Grev and H. F. Schaefer III, J. Chem. Phys. 80, 3552 (1984).

5. W. Weltner, Jr. and D. McLeod, Jr., J. Chem. Phys. 41, 253 (1964).

6. V. E. Bondybey, J. Phys. Chem. 86, 3396 (1982).

7. G. Herzberg, Molecular Spectra and Molecular Structure II. Infrared and Raman Spectra of Polyatomic Molecules (Van Nostrand, Princeton, N.J., 1945), pp. 172-173.

8. R. A. Shepherd and W.R.M. Graham, J. Chem. Phys. 82, 4788 (1985).

9. M. E. Jacox, private communication.

10. G. Herzberg and A. Lagerquist, Can. J. Phys. 46, 2363(1968).

RADIO OBSERVATIONS OF MOLECULES IN SPACE

L. E. Snyder
Astronomy Dept., University of Illinois, Urbana, IL, U.S.A.

I. Introduction: The Known Interstellar Molecules

In this paper, an inventory of some of the current astronomical molecular studies will be given, but it will not be a comprehensive guide to the future by any means, because one of the exciting aspects of astronomical molecular work is its serendipity. As a guide to begin to discuss this topic, Table 1 gives a list of the 68 interstellar molecular species which have been reported as of this meeting. Individual isotopes and a few unconfirmed species have not been listed. Square brackets mean that further confirmation of the detection is needed. Lists of the transition frequencies have been prepared by Lovas,

Table 1. The 68 Reported Interstellar Molecules Listed in Order by Number of Atoms

2	3	4	5	6	7	8	9	10	11	13
H_2	H_2O	H_2CO	H_2C_2O	$HCONH_2$	HC_5N	$HCOOCH_3$	HC_7N	$[CH_3C_5N]$	HC_9N	$HC_{11}N$
CH	H_2S	H_2CS	H_2CNH	CH_3CN	$HCOCH_3$	CH_3C_3N	$(CH_3)_2O$			
CH+	HCN	$HCNH^+$	H_2NCN	$[CH_3NC]$	CH_3C_2H		CH_3CH_2CN			
C_2	HNC	HNCO	HC_3N	CH_3OH	CH_2CHCN		CH_3CH_2OH			
CN	HCO	HNCS	HCOOH	CH_3SH	NH_2CH_3		CH_3C_4H			
CO	HCO^+	$HOCO^+$	C_3H_2							
CS	$[HOC^+]$	C_3H	C_4H							
NO	HCS^+	C_3N								
NS	[HNO]	C_3O								
OH	N_2H^+	NH_3								
SiO	C_2H									
SiS	OCS									
SO	SO_2									
[HCl]	SiC_2									
[PN]	[NaOH]									
	$[H_3^+]$									

Snyder, and Johnson (1979), Mann and Williams (1980), and Lovas (1985). Many of the interstellar molecular species have also been found in circumstellar shells. Over the years, the list in Table 1 has grown too long to address in only one lecture, so only a few of the more interesting aspects will be addressed here. Because of excitation and partition function arguments, it is generally expected that the smaller molecules will be found to predominate in the short millimeter and submillimeter range of the spectrum while the large species will be observed in the longer millimeter and centimeter range. There are exceptions, of course, such as the short millimeter wavelength emission of methanol, dimethyl ether, and methyl formate from dense, high temperature clumps.

Some interesting things to note from Table 1 are:

a) Two small rings, SiC_2 and C_3H_2, have been found (Thaddeus et al. 1984; 1985).

b) Protonated species are starting to appear, such as N_2H^+ (protonated nitrogen) and HCNH+ (protonated HCN).

c) The large molecules are important because each complex molecule represents many other species that can't be seen.

d) There are tentative detections of molecules which contain sodium and chlorine-potential tracers of stellar processing.

e) Three molecules contain the amide group: H_2NCN (cyanamide), $HCONH_2$ (formamide), and NH_2CH_3 (methylamine).

These interesting facts are related to some of the most exciting astrophysical and astrochemical reasons for studying molecules in space-studies which concern stellar birth, stellar death, interstellar chemistry, and the related questions about the existence of biomolecules and about the importance of their potential delivery systems, comets. An overview of these areas will be given in this paper, and the details of many of the interesting specific studies will be left to the references.

II. Stellar Birth

Studies of star-forming regions have been aided greatly by molecular observations. For example, the picture of the Orion infrared source IRc2, which is emerging from telescopes at Berkeley, Bonn, Onsala, and the VLA, is that IRc2 is surrounded by a dense disk of gas which has a high-veloci-

ty bipolar outflow (Erickson et al. 1982; Plambeck et al. 1982). The disk is composed of molecules such as SO, HCN, SiO, and NH_3. The NH_3 seems to be central to the clumps or condensations in the disk (Pauls et al. 1983), the OH masers are scattered around inside the dense gas disk, and the inner edges seem to support the SiO masers, within 35 AU of the infrared source IRc2 (Wright and Plambeck 1983; Lane 1982; Wright et al. 1983). The outflow is traced in HCO+ and appears to originate either from the surface of the disk or from the central star itself. The diameter of activity is less than one arc min. and, within this region, IRc2 is believed to drive the flow. In apparent contrast to the Orion picture, W3 is an example of high velocity outflow with no constraining disk (Wright, Dickel, and Ho 1984); it has HCN emission as well as OH and H_2O masers. In general, OH, H_2O, and CH_3OH maser observations show that active star forming regions typically have dense clumps of gas. Short millimeter and submillimeter wavelength observations are expected to be very useful for probing these clumps.

III. Stellar Death

The clouds of gas and dust found around many evolved stars are produced by a high mass loss phase (10^{-6} to 10^{-4} $M_\odot$ yr^{-1}) which is thought to be the dominant source of metal-rich gas for the interstellar medium. Some common types of evolved stars are O stars (Mira variables with [O]>[C]), C stars (carbon stars with [C]>[O]), and S stars ([O]$\cong$ [C]). Knapp and Morris (1985) have derived a useful formula for the mass loss rate where D = distance (pc) and f = $[CO]/[H_2]$. The total rate of mass

$$\dot{M} = \frac{T_A^* V_o^2 D^2}{2.0\times10^{15} f 0.85} \; M_\odot \; yr^{-1}$$

returned to the interstellar medium is estimated to be about 0.3 $M_\odot$ yr^{-1}. Usually, radio studies of the circumstellar envelopes of evolved carbon stars are conducted using spectra of the CO molecule. Typically, CO is used to find the stellar radial velocity, the outflow velocity, and as a temperature probe. Therefore, to get away from CO momentarily, the first example illustrates what can be learned from the combination of centimeter and millimeter wavelength spectra of the asymmetric rotor SiC_2,

a small ring molecule which is part of the interesting molecular mix fed back into the interstellar medium by evolved stars. Fig. 1 shows the spectrum of the 1_{01}-0_{00} transition of SiC_2 in the envelope of the evolved carbon star IRC+10216, observed with the Effelsberg 100 m radio telescope

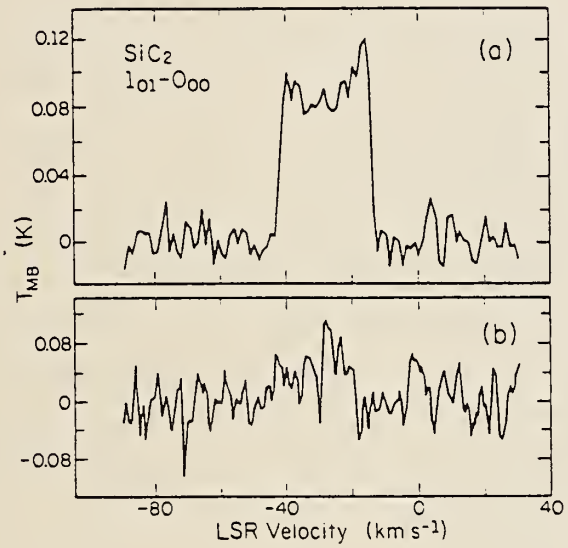

Fig. 1 - (a) Spectrum of the 1_{01}-0_{00} transition of SiC_2 toward IRC+10216 taken with the Effelsberg 100 m radio telescope of the MPIfR (from Snyder et al. 1985b). The ordinate is main beam brightness temperature and the abscissa is LSR radial velocity. (b) The average of all offset spectra (N, S, E, and W) taken from a five point cross map in R.A. and dec., centered on IRC+10216 with one beamwidth offsets.

of the MPIfR. The telescope beam size was 42" (FWHP). The double-peaked profile in Fig. 1 (a) suggests that the SiC_2 is optically thin and partially resolved by the beam (see, for example, Olofsson et al. 1982). The signal-to-noise ratio in Fig. 1 (a) is high enough to allow the stellar radial velocity (about -26 km s^{-1}) to be determined if the rest frequency (23,600.2 MHz) is known accurately, or vice versa. Fig. 2 shows the rotational temperature diagram constructed from the data in Fig. 1 and from the three SiC_2 millimeter transitions reported by Thaddeus et al. (1984). The usual expression for the intensity of optically thin rotational lines has been used: $\log I = \log [(3kW)/(8\pi^3 \nu S\mu_a^2)] = \log (N/Z) - (E \log e)/(kT_{rot})$. The values of these parameters have been defined by Thaddeus et al. (1984) and by Snyder et al. (1985b). There is little signifi-

cant difference in Fig. 2 between the least squares fit to the millimeter data only (solid line) and the least squares fit to all four transitions. From the fit, a rotational temperature of 15 ± 2 K and a column density of 1.5×10^{14} cm^{-2} was found. Furthermore, it is possible to use SiC_2 line profile

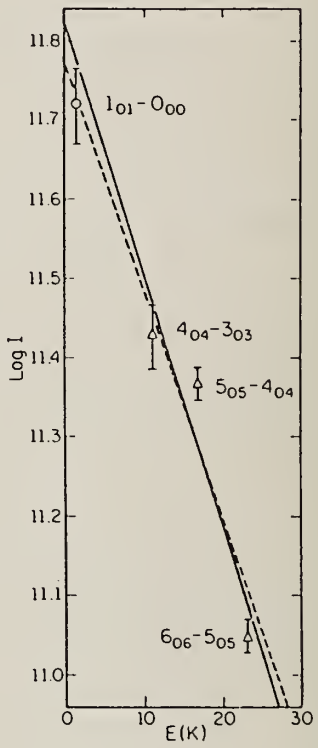

Fig. 2 - Rotational temperature diagram of the SiC_2 1_{01}-0_{00}, 4_{04}-3_{03}, 5_{05}-4_{04}, and 6_{06}-5_{05} transitions in IRC+10216. The ordinate is log I, where $I = [(3kW)/(8\pi^3 \nu S \mu_a^2)]$, and the abscissa is rotational energy of the upper state in K. All points have been corrected to a 90" HPBW. The solid line is a least squares fit based only on the previously reported SiC_2 millimeter transitions 6_{06}-5_{05}, 5_{05}-4_{04}, and 4_{04}-3_{03}. The dashed line is a least squares fit to all data (from Snyder et al. 1985b).

and mapping information and all measured line intensities in the constant excitation temperature model of Olofsson et al. (1982) to determine that (a) the emission radius R_e of the IRC+10216 circumstellar envelope is approximately 29" in the SiC_2 1_{01}-0_{00} transition, (b) the abundance of SiC_2 relative to H_2 in IRC+10216 appears to be intermediate between that of SiS and SiO, and (c) the emission radius R_e decreases with increased excitation, which is to be expected if the SiC_2 is excited by infrared radiation from a central exciting star. The second example is a brief discussion of maser stars. SiO, OH, and H_2O are the three molecular species exhibiting widespread maser emission in stellar objects. Approximately 325 OH, 110 H_2O, and 130 SiO circumstellar

maser sources are known (Engels 1979; Winnberg et al. 1985; Jewell et al. 1985) and a summary of their observational characteristics has been given by Snyder (1980). Interferometric observations show that the OH lies in expanding spherical shells typically about 10^{16} cm in diameter (see, for example, Booth, Diamond, and Norris 1984) while the SiO resides closest to the central star, nominally a long period variable undergoing mass loss. Fig. 3 from Moran et al. (1985) shows the distribution of 1612 MHz OH and H_2O masers near VX Sgr. VLBI measurements have determined the radius of the SiO masering region to be $\sim 10^{14}$ cm for the Mira variable R Cas and $\sim 10^{15}$ cm for the supergiant VY CMa (Moran et al. 1979). The determination of the distances to the maser stars is an important application which utilizes the angular diameters from interferometric measurements. It has been shown by Jewell et al. (1980) and by Herman and Habing (1981) that the phase lag between the blue and red shifted OH emission peaks may be used to determine the light travel time across the shell and hence a shell diameter to $\sim$ 10% accuracy. Division of shell diameter by angular diameter gives a direct measure of distance to the source which involves no assumptions. This technique should be of great value in the measurement of the galactic distance scale.

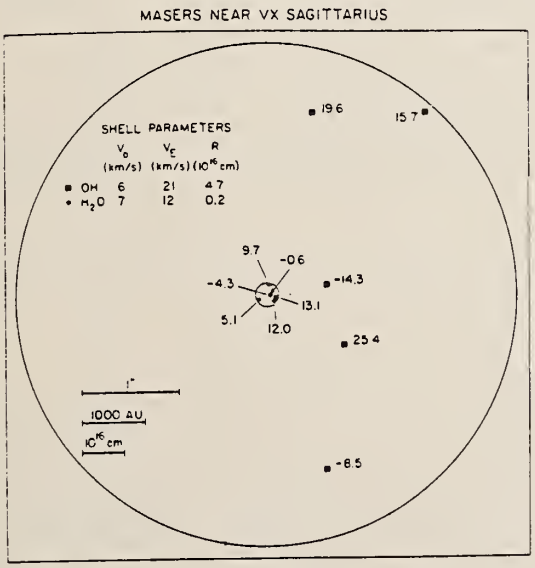

Fig. 3 - The distribution of 1612 MHz OH and H_2O masers near VX Sgr (from Moran et al. 1985).

IV. Interstellar Chemistry

Many astronomers regard interstellar chemistry as a rather dull subject which is cut and dried: a theoretician runs an ion-molecule code and an observer confirms the results. In the real world, however, things rarely work that way. All of the large molecules and many of the small molecules in Table 1 have abundances which are not predicted accurately by theory or measured correctly by observation. One excellent example of an unpredictable molecule is the interstellar formyl radical, HCO. Almost every serious chemical code predicts a measurable abundance of HCO and almost every observational bandscan in the 3 millimeter wavelength region of the spectrum covers hyperfine components of the J = 1-0 transition of HCO. The first problem is that HCO is hard to detect. Fig. 4 shows the lowest rotational energy levels of HCO; it

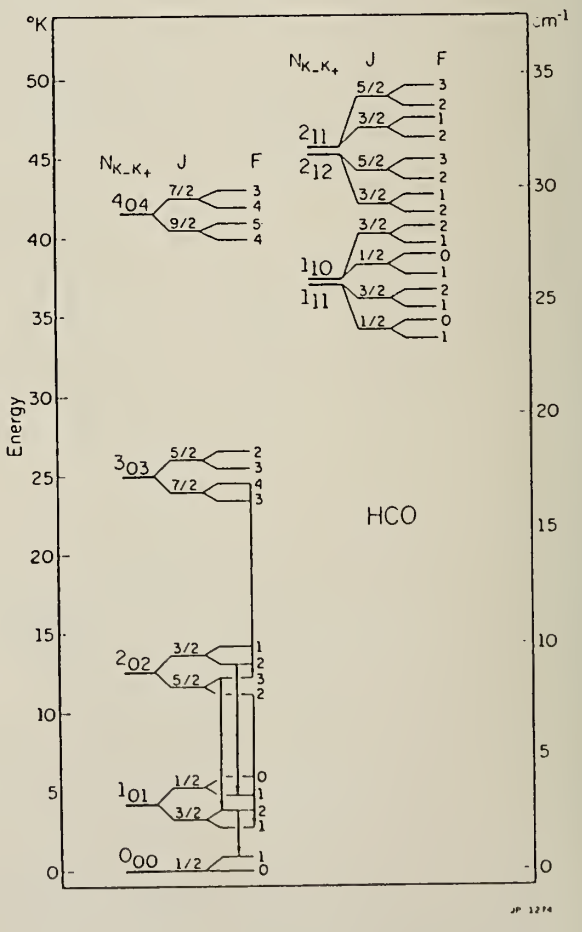

Fig. 4. - The lowest rotational energy levels of HCO. All interstellar HCO transitions reported to date are in emission and are indicated by downward arrows. The fine and hyperfine structure levels are not drawn to scale (from Snyder, Schenewerk, and Hollis 1985c).

is clear that the hyperfine level structure severely dilutes the intensities of the rotational transitions, which explains why HCO is hard to detect and rarely ever found in bandscans (see, for example, Johansson et al. 1984). The second problem is that when HCO is detected, it is not observed in the major molecular clouds, such as Orion KL, but rather in clouds which aren't usually outstanding sources of other species, such as NGC 2024, W3, W51, and K3-50. In the best HCO source, NGC 2024, there is fairly good agreement between observation and theoretical prediction from ion-molecule codes, but it is not clear why NGC 2024 is the best source. It is important to understand this anomalous behavior, however, because in the future small species like HCO will be observed frequently in the short millimeter and submillimeter wavelength regions of the spectrum. Large molecules also have interesting abundance peculiarities. Fig. 5 shows the excellent signal-to-noise ratio found for the

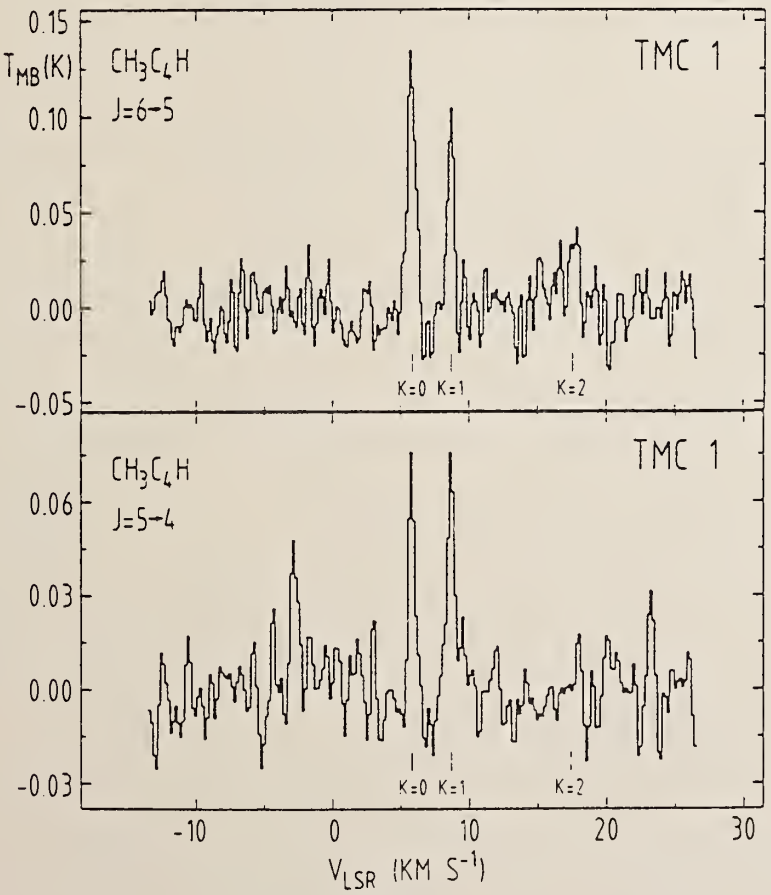

Fig. 5. - The CH_3C_4H spectrum toward TMC 1 (from Walmsley et al. 1984).

large interstellar molecule CH_3C_4H in TMC 1, a dark dust cloud believed to be a site for formation of low mass stars such as our Sun. The largest known interstellar molecules are found in TMC 1, but in many cases the column density results have been computed using rough estimates for the dipole moment values, which in some cases leads to large errors in the abundances. Fig. 6 shows the interesting relationship between m, the number of atoms in a molecule, and the logarithm of column density in TMC 1 which emerges when the correct dipole moments are applied to the column density computation. The solid line in Fig. 6 shows the results of a least squares fit to log N for the revised column densities of HC_3N through $HC_{11}N$, which gives a decrement $N(HC_{2n+1}N)/N(HC_{2n+3}N) = 3.06$. The dashed line is a fit for HC_3N through HC_9N only, which gives a decrement of 2.51. The simplicity of the relationship in Fig. 6 is not predicted by straightforward modeling, but it strongly suggests that there may be key formation reactions which dominate the abundances of the long carbon chain molecules in quiescent interstellar dust clouds (Herbst 1985).

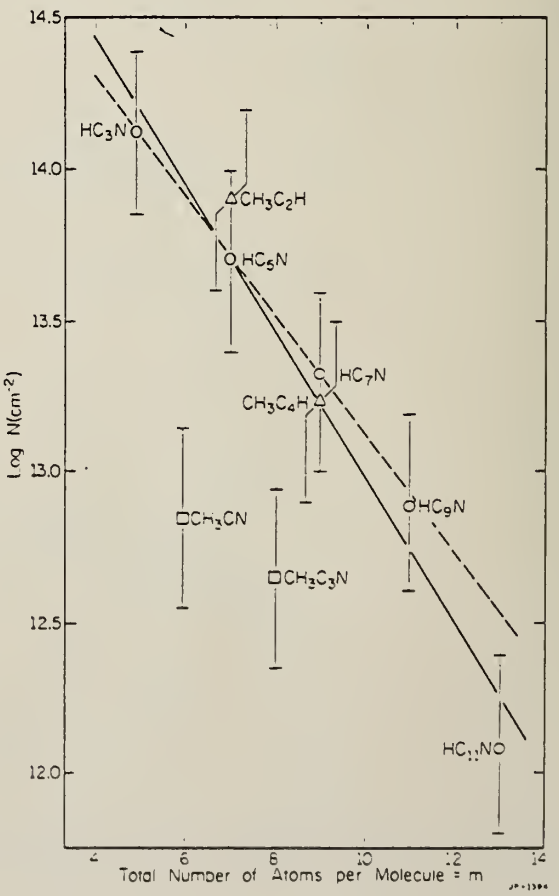

Fig. 6 - The logarithms of the revised column densities (ordinate) plotted against m, the total number of atoms per molecule (abscissa) for the dark dust cloud TMC 1 (from Snyder, Dykstra, and Bernholdt 1985a). Solid line-least squares fit for HC_3N through $HC_{11}N$ (circles). Dashed line-least squares fit for HC_3N through HC_9N only. The logarithms of the column densities of the CH_3CN-CH_3C_3N (squares) and CH_3C_2H-CH_3C_4H (triangles) families are plotted but not included in the least squares fitting.

V. Are There Biomolecules in the Interstellar Clouds?

Commission 51, also called Bioastronomy or the Search for Extraterrestrial Life, is the fastest growing group in the International Astronomical Union. Among the commission's stated areas of interest is, "the search for, and study of, biologically relevant interstellar molecules". Are there really biologically relevant molecules, i.e. biomolecules, in the interstellar clouds? If so, can they be found or have they already been found? To try to answer these questions, it is necessary to think about the building blocks of biological systems. Deevey (1970) pointed out that if minor elemental constituents can be neglected, an empirical formula for living matter would contain 49.84% hydrogen, 24.92% oxygen, 24.92% carbon, 0.27% nitrogen, 0.03% phosphorus and 0.02% sulfur. Interstellar searches have detected compounds containing all of the above elements including phosphorus, if the tentative detection of PN in Table 1 is verified. Even if interstellar PN is not confirmed, interstellar ionized phosphorus is easily detected via ultraviolet observations. Other authors have advocated sulfur as the fountainhead of life (based partly on descriptions of nucleosynthesis during explosive oxygen-burning in the supernova phase of stellar evolution which produces a high sulfur yield), or drawn "trees of life" with common interstellar atoms and molecules in the roots, RNA and DNA in the trunk, and advanced creatures such as horses and humans in the branches. All of these approaches are useful, but is there any hard evidence that the energy sources available in interstellar (or circumstellar) molecular clouds drive the synthesis of organic compounds into a biological chemistry? Is biomolecular ordering present in these clouds of gas and dust? Hoyle and Wickramasinghe (1984) have argued that the dust grains in interstellar clouds contain bacteria such as E coli. When the clouds condense to form stars and planets, the bacteria survive in comets. Those bacteria caught inside periodic comets are further processed into micro-organisms via successive perihelion passages, trapped by the outer cometary crust which acts much like the lid on a pressure cooker. Hoyle and Wickramasinghe (1977) have suggested that a cometary impact on the Earth about 4 billion years ago could have led to the start of terrestrial life and even today the continuing influxes of cometary debris may be responsible for major pandemics, such as influenza, which sweep the planet. Much of the experimental evidence for bacterial interstellar grains has centered on the comparison

of the shapes of interstellar extinction curves with laboratory opacity curves for various preparations of E coli. It is enough to say that these comparisons have been controversial (Moore and Donn 1982), mostly because solid state spectra generally do not have any sharply localized spectral features like the well defined rotational or vibrational-rotational lines found in gas phase spectra. Therefore, it would be extremely useful if the bacterial grain controversy could be formulated in terms of gas phase spectroscopy, where well-defined patterns of spectral lines can uniquely identify interstellar compounds.

What mechanisms conventionally believed to be important for the evolution of biology on the early earth might instead be active in the interstellar clouds? The idea that life arose when self-replicating crystals of clay assembled organic molecules which in turn eventually learned to become self-replicating (see, for example, Cairns-Smith 1985) may be applicable to dense interstellar molecular clouds with clay-like grains. If there are certain molecules which play a central role in the formation of gene materials via this process, perhaps it would be possible to detect them astronomically. Another approach might be to ask if the molecules produced in the Miller-Urey type of experiments (see Dickerson 1978, for example) can be found in space. Sagan and Khare (1979) have advocated the possible astronomical importance of the tarry residues (or "tholins") produced in these types of experiments, but the gas phase components have not been emphasized at all. Of the 20 some molecules produced in quantity in the experiments of Miller and Urey, the fairly small molecules formic acid, glycine, acetic acid, and urea have assigned microwave spectra. Of these, only formic acid has been detected in the galactic clouds. Glycine may be impossible to find with present telescopes because of its three conformers (see Hollis et al. 1980; Snyder et al. 1983, and references therein) but clearly its 10 atom complexity has been surpassed already by several molecules in Table 1. This suggests that interstellar searches for acetic acid and urea could be pursued in order to obtain abundance comparisons with formic acid and thereby perhaps provide some insight about whether chemical processes analogous to Miller-Urey cycles are ongoing in the interstellar clouds.

VI. Comets--Do They Preserve the Interstellar Chemistry?

Donn (1982) has summarized the historical background of the idea that comets may have played a role in biochemical evolution on the early Earth. Radio molecular observations of comets are important because they have the potential to probe deep into the coma and sample the potentially rich chemistry near the nucleus - which may contain many elements of the preserved interstellar chemistry. Molecular observations have been reviewed elsewhere by Snyder (1982) and Crovisier (1985) so it is sufficient to say that cometary radio signals from NH_3 and H_2O and hints of signals from HCN and CH_3CN have been reported, but these species have not been detected consistently in major comets. This lack of consistency has caused some to doubt that comets actually have a very complex chemistry. A most important clue that this viewpoint may be incorrect comes from radio observations of cometary OH - to date 16 comets have been found to have detectable radio lines of OH so it is safe to say that almost every major comet has observable OH (see Snyder 1984, for example). OH was the key molecule observed by radio astronomers in interstellar molecular clouds 20 years ago, long before all of the other molecules in Table 1 (except CH, CH^+ and CN) were known. Its abundant presence in comets may signal the existence of a rich chemistry near the cometary nucleus, far beyond the simple dissociation of H_2O, which will be uncovered by new millimeter and submillimeter instruments which have both high sensitivity and good spatial resolution. Already Hasegawa *et al.* (1984) have used the unprecedented millimeter-wavelength sensitivity of the 45 m telescope of the Nobeyama Radio Observatory to detect a hint of the long carbon chain molecule HC_3N in Comet Sugano-Saigusa-Fujikawa (1983e).

Another very important point is that OH is pumped by solar ultraviolet radiation. Time variations in the OH pumping mechanism, often called the Swings effect, happen when cometary OH absorbs Doppler-shifted solar ultraviolet Fraunhofer bands. This causes steady-state fluorescent pumping of the $X^2\Pi$ ground state Λ doublet levels to the electronically excited $A^2\Sigma^+$ state. The OH molecules cascade back to the ground state, thereby establishing the relative populations of the ground state Λ doublets. Hence this mechanism determines whether cometary radio OH signals will be observed in absorption, emission, or not at all. Other cometary molecules with greater chemical complexity may also undergo radiative or collisional pumping which ultimately determines whether they are detectable with current radio observa-

tional approaches.

VII. Conclusions

The list of interstellar molecules in Table 1 has grown so large that the detection of new interstellar molecular species no longer has the impact that it once did. However, specific subfields have evolved which use astrophysical and astrochemical molecular studies. The areas of stellar birth, stellar death, interstellar chemistry, bioastronomy, and comets have been briefly overviewed in this paper; given enough time, other important areas of molecular astronomy such as galactic structure, magnetic field measurements, and extragalactic molecular studies could have been discussed as well. The point to emphasize here is that when astronomical molecules are studied-whether mapping known species or detecting new-it is important to use the results to advance understanding in particular areas of astrophysics or astrochemistry rather than mapping for the sake of mapping or discovering the 69th molecule in order to get newspaper publicity. A second important consideration is that it is important to reach agreement on which species are candidates for biomolecules, and establish their relationships to astronomically interesting regions such as regions of stellar birth and stellar death. The final point of this paper is to emphasize that the important question of how well comets preserve the interstellar chemistry has not yet been answered observationally. Therefore it remains to be established whether comets could have been the delivery system between the interstellar clouds and the early Earth. It is important to use the next generation of sensitive new millimeter and submillimeter radio telescopes for molecular observations which will bring comets past the OH stage of radio molecular knowledge.

The author thanks Dr. Thomas Leo Wilson for supplying advice useful for the preparation of this article. This work was supported in part by NSF grant AST-8217547 to the University of Illinois.

VIII. References

Booth, R.S., Diamond, P.J., and Norris 1984, in VLBI and Compact Radio Sources, ed. R. Fanti, K. Kellerman, and G. Seti (Dordrecht: Reidel), p. 313.

Cairns-Smith, A.G. 1985, Sci. Am., 252, 90.

Crovisier, J. 1985, A.J., 90, 670.
Deevey, E.S. Jr. 1970, Sci. Am., 223, 149.
Dickerson, R.E. 1978, Sci. Am., 239, 70.
Donn, B. 1982, J. Mol. Evol., 18, 157.
Engels, D. 1979, Astr. Ap. Suppl., 36, 337.
Erickson, N.R., Goldsmith, P.F., Snell, R.L., Berson, R.L., Huguenin, G.R., Ulich, B.L., and Lada, C.J. 1982, Ap. J. (Letters), 261, L103.
Hasegawa, T., Ohishi, M., Morimoto, M., Suzuki, H., and Kaifu, N. 1984, Icarus, 60, 211.
Herbst, E. 1985, private communication.
Herman, J., and Habing, H.J. 1981, in Physical Processes in Red Giants, ed. I. Iben and A. Renzini (Dordrecht: Reidel), p. 383.
Hollis, J.M., Snyder, L.E., Suenram, R.D., and Lovas, F.J. 1980, Ap. J., 241, 1001.
Hoyle, F.W., and Wickramasinghe, C. 1977, New Sci., 17 Nov., 402.
Hoyle, F.W., and Wickramasinghe, C. 1984, From Grains to Bacteria (Cardiff: University College Cardiff Press).
Jewell, P.R., Walmsley, C.M., Wilson, T.L., and Snyder, L.E. 1985, Ap. J. (Letters), in press.
Jewell, P.R., Webber, J.C., and Snyder, L.E. 1980, Ap. J. (Letters), 242, L29.
Johansson, L.E.B., Andersson, C., Elldér, J., Friberg, P., Hjalmarson, Å., Höglund, B., Irvine, W.M., Olofsson, H., and Rydbeck, G. 1984, Astr. Ap., 130, 227.
Knapp, G.R., and Morris, M. 1985, Ap. J., 292, 640.
Lane, A.P. 1982, Ph.D. Dissertation, University of Massachusetts.
Lovas, F.J. 1985, in preparation.
Lovas, F.J., Snyder, L.E., and Johnson, D.R. 1979, Ap. J. Suppl., 41, 451.
Mann, A.P.C., and Williams, D.A. 1980, Nature, 283, 721.
Moore, M.H., and Donn, B. 1982, Ap. J. (Letters), 257, L47.
Moran, J.M., Ball, J.A., Predmore, C.R., Lane, A.P., Huguenin, G.R., Reid, M.J., and Hansen, S.S. 1979, Ap. J. (Letters), 231, L67.
Moran, J.M., Lichten, S., Reid, M., Huguenin, R., and Predmore, R. 1985, in preparation.
Olofsson, H., Johanson, L.E.B., Hjalmarson, Å., and Nguyen-Quang Rieu 1982, Astr. Ap., 107, 128.
Pauls, T.A., Wilson, T.L., Bieging, J.H., and Martin, R.N. 1983 Astr. Ap., 124, 23.
Plambeck, R.L., Wright, M.C.H., Welch, W.J., Bieging, J.H., Baud, B., Ho, P.T.P., and Vogel, S.N. 1982, Ap. J., 259, 617.
Sagan, C., and Khare, B.N. 1979, Nature, 277, 102.
Snyder, L.E. 1980, in Interstellar Molecules, ed. B.H. Andrew (Dordrecht: Reidel) p. 525.
Snyder, L.E. 1982, Icarus, 51, 1.
Snyder, L.E. 1984, in session "Radio Science Studies of Comets", URSI 21st General Assembly, Florence, Italy.
Snyder, L.E., Dykstra, C.E., and Bernholdt, D. 1985a, in proceedings of Haystack Observatory conference, "Masers, Molecules, and Mass Outflows in Star Forming Regions".
Snyder, L.E., Henkel, C., Hollis, J.M., and Lovas, F.J. 1985b, Ap. J. (Letters), 290, L29.
Snyder, L.E., Hollis, J.M., Suenram, R.D., Lovas, F.J., Brown, L.W., and Buhl, D. 1983, Ap. J., 268, 123.
Snyder, L.E., Schenewerk, M.S., and Hollis, J.M. 1985c, Ap. J., in press for Nov.

Thaddeus, P., Cummins, S.E., and Linke, R.A. 1984, Ap. J. (Letters), 283, L45.
Thaddeus, P., Gottlieb, C.A., Hjalmarson, Å., Johansson, L.E.B., Irvine, W.M., Friberg, P., and Linke, R.A. 1985, Ap. J. (Letters), 294, L53.
Walmsley, C.M., Jewell, P.R., Snyder, L.E., and Winnewisser, G. 1984, Astr. Ap., 134, L11.
Winnberg, A., Baud, B., Matthews, H.E., Habing, H.J., and Olnon, F.M. 1985, Ap. J. (Letters), 291, L45.
Wright, M.C.H., Dickel, H.R., and Ho, P.T.P. 1984, Ap. J. (Letters), 281, L71.
Wright, M.C.H., and Plambeck, R.L. 1983, Ap. J. (Letters), 267, L115.
Wright, M.C.H., Plambeck, R.L., Vogel, S.N., Ho, P.T.P., and Welch, W.J. 1983, Ap. J. (Letters), 245, L87.

α-DICARBONYL YIELDS FROM THE NO_x-AIR PHOTOOXIDATIONS OF A SERIES OF AROMATIC HYDROCARBONS IN AIR

Ernesto C. Tuazon, Hélène Mac Leod,
Roger Atkinson and William P. L. Carter

Statewide Air Pollution Research Center
University of California
Riverside, California 92521

Abstract. The yields of the ring cleavage products glyoxal, methylglyoxal and biacetyl from the reactions of OH radicals with benzene, toluene, o-, m- and p-xylene and 1,2,3-, 1,2,4- and 1,3,5-trimethylbenzene in the presence of part-per-million concentrations of NO have been determined in one atmosphere of air at 298 ± 2 K using in situ long pathlength Fourier transform infrared absorption spectroscopy and differential optical absorption spectroscopy with supplementary gas chromatographic analyses. These data are important inputs to chemical models of the NO_x-air photooxidations of these aromatic hydrocarbons.

Introduction

Aromatic hydrocarbons are important constituents of commercial fuels and of emissions from mobile sources [1,2]. However, despite numerous experimental and computer modeling studies, the reaction pathways occurring during their atmospheric photooxidations are still not well understood [3-8].

Kinetic and environmental chamber studies have shown that under atmospheric conditions the sole loss process of the aromatic hydrocarbons is due to reaction with the hydroxyl radical [6-10]. These OH radical reactions have been shown to proceed via two pathways, namely H-atom abstraction from the substituent alkyl groups, which is a minor process [10], and OH radical addition to the aromatic ring. Reaction of the OH-aromatic adducts with O_2 is expected to lead to the formation of hydroxyaromatics [6,9,10]. However, the observation of the α-dicarbonyls glyoxal, methylglyoxal and biacetyl in significant yields from the methyl-substituted aromatic hydrocarbons [7,11-14] and of a variety of other acyclic oxygenated products from toluene [4,5,15] o-xylene [4], and 1,2,4-trimethylbenzene [16] shows that ring cleavage is also an important overall reaction pathway.

In this work, we have used long pathlength Fourier transform infrared (FT-IR) absorption spectroscopy, long pathlength differential optical absorption spectroscopy (DOAS), and gas chromatography (GC) to determine the yields of the α-dicarbonyls glyoxal, methylglyoxal and biacetyl from the NO_x-air photooxidations of benzene, toluene, the xylene isomers and the trimethylbenzene isomers at ~740 torr total pressure of air and 298 ± 2 K.

Experimental

The experimental techniques used were essentially identical to those described previously [7]. NO_x-air photooxidations of the aromatic hydrocarbons were carried out in the SAPRC 5800 liter evacuable, Teflon-coated environmental chamber, with radiation being provided by a 25 KW Xenon arc. This environmental chamber is equipped with two sets of multiple-reflection White-type optical systems. One set, with a base path of 1.30 m, was interfaced to an FT-IR Nicolet spectrometer. The second set, with a base path of 3.77 m, was interfaced to a differential optical absorption spectrometer.

As in our previous study [7], DOAS measurements of glyoxal were carried out using pathlengths from 45.2 m to 150.8 m, utilizing the wavelength region 430-460 nm. The optimum detection sensitivity for glyoxal was ~3 x 10^{11} molecule cm^{-3} for the maximum pathlength used (150.8 m). Due to the much weaker spectral features of methylglyoxal (for which the detection sensitivity was ~ 5 x 10^{12} molecule cm^{-3} at 150 m) its unambiguous detection and measurement by DOAS during these experiments could not be carried out, particularly in the presence of interfering NO_2 absorption bands.

Glyoxal, methylglyoxal, and the aromatic hydrocarbons were monitored by FT-IR absorption spectroscopy simultaneously with the DOAS measurements of glyoxal. For the FT-IR measurements, a pathlength of 62.9 m was routinely used with a spectral resolution (unapodized) of 1 cm^{-1} (optical path difference = 1 cm). The absorption bands of the aromatic hydrocarbons in both of the regions 650-850 cm^{-1} and 2850-3100 cm^{-1} were used to measure their concentrations. Glyoxal and methylglyoxal were monitored at their absorptions centered respectively at ~2835 and 2829 cm^{-1}. Analyses of these superimposed glyoxal and methylglyoxal absorption bands were

carried out using standard spectra recorded from authentic samples. FT-IR detection sensitivities for glyoxal and methylglyoxal were similar, being ~4 x 10^{12} molecule cm^{-3} at the pathlength and resolution employed. Biacetyl was analyzed by gas chromatography with electron capture detection.

Hydroxyl radicals were generated by the photolysis of methyl nitrite in air at wavelengths $\gtrsim$300 nm [6]

$$CH_3ONO + h\nu \rightarrow CH_3O + NO$$

$$CH_3O + O_2 \rightarrow HCHO + HO_2$$

$$HO_2 + NO \rightarrow OH + NO_2$$

NO was included in the reaction mixtures in order to minimize the formation of O_3 and of NO_3 radicals. The initial concentrations of the CH_3ONO-NO-aromatic hydrocarbon-air mixtures were: CH_3ONO ~2.4 x 10^{14} molecule cm^{-3}; NO ~1.2 x 10^{14} molecule cm^{-3}; aromatic hydrocarbon ~(2.5-5) x 10^{14} molecule cm^{-3}; with one atmosphere of synthetic air (80% N_2 + 20% O_2) as the diluent gas.

Each experiment consisted of cumulative, short-period (3 to 10 minutes) irradiations, with total irradiation times up to 60 minutes. DOAS and FT-IR spectra were recorded and GC samples were taken between these irradiation periods. This procedure minimized the effect of stray radiation on the DOAS instrument and ensured that all the analyses corresponded to the same extent of reaction. The light intensity in these experiments, as determined from an irradiation of a biacetyl-air mixture, corresponded to a biacetyl photolysis rate of 1.25 x 10^{-4} sec^{-1}.

Results

CH_3ONO-NO-air irradiations of benzene, toluene, o-, m- and p-xylene and 1,2,3-, 1,2,4- and 1,3,5-trimethylbenzene were carried out at 298 K and ~740 torr total pressure of air.

The observed α-dicarbonyl yields had to be corrected for reaction with OH radicals and photolysis [7] in order to derive the formation yields of these compounds. The reaction sequence is:

$$\text{OH + aromatic} \xrightarrow{\text{NO, } O_2} \text{Y } \alpha\text{-dicarbonyl} \qquad (3)$$

$$\text{OH + } \alpha\text{-dicarbonyl} \rightarrow \text{products} \qquad (4)$$

$$\alpha\text{-dicarbonyl + h}\nu \rightarrow \text{products} \qquad (5)$$

where reaction (3) is complex [7] and Y is the formation yield of the individual α-dicarbonyls from the aromatic hydrocarbon studied. Assuming that the OH radical concentrations were essentially constant over the small irradiation periods, then [7]:

$$[\text{aromatic}]_{t_2} = [\text{aromatic}]_{t_1} e^{-k_3[OH](t_2 - t_1)} \qquad (I)$$

and

$$[\alpha\text{-dicarbonyl}]_{t_2} = [\alpha\text{-dicarbonyl}]_{t_1} e^{-(k_4[OH] + k_5)(t_2-t_1)}$$

$$+ \frac{Y_{t_1-t_2}[\text{aromatic}]_{t_1} k_3[OH]}{[(k_4-k_3)\,[OH] + k_5]} \left[e^{-k_3[OH](t_2-t_1)} - e^{-(k_4[OH] + k_5)(t_2-t_1)} \right] \qquad (II)$$

where $[\text{aromatic}]_{t_1}$, $[\alpha\text{-dicarbonyl}]_{t_1}$ and $[\text{aromatic}]_{t_2}$, $[\alpha\text{-dicarbonyl}]_{t_2}$ are the aromatic hydrocarbon and α-dicarbonyl concentrations observed at times t_1 and t_2, respectively, and $Y_{t_1-t_2}$ is the formation yield of the individual α-dicarbonyls over the time period t_1 to t_2. Computer calculations showed that this formula was valid under the conditions employed.

OH radical concentrations were calculated from the aromatic hydrocarbon decays [equation (I)]. Rate constants k_3 and k_4 were taken from the literature [10,17], and values of k_5 were obtained by ratioing the previously determined photolysis rates for glyoxal, methylglyoxal and biacetyl [17] with the presently determined photolysis rate of biacetyl. Use of these rate constants together with equations (I) and (II) allow $Y_{t_1-t_2}$ to be calculated, and the α-dicarbonyl concentrations, corrected for reaction with OH radicals and photolysis, are then given by:

$$[\alpha\text{-dicarbonyl}]_{t_2}^{corr} = [\alpha\text{-dicarbonyl}]_{t_1}^{corr} + Y_{t_1-t_2}([aromatic]_{t_2} - [aromatic]_{t_1}) \quad \text{(III)}$$

where $[\alpha\text{-dicarbonyl}]_{t_1}^{corr}$ and $[\alpha\text{-dicarbonyl}]_{t_2}^{corr}$ are the corrected α-dicarbonyl concentrations at times t_1 and t_2, respectively. The correction factors, $[\alpha\text{-dicarbonyl}]_t^{corr} / [\alpha\text{-dicarbonyl}]_t$, were in all cases $\lesssim 1.67$ for glyoxal and $\lesssim 1.55$ for methylglyoxal, and were typically ~1.2.

The corrected glyoxal and biacetyl concentrations, $[\alpha\text{-dicarbonyl}]_t^{corr}$, are plotted against the amounts of aromatic hydrocarbon consumed, $-\Delta[aromatic] = [aromatic]_t - [aromatic]_{t_o}$, according to equation (III) in Figure 1. The yields, Y, of glyoxal, methylglyoxal and biacetyl derived from the slopes of such plots by least squares analyses are listed in Table 1.

Discussion

The glyoxal and methylglyoxal yields obtained in this work are compared in Table 1 with our previous glyoxal and methylglyoxal yields for toluene and m- and p-xylene [7], and with other available literature data for toluene, the xylenes and the trimethylbenzenes.

It can be seen that the present glyoxal and methylglyoxal yields for toluene, the xylenes and the trimethylbenzenes are generally in good agreement with those reported by Bandow et al. [14] with the only discrepancies outside of the combined stated error limits occurring for the glyoxal yields from 1,2,3- and 1,2,4-trimethylbenzene.

Consistent with our previous conclusions [7], it is obvious that the α-dicarbonyl yields do not fully account for the reaction pathways occurring. Thus these α-dicarbonyl yields account for ~20% of the overall reactions for benzene, ~25-30% for toluene, ~30-50% for the xylenes, and ~60% for the trimethylbenzenes if it is assumed that the corresponding unsaturated 1,4-dicarbonyls are formed together with the α-dicarbonyls. However, if the unsaturated 1,4-dicarbonyls are not formed in yields corresponding to the α-dicarbonyl co-products, then these carbon balances are drastically lower.

Clearly, while the present data set is an important input to chemical computer models concerning the atmospheric chemistry of the aromatic

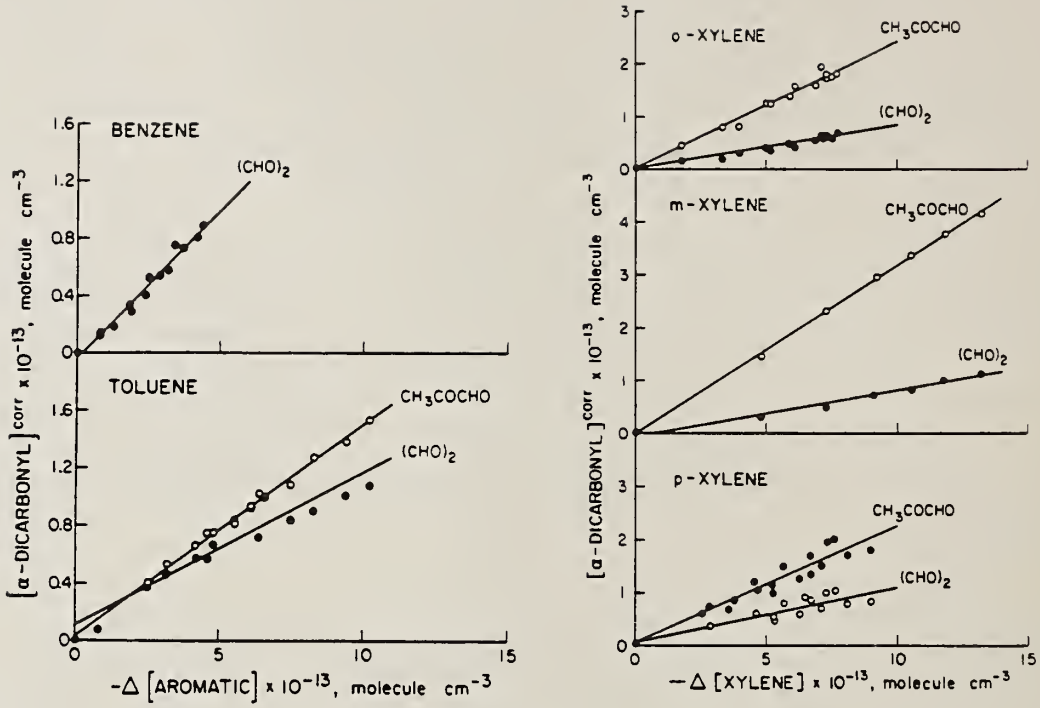

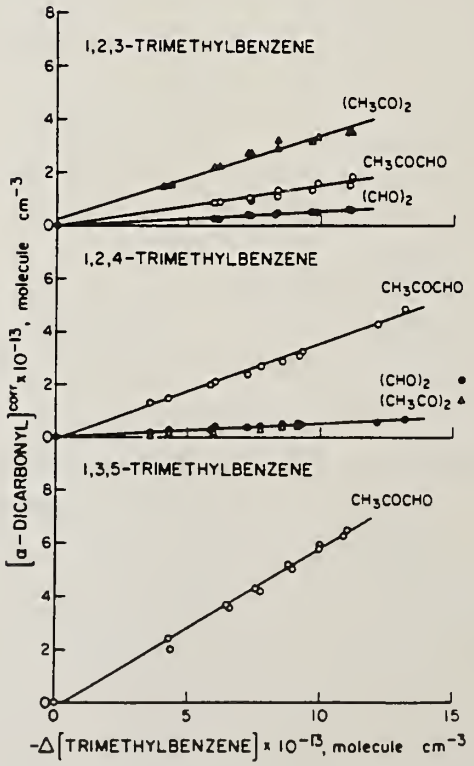

Figure 1. Plots of the glyoxal and methylglyoxal yields (corrected for photolysis and reaction with OH radicals; see text) against the amounts of aromatic hydrocarbon consumed.

TABLE 1. Formation Yields of the α-Dicarbonyls Glyoxal, Methylglyoxal and Biacetyl from Benzene and the Methyl-Substituted Benzenes at Room Temperature and Atmosphere Pressure, Together with Literature Data

Aromatic	α-Dicarbonyl Yield[a]			Reference
	Glyoxal	Methylglyoxal	Biacetyl	
Benzene	0.207 ± 0.019			This work
Toluene	0.15 ± 0.04	0.14 ± 0.04		14
	0.111 ± 0.013	0.146 ± 0.014		7
	0.105 ± 0.019	0.146 ± 0.006		This work
o-Xylene			0.18 ± 0.04	11
			0.260 ± 0.102	12
			0.137 ± 0.016	13
	0.08 ± 0.04	0.23 ± 0.3	0.10 ± 0.02	14
	0.087 ± 0.012	0.246 ± 0.020		This work
m-Xylene	0.13 ± 0.03	0.42 ± 0.05		14
	0.104 ± 0.020	0.265 ± 0.035		7
	0.086 ± 0.011	0.319 ± 0.009		This work
p-Xylene	0.24 ± 0.02	0.12 ± 0.02		14
	0.120 ± 0.020	0.111 ± 0.015		7
	0.225 ± 0.039	0.105 ± 0.034		This work
1,2,3-Trimethylbenzene	0.078 ± 0.001	0.18 ± 0.01	0.45 ± 0.02	14
	0.058 ± 0.008	0.152 ± 0.025	0.316 ± 0.036	This work
1,2,4-Trimethylbenzene	0.078 ± 0.005	0.37 ± 0.01	0.11 ± 0.01	14
	0.048 ± 0.005	0.357 ± 0.017	0.048 ± 0.009	This work
1,3,5-Trimethylbenzene		0.64 ± 0.03		14
		0.602 ± 0.033		This work

[a]Indicated error limits are two standard deviations.

hydrocarbons, work is urgently needed to quantify other products such as those reported by Shepson et al. [4] and Dumdei and O'Brien [5] and to further elucidate the reaction pathways occurring during these NO_x-air photooxidations subsequent to the initial OH radical reaction with the parent aromatic hydrocarbons.

Acknowledgments

The authors gratefully acknowledge the financial support of the U. S. Environmental Protection Agency under Cooperative Agreement No. CR-810964-01 (Project Monitor, Dr. Marcia C. Dodge), and thank Mr. William D. Long and Ms. Sara M. Aschmann for assistance in conducting these experiments. Although this research has been funded by the United States Environmental Protection Agency, it has not been subjected to the Agency's required peer and policy review and therefore does not necessarily reflect the views of the Agency and no official endorsement should be inferred.

References

(1) Black, F. M.; High, L. E.; Lang, J. M. J. Air Pollut. Control Assoc. **1980**, 30, 1216-1221.

(2) Nelson, P. F.; Quigley, S. M.; Smith, M. Y. Atmos. Environ. **1983**, 17, 439-449.

(3) Leone, J. A.; Seinfeld, J. H. Int. J. Chem. Kinet. **1984**, 16, 159-193.

(4) Shepson, P. B.; Edney, E. O.; Corse, E. W. J. Phys. Chem. **1984**, 88, 4122-4126.

(5) Dumdei, B. E.; O'Brien, R. J. Nature **1984**, 311, 248-250.

(6) Atkinson, R.; Lloyd, A. C. J. Phys. Chem. Ref. Data **1984** 13, 315-444.

(7) Tuazon, E. C.; Atkinson, R.; Mac Leod, H.; Biermann, H. W.; Winer, A. M.; Carter, W. P. L., Pitts, J. N., Jr.; Environ. Sci. Technol. **1984**, 18, 981-984.

(8) Leone, J. A.; Flagan, R. C.; Grosjean, D.; Seinfeld, J. A.; Int. J. Chem. Kinet. **1985** 17, 177-216.

(9) Atkinson, R.; Carter, W. P. L.; Darnall, K. R.; Winer, A. M.; Pitts, J. N., Jr. Int. J. Chem. Kinet. **1980**, 12, 779-836.

(10) Atkinson, R.; Chem. Rev. **1985**, in press.

(11) Darnall, K. R.; Atkinson, R.; Pitts, J. N., Jr. J. Phys. Chem. **1979**, 83, 1943-1946.

(12) Takagi, H.; Washida, N.; Akimoto, H.; Nagasawa, K.; Usui, Y.; Okuda, M. J. Phys. Chem. **1980**, 84, 478-483.

(13) Atkinson, R.; Carter, W. P. L.; Winer, A. M. J. Phys. Chem. **1983**, 87, 1605-1610.

(14) Bandow, H.; Washida, N.; Akimoto, H. 11th International Conference on Photochemistry, University of Maryland, College Park, MA, August 21-26, 1983.

(15) Besemer, A. C. Atmos. Environ. **1982**, 16, 1599-1602.

(16) Takagi, H.; Washida, N.; Akimoto, H.; Okuda, M. Spectros. Lett. **1982**, 15, 145-152.

(17) Plum, C. N.; Sanhueza, E.; Carter, W. P. L.; Atkinson, R.; Winer, A. M.; Pitts, J. N., Jr. Environ. Sci. Technol. **1983**, 17, 479-484.

GASEOUS REACTIONS OF THERMAL TRITIUM ATOMS WITH ETHYLENE AND H_2S

NUN YII WANG, R.S. IYER AND F. S. ROWLAND

DEPARTMENT OF CHEMISTRY
UNIVERSITY OF CALIFORNIA AT IRVINE
IRVINE, CALIFORNIA 92717

I. THEORY

HYDROGEN ATOM REACTIONS CAN BE STUDIED BY USING RADIOACTIVE TRITIUM ATOMS PRODUCED BY THE NUCLEAR REACTION $^{3}He(n,p)^{3}H$ WITH KINETIC ENERGY OF 192,000 ELECTRON VOLTS. THESE ENERGETIC TRITIUM ATOMS ARE THERMALIZED BY MULTIPLE COLLISIONS WITH NON-REACTIVE MODERATORS. THE TRITIUM ATOMS ARE FORMED IN MIXTURES OF MODERATOR AND REACTIVE SUBSTRATE, AND ENERGETIC ("HOT ATOM") REACTIONS CAN OCCUR WITH THE REACTIVE SUBSTRATE IF COLLISIONS OCCUR WHEN THE TRITIUM STOM HAS 0.1 TO 100 E.V. KINETIC ENERGY. THESE HOT ATOM REACTIONS CAN BE AVOIDED BY GOING TO LOWER AND LOWER MOLE FRACTIONS OF REACTIVE SUBSTRATE. THE ANALYTICAL ANALYSES FOR TRITIUM-LABELED PRODUCTS HAVE BEEN CARRIED OUT BY THE STANDARD TECHNIQUE OF RADIO GAS CHROMATOGRAPHY WITH DETECTION OF THE DECAY OF TRITIUM WITH AN INTERNAL GAS PROPORTIONAL COUNTER AFTER CHROMATOGRAPHIC SEPARATION. USEFUL INFORMATION ABOUT THE MECHANISMS AND RELATIVE REACTION RATES OF THERMALIZED RADIOACTIVE TRITIUM ATOMS WITH A VARIETY OF SUBSTRATES CAN OFFERED.

II. REACTION MECHANISM

$$ {}^{3}_{2}HE + {}^{1}_{0}N \longrightarrow {}^{1}_{1}P + {}^{3}_{1}T^{*} $$

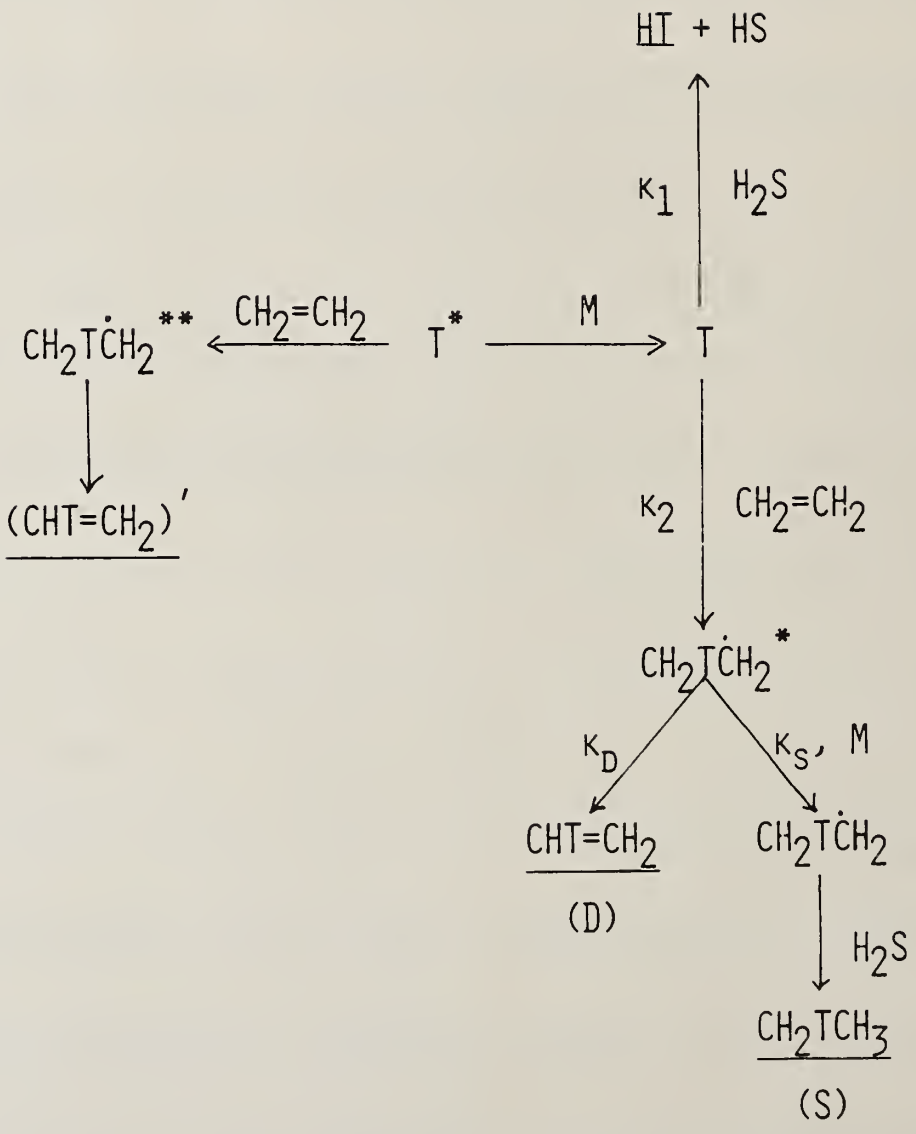

M: CF_4 OR KR

III. EXPERIMENT

PREPARATION: $^3He/C_2H_4/H_2S/CF_4$ OR $^3He/C_2H_4/H_2S/Kr$ GAS MIXTURES WITH DESIGNED MOLE RATIOS AND PRESSURE ARE SEALED IN 10 ML BULBS.

IRRADIATION: 8 MINUTES WITH A NEUTRON FLUX OF $3x10^{11}$ NEUTRONS $CM^{-1}SEC^{-1}$ IN THE UCI MARK I TRIGA NUCLEAR REACTOR.

ANALYSIS:

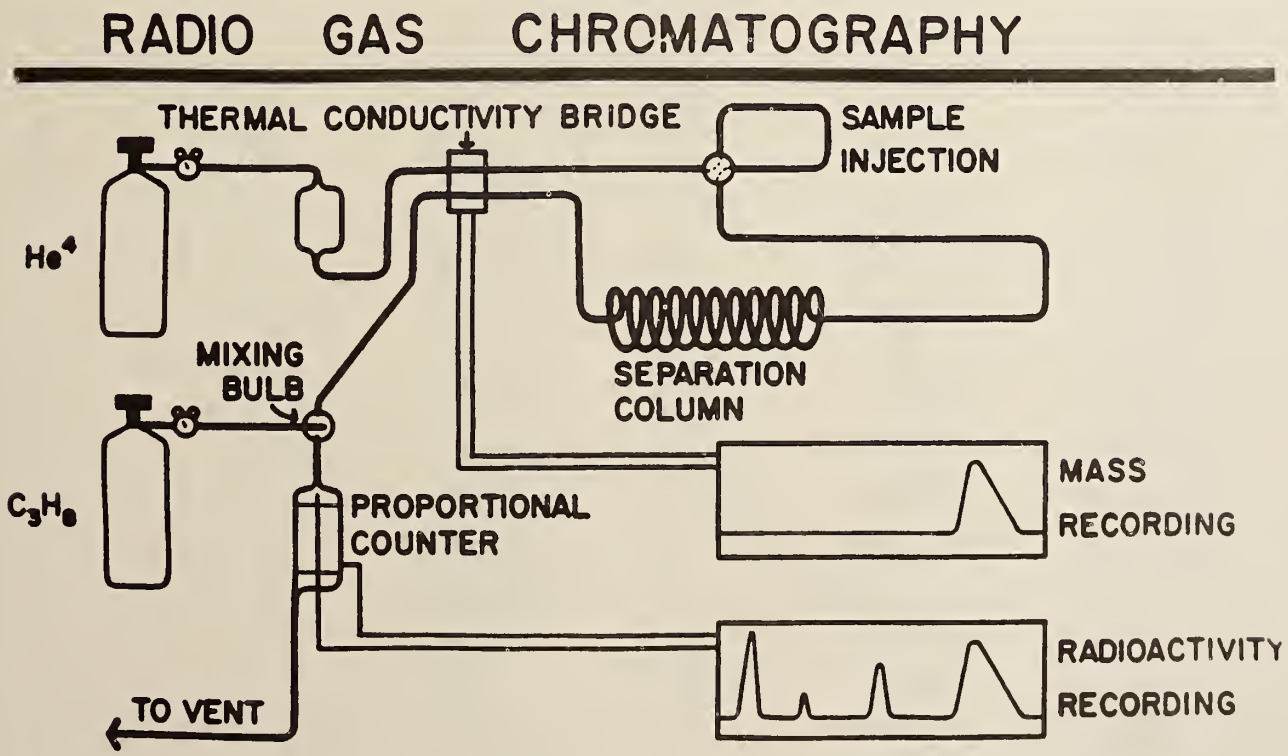

IV. RESULTS

A. CF_4

TABLE I

VOLATILE TRITIUM-LABELED PRODUCTS FROM THE REACTIONS OF TRITIUM ATOMS IN MIXTURES CONTAINING $CH_2=CH_2$ AND H_2S IN A 2/1 RATIO AND CF_4 AS MODERATOR GAS

MOLE FRACTION OF $CH_2=CH_2$	TOTAL PRESS. TORR	PRODUCT YIELD, PERCENT HT	$CHT=CH_2$	CH_2TCH_3	CTF_3
0.0030	606	29.3	1.70	41.0	0.27
0.0030	1212	28.5	1.01	44.0	0.24
0.0029	1357	27.4	1.03	43.0	0.33
0.0030	1560	29.1	0.93	45.9	0.37
0.0030	1954	26.4	0.84	43.3	0.37
0.0030	2093	25.9	0.56	42.3	0.26
0.0052	833	27.5	1.69	42.6	0.20
0.0055	1033	31.4	1.61	50.2	0.19
0.0055	1597	26.3	1.12	44.3	0.22
0.0055	1710	26.8	0.94	44.9	0.25
0.0055	2073	24.4	0.88	42.2	0.28
0.0101	673	29.1	2.58	47.4	0.17
0.0100	1010	28.6	2.05	47.8	0.30
0.0099	1652	27.7	1.47	47.4	0.26
0.0100	1990	27.7	1.50	45.9	0.28
0.0240	738	30.3	4.26	50.0	0.28
0.0248	1004	27.9	4.35	46.9	0.20
0.0242	1647	26.0	3.08	44.8	0.24
0.0247	1944	27.7	3.52	47.8	0.34

FIGURE 1

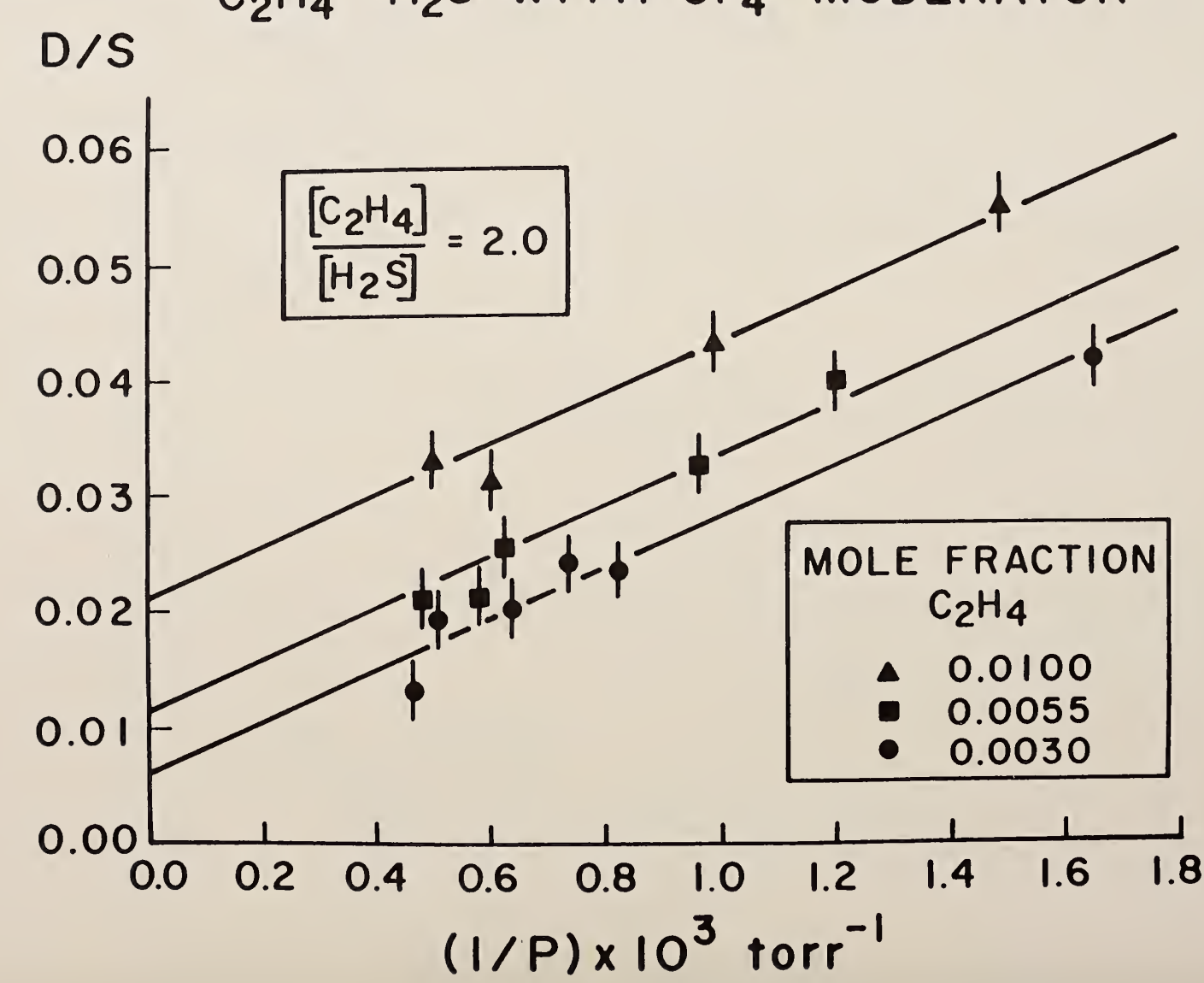
$C_2H_4 - H_2S$ WITH CF_4 MODERATOR
D/S
0.06
0.05
0.04
0.03
0.02
0.01
0.00
$\frac{[C_2H_4]}{[H_2S]} = 2.0$
MOLE FRACTION C_2H_4
0.0100
0.0055
0.0030
0.0
0.2
0.4
0.6
0.8
1.0
1.2
1.4
1.6
1.8
$(1/P) \times 10^3$ torr^{-1}

FIGURE 2 $C_2H_4 - H_2S$ WITH CF_4 MODERATOR

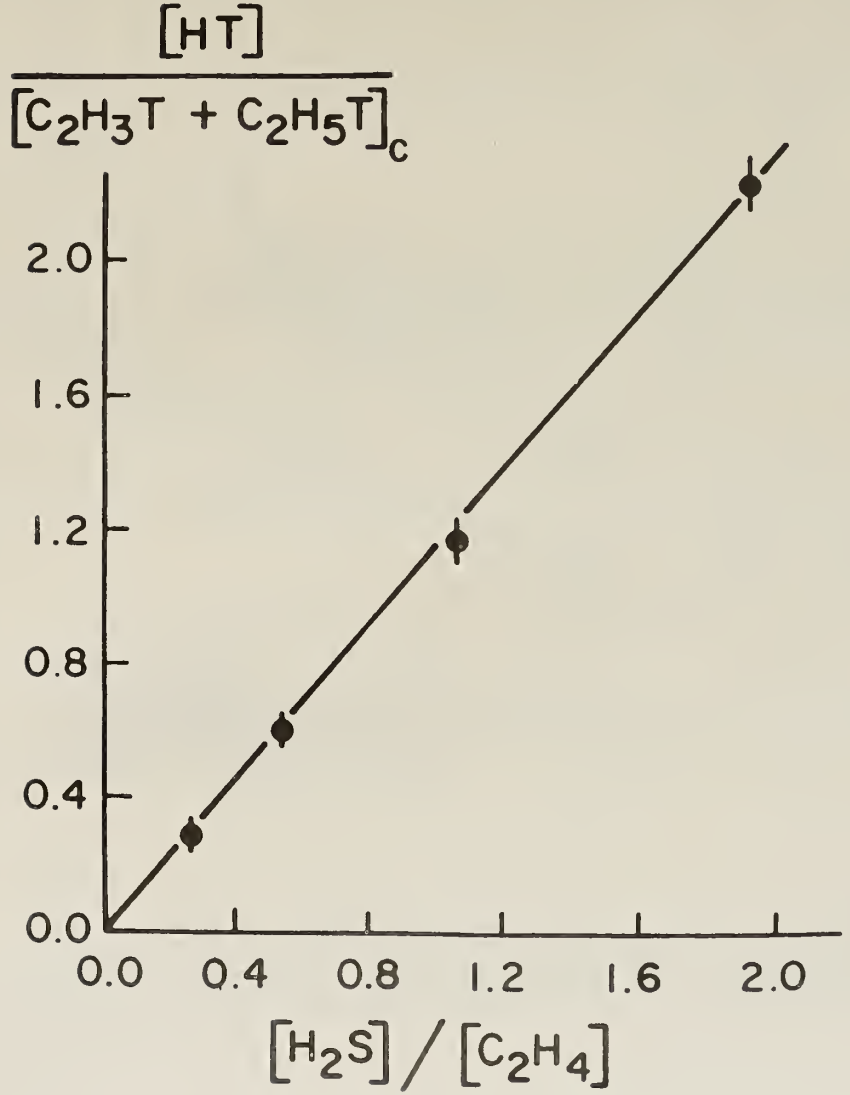

B. Kr

TABLE II

VOLATILE RADIOACTIVE PRODUCTS FROM REACTIONS OF TRITIUM ATOMS IN MIXTURES CONTAINING $CH_2=CH_2$ AND H_2S IN A 2/1 RATIO AND Kr AS MODERATOR GAS

MOLE FRACTION OF $CH_2=CH_2$	TOTAL PRESS. TORR	PRODUCT YIELD, PERCENT HT	$CHT=CH_2$	CH_2TCH_3
0.0030	571	35.8	5.69	40.3
0.0032	620	33.9	5.91	36.8
0.0027	1038	35.1	4.37	41.2
0.0029	1045	33.4	5.28	43.4
0.0030	1613	36.6	4.19	49.3
0.0030	1950	35.8	3.82	45.4
0.0055	618	37.2	7.77	46.2
0.0050	650	34.2	7.09	40.9
0.0055	973	35.3	6.84	48.1
0.0055	1632	37.2	5.38	55.8
0.0055	1944	35.2	6.01	54.6
0.0114	599	34.9	10.8	46.1
0.0100	1563	29.8	6.36	37.0
0.0100	2063	31.4	6.60	40.9

FIGURE 3 $C_2H_4 - H_2S$ WITH KRYPTON MODERATOR

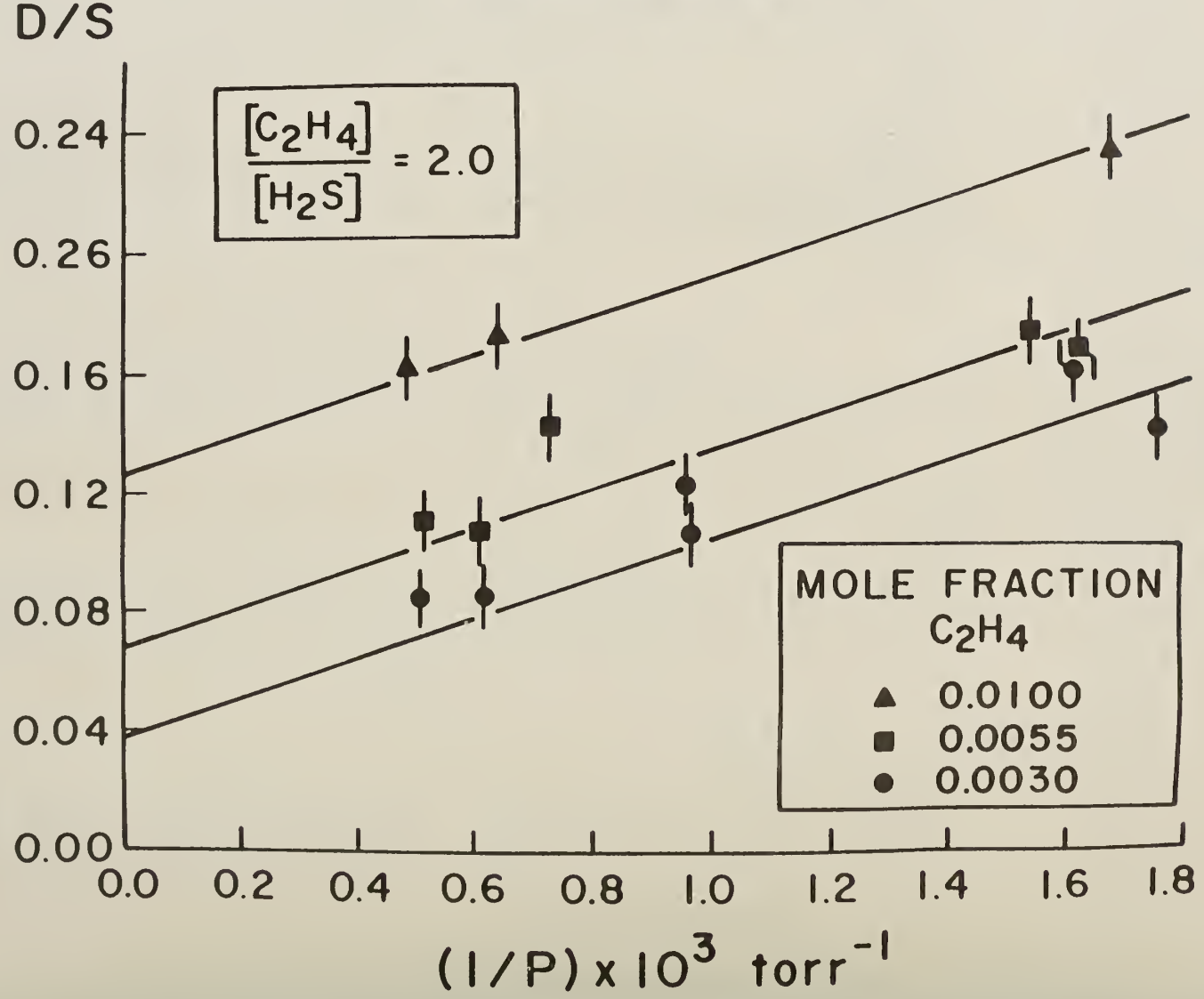

FIGURE 4 $C_2H_4 - H_2S$ WITH KRYPTON MODERATOR

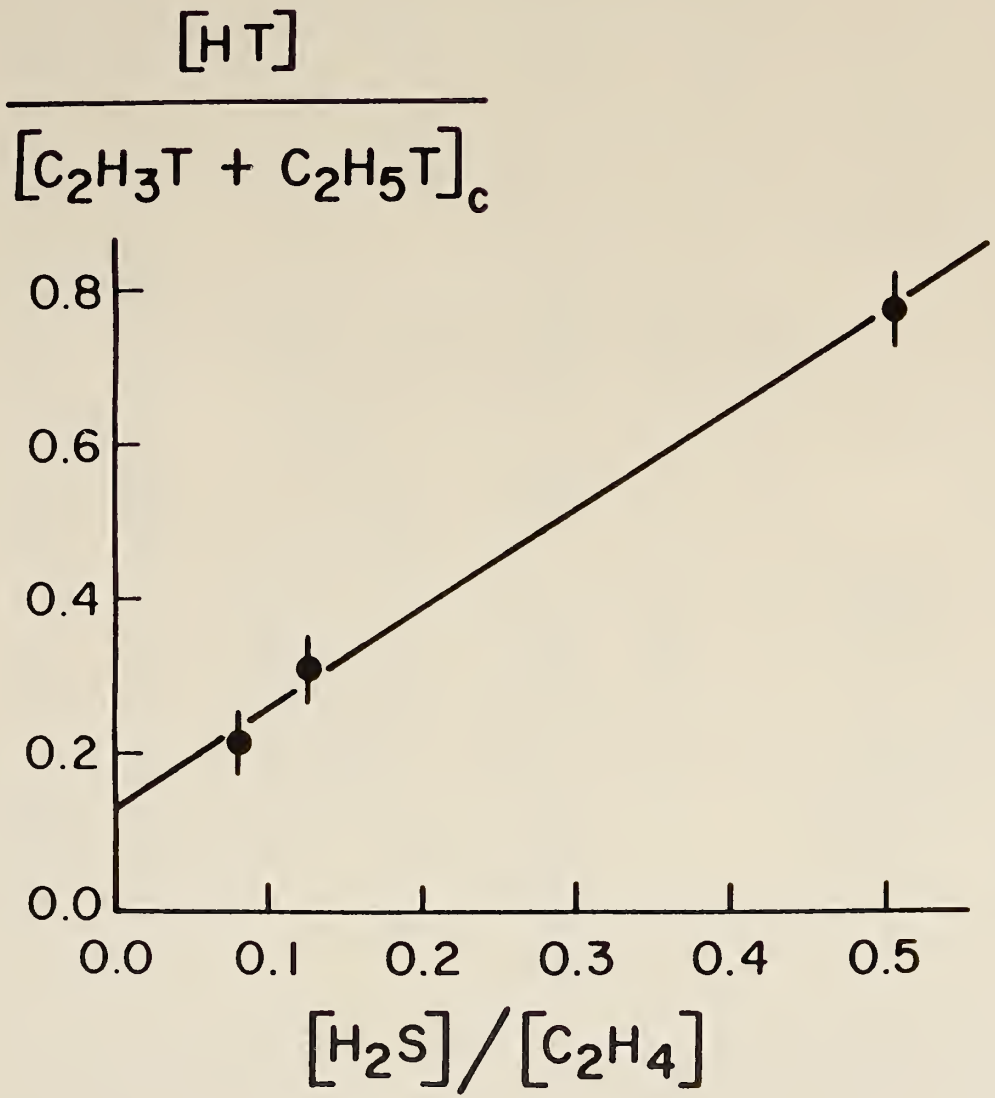

V. CONCLUSIONS

I) FIGURE 1 AND 3

SLOPE: HALF STABILIZATION PRESSURES ($P_{1/2}$) FOR $CH_2\dot{T}CH_2$

SINCE $\frac{D}{S} = \frac{K_D}{K_S P}$; WHEN $\frac{D}{S} = 1$, $\frac{K_D}{K_S} = P_{1/2}$

	CF_4	Kr
$P_{1/2}$ (TORR):	22±2	67±8

INTERCEPT: $(CHT{=}CH_2)'$ FORMED FROM HOT PROCESSES; PROPORTIONAL TO THE MOLE FRACTION OF $CH_2{=}CH_2$.

	CF_4	Kr
% OF $(CHT{=}CH_2)'$ IN SUM OF $(CHT{=}CH_2 + CH_2TCH_3)$ AT 0.0030 MOLE FRACTION OF $CH_2{=}CH_2$.	0.60%	3.8%

A) LINEAR RELATIONSHIP SHOWS THAT MOST OF THE $CH_2\dot{T}CH_2^*$ RADICALS POSSESS ESSENTIALLY THE SAME EXCITATION ENERGY, CORRESPONDING TO THE ADDITION OF THERMAL TRITIUM TO $CH_2{=}CH_2$.

B) LESS EFFICIENT MODERATION BY Kr THAN BY CF_4

II) FIGURE 2 AND 4

$$\text{SINCE } \frac{(HT)}{(CHT{=}CH_2 + CH_2TCH_3)} = \frac{K_1}{K_2} \cdot \frac{(H_2S)}{(CH_2{=}CH_2)}$$

$$\text{THEREFORE} \quad \text{SLOPE} = \frac{K_1}{K_2}$$

ATOMS	SUBSTRATES	K_1 OR K_2 (10^{-13} CM^3 MOLECULE^{-1} SEC^{-1})	$\frac{K_1}{K_2}$	REF.
T	H_2S & $CH_2{=}CH_2$	—	$\frac{CF_4}{KR}$ $\frac{1.17\pm0.04}{1.29\pm0.09}$	THIS WORK
D	H_2S	~7.3	0.84	A
	$CH_2{=}CH_2$	8.7		B,C
H	H_2S	7.3	0.65	D
	$CH_2{=}CH_2$	~11.3		B,E,F,G,H
	H_2S & $CH_2{=}CH_2$	—	0.83 ~ 1.6	J,K,L,M

A)D. Mihelcic; R. N. Schindler, Ber. Bunsenges. Phys. Chem., (74), 1280,1970.
B)D. Mihelcic; V. Schubert; F. Hofler; P. Potzinger, Ber. Bunsenges. Phys. Chem., (79), 1230, 1975.
C)S. Nagase; T Fueno; K. Morokuma; J. Am. Chem. Soc., (101), 5849, 1979.
D)M. J. Kurylo; N. C. Peterson; W. Braun, J. Chem. Phys., (54), 943. 1971.
E)J. H. Lee; J. V. Michael; W. A. Payne; L. J. Stief, J. Chem. Phys., (68), 1817, 1978.
F)Y. Ishikawa; M. Yamabe; A. Noda; S. Sato, Bull. Chem. Soc., Japan, (51). 2488, 1978.
G)J. V. Michael; D. T. Osborne; G. N. Suess, J. Chem. Phys., (58), 2800, 1973.
H)M. J. Kurylo; N. C. Peterson; W. Braun, J. Chem. Phys., (53), 2776, 1970.
J)B. deB. Darwent; R. Roberts, Disc. Faraday Soc., (14), 55, 1953.
K)G. R. Wooley; R. J. Cvetanovic, J. Chem. Phys., (50), 4697, 1969.
L)B. deB. Darwent; R. L. Waslinger; M. J. Allard, J. Phys. Chem., (71). 2346, 1967.
M)B. G. Dzantiez; A. V. Shishkov, Khim Vysokikh Energii, (1), 192, 1967.

VIBRATION-ROTATION STRUCTURE IN THE ELECTRONIC SPECTRUM OF THE AMMONIUM RADICAL

James K. G. Watson

Herzberg Institute of Astrophysics, National Research Council of Canada

Ottawa, Ontario, Canada K1A 0R6

ABSTRACT

An emission band observed by Schüler, Michel and Grün in 1955 near 15078 cm^{-1} by excitation of ammonia was shown by Herzberg in 1981 to be due to the ammonium radical, NH_4. On the other hand the Schuster band near 17670 cm^{-1}, first reported in 1872 and once thought to be another transition of NH_4, is now identified as a transition of the NH_3 molecule, from the rotational structure of the corresponding band at 17227 cm^{-1} in ND_3. The lifetime of the ground state $3s^2A_1$ of ND_4 is about 30 μs, and the main Schüler band of ND_4 at 14828 cm^{-1}has been observed by various techniques, both in emission and absorption. This band is the 0–0 band of the electronic transition $3p^2F_2 - 3s^2A_1$, and a number of vibrational bands of this transition are known. The present status of the analysis of these bands is reviewed, particularly for the 0–1 and 1–0 bands of the bending modes ν_2 and ν_4.

I. OBSERVED SPECTRA

This paper presents an interim report on the analysis of the electronic spectrum of the ammonium radical, NH_4. The possible stability of NH_4 was discussed some time ago by Mulliken[1] and Bernstein[2]. Recent *ab initio* calculations of the ground state potential energy surface[3–5] show that on the minimum-energy path between NH_4 and $NH_3 + H$ the molecule preserves C_{3v} symmetry and that there is a C_{3v} saddle point at an energy of about 5000 cm^{-1} above the NH_4 minimum. The latter has T_d symmetry with electronic species $^2A_1$, and its energy is nearly equal to that of $NH_3 + H$. Very good calculations will probably be required to decide which is the absolute minimum, but NH_4 in its lowest vibrational state is probably unstable on account of the fact that its zero-point energy is greater than that of NH_3, whether or not the actual minimum is lower. On the other hand, the existence of the barrier to dissociation implies that NH_4 should have a significant lifetime, determined by the rate of tunneling through the barrier.

The first spectrum of the ammonium radical seems to have been observed by Schüler, Michel and Grün[6], who studied the visible light emitted by ammonia gas when excited by electron impact. At low ammonia pressures they observed the Schuster band[7], previously known from discharges through ammonia, together with a number of other bands probably associated with the Schuster band. At higher pressures, up to about 1 atm, a new system of bands, now called[8] the Schüler system, becomes predominant. The two systems were studied by Schüler *et al.* in excitation of both NH_3 and ND_3 and, in a note added in proof, they state that experiments with isotopic mixtures show that for both systems the molecule responsible for the spectrum contains four hydrogen atoms.

The appearance of the mixed H/D isotope emission spectra were confirmed by Herzberg[8], who also studied the emission excited in $^{15}NH_3$ and $^{15}ND_3$ and showed that the carrier of each spectrum has one nitrogen atom. It thus appeared that both the Schuster and the Schüler systems are due to transitions of the ammonium radical, NH_4, although it proved difficult to assign them to specific electronic transitions by comparison with *ab*

initio predictions. The most probable mechanism of production of the spectrum is by electron capture by the ammonium ion, NH_4^+, and the electronic states of the ammonium radical are most easily specified by giving the nature of the Rydberg orbital of the odd electron, together with the electronic species symbol. Thus the ground state is $3s^2A_1$ and the lowest excited state is $3p^2F_2$.

Under high resolution the Schuster band excited in NH_3 is very diffuse, but the corresponding band in ND_3 shows reasonable rotational structure. Herzberg and Hougen[9] showed that the latter could be fitted with a spherical top model assuming no doublet splitting, with an electronic Coriolis coefficient $\zeta_{\text{eff}} \approx -0.8$. These results would be consistent with the electronic transition $3d^2F_2 - 3s^2A_1$, but this transition is calculated to be very weak[10–12] and actually becomes forbidden in the united atom limit. Although the absolute intensity of this transition has not been measued, the emission can be quite strong to the naked eye when the conditions are optimized, and it seems to behave more like a normal allowed transition than an essentially forbidden transition.

In view of this and other difficulties, the assignment of the Schuster band has recently been reconsidered[13]. The first notable observation[14] was that when NH_3 or ND_3 molecule is pumped with a dye laser by two-photon absorption into the recently-discovered $\tilde{C}'^1A_1'(D_{3h})$ state[15] it emits in the visible to the $\tilde{A}^1A_2''(D_{3h})$ state, which is also known fron one-photon absorption from the ground state $\tilde{X}^1A_1(C_{3v})$[16,17]. The most favorable Franck-Condon factors for the pumping are in the bands 2_0^n of $\tilde{C}' \leftarrow \tilde{X}$, where $n \gg 0$, and then emission occurs in the bands 2_n^n of $\tilde{C}' \rightarrow \tilde{A}$. These bands are in the visible region, in the vicinity of the Schuster band. In addition, the rotational structure of the Schuster band excited in ND_3 [9] is very similar to that in the absorption bands of ND_3 studied by Douglas[17]. In fact, with essentially the same J' and J'' numbering as Herzberg and Hougen[9] and with the 'tetrahedral splittings' reinterpreted as K-structure, the Schuster band can be assigned as a parallel band of ND_3[13]. The resulting constants shown in Table 1 as well as the intensity alternation are all consistent with assignment to the band 2_1^1 of the $\tilde{C}' \rightarrow \tilde{A}$ system. A few additional weak lines may belong to the 2_0^0 band[13], but the excitation mechanism appears to strongly favor the 2_1^1 band over the other 2_n^n sequence bands. The difficulty with the mixed-isotope spectrum[9] that led to the assignment of the Schuster band to NH_4 is due to the overlapping of the bands of different isotopes, which makes it difficult to count them unambiguously. The published mixed-isotope spectrum of the Schuster band[9] is actually quite similar to the 25% D mixed-isotope spectrum of

the $\tilde{B}^2A_1' - \tilde{X}^2A_2''$ band of the methyl radical[18], where the problem of overlapping also arises. Finally, the $\tilde{C}' \rightarrow \tilde{A}$ electronic transition of NH_3 can be described approximately as $...(2p_z)(3p_z) \rightarrow ...(2p_z)(3s)$, *i.e.* as a $3p_z \rightarrow 3s$ one-electron transition, and qualitatively this is consistent with the strength of the Schuster band. Further evidence for this interpretation of the Schuster band has been obtained in recent work of Ashfold *et al.*[19].

The main Schüler band is sharper than the Schuster band and shows a double-headed structure with a separation of about 6 cm^{-1} that was assigned by Herzberg[8] as due to the spin-orbit coupling of the odd electron, most probably in the $3p^2F_2$ electronic state. This band is quite compact, and there is no serious overlapping in the mixed-isotope spectrum. Thus the isotopic evidence for the NH_4 assignment is more secure, and is substantiated by the detailed analysis[20,21]. Rotational structure is observed for both NH_4 and ND_4, and in the latter case at least is probably limited by the present instrumental resolution. The implied limits of the lifetimes of both the states involved are approximately $\tau > 0.2$ ns for NH_4, and $\tau > 1$ ns for ND_4. Thus an important question is whether the lifetimes of the ground states satisfy these conditions. For ND_4, at least, this question was answered by a neutralized-ion-beam experiment of Gellene, Cleary, and Porter[22], in which beams of $NH_nD_{4-n}^+$ ions were neutralized and the dissociations of the resulting neutrals were studied. It was found that the time-of-flight lifetimes of some ND_4 molecules were greater than 20 μsec, whereas the other isotopes all had shorter lives than 20 μsec. From the experimental data, Gellene *et al.*[22] deduced a dissociation barrier near 3000 cm^{-1}, which agrees in approximate order with the *ab initio* values[3–5].

These beam results show that the lifetimes of the ground states of ND_4 and in all probability NH_4 are long enough to be consistent with the linewidths observed in the Schüler band. Then the observed spin splitting strongly suggests the assignment $3p^2F_2 - 3s^2A_1$, between the two lowest electronic states. Detailed confirmation is obtained from the rotational structure of the Schüler band of ND_4, as described in Sec. 2.

In addition to the conventional emission spectra discussed so far, the Schüler band of ND_4 has been observed more recently by other techniques, although none of these has been successful with NH_4. Using a combination of photochemical modulation with laser frequency-modulation spectroscopy, Whittaker *et al.*[23] were able to observe the Schüler band of ND_4 in absorption in the mercury-photosensitized reaction of ND_3. In this system it is possible to discriminate between the lines of ND_4 and of ND_2 in the same spectral region because the latter turn 90° out of phase at the higher photochemical modulation

frequencies employed (up to 12 kHz). Another absorption experiment was performed in Ottawa[21] using the flash discharge technique[24]. It was found that the Schüler band was observed for short delay times ($< 50\mu s$) between the initiation of the discharge and the absorption flash. while at longer delays, after electrical breakdown. it was replaced by the multiline spectrum of ND_2. The lifetime of the ground state of ND_4 in this experiment was about 30 μs. fully consistent with the lower limit of 20 μs from the beam experiment[22] and the upper limit of about 80 μs implied by the photochemical modulation frequency[23].

Rotationally-cooled spectra of ND_4 have been obtained[25] in a discharge through supersonically expanding argon gas containing a trace of ND_3, using a nozzle of Droege-Engelking type[26]. Both this spectrum and the flash-discharge absorption spectrum were very important in the rotational analysis[21], because they show clearly the low-J lines of the various rotational branches. Nevertheless, the rotational temperature of the expansion-cooled ND_4 is still remarkably high, of the order of 250 K, whereas in a similar experiment[25] the rotational temperature of the NO molecule was 20–30 K. In the flash discharge experiment the rotational temperature of the ND_4 was near 300 K, whereas the conventional discharge or electron-beam emission sources give much higher temperatures, of order 600 K.

Other bands of the Schüler system were reported in the original paper[6] and have recently been studied at higher resolution by Herzberg[27]. Some of these show extensive rotational structure in ND_4. Probably the most interesting are the 0–1 and 1–0 bands in the bending vibrational modes $\nu_2(e)$ and $\nu_4(f_2)$. These occur at intervals of 1100 cm^{-1} below and above the 0–0 band. Obviously it would be desirable to obtain spectra of these bands with lower rotational temperatures. For the 0–1 bands one obvious possibility is the supersonic nozzle discharge, which has given good emission spectra[25] with the same upper state. Unfortunately, attempts to observe this band under these conditions have so far been unsuccessful[28]. This must be due to a combination of factors. As discussed in Sec. 4, the intrinsic intensity of these bands is about an order of magnitude down from the 0–0 band, but this intensity is distributed over a much larger number of rotational lines. Also, photographic plates are less sensitive at these longer wavelengths. Compared to a conventional discharge, the emitting volume of the nozzle source is very small, and the rapid consumption of materials places a practical limit on exposure times.

In the case of the 1–0 bands, attempts to observe them by the flash discharge technique, which has given absorption spectra from the same lower state[21], have also failed[28].

For this band the weakness of the individual lines is compounded by the presence of fairly strong overlapping ND_2 lines. The latter have not been fully assigned in this region.

Possibly the best way to gain additional information on these bands is to introduce laser-induced fluorescence techniques, possibly in combination with the supersonic expansion nozzle. The ND_4 bands are in a convenient region for the use of dye lasers. By pumping the lines of the 0–0 band, it may be feasible to observe the dispersed fluorescence from individual rotational levels in the 0–1 bands. For the 1–0 bands, a fluorescence excitation spectrum may be obtainable with both higher resolution and a lower rotational temperature than the present emission spectrum.

Recently another type of NH_4 spectrum has been observed by Coe *et al.*[29]. This is a photoelectron spectrum of the negative ion NH_4^-. Unfortunately the geometrical structure of NH_4^-, which can be roughly described as an H^- ion attached to one of the hydrogen atoms of NH_3, is far from tetrahedral, and so its photoelectron spectrum produces NH_4 in a completely different region of the potential energy surface.

2. ROTATIONAL ANALYSIS OF 0–0 BAND

As discussed in Sec. 1, the main Schüler band is assigned to the 0–0 band of the transition $3p^2F_2 - 3s^2A_1$. This assignment was originally suggested by Gellene *et al.*[22] and by Havriliak and King[10]. The rotational structure is similar to that of an infrared fundamental, with the added complication of the electron spin doubling in the upper state. The lower $3s$ state has no spin-orbit coupling and negligible spin-rotation coupling, and the rotational levels are given to a good approximation by

$$F_0(N,\kappa) = B_0 N(N+1) - D_S^0 N^2(N+1)^2 + D_T^0 f(N,\kappa), \tag{1}$$

where $f(N,\kappa)$ is the tetrahedral splitting function of Hecht[30]. The levels are degenerate in J with $J = N \pm 1/2$, except for $N = 0$ with $J = 1/2$ only.

The rotational Hamiltonian of the upper state contains the usual Coriolis term to-

gether with scalar and tensor Λ-doubling and centrifugal corrections[20],

$$H_{\rm rot} = T_0 + B_0\mathbf{N}^2 - 2(B\zeta)_0\mathbf{N}\cdot\mathbf{\Lambda} + (q_S^0 + q_S^N\mathbf{N}^2)O^{\rm scalar}_{NN\Lambda\Lambda} + q_T^0 O^{\rm tensor}_{NN\Lambda\Lambda} - D_S^0\mathbf{N}^4 - D_T^0 O^{\rm tensor}_{NNNN} + F_S^0\mathbf{N}^2\mathbf{N}\cdot\mathbf{\Lambda}, \tag{2}$$

where the notation for the O operators follows Hecht[30]. In the *dominant approximation*[30] it is sufficient to take the matrix elements of $H_{\rm rot}$ diagonal in the quantum number R of the vector $\mathbf{R} = \mathbf{N} - \Lambda$, which describes the Coriolis substates.

The effective spin-orbit coupling is

$$H_{\rm so} = \frac{1}{2}[\xi_0 + \xi_0^N\mathbf{N}^2, \mathbf{S}\cdot\mathbf{\Lambda}]_+, \tag{3}$$

and this commutes with $\mathbf{J}$ and $\mathbf{R}$, but has matrix elements both diagonal and off-diagonal in N, which can be evaluated in terms of $6j$ symbols[20]. Then in dominant approximation we use (J, R, κ) as good quantum numbers, and set up a 2×2 matrix for $N = J \pm 1/2$, or a 1×1 matrix if only one of these values satisfies the triangle conditions for $(N, R, \Lambda = 1)$. Diagonalization of the 2×2 matrices for each (J, R, κ) gives two levels which can be formally labeled $N = J - 1/2$ and $N = J + 1/2$ in order of increasing energy. For the 1×1 matrices, the value of N is unique.

To complete the calculation of the ${}^2F_2 - {}^2A_1$ rotational structure we need the selection rules

$$\begin{aligned} \Delta N &= 0, \pm 1, \\ \Delta R &= R' - N'' = 0, \\ \kappa' &= \kappa''. \end{aligned} \tag{4}$$

The line strength summed over the two degenerate J values of the lower state is just $(2J' + 1)g_\kappa$, where the nuclear spin statistical weight factor g_κ is (5,2,3) or (15,12,18) for (A, E, F) rovibronic levels of NH_4 or ND_4 respectively.

This theory proved very successful, and the flash discharge spectrum, which was recorded with the highest resoution, could be fitted essentially to experimental precision[21]. The constants are presented in Table 2. As usual in this type of band, the $\Delta R = 0$ selection rule means that only differences in B_0, D_S^0 and D_T^0 could be determined.

The corresponding band of NH_4 is at 15078 cm^{-1}, and an approximate correction for the zero-point energy and the small Jahn-Teller effect gives $T_e = 14300$ cm^{-1} for the pure electronic transition in the T_d geometry. Various predicted values are 12755[10a], 11933[11], 16575[31], 17100[32], 13796[12], 15170[10b], all in cm^{-1}.

3. ROTATIONAL ANALYSIS OF 0–1 BANDS

The new spectra[27] of ND_4 show a complex structure in the region 900–1250 cm^{-1} below the 0–0 band, representing the 0–1 bands in the two bending modes $\nu_2(e)$ and $\nu_4(f_2)$. The one-quantum levels involving these modes in the upper and lower states are shown schematically in Fig. 1. The 0–1 bands are of types $^2F_2 - {}^2E$ and $^2F_2 - {}^2F_2$ respectively, and both are fully allowed by symmetry. Their intensities relative to the 0–0 band are discussed in Sec. 4. Since one expects $\nu_2 > \nu_4$, as in CD_4[33,34] , it seems likely that the rather regular branch extending to low wavenumbers from the head at 13675 cm^{-1} is part of the rotational structure of the 2_1^0 band, and that this is a convenient feature to start with. As a first attempt, 2_1^0 is treated as an isolated band, but eventually it will probably be necessary to include the Coriolis coupling between ν_2 and ν_4 explicitly, as has been done for CD_4[33,34].

The two components $|E_a\rangle$ and $|E_b\rangle$ of an E vibronic state transform under rotations like $(2z^2 - x^2 - y^2)/\sqrt{6}$ and $(x^2 - y^2)/\sqrt{2}$, respectively, and so can be treated as two of the five angular momentum states with $\Lambda = 2$, namely

$$\begin{aligned} |E_a\rangle &\equiv |2,0\rangle, \\ |E_b\rangle &\equiv |2,2^+\rangle = \{|2,2\rangle + |2,-2\rangle\}/\sqrt{2}. \end{aligned} \tag{5}$$

(In the treatment of Berger[35], the ν_4 F_2 bending modes correspond to the other three components of $\Lambda = 2$.) The effective rotational Hamiltonian of Herranz and Thyagarajan[36] for the ν_2 state can be written

$$\begin{aligned} H_2 =& \nu_2 + B_2\mathbf{N}^2 + b_2\Theta + d_2\Upsilon \\ & - D_{2S}\mathbf{N}^4 + D_{2T}(4\mathbf{N}^4/15 - \Theta^2/6 - \Upsilon). \end{aligned} \tag{6}$$

Here Θ and Υ correspond to the operators $\mathbf{N}$ and $\mathbf{T}$ of Herranz and Thyagarajan[36],

$$\begin{aligned} \Theta &= (\mathbf{\Lambda}^2 - 3\Lambda_z^2)(\mathbf{N}^2 - 3N_z^2)/6 + (\Lambda_+^2 + \Lambda_-^2)(N_+^2 + N_-^2)/8, \\ \Upsilon &= -(\Lambda_+\Lambda_z\Lambda_+ - \Lambda_-\Lambda_z\Lambda_-)(N_+N_zN_+ - N_-N_zN_-)/4. \end{aligned} \tag{7}$$

There is no first-order Coriolis coupling, so $R = N$. The eigenvalues of the operator Θ give the principal splitting $b_2\Theta(N,\kappa)$, and then the expectation values of the operator Υ give the main higher-order contributions to the splittings.

If tetrahedral splittings are unresolved and nuclear spin statistics are ignored, the line strengths of the scalar spectrum are proportional to

$$(2J'+1)(2R'+1)(2N''+1)\begin{Bmatrix} 1 & 1 & 2 \\ N'' & R' & N' \end{Bmatrix}^2. \tag{8}$$

The $6j$ symbol gives the selection rules

$$\begin{aligned} \Delta N &= 0, \pm 1, \\ \Delta R &= R' - N'' = 0, \pm 1, \pm 2, \end{aligned} \tag{9}$$

together with the other triangle conditions. The relative intensities of the tetrahedral substructure are obtained by multiplying eq. (8) by the square of a $3j$ symbol involving the angular momenta $(R', N'', \Lambda'' = 2)$, projected onto the tetrahedral eigenstates.

The strongest branches according to eq. (8) have $\Delta R = 2\Delta N = \pm 2$, with an approximate spacing of $2B(1+\zeta') \approx 11.2$ cm^{-1}. Thus the prominent low wavenumber branch in the observed spectrum can be assigned as the ${}^{O}P$ branch. The observable part of this branch consists of two regions, the first from near 13675 cm^{-1} to about 13600 cm^{-1} with relatively simple substructure, and the second from 13600 cm^{-1} to lower wavenumbers with more complex substructure. The former corresponds to the scalar spectrum with spin splittings and the latter to increasing tetrahedral splittings. Using the fact that the upper state is common to the 0–0 band, it is seen that the ${}^{O}P_1(N) - {}^{O}P_2(N)$ separations in the 2_1^0 band should agree with the $R_1(N-2) - R_2(N-2)$ separations in the 0–0 band. These separations change sufficiently rapidly with N that they can be used to determine the N-numbering of the ${}^{O}P$ branches. We can then adjust the ν_2 constants to obtain a good representation of this branch, as shown in Fig. 2. The constants determined mainly from this branch, together with a few other strong lines, are given in Table 3. Here the information available from the 0–0 band is used to constrain the upper-state parameters, but because $\Delta R \neq 0$ it is possible to separate the B values in the two states. However, the negative values obtained for the D_S values in the two states are probably not physically correct, and are more an indication of the limitation on the types of branches used in the present data set. The value obtained for ν_2 is only 11.4 cm^{-1} below the CD_4 value[33,34].

These constants reproduce the general character of the remainder of the 2_0^1 band, but some aspects such as the intensity of the $\Delta R = -1$ head at 13675 cm^{-1} have so far evaded simulation. One possible reason may be the Coriolis interaction with the 4_1^0 band. If the latter is treated as an isolated band it has branches with

$$\begin{aligned} \Delta N &= 0, \pm 1, \\ \Delta R &= 0, \pm 1, \pm 2, \pm 3. \end{aligned} \tag{10}$$

Possibly because of congestion, there are no very prominent branches in the observed spectrum. Thus it will be best to have an accurate model, including the (ν_2 , ν_4) Coriolis coupling, to simulate the entire 2_1^0 and 4_1^0 complex and then try to adjust the ν_4 parameters to fit the observed structure. Because the number of principal parameters is comparatively small, I am optimistic that this will be successful. However, the computations required are larger than those for the 0–0 or the isolated 2_1^0 bands, which were performed on an HP microcomputer, and I am developing programs on the main NRC computer to try to complete the analysis of the 0–1 bands.

4. JAHN-TELLER EFFECTS AND THE 1–0 BANDS

The upper electronic state $3p^2F_2$ of the Schüler bands is orbitally degenerate and therefore by symmetry can have linear potential energy terms in the e and f_2 vibrational displacements from the T_d configuration. This is the Jahn-Teller effect[37,38]. The dimensionless linear potential constants are denoted k_t for the e mode ($t = 2$), and k_u for the f_2 mode ($u = 3,4$), and their values give essentially the size of the Jahn-Teller distortions relative to the zero-point amplitudes of vibrations. The precise definitions used here are given in ref. 39.

Rotational evidence for the size of the Jahn-Teller distortions comes from the parameters q_S^0, q_T^0 and ζ_0 of the zero-point level. Normally[39] these parameters are contaminated by the effects of matrix elements of $\mathbf{L}$ to other electronic states, but in the case of a good np Rydberg state of a spherical top these matrix elements are very small and can be ignored. The q parameters result from the effects of the Jahn-Teller distortions on the moments of inertia,

$$\begin{aligned} q_S^0 &= (3B_e/5I_e)\{\sum_t k_t(\partial I_{zz}/\partial q_{ta}) + 2\sum_u k_u(\partial I_{xy}/\partial q_{uz})\}, \\ q_T^0 &= (B_e/20I_e)\{3\sum_t k_t(\partial I_{zz}/\partial q_{ta}) - 4\sum_u k_u(\partial I_{xy}/\partial q_{uz})\}. \end{aligned} \tag{11}$$

The Jahn-Teller effect on ζ_0 consists partly of a quenching of the electronic orbital angular momentum ζ_{elec} and partly of an excitation of the vibrational angular momenta ζ_{tu} and

$\zeta_{uu'}$. To terms quadratic in the k's. the formula is[39]

$$\begin{aligned}\zeta_0 = \zeta_{\text{elec}}\Big(1 &- \frac{3}{4}\sum_t k_t^2 - \frac{3}{2}\sum_u k_u^2\Big) \\ &+ \frac{\sqrt{3}}{4}\sum_{tu} k_t k_u \frac{(\omega_t + \omega_u)}{(\omega_t\omega_u)^{1/2}}\zeta_{tu} \\ &- \frac{1}{4}\sum_{uu'} k_u k_{u'} \frac{(\omega_u + \omega_{u'})}{(\omega_u\omega_{u'})^{1/2}}\zeta_{uu'}.\end{aligned} \tag{12}$$

The parameters in eqs. (11) and (12) can be calculated from the *ab initio* data of Havriliak and King[10a]. It is found that the observed q_S^0 and q_T^0 are larger and the observed ζ_0 is smaller than calculated. These differences are all in the direction of larger Jahn-Teller effects. To make this comparison more quantitative we can use the *ab initio* ζ_{elec} and harmonic parameters, and use eqs. (11) and (12) to derive 'observed' values of (k_2, k_3, k_4). The results[21] are (0.358, 0.011, 0.330) compared to the predicted (0.264, 0.021, 0.161). The implication of both the observed and the predicted constants is that the Jahn-Teller distortions are principally in the bending modes q_2 and q_4, and are of comparable magnitude in the two.

Another manifestation of the Jahn-Teller effect is occurrence of the 2_1^0 and 4_1^0 bands discussed in Sec. 3. This is essentially a Franck-Condon effect due to the distortions along the corresponding coordinates in the upper state. If the harmonic frequencies and normal coordinates are similar in the two states, then the intensities of these bands relative to the 0–0 band are just $k_2^2/2$ and k_4^2 respectively. The two observed bands clearly have similar intensities, as required by these formulas, but they are difficult to compare with the 0–0 band because their rotational structures are quite different. Herzberg[27] estimates a relative intensity of less than 1/50 for these bands. This comparative weakness probably results from the effect of the spreading out of the rotational structure among the different ΔR branches, because the 0–0 band has only one value of ΔR, whereas 2_1^0 has five and 4_1^0 has seven. Clearly, quantitative line intensity measurements in these bands would be of great interest, to provide an independent estimate of the constants k_2 and k_4.

Jahn-Teller effects on the energies of vibronic levels will clearly be important in the interpretation of the 1–0 bands. The linear Jahn-Teller effect does not split the $({}^2F_1 + {}^2F_2)$ components of the ν_2 level of the $3p$ state, whereas the ν_4 level is split into three components ${}^2A_1$, ${}^2F_1$, and $({}^2E + {}^2F_2)$, with approximate energies $(\nu_4 - k_4^2\omega_4)$, $(\nu_4 - k_4^2\omega_4/2)$, and $(\nu_4 + k_4^2\omega_4/2)$, respectively. However, quadratic Jahn-Teller effects, which may amount to a few

cm^{-1}, will split the degeneracy of the $\nu_2(^2F_1 - {}^2F_2)$ and $\nu_4(^2E - {}^2F_2)$ pairs. Formally there are only two allowed bands, to the $^2F_2$ levels. and these should each have a simple $\Delta R = 0$ structure similar to the 0–0 band, but these will be heavily perturbed by Coriolis coupling with their near-degenerate partners. Furthermore. the raising of the top components of ν_4 by the Jahn-Teller effect will bring them close to the ν_2 levels, and so the (ν_2, ν_4) Coriolis interactions will be more important than in the ground state. Added to these complications are the matrix elements of the effective spin-orbit operator, which will vary between different vibronic levels, depending upon how the matrix elements of the purely electronic operator **L** are redistributed by the vibronic mixings.

While some rotational structure is observed in the 1–0 bands[27], in view of the above complications it seems unlikely that there will be much progress in the analysis of them until spectra are available that are improved in two respects:

(a) decreased rotational temperature; and

(b) increased resolving power.

Clearly the 1–0 bands present a particularly fascinating challenge for both experimentalists and theoreticians, and they provide an opportunity to test in detail some of the rovibronic predictions associated with Jahn-Teller interactions. Anyone who solves this problem can then proceed to the 1–1 bands in ν_2 and ν_4. Fig. 1 shows that in this case a total of ten vibronic transitions are allowed by symmetry.

REFERENCES

[1] R. S. Mulliken, J. Chem. Phys. **1**, 492–503 (1933).

[2] H. J. Bernstein, J. Amer. Chem. Soc. **85**, 484–485 (1963).

[3] B. N. McMaster, J. Mrozek, and V. H. Smith Jr., Chem. Phys. **73**, 131–143 (1982).

[4] H. Cardy, D. Liotard, A. Dargelos, and E. Poquet, Chem. Phys. **77**, 287–299 (1983).

[5] J. Kaspar, V. H. Smith Jr., and B. N. McMaster, to be published.

[6] H. Schüler, A. Michel, and A. E. Grün, Z. Naturforsch. A **10**, 1–3 (1955).

[7] A. Schuster, Rep. Brit. Assoc. p. 38 (1872).

[8] G. Herzberg, Faraday Disc. Roy. Soc. Chem. **71**, 165–173 (1981).

[9] G. Herzberg and J. T. Hougen, J. Mol. Spectrosc. **97**, 430–440 (1983).

[10] (a) S. Havriliak and H. F. King, J. Amer. Chem. Soc. **105**, 4–12 (1983); (b) S. Havriliak, T. R. Furlani, and H. F. King, Can. J. Phys. **62**, 1336–1346 (1984).

[11] S. Raynor and D. R. Herschbach, J. Phys. Chem. **86**, 3592-3598 (1982).

[12] K. Hirao, J. Amer. Chem. Soc. **106**, 6283–6285 (1984).

[13] J. K. G. Watson, W. A. Majewski, and J. H. Glownia, J. Mol. Spectrosc., in press.

[14] C. R. Quick Jr., J. H. Glownia, J. J. Tiee, and F. L. Archuleta, Proc. SPIEE Int. Soc. Opt. Eng. **380**, 156–159 (1983).

[15] G. C. Nieman and S. D. Colson, J. Chem. Phys. **71**, 571–577 (1979).

[16] A. D. Walsh and P. A. Warsop, Trans. Faraday Soc. **57**, 345–358 (1961).

[17] A. E. Douglas, Disc. Faraday Soc. **35**, 158–174 (1963).

[18] G. Herzberg, Proc. Roy. Soc. Lond. A **262**, 291–317 (1961).

[19] M. N. R. Ashfold, C. L. Bennett, R. N. Dixon, P. Fielden, and R. J. Stickland, J. Mol. Spectrosc., to be published.

[20] J. K. G. Watson, J. Mol. Spectrosc. **107**, 124–132 (1984).

[21] F. Alberti, K. P. Huber, and J. K. G. Watson, J. Mol. Spectrosc. **107**, 133–143 (1984).

[22] G. I. Gellene, D. A. Cleary, and R. F. Porter, J. Chem. Phys. **77**, 3471–3477 (1982).

[23] E. A. Whittaker, B. J. Sullivan, G. C. Bjorklund, H. R. Wendt, and H. E. Hunziker, J. Chem. Phys. **80**, 961–962 (1984).

[24] G. Herzberg and A. Lagerqvist, Can. J. Phys. **46**, 2363–2373 (1968).

[25] K. P. Huber and T. J. Sears, Chem. Phys. Lett. **113**, 129–134 (1985).

[26] A. T. Droege and P. C. Engelking, Chem. Phys. Lett. **96**, 316–318 (1983).

[27] G. Herzberg, J. Astrophys. Astron. **5**, 131–138 (1984).

[28] K. P. Huber, private communication.

[29] J. V. Coe, J. T. Snodgrass, C. B. Freidhoff, K. M. McHugh, and K. H. Bowen, J. Chem. Phys., in press.

[30] K. T. Hecht, J. Mol. Spectrosc. **5**, 355–389, 390–404 (1960).

[31] E. Broclawik, J. Mrozek, and V. H. Smith Jr., Chem. Phys. **66**, 417–423 (1982).

[32] J. Kaspar and V. H. Smith Jr., Chem. Phys. **90**, 47–53 (1984).

[33] W. A. Kreiner and A. G. Robiette, Can. J. Phys. **57**, 1969–1981 (1979).

[34] M. Loete, J. C. Hilico, A. Valentin, J. Chazelas, and L. Henry, J. Mol. Spectrosc. **99**, 63–86 (1983).

[35] H. Berger, J. Mol. Spectrosc. **55**, 48–55 (1975).

[36] J. Herranz and G. Thyagarajan, J. Mol. Spectrosc. **19**, 247–265 (1966).

[37] G. Herzberg, *Electronic Spectra of Polyatomic Molecules*, Van Nostrand (1966).

[38] R. Englman, *The Jahn-Teller Effect in Molecules and Crystals*, Wiley-Interscience (1972).

[39] J. K. G. Watson, J. Mol. Spectrosc. **103**, 125–146 (1984).

Table 1

Parameters of the 2_1^1 Band of the $\tilde{C}' - \tilde{A}$ System of Ammonia

Parameter (cm^{-1})	From Schuster band	From $\tilde{C}' - \tilde{X}$ and $\tilde{A} - \tilde{X}$ systems
$\nu_{00}(ND_3)$	17227.39(8)	17228.6(head)[ab]
$B'(ND_3)$	5.230(17)	5.20[a], 5.26[c]
$B''(ND_3)$	4.768(15)	4.780[d]
$\Delta C(ND_3)$	0.1948(12)	0.22[ad], 0.18[cd]
$\nu_{00}(NH_3) - \nu_{00}(ND_3)$	440	436[ae]

[a]G.C. Nieman and S.D. Colson, *J. Chem. Phys.*, **71**, 571–577 (1979).

[b]A.E. Douglas, *Disc. Faraday Soc.*,**35**,158–174(1963).

[c]M.N.R. Ashfold, R.N. Dixon, and R.J. Stickland, *Chem. Phys.*,**88**,463–478 (1984).

[d]M.N.R. Ashfold, C.L. Bennett, and R.N. Dixon, *Chem. Phys.*,**93**, 293–306 (1985).

[e]A.D. Walsh and P.A. Warsop, *Trans. Faraday Soc.*,**57**,345–358 (1961).

Table 2

Parameters of the 0–0 Band of ND_4[a]

Parameter	Value[b]
T_0	14828.2853(36)
ξ_0'	6.1033(39)
ΔB_0	0.081096(62)
$B_0' - (B\zeta)_0'$	0.64793(28)
$(q_S^0)'$	0.112776(85)
$(q_T^0)'$	0.003075(10)
$10^4(\xi_0^N)'$	2.82(27)
$10^6\Delta D_S^0$	–1.402(252)
$10^4(F_S^0)'$	1.462(39)
$10^6(q_S^N)'$	–6.71(44)
$10^6\Delta D_T^0$	0.498(26)

[a] Ref. 21.

[b] Values in cm^{-1} with standard deviations in units of the last decimal place in parentheses.

Table 3

Parameters of the 2_1^0 Band of ND_4[a]

Parameter	Value[b]
B_0'	3.0680(25)
$10^4(D_S^0)'$	–1.99(24)
ν_2''	1080.255(74)
B_2''	3.0115(25)
$10^3 b_2''$	2.56(66)
$10^3 d_2''$	–0.28(12)
$10^4 D_{2S}''$	–1.50(20)
$10^4 D_{2T}''$	–0.95(12)

[a] Other upper state parameters are constrained to values in Table 2.

[b] Values in cm^{-1} with standard deviations in units of the last decimal place in parentheses.

FIGURE CAPTIONS

1 Schematic diagram of the lowest vibrational levels in the upper and lower states of the $3p^2F_2 - 3s^2A_1$ transition of the ammonium radical. All the levels are electron-spin doublets.

2 (a) Portion of the emission spectrum of ND_4 recorded on a Bomem Fourier transform spectrometer (G. Herzberg, to be published). (b) Calculated spectrum of the 2_1^0 band of ND_4 employing the constants of Tables 2 and 3, assuming a rotational temperature of 500 K.

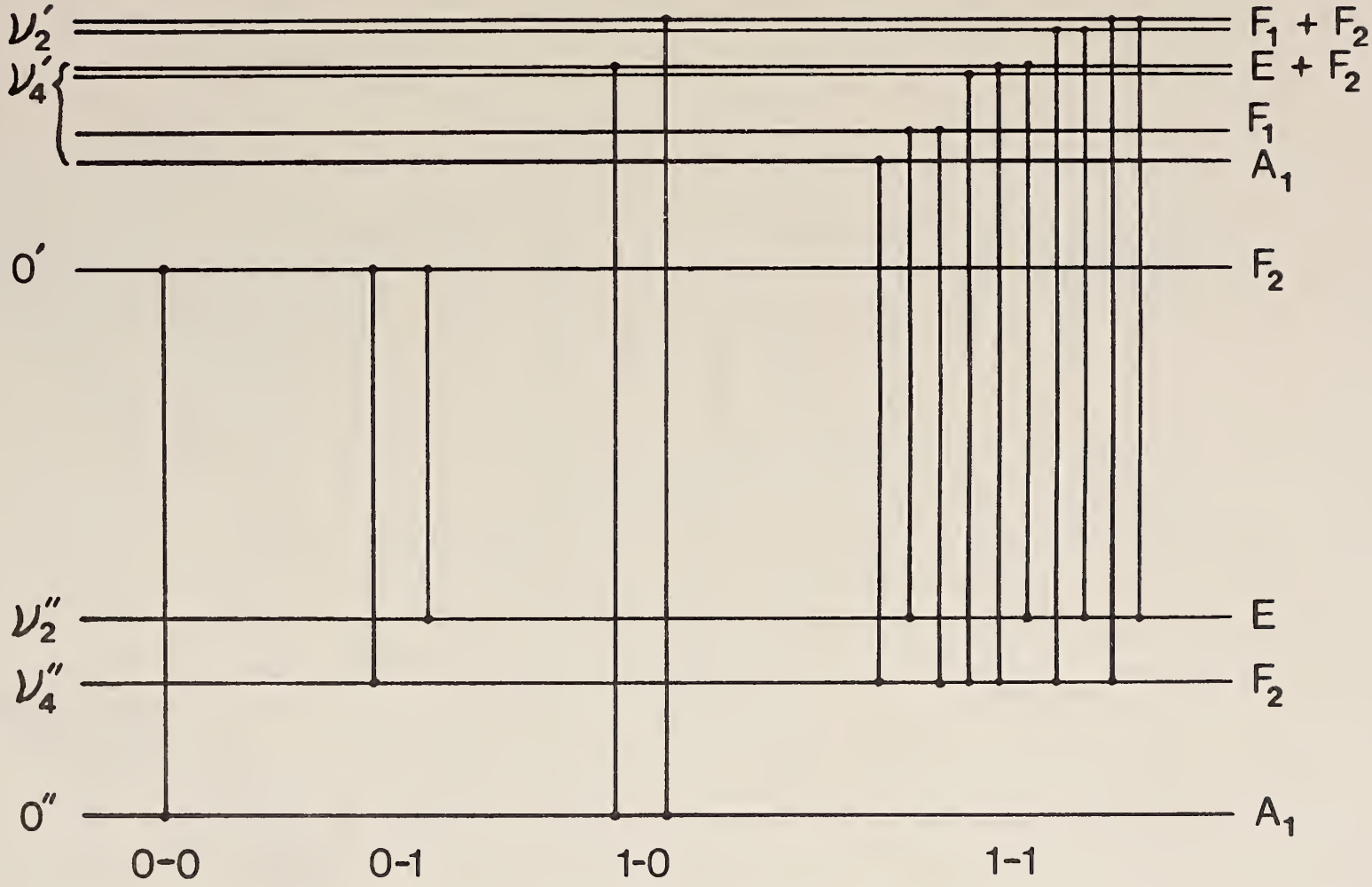

FIGURE 1

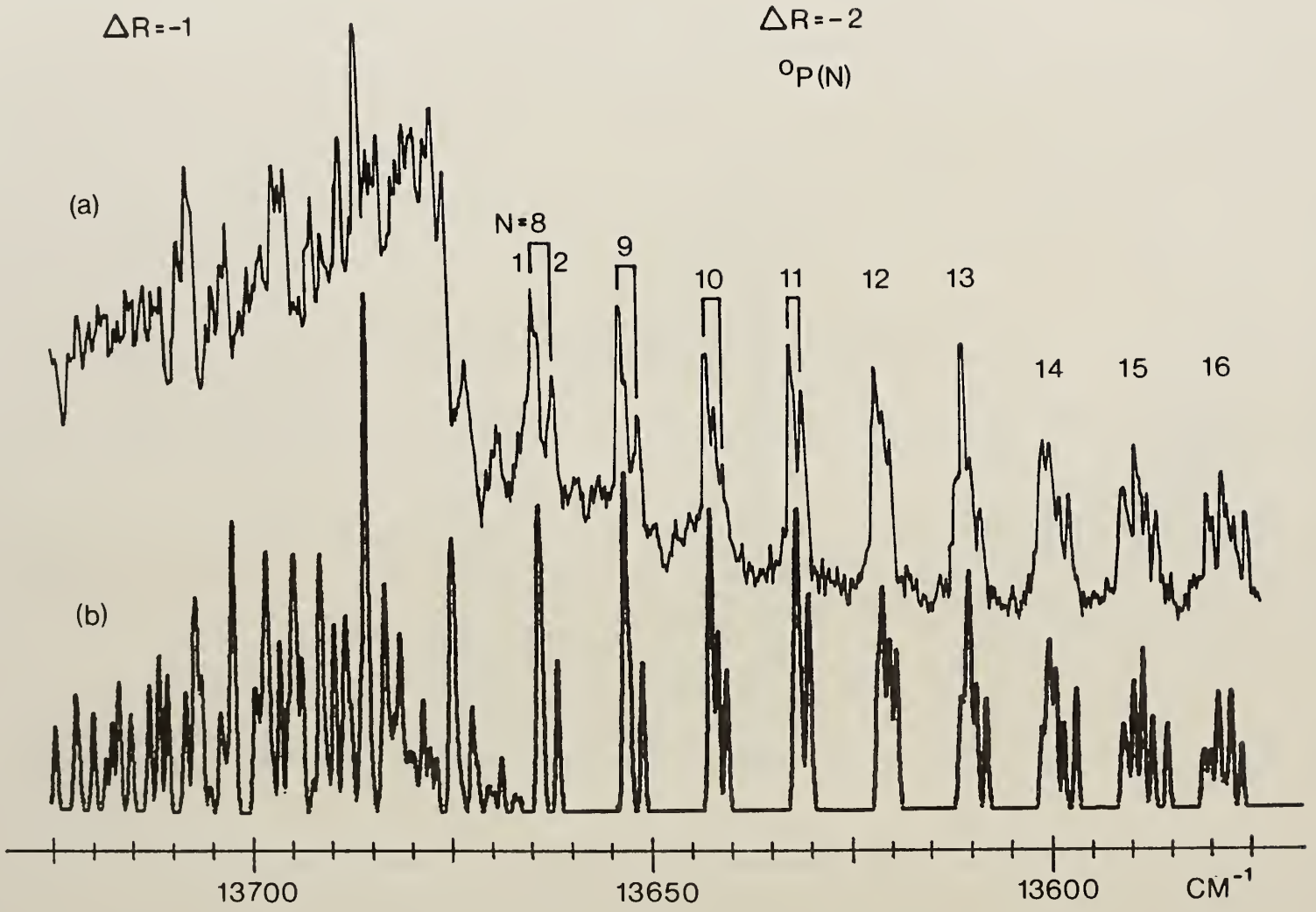

FIGURE 2

EFFECTS OF FREE RADICALS GENERATED BY PHEOMELANIN ON RAT MAST CELLS

D.C.P. Wong, N.S. Ranadive and S.Shirwadkar
Department of Pathology, University of Toronto, Toronto, Ontario, Canada.
I.A. Menon and S. Persad
Clinical Science Division, University of Toronto, Toronto, Ontario, Canada.

INTRODUCTION

The characteristic manifestations of the sunburn reactions such as erythema, edema, determal infiltrate, hyperpigmentation and peeling off or scaling of the skin are more common in people with fair skin than in those with darker skin (1). It is generally believed that this is due to the lesser protection afforded by the melanin in the skin of the former, and that this is probably due to the lower concentrations of melanin in their skin (2). Clinical evidence indicates that in addition to sunburn reactions, many cutaneous cancers are more prevalent and severe among people with red hair and 'celtic type' skin (3). Irradiation of pheomelanin produces more superoxide as well as free radical-mediated cell lysis than irradiation of eumelanin (4-7). These suggest that pheomelanin in the skin may be positively contributing to the inflammatory response in the skin induced by UV radiation.

The solar erythemogenesis and subsequent delayed reactions seem to be due to mediators released by direct injury to the

target cells as well as the cascade of secondary events leading to inflammation (8). The initial reaction may be due to the interaction between cutaneous mast cells and reactive species and/or oxygen-based free radicals generated during irradiation. The release of histamine from mast cells by H_2O_2 (9) and myeloperoxidase-H_2O_2-halide system (10) has been shown to occur in the isolated cell system. Late phase inflammatory reactions have been shown to be propagated by mast cell degranulation (11). In this paper, the effects of reactive species generated from melanins by exposure to light on isolated mast cells are reported.

MATERIALS AND METHODS

Red hair melanin (RHM) and black hair melanin (BHM) were isolated from human hair as described previously (12). Rat peritoneal mast cells were isolated, labeled with ^{51}Cr and the release of ^{51}Cr was determined according to Ranadive et al (13). Histamine was assayed fluorometrically (14). Mast cells were irradiated at 21° using a Westinghouse mercury vapor lamp (5) and the release of ^{51}Cr and histamine was determined.

RESULTS

Irradiation of mast cells in the presence of RHM released histamine; this was dependent upon the concentration of the melanin (Fig. 1). Mast cells incubated in the dark in the presence of RHM did not release histamine. At high concentrations of RHM (100 ug/ml) a slight increase of histamine release was observed. Mast cells either incubated in the dark or irradiated in the presence of BHM did not release appreciable amounts of histamine.

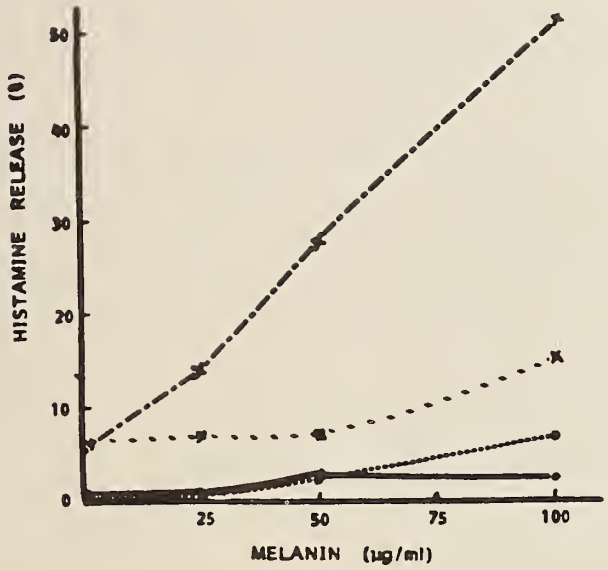

Figure 1

Release of histamine from mastg cell irradiated in the presence of various concentrations of melanins for 60 minutes at room temperature.

●—●—●—●—● RHM in dark; x—x—x—x—x RHM in light;

o———o BHM in dark; x- - - -x BHM in light.

The release of histamine was found to be related to the dose of radiation and the maximum release by 100 ug/ml of RHM occurred at 60 min (fig. 2).

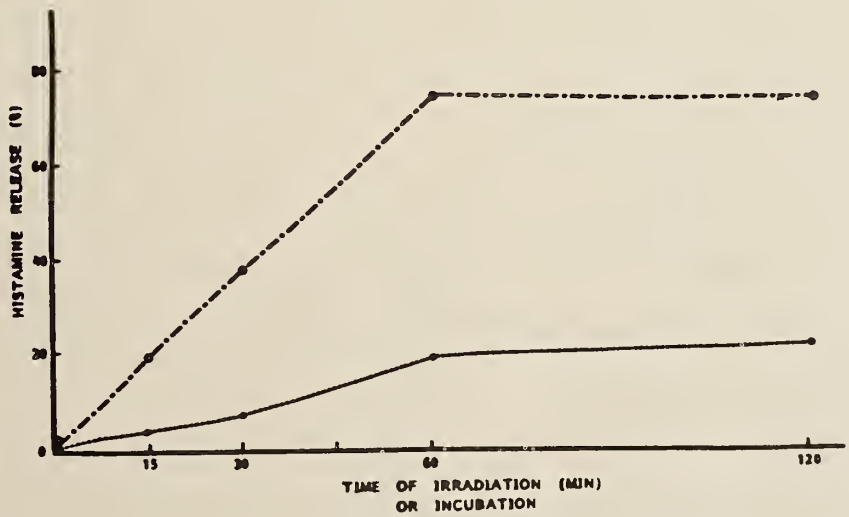

Figure 2

Release of histamine from mast cells by 100 ug/ml of RHM as a function of period of irradiation at room temperature.

●—●—●—●—● Cells in dark; o—o—o—o—o Cells in light.

Figure 3 shows a comparison of the release of histamine and that of ^{51}Cr from mast cells during irradiation in the presence of RHM. At lower concentrations of RHM the release of histamine was not accompanied by the release of ^{51}Cr; however at higher concentrations of RHM, the amount of histamine released was comparable to that of ^{51}Cr released.

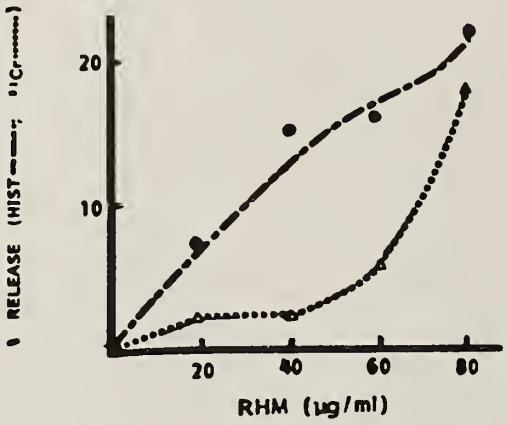

Figure 3

Comparison of histamine release and ^{51}Cr release from chromium loaded mast cells by various concentrations of RHM in the presence of light for 60 minutes atg room temperature.

Δ·····Δ ^{51}Cr Release; o—·—·—o Histamine Release.

Table 1 shows the effects of catalase and superoxide dismutase (SOD) on the release of histamine by irradiation of mast cells in the presence of RHM. There was only a slight release of histamine after incubation in the dark of the cells in the presence of RHM and it was This release was inhibited by catalase. Histamine release during irradiation of mast cells in the presence of RHM was slightly enhanced by SOD but was completely abolished by catalase. However, catalase inhibited

only partially the histamine release from irradiated cells when SOD was present.

Table 1

Effects of SOD and catalase on the release of histamine from mast cells during irradiation in the presence of RHM.

Reagents added	Histamine release (%)	
	Dark	Irradiated
None	8	10
RHM (40 ug/ml)	15	35
RHM, SOD (160 U/ml)	17	41
RHM, catalase (3400 U/ml)	6	10
RHM, SOD, catalase	16	25

The cells were incubated in the dark or irradiated for 60 min.

DISCUSSION

Mast cells are known to participate in various cutaneous phototoxic reactions (15-17). It is also known that melanin can act as an electron exchange polymer (18, 19) and contains free radicals are increased by UV-visible radiation (20, 21). Although, as found by the ESR experimewnts both eumelanin and pheomelanin contain one common signal, pheomelanin contains a specific kind of free radical(s) which is not present in eumelanin (22, 23). The present studies have shown that irradiation of mast cells alone or in the presence of BHM had no significant effect on the release of histamine. On the other hand

the cells which were irradiated in the presence of RHM released histamine. Comparison of the releases of histamine and ^{51}Cr suggests that at lower concentrations of RHM the release of histamine is of cytotropic nature while at higher concentrations cell lysis occurs.

Irradiation of RHM produces superoxide and hydrogen peroxide (4). The histamine release during irradiation of mast cells in the presence of RHM inhibited by catalase suggesting this release is due to the hydrogen peroxide formed. Previous observations with Ehrlich ascites carcinoma showed cell lyses by irradiation in the presence of RHM; however this was not inhibited by catalase. Therefore it appears that the histamine release from mast cells is mediated by mechansims different from the one(s) responsible for the lysis of the Ehrlich ascites carcinoma cells (5).

A few implications of these in vitro studies in cutaneous phototoxicity are worth noting. In the skin, melanin is mostly present within the melanocytes and keratinocytes, while in in vitro experiments melanin was added to the cell suspension. However the following cosiderations suggest that the results of the present studies may be relevant to in vivo conditions. Although we have not yet examined whether melanin penetrates into the mast cells, electron microscopic studies have shown that under similar conditions melanin penetrated into Ehrlich ascites carcinoma cells (24). Morphological studies have also shown occasional presence of melanin granules in mast cells (25). Although melanin is present in the skin mostly within the

melanosomes, it is also present in a more diffused state as melanin dust (26).

Irradiation of melanin, especially in the presence of naturally occurring sulfhydryl compounds such as cysteine produces H_2O_2 (7) which is relatively stable and could diffuse across a number of cell layers. The irradiation of melanin in the presence of free fatty acid has been shown to produce lipid peroxidation (27, 28). Peroxiation of cellular lipid components by irradiation of cells in the presence of melanin has also been reported (28). Some of the intermediates in lipid peroxidation such as hydroperoxides are fairly stable (29, 30). Thus, although the reactive free radicals in melanin produced by irradiation are short-lived, it is conceivable that these free radicals could react with several biomolecules producing reactive compounds which are relatively long-lived and could permeate to other sites in the skin.

The studies reported here show that the RHM on exposure to UV-visible radiation produces reactive species which can induce release of histamine by both cytotropic and cytotoxic mechanisms. Mast cells represent the effector cells capable of elaborating the essential mediators of inflammation (31). The fact that the exposure of RHM to UV-visible radiations generates active compounds suggests that the susceptibility of celtic skin to sunburn reactions may be related to the type of melanin present in the skin.

REFERENCES

1. Epstein JH: Free Radicals in Biology. Vol 3. Ed.WA Pryor. Academic Press. New York. 1977. pp. 219-249.
2. Cripps D: J Invest Dermatol 76: 154-57, 1981
3. McGovern VJ: Malignant melanoma of skin and mucous membrane, Ed. Milton GW Churchill Livingstone Publication. New York 1977. pp. 1-25.
4. Persad S, Menon IA, Haberman HF: Photochem. Photobiol. 37: 63-68, 1983.
5. Menon, IA, Persad S, Ranadive NS, Haberman, HF: Cancer Res 43: 3165-69, 1983.
6. Menon IA, Persad S, Ranadive NS, Haberman HF: Oxygen radicals in Chemistry and Biology, edited by W Bors, M Saran, D Tait. Walter de Gruyter & Co, Berlin, 1984, pp. 673-679.
7. Menon IA, Persad S, Ranadive NS, Haberman HF: Can J Biochem Cell Biol 63: 278-83, 1985.
8. Gilchrist BA, Soter NA, Stoff JS, Mihm MC Jr: J Amer Acad Dermatol 5: 411-422, 1981.
9. Ohmori H, Komoriya K, Azuma A, Kuruzomi S, Otto YH: Biochem. Pharmacol 28: 333-35, 1979.
10. Henderson WR, Chi EY, Klebanoff SJ: J Exp Med 152: 265-79, 1980.
11. Kaliner M, Lemanske R: Fed Proc 43: 2846-51, 1984.
12. Menon IA, Persad S, Haberman HF, Kurian, CJ: J Invest Dermatol 80: 202-06, 1983.
13. Ranadive, NS, Menon IA, Haberman HF: Acta Dermato-Vener 59:

13. Ranadive, NS, Menon IA, Haberman HF: Acta Dermato-Vener 59: 493-97, 1979.

14. Siraganian RP: Manual of clinical immunology. Ed. NR Rose and H Friedman Amer Soc Microbiol, Washington DC 1976

15. Soter NA, Austen KF: Fed Proc 36: 1736-41, 1977.

16. Lim HW, Young L, Hagan M, Gigli I: J Invest Dermatol 84: 114-17, 1985.

17. Gendimenico GJ, Kochevar I: Toxicol Appl Pharmacol 76: 374-82, 1984.

18. Mason HS, Ingram DJE, Allen B: Arch Biochem Biophys 86: 225-330, 1960.

19. Gan EV, Haberman HF, Menon IA: Arch Biochem Biophys 173: 666-72, 1976.

20. Sarna T, Menon, IA, Sealy, RC: Photochem. Photobiol 39: 805-809, 1984.

21. Sealy RC, Felix CC, Hyde JS, Swartz, HM: Free Radicals in Biology, Vol IV, Edited by WA Pryor, New York, Academic Press 1980, pp.209-59.

22. Sealy RC, Hyde JS, Felix CC, Menon, IA, Prota G, Swartz, HM, Persad, S, Haberman HF: Proc. Natl. Acad. Sci. USA 79: 2885-89, 1982.

23. Sealy RC, Hyde JS, Felix CC, Menon IA, Prota G: Science 217: 545-47, 1982

24. Lea PJ Pawlowski A, Persad S, Menon IA, Haberman HF: This volume pp.

25. Okun MR. Internatl J Dermatol 15: 711-22, 1976.

26. Klein LM, Nordlund JJ: Internatl J Dermatol 20: 621-631, 1981.

27. Chedekel MR: Photochem Photobiol 35: 881-885, 1982.

28. Menon IA, Persad S, Ranadive NS, Haberman HF: Pigment Cell, University of Tokyo Press, 1985 (in press).

29. Dixit R, Mukhtar H, Bickers DR: J Invest Dermatol 81: 369-75, 1983.

30. Girotti AW, Thomas JP, Jordan JE: Arch Biochem Biophys 236: 238-51, 1985.

31. Soter NA, Austen KF J Invest Dermatol 67: 313-319, 1976.

UV Multiphoton Photodissociation of the $C_4H_2N_2$ Molecule

Xiaoxiang Xie*, E. Pugh, V. R. McCrary,
J. B. Halpern and W. M. Jackson
Department of Chemistry, Howard University, Washington,
D. C. 20059, U. S. A.

Abstract

The UV absorption spectrum in the region of 190 -- 300 nm at room temperature has been observed and the absorption cross-section at 193 nm is $(5.7 \pm 0.6)X10^{-19}$ cm^2. A study has been done of the UV dissociation of $C_4H_2N_2$ at 193 nm. The emission spectra of excited photofragments in the $CN(B^2\Sigma^+)$ --> $CN(X^2\Sigma^+)$ and $CN(A^2\Pi)$ --> $CN(X^2\Sigma)$ systems are observed. Laser induced fluorescence (LIF) has been used to determine the nascent energy distribution of ground state CN radicals. At laser fluence of 4.2 mJ/cm^2pulse the ratio of v" = 1 to v" = 0 $CN(X^2\Sigma^+)$ products is 0.2:0.8. The rotational distribution of v" = 0 fragments is Boltzmann in nature, and characterized by a temperature of 1950 $\pm$ 60 K. At an ArF laser fluence of 24 mJ/cm^2pulse the ground state radicals were found to have an effective vibrational temperature of 2900 $\pm$ 200 K. The nascent rotational distributions of $CN(X^2\Sigma^+$, v" = 0) could also be characterized by a Boltzmann distribution, with a T_{rot} of

2350 ± 60 K. The two-photon photolysis mechanisms were discussed.

---

* Permanent address: Anhui Institute of Optics and Fine Mechanics, P. O. Box 25 Hefei, Anhui, People's Republic of China.

Introduction

There have been many studies on the photodissociation dynamics of CN containing compounds [1], but most of these were concerned with relatively simple molecules. The more complicated molecules that have been studied in the past ten years are dicyanoacetylene (C_4N_2) [2], acrylonitrile (C_3H_3N) [3], and cyanoacetylene (C_3HN) [4,5]. The discovery of these molecules in outer space [6,7] suggests that fundamental laboratories studies of their photochemistry would be of value. Photochemical investigations using lasers to dissociate and to detect the fragments can supply information about the product energy distributions and the detailed reaction mechanisms [8,9]. Recent experiments have also increased our understanding of the UV multiphoton photodissociation process (UVMPDP) [3,10-18]. The actual mechanism in a particular molecule at a particular laser intensity is sensitive to the lifetime of the dissociative

state, which, in turn, depends on the number of effective vibrational modes [19].

Fumaronitrile (trans-1,2,-dicyanoethylene) is a large molecule consisting of eight atoms. It has a conjugated bond system and a planar structure:

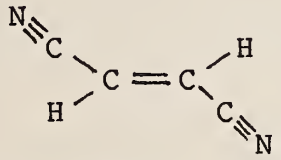

While the UV absorption spectra [21,22] has been measured in the liquid-phase, nothing has been reported on the photodissociation dynamics of this molecule.

In the present work, we have measured the UV absorption spectrum from 190 --> 300 nm in the gas-phase and used an ArF laser to dissociate the $C_4H_2N_2$ molecule. One and two-photon photochemical reactions were observed.

Experimental

UV Absorption Spectrum:

A Beckman DU-7 Spectrophotometer (a high-speed microprocessor-controlled UV-Visible Instrument operating from 190 nm to 800 nm) with a 10 cm long absorption cell equipped with two CaF windows was used to measure the gas-phase UV absorption spectrum of the $C_4H_2N_2$ molecule. The graphic output of the DU-7 spectrophotometer has a resolution of 100 by 200 points and the wavelength accuracy

is ± 0.5 nm. The resolution of the spectrophotomenter is 2 nm with 2 mm slit. In order to get equilibrium vapor pressure of this molecules, the spectrum of each molecule was measured one hour after it was put into the cell. The scan speed of the spectrophotometer is 120 nm/min. A capacitance manometer (ABS Gauge 10 torr) was used to measure the vapor pressure at room temperature.

Laser-Induced Fluorescence Spectrum:

The LIF experimental apparatus has been previously described [20]. Briefly, an apertured ArF laser beam (Lambda Physik EMG 101) of 0.7 cm diameter with a 20 ns pulsewidth was passed through a fluorescence cell. The cell has CaF_2 windows and long baffle arms to reduce the scattered laser light. The laser had a maximum energy of 60 mJ/pulse at a pulse repetition rate of 6 Hz.

A Molectron UV 12 nitrogen laser was used to pump a Molectron DL-II dye laser that generated narrow band (0.3 cm^{-1}) tunable laser radiation using BBQ as the dye in p-dioxane solution. The dye laser beam with a 0.2 cm diameter was propagated in a direction opposing the ArF laser beam and passing co-linearly through it.

Induced fluorescence excited by the dye laser was observed in a direction perpendicular to the laser beams. A lens imaged the fluorescence through an interference filter, with a central wavelength of 388 nm, onto a photomultiplier

tube (EMI 9789 QB). The signal from the PMT was averaged by a boxcar integrator (PAR 160).

Emission spectra were measured with a 0.25 m monochromator (Jobin-Yvon) using a slit width of 0.25 mm for the violet system of CN , and 1 mm for the red system. The resolution of the monochromator was about 1 nm and 4 nm, respectively. A Hammamatsu photomultiplier tube (R666) was used to observe the red emission of the transition CN(A) --> CN(X). The monochromator and phototube response as a function of wavelength have been calibrated with a standard lamp.

The solid $C_4H_2N_2$, with a stated purity of 98%, was obtained from Aldrich Chemical Co., and used without further purification.

Results

The absorption spectrum in the gas-phase:

There are two papers reporting the absorption spectra of the $C_4H_2N_2$ molecule in the liquid-phase [21,22]. The vapor pressure we measured is 0.19 $\pm$ 0.02 torr. Because it has a large absorbance in the UV region, so it is simple to observe the absorption spectrum at room temperature shown in Fig.1. The maximum absorbance is at 216 nm, which is very close to the value of 220 nm reported for the liquid-phase [22]; the slight shift to longer wavelength in the liquid-phase can be attributed to a solvent effect. According to

the vapor pressure at room temperature, the absortion cross-section at 193 nm is $(5.7 \pm 0.6) \times 10^{-19}$ cm^2. No absorbance at 248 nm can be seen in the Fig.1.

The LIF spectra of CN ($X\ ^2\Sigma^+$)

Typical LIF spectra of the $\Delta v = 0$ sequence of $CN(X^2\Sigma^+)$ are shown in Fig. 2. They were obtained following the photolysis of $C_4H_2N_2$ at 193 nm with a nominal delay between photolysis and probing lasers of 0.5 μs at a total gas pressure of 1 mtorr. The figure shows that under these collision free conditions the CN(X) radicals were formed rotationally excited in the v" = 0 and v" = 1 levels. This is shown by the prominent (0,0) and (1,1) bandheads at 388.34 and 387.14 nm, respectively. Fig. 2 (a) shows that a prominent bandhead for the v" = 2 vibrational level of CN (X) state was observed when the excimer laser fluence was 24 mJ/cm^2pulse, but not in Fig. 2 (b) when it was 4.2 mJ/cm^2pulse.

The LIF intensity of CN(X) radicals at 388.3 nm as a function of the excimer laser power was measured at the pressure of 13 mtorr shown in Fig.3. A linear relation between them shows the slope of the line in Fig.3 is 1.1 $\pm$ 0.1 in the condition of low laser intensity.

The spectra shown in Fig. 2 (a) and (b) can be used to determine the relative ratios for the various vibrational levels. In the high fluence case they were determined to be

0.7:0.2:0.1 for the first three vibrational levels of CN ground state fragments. This corresponds to a Boltzmann distribution with a vibrational temperatures of 2900 ±200 K. For low fluence only the first two vibrational levels were observed in the ratio 0.8:0.2.

The relative intensities of the rotational lines obtained from the R_{00} branch of Fig. 2 (a) and (b) are plotted in Fig. 4. For a Boltzmann type of behavior the quantity $\ln(I/(N' + N'' + 1)$ will be proportional to $N''(N''+1)$, where I is the LIF intensity, and N" and N' are the rotational quantum numbers of the X and B states. Effective rotational temperatures of 2350 ± 60 K and 1950 ± 60 K can be defined for the high and low fluence cases, respectively.

Multi-Photon Processes

The absorption spectrum shown in Fig.1 shows the maximum absorbance is at 193 nm corresponding to a cross-section of $5.7X10^{-19}$ cm^2, but no absorbance at 248 nm. Thus, when we tried to dissociate the $C_4H_2N_2$ molecule with a 248 nm KrF laser we did not observe any LIF signal from CN(X) state fragments at the fluence levels above 43 mJ/cm^2pulse, nor did we see any emission from excited CN radicals.

The $CN(B\ ^2\Sigma^+) \rightarrow CN(X\ ^2\Sigma^+)$ Emission

The ArF laser was used to dissociate the molecule $C_4H_2N_2$. A strong fluorescence emission which originated from the CN(B) --> CN(X) transition shown in Fig. 5, was observed in 50 mtorr of the $C_4H_2N_2$. The resolution is not sufficient to completely separate the bands. When the wavelength was fixed at 388.3 nm, the emission intensity of the CN violet bands is a function of the ArF laser intensity shown ih Fig.6, and the linear relation shows the slope of the line is 1.6 ± 0.1. This data suggested the the processes to produce the CN(B) radicals is the two-photon absorption processes. As a result of the data in Table 1 which suggest that the $NC-C_3H_2N$ bond is 5.83 ev, a single 193 nm photon (6.4 ev) will not have enough energy to both dissociate and pump the CN radical to B state, thus the observed emission spectrum must be due to a two photon absorption process.

The $CN(A^2\Pi)$ --> $CN(X^2\Sigma^+)$ Emission

A red fluorescence due to the CN(A) --> CN(X) transition can be easily observed by eye. The spectra of this emission obtained in 10 mtorr of the $C_4H_2N_2$, in the region between 500 nm to 800 nm, is shown in Fig. 7. The spectrum was taken in sections because the intensity of the emission is very dependent on the excimer laser power, and the cleanliness window of the cell. Even though the laser energy varies about 30% during a run, a quantitative measurement of the vibrational distribution of some of the red bands of CN radical can be determined. From Fig. 7 it

can be seen that levels as high as v' = 10 of the CN(A) state were reached. Emission was not seen from higher levels, although we scanned regions of the spectrum where the Franck-Condon factors for such transitions are substantial. The general shape of the spectrum indicates that the distribution is vibrationally inverted which is confirmed by the vibrational distribution of the A state obtained from the spectra shown in Figure 8.

Discussion

Table 1 summarizes the thermochemical data for the various possible photochemical processes that may occur in the 193 nm photolysis of the $C_4H_2N_2$. The $C_4H_2N_2$ molecule belongs to the C_{2h} point group, and the term symbol for the ground state is X^1A_g. The absorption at 216 nm (see Fig.1) is probably due to excitation to an excited state with ^1A_u symmetry [26].

In the case of the low ArF laser fluence, the possible photodissociation process following one photon absorption is

$$C_4H_2N_2(^1A_g) + h\nu \longrightarrow C_4H_2N_2^* (^1A_u) \quad (1)$$

$$C_4H_2N_2^*(^1A_u) \longrightarrow C_4H_2N_2(^1A_g) + h\nu_1 \quad (2)$$

$$C_4H_2N_2^*(^1A_u) \longrightarrow H_2 + C_4N_2 \qquad \Delta H = 2.41 \text{ ev} \quad (3)$$

$$C_4H_2N_2^*(^1A_u) \longrightarrow CN(X^2\Sigma^+, v'' \leqslant 1) + C_3H_2N \qquad \Delta H = 5.83 \text{ ev} \quad (4)$$

where the $h\nu$ represents the 193 nm photon. Although the reaction (3) is the low energy channel, it is expected that

there is a high barrier for the H_2 elimination because the H atoms are in the different side of the C = C bond and in the different C atom. In the other hand. If the reaction (3) is the main channel, no CN(X) radical should be observed in the condition of the low laser intensity. In fact we observed great LIF signal from the CN(X) radical, this fact means reaction (3) is not the main single-photon absorption process.

If the reaction (4) is proceeded, 0.57 ev of available energy can be distributed between recoil translation motion and the internal energy of the fragments. In Fig. 2 (b), only the (0,0) and (1,1) bandheads are observed, indicating that CN is not produced in the v" = 2 level by reaction (4). Reaction (4) is the only observed CN producing reaction which is energetically possible via a single-photon absorption.

There are three mechanistic possibilities that could explain the change in the ground state population distribution and the increased amount of emission in the violet and red bands when the laser fluence is increased. The first is the sequential two photon absorption processes,

$$C_4H_2N_2 + h\nu \longrightarrow C_4H_2N_2^* \ (^1A_u) \qquad (5)$$

$$C_4H_2N_2^*(^1A_u) + h\nu \longrightarrow CN(A\ ^2\Pi) + C_3H_2N \quad \Delta H = 6.96 \text{ ev} \qquad (6)$$

$$C_4H_2N_2^*(^1A_u) + h\nu \longrightarrow CN(B\ ^2\Sigma^+) + C_3H_2N \quad \Delta H = 9.03 \text{ ev} \qquad (7)$$

$$CN\ (B\ ^2\Sigma^+) \longrightarrow CN\ (X\ ^2\Sigma^+,\ v" \leqslant 2) + h\nu_2 \qquad (8)$$

$$CN\ (A\ ^2\Pi) \longrightarrow CN\ (X\ ^2\Sigma^+) + h\nu_3 \qquad (9)$$

In reaction (5) it is postulated that the $C_4H_2N_2$ molecules are excited to high vibrational levels of ^1A_u electronic state by the first photon, and if the $C_4H_2N_2^*$ has a long dissociative lifetime as compared with the mean time for absorbing a photon from the laser beam, the second photon could easily match a transition from these high vibrational levels to a super-excited state. This super-excited state may be a dissociation continuum, a predissociating Rydberg level, or a state in the ionization region. Although information on the super-excited state is lacking, the cross-section for the second step of the sequential two photon excitation to such a highly excited electronic state may be very large.

There is a another channel which may be proceeded in the sequential absorption:

$$C_4H_2N_2^* + h \text{ ---> } CN(A) + H_2 + C_3N \quad \Delta H = 8.94 \text{ ev} \quad (10)$$

Because the C_3N radical has a high heat of formation, this channel is a high energy process. If the conditions are the same as reactions (6) and (7), reaction (10) is impossible to be proceeded.

The simultaneous photodissociation process proceeds directly to the super-excited state by simultaneous absorption of two laser photons. In general simultaneous two photon absorption has a fairly low cross-section relative to any allowed one photon process. Since the UVMP process is observed at low laser fluence with an unfocused

laser, it is not likely that this mechanism is responsible for the process observed.

The third possibility is the secondary photon dissociation processes described as follows,

$$C_4H_2N_2 + h\nu \text{ ---> } CN(X\ ^2\Sigma^+) + C_3H_2N \qquad \Delta H = 5.83 \text{ ev} \qquad (11)$$

$$C_3H_2N + h\nu \text{ ---> } H_2 + C_3N \qquad \Delta H = 1.98 \text{ ev} \qquad (12)$$

$$C_3H_2N + h\nu \text{ ---> } CN(B\ ^2\Sigma^+) + C_2H_2 \qquad \Delta H = 5.71 \text{ ev} \qquad (13)$$

$$\text{or} \quad C_3H_2N + h\nu \text{ ---> } CN(A\ ^2\Pi) + C_2H_2 \qquad \Delta H = 3.64 \text{ ev} \qquad (14)$$

The reaction (12) is possible to preceeded in the point of the energy. But if the CN(A) and CN(B) radical which were observed in the experiments are produced from the photolysis of C_3N radical, the third photon is needed to dissociate the C_3N radical because the energy is not enough after overcoming the energy barrier for H_2 elimination. In this case it is not the low energy channel to be considered. In either reaction (13) or (14) there is more than 1 ev of energy left to partition into the internal degrees of freedom and translational energy of the CN(B), CN(A) and C_2H_2 products.

One might argue that in addition to the channels (13) and (14), it would be possible to excite the CN radicals, producing the emission. However, the Franck-Condon factor for one photon excitation of the CN(X) --> CN(B) transition at 193 nm is of the order of 10^{-13} to 10^{-14} [11]. The situation is even worse for the direct excitation of CN(A) radicals. Another possibility would be excitation of CN(E)

and CN(F), followed by radiative decay of these states to CN(A) and CN(X). We have attempted to measure whether these states are present. At the fluence levels used in these experiments, there is no observable emission from these states. Thus, it is unlikely that direct secondary excitation of the CN radical could explain the observations.

As shown in Figure 8, we can not observe the emission from the v' = 11 level of the CN(A) and little from v' > 8. It is interesting to note that the energy of the v' = 10 level of the CN(A) is very close to the energy of the v' = 0 level of the CN(B). This suggests that if sufficient energy is available to internal excitation of the CN fragment, it will preferentially be partitioned to CN B state rather than being distributed into vibrationally excited A state. This may be justified on the basis of a Franck-Condon argument. The CN equilibrium distance in the ground state of the fumaronitrile is roughly the same as in the free radical. If this distance remains the same in the C_3H_2N or internal redistribution of the energy, then production of the B state will be favored if enough energy is available because its equilibrium separation is closer to ground state than the A states equilibrium distance. The cutoff in the A state distribution at v' = 8 may have the same cause.

Nishi et al. [3] found the acrylonitrile (C_3H_3N) can absorb three 193 nm photons to produce the C_2 radical. The $D_0(C_2H_3\text{-}CN)$ is 5.23 ev. In the case of $C_4H_2N_2$ molecule, one

more CN group increases the conjugation of π electrons so that the equivalent bond is stronger than that of the C_3H_3N molecule and no C_2 radical was produced at the fluence levels used.

The two photon photodissociation processes that are observed for the $C_4H_2N_2$ molecules at 193 nm can be described by three competing processes with two mechanisms. In the case of the low laser fluence, reaction (4) or (11) is the main reaction channel. The energy is partitioned into the v" = 0 and v" = 1 vibrational levels of the CN(X) state. When the laser fluence increases, the reactions (6) and (7) or (13) and (14) become more important. Energy from a second absorbed photon can partition into the internal degrees of freedom of the CN(A) and CN(B) state. The fast CN(B) --> CN(X) transition will increase the vibrational temperature of the CN ground state as shown in Fig. 2 and Fig. 4. From Fig.2 (a) the population in the v" = 2 vibrational level obviously increased. We would conclude that the two-photon excitation of the parent molecule is dominant in the laser photolysis of large molecules with a high laser power.

Acknowledgments

The authors are grateful to Dr. H. Okabe for the helpful discussion. Xioaxiang Xie and V. R. McCrary are grateful for the support under NASA grant NSG-5071. E. Pugh is grateful

for the support under NASA grant NAGW-446. Joshua B. Halpern acknowledges the support of NSF under grant CHE-82099.

Table 1: Thermochemical data used to calculate the heats of reaction of dissociative processes in the UV multiphoton dissociation of $C_4H_2N_2$.

Species	ΔH_f (ev)	Ref.
$C_4H_2N_2$	2.78	[23]
C_3H_2N	4.23	[24]
C_3HN	3.68	[25]
C_2H_2	2.36	[18]
C_4N_2	5.19	[23]
C_3N	6.21	a
HCN	1.40	[25]
CN	4.38	[25]
H	2.24	[25]

Dissociative processes	ΔH(ev)
$C_4H_2N_2$ ---> CN + C_3H_2N	5.83
$C_4H_2N_2$ ---> H_2 + C_4N_2	2.41
C_3H_2N ---> H_2 + C_3N	1.98
C_4N_2 ---> CN + C_3N	5.4 [27]
C_3H_2N ---> CN + C_2H_2	2.51
C_3H_2N ---> H + C_3HN	1.69
C_2H_2 ---> C_2 + 2H	10.80

a calculated According to the data of [27].

Reference

[1] W. M. Jackson and H. Okabe, Photodissociation Dynamics of Small Molecules, to appear in Vol.13 of the Advances in Photochemistry, (1985).

[2] M. J. Sabety-Dzvonik, R. J. Cody and W. M. Jackson, Chem. Phys. Lett., 44 (1976) 131.

[3] N. Nishi, H. Shinohara and I. Hanazaki, J. Chem. Phys., 77 (1982) 246.

[4] R. E. Connors, J. L. Roebber and K. Weiss, J. Chem. Phys., 60 (1974) 5011.

[5] H. Okabe and V. H. Dibeler, J. Chem. Phys., 59 (1973) 2430.

[6] B. E. Turner, International Astron. Circular,(1970) 2268.

[7] B. E. Turner, Astrophys. J. 163 (1971) L35; P. M. Solomon, ibid. 168 (1971) L107.

[8] G. A. West and M. J. Berry, J. Chem. Phys., 61 (1974) 4700.

[9] J. H. Ling and K. R. Wilson, J. Chem. Phys., 63 (1975) 101.

[10] W. M. Jackson, J. B. Halpern and C. S. Lin, Chem. Phys. Lett., 55 (1978) 254.

[11] W. M. Jackson and J. B. Halpern, J. Chem. Phys., 70 (1979) 2373.

[12] A. P. Baronavski and J. R. McDonald, Chem. Phys. Lett.,

56 (1978) 369.

[13] C. Fotakis, M. Martin, K. P. Lawley and R. J. Donovan, Chem. Phys. Lett., 67 (1979) 1; D. J. Kligler, H. Plummer, W. K. Bischhel and C. K. Rhodes, J. Chem. Phys., 69 (1978) 4652.

[14] J. J. Tiee, F. B. Wampler and W. W. Rice, Chem. Phys. Lett., 68 (1979) 403.

[15] N. Nishi, H. Shinohara and I. Hanazaki, Chem. Phys. Lett., 73 (1980) 473.

[16] H. K. Haak and F. Stuhl, Chem. Phys. Lett., 68 (1979) 399.

[17] D. Krahnovich, Z. Zhang, L. Butter and Y. T. Lee, J. Phys. Chem., 88 (1984) 4561; C. L. Sam and J. T. Yardley, Chem. Phys. Lett., 61 (1979) 509; F. B. Wampler, J. J. Tiee, W. W. Rice and R. C. Oldenbory, J. Chem. Phys., 71 (1979) 3926.

[18] J. R. McDonald, A. P. Baronavski and V. M. Donnelly, Chem. Phys., 33 (1978) 161.

[19] R. A. Marcus, J. Chem. Phys., 62 (1975) 1372.

[20] J. B. Halpern and W. M. Jackson, J. Phys. Chem. 86, (1982) 3528

[21] C. S. Rondestvedt, Jr, M. J. Kalm and O. Vogl, J. Amer. Chem. Soc., 78 (1956) 6115.

[22] R. L. Webb, S. Frank and W. C. Schneider, J. Amer. Chem. Soc., 77 (1955) 3491.

[23] J. A. Dean, Handbook of Chemistry, Twelfth Edition, (McGraw-Hill Book Co., New York, 1979).

[24] M. H. Yu, M. R. Levy and C. Wittig, J. Chem. Phys., 72 (1980) 3789.

[25] H. Okabe, Photochemistry of Small Molecules, (John Wiley & sons, New York, 1978).

[26] G. Herzberg, Molecular Spectra and Molecular Structure, Vol.3 (D. Van Nostrand Co., Inc., New Jersey, 1966).

[27] J. B. Halpern has measured this value which is 5.4 ± 0.2 ev using the flash lamp apparatus recently (1985).

Fig.1: The UV absorption spectrum of the $C_4H_2N_2$ molecule at room temperature. The absorption croos-section at 193 nm is $(5.7 \pm 0.6)X10^{-19}$ cm^2.

Fig.2: The LIF spectra of CN ($X\ ^2\Sigma^+$) are plotted as a function of the laser wavelength. These spectra are uncorrected for excimer and dye laser energy variations as a function of wavelength. The pressure of the fumaronitrile is 1 mtorr and delay time between pump and probe laser is 0.5 μs. (a) is a spectrum measured in the condition of ArF fluence of 24 mJ/cm^2pulse, and (b) was measured in the 4.2 mJ/cm^2pulse.

Fig.3: The relation of the LIF intensity of CN(X) radicals at 388.3 nm as a function of the excimer laser power.

Fig.4: The relative intensities of the rotational lines for the R_{00} branch are plotted assuming a Boltzmann distribution function. The quantity log(I/(N' + N" + 1)) is plotted as a function of N'(N' + 1), where N" and N' are the quantum numbers of the X and B states, respectively. The line intensities were taken from the two spectra of Fig.1 and were corrected for the variation in

power of two lasers.

T_{rot} = 2350 ± 60 K (Fig.2 (a))

T_{rot} = 1950 ± 60 K (Fig.2 (b))

Fig.5: The $CN(B^2\Sigma^+)$ ---> $CN(X^2\Sigma^+)$ emission spectrum of $C_4H_2N_2$ illuminated by the ArF laser at 193 nm. The resolution of the monochromator is 1 nm and the pressure of the $C_4H_2N_2$ is 50 mtorr.

Fig.6: The relation of the emission intensity fron the CN(B) radicals at 388.3 nm as a function of ArF laser intensity.

Fig.7: The $CN(A^2\Pi)$ ---> $CN(X^2\Sigma^+)$ emission spectrum observed in the 193 nm laser photolysis of the $C_4H_2N_2$ molecule. The resolution of the monochromator is 4 nm and the pressure of the $C_4H_2N_2$ is 10 mtorr.

Fig.8: The normalized relative population of the CN A state.

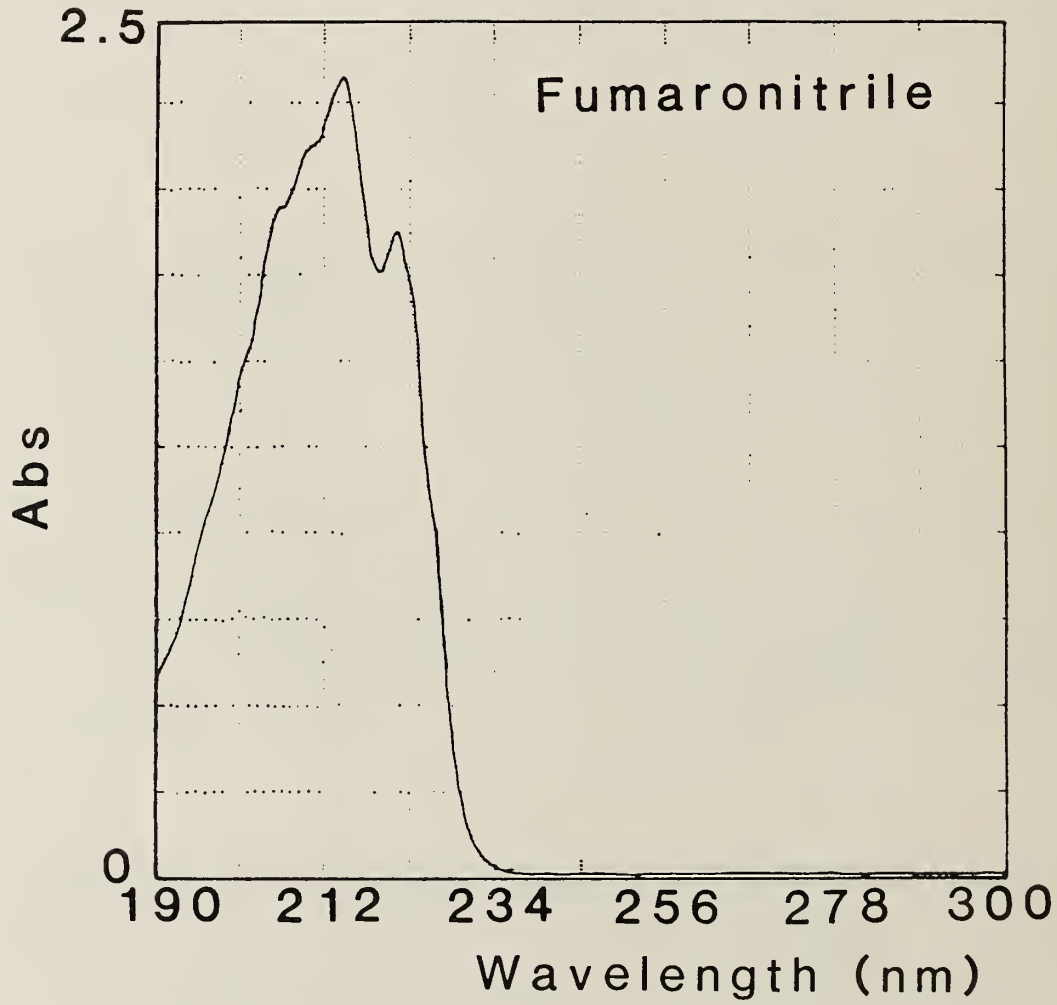

FIGURE 1

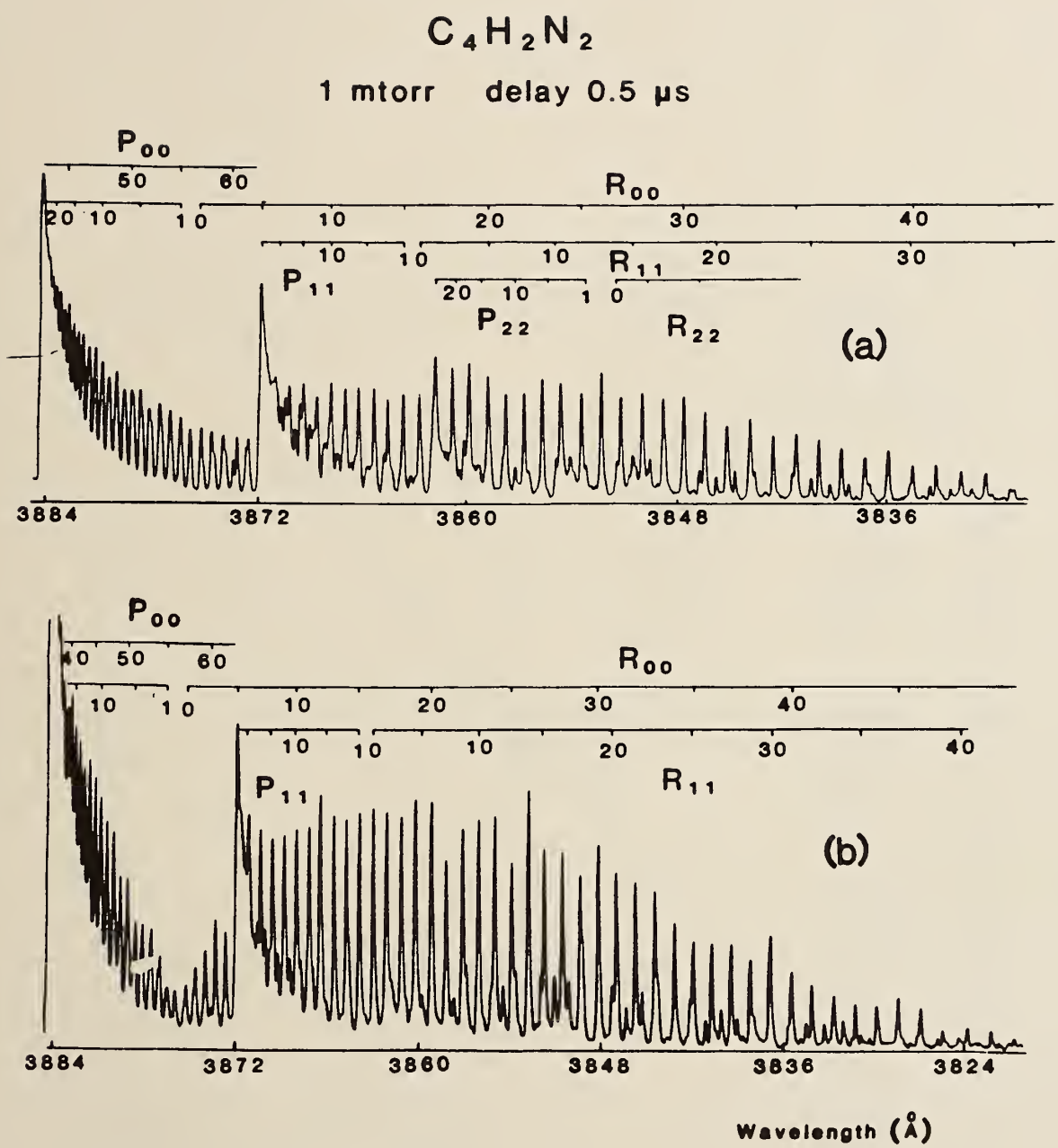
C4H2N2
1 mtorr delay 0.5 μs
Poo
50
60
20 10
10
Roo
10
20
30
40
10
10
10
R11
20
30
P11
20 10
1 0
P22
R22
(a)
3884
3872
3860
3848
3836
Poo
0 50
60
10
10
Roo
10
20
30
40
10
10
10
20
30
40
P11
R11
(b)
3884
3872
3860
3848
3836
3824
Wavelength (Å)

FIGURE 2

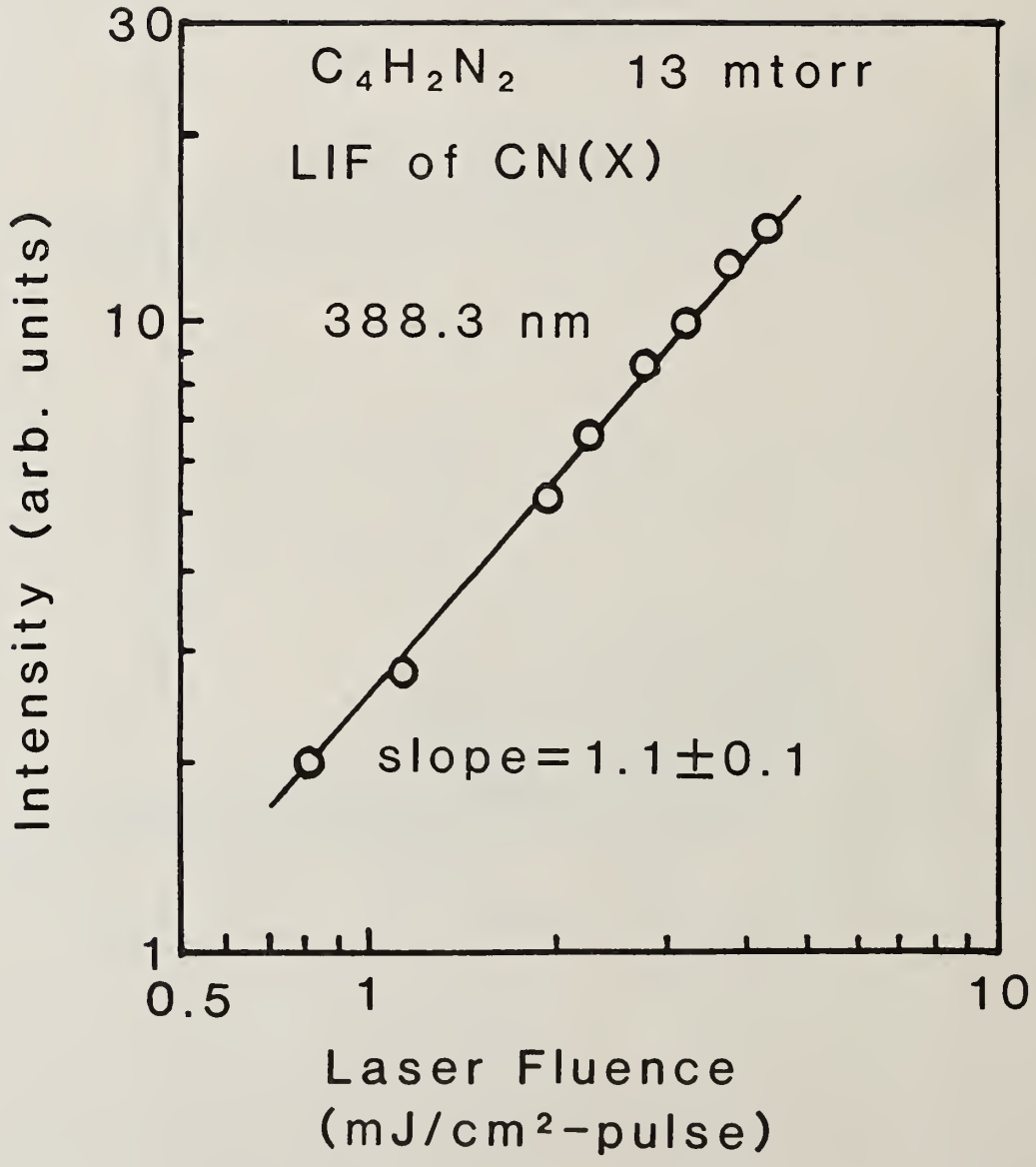
30
10
1
0.5
1
10
$C_4H_2N_2$ 13 mtorr
LIF of CN(X)
388.3 nm
slope=1.1±0.1
Intensity (arb. units)
Laser Fluence
(mJ/cm²-pulse)

FIGURE 3

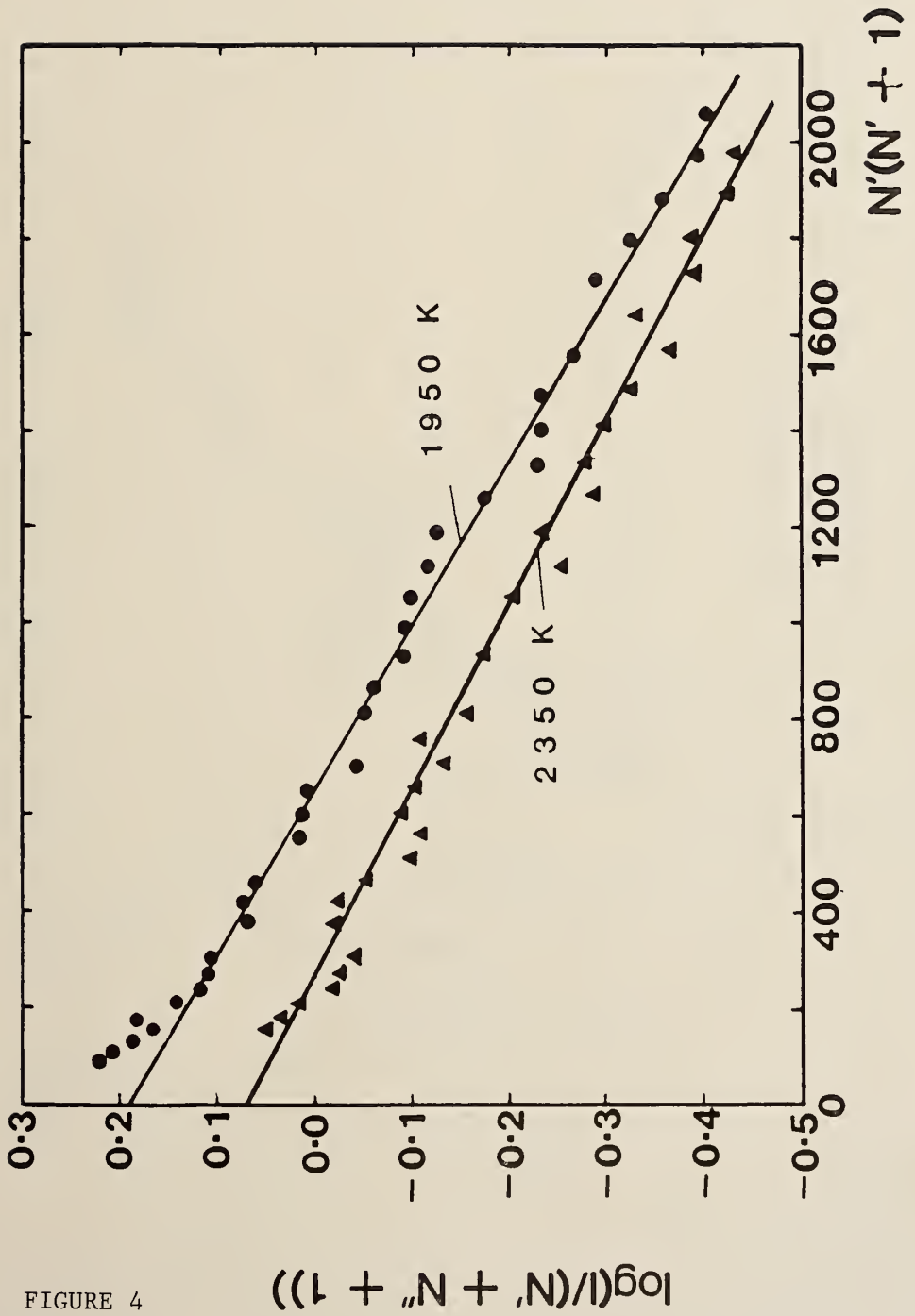
log(I/(N' + N'' + 1))
N'(N' + 1)
0·3
0·2
0·1
0·0
−0·1
−0·2
−0·3
−0·4
−0·5
0
400
800
1200
1600
2000
1950 K
2350 K

FIGURE 4

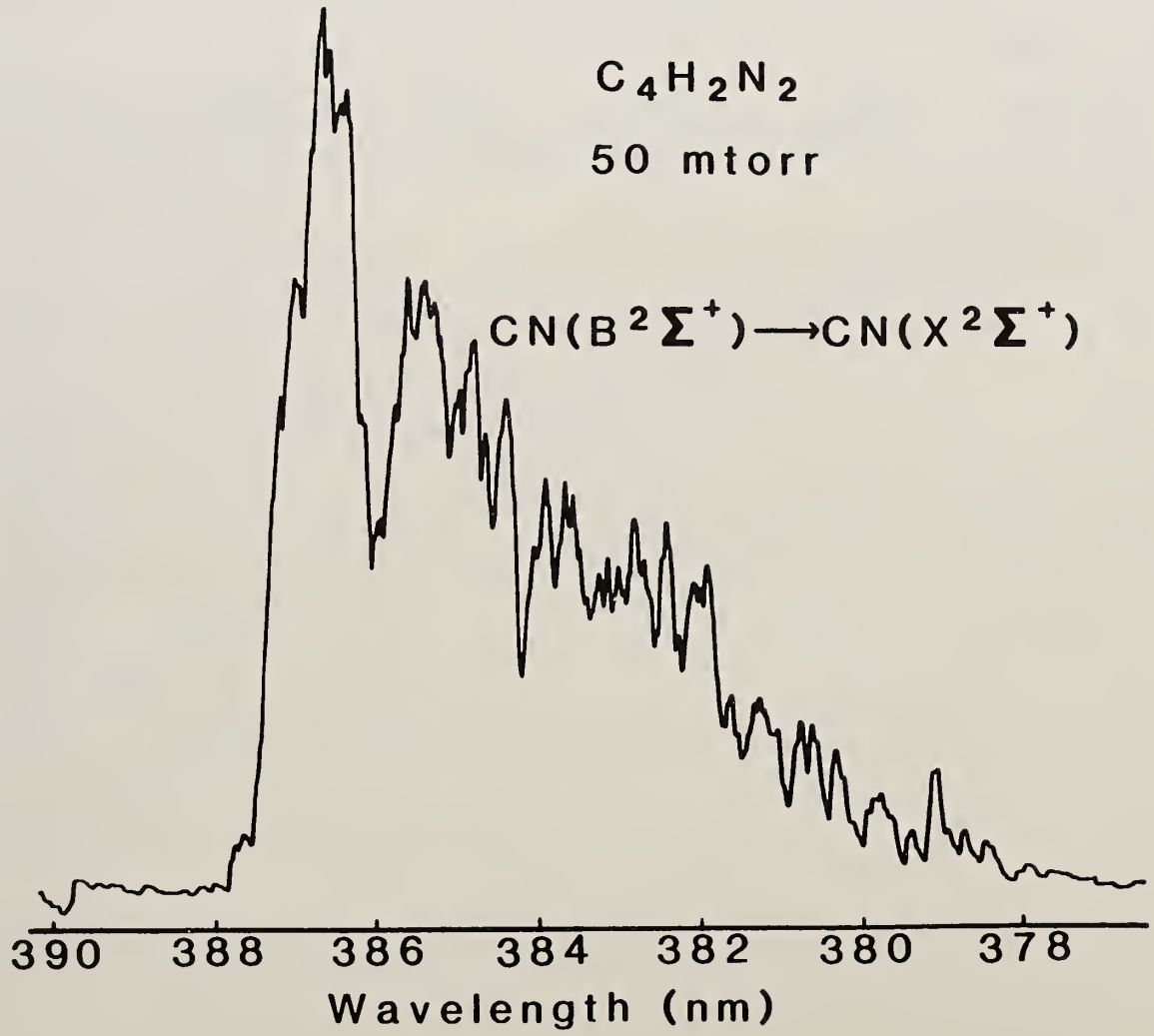
$C_4H_2N_2$
50 mtorr
$CN(B^2\Sigma^+) \longrightarrow CN(X^2\Sigma^+)$
390
388
386
384
382
380
378
Wavelength (nm)

FIGURE 5

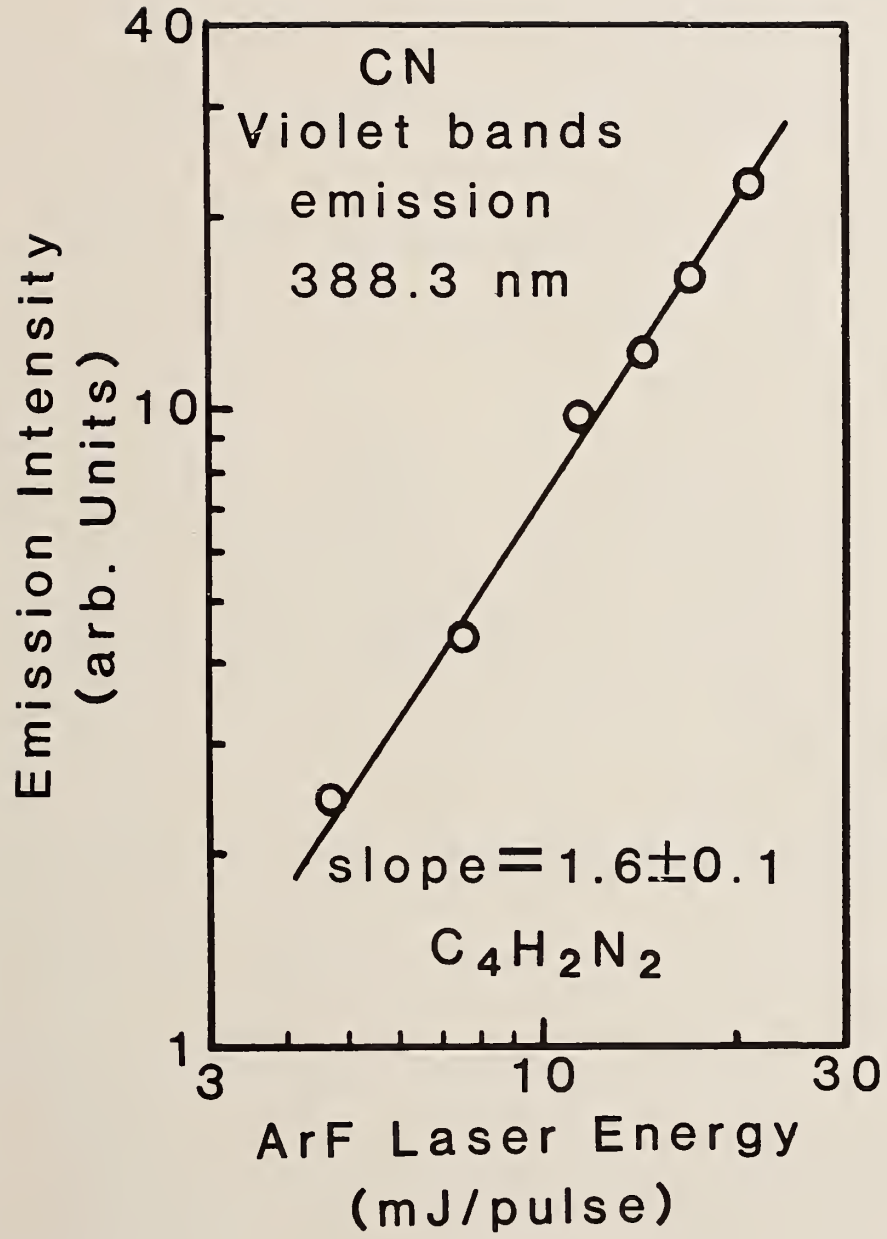
40
10
1
3
10
30
CN
Violet bands
emission
388.3 nm
slope = 1.6±0.1
$C_4H_2N_2$
Emission Intensity
(arb. Units)
ArF Laser Energy
(mJ/pulse)

FIGURE 6

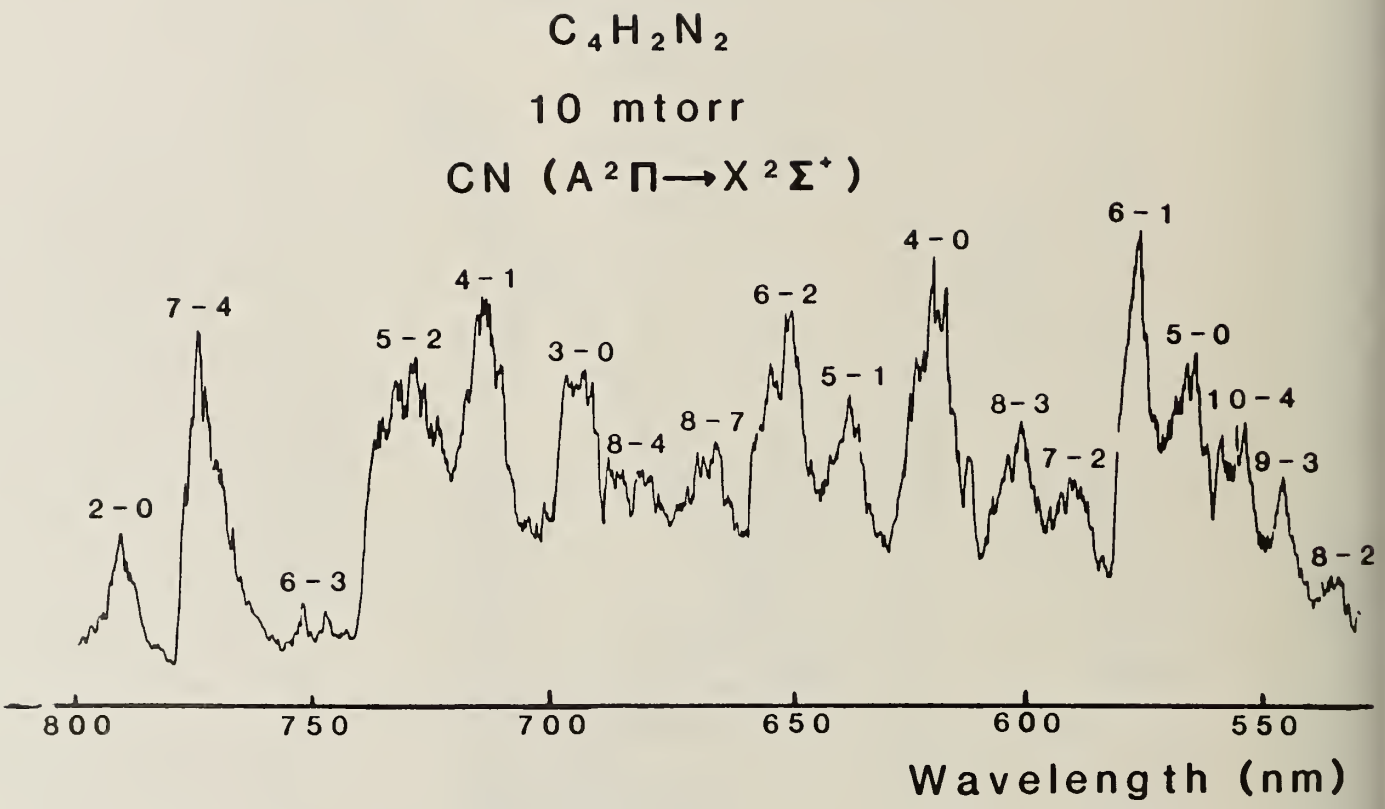
C4H2N2
10 mtorr
CN (A 2Π⟶X 2Σ+)
2 - 0
7 - 4
6 - 3
5 - 2
4 - 1
3 - 0
8 - 4
8 - 7
6 - 2
5 - 1
4 - 0
8 - 3
7 - 2
6 - 1
5 - 0
10 - 4
9 - 3
8 - 2
800
750
700
650
600
550
Wavelength (nm)

FIGURE 7

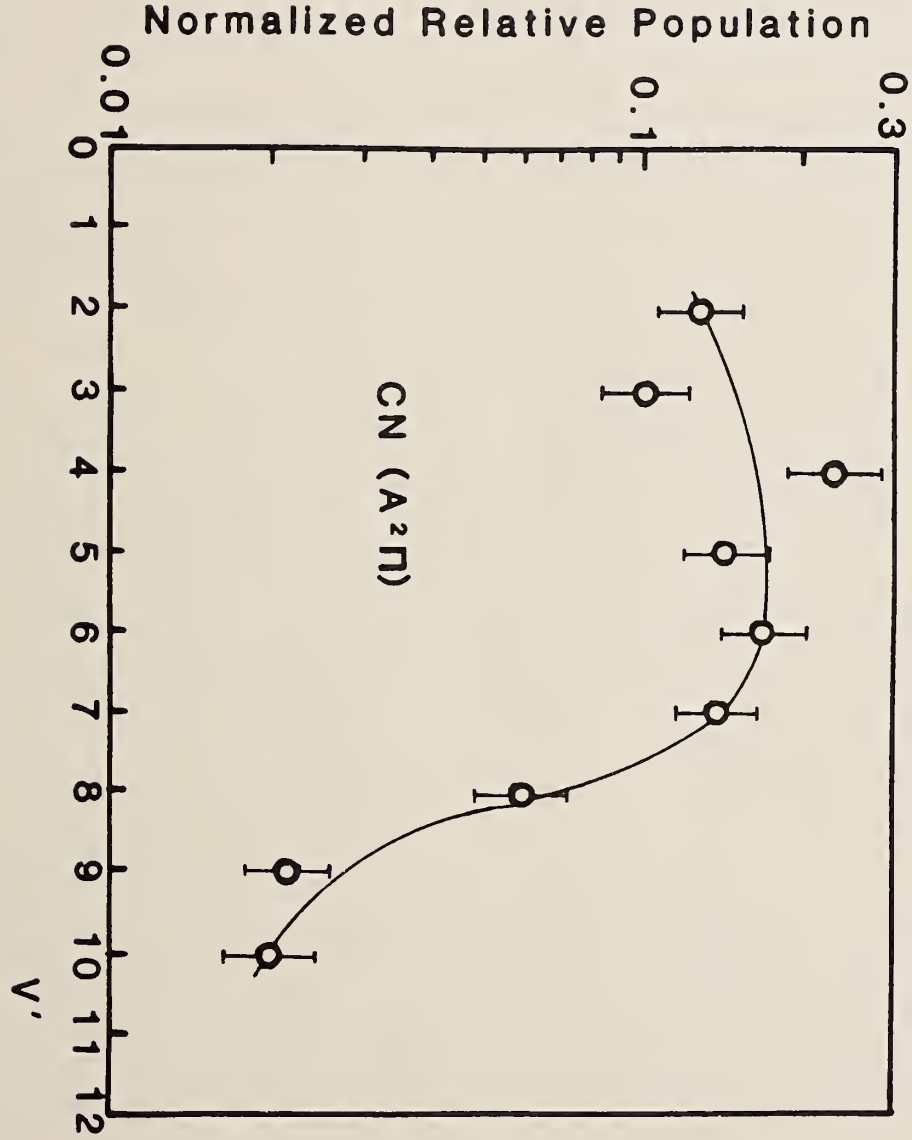
Normalized Relative Population
0.01
0.1
0.3
0
1
2
3
4
5
6
7
8
9
10
11
12
v'
CN (A²Π)

FIGURE 8

CHEMILUMINESCENCE IN THE FREE RADICAL REACTION OF SH + O_3 AND THE INTERNAL ENERGY DISTRIBUTIONS.

Yasunori Yoshimura, Toshio Kasai, and Keiji Kuwata
Department of Chemistry, Faculty of Science, Osaka University, Toyonaka, Osaka 560 Japan

Abstract

The chemiluminescence in the free radical reaction of SH + $O_3 \rightarrow HSO^*(^2A'') + O_2$ was observed using the crossed beam method, and the initial energy distributions among the internal states of the reaction product were discussed.

The vibrational bands of the emission from the elctronically exited state of $HSO^*(^2A')$ were highly broadened due to the inverted rotational distribution centered at the higher levels. The vibrational distribution centered at v=2 was found to be non-statistical. These results indicate that the reaction proceeds via direct collision.

Introduction

Sulfur containing chemical species such as hydrogen sulfide, mercaptane, and sulfric oxide are regarded to be one of the major pollutants in the atomosphere. These compounds are easily oxidezed by atomic or molecular oxygen and also by ozone.

So far, not many details have been known about mechanisms on the oxidation of these compounds. One of the reasons for this is that the sulfur atom can change its valency very easily over the range from S(I) to S(VI). Thus, complexity on the reaction mechanisms of sulfur compounds may arise from this multi-valent character of the sulfur atom. There are variety of intermediates of sulfur compounds containing hydrogen or oxygen, which are expected to be chemically active and should play an important role in the oxidation reactions.

In the reaction of H_2S with ozone, SO_2 and H_2O are obtained as the final products and possibly the intermediates known as HSO, SH, and SO may be formed during the reaction[2]. It is of great necessity to investigate directly the elementary reactions of those sulfur compounds; whether reaction intermediate is really formed or not, and in which electronic and internal states they are. In this paper, we studied the elementary reaction of SH with O_3, which is known to be one of the most important oxidation s.

In the $H_2S/O/O_3$ reaction at 1 Torr of total pressure, Schrath et al. have obseved the HSO chemiluminescence with vibrational structure in the range of 550 to 850 nm, i.e. outside the region of the SO_2 chemiluminescence which is confined to

shorter wavelengh [3]. They have assigned these structured bands to be a series of the vibrational bands of the S-O stretching of HSO and proposed the two steps of reactions.

$$H_2S + O \rightarrow SH + OH$$

$$SH + O_3 \rightarrow HSO^* + O_2$$

No direct evidence, however, for those reactions in the formation of HSO^* has been given. Tolby et al. have observed similar chemiluminescence in the oxidation of thiophene (C_4H_4S)[4]. It is expected that HSO^* formed in the reaction suffers collisional relaxation frequently under a few Torr pressures, thus the initial distribution of internal energy may not be revealed.

Recently, the HSO cemiluminescence at 1 mTorr of total pressure has been investigated in the SH/O_3 system initiated by laser irradiation[5]. Under this pressure the rotational relaxation by collision becomes less probable, thus spectral broadening resulted from high rotational temperature undergoes. They have estimated the rotational temperature of 700 K.

It is preferable to observe HSO directly in the reaction of SH with ozone under the crossed beam conditions where the initial vibrational rotational distributions are expected to be preserved.

Experimental

The experimental apparatus is schematically shown in Fig. 1.

Figure 1

The SH radicals are effused from a teflon nozzle which is placed in a forechamber and are introduced through a skimmer into a reaction chamber as a beam. Ozone molecules directly effuse into the reaction chamber and cross the SH beam at a right angle. The HSO chemiluminescence at the crossing point of the beams are observed in the direction of the third right angle. The method to obtain the SH radcals by reaction is briefly given below. The detail discussion on the reaction will be represented elsewhere[6].

Formation of the SH radical beam

$$H_2S + F \rightarrow SH + HF \quad (1)$$

The rate of reaction (1) is reported to be significantly large among a few reactions with H_2S to produce the SH radicals[7], $k_{300K} = 7.4 \times 10^{-12}$ cm^3 $molecule^{-1}s^{-1}$.

The beam intensity of SH is monitored by detecting the simultaneously obtained HF emission in the forechamber. The preparation of the ozone beam is similar to the previously reported experiment[8,9]. The reagent gases were commercially available ones and were used without further purification.

Results and discussion

$HSO(^2A'-^2A")$ emisssion spectrum

The emission spectrum in the beam reaction of SH with ozone is shown in Fig. 2.

Figure 2

The stray light of HF† (around 670 nm) from the SH nozzle

head is alredy subtructed. The SH radical beam was prepared at the flow rates of 0.5 and 0.3 μ mol s^{-1} for CF_4 and H_2S, respectively and the flow rate of ozone was 1.0 μ mol s^{-1}[10]. The background pressure raised to 1.5 X 10^{-4} Torr in the reaction chamber. The spectral resolution was 3 nm.

Unlike the already reported HSO emission spectrum in the flow methods at higher pressures[2,3,4], the broad spectrum with almost dispersed vibrational structure is characteristic.

Dependence of the emission intensity on the ozone and H_2S beam intensities

$$HS + O_3 \rightarrow HSO^* + O_2 \quad (2)$$

Suppose the chemiluminescence in Fig. 2 is resulted from HSO^* in reaction (2), the intensity of emission should exhibit linear relationship against the beam intensities(i.e. the total flow rates) of ozone and SH.

Logarithmic display of the emission intensity at 600 nm vs. the ozone beam intensity is represented in Fig. 3.

Figure 3

Approximately, first-order dependence of the emission intensity on the ozone beam appears to be obvious and this indicates that the rate of formation of HSO^* should be first order with respect to O_3. The HF emission due to reaction (1) in the forechamber provides a meaure to estimate the SH radical beam intensity. By varying the H_2S flow rate, we can adjust the SH beam intensity. Fig. 4 displays the dependence of the HSO

emission on the monitored HF emission that is regarded to be proportional to the SH beam intensity.

Figure 4

The logarithmic plot has the slop of approximately one($\sim$ 1.3) that implies first order formation of the emissive product HSO with respect to the SH radical.

It should be noted that there remains a possibility that the unreacted F atoms or H_2S in the SH beam might produce emissive products at the encounter of the ozone beam. This possibility can be denied by the experiment that the reactions F + O_3 and H_2S + O_3 did not offer any emission. In addition, we merely chang the flow rate of H_2S while the flow rate of fluorine atom is kept constant. Thus the increase in the emission intensity in reaction (2) depends solely upon the SH beam intensity.

The reaction $HF(v\leq 4) + O_3 \rightarrow HFO + O_2$ can be ruled out as the source of the chemiluminescence in question because of lack of the reaction energy released[11].

The rotationally relaxed HSO emission spectrum

It is desired to see the individual vibrational bands of HSO spectrum more clearly, so that the vibrational distribution can be obtained more precisely. Making use of narrowing effect on the vibrational bands due to collisional relaxation(simulation on this effect is discussed in the next section), more resolved spectrum of HSO was obtained in Fig. 5.

Figure 5

Experimentally, we increased the background pressure by two order of magnitude($\sim 10^{-2}$ Torr) by reducing the pumping speed of the reaction chamber. The emission intensity increased by a factor of 10. Quantitative comparison in the intensity with the previously obtaioned spectrum (see Fig. 2) is difficult, since the additional emission due to the substantial background pressure contributes with significant weight under the sub mTorr pressures. Nevertheless it may be clear qualitatively that rotational relaxation undergoes frequently, the vibrrational bands become narrower under this pressure. This resolved spectrum confirms that the series of the vibrational bands can be assigned to the S-O stretching of HSO in the $^2A'-^2A''$ transition.

The vibrational distribution of HSO

Fig. 6 shows the vibrational distribution, using the relative Franck-Condon factors obtained from the lifetimes and transition moments for the $^2A'-^2A''$ transition[3,12].

In calculating the relative populations, the peak height of each band head was used in place of the total band intensity.

Figure 6

The circles in the figure represent the result from Fig. 2, and the squres represent the result from Fig. 5. As seen easily, the two plots are very close to one another, thus we may regard

that there is no vibrational relaxation at the pressures of sub mTorr. Therefore, either of the distributions in Fig. 6 reflects the initial vibrational distribution of HSO in the title reaction.

The rotational distribution of HSO

Owing to the fact that the chemiluminescent electronic state A^2A' and the ground state X^2A' of HSO have almost similar spectroscopic constants[14], the halfwidth of each vibrational band becomes wider as K, the quantum number for rotation along S-O axis, increases.

As an example, Fig. 7 exhibits the widely dispersed rotational lines which are supposed to appear in the (030)-(000) vibrational band.

Figure 7

HSO could be excited up to v=15 of the $^2A'$ state in the SH + O_3 reacion, supposing the reaction energy is released entirely to the S-O vibrational excitation[15].

It should be noted that the resultant spectrum of many vibrational bands characterized by high rotational temperatures might become the broad spectrum in vibrational structure.

Fig. 8 demonstrates the simulated spectra at two different rotational temperatures 700 and 3000 K, in each spectrum we asusmed single rotational temperature for all vibrational states.

Figure 8

We also assumed that the all band have the same band shape as the (030)-(000) band.

Neither of the spectra in the figure was found to agree with the observed spectrum. One of the reasons for this disagreement is that in this simulation we confined the rotaional distribution as Boltzmann distribution where the contribution of the higher K levels are underestimated. It may be necessary to take non-Boltzmann distribution weighted in favour of the higher K levels. In the case of HSO, the rotational lines with higher K are widely distributed apart from its band origins and this wide distribution of the rotational lines may give the broad spectrum observed in this investigation.

Due to the fact that the rotaional and vibrational distributions of the product HSO are non-statistical, it is likely that the SH + O_3 reaction takes place under the mechanism of rather direct collision than reaction-complex formation.

In many chemical reactions, a newly formed bond can be preferentially excited while the other bonds are not excited. If this is the case, it may be concluded that the vibrational excitaion of O_2 in this reaction is unlikely. It leaves the possibility, however, as implied by Kendall that the electronic excitation of oxygen to $O_2(^1\Delta_g)$ might take place together with the HSO^* vibrational excitation to $v \leq 3$(note that the excitation above v=4 is not energetically allowed), where total spin angular

momentum is conserved.

As for the HSO^* vibrational excitation above v=4, the recoiling O_2 should stay in the electronically ground state, thus a large amount of energy must be released as the rotational excitaions of HSO^* and O_2, confined in the reversed directions of rotation to one another in order to conserve total angular momentum.

Figure captions

Fig. 1 Schematic diagram of the experimental apparatus for the HSO chemiluminescent reaction.

Fig. 2 Emission spectrum of HSO(^{2}A'-^{2}A") with the spectral resolution of 3 nm. Flow rates of F(CF_4), H_2S, and O_3 are 0.5, 0.3, and 1.5 μ mol s^{-1}, respectively.

Fig. 3 Dependence of HSO emission intensity at 600 nm on the flow rate of O_3.

Fig. 4 Dependence of HSO emission intensity at 630 nm on the intensity of HF stray light(670 nm).

Fig. 5 Emission spectrum of HSO(^{2}A'-^{2}A") with the spectral resolution of 3 nm. Flow rates of F(CF_4), H_2S, and O_3 are 0.5, 0.4, and 0.9 μ mol s^{-1}, respectively.

Fig. 6 Relative populations of vibration for HSO(^{2}A').

Fig. 7 Rotational structure of the A'(003)-A"(000) vibrational band of HSO.

Fig. 8 Spectral simulations of HSO at the rotational temperatures of 700 and 3000 K, respectively.

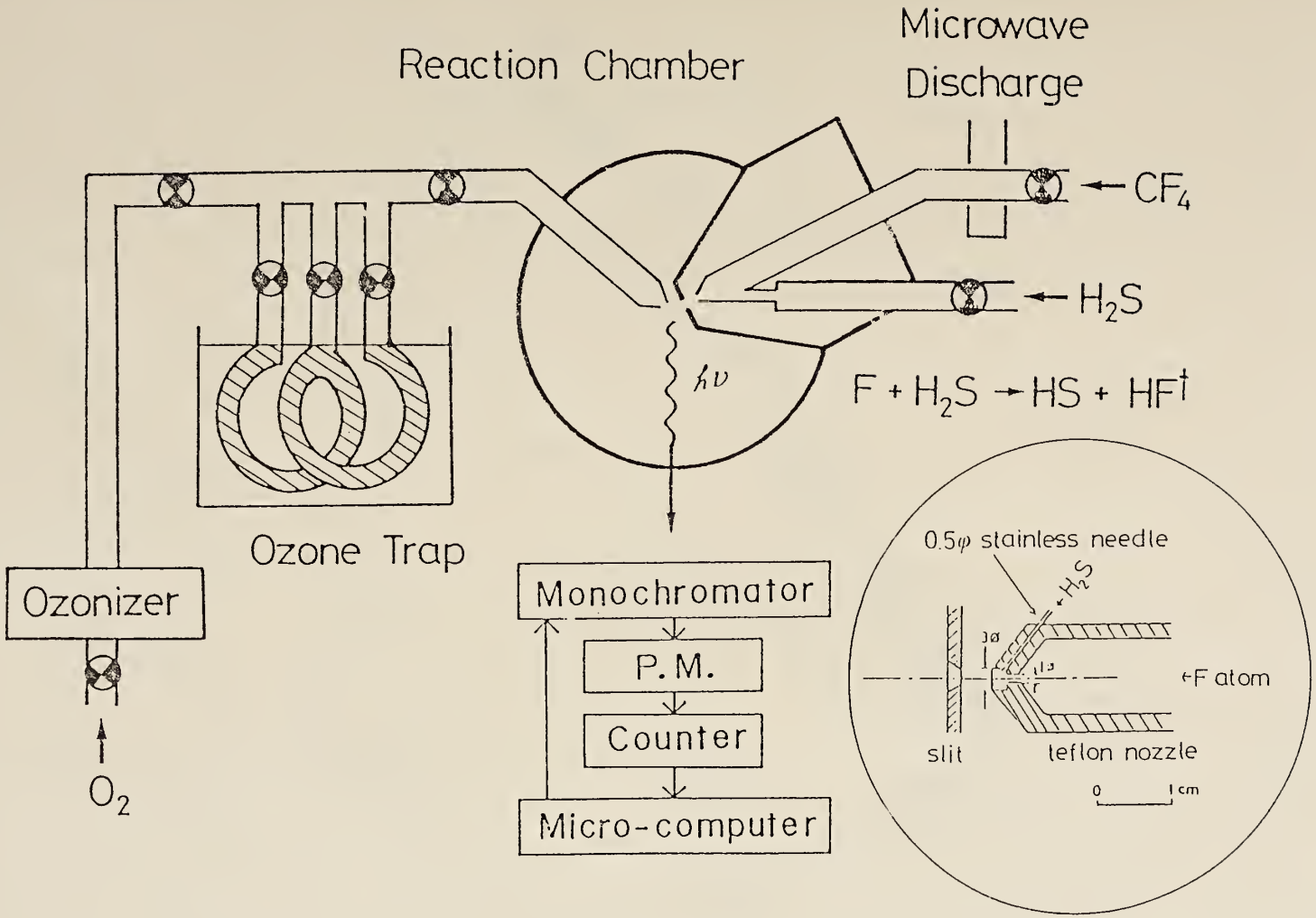
Reaction Chamber
Microwave Discharge
CF_4
H_2S
$h\nu$
$F + H_2S \rightarrow HS + HF^{\dagger}$
Ozone Trap
Ozonizer
O_2
Monochromator
P.M.
Counter
Micro-computer
0.5φ stainless needle
H_2S
3ø
1.5
F atom
slit
teflon nozzle
0
1cm

FIGURE 1

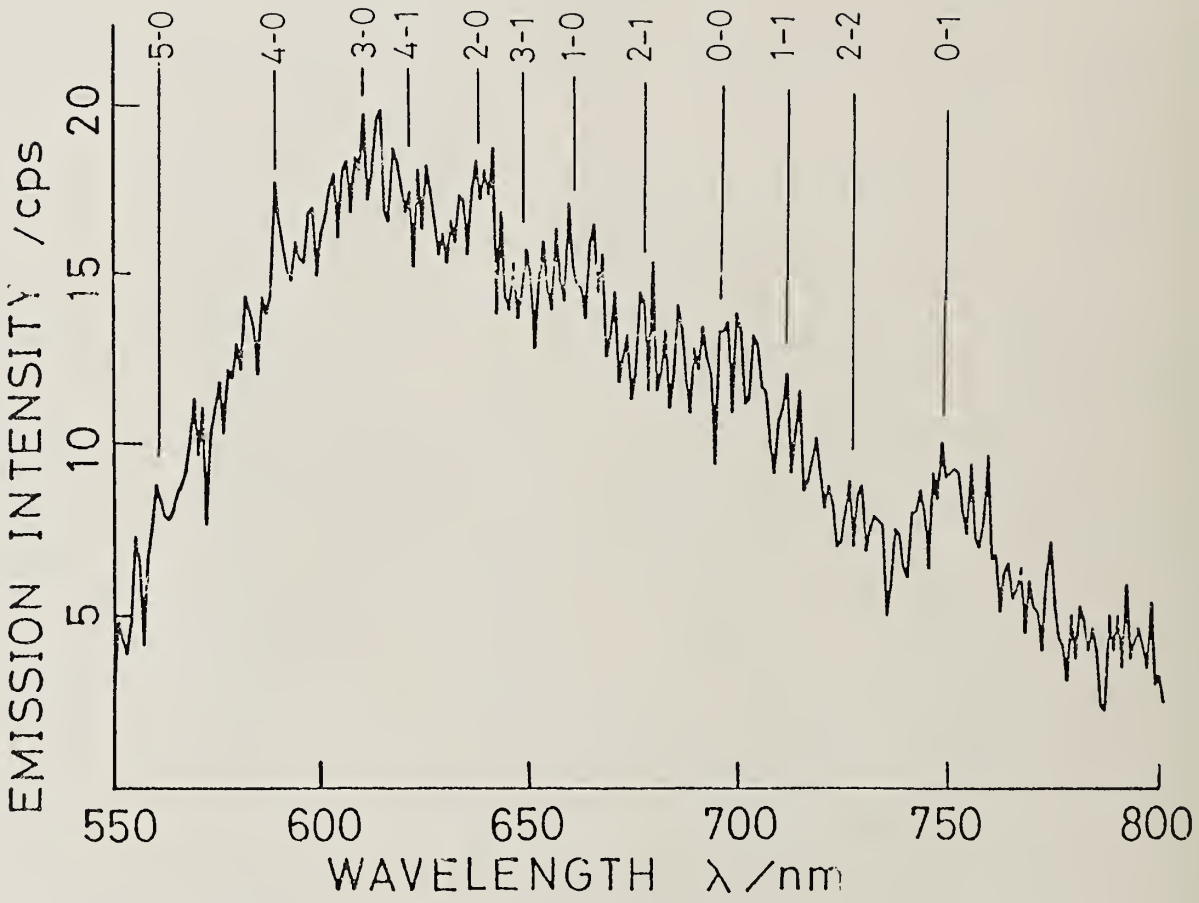
5-0
4-0
3-0
4-1
2-0
3-1
1-0
2-1
0-0
1-1
2-2
0-1
EMISSION INTENSITY /cps
5
10
15
20
550
600
650
700
750
800
WAVELENGTH λ/nm

FIGURE 2

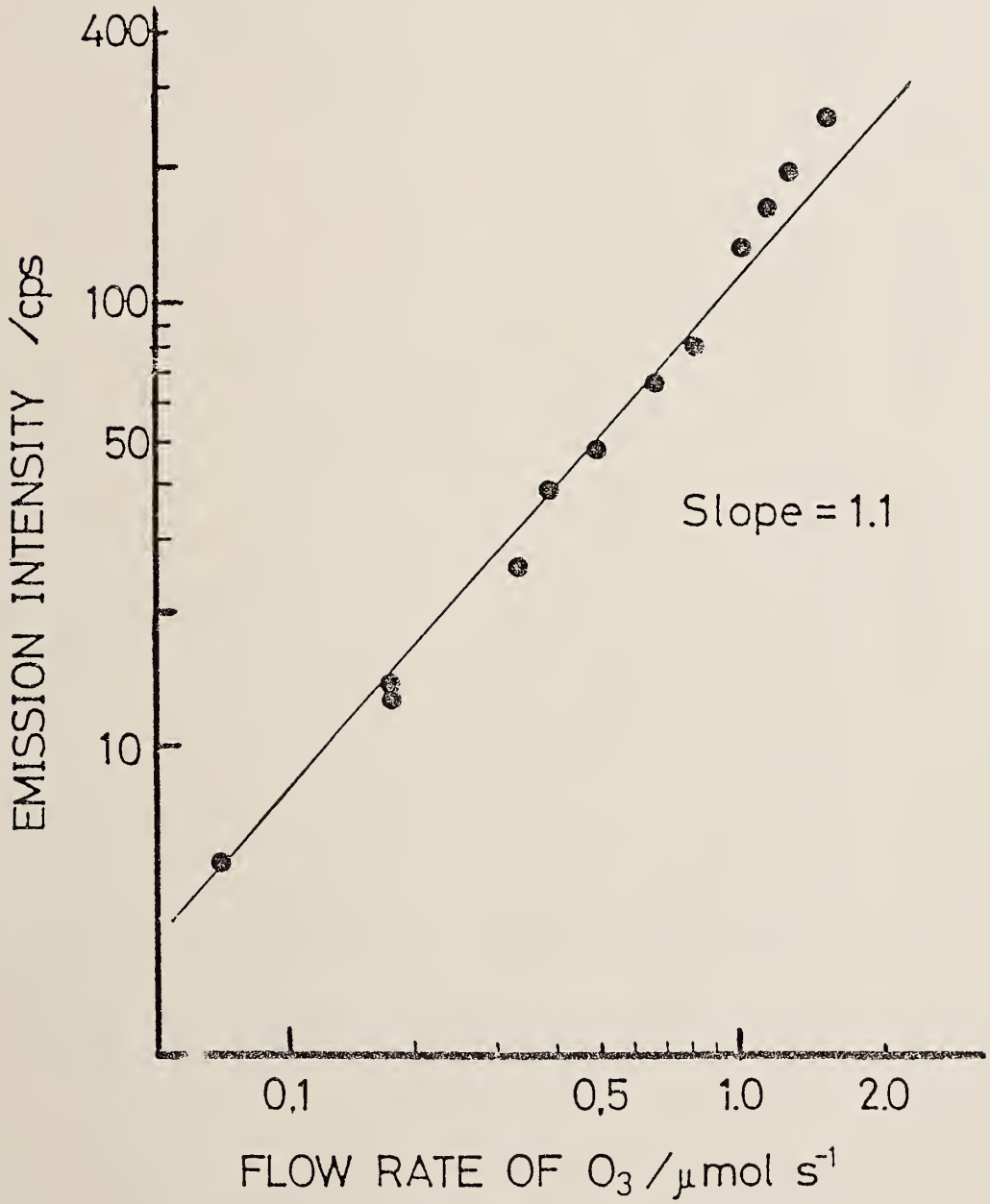
400
100
50
10
EMISSION INTENSITY /cps
Slope = 1.1
0.1
0.5
1.0
2.0
FLOW RATE OF O_3 /μmol s^{-1}

FIGURE 3

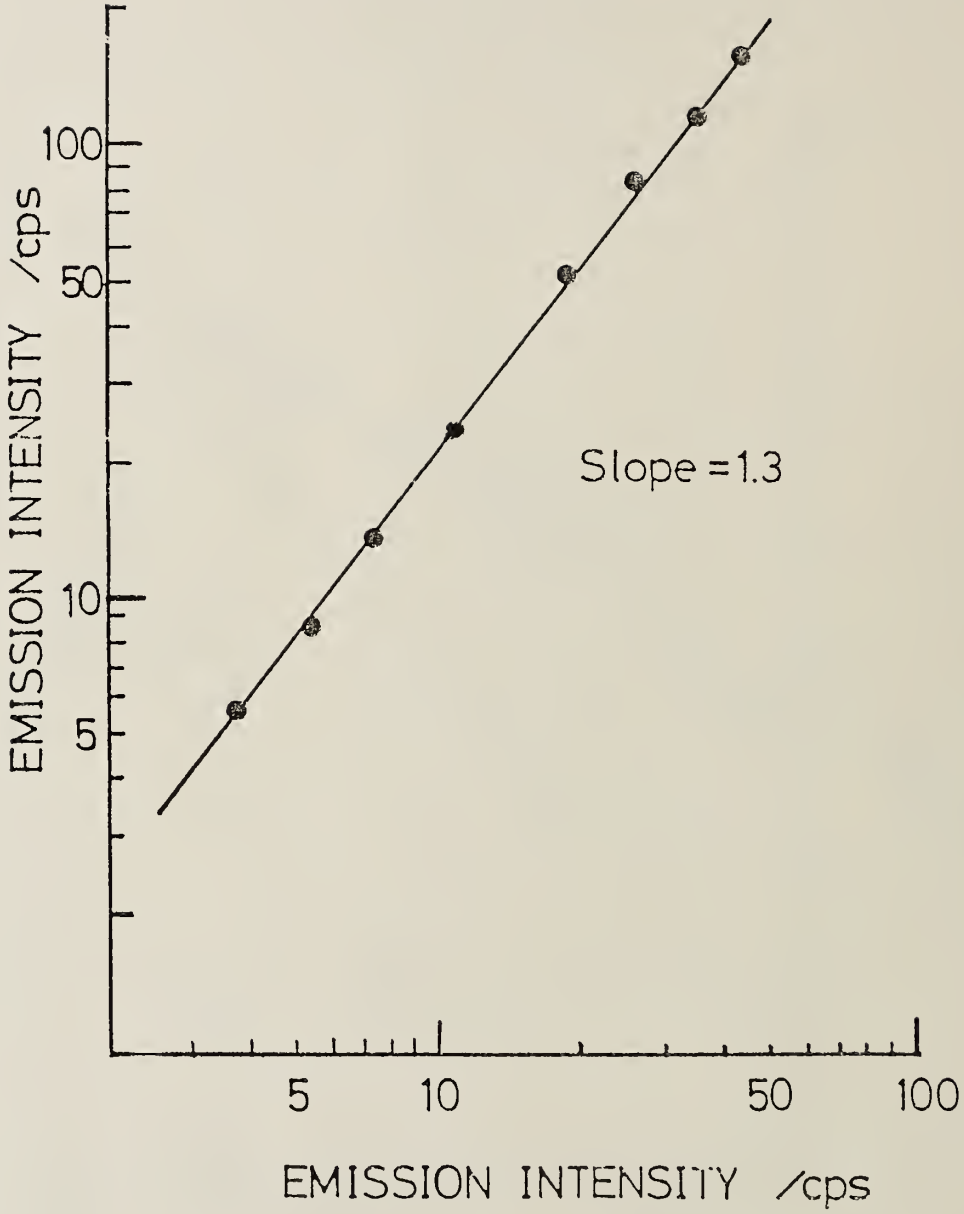
EMISSION INTENSITY /cps
100
50
10
5
Slope = 1.3
5
10
50
100
EMISSION INTENSITY /cps

FIGURE 4

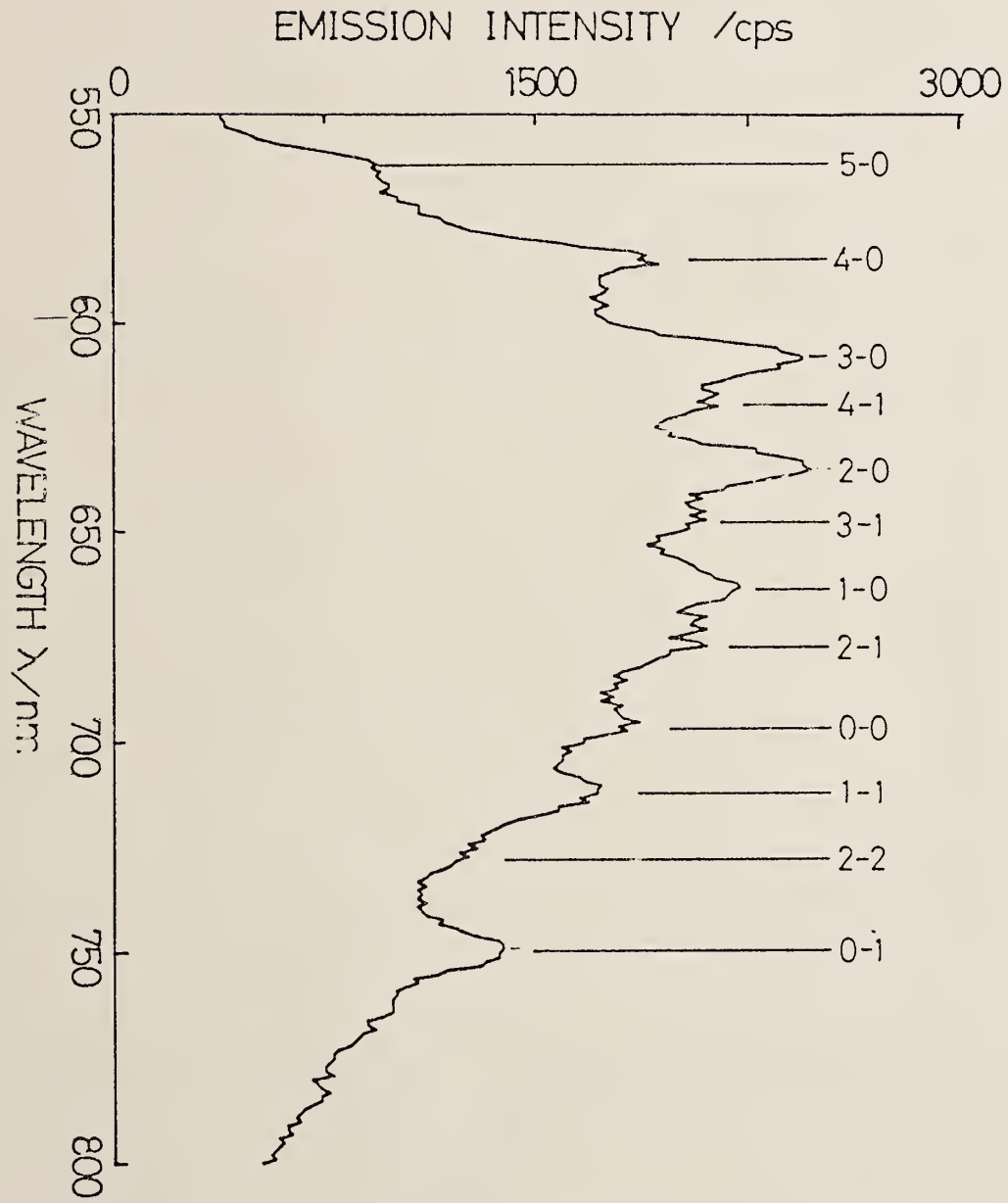
EMISSION INTENSITY /cps
0
1500
3000
550
600
650
700
750
800
WAVELENGTH λ/nm
5-0
4-0
3-0
4-1
2-0
3-1
1-0
2-1
0-0
1-1
2-2
0-1

FIGURE 5

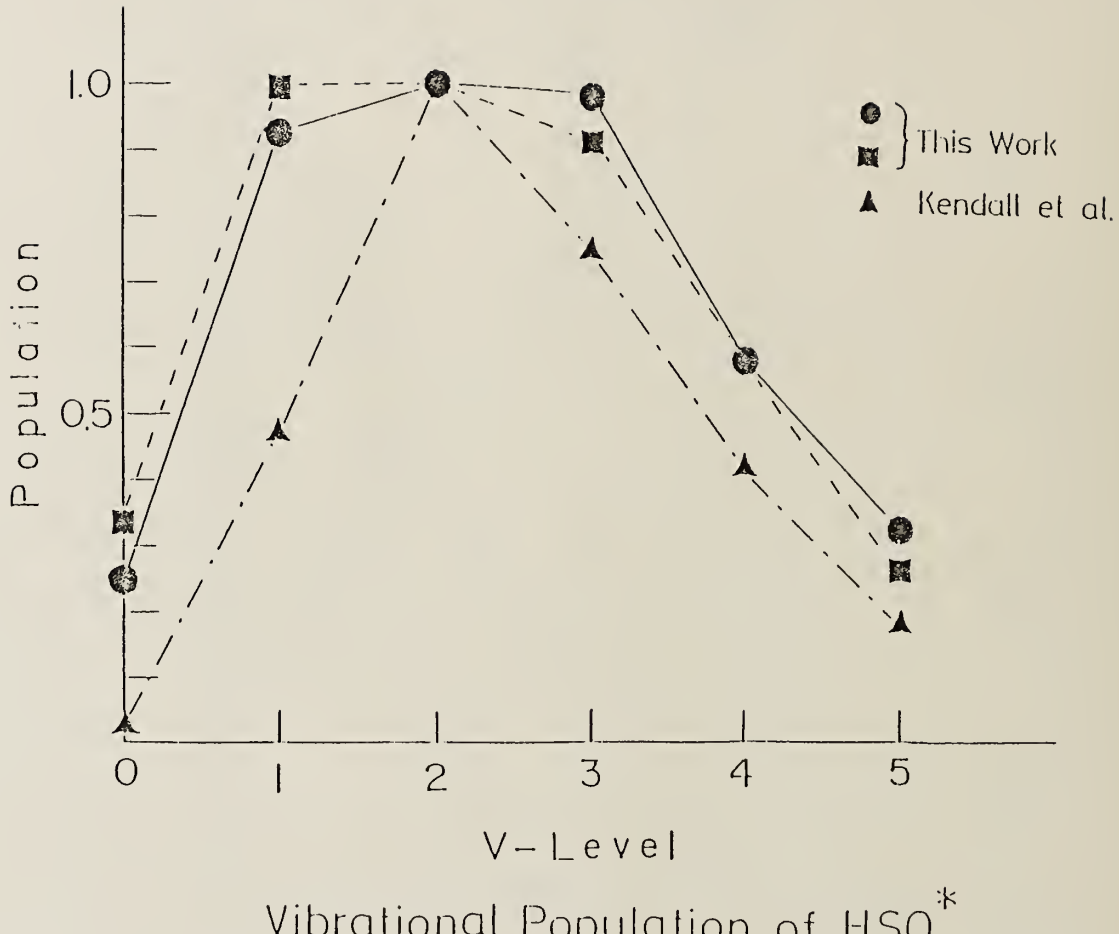
1.0
0.5
Population
0
1
2
3
4
5
V-Level
This Work
Kendall et al.
Vibrational Population of HSO*

FIGURE 6

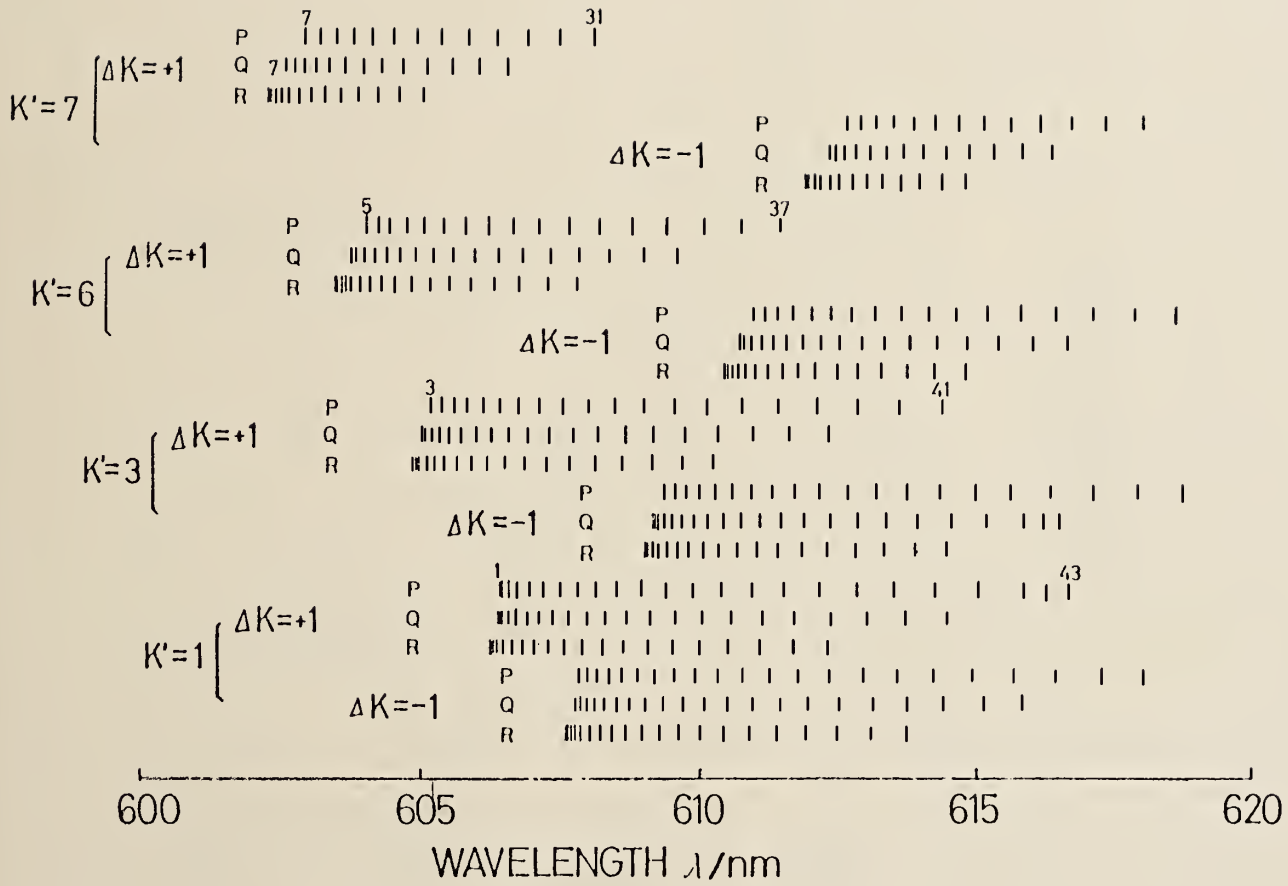
K'=7
ΔK=+1
ΔK=-1
K'=6
ΔK=+1
ΔK=-1
K'=3
ΔK=+1
ΔK=-1
K'=1
ΔK=+1
ΔK=-1
P
Q
R
7
31
5
37
3
41
1
43
600
605
610
615
620
WAVELENGTH λ/nm

FIGURE 7

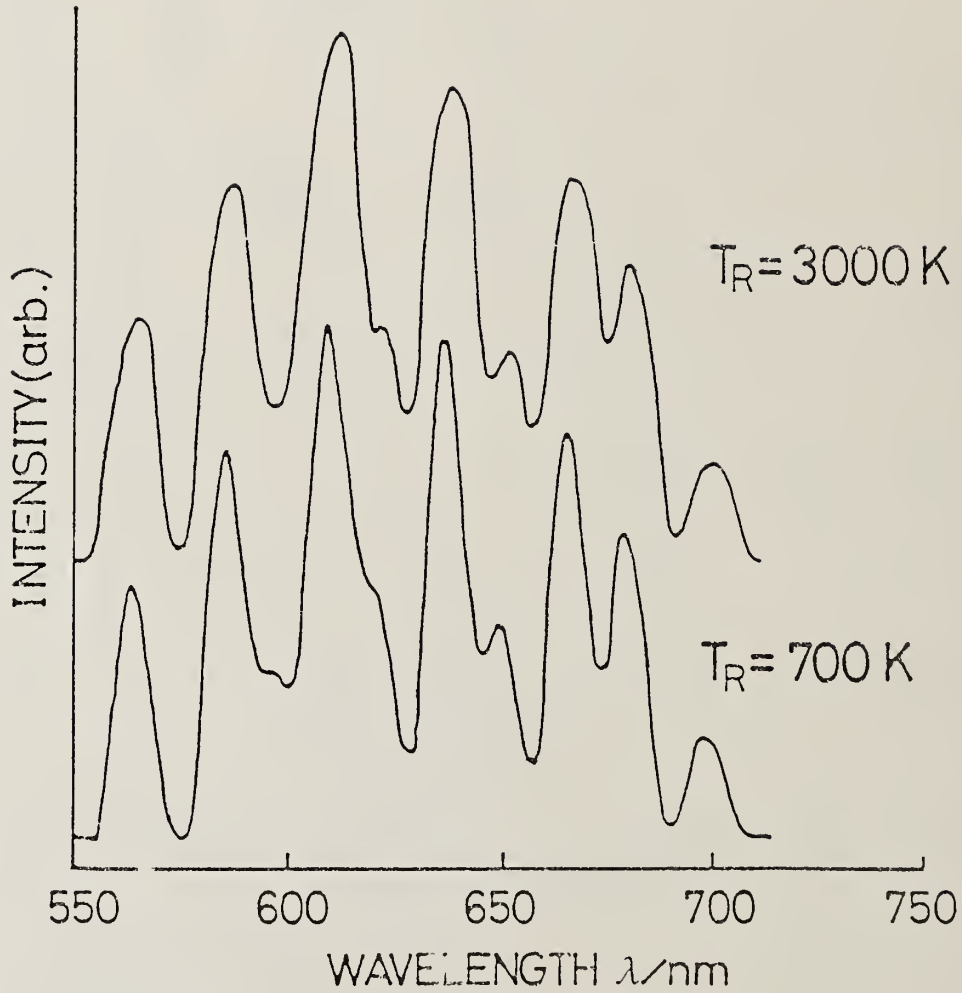
INTENSITY(arb.)
T_R= 3000 K
T_R= 700 K
550
600
650
700
750
WAVELENGTH λ/nm

FIGURE 8

References

[1] S. W. Benson, Chem. Rev., 78, 23(1978); I. R. Slagle, F. Baiocchl, and D. Gutman, J. Phys. Chem., 82, 1333(1978)

[2] S. Glavas, and S. Toby, J. Phys. Chem., 79, 779(1975)

[3] U. Schurath, M. Weber, and K. H. Becker, J. Chem. Phys., 67, 110(1977)

[4] S. Toby, F. S. Toby, and B. Kaduk, 12th International Conference on Photochemistry, Gaithersburg, Maryland Extended Abstracts 1976

[5] D. J. Kendall, J. J. A. O'brien, J. J. Sloan, and R. G. Macdonald, Chem. Phys. Lett., 110, 183(1984)

[6] Y. Yoshimura, T.Kasai, and K.Kuwata, J. Phys. Chem., in preparation.

[7] a)D. A. Whytock, R. B. Timmons, J. H. Lee, J. V. Michael, W. A. Payne, and L. J. Stief, J. Chem. Phys., 65, 2052(1976); b)M. J. Kurylo, N. C. Peterson, and W. Braun, J. Chem. Phys., 54, 943(1971); c)R. R. Friedl, Wm. H. Brune, and J, G. Anderson, J. Chem. Phys., 79, 4227(1983)

[8] H. Ohoyama, T. Kasai, Y. Yoshimura, H. Kimura, and K.Kuwata, Chem. Phys. Lett., in press.

[9] G. A. Cook, A. D. Kiffer, C. V. Klumpp, A. H. Malik, and L. A. Spence, Ozone Chemistry and Technology, Advances in Chemistry Series, ACS Staff. Ed.(American Chemical Society, Washington, D. C., 1959)

[10] A beam intensity in the text is expressed in terms of the total flow rate at the nozzle, and about one tenth of the flow is introduced into the reaction volume.

[11] H. Okabe, "Photochemistry of Small Molecules", p379, Wiley Interscience

[12] M. Kawasaki, K. Kasatani, S. Tanahashi, and H. Sato, J. Chem. Phys., 78, 7146(1983)

[13] G. Hancock, and I. W. M. Smith, Appl. Opt., 10, 1827(1971)

[14] M. Kakimoto, S. Saito, and E. Hirota, J. Mol. Spectr., 80, 334(1980)

[15] F. E. Davidson, A. R. Clemo, C. L. Duncan, R. J. Browett, J. H. Hobson, and R. Grice, Chem. Phys., 46, 33(1982)

[16] H. W. Chang, D. W. Setser, M. J. Perona, and R. L. Johnson, Chem. Phys. Lett., 9, 587(1971)

REACTION KINETICS OF OH WITH NITROMETHANE, DIMETHYLNITROSAMINE, AND 1,3,5-TRIOXANE; PHOTOLYTIC PRODUCTION OF OH FROM NITROMETHANE AT 266 NM

S.S. Zabarnick*, J.W. Fleming, A.P. Baronavski, and M.C. Lin

Chemistry Division
Naval Research Laboratory
Washington, D.C. 20375-5000

*NRL/NRC Postdoctoral Research Associate

ABSTRACT

A two-laser photolysis/LIF probe technique is employed to investigate the kinetics of the reaction of OH with nitromethane, dimethylnitrosamine, and 1,3,5-trioxane. At 296±2K, measured rate constants were: $<1 \times 10^{-14}$ cm^3s^{-1} for nitromethane, $(3.6\pm0.1) \times 10^{-12}$ cm^3s^{-1} for dimethylnitrosamine, and $(7.9\pm0.6) \times 10^{-12}$ cm^3s^{-1} for trioxane. Laser photolysis of nitromethane at 266 nm produces OH radicals in a single-photon collision-free process, with a quantum yield of 0.004±0.001.

I. INTRODUCTION

The hydroxyl radical, OH, is an important species in combustion, photochemical smog, flames, gas discharges, etc.[1,2] Its role in these processes is far from being completely understood. It can be an important chain carrier in these systems. Also, the processes that form the initial OH in combustion and smog systems is not well understood. In addition, OH has been implicated in the decomposition of energetic materials. However, the reaction of OH with nitrogen and oxygen containing organic compounds has not been well studied.

We have undertaken a study to directly measure rate constants for reaction of hydroxyl radicals with nitrogen and oxygen containing compounds in the gas phase over a wide range of temperatures. Here we report initial results for room temperature rate constants with dimethylnitrosamine, nitromethane, perdeuterated nitromethane, and 1,3,5-trioxane.

During these studies it was discovered that OH is produced directly from the photolysis of CH_3NO_2. This rather suprising result lead us to inquire as to the primary processes that form OH. Therefore, we have undertaken a study of the collision-free, single-photon photodissociation of CH_3NO_2 at 266 nm. We have spectroscopically probed the hydroxyl radical that is produced and attempted to measure a primary quantum yield for this channel.

II. EXPERIMENTAL

(a) Kinetic Studies

The kinetics of OH radical reactions have been studied using a two-laser photolysis/probe technique. The experimental apparatus is shown in Fig. 1. OH radicals were produced by the photodissociation of H_2O_2 using the fourth harmonic of a Nd^{+3}:YAG laser (Quanta-Ray) at 266 nm. The photolysis laser power was typically 1-8 mJ/pulse at 10 Hz. At an adjustable time delay after the photolysis pulse (jitter <1 us), a dye laser (Lambda Physik FL-2002) pumped at 532 nm by a doubled Nd^{+3}:YAG laser (Quanta-Ray) at 10 Hz, was frequency doubled (~100 uj/pulse) and used to excite LIF from the OH radicals on the $Q_1(2)$ rotational line at 307.99 nm of the $(A^2\Sigma - X^2\Pi)$, (0,0) vibronic band. The dye and photolysis laser beams were collinearly counterpropagated through the reaction cell.

Flourescence from the reaction zone was collected at right angles to the laser beams with quartz lenses and appropriate filters designed to pass the region around 308 nm. An RCA 31000B photomultiplier tube was used to detect the flourescence. The output of the photomultiplier was sent to a boxcar averager/ gated integrator (SRS-250) operating as a gated integrator. The output of the boxcar was digitized and stored by a laboratory minicomputer (DEC MNC 11/23). Facilities were also available to

monitor the power output of the dye and photolysis lasers by the boxcar/computer system. The computer controlled the delay between the lasers, stored the data, and was also utilized to analyze the data. Typical kinetic runs spanned time delays between -10 to 1000 us.

The reaction cell was a resistively heated Pyrex cross that has been previously described [3]. Temperatures were measured by a thermocouple that was positioned ~5 mm above the laser beams. All experiments were conducted on slowly flowing gas mixtures in order to minimize the interference by photolysis and reaction products. All reactants were diluted in Argon and stored in 20 l glass reservoirs. The H_2O_2 was introduced into the cell by an Ar bubbler. The partial pressure of H_2O_2 was typically ~40 mtorr. Pressures were measured by a capacitance manometer (MKS). The concentration of each gas was computed from the partial pressure of its mixture used in the flow. All experiments were performed at 100 torr total pressure using Ar as the bath gas.

Nominal 99% H_2O_2 from FMC was employed without purification. O_3 was produced by a Tesla coil discharge of O_2. Argon was obtained from Air Products and used without purification. CH_3NO_2 was obtained from Eastman and distilled on an auto annular spinning band column. CD_3NO_2, from Wilmad Glass Co., was used without further purification. 1,3,5-trioxane, from Aldrich, was used without purification. $(CH_3)_2NNO$ was synthesized by a well known technique [4].

(b) Photodissociation Study

The photodissociation experiments demanded a higher power laser and optical delay between the lasers to decrease the time jitter. The laser (Fig. 2) was a Quantel Datachrome 5000 (10 ns pulse width) Nd^{+3}:YAG pumped dye laser system. The Nd^{+3}:YAG laser was doubled to 532 nm; a portion of this beam was split off and doubled again to provide the 266 nm photolysis beam. The remaining 532 nm beam was used to pump the dye laser. A delay of ~10 ns was obtained between photolysis and probe laser beams by optical delay. The beams were left unfocused.

The laser beams were counterpropagated through the photolysis chamber. All experiments were conducted on "slow flows" so that reaction products did not build up for successive 10 Hz pulses. The OH was probed at the (1,0) vibrational transition of the $A^2\Sigma - X^2\Pi$ electronic transition at 281.1 nm. Flourescence was observed at >300 nm; Hoya U-28 and U-30 filters were utilized to reduce scattered laser light. The laser power of both the photolysis and probe lasers were monitored by 1P28 PMT's. An RCA 31034 PMT along with SRS-250 boxcar averagers and an IBM PC-XT computer completed the data acquisition system. Flourescence intensity studies were performed at the bandhead, ($R_1(5)$, $R_1(6)$), of the (1,0) vibrational level of OH at 281.1 nm. HNO_3 was synthesized from the reaction of H_2SO_4 with KNO_3.[5]

III. RESULTS AND DISCUSSION

(a) OH REACTION KINETICS

The LIF intensity was taken as a relative measure of the $OH(X^2\Pi)$ concentration. The LIF signal decayed exponentially as a function of delay time t after the photolysis pulse. The data were fitted by a non-linear least-squares program to the function

$$I = Ae^{-k_1 t} + B$$

where k_1 is the pseudo-first-order decay rate constant for OH due to all loss processes, i.e. reaction and diffusion out of the beam. The OH decay rate should be proportional to the concentration of added reactant gas. Second-order rate constants, k_2, for OH + reactant were obtained by linear least-squares fits to the equation

$$k_1 = k_n + k_2[\text{Reactant}]$$

where k_n is the loss rate for OH due to all other removal mechanisms including reaction (with H_2O_2) and diffusion.

As a test of the experimental apparatus, the rate constant for OH + C_2H_6 was measured as a function of temperature. Our measured rate constants were within 10% of accepted literature values [6].

(i) OH + $(CH_3)_2NNO$

In the reaction of OH + $(CH_3)_2NNO$, some photochemistry was expected at 266 nm. Under conditions of 3 mJ/pulse at 266 nm the decay of the OH radical concentration could not be adequately fit by a single exponential. The decay could be fit very nicely to a function that is the sum of two exponentials. The 266 nm beam was then attenuated to 300 uj/pulse and single exponential decays were observed, the rate coefficients are presented in Table 1. The laser was further attenuated to 100 uj/pulse, where single exponential decays were also obtained. We were limited by signal-to-noise and were not able to observe decays when the photolysis laser was attenuated to less than 100 uj/pulse.

Dimethylnitrosamine, $(CH_3)_2NNO$, exhibits an extinction coefficient of ~270 $M^{-1}cm^{-1}$ at 266 nm. As a result of this relatively large extinction coefficient, significant photodissociation is to be expected under our experimental conditions. It is believed [7] that excitation of $(CH_3)_2NNO$ into its second absorption band ($S_2(\pi\pi^*) - S_0$) results in N-N bond cleavage by process 1.

$$(CH_3)_2NNO + h\nu \longrightarrow (CH_3)_2N + NO \qquad (1)$$

As the photolysis laser power is lowered, single exponential decays are obtained. Any influence from the photodissociation

products will be smaller at lower powers. Single exponential decays were observed at 300 uJ/pulse photolysis power and lower. Data for 300 uJ/pulse photolysis is shown in Fig. 3. The rate coefficient decreases from (5.8±0.1) x $10^{-12}cm^3s^{-1}$ to (3.6±0.1) x $10^{-12}cm^3s^{-1}$ in going from 300 to 100 uj/pulse (see Table 1). Low signal to noise limited obtaining a series of rate constants at sucessively lower laser powers that would permit extrapolation to zero power, where presumably no photochemistry would occur. The second order rate plot for 100 uJ/pulse photolysis power is shown in Fig. 4. Our rate constant at 100 uj/pulse should be near the low power limit, and this result is not far from that of Tuazon et al.[8], as shown in Table 1. Thus, our direct method for OH reaction rate coefficient determination supports the relative rate method of Tuazon et al.

(ii) OH + CH_3NO_2, CD_3NO_2

The reaction of OH with nitromethane, CH_3NO_2, resulted in an OH versus time curve that initially increased up to ~20 us and subsequently decayed. CH_3NO_2 has an absorption at 266nm of ~8 $M^{-1}cm^{-1}$. The OH concentration did not decay faster with an increase in the CH_3NO_2 concentration. Thus it appears that the rate constant is $<1 \times 10^{-14}cm^3s^{-1}$, the lower limit that we are able to measure. The only literature rate constant for this reaction that we are aware of is that of Campbell and Goodman [9], who obtained $9.2 \times 10^{-13}cm^3s^{-1}$ by a relative rate

technique. These workers also measured a rate constant of 1.3 x $10^{-12}cm^3s^{-1}$ for OH + CH_3ONO. And recently, Baulch et al. [10] measured the rate coefficients of OH with a series of alkyl nitrites by discharge flow, a direct technique. They obtained 1.0 x $10^{-12}cm^3s^{-1}$ for OH + CH_3ONO, a result consistent with that obtained by the relative technique utilized by Campbell and Goodman.

In an attempt to sort out this discrepancy we looked to a second source for the generation of OH radicals. The photolysis of O_3 in the presence of H_2O produces OH by the following reactions.

$$O_3 + h\nu(266nm) \longrightarrow O(^1D) + O_2 \qquad (2)$$

$$O(^1D) + H_2O \longrightarrow 2OH \qquad (3)$$

Ozone has a very large extinction coefficient at 266 nm (~2440 $M^{-1}cm^{-1}$) so that we should be able to attenuate to a photolysis laser power where CH_3NO_2 photolysis is negligible. In all cases no increase in the OH decays were observed when CH_3NO_2 was added to the system. Additionally, we attempted to measure the rate coefficient for OH + CD_3NO_2; once again, only an upper limit could be obtained. Since our results for OH + CH_3NO_2 are reproducible for two different OH sources, the slow rate obtained is difficult to reconcile with the result of Campbell and Goodman.

Assuming the OH + CH_3ONO rate constant of Campbell and Goodman and that of Baulch et al. are correct, it is difficult to

reason that the OH + CH_3NO_2 rate constant would be two orders of magnitude lower. Our experimentally measured rate constant would be low if OH radicals are being regenerated subsequent to the OH + CH_3NO_2 reaction. As a consequence of the OH + CD_3NO_2 results, a system in which OH could not be regenerated from the reactant, the sole explanation is that somehow OH is regenerated from H_2O_2. Obviously, more work needs to be performed to confirm the OH + CH_3NO_2 rate coefficient.

(iii) OH + 1,3,5-TRIOXANE

The reaction

$$OH + 1,3,5\text{-trioxane} \longrightarrow \text{products} \qquad (4)$$

has not been previously measured in the gas phase. We obtained a rate coefficient of $k = (7.9 \pm 0.6) \times 10^{-12} cm^3 s^{-1}$ at room temperature. Temperature studies are now in progress in our lab so that the Arrhenius parameters for reaction 4 can be determined.

(b) PHOTODISSOCIATION OF NITROMETHANE

CH_3NO_2 (550 mtorr) was photolyzed with 266 nm radiation and the intensity of the LIF signal from OH was monitored. The 266 nm laser radiation was varied from 1.6 to 18 mJ/pulse; the results are plotted on a log-log scale in Fig. 5. The least-squares slope of the line is 1.1±0.1, where the uncertainty

is 1σ. This plot indicates that the OH radicals produced are probably generated in a single-photon process.

An excitation spectrum of OH obtained by photolysis of 400 mtorr of CH_3NO_2 over the wavelength range 281-285 nm is shown in Fig. 6. The time delay between photolysis and probe lasers was ~10 ns. OH signals were observed at CH_3NO_2 pressures as low as 100 mtorr. Thus under these conditions, where collisions should not be important, our observations support that OH is likely produced from a primary photodissociation step in a single-photon process. Analysis of the rotational branches of the excitation spectrum by plotting log[I(J)/B(J)(2J+1)] versus the rotational energy is shown in Fig. 7. I(J) is the LIF signal intensity for rotational line J, B(J) is the Einstein coefficient for the transition from Dimpfl and Kinsey [11], and 2J+1 is the degeneracy. The rotational energies are from Dieke and Crosswhite [12]. The plot yields a rotational "temperature" of 1447±227K for the nascent OH that is produced. This is much hotter than the OH produced in the photodissociation of 2-nitro propane at 249 nm [13]. 2-nitropropane photodissociation can occur through the formation of a five-membered ring, which can then yield OH radicals readily. The process that gives OH in CH_3NO_2 photodissociation cannot be as easily explained. The formation of a four-membered ring is possible but seems unlikely. The hotter rotational "temperature" of OH from CH_3NO_2 at 266 nm indicates that a very different process occurs than in the 2-nitropropane system. There are several possible pathways

for CH_3NO_2 photodissociation at 266 nm [14]. However, the energetics of an OH producing path is very uncertain. The formation of OH in the photolysis of CH_3NO_2 has not, to our knowledge, been previously reported or proposed. This interesting route must now be considered as a possible pathway that generates OH radicals in the thermal decomposition of CH_3NO_2.

In an effort to assess the importance of the OH channel, CH_3NO_2 was photolyzed as a function of pressure while the LIF intensity was monitored. This was also performed for nitric acid, HNO_3. The photolysis of HNO_3 apparently yields OH + NO_2 with a quantum yield of unity in the region 200 to 300 nm [15]. LIF intensity versus pressure plots can be utilized to determine the quantum yield for the OH production pathway in the photodissociation of CH_3NO_2 by the following equation:

$$\Phi^{NM} = \frac{I^{NM} \in^{REF} C^{REF} \Phi^{REF}}{I^{REF} \in^{NM} C^{NM}}$$

where Φ^A is the quantum yield of OH for molecule A, I^A is the observed LIF intensity for concentration of molecule A, C^A, and $\in^A$ is the extinction coefficient of molecule A. NM is nitromethane and REF is the reference molecule , in this case HNO_3. The plots that yield I/C are shown in Fig. 8. Good straight line fits are obtained with intercepts equal to zero.

Using the extinction coefficients in Calvert and Pitts [16] for CH_3NO_2 and the extinction coefficients of Johnston and Graham [5] for HNO_3 give a quantum yield of 0.004±0.001 for the production of OH radicals in the photodissociation of CH_3NO_2 at 266 nm in the gas phase.

IV. CONCLUSION

This paper has presented laser photolysis/LIF probe kinetics and photodissociation studies in order to measure the room temperature reaction rate coefficients of OH with certain reactants whose properties, including containing NO or NO_2 groups, make them relevant or important in the study of energetic materials. Most of the systems studied exhibit some absorption at the photolysis laser wavelength, 266 nm, so that details of their photochemistry had to be considered. In this work these systems included 1,3,5-trioxane, dimethylnitrosamine, and nitromethane.

Trioxane photolysis is negligible at the photolysis wavelength so that determination of the rate coefficient is straightforward. Even at low photolysis laser powers, dimethylnitrosamine experiments resulted in dramatic non-single exponential behavior in first order decay plots so that only severe attenuation of the photolysis laser power produced reliable first order decay rates. Our results for OH + nitromethane indicate an

upper limit of $k = 1 \times 10^{-14}$ $cm^{-3}s^{-1}$. This is supported by work at different photolysis laser powers, with two different OH sources, and by the result for the reaction of OH with CD_3NO_2. However, our rate coefficient is two orders of magnitude lower than a result from an indirect method. The production of OH from CH_3NO_2 photolysis was investigated and is believed to be a prompt, single-photon process. Although the rotational distribution for OH indicates a "temperature" of 1447K, an exact mechanism and the energetic pathway for production are still under investigation.

REFERENCES

1. J.N. Bradley, "Flame and Combustion Phenomena," Methuen, London, 1969.

2. J. Heicklen, "Atmospheric Chemistry," Academic Press, New York, 1976.

3. D. Gutman, N. Sanders and J.E. Butler, J. Phys. Chem. 86 (1982) 66.

4. W.E. Bull, J.A. Seaton and L.F. Audrieth, J. Am. Chem. Soc. 80 (1958) 2516.

5. H. Johnston and R. Graham, J. Phys. Chem. 77 (1973) 62.

6. F.P. Tully, A.R. Ravishankara and K. Carr, Int. J. Chem. Kin. 15 (1983) 1112.

7. G. Geiger, H. Stafast, U. Bruhlmann and J.R. Huber, Chem. Phys. Lett. 79 (1981) 521.

8. E.C. Tuazon, W.P.L. Carter, R. Atkinson, A.M. Winer, and J.N. Pitts Jr., Environ. Sci. Tech. 18 (1984) 49.

9. I.M. Campbell and K. Goodman, Chem. Phys. Lett. 36 (1975) 382.

10. D.L. Baulch,I.M. Campbell and S.M. Saunders, Int. J. Chem. Kin. 17 (1985) 355.

11. W.L. Dimpfl and J.L. Kinsey, J. Quant. Spec. Rad. Trans. 21 (1979) 233.

12. G.H. Dieke and H.M. Crosswhite, J. Quant. Spec. Rad. Trans. 2 (1962) 97.

13. G. Radhakrishnan, T. Parr and C. Wittig, Chem. Phys. Lett. 111 (1984) 25.

14. L.J. Butler, D. Krajnovich, Y.T. Lee, G. Ondrey and R. Bersohn, J. Chem. Phys. 79 (1983) 1708.

15. H. Okabe, "Photochemistry of Small Molecules," Wiley, New York, 1978, p. 315.

16. J.G. Calvert and J.N. Pitts Jr., "Photochemistry," Wiley, New York, 1966, p. 454.

TABLE 1 Kinetic Data for OH Reactions at 296±2K

Reactant	Photolysis Laser Power	Rate Constant($cm^3 s^{-1}$)	Reference
1,3,5-trioxane		$(7.9\pm0.6) \times 10^{-12}$	this work
$(CH_3)_2NNO$	300 uJ/pulse	$(5.8\pm0.1) \times 10^{-12}$	this work
$(CH_3)_2NNO$	100 uJ/pulse	$(3.6\pm0.1) \times 10^{-12}$	this work
$(CH_3)_2NNO$		$(3.0\pm0.4) \times 10^{-12}$	[8]
CH_3NO_2		$< 1.0 \times 10^{-14}$	this work
CH_3NO_2		$(9.2\pm1.0) \times 10^{-13}$	[9]
CD_3NO_2		$< 1.0 \times 10^{-14}$	this work

FIGURE CAPTIONS

Fig. 1 Experimental apparatus for the kinetics experiments.

Fig. 2 Experimental apparatus for the photodissociation experiments.

Fig. 3 First order decay; semi-log plot of LIF signal vs. time for dimethylnitrosamine.

Fig. 4 Second order plot; plot of k_1 vs. concentration of dimethylnitrosamine.

Fig. 5 Log-log plot of LIF signal intensity vs. photolysis laser power for nitromethane.

Fig. 6 Excitation spectrum of OH, (1,0) band, produced in the photolysis of 400 mtorr nitromethane (10 ns delay).

Fig. 7 Semi-log plot of I(J)/B(J)(2J+1) vs. rotational energy for Q_1, Q_2, R_1, R_2 branches of OH.

Fig. 8 Plot of LIF intensity vs. HNO_3 and CH_3NO_2 pressure.

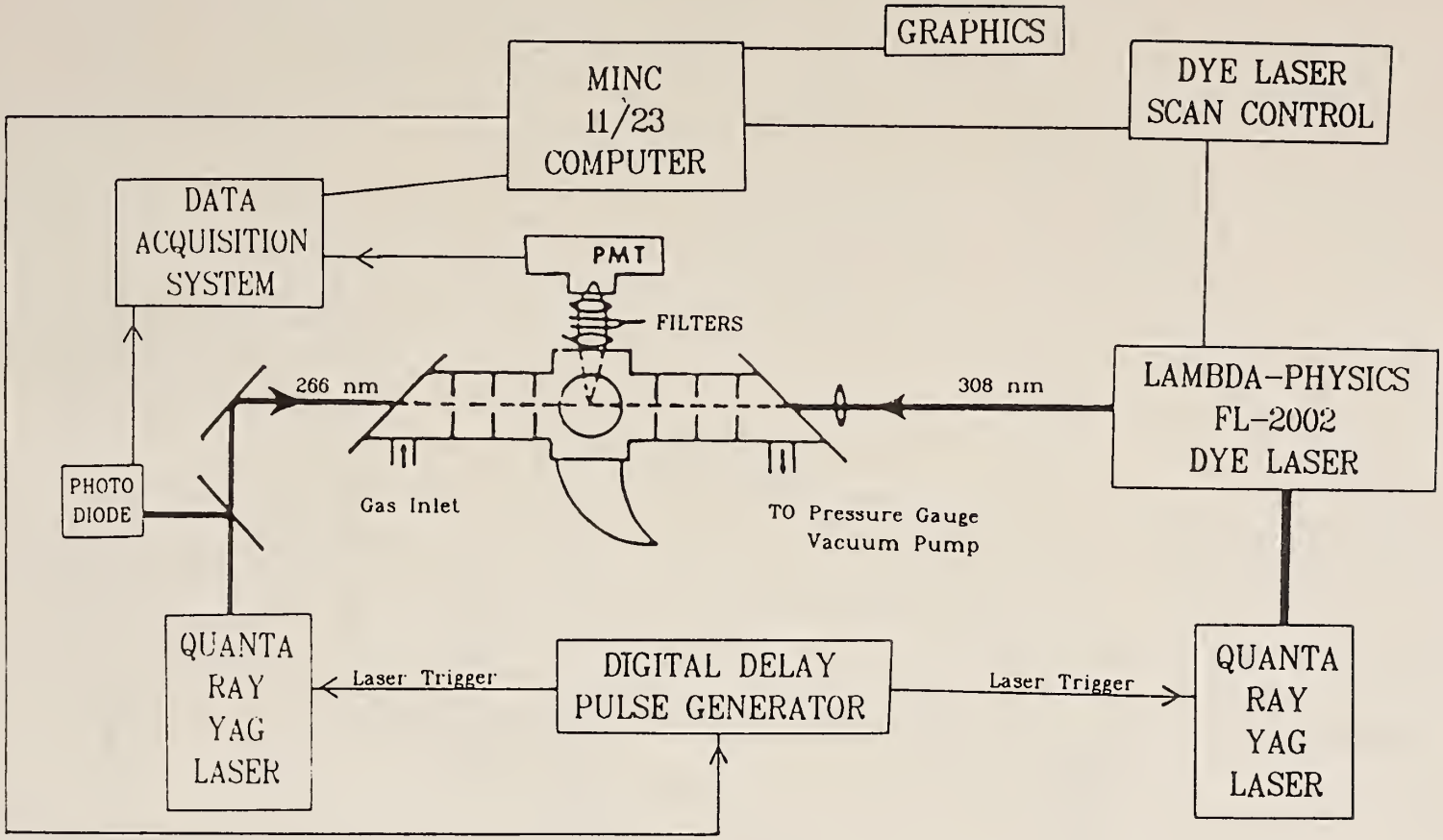
GRAPHICS
MINC
11/23
COMPUTER
DYE LASER
SCAN CONTROL
DATA
ACQUISITION
SYSTEM
PMT
FILTERS
266 nm
308 nm
LAMBDA-PHYSICS
FL-2002
DYE LASER
PHOTO
DIODE
Gas Inlet
TO Pressure Gauge
Vacuum Pump
QUANTA
RAY
YAG
LASER
Laser Trigger
DIGITAL DELAY
PULSE GENERATOR
Laser Trigger
QUANTA
RAY
YAG
LASER

FIGURE 1

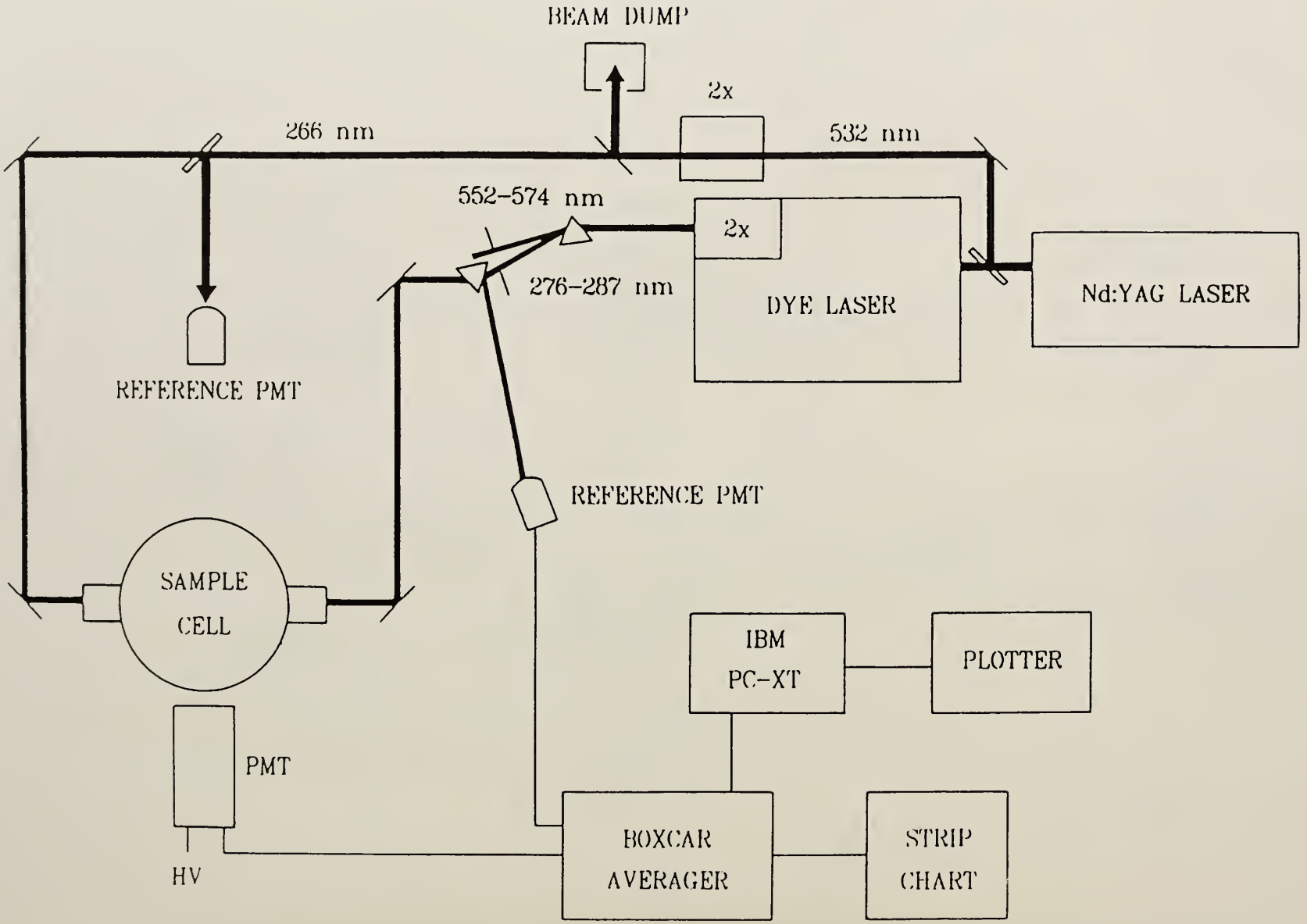
BEAM DUMP
2x
266 nm
532 nm
552-574 nm
2x
276-287 nm
DYE LASER
Nd:YAG LASER
REFERENCE PMT
REFERENCE PMT
SAMPLE
CELL
IBM
PC-XT
PLOTTER
PMT
HV
BOXCAR
AVERAGER
STRIP
CHART

FIGURE 2

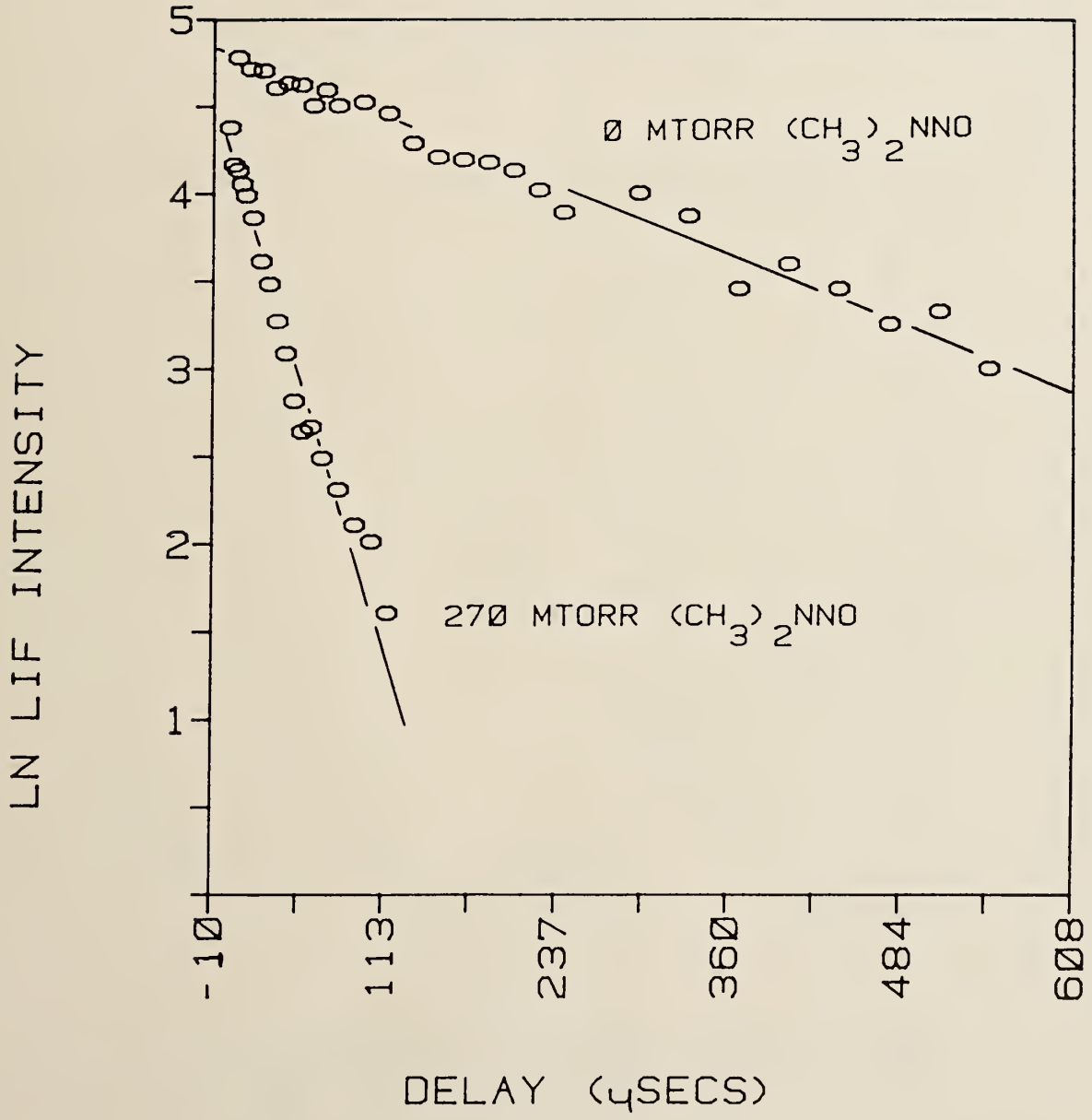
LN LIF INTENSITY
5
4
3
2
1
Ø MTORR (CH3)2NNO
270 MTORR (CH3)2NNO
-10
113
237
360
484
608
DELAY (μSECS)

FIGURE 3

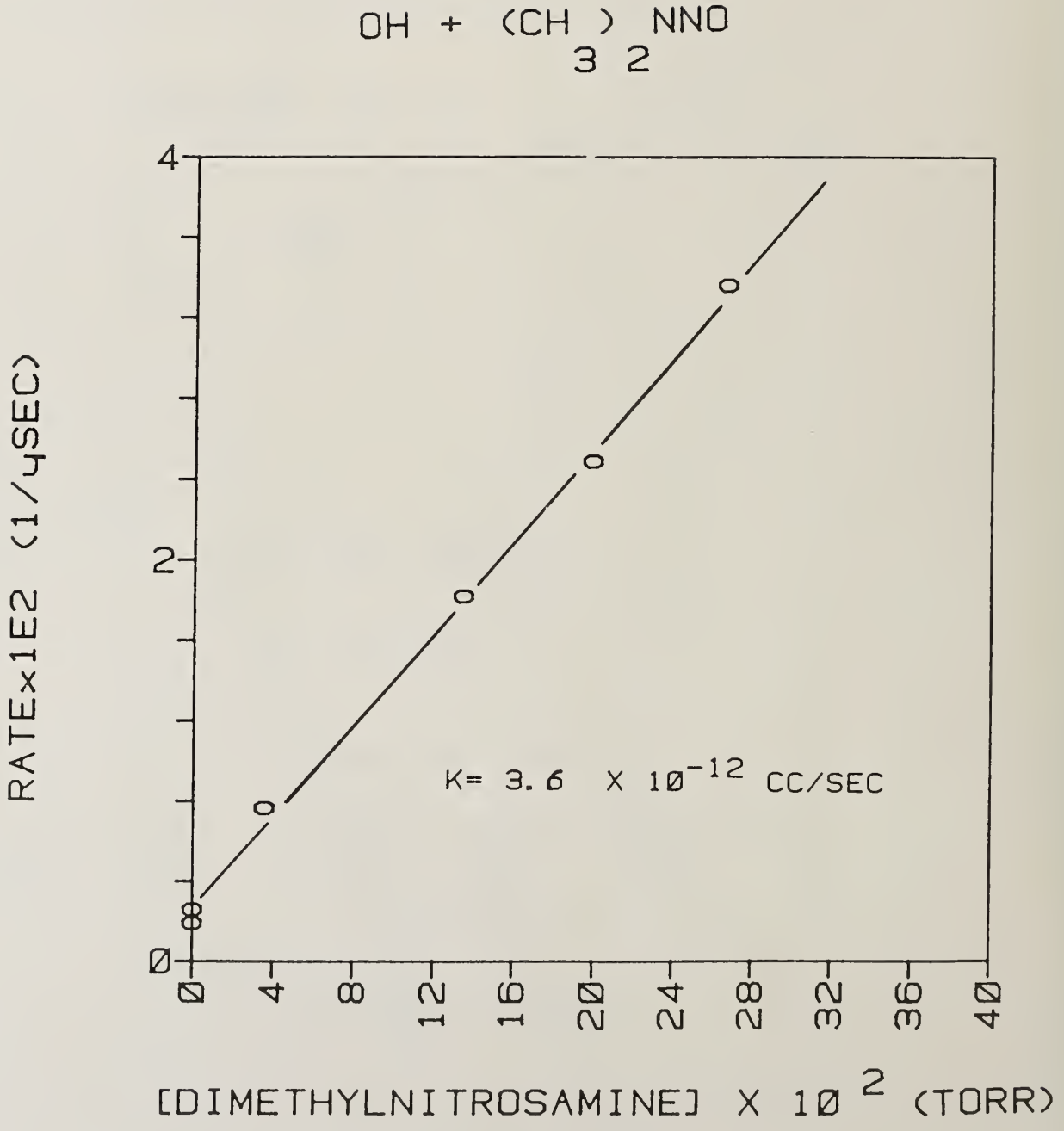
OH + (CH3)2NNO
RATE×1E2 (1/4SEC)
K= 3.6 X 10-12 CC/SEC
[DIMETHYLNITROSAMINE] X 10 2 (TORR)
0
2
4
0
4
8
12
16
20
24
28
32
36
40

FIGURE 4

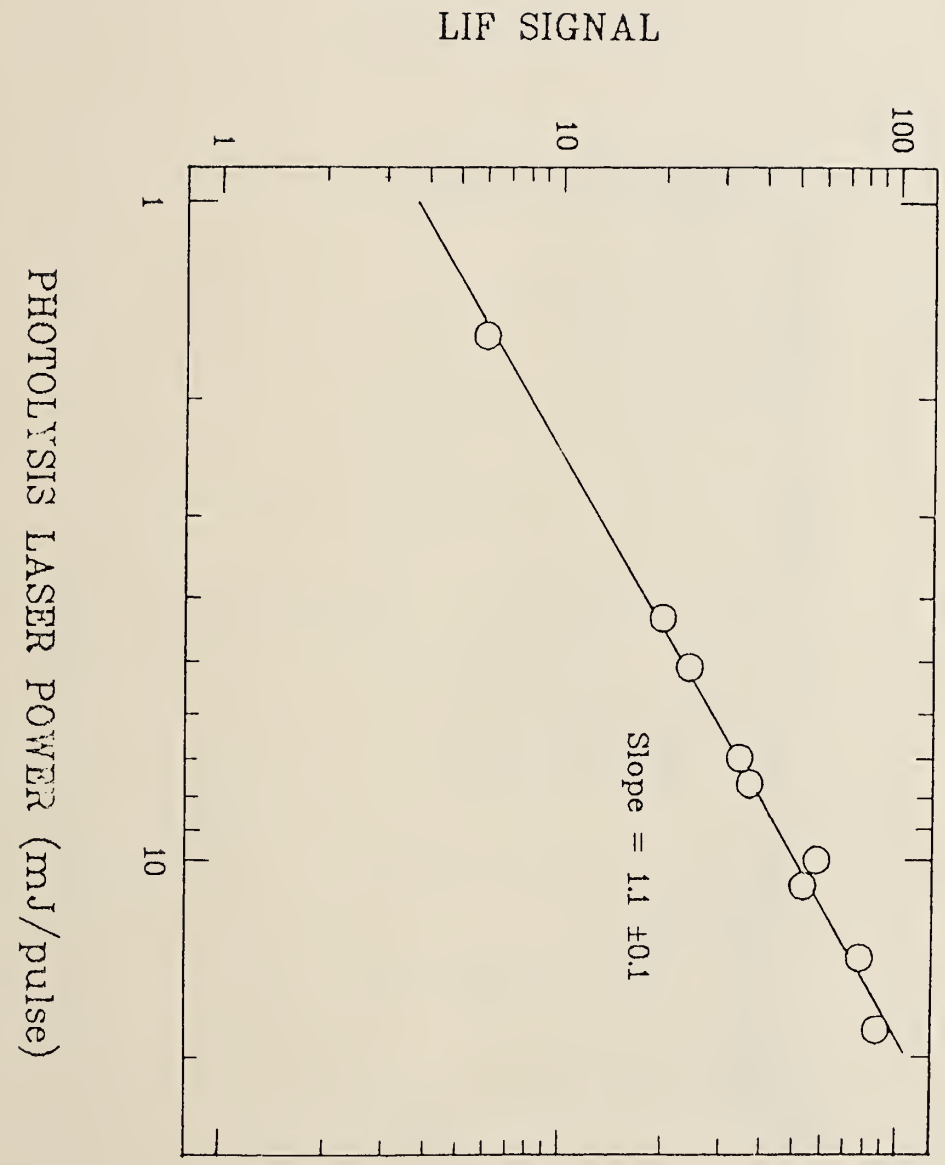
LIF SIGNAL
1
10
100
1
10
PHOTOLYSIS LASER POWER (mJ/pulse)
Slope = 1.1 ±0.1

FIGURE 5

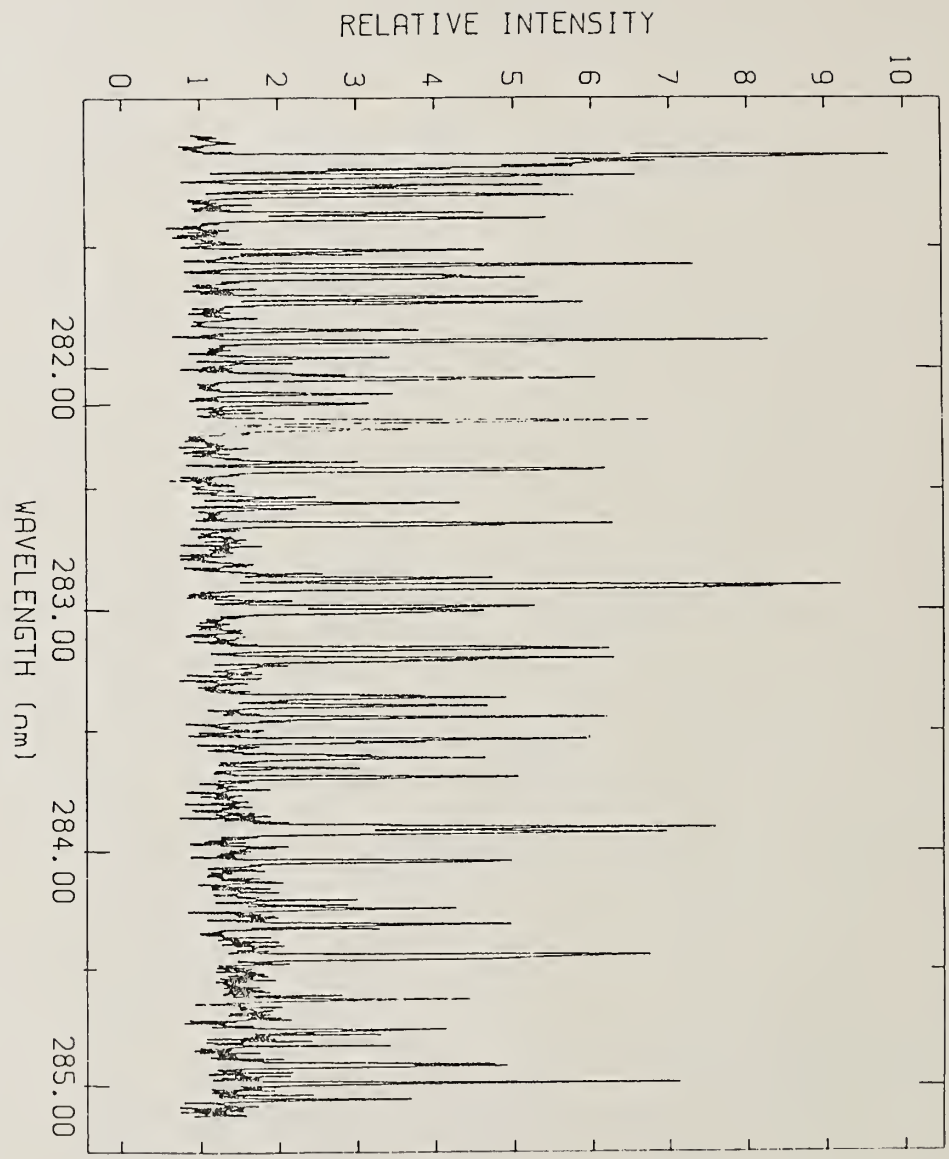
RELATIVE INTENSITY
0
1
2
3
4
5
6
7
8
9
10
282.00
283.00
284.00
285.00
WAVELENGTH (nm)

FIGURE 6

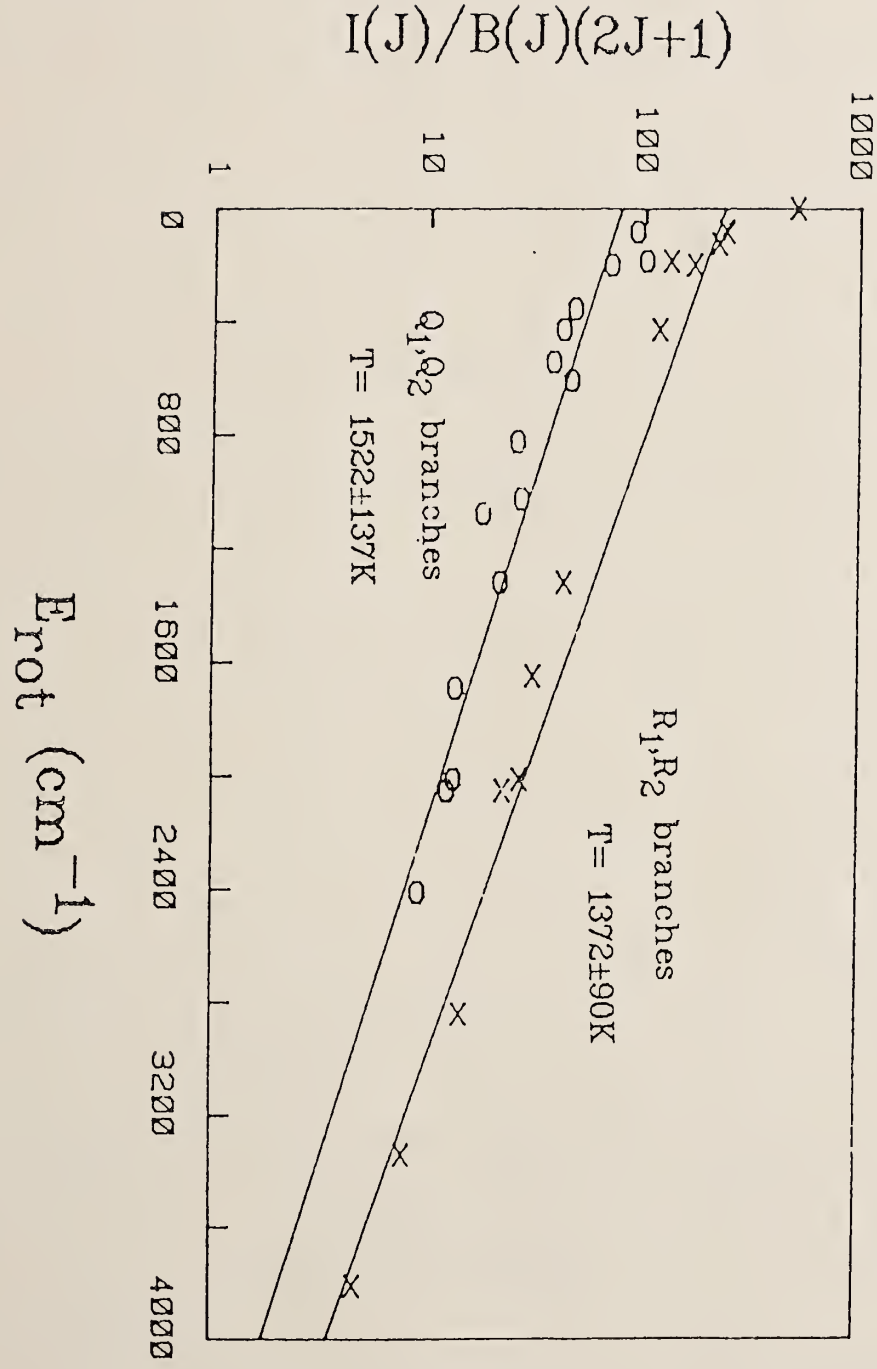
I(J)/B(J)(2J+1)
1000
100
10
1
0
800
1600
2400
3200
4000
E_{rot} (cm^{-1})
Q_1,Q_2 branches
T= 1522±137K
R_1,R_2 branches
T= 1372±90K

FIGURE 7

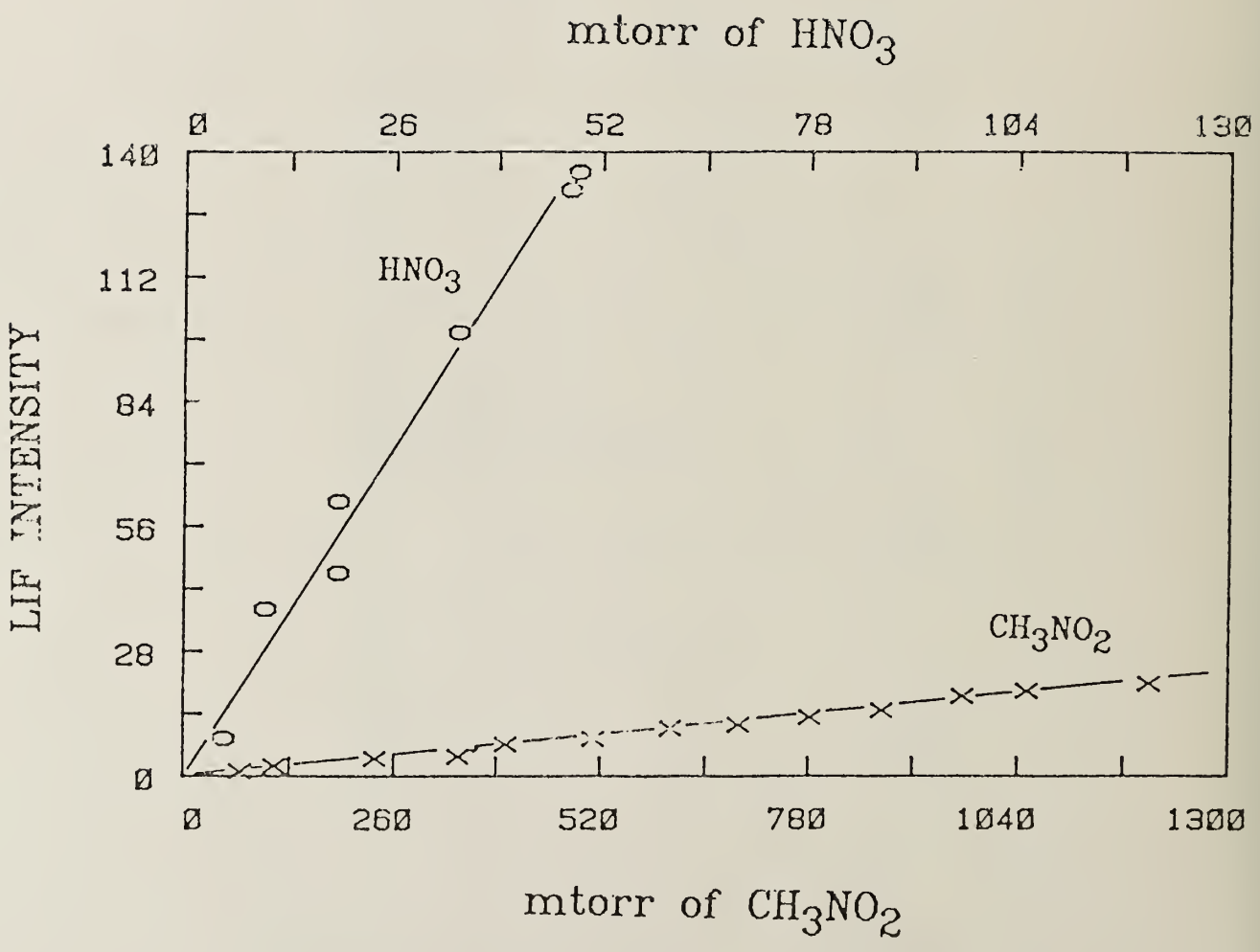
mtorr of HNO_3
0
26
52
78
104
130
140
112
84
56
28
0
LIF INTENSITY
HNO_3
CH_3NO_2
0
260
520
780
1040
1300
mtorr of CH_3NO_2

FIGURE 8

New Detections of Interstellar Transient Species

L.M. Ziurys
Five College Radio Astronomy Observatory, U. Mass., Amherst
B.E. Turner
National Radio Astronomy Observatory, Charlottesville, Va.

INTRODUCTION:

To date, over fifty-seven different chemical species have been detected in the interstellar medium, a good fraction of which are free radicals and molecular ions, i.e. transient species. These molecules have been identified primarily on the basis of their high resolution rotational spectra, which were obtained using techniques of radio and millimeter-wave astronomy. Aside from the intrinsic interest of molecular spectroscopy, radio astronomical studies of transient species is important for the investigation of interstellar chemistry. Indeed, the presence of such species, many of which are very abundant, is clearly indicative of the unique, "non-laboratory"-type conditions that exist in interstellar gas. The detection and study of transient molecules in space has lead to key formulations concerning interstellar chemistry. For example, the observation of HCO+, N_2H+, HCS+, and HCOO+, which are all formed via a proton transfer from H_3+, is the strongest evidence to date of the ion-molecule theory of interstellar chemistry, which is accepted to be principle pathway for interstellar synthesis. Observations of free radicals in circumstellar shells of late-type stars has been crucial to the development of the current model of circumstellar chemistry, the so-called "freeze-out" model. In addition, certain free radicals, such as diatomic hydrides are thought to be indicators of "shock" or "high temperature" chemisty.

Here we present detections of three new interstellar transient molecules: rotationally-excited CH, vibrationally-excited HCN, and a new molecular ion, HCNH+. Recent, high resolution laboratory spectroscopy made all of these detections possible.

ROTATIONALLY EXCITED CH:

The CH radical ($^2\Pi$) was first detected in the interstellar medium in 1973, when the three hyperfine lines of the ground state Λ-doubling transition (F_2,

N=1, J=1/2) were observed. Unfortunately, these CH lines almost universally exhibited weak maser action, which made the derivation of the molecule's abundances uncertain. Detection of the excited rotational states of CH were thus of major astrophysical interest, because they would enable better determination of the abundance of the species, certainly one of the building blocks of interstellar chemistry, and because they could provide further data on the maser mechanism of the ground state.

Rotationally-excited CH has thus been the subject of astronomical searches for many years, both at radio and FarIR wavelengths. These searches were unsucessful, in part because the rest frequencies for transitions of the excited states were not well known. The recent work of Brown and Evenson (Ap.J. 268, L51, 1983), Brazier and Brown (J.Chem.Phys. 78, 1608, 1983), and Bogey, Demuynck, and Destombes (Chem.Phys.Lett. 100, 105, 1983), however, has resulted in highly accurate frequencies for these transitions. Using the new measurements, rotationally excited CH was finally detected (Ziurys and Turner 1985, Ap.J. 292, L25). The first excited rotational state (F_1, N=1, J=3/2) was observed via its Λ-doubling transitions at 700 MHz towards W51, a dense molecular cloud, using the 1000 ft. antenna at Arecibo. Initially only the two main hyperfine components observed, but subsequent measurements have resulted in the probable detection of the weaker hyperfine lines.

Additional observations using the 300 ft. telescope at NRAO: Green Bank in April 1984 and 1985 resulted in the detection of the first excited state in other dense molecular clouds, including OriB, W3, W33, W43, and K3-50 (Ziurys and Turner 1985, in preparation). In several of these sources both main hyperfine transitions were observed. As in W51, all transitions were observed in absorption, which means that the lines are thermally-excited and abundances can be accurately derived. Column densities thus calculated from these excited state observations are on the order of 10^{18} cm-2 in several clouds, implying a CH abundance 1000 times higher than what was previously derived from the non-thermal ground state transition. Such abundances have to be present in dense

gas as well, for a high gas density is needed to explain the excitation of the first excited state. This CH abundance is about four orders of magnitude larger than what has been predicted by ion-molecule models of interstellar chemistry at the given gas density (e.g. Graedel, et al. 1982, Ap.J. Suppl. 48, 321); contrary to past conclusions, CH may be one of the most abundant interstellar molecules. Such an unexpected high CH concentration is suggestive that the species may be formed by "shock chemistry" in dense clouds. The detection of this excited state of CH also provides further evidence for the proposed Λ-doublet-selective collisional pump of the ground state maser, the so-called "Gwinn-Townes" model.

VIBRATIONALLY EXCITED HCN:

Several molecules thus far have been detected in the interstellar medium in vibrationally excited states, including SiO, HCCCN, and CH_3CN. Unfortunately, past studies of vibrationally excited species in space have been somewhat incomplete, involving measurements of ro-vibrational transitions, done in the IR where astronomical sensitivity is limited; or else, they have concerned radio/mmwave observations of rotational lines of low-excitation bending modes of large polyatomics as CH_3CN. Such large species are not very abundant and have many low-lying vibrational states, making transitions originating in such states quite weak. Nonetheless, observations of interstellar molecules in vibrationally excited modes have a definite impact on interstellar chemistry, because they indicate that much molecular material is present at high temperatures. In such gas "shock chemistry" must occur. The role of this type of chemistry in overall interstellar synthesis is one of the important unanswered questions in astrochemistry.

It was therefore most interesting when a search for interstellar vibrationally excited HCH resulted in the detection of the $(0,1^{1c,1d},0)$ ℓ-doublets. The J=3-2 transitions of this bending mode were observed in Orion-KL and late-type carbon star IRC+10216, using the NRAO 12 meter antenna at 265-267 GHz (Ziurys and Turner 1985, Ap.J., submitted). This particular mode lies 1025 K above

ground state in energy and has an Einstein A coefficient for decay to ground of 3.7 s-1.

The J=3-2 rotational lines in the (0,1,0) vibrational mode are particularly strong in Orion-KL, with T_R*=1.5 K. Such intensities are somewhat amazing, considering how high this mode lies in energy and its short lifetime. The column density estimated for the excited state gas alone in HCN is 10^{16} cm-2, which is substantial and implies a ground state HCN column density of 10^{18} cm-2 and a vibrational temperature of 200 K. Thus, a considerable amount of HCN is present in conditions where shock chemistry must govern chemical abundances. Also, the excitation of the (0,1,0) mode, if collisional, implies that gas densities of 10^{11} cm-3 , which means 3-body collisions can occur. Furthermore, the particular "clump" of gas which contains the vibrationally excited HCN, known as the "hot core", contains the highest column of HCN in all of the Orion molecular cloud. Yet, because of foreground optical depth effects, this is the first instance in which HCN has been clearly detected in this region.

These observations suggest that other common interstellar molecules may have large abundances in vibrationally excited states, and the extent of vibrational excitation in the ISM, and its affect on interstellar chemistry, may be more widespread than previously thought.

HCNH+:

Although predictions of the ion-molecule reaction scheme of interstellar chemistry have had considerable success, definitive tests of the theory are few. Only four molecular ions have been detected in interstellar gas thus far, and only two of these, HCO+ and N_2H+, have served the theory in a predictive sense. HCNH+, the protenated form of HCN, however, has long been regarded as a definite test of ion-molecule theory, because it is predicted to be intimately involved in the chemistry of such well known and abundant interstellar species HCN and HNC. There were a long series of unsuccessful searches over the past decades for HCNH+, based on crudely known rotational frequencies. Thus it was of interest when Altman, et al. 1984 (J.Chem.Phys. 80, 3911) finally obtained the

mid-IR ro-vibrational spectrm of HCNH+, from which accurate rotational transitions could be predicted.

Based on these results, we (Ziurys and Turner, in preparation) have succeeded in detecting interstellar HCNH+. The J=1-0, J=2-1, and J=3-2 rotational transitions were observed toward Sgr B2. HCNH+ may have been seen in W51 and Orion(3,1) as well, but was not observed in several dark clouds, where supposedly ion-molecule chemistry must dominate. The observed fractional abundance in Sgr B2 is roughly that predicted by ion-molecule chemistry, but such agreement could be fortuitous. Sgr B2 is a highly complex region whose chemistry may not be predominantly ion-molecule, and for which reliable abundances are notoriously difficult to obtain because of dynamical complexity. Although the permanent dipole moment of HCNH+ is not large, the results thus far suggest that the ion is not particularly widespread; such results conflict with ionmolecule theory. Additional observations are planned to search for this species in many additional sources, especially dark clouds, in order to resolve this puzzling question of the abundance and distribution of this important molecule.

	SUNDAY	MONDAY	TUESDAY	WEDNESDAY	THURSDAY	FRIDAY
7:15 to 8:30		Breakfast	Breakfast	Breakfast	Breakfast	Breakfast
8:00		Keynote: J.T. Hougen	J.G. Anderson --- Guest Program	T.A. Miller	P.B. Davis	W.C. Lineberger
9:00		NS Poster Introduction	NS Poster Introduction	NS Poster Introduction	NS Poster Introduction	NS Poster Introduction
9:15		S. Saito	J.M. Brown	R.J. Saykally	J.K.G. Watson	C. Demuynck
9:45			T.Oka	S.F.J. Cox	A. Dymanus	Summary: S. Leach (Check-Out- 10:00)
10:15		TE Poster Introduction	TE Poster Introduction	TE Poster Introduction	TE Poster Introduction	TE Poster Introduction
10:30 to 12:00		Poster Sess. #1 And Coffee	Poster Sess. #2 And Coffee	Poster Sess. #4 And Coffee	Poster Sess. #5 And Coffee	Poster Sess. #7 And Coffee
12:00 to 1:30		Box Lunch Trip to Top of Trail Ridge Road Rocky Mountain National Park Bus Leaves at 12:30 after Group Photo	Lunch	Lunch	Lunch, SMR, or Picnic Lunch at Mary Jane Ski Center Winter Park	Lunch
1:00	Registration at Snow Mountain Ranch (Main Admin. Building) 1:00 - 5:00		Nature Hike #1 (1:00-5:30) (Meet at Chapel)			1:00 First Bus to Stapleton Airport Denver
1:30				Nature Hike #2 (1:30 - 3:00) (Meet at Chapel)		1:30 Second Bus to Stapleton Airport Denver
4:00	Wine and Cheese Reception (4:00 - 9:00)					
5:00	Registration Continues Aspenbrook Lounge					
5:30 to 6:45	Dinner	Dinner	Dinner	6:00 PM	Dinner	
7:00	Reception and	L.E. Snyder	J.P. Simons	Western Bar-B-Q	C.J. Howard	
8:00	Registration Continues	Paul Gilbert	NS Poster Introduction	with Authentic	NS Poster Introduction	
8:15	Until	Slide Show	E.E. Ferguson	Western Entertainment	W. Urban	
8:45	9:00 PM	"Then And Now"	TE Poster Introduction		TE Poster Introduction	
9:00 to 10:30		Refreshments	Poster Sess. #3 And Beer		Poster Sess. #6 and Beer	

COUNTRIES REPRESENTED

UNITED STATES	94
CANADA	11
ENGLAND	8
FRANCE	6
WEST GERMANY	5
JAPAN	4
DENMARK	2
SWEDEN	2
ITALY	2
BRAZIL	1
IRAQ	1
MEXICO	1
THE NETHERLANDS	1
PEOPLES REPUBLIC OF CHINA	1
ROMANIA	1
SWITZERLAND	1
TURKEY	1
USSR	1

UNITED STATES

August 18, 1985

NAME	AFFILIATION	CITY AND STATE	ROOM NUMBER
Ager, Joel	NOAA	Boulder, Colorado	Camping
Allen, John E. Jr.	NASA/Goddard Space Flight Ctr.	Greenbelt, Maryland	Aspenbrook 3212
Anderson, J.G.	Harvard University	Cambridge, Massachusetts	Aspenbrook 2042
Anderson, Larry	University of Colorado/Denver	Denver, Colorado	
Apel, Eric	Los Alamos National Labs	Los Alamos, New Mexico	Silver Creek
Atkinson, Roger	University of Calif./Riverside	Riverside, California	Silver Sage 2213
Balla, R. Jeffrey	Naval Research Lab	Washington, D.C.	Aspenbrook 1212
Baughcum, Steven L.	Los Alamos National Labs	Los Alamos, New Mexico	Silver Creek
Bernath, Peter	University of Arizona	Tucson, Arizona	Silver Sage 3023
Bernheim, Robert	Pennsylvania State	University Park, Penn.	Silver Creek
Berry Ann	University of Houston	Houston, Texas	Camping
Blackburn, Thomas	NASA/Ames Research Ctr.	Moffett Field, Calif.	Silver Creek
Bomse, David S.	Exxon Research & Eng. Co.	Annedale, New Jersey	Aspenbrook 1132
Bonilla, Juan L.	University of Colorado/Denver	Denver, Colorado	
Brazier, Chris	University of Arizona	Tucson, Arizona	Aspenbrook 3112
Cantrell, Chris	Nat'l Ctr. for Atmos. Resch.	Boulder, Colorado	
Chance, Kelly	Smithsonian Astro. Observ	Cambridge, Massachusetts	Aspenbrook 3132
Cody Regina	NASA/Goddard Space Flight Ctr.	Greenbelt, Maryland	Silver Sage 2093

UNITED STATES

(continued)

August 18, 1985

NAME	AFFILIATION	CITY AND STATE	ROOM NUMBER
Colson, Steven D.	Yale University	New Haven, Connecticutt	Aspenbrook 1192
Crofton, Mark	University of Chicago	Chicago, Illinois	Aspenbrook 1092
Curl, R. F.	Rice University	Houston, Texas	Silver Sage 2203
Dane, Betsy	University of Houston	Houston, Texas	Camping
Dane, C. Brent	Rice University	Houston, Texas	Camping
Davidson, James A.	Nat'l Ctr. for Atmos. Resch.	Boulder, Colorado	
DeBarber, Peter	University of Calif./Irvine	Irvine, California	Silver Sage 3023
Ellingboe, Leah C.	University of Arizona	Tucson, Arizona	Aspenbrook 2222
Ellison, B.G.	University of Colorado	Boulder, Colorado	
Engleman, Rolf Jr.	Los Alamos National Labs	Los Alamos, New Mexico	
Evenson, Kenneth	National Bureau of Standards	Boulder, Colorado	Aspenbrook 2022
Fahr, Askar	National Bureau of Standards	Gaithersburg, Maryland	Silver Sage 2183
Ferguson, Eldon E.	Nat'l Oceanic & Atmos. Adm.	Boulder, Colorado	Aspenbrook 3232
Fessenden, Richard W.	University of Notre Dame	Notre Dame, Indiana	Silver Sage 3233
Francisco, Joseph S.	MIT	Cambridge, Massachusetts	Aspenbrook 1032
Friberg, Per	University of Massachusetts	Amherst, Massachusetts	Silver Sage
Gellene, Gregory I.	University of Notre Dame	Notre Dame, Indiana	Silver Sage 2063
Goldstein, Neil	University of Arizona	Tucson, Arizona	Aspenbrook 2202

UNITED STATES

(continued)

August 18, 1985

NAME	AFFILIATION	CITY AND STATE	ROOM NUMBER
Gottlieb, Carl A.	Columbia University	New York, New York	Silver Sage 2193
Graham, W.R.M. (Bill)	Southern Texas Christian Univ.	Fort Worth, Texas	Silver Sage 3203
Hammer, Philip D.	Nat'l Oceanic & Atmos. Adm.	Boulder, Colorado	Silver Sage 3193
Heikes, Brian	Nat'l Ctr. for Atmos. Resch.	Boulder, Colorado	Camping
Holloway, John	Aerospace Corporation	Los Angeles, California	Silver Creek
Hougen, Jon T.	National Bureau of Standards	Gaithersburg, Maryland	Silver Sage 3013
Howard, Carleton J.	Nat'l Oceanic & Atmos. Adm.	Boulder, Colorado	Silver Sage 2233
Jacox, Marilyn	National Bureau of Standards	Washington, D.C.	Aspenbrook 2052
Jen, C.K.	Johns Hopkins University	Laurel, Maryland	Silver Creek
Jennings, Donald A.	National Bureau of Standards	Boulder, Colorado	Aspenbrook 2012
Johnson, Donald R.	National Bureau of Standards	Gaithersburg, Maryland	Silver Sage 2163
Koffend, Brooke	Aerospace Corporation	Los Angeles, California	Silver Creek
Laufer, Allan H.	Department of Energy	Washington, D.C.	Silver Sage 3173
Lawrence, Barbara	University of Calif./Irvine	Irvine, California	Aspenbrook 2222
Lee, Edward K.C.	University of Calif./Irvine	Irvine, California	Aspenbrook 3192
Leopold, Kenneth	National Bureau of Standards	Boulder, Colorado	Silver Creek
Lineberger, Carl W.	University of Colorado	Boulder, Colorado	Silver Sage 2073
Loewenstein, Lee	Texas Instruments	Dallas, Texas	Silver Sage 3093

UNITED STATES

(continued)

August 18, 1985

NAME	AFFILIATION	CITY AND STATE	ROOM NUMBER
Loper, Gary	Aerospace Corporation	Los Angeles, California	Silver Creek
MacLeod, Helene	Univ. of Calif./Riverside Research Ctr.	Riverside, California	Aspenbrook 2072
Magnotta, Frank	Lawrence Livermore Labs	Livermore, California	Silver Creek
McRae, Glenn	Cal Tech	Pasadena, California	Silver Creek
Miller, Terry A.	Ohio State University	Columbus, Ohio	Aspenbrook 3042
Mizushima, M.	University of Colorado	Boulder, Colorado	Aspenbrook 3012
Mozurkewich, Michael	Nat'l Ctr. for Atmos. Resch.	Boulder, Colorado	
Murrells, T.P.	Nat'l Oceanic & Atmos. Adm.	Boulder, Colorado	Silver Sage 3193
Nava, David F.	NASA/Goddard Space Flight Ctr.	Greenbelt, Maryland	Aspenbrook 1072
Nee, Jan B.	San Diego State University	San Diego, California	Aspenbrook 1112
Nimlos, Mark R.	University of Colorado	Boulder, Colorado	Camping
Oka, Takeshi	University of Chicago	Chicago, Illinois	Aspenbrook 1092
Pickett, Herbert M.	Jet Propulsion Lab	Pasadena, California	Silver Sage 3113
Podolske, James	NASA/Ames Research Center	Moffett Field, Calif.	Silver Creek
Porter, Richard	Cornell University	Ithaca, New York	Silver Sage 3033
Radford, Harrison E.	Harvard/Smithsonian Astro. Observ.	Cambridge, Massachusetts	Aspenbrook 2192
Saykally, Richard J.	University of Calif/Berkeley	Berkeley, California	Silver Sage 3013

UNITED STATES

(continued)

August 18, 1985

NAME	AFFILIATION	CITY AND STATE	ROOM NUMBER
Sears, Trevor J.	Brookhaven National Lab.	Upton, New York	Silver Sage 3073
Sinha, Amit	Nat'l Oceanic & Atmos. Adm.	Boulder, Colorado	Silver Sage 3193
Snyder, Lewis E.	University of Illinois	Urbana, Illinois	Aspenbrook 3182
Softley, Tim	Stanford University	Stanford Univ, Calif.	
Stachnik, Robert	Cal Tech/Jet Propulsion Lab.	Pasadena, California	Silver Creek
Stedman, Donald	University of Denver	Denver, Colorado	Camping
Steinfeld, Jeffrey	MIT	Cambridge, Massachusetts	Aspenbrook 1032
Stephens, James W.	Rice University	Houston, Texas	Camping
Sullivan, Donald B.	National Bureau of Standards	Boulder, Colorado	Silver Creek
Tom, Roderick	Ca. Tech/Jet Propulsion Lab.	Pasadena, California	Silver Creek
Toohey, Darin	Harvard University	Cambridge, Massachusetts	Silver Creek
Tripathi, G.N.R.	University of Notre Dame	Notre Dame, Indiana	Silver Sage 3213
Vasconcellos, Elza	National Bureau of Standards	Boulder, Colorado	Aspenbrook 2092
Wang, Nun YII	University of Calif./Irvine	Irvine, California	Aspenbrook 3022
Wells, Joseph	National Bureau of Standards	Boulder, Colorado	Silver Creek
Wen-Bin, Yan	Rice University	Houston, Texas	Camping
Wing, William H.	University of Arizona	Tucson, Arizona	Silver Creek
Wodtke, Alec	University of Calif./Berkeley	Berkeley, California	Aspenbrook 1192

UNITED STATES

(continued)

August 18, 1985

NAME	AFFILIATION	CITY AND STATE	ROOM NUMBER
Xie, Xiaoxiang	Howard University	Washington, D.C.	Silver Creek
Zabarnick, Steven	Naval Research Lab.	Washington, D.C.	Aspenbrook 1052
Zeitz, Dieter	Rice University	Houston, Texas	Camping
Zink, Lyndon	National Bureau of Standards	Boulder, Colorado	Camping
Ziurys, Lucy M.	University of Massachusetts	Amherst, Massachusetts	Silver Creek

CANADA

August 18, 1985

NAME	AFFILIATION	CITY AND STATE	ROOM NUMBER
Jones, William E.	Dalhousie University	Halifax, Nova Scotia	Silver Sage 3043
Kerr, Caroline M.L.	National Research Council	Ottawa, Ontario	Silver Sage 3063
Klapstein, Dieter	St. Francis Xavier Univ.	Antigonish, Nova Scotia	Aspenbrook 3112
Lewis-Bevan, Wyn	University of British Columbia	Vancouver, British Col.	Aspenbrook 3172
Menon, I.A.	University of Toronto	Toronto, Ontario	
Merer, Anthony J.	University of British Columbia	Vancouver, British Col.	Aspenbrook 3062
Percival, Paul W.	Simon Fraser University	Burnaby, British Col.	Aspenbrook 1232
Ramsay, D.A.	National Research Council	Ottawa, Ontario	Aspenbrook 3032
Rayner, David M.	National Research Council	Ottawa, Ontario	Aspenbrook 3152
Smith, Donald R.	McMaster University	Hamilton, Ontario	Aspenbrook 2182
Watson, James K.G.	National Research Council	Ottawa, Ontario	Silver Sage 3063

ENGLAND

Borrell, Peter	Keele University	Staffordshire	Silver Creek
Brown, J.M.	Oxford University	Oxford	Silver Sage 2173
Cox, Steven	Rutherford Appleton Lab	Osfordshire	Camping
Curtis, Michael C.	University of Nottingham	Nottingham	Aspenbrook 3112
Davies, Paul B.	Cambridge University	Cambridge	Silver Sage 2173
Hamilton, Peter	Queen Mary College	London	Aspenbrook 3092

ENGLAND

(continued)

August 18, 1985

NAME	AFFILIATION	CITY AND STATE	ROOM NUMBER
Rothwell, William	Cambridge University	Cambridge	Aspenbrook 2212
Simons, John P.	University of Nottingham	Nottingham	Silver Sage 2173

FRANCE

Cossart-Magos, Claudina	University de Paris	Orsay	Silver Sage 2223
Demuynck, Claire	University de Lille I	Villeneuve D'Asco Cedex	Aspenbrook 2032
Le Bras, Georges	CNRS/Centre de Rech. Sur	Orleans Cedex	Silver Sage 3153
Leach, Sydney	University de Paris	Orsay	Aspenbrook 2062
Poulet, Gilles	CNRS (CRCCHT)	Orleans Cedex	Silver Sage 3153
Rostas, Joelle	University de Paris	Orsay	Silver Sage 2223

WEST GERMANY

Burrows, J.P.	Max-Planck Institute	Mainz	Aspenbrook 3092
Halpern, Alexander	Institute of Chemistry Nuclear Research Center	KFA Juelich	Silver Sage 3183
Hinz, Alexander	University of Bonn	Bonn	Camping
Temps, Frederich	Max-Planch Institute	Goettingen	Silver Sage 2153
Urban, Wolfgang	Inst. fur Angewandte Physik	Bonn	Aspenbrook 3052

JAPAN

August 18, 1985

NAME	AFFILIATION	CITY AND STATE	ROOM NUMBER
Akimoto, Hajemi	Nat'l Inst. for Environ. Study	Tsukuba, Ibaraki	Aspenbrook 1012
Kasai, Toshio	Osaka University	Toyokaka, Osaka	Aspenbrook 3202
Saito, Shuju	Inst. for Molecular Science	Myodaiji, Okazaki	Silver Sage 2133
Sato, Hiroyasu	MI'E University	TSU	Blue Ridge 3194

DENMARK

Pagsberg, Palle	Riso National Lab.	Roskilde	Aspenbrook 1152
Sillesen, Alfred	Riso National Lab	Roskilde	Aspenbrook 1172

SWEDEN

Davidsson, Jan	Chalmers Univ. of Technology	Goteborg	Silver Sage 3223
Erman, Peter	Royal Inst. of Technology	Stockholm	Aspenbrook 3072

ITALY

Cazzoli, Gabriele	University of Bologna	Bologna	Silver Creek
Enso, Tiezzi	Degli, Studi di Siena	Siena	Silver Creek

BRAZIL

Vasconcellos, Elza	National Bureau of Standards		Aspenbrook 2092

August 18, 1985

NAME	AFFILIATION	CITY AND STATE	ROOM NUMBER
	IRAQ		
Zainel, Hanaa	University of Baghdad	Jadria Baghdad	Silver Creek
	MEXICO		
Vasquez, G. J.	Instituto de Fisica	Cuernavaca, Morroco	Silver Sage 3053
	THE NETHERLANDS		
Dymanus, Antony	Katholieke Univ. Nijmegen Toernooiveld	Nijmegen	Aspenbrook 2152
	PEOPLES REPUBLIC OF CHINA		
Zhang, Rong	Dalian Inst. of Chem. Physics	Dalian	Aspenbrook 2232
	ROMANIA		
Balaban, A.T.	Polytechnic Bucharest	Bucharest	Silver Sage 3213
	SWITZERLAND		
Loliger, Jurg	Nestec Ltd. Research Lab.	Vevy	Silver Sage 3133

TURKEY

August 18, 1985

NAME	AFFILIATION	CITY AND STATE	ROOM NUMBER
Bayrakceken, Faut	Orta Cogu Teknik University	Ankara	Silver Creek

USSR

Pokhodenko, V.D.	Pisarzhevsky Inst. of Phys Acad of Sciences	Kiev	Aspenbrook 2172

NBS-114A (REV. 2-8C)

U.S. DEPT. OF COMM. BIBLIOGRAPHIC DATA SHEET (See instructions)	1. PUBLICATION OR REPORT NO. NBS/SP-716	2. Performing Organ. Report No.	3. Publication Date April 1986

4. TITLE AND SUBTITLE

Proceedings of the Seventeenth International Symposium on Free Radicals

5. AUTHOR(S)

Kenneth M. Evenson, Editor

6. PERFORMING ORGANIZATION (If joint or other than NBS, see instructions)

NATIONAL BUREAU OF STANDARDS
DEPARTMENT OF COMMERCE
WASHINGTON, D.C. 20234

7. Contract/Grant No.

8. Type of Report & Period Covered

9. SPONSORING ORGANIZATION NAME AND COMPLETE ADDRESS (Street, City, State, ZIP)

National Bureau of Standards
Laser Analytics Division of Spectra Physics, Inc.
National Aeronautics and Space Administration
Smithsonian Astrophysical Observatory
Lambda Physik
Oriel Optics

10. SUPPLEMENTARY NOTES

☐ Document describes a computer program; SF-185, FIPS Software Summary, is attached.

11. ABSTRACT (A 200-word or less factual summary of most significant information. If document includes a significant bibliography or literature survey, mention it here)

This publication contains papers presented at the Seventeenth International Symposium on Free Radicals, held at Snow Mountain Ranch in Granby, Colorado, on August 18-23, 1985.

The Symposium was attended by 147 people, representing industry, government, and academia, from 18 countries. A total of 67 papers appear in written form in this document.

12. KEY WORDS (Six to twelve entries; alphabetical order; capitalize only proper names; and separate key words by semicolons)

free radicals; 17th international symposium on free radicals

13. AVAILABILITY

☒ Unlimited

☐ For Official Distribution. Do Not Release to NTIS

☒ Order From Superintendent of Documents, U.S. Government Printing Office, Washington, D.C. 20402.

☐ Order From National Technical Information Service (NTIS), Springfield, VA. 22161

14. NO. OF PRINTED PAGES

788

15. Price

USCOMM-DC 6043-P80

☆U.S. GOVERNMENT PRINTING OFFICE:1986—671-494 / 45163

NBS Technical Publications

Periodical

Journal of Research—The Journal of Research of the National Bureau of Standards reports NBS research and development in those disciplines of the physical and engineering sciences in which the Bureau is active. These include physics, chemistry, engineering, mathematics, and computer sciences. Papers cover a broad range of subjects, with major emphasis on measurement methodology and the basic technology underlying standardization. Also included from time to time are survey articles on topics closely related to the Bureau's technical and scientific programs. Issued six times a year.

Nonperiodicals

Monographs—Major contributions to the technical literature on various subjects related to the Bureau's scientific and technical activities.

Handbooks—Recommended codes of engineering and industrial practice (including safety codes) developed in cooperation with interested industries, professional organizations, and regulatory bodies.

Special Publications—Include proceedings of conferences sponsored by NBS, NBS annual reports, and other special publications appropriate to this grouping such as wall charts, pocket cards, and bibliographies.

Applied Mathematics Series—Mathematical tables, manuals, and studies of special interest to physicists, engineers, chemists, biologists, mathematicians, computer programmers, and others engaged in scientific and technical work.

National Standard Reference Data Series—Provides quantitative data on the physical and chemical properties of materials, compiled from the world's literature and critically evaluated. Developed under a worldwide program coordinated by NBS under the authority of the National Standard Data Act (Public Law 90-396). NOTE: The Journal of Physical and Chemical Reference Data (JPCRD) is published quarterly for NBS by the American Chemical Society (ACS) and the American Institute of Physics (AIP). Subscriptions, reprints, and supplements are available from ACS, 1155 Sixteenth St., NW, Washington, DC 20056.

Building Science Series—Disseminates technical information developed at the Bureau on building materials, components, systems, and whole structures. The series presents research results, test methods, and performance criteria related to the structural and environmental functions and the durability and safety characteristics of building elements and systems.

Technical Notes—Studies or reports which are complete in themselves but restrictive in their treatment of a subject. Analogous to monographs but not so comprehensive in scope or definitive in treatment of the subject area. Often serve as a vehicle for final reports of work performed at NBS under the sponsorship of other government agencies.

Voluntary Product Standards—Developed under procedures published by the Department of Commerce in Part 10, Title 15, of the Code of Federal Regulations. The standards establish nationally recognized requirements for products, and provide all concerned interests with a basis for common understanding of the characteristics of the products. NBS administers this program as a supplement to the activities of the private sector standardizing organizations.

Consumer Information Series—Practical information, based on NBS research and experience, covering areas of interest to the consumer. Easily understandable language and illustrations provide useful background knowledge for shopping in today's technological marketplace.

Order the **above** *NBS publications from: Superintendent of Documents, Government Printing Office, Washington, DC 20402.*

Order the **following** *NBS publications—FIPS and NBSIR's—from the National Technical Information Service, Springfield, VA 22161.*

Federal Information Processing Standards Publications (FIPS PUB)—Publications in this series collectively constitute the Federal Information Processing Standards Register. The Register serves as the official source of information in the Federal Government regarding standards issued by NBS pursuant to the Federal Property and Administrative Services Act of 1949 as amended, Public Law 89-306 (79 Stat. 1127), and as implemented by Executive Order 11717 (38 FR 12315, dated May 11, 1973) and Part 6 of Title 15 CFR (Code of Federal Regulations).

NBS Interagency Reports (NBSIR)—A special series of interim or final reports on work performed by NBS for outside sponsors (both government and non-government). In general, initial distribution is handled by the sponsor; public distribution is by the National Technical Information Service, Springfield, VA 22161, in paper copy or microfiche form.

U.S. Department of Commerce
National Bureau of Standards
Gaithersburg, MD 20899

Official Business
Penalty for Private Use $300

POSTAGE AND FEES PAID
U.S. DEPARTMENT OF COMMERCE
COM-215

SPECIAL FOURTH-CLASS RATE
BOOK